Petrogenesis of the cenozoic Meghri-Ordubad pluton, southernmost Lesser Caucasus: implications for the formation of large porphyry Cu-Mo(-Au) systems during the Arabia-Eurasia accretionary orogenesis

Rezeau, Hervé

UNIVERSITƒ DE GENé VE
DŽpartement des Sciences de la Terre

FACULTƒ DES SCIENCES
Prof. Robert Moritz

Petrogenesis Of The Cenozoic Meghri-Ordubad Pluton, Southernmost Lesser Caucasus: Implications For The Formation Of Large Porphyry Cu-Mo(-Au) Systems During The Arabia-Eurasia Accretionary Orogenesis

THé SE

PrŽsentŽe ^ la FacultŽ des Sciences de lÕUniversitŽ de Gen•ve
pour obtenir le grade de Docteur •s sciences, mention sciences de la Terre.

par

HervŽ Rezeau

de

Mazi•res en Mauges (France)

Th•se N¡ 5119

GENé VE
2017

UNIVERSITÉ DE GENÈVE

FACULTÉ DES SCIENCES

DOCTORAT ÈS SCIENCES, MENTION SCIENCES DE LA TERRE

Thèse de Monsieur Hervé REZEAU

intitulée :

«Petrogenesis of the Cenozoic Meghri-Ordubad Pluton, Southernmost Lesser Caucasus: Implications for the Formation of Large Porphyry Cu-Mo(-Au) Systems during the Arabia-Eurasia Accretionary Orogenesis»

La Faculté des sciences, sur le préavis de Monsieur R. MORITZ, professeur associé et directeur de thèse (Département des sciences de la Terre), Monsieur M. CHIARADIA, docteur (Département des sciences de la Terre), Monsieur S. PILET, docteur (Institut des sciences de la Terre, Université de Lausanne, Suisse), Monsieur J. RICHARDS, professeur (School of Earth Sciences, Laurentian University, Sudbury, Ontario, Canada), autorise l'impression de la présente thèse, sans exprimer d'opinion sur les propositions qui y sont énoncées.

Genève, le 12 septembre 2017

Thèse - 5119 -

Le Doyen

N.B. - La thèse doit porter la déclaration précédente et remplir les conditions énumérées dans les "Informations relatives aux thèses de doctorat à l'Université de Genève".

ÒImagination is more important than knowledge. Knowledge is limited.
Imagination encircles the world.Ó

Albert Einstein, October 26th, 1929 in The Saturday Evening Post

The research presented in this thesis was accomplished with financial support through the Swiss National Science Foundation (SNSF) under grants agreement no. [200020_138130], [200020_155928] and [200020_168996]. Additional funding have contributed to this thesis, including the Scientific Cooperation between Eastern Europe and Switzerland (SCOPES) Joint Research Project [IB7620 - 118901] and [IZ73Z0 - 128324], the Augustin-Lombard Foundation of the SociŽtŽ de Physique et dÕHistoire Naturelle de Gen•ve, and the Economic Geologists student grant from the H.E. McKinstry Fund. The research was carried out in the Department of Earth Sciences at the University of Geneva, within the framework of the ***Doctoral Program in Mineral Sciences (DPMS)***.

Thesis director:

Prof. Dr. Robert Moritz
Department of Earth and Environmental Sciences,
University of Geneva, Switzerland

Members of the Dissertation committee:

Dr. Massimo Chiaradia
Department of Earth and Environmental Sciences,
University of Geneva, Switzerland

Dr. SŽbastien Pilet
Institute of Earth Sciences,
University of Lausanne, Switzerland

Prof. Dr. Jeremy P. Richards
School of Earth Sciences
Laurentian University, Sudbury, Ontario, Canada

TABLE OF CONTENTS

THESIS SUMMARY

This thesis, entitled ÒPetrogenesis of the Cenozoic Meghri-Ordubad pluton, southernmost Lesser Caucasus: implications for the formation of large porphyry Cu-Mo(-Au) systems during the Arabia-Eurasia accretionary orogenesisÓ is a multi-disciplinary study including field work, petrography, whole-rock and mineral geochemistry, trace element whole-rock geochemical modelling, zircon U-Pb and molybdenite Re-Os geochronology to respectively date magma emplacement and ore mineralization. This study area represents the largest mineralized district in the Lesser Caucasus and the main Cu and Mo producer in the region, encompassing Eastern Turkey, Caucasus and Iran. The main aim is to establish (1) a better general understanding between the magmatism and the formation of Cu-Mo(-Au) ore deposits, (2) a petrogenetic model for the Meghri-Ordubad incrementally assembled over 30 m.y. and associated with ore-forming pulses, and (3) a new genetic model for the large Kadjaran porphyry Cu-Mo deposit. The multi-disciplinary approach allows to reveal a very complex magmatic-hydrothermal system operating over several tens of million years, which is very attractive to investigate the magmatic evolution in a geodynamic framework linked to the Alpine orogenesis and more specifically related to the closure of the NeotŽthys ocean during the final convergence of the Arabian toward the Eurasian plate leading to a continental collision followed by a progressive post-collisional relaxation along the Turkish-Iranian plateau. Finally, the link with the formation of ore deposits allows us to assess optimal magmatic, tectonic and hydrothermal conditions leading to the formation of large economic resources. This thesis is subdivided in four chapters.

CHAPTER 1 ÒTemporal and genetic link between incremental pluton assembly and pulsed porphyry Cu-Mo formation in accretionary orogensÓ Economically important porphyry Cu-Mo deposits (PCDs) are generally hosted by upper crustal plutons of variable chemical compositions related to distinct geodynamic settings. The absolute timing and duration of pluton assembly and PCD formation is critical to understand the genetic relationship between these interrelated processes. Here we present new comprehensive zircon U-Pb and molybdenite Re-Os ages that tightly constrain the timing and duration of pluton assembly and the age of mineralization in one of the largest ore-bearing plutons of the central Tethyan metallogenic belt, the Meghri-Ordubad pluton, southern Armenia and Nakhitchevan, Lesser Caucasus. This composite pluton was incrementally assembled during three compositionally distinct magmatic episodes over about 30 m.y., comprising Middle Eocene (48.9-43.1 Ma) calc-alkaline subduction-related magmatism lasting 5.8 ± 0.8 m.y., followed by post-subduction Late Eocene - Middle Oligocene (37.8-28.1 Ma) shoshonitic magmatism over 9.7 ± 0.9 m.y., and Late Oligocene - Early Miocene (26.6-21.2 Ma) adakitic magmatism consisting of shoshonitic dikes and

high-K calc-alkaline granodioritic magmas emplaced over 5.4 ± 0.4 m.y.. Despite the distinct geodynamic settings and magma compositions, each intrusive suite culminated in the formation of variably sized PCDs, including the giant Oligocene Kadjaran porphyry Cu-Mo deposit associated with high Sr/Y shoshonitic magmas. Complementary in-situ zircon hafnium (εHfzircon = +8 to +11.3) and oxygen (δ18Ozircon = +4.6 to +6.0 ä) isotope data support a mantle-dominated magma source with limited crustal contribution and/or cannibalization of young and juvenile lower crustal cumulates. We conclude that, independently of geodynamic setting and magma composition, long-lived (5-10 m.y.) incremental mantle-derived magmatism is a pre-requisite to form fertile magmatic-hydrothermal systems, and especially giant PCDs. This chapter is published in *Geology*.

CHAPTER 2 ÒƁ0 Myr of Cenozoic magmatism along the Tethyan margin during Arabia-Eurasia accretionary orogenesis (Meghri-Ordubad pluton, southernmost Lesser Caucasus)Ó
Three magmatic series of substantially different ages and compositions were successively emplaced to form the composite Meghri-Ordubab pluton (MOP) in the southernmost Lesser Caucasus. The protracted incremental assembly during 30 m.y., from Middle Eocene to Early Miocene, renders this location particularly suitable to characterize the petrogenetic evolution of Cenozoic magmatism during the final stage of the Neotethyan subduction. Based on whole-rock geochemistry, two main transitions tightly constrained in time are recognized. The first transition from Middle Eocene medium- to high-K calc-alkaline to Late Eocene - Middle Oligocene shoshonitic magmatism corresponds to a marked increase in LREE and MREE and more juvenile 87Sr/86Sr and 143Nd/144Nd ratios. The second transition to Late Oligocene - Early Miocene high-K calc-alkaline "adakite-like" magmatism is coeval with a marked increase in Mg#, and Ni and Cr contents together with a depletion in MREE and HREE. Although the three differentiation series are derived from lower to mid-crustal hydrous magma fractionation, temporal variations of the magmatic source conditions are required to explain the contrasting chemistry of the parental magmas over time. Medium- to high-K calc-alkaline parental magmas were generated by high degree of partial melting (~15%) of a garnet lherzolite. The shoshonitic and adakitic magmatic series represent magmas produced by low degree of partial melting (1-5%) of a garnet lherzolite, but a higher amount of residual garnet is required to reproduce the "adakite-like" signature. The timing of the two main geochemical transitions in the MOP is correlated with a progressive evolution from a compressional to an extensional stress regime linked to (1) the final stage of the Neotethyan subduction followed by the Arabia-Eurasia continental collision during the Eocene-Oligocene, and (2) the transition toward post-collisional magmatism, combined with a switch toward transcurrent tectonics during the Late Oligocene - Early Miocene. This chapter is published in *Lithos*.

CHAPTER 3 ÒPetrological characterization of subduction- and collision-related magmatism in the composite Meghri-Ordubad pluton, Lesser Caucasus (Tethyan Orogenic Belt)Ó The composite Meghri-Ordubad pluton belongs to the southernmost Lesser Caucasus located in the central segment of the Tethyan orogenic belt. It is characterized by nested intrusions incrementally emplaced from Middle Eocene to Early Miocene coeval to the closure of the Neotethyan ocean and the regional Arabia-Eurasia continental collision. The recognition of three compositionally distinct magmatic series includes the early emplacement of subduction-related medium- to high-K calc-alkaline series 1, followed by syn-collisional shoshonitic to high-K calc-alkaline series 2, and post-collisional high-K calc-alkaline adakitic series 3. This study presents detailed petrography and mineral chemistry on representative dated intrusions for each differentiation series to shed light on the complex magmatic plumbing system that generated the composite Meghri-Ordubad pluton. The Middle Eocene magmatic series 1 is dominated by dioritic to tonalitic intrusions characterized by early plagioclase fractionation indicative of shallow crystallization (<200-350 MPa), and by the presence of hornblende gabbro displaying early amphibole crystallized at higher pressure (>200-350 MPa). The Late Eocene - Middle Oligocene K-rich magmatic series 2 is dominated by gabbro - monzogabbro - monzodiorite - monzonite - syenite intrusions and dikes characterized by a contrasting mineral assemblage, including crystallization of peritectic biotite at the expense of amphibole and the occurrence of abundant poikilitic K-felspar and occasionally nepheline. Based on the sequence of mineral crystallization and mineral chemistry, intrusions and dikes display crystallization at relatively high (>200-350 MPa) and low (<200-350 MPa) pressure representative of storage at various crustal levels. Subsidiary hornblende gabbro shows early amphibole fractionation suggesting crystallization in the mid- to lower crust. The Late Oligocene - Early Miocene high-K calc-alkaline adakitic magmatic series 3 includes early emplacement of lamprophyres followed by porphyritic granodioritic intrusions and dikes. Calc-alkaline lamprophyres are composed of high Mg# phlogopite, and clinopyroxene and amphibole phenocrysts characterized by reverse chemical zoning characterized by high Mg#, high Cr and Ni contents together with the lowest REE contents and a lack Eu negative anomalies. This suggests ascent of primitive-like melt to the upper crust and host-rock assimilation and hybridization. Younger porphyritic granodioritic magmas indicate crystallization at shallower crustal levels (<200 MPa). Plagioclase textures and in-situ mineral chemistry reveal magma interactions indicative of open-system magmatic processes and crystallization dominated by cooling. Reverse chemical zoning displayed by amphibole and clinopyroxene phenocrysts combined with dendritic amphibole and phlogopite in the groundmass of calc-alkaline lamprophyres indicate hybridization in the upper crust and fast crystallization through rapid decompression and/or cooling, respectively. Such detailed petrological characterization allows us to identify various crustal levels of magma crystallization and to reveal interactions between magmas reservoirs through mafic resplenishment and recycling of crystal mushes. Although magmatic source processes control the liquid line of descent and

consequently the sequence of mineral crystallization, each magmatic differentiation series is dominated by fractional crystallization ± crustal assimilation. In conclusion, we propose the first temporal and spatial petrogenetic model for the composite Meghri-Ordubad pluton encompassing three long-lived magmatic series incrementally emplaced over 30 million years. This chapter is in preparation to be submitted to ***Journal of Petrology***.

CHAPTER 4 ÒOptimal tectonic, magmatic and hydrothermal conditions for the generation of large porphyry Cu-Mo systems in a collision zone: Insights from the Meghri-Ordubad pluton, southernmost Lesser CaucasusÓ The Afro-Arabian collision zone, which encompasses Eastern Turkey, Lesser Caucasus, Iran and western Pakistan, represents a highly metal endowed segment along the Alpine-Himalayan orogenic belt. Mesozoic and mid-Paleogene magmatism results from the subduction of the northern branch of the Neotethyan Ocean, followed by mid-Paleogene to Quaternary syn- to post-collisional magmatism linked to the final closure of the southern branch of the Neotethyan ocean and the Arabia-Eurasia continental collision. The majority of economical porphyry Cu-Mo(-Au) deposits (PCDs) in the region is associated with subduction and post-subduction magmatism during the Cenozoic. The southernmost Lesser Caucasus hosts the composite Meghri-Ordubad pluton, which was incrementally assembled over 30 m.y., from the Middle Eocene to Early Miocene. The composite pluton is composed of three temporally and compositionally distinct magmatic differentiation series: (1) Middle Eocene subduction-related medium- to high-K calc-alkaline series, (2) Late Eocene Ð Middle Oligocene collisional shoshonitic to high-K calc-alkaline series, and (3) Late Oligocene Ð Early Miocene post-collisional high-K calc-alkaline "adakite-like" series. The evolution of magma chemistry over time reflects variable degrees of partial melting of the mantle source concomitant with progressive metasomatism of the subcontinental lithospheric mantle and a change in regional stress from a compressive to extensional regime. The subduction-related magmatism is associated with small PCDs, whereas the syn- to post-collisional magmatism is linked to the formation of the world-class Kadjaran Cu-Mo porphyry-epithermal deposit. This emphasizes the crucial role of magmatic source and crustal processes in metal crustal endowment and their availability to the exsolved magmatic hydrothermal fluids responsible for the formation of economic PCDs. A careful review of geochemical, petrological, geochronological and tectonic features allows a comparison of different tectono-magmatic conditions associated with variably-sized PCDs in the upper crust. In conclusion, the Meghri-Ordubad pluton offers a unique opportunity to assess a set of key controlling factors leading to the formation of large PCDs in a collision zone and this study aims at providing new insights for mining compagnies to identify fertile magmatic provinces during greenfield mineral exploration campaigns in order to optimize their quest for the "Giants" in continental collision zone. This chapter is in preparation to be submitted to ***Economic Geology in a special thematic issue entitled ÒThe Southeast European - Turkish - Caucasian segment of the Tethyan Metallogenic BeltÓ***.

Rf SUMf DE THé SE

Cette th•se intitulŽe "Petrogenesis of the Cenozoic Meghri-Ordubad pluton, southernmost Lesser Caucasus: implications for the formation of large porphyry Cu-Mo(-Au) systems during the Arabia-Eurasia accretionary orogenesis ", est une Žtude multi-disciplinaire incluant la gŽologie de terrain, des descriptions pŽtrographiques, des analyses chimiques sur roche totale et sur les minŽraux, des modŽlisations gŽochimiques, de la datation par U-Pb sur zircon des Žv•nements magmatiques et par Re-Os sur molybdŽnite pour les minŽralisations. Cette rŽgion d'Žtude reprŽsente le plus grand district minŽralisŽ du Petit Caucase et le principal producteur de cuivre et de molybd•ne de la rŽgion, incluant l'Est de la Turquie, le Caucase et l'Iran. Le but ultime est d'Žtablir (1) une meilleure comprŽhension gŽnŽrale entre le magmatisme et la formation de gisements de minerais de cuivre, molybd•ne et d'or, (2) un mod•le pŽtrogŽnŽtique pour le Meghri-Ordubad pluton construit incrŽmentalement sur 30 millions d'annŽes, associŽ ˆ des pulses minŽralisateurs, et (3) un nouveau mod•le de formation pour le gisement de Kadjaran. L'approche multi-disciplinaire a permis de rŽvŽler un syst•me magmatique-hydrothermal tr•s complexe opŽrant durant des dizaines de millions d'annŽes, ce qui est tr•s intŽressant pour la comprŽhension de l'Žvolution du magmatisme dans un cadre gŽodynamique rŽgional liŽ ˆ l'orog•ne alpine et plus particuli•rement ˆ la fermeture de l'ocŽan NŽotŽthys, dže ˆ la convergence de la plaque Arabe vers l'Eurasie, et la rŽsultante collision Žvoluant progressivement vers une relaxation post-collisionelle de la rŽgion. Finalement, le lien avec la formation de gisements mŽtallif•res permet d'Žvaluer les conditions magmatiques, tectoniques et hydrothermales optimales, tous favorables ˆ la formation de gisements Žconomiques majeurs. Cette th•se est divisŽe en quatre chapitres.

CHAPTER 1 "Temporal and genetic link between incremental pluton assembly and pulsed porphyry Cu-Mo formation in accretionary orogensÓ Les gisements types porphyres Cu-Mo sont Žconomiquement importants et sont gŽnŽralement associŽs ˆ des intrusions de compositions variables, mises en place dans la crožte continentale supŽrieure liŽs ˆ des environnements gŽodynamiques diffŽrents. Le timing absolu et la durŽe de la formation du pluton et des porphyres Cu-Mo sont critiques pour comprendre le lien gŽnŽtique entre ces processus intrins•quement liŽs. Cette Žtude prŽsente de nouveaux %ges U-Pb sur zircons et Re-Os sur molybdenite, qui contraignent fortement le timing et la durŽe de l'assemblage du pluton ainsi que l'%ge de la minŽralisation dans l'un des plus larges plutons minŽralisŽs, mis en place dans la partie centrale de la ceinture mŽtallogŽnique TŽthysienne: le Meghri-Ordubad pluton localisŽ au sud de la RŽpublique d'ArmŽnie et Nakhitchevan dans le Petit Caucase. Ce pluton composite s'est construit incrŽmentalement durant trois Žpisodes

magmatiques de compositions diffŽrentes sur une pŽriode de 30 millions d'annŽes, incluant le magmatisme calc-alcalin pendant 5.8 ± 0.8 m.a. liŽ ^ une subduction durant l'Eoc•ne Moyen (48.9Ð43.1 Ma), suivi d'un magmatisme post-subduction caractŽrisŽ par des intrusions shoshonitiques pendant 9.7 ± 0.9 m.a. ^ l'Eoc•ne SupŽrieur - Oligoc•ne InfŽrieur (37.8Ð28.1 Ma) et d'un magmatisme adakitique illustrŽ par des dikes shoshonitiques et des intrusions granodioritiques potassiques calc-alcalines mises en place sur 5.4 ± 0.4 m.a. ^ l'Oligoc•ne SupŽrieur - Mioc•ne InfŽrieur. MalgrŽ des environnements gŽodynamiques et des compositions magmatiques diffŽrents, chaque sŽrie d'intrusions se rŽv•le •tre temporellement associŽe ^ la formation de gisements porphyriques, incluant le large gisement Kadjaran formŽ ^ l'Oligocene associŽ avec des magmas shoshonitiques caractŽrisŽs par des ratios Sr/Y ŽlevŽs. En complŽment, des analyses in situ isotopiques d'hafnium et d'oxyg•ne sur zircons supportent une source magmatique dominŽe par le manteau et tr•s peu contaminŽe par la crožte continentale et/ou un cannibalisme de cumulats juvŽniles en crožte infŽrieure. En conclusion, indŽpendemment de l'environnement gŽodynamique et de la composition magmatique, un magmatisme incrŽmentalement mis en place sur une longue pŽriode est un prŽ-requis pour la formation d'un syst•me magmatique-hydrothermal fertile, et surtout pour les larges porphyres ^ Cu-Mo. Ce chapitre est publiŽ dans le journal *Geology*.

CHAPTER 2 Ò30 Myr of Cenozoic magmatism along the Tethyan margin during Arabia-Eurasia accretionary orogenesis (Meghri-Ordubad pluton, southernmost Lesser Caucasus)Ó Trois sŽries magmatiques d'‰ges et compositions diffŽrents se sont successivement mis en place pour former le composite Meghri-Ordubab pluton (MOP) dans le sud du Petit Caucase. L'assemblage incrŽmental prolongŽ sur 30 millions d'annŽes de l'Eoc•ne Moyen au Mioc•ne InfŽrieur rend ce terrain d'Žtude particuli•rement attractif pour caractŽriser l'Žvolution pŽtrogŽnŽtique du magmatisme CŽnozo•que durant la fermeture de la branche sud de l'OcŽan NŽothŽtysien. La gŽochimie sur roche totale permet de distinguer deux transitions majeures temporellement contraintes. La premi•re transition entre le magmatisme calc-alcalin de l'Eoc•ne Moyen et le shoshonitique de l'Eoc•ne SupŽrieur - Oligoc•ne InfŽrieur est marquŽe par une forte augmentation en terres rares l•g•res et moyennes, accompagnŽes par une signature plus juvŽnile des $^{87}Sr/^{86}Sr$ et $^{143}Nd/^{144}Nd$ ratios isotopiques. La seconde transition vers le magmatisme adakitique de l'Oligoc•ne SupŽrieur - Mioc•ne InfŽrieur est contemporain d'une augmentation significative du Mg# et des concentrations en Ni et Cr ainsi qu'une diminution des concentrations en terres rares moyennes et lourdes. Bien que les trois sŽries de diffŽrentiation magmatique sont issues d'un magma hydratŽ fractionnŽ en milieu ou en base de crožte continentale, des variations temporelles liŽes ^ la source magmatique sont requises pour expliquer l'Žvolution de la chimie des magmas sources au fil du temps. Les magmas calc-alcalins sources de l'Eoc•ne Moyen sont gŽnŽrŽs par un taux ŽlevŽ de fusion partielle (~15%) d'une l'herzolite ^ grenat. Les sŽries magmatiques shoshonitiques et adakitiques sont produites par un faible taux de

fusion partielle (1-5%) d'une l'herzolite ˆ grenat, mais une quantitŽ plus importante de grenat rŽsiduel est requis pour le magmatisme adakitique. Le timing des deux transitions marquŽes par un changement gŽochimique est corrŽlŽ avec une Žvolution progressive d'un rŽgime en compression puis en extension liŽ (1) au stade final de la subduction NŽotŽthysienne suivi de la collision continentale entre l'Arabie et l'Eurasie durant l'Eoc•ne - Oligoc•ne, et (2) la transition vers un magmatisme post-collisionelle en transtension-extension durant l'Oligoc•ne SupŽrieur - Mioc•ne InfŽrieur. Ce chapitre est publiŽ dans le journal *Lithos*.

CHAPTER 3 ÒPetrological characterization of calc-alkaline and shoshonitic differentiation series successively emplaced in the Meghri-Ordubad pluton, southernmost Lesser CaucasusÓ Le pluton composite Meghri-Ordubad s'est mis en place dans l'extrŽmitŽ sud du Petit Caucase qui se situe dans la partie centrale de la ceinture orogŽnique TŽthysienne. Il est caractŽrisŽ par l'imbrication d'intrusions mises en place incrŽmentalement de l'Eoc•ne moyen au Mioc•ne infŽrieur en m•me temps que la fermeture rŽgionale de l'ocŽan NŽotŽthys et de la collision continentale entre l'Arabie et l'Eurasie. La reconnaissance de trois sŽries magmatiques de compositions distinctes inclut l'emplacement prŽcoce de la sŽrie 1 calco-alcaline liŽ ˆ la subduction, suivi de la sŽrie 2 shoshonitic ˆ calco-alcaline associŽ ˆ la collision, et de la sŽrie 3 adakitique formŽ apr•s l'Žpisode de collision. Cette Žtude prŽsente des observations pŽtrographiques et des analyses chimiques sur minŽraux dŽtaillŽes, sur des intrusions reprŽsentatives datŽes pour chaque sŽrie magmatique de diffŽrentiation dans le but de mieux comprendre la formation de cette complexe plomberie magmatique ˆ l'origine du Meghri-Ordubad pluton composite. La sŽrie magmatique de l'Eoc•ne moyen est dominŽe par des intrusions dioritiques ˆ tonalitiques caractŽrisŽes par le fractionement prŽcoce de plagioclase indiquant une cristallisation ˆ faible pression (<200-350 MPa), et par la prŽsence de gabbro ˆ amphibole prŽsentant une cristallisation prŽcoce des amphiboles ˆ plus haute pression (>200-350 MPa). La sŽrie magmatique riche en potassium mise en place de l'Eoc•ne supŽrieur ˆ l'Oligoc•ne moyen est dominŽe par des intrusions et des dikes de gabbro, monzogabbro, monzodiorite, monzonite et de syenite, toutes caractŽrisŽes par des assemblages minŽralogiques qui contrastent, incluant la cristallisation de biotite pŽritectique aux dŽpends des amphiboles et la prŽsence en abondance de feldspath potassique poikilitique et pus occasionellement nŽphŽline. En se basant sur la sŽquence de cristallisation des minŽraux et sur la chimie des minŽraux, les intrusions et les dikes exposent une cristallisation ˆ des pressions relativement hautes (>200-350 MPa) et basses (< 200-350 MPa) qui sont reprŽsentatives d'un stockage magmatique ˆ diffŽrentes profondeurs dans la crožte continentale. Un petit affleurement de gabbro ˆ amphibole montre une cristallisation prŽcoce des amphiboles ce qui sugg•re une cristallisation dans les niveaux moyens ˆ profonds de la crožte continentale. La sŽrie magmatique 3 mise en place de l'Oligoc•ne supŽrieur au Mioc•ne infŽrieur se caractŽrise par l'emplacement de lamprophyres calco-alcalins suivi par des intrusions et dikes granodioritique et porphyrique montrant

une signature adakitique. Les lamprophyres calco-alcalins sont composŽs de phlogopite ˆ Mg# ŽlevŽ, et des phŽnocristaux de clinopyrox•nes et d'amphiboles caractŽrisŽs par une zonation chimique inverse illustrŽe par des Mg# ŽlevŽs, des teneurs ŽlevŽes en Cr et Ni, par les plus petites teneurs en terres rares et une absence d'anomalie nŽgative en Eu. Cela sugg•re une remontŽe de magma primitif vers la crožte supŽrieure suivi de l'assimilation de la roche encaissante et une hybridation du magma. Les intrusions granodioritiques plus jeunes indiquent une cristallisation ˆ des niveaux peu profonds dans la crožte continentale (<200 MPa). La texture des plagioclases et la chimie des minŽraux rŽv•lent des intŽractions entre les magmas ce qui indique des processus magmatiques en syst•me ouvert suivi par une cristallisation dominŽe par le refroidissement. Les zonations chimiques inverses prŽsentŽes par les phŽnocristaux d'amphiboles et de clinopyroxenes combinŽes ˆ la prŽsence d'amphiboles squelettiques et de phlogopite dans la matrice des lamprophyres calco-alcalins indiquent hybridation dans la crožte supŽrieure et une cristallisation tr•s rapide par une dŽcompression rapide et/ou un refroidissement du magma, respectivement. Une telle caractŽrisation pŽtrologique nous permet d'identifier diffŽrents niveaux crustaux de cristallisation du magma et de rŽvŽler des interactions entre des rŽservoirs magmatiques par des recharges de magma mafique et un recyclage d'amas de cristaux prŽalablement formŽs. Bien que les processus magmatiques de source contr™lent la sŽquence de cristallisation, chaque sŽrie magmatique de diffŽrentiation est dominŽe par la cristallisation fractionnŽe avec plus ou moins d'assimilation crustale. En conclusion, nous proposons pour la premi•re fois un mod•le pŽtrogŽnŽtique d'Žvolution spatio-temporelle pour le Meghri-Ordubad pluton incluant trois sŽries magmatiques incrŽmentallement mis en place sur 30 millions d'annŽes. Ce chapitre est en prŽparation pour •tre soumis ˆ ***Journal of Petrology***.

CHAPTER 4 ÒOptimal tectonic, magmatic and hydrothermal conditions for the generation of large porphyry Cu-Mo systems in a collision zone: Insights from the Meghri-Ordubad pluton, southernmost Lesser CaucasussÓ La zone de collision Afro-Arabe, qui comprend l'Est de la Turquie, le Petit Caucase, l'Iran et l'Ouest du Pakistan, reprŽsente un segment tr•s enrichi en mŽtaux le long de la ceinture orogŽnique Alpine-Himalayenne. Le magmatisme MŽsoso•que et PalŽog•ne moyen rŽsulte de la subduction de la branche nord et sud de l'ocŽan NŽotŽthysien, suivi du magmatisme syn- ˆ post-collisionel du PalŽog•ne moyen jusqu'au Quaternaire liŽ ˆ la fermeture dŽfinitive de l'ocŽan NŽotŽthysien et de la rŽsultante collision continentale entre la plaque Arabe et Eurasienne. La majoritŽ des gisements Žconomiques porphyriques ˆ Cu-Mo(-Au) de la rŽgion est associŽe ˆ du magmatisme de subduction et de collision durant le CŽnozo•que. L'extrŽmitŽ sud du Petit Caucase expose le Meghri-Ordubad pluton, qui a ŽtŽ incrŽmentalement assemblŽ sur une pŽriode de 30 millions d'annŽes, depuis l'Eoc•ne moyen jusqu'au Mioc•ne infŽrieur. Le pluton composite est composŽ de trois sŽries de diffŽrentiation magmatique temporellement et chimiquement distinctes: (1) la sŽrie calco-alcaline moyennement potassique de l'Eoc•ne moyen liŽ ˆ la subduction, (2) la sŽrie shoshonitique ˆ calco-

alcaline hautement potassique de l'Eoc•ne supŽrieur ˆ l'Oligoc•ne moyen liŽ ˆ la collision, et (3) la sŽrie adakitique calco-alcaline hautement potassique de l'Oligoc•ne supŽrieur au Miocene infŽrieur liŽ ˆ la relaxation orogŽnique qui suit la collision. L'Žvolution chimique des magmas refl•te des degrŽs variables de fusion partielle de la source mantellique parall•lement ˆ une mŽtasomatisation progressive du manteau lithosphŽrique supŽrieur et ˆ un changement de stress rŽgional Žvoluant d'un regime en compression vers de l'extension avec le temps. Le magmatisme liŽ ˆ la subduction est associŽ ˆ la formation de petits gisements porphyriques ˆ Cu et Mo, alors que le magmatisme de collision ˆ post-collision est liŽ ˆ la formation du gisement de classe mondial, le gisement porphyrique-Žpithermale de Kadjaran. Cela met de l'emphase sur le r™le crucial des processus magmatiques s'opŽrant dans la source mantellique et dans la crožte continentale sur l'enrichissement crustal des mŽtaux et leur disponibilitŽ pour •tre transfŽrŽs dans les fluides magmatiques hydrothermaux responsables de la formation de gisements Žconomiques. Une examination minutieuse des caractŽristiques gŽochimiques, pŽtrologiques, gŽochronologiques et tectoniques permet une comparaison des diffŽrentes conditions tectoniques et magmatiques associŽes ˆ des gisements de tailles variables. En conclusion, le Meghri-Ordubad pluton offre une opportunitŽ unique d'Žvaluer un ensemble de facteurs clefs favorisant la formation de larges gisements Žconomiques dans une zone de collision, et cette Žtude a pour but de fournir de nouveaux ŽlŽments aux compagnies mini•res, afin d'identifier des provinces magmatiques fertiles durant les campagnes d'exploration mini•re en milieu vierge, ceci dans le but d'optimiser leur qu•te de dŽcouvrir des "GŽants" en zone de collision continentale. Ce chapitre est en prŽparation pour •tre soumis ˆ ***Economic Geology*** dans un volume spŽcial intitulŽ ***ÒThe Southeast European - Turkish - Caucasian segment of the Tethyan Metallogenic BeltÓ***.

INTRODUCTION

Over the last decades, the rise of emerging economies and the evolution of technologies are correlated with an increase of a global demand of metals. Metals resources, and notably copper (Cu), are critical for the development of our modern societies worldwide. Copper represents one the most important industrial metals and current markets consist of electrical and electronic equipment (31%), construction (30%), infrastructure (12%), transport (12%), and industrial machinery (12%) (Arndt et al., 2017). This is especially shown by the development of the Republic of China that mainly impacted the global Cu market (Fig. 1), and also metals in general, i.e., gold (Au), molybdenum (Mo), iron (Fe), lead (Pb), zinc (Zn) and nickel (Ni).

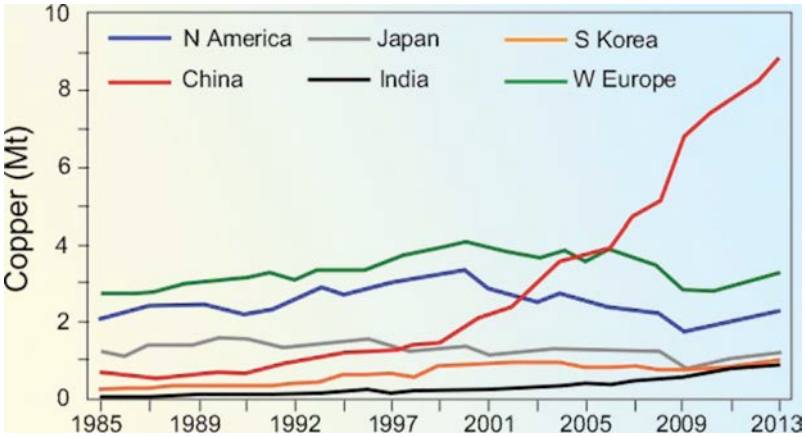

Figure 1: Copper consumption by major producers and consumers showing increase for emerging countries (China, India) and a constant demand from developped countries (Europe, USA, Japan, S. Korea). After Arndt et al. (2017) based on data of the U.S. Geological Survey (USGS); World Copper Factbook, 2015.

Meanwhile, there is a significant increase of exploration spending (up to 30-35 US$ billions) coeval with a decrease of major discoveries since 2010 (Fig. 2; Min Ex consulting, 2017). This illustrates our current lack of ability to predict the location of new resources emplaced deeper than 1 km in the continental crust, and therefore the necessity to develop new exploration proxies applied to deeper resources. A large portion of the continental crust has not been explored yet, as illustrated by the very shallow depth of discoveries since 1900 (Fig. 3a). This speaks for abundant undiscovered resources such as porphyry copper deposits form at depth between 1 and 5 km (Fig. 3b; Kesler and Wilkinson, 2008; Sillitoe, 2010; Arndt et al., 2017) and a promising future for mining exploration if joint effort from both the mining industry and the academic research take up the challenge to assess key exploration vectors leading to future hidden major discoveries.

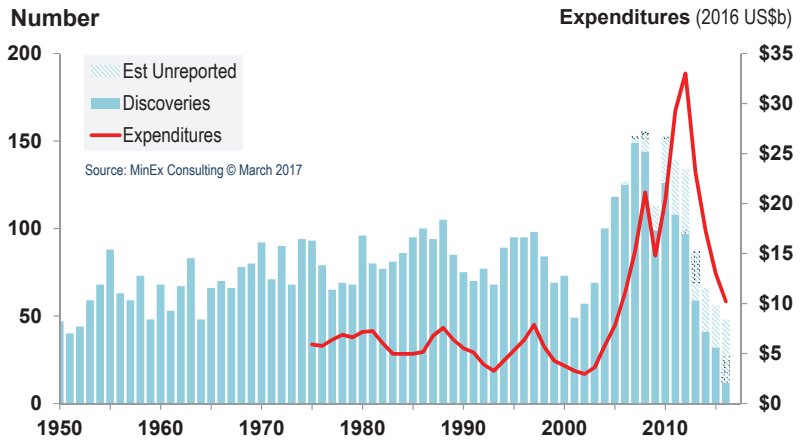

Figure 2: Number of discoveries versus expenditures Mineral discoveries in the World for all Commodities from 1950 to 2016. Note: Discoveries based on deposits >=ÒModerateÓin size i.e. >100koz Au, >10kt Ni, >100Kt Cu, 250kt Zn+Pb, >5kt U_3O_8 , > 10Mt Fe, >20Mt Thermal Coal. Source: Min Ex presentation at PDAC March 2017.

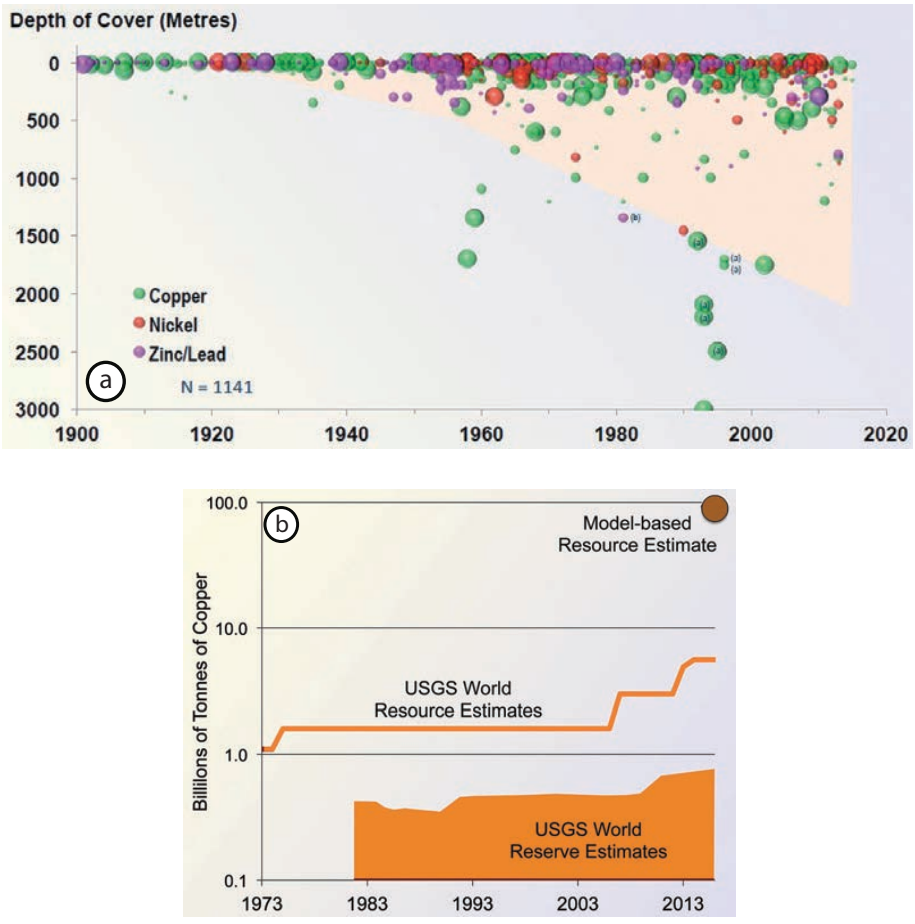

Figure 3: a) Depth of base metals deposits (Cu, Pb, Zn, Ni) discovered since 1900 after Arndt et al. (2017). b) Comparison of changing USGS estimates for copper reserves (filled shape), and resources (line) and based resources to depth of 3.3 km based on tectonic diffusion model (filled circle, Kesler and Wilkinson, 2008). The reader is referred to Arndt et al. (2017) for the discussion about the official definition and distiction between "Resource" and "Reserve" estimates.

Porphyry systems provide three quarters of the worldÕs Cu and significant proportions of Mo, Zn, Pb and precious metals (Au, Ag) to our economy (Sillitoe, 2010). They are typically hosted by upper crustal plutons along convergent margin including subduction, collision, and post-collision geodynamic setting (e.g., Richards, 2003, 2009, 2011, 2015; Cooke et al. 2005; Sillitoe, 2010; Hou et al., 2011; Moritz et al., 2016). For decades, the most popular genetic model for porphyry systems described a subduction-related magmatism consisting of oceanic slab dehydration leading to melting of a metasomatised mantle wedge (Fig. 3a), followed by basaltic underplating at the mantle-crust boundary initiating melting, assimilation, segregation and hybridization, known as MASH zone (Hildreth and Moorbath, 1989) or Deep Crustal Hot zone (Annen et al. 2006). Metal enrichment are assumed to be sourced from mantle-derived mafic magmas that experience Assimilation-Fractional Crystallization (AFC) processes and subsequently ascend to the upper crust, where felsic magmas crystallize progressively to expel magmatic-hydrothermal ore-forming fluids upon cooling (e.g., Burnham, 1979; Richards, 2003, 2011). The general accepted view consists of a reservoir at depth acting as metals, sulfur and volatiles suppliers to the upper crustal felsic plutons through pulsed mafic recharges (Hattori et al. 1993; Hattori and Keith, 2001; Richards, 2011b; AudÉtat and Simon, 2012; Wilkinson, 2013; Buret et al., 2016; Tapster et al. 2016). Finally, a common association between high-Sr/Y "adakite-like" magmas and porphyry copper systems has been revealed and interpreted as representative of an ore fertility proxy resulting from an early amphibole (± garnet) crystallization and delay of plagioclase fractionation as a consequence of high pressure crystallization in the mid- to lower crust of a water-rich parental melt (e.g., Rohrlach and Loucks, 2005; Richards 2011a; Loucks, 2014; Chiaradia et al, 2012, Chiaradia and Caricchi, 2017).

Most studies dedicated to the formation of economic porphyry systems primarily focused on upper crustal magmatic processes in felsic batholith-hosted porphyry systems emplaced within a pressure range of 100-300 MPa and associated with magmatic-hydrothermal processes (e.g., Richards, 2016). They can be summarized as follow using numbers of Figure 3b: (1) volcano fumaroles are characterized by the abundance of sulfur and metals within vapor phase (Nadeau et al. 2010, 2016), (2) and (3) the recognition of exploration vector including the systematic alteration pattern as a guide to find the ore body (Seedorf et al. 2005; Sillitoe, 2010; Wilkinson et al. 2015), (4) the mixing of metal-rich brines with sulfur-rich, magmatic gases (Blundy et al. 2015), (5) reactions between sulfur dioxide gas and plagioclase in the surrounding rocks to precipitate sulfide minerals (Henley et al. 2015), (6) the flotation of sulfide melt droplets attached to vapour bubbles to enrich shallower parts of magma chambers in metals (Mungall et al. 2015), (7) high aluminum discrete zoning in plagioclase crystals mark discrete pulses of hydrothermal fluid, which may correspond to individual ore-forming events (Williamson et al., 2016), (8) study of fluid inclusions to track the behavior of metals and ligands (Cl, S) with respect to vapor and brines during hydrothermal processes at shallow crustal levels (Williams-Jones and Heinrich, 2005; Kouzmanov and Pokrovski, 2012; Lerchbaumer and

AudŽat, 2012), (9) melt inclusion study illustrating the role of volatiles (H_2O, CO_2, S, Cl) as chalcophile scavengers (Wallace, 2005; Simon et al. 2006; AudŽat, 2010; Simon and Ripley, 2011; Zajacz et al. 2012, 2013), (10) accumulation of magmatic sulfides in the mid- to lower crust potentially remobilized by new magma input (e.g., Core et al. 2006; Richards, 2009; Jenner et al., 2010; Lee et al. 2012; Chiaradia, 2014; FontbotŽ et al., 2017; Jenner, 2017).

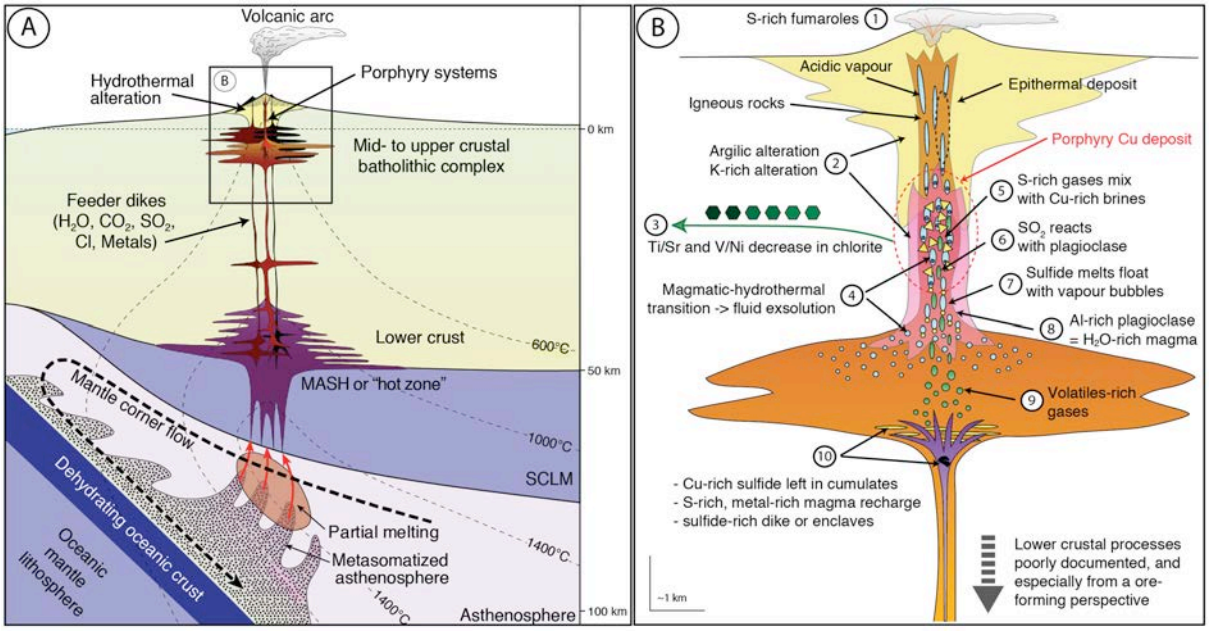

Figure 3: A. Schematic section through a continental arc, showing the development of a MASH or Òhot zoneÓat the base of the crust where basaltic arc magmas pool, differentiate, and interact with crustal rocks and melts. Evolved, less dense, andesitic magmas rise into the mid-to-upper crust where they pool to form batholithic complexes. Modified after Richards (2011) B. Summary of scenarios for porphyry copper ore formation modified after Richards (2016).

The Meghri-Ordubad pluton belongs to the Lesser Caucasus located in the central part of the Alpine-Himalayan orogenic belt. The Zangezur-Ordubad region, located in southern Armenia, hosts the composite Meghri-Ordubad pluton, which outcrops over 1000 km^2 and represents one of the largest Cu-Mo mineralized district in the Lesser Caucasus (Moritz et al., 2016). Its regional geodynamic context of formation is related to the Cenozoic Arabia-Eurasia continental collision and the composite Meghri-Ordubad pluton is composed of intrusions of variable chemistry dated from Middle Eocene to Early Miocene (Moritz et al., 2016). However, there is a lack of understanding regarding the link between the different intrusions of variable age sand no petrological characterization has been carried out yet. This renders difficult to build a comprehensive genetic magmatic-hydrothermal model regarding the formation of porphyry Cu-Mo systems in the Meghri-Ordubad pluton. Therefore, the study area provides a unique opportunity (1) to propose petrogenetic model tightly constrained in time for the incremental construction of the Meghri-Ordubad pluton over 30 million years associated with the formation of variably sized porphyry Cu-Mo deposits, (2) to

evaluate a general set of favourable tectonic, magmatic and hydrothermal conditions leading to the formation of giant porphyry copper systems and suggest exploration strategy views, and (3) to reassess the genetic model of the giant Kadjaran Cu-Mo porphyry systems representing the main Cu and Mo producer of the country, if not to the Lesser Caucasus.

This thesis, entitled ÒPetrogenesis of the Cenozoic Meghri-Ordubad pluton, southernmost Lesser Caucasus: implications for the formation of large porphyry Cu-Mo(-Au) systems during the Arabia-Eurasia accretionary orogenesisÓ aims at understanding magmatic-hydrothermal systematics from a multi-disciplinary approach, including U-Pb zircon and Re-Os molybdenite geochronology combined with *in-situ* zircon oxygen and hafnium isotope (Chapter 1), whole-rock elemental and isotope geochemistry (Chapter 2), igneous petrography and mineral geochemistry (Chapter 3), and tectono-magmatic controls on the formation of porphyry Cu-Mo deposits (Chapter 4). General implications are two folds: (1) a fundamental research aspect dedicated to the characterization of magmatic processes shaping long-lived composite pluton, and (2) an applied research aspect by providing new insights regarding the generation of large porphyry Cu-Mo(-Au) systems in collision zone, which ultimately allows us to suggest new exploration proxies for the mining industry and mineral exploration campaigns.

REFERENCES

Annen, C., Blundy, J. D., and Sparks, R. S. J. (2006). The genesis of intermediate and silicic magmas in deep crustal hot zones : Journal of Petrology, 47, 505-539.

Arndt, N. T., FontbotŽ, L., Hedenquist, J. W., Kesler, S. E., Thompson, J. F., and Wood, D. G. (2017). Metals and Minerals, Now and in The Future. Geochemical Perspectives, 6(1), pp. 171.

AudŽtat, A. (2010). Source and evolution of molybdenum in the porphyry Mo (±Nb) deposit at Cave Peak, Texas. Journal of Petrology, 51(8), 1739-1760.

AudŽtat, A., and Simon, A. C. (2012). Magmatic controls on porphyry copper genesis. In: Hedenquist JW, Harris M, Camus F (eds) Geology and Genesis of Major Copper Deposits and Districts of the World: A Tribute to Richard H. Sillitoe. Society of Economic Geologists Special Publication, 16, 553-572.

Blundy, J., Mavrogenes, J., Tattitch, B., Sparks, S., and Gilmer, A. (2015). Generation of porphyry copper deposits by gas-brine reaction in volcanic arcs. Nature Geoscience, 8(3), 235.

Buret, Y., Wotzlaw, J. F., Roozen, S., Guillong, M., von Quadt, A., and Heinrich, C. A. (2017) Zircon petrochronological evidence for a plutonic-volcanic connection in porphyry copper deposits: Geology, 45, 623-626.

Burnham, C. W. (1979). Magmas and hydrothermal fluids. Geochemistry of Hydrothermal Ore Deposits., 71-136.

Cooke, D. R., Hollings, P., and Walshe, J. L. (2005). Giant porphyry deposits: Characteristics, distribution, and tectonic controls: Economic Geology, 100, 801-818.

FontbotŽ, L., Kouzmanov, K., Chiaradia, M., and Pokrovski, G. S., (2017). Sulfide minerals in hydrothermal deposits: Elements, 13, 97-103.

Chiaradia, M. (2014). Copper enrichment in arc magmas controlled by overriding plate thickness: Nature Geoscience, 7, 43-46.

Chiaradia, M., and Caricchi, L. (2017). Stochastic modelling of deep magmatic controls on porphyry copper deposit endowment: Scientific Reports, v. 7.

Chiaradia, M., Ulianov, A., Kouzmanov, K., and Beate, B. (2012). Why large porphyry Cu deposits like high Sr/Y magmas?: Scientific reports, 2.

Core, D. P., Kesler, S. E., and Essene, E. J. (2006). Unusually Cu-rich magmas associated with giant porphyry copper deposits: Evidence from Bingham, Utah: Geology, 34, 41-44.

Hattori, K., (1993). High-sulfur magma, a product of fluid discharge from underlying mafic magma: evidence from Mount Pinatubo, Philippines : Geology, 21,1083-1086.

Hattori, K. H., and Keith, J. D. (2001). Contribution of mafic melt to porphyry copper mineralization: evidence from Mount Pinatubo, Philippines, and Bingham Canyon, Utah, USA. Mineralium Deposita, 36(8), 799-806.

Henley, R. W., King, P. L., Wykes, J. L., Renggli, C. J., Brink, F. J., Clark, D. A., and Troitzsch, U. (2015). Porphyry copper deposit formation by sub-volcanic sulphur dioxide flux and chemisorption. Nature Geoscience, 8(3), 210.

Hildreth, W., and Moorbath, S. (1988). Crustal contributions to arc magmatism in the Andes of central Chile: Contributions to mineralogy and petrology, 98, 455-489.

Hou, Z., Zhang, H., Pan, X., and Yang, Z. (2011). Porphyry Cu (ÐMoÐAu) deposits related to melting of thickened mafic lower crust: examples from the eastern Tethyan metallogenic domain: Ore Geology Reviews, 39, 21-45.

Jenner, F. E. (2017). Cumulate causes for the low contents of sulfide-loving elements in the continental crust. Nature Geoscience, 10(7), 524-529.

Jenner, F. E., OÕneill, H. S. C., Arculus, R. J., and Mavrogenes, J. A. (2010). The magnetite crisis in the evolution of arc-related magmas and the initial concentration of Au, Ag and Cu. Journal of Petrology, 51(12), 2445-2464.

Kesler, S. E., and Wilkinson, B. H. (2008). Earth's copper resources estimated from tectonic diffusion of porphyry copper deposits. Geology, 36(3), 255-258.

Kouzmanov, K., and Pokrovski, G. S. (2012). Hydrothermal controls on metal distribution in porphyry Cu (-Mo-Au) systems. In: Hedenquist JW, Harris M, Camus F (eds) Geology and Genesis of Major Copper Deposits and Districts of the World: A Tribute to Richard H. Sillitoe. Society of Economic Geologists Special Publication, 16, 573-618.

Lee, C. T. A., Luffi, P., Chin, E. J., Bouchet, R., Dasgupta, R., Morton, D. M., Le Roux, V., Yin, Q-Z and Jin, D. (2012). Copper systematics in arc magmas and implications for crust-mantle differentiation. Science, 336(6077), 64-68.

Lerchbaumer, L., and AudŽtat, A. (2012). High Cu concentrations in vapor-type fluid inclusions: An artifact?. Geochimica et Cosmochimica Acta, 88, 255-274.

Loucks, R. R. (2014). Distinctive composition of copper-ore-forming arc magmas: Australian Journal of Earth Sciences, 61, 5-16.

Moritz, R., Rezeau, H., Ovtcharova, M., Tayan, R., Melkonyan, R., Hovakimyan, S., Ramazanov, V., Selby, D., Ulianov, A., Chiaradia, M., andPutlitz, B. (2016). Long-lived, stationary magmatism and pulsed porphyry systems during Tethyan subduction to post-collision evolution in the Southernmost Lesser Caucasus, Armenia and Nakhitchevan: Gondwana Research, 37, 465-503.

Mungall, J. E., Brenan, J. M., Godel, B., Barnes, S. J., and Gaillard, F. (2015). Transport of metals and sulphur in magmas by flotation of sulphide melt on vapour bubbles. Nature Geoscience, 8(3), 216.

Nadeau, O., Stix, J., and Williams-Jones, A. E. (2016). Links between arc volcanoes and porphyry-epithermal ore deposits. Geology, 44(1), 11-14.

Nadeau, O., Williams-Jones, A. E., and Stix, J. (2010). Sulphide magma as a source of metals in arc-related magmatic hydrothermal ore fluids. Nature Geoscience, 3(7), 501.

Richards, J. P. (2016). Economic geology: Clues to hidden copper deposits: Nature Geoscience, 9, 195-196.

Richards, J. P. (2015) Tectonic, magmatic, and metallogenic evolution of the Tethyan orogen: From subduction to collision: Ore Geology Reviews, 70, 323-345.

Richards, J. P. (2011a). High Sr/Y arc magmas and porphyry Cu±Mo±Au deposits: just add water. Economic Geology, 106, 1075-1081.

Richards, J. P. (2011b). Magmatic to hydrothermal metal fluxes in convergent and collided margins. Ore Geology Reviews, 40, 1-26.

Richards, J. P. (2009). Postsubduction porphyry Cu-Au and epithermal Au deposits: Products of remelting of subduction-modified lithosphere: Geology, 37, 247-250.

Richards, J. P. (2003). Tectono-magmatic precursors for porphyry Cu-(Mo-Au) deposit formation: Economic Geology, 98, 1515-1533.

Rohrlach, B. D., Loucks, R. R., and Porter, T. M. (2005). Multi-million-year cyclic ramp-up of volatiles in a lower crustal magma reservoir trapped below the Tampakan copper-gold deposit by Mio-Pliocene crustal compression in the southern Philippines: Super porphyry copper and gold deposits: A global perspective: Adelaide, PGC Publishing, 2, 369-407.

Seedorff, E., Dilles, J. H., Proffett, J. M., Einaudi, M. T., Zurcher, L., Stavast, W. J. A., Johnson, D. A., and Barton, M. D. (2005). Porphyry deposits: Characteristics and origin of hypogene features: Economic Geology 100th anniversary, 29, 251-298.

Sillitoe, R. H. (2010). Porphyry copper systems. Economic geology, 105(1), 3-41.

Simon, A. C., and Ripley, E. M. (2011). The role of magmatic sulfur in the formation of ore deposits. Reviews in Mineralogy and Geochemistry, 73(1), 513-578.

Simon, A. C., Pettke, T., Candela, P. A., Piccoli, P. M., and Heinrich, C. A. (2006). Copper partitioning in a melt–vapor–brine–magnetite–pyrrhotite assemblage. Geochimica et Cosmochimica Acta, 70(22), 5583-5600.

Tapster, S., Condon, D. J., Naden, J., Noble, S. R., Petterson, M. G., Roberts, N. M. W. Saunders, A.D., and Smith, D. J. (2016). Rapid thermal rejuvenation of high-crystallinity magma linked to porphyry copper deposit formation; evidence from the Koloula Porphyry Prospect, Solomon Islands: Earth and Planetary Science Letters, 442, 206-217.

Wallace, P. J. (2005). Volatiles in subduction zone magmas: concentrations and fluxes based on melt inclusion and volcanic gas data. Journal of Volcanology and Geothermal Research, 140(1), 217-240.

Wilkinson, J. J. (2013). Triggers for the formation of porphyry ore deposits in magmatic arcs: Nature Geoscience, 6, 917-925.

Wilkinson, J. J., Chang, Z., Cooke, D. R., Baker, M. J., Wilkinson, C. C., Inglis, S., Chen, H., and Gemmell, J. B. (2015). The chlorite proximitor: A new tool for detecting porphyry ore deposits. Journal of Geochemical Exploration, 152, 10-26.

Williamson, B. J., Herrington, R. J., and Morris, A. (2016). Porphyry copper enrichment linked to excess aluminium in plagioclase. Nature Geoscience, 9(3), 237.

Williams-Jones, A. E., and Heinrich, C. A. (2005). 100th Anniversary special paper: vapor transport of metals and the formation of magmatic-hydrothermal ore deposits. Economic Geology, 100(7), 1287-1312.

Zajacz, Z., Candela, P. A., Piccoli, P. M., Sanchez-Valle, C., and WŠlle, M. (2013). Solubility and partitioning behavior of Au, Cu, Ag and reduced S in magmas. Geochimica et Cosmochimica Acta, 112, 288-304.

Zajacz, Z., Candela, P. A., Piccoli, P. M., WŠlle, M., and Sanchez-Valle, C. (2012). Gold and copper in volatile saturated mafic to intermediate magmas: Solubilities, partitioning, and implications for ore deposit formation. Geochimica et Cosmochimica Acta, 91, 140-159.

CHAPTER 1

Temporal and genetic link between incremental pluton assembly and pulsed porphyry Cu-Mo formation in accretionary orogens

HervŽ Rezeau[1], Robert Moritz[1], Jš rn-Frederik Wotzlaw[2], Rodrik Tayan[3], Rafael Melkonyan[3], Alexey Ulianov[4], David Selby[5], Fran•ois-Xavier d'Abzac[1] and Richard A. Stern[6]

[1]Department of Earth Sciences, University of Geneva, 1205 Geneva, Switzerland; [2]Institute of Geochemistry and Petrology, ETH ZŸrich, 8092 ZŸrich, Switzerland; [3]Institute of Geological Sciences, National Academy of Sciences, 0019 Yerevan, Armenia [4]Institute of Earth Sciences, University of Lausanne, 1015 Lausanne, Switzerland; [5]Department of Earth Sciences, University of Durham, DH1 3LE Durham, United Kingdom; [6]Canadian Centre for Isotopic Microanalysis, University of Alberta, Edmonton, Canada

ABSTRACT

Economically important porphyry Cu-Mo deposits (PCDs) are generally hosted by upper crustal plutons of variable chemical compositions related to distinct geodynamic settings. The absolute timing and duration of pluton assembly and PCD formation is critical to understand the genetic relationship between these interrelated processes. Here we present new comprehensive zircon U-Pb and molybdenite Re-Os ages that tightly constrain the timing and duration of pluton assembly and the age of mineralization in one of the largest ore-bearing plutons of the central Tethyan metallogenic belt, the Meghri-Ordubad pluton, southern Armenia and Nakhitchevan, Lesser Caucasus. This composite pluton was incrementally assembled during three compositionally distinct magmatic episodes over about 30 m.y., comprising Middle Eocene (48.9-43.1 Ma) calc-alkaline subduction-related magmatism lasting 5.8 ± 0.8 m.y., followed by post-subduction Late Eocene - Middle Oligocene (37.8-28.1 Ma) shoshonitic magmatism over 9.7 ± 0.9 m.y., and Late Oligocene - Early Miocene (26.6-21.2 Ma) adakitic magmatism consisting of shoshonitic dikes and high-K calc-alkaline granodioritic magmas emplaced over 5.4 ± 0.4 m.y.. Despite the distinct geodynamic settings and magma compositions, each intrusive suite culminated in the formation of variably sized PCDs, including the giant Oligocene Kadjaran porphyry Cu-Mo deposit associated with high Sr/Y shoshonitic magmas. Complementary in-situ zircon hafnium (εHf_{zircon} = +8 to +11.3) and oxygen ($\delta^{18}O_{zircon}$ = +4.6 to +6.0 ä) isotope data support a mantle-dominated magma source with limited crustal contribution and/or cannibalization of young and juvenile lower crustal cumulates. We conclude that, independently of geodynamic setting and magma composition, long-lived (5-10 m.y.) incremental mantle-derived magmatism is a pre-requisite to form fertile magmatic-hydrothermal systems, and especially giant PCDs.

Keywords: Geochronology; Cu-Mo porphyry deposits; Isotope geochemistry; Lesser Caucasus; Tethyan orogenic belt

1. INTRODUCTION

The majority of porphyry Cu-Mo deposits (PCDs) are associated with subduction-related calc-alkaline upper-crustal plutons (Sillitoe, 2010). However, porphyry Cu-Mo systems have recently also been recognized in post-subduction settings, particularly along the Tethyan metallogenic belt (e.g., Richards, 2015; Hou et al., 2015a, b; Moritz et al., 2016). This raises a number of questions concerning the primary control on PCD formation, as most models require active oceanic subduction to generate large volumes of hydrous, oxidized, S-rich, and Cu-rich magmas derived from a subcontinental lithospheric mantle metasomatized by slab-related fluids, and repeated mafic magma injections to provide and transfer sulfur, metals and volatiles into upper crustal reservoirs (e.g., Hattori & Keith, 2001; Scaillet, 2010; AudŽtat & Simon, 2012; Tapster et al., 2016). Ore-forming processes in PCDs occur over short timescales of $<10^3$ to 10^4 years (e.g., von Quadt et al., 2011; Chiaradia et al., 2013), which are in marked contrast to the duration of incremental assembly of the host plutons lasting 10^5 to 10^6 years (Rohrlach and Loucks, 2005; Chelle-Michou et al., 2014; Correa et al., 2016). In most magmatic-hydrothermal systems, ore formation occurs late in the magmatic evolution (e.g., Sillitoe, 2010; AudŽtat & Simon, 2012), but the precise temporal and genetic relationships between the entire pluton construction and PCD formation remains poorly documented.

Recently, Moritz et al. (2016) documented the regional tectonic evolution of the southernmost Lesser Caucasus from a subduction to post-collisional setting with coeval mineralization pulses, however the absolute temporal link between intrusions and PCDs remained elusive due to limited geochronological data. Here we investigate the absolute temporal relationship between incremental pluton construction and PCD formation using a large data set of new zircon U-Pb and molybdenite Re-Os data from one of the largest ore-bearing plutons of the central Tethyan metallogenic belt, the Meghri-Ordubad pluton (MOP) in southern Armenia and Nakhitchevan, Lesser Caucasus. The MOP comprises three long-lived intrusive suites, which culminated in the formation of variably sized PCDs, including the giant Oligocene Kadjaran PCD. Our comprehensive U-Pb and Re-Os geochronological framework documents in detail the incremental construction of the MOP over 30 m.y. and the timing of ore formation allowing improved understanding of the conditions and processes required to form PCDs. Complementary ***in-situ*** zircon hafnium and oxygen isotope data are used to estimate mantle and crustal contributions to the ore-forming magmas.

2. GEOLOGICAL SETTING

The ore-bearing MOP belongs to the regional fertile Cenozoic magmatic belt extending from Turkey to Iran that formed during the final convergence and collision of the Arabian and Eurasian plates (Fig. 1). The MOP represents the largest composite intrusion of the Lesser Caucasus (1000 km^2) and intrudes a thick sequence of Cenozoic terrigenous sedimentary and subalkaline to calc-alkaline basaltic to andesitic volcanic rocks (Karamyan et al., 1974). The MOP is the result of a long-lasting Middle Eocene to Early Miocene evolution, including subduction-related calc-alkaline magmatism followed by post-subduction shoshonitic to high-K calc-alkaline magmatism (Fig. 2; Moritz et al., 2016). The MOP is bordered by two regional NNW-oriented faults with both vertical and dextral strike-slip movements, and another parallel fault extends through its central part and controls the location of PCDs (Fig. 3; Tayan, 1998). For detailed descriptions about the regional and local geology, the reader is referred to the Chapter 2.

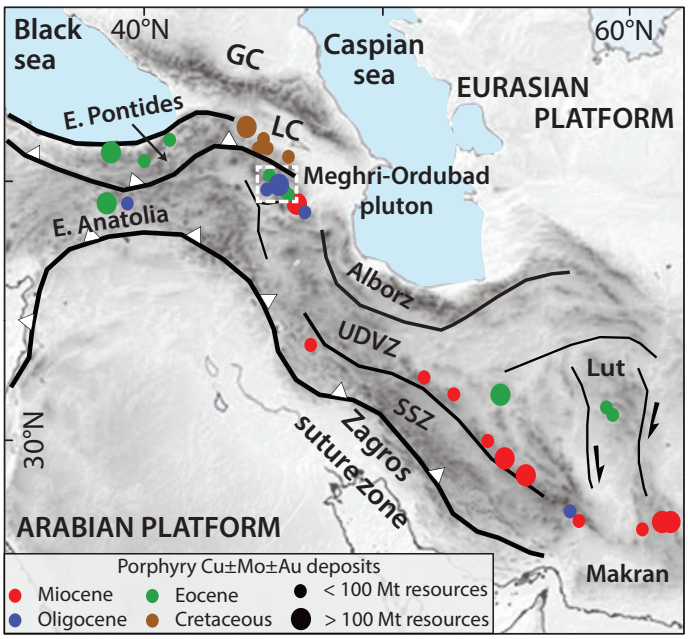

Figure 1: Distribution of porphyry Cu±Mo±Au deposits grouped by ages and sizes along the Afro-Arabian collision zone located in the central Tethyan metallogenic belt. Locations and ages of porphyry deposits are derived from Aghazadeh et al. (2015) and Richards (2015). Suture zones and structures are derived from Mouthereau et al. (2012) and the topographic relief background map from ETOPO1 (1'×1' resolution) Global Relief data (http://www.ngdc.noaa.gov). Abbreviations are Greater Caucasus (GC), Lesser Caucasus (LC), Sanandaj-Sirjan Zone (SSZ) and Urumieh-Dokhtar Volcanic Zone (UDVZ).

3. ANALYTICAL METHODS

New zircon U-Pb ages were obtained by laser ablation–inductively coupled plasma–mass spectrometry (LA-ICP-MS) from 30 representative magmatic rock samples covering the entire

temporal and compositional range of the MOP (Tables 1 and 2). Nine molybdenite Re-Os ages were obtained by isotope dilution–negative thermal ionization–mass spectrometry (ID-N-TIMS) from mineralization events associated with all three magmatic episodes. In situ multiple collector ICP-MS (MC-ICP-MS) hafnium and secondary ion mass spectrometry (SIMS) oxygen isotope data were obtained on selected zircon grains. The complete analytical details and data set are provided in Appendix A and B, respectively. Zircon textures revealed by scanning electron microscope cathodoluminescene (SEM-CL) and the location of *in situ* zircon U-Pb, Hf and O isotope spot analyses are shown in Appendix C. Detailed geochemical characterization is further presented and discussed in Chapter 2.

4. INCREMENTAL PLUTON CONSTRUCTION

A total of 601 new LA-ICP-MS zircon U-Pb dates (Supplementary Table B.1), together with previously published chemical abrasion isotope dilution thermal ionization mass spectrometry (CA-ID-TIMS) zircon U-Pb ages (Table 1; Moritz et al., 2016), place tight spatial-temporal constraints on the MOP incremental assembly (Figs. 2a and 3).

In the southern part of the MOP (Fig. 3), the subduction-related calc-alkaline magmatism starts with two granitic and tonalitic intrusions at 48.9 ± 0.6 and 47.6 ± 0.6 Ma, followed by gabbro-diorite-tonalite-granodiorite intrusions and NNW-oriented basaltic andesite dikes emplaced between 45.9 ± 0.9 and 43.8 ± 0.6 Ma (Fig. 2a). These ages are in agreement with CA-ID-TIMS ages from similar samples (Fig. 2a; Table 1). In the northern part of the MOP (Fig. 3), a monzodiorite is intruded by a tonalite and yield slightly younger U-Pb ages of 42.9 ± 0.5 and 43.1 ± 0.5 Ma, respectively (Fig. 2a). The Middle Eocene intrusive suite documents 5.8 ± 0.8 m.y. of incremental magmatism.

Following a magmatic lull of 5.1 ± 0.9 m.y., pluton assembly resumed with emplacement of post-subduction high Sr/Y shoshonitic intrusions (Fig. 2a). In the southeastern part of the MOP (Fig. 3), a monzogabbro and a monzodiorite yield indistinguishable ages of 37.8 ± 0.8 and 37.0 ± 0.4 Ma, respectively (Fig. 2a). Further north along the Vank-Kaler road and along the Meghri ridge (Fig. 3), five monzogabbroic-monzodioritic intrusions were emplaced between 35.7 ± 0.6 and 33.5 ± 0.6 Ma, and are crosscut by trachyandesitic and syenitic dikes that yield ages of 33.7 ± 0.5 and 33.6 ± 0.6 Ma, respectively (Fig. 2a). Along the Meghri ridge, a hornblende gabbro was dated at 33.43 ± 0.02 Ma by CA-ID-TIMS (Fig. 2A; Table 1). Further north and west (Fig. 3), the Kadjaran ore field exposes a monzonite with an age of 31.9 ± 0.5 Ma, which is in agreement with a CA-ID-TIMS U-Pb age of 31.83 ± 0.02 Ma, and crosscut by a syenitic sill dated at 31.1 ± 0.5 Ma (Fig. 2a; Table 1). Younger monzonite and

Table 1. Summary of location, classification, weighted mean U-Pb zircon ages, median εHf and $\delta^{18}O$ for 30 representative samples from this study and 6 additional samples from Moritz et al. (2016).

							zircons		
Samples	***Nj Figs. 1 & 2***	***Location***	***Longitude***	***Latitude***	***Altitude***	***Rock type (TAS classification)***	***Mean Age ± 2SD (Ma)***	***Mean εHf ± 2SD***	***Mean $\delta^{18}O$ (SMOW) ± 2SD***
					(m)		***(Ma)***		***(ä)***
AG1304A	1	Agarak area	E46 11.734	N38 53.804	923	Granodiorite/Granite	48.9 ± 0.6	8.7 ± 1.1	5.20 ± 0.19
AG1006A	-	Agarak area	E46 11.780	N38 53.735	-	Granite	**48.99 ± 0.07**	-	-
MR1501	2	Alvank area	E46 19.892	N38 56.303	772	Tonalite	47.6 ± 0.6	8.0 ± 0.6	-
AG1401	3	Vahravar area	E46 10.329	N38 57.179	1345	Hornblende Gabbro	45.9 ± 0.9	8.8 ± 1.0	4.51 ± 0.19
AG1404	4	Araksashen area	E46 17.324	N38 55.012	749	Diorite/Tonalite	44.8 ± 0.9	9.0 ± 0.9	-
VK1403	5	Vank-Kaler road	E46 13.036	N39 02.034	1787	Quartz monzonite	44.3 ± 0.7	9.3 ± 0.9	-
AG1403	6	Araksashen area	E46 17.324	N38 55.012	749	Diorite	44.1 ± 1	9.4 ± 0.9	-
AG1007*	-	Agarak area	E46 13.274	N38 53.862	-	Granodiorite	**44.03 ± 0.02**	-	-
AG1406	7	Alvank area	E46 19.892	N38 56.303	772	Basaltic-andesite dike	44 ± 0.9	8.8 ± 0.9	-
AG1402	8	Vahravar area	E46 10.329	N38 57.179	1345	Diorite	43.8 ± 0.6	8.5 ± 0.9	5.32 ± 0.19
HQ1402	9	Hanqasar area	E46 08.393	N39 13.702	1626	Monzodiorite	42.9 ± 0.5	11.3 ± 1.0	-
HQ1403	10	Hanqasar area	E46 07.348	N39 13.805	1699	Tonalite	43.1 ± 0.5	10.4 ± 1.0	5.42 ± 0.20
AG1308A1	11	Schvanidzor area	E46 22.594	N38 56.873	849	Monzogabbro (Tephrite?)	37.8 ± 0.8	8.4 ± 1.3	-
AG1308A	12	Schvanidzor area	E46 22.594	N38 56.873	849	Monzodiorite	37 ± 0.4	8.4 ± 1.3	5.37 ± 0.19
VK1404	13	Near Kaler	E46 16.975	N39 03.411	2267	Monzogabbro	35.7 ± 0.6	8.9 ± 1.0	-
VK1405	14	Near Kaler	E46 16.975	N39 03.411	2267	Monzodiorite	34.8 ± 0.5	8.6 ± 1.2	5.26 ± 0.20
MR1403	15	Meghri ridge	E46 14.495	N39 05.877	2762	Monzodiorite	34.6 ± 0.6	9.1 ± 1.3	5.58 ± 0.18
LI1303A1	16	Vank.Kaler road	E46 15.578	N39 03.458	2000	Monzogabbro	33.5 ± 0.6	8.8 ± 1.0	5.64 ± 0.19
LI1303	17	Vank-Kaler road	E46 15.578	N39 03.458	2000	Syenitic dike	33.6 ± 0.6	8.8 ± 1.5	-
MR1402/KJ1207	-	Meghri ridge	E46 13.287	N39 06.159	2685	Hornblende Gabbro	**33.49 ± 0.02**	9.5 ± 0.6	5.51 ± 0.18
KJ1316	18	Meghri ridge	E46 13.287	N39 06.159	2685	Trachyandesite dike	33.7 ± 0.5	9.4 ± 0.5	5.62 ± 0.19
KJ1006A	19	Atkis	E46 12.745	N39 09.076	1662	Monzonite	31.9 ± 0.5	9.4 ± 0.8	-
KJ1002	-	Atkis	E46 09.528	N39 09.584	-	Monzonite	**31.83 ± 0.02**	-	5.47 ± 0.19

KJ1308	20	Road to Meghri	E46 11.134	N39 08.656	1929	Syenitic dike	31.1 ± 0.5	8.7 ± 1.0	-
KJ1508	21	Kadjaran open pit	E46 08.026	N39 08.972	1866	Gabbro (weakly altered)	28.3 ± 0.4	9.5 ± 0.6	-
KJ1509	22	Kadjaran open pit	E46 08.026	N39 08.972	1866	Monzonite (heavily altered)	28.1 ± 0.4	9.6 ± 0.5	-
KJ1302A	23	Kadjaran Open pit	E46 08.414	N39 08.757	1887	Trachyandesite dike	26.6 ± 0.3	9.7 ± 0.9	5.54 ± 0.19
KJ1303A1	24	Near Katnarat	E46 12.629	N39 07.513	2142	Trachybasalt dike	25.5 ± 0.3	9.9 ± 1.1	-
MR1401	25	Meghri Ridge	E46 12.808	N39 06.430	2547	Trachyandesite dike	24.5 ± 0.4	11.2 ± 0.9	-
KJ1307	26	Road to Pukhrut	E46 12.907	N39 08.182	1865	Trachybasalt dike	24.3 ± 0.3	10.4 ± 0.8	-
LI1301	27	Lichk area	E46 10.368	N39 01.780	1797	Porphyritic Granodiorite	22.6 ± 0.5	11.2 ± 1.2	5.97 ± 0.19
LI1003	-	Lichk area	E46 10.375	N39 02.777	-	Porphyritic Granodiorite	**22.46 ± 0.02**	-	-
KJ1325A	28	Kadjaran Open pit	E46 08.416	N39 08.840	1901	porphyritic granodioritic dike	22.2 ± 0.3	10.7 ± 0.8	-
KJ1324A	29	Kadjaran Open pit	E46 08.026	N39 08.972	1866	porphyritic granodioritic dike	22.2 ± 0.3	10.5 ± 1.0	5.92 ± 0.19
KJ1211A	-	Kadjaran Open pit	E46 08.316	N39 08.610	-	Basalt-Andesite dike	**22.22 ± 0.01**	-	-
KJ1313	30	Road to Meghri	E46 11.054	N39 08.547	1952	Trachyandesite dike	21.2 ± 0.3	10.9 ± 0.8	-

Bold ages refer to CA-ID-TIMS ages from Moritz et al. (2016)

Table 2: Summary of whole-rock major and selected trace elements geochemistry for 29 representative samples from this study and 6 samples from Moritz et al. (2016).

Samples	***SiO_2***	***TiO_2***	***Al_2O_3***	***Fe_2O_3***	***MnO***	***MgO***	***CaO***	***Na_2O***	***K_2O***	***P_2O_5***	***LOI***	***Mg#***	***Cr***	***Ni***	***Sr***	***Y***
	(wt. %)												***(ppm)***			
AG1304A	70.26	0.34	15.28	2.52	0.01	0.48	2.38	5.81	0.55	0.09	0.86	0.27	26.69	2.00	332.44	14.70
AG1006A*	71.20	0.35	15.51	2.77	0.01	0.91	2.58	5.30	0.72	0.11	0.67	0.39	13.00	b.d.	380.00	17.00
MR1501	64.92	0.51	15.75	5.22	0.13	1.92	4.99	3.47	2.08	0.15	0.33	0.42	16.00	3.00	269.00	16.00
AG1401	45.77	0.90	20.17	10.61	0.17	5.41	11.54	2.27	1.10	0.44	0.65	0.50	10.29	14.19	467.73	20.36
AG1404	60.61	0.64	16.36	6.63	0.14	2.82	5.85	3.38	2.31	0.16	0.48	0.46	21.72	5.56	407.44	22.81
VK1403	65.87	0.65	14.99	4.65	0.09	1.11	3.35	3.22	4.45	0.16	0.57	0.32	15.70	2.97	179.93	37.88
AG1403	58.34	0.90	13.86	9.96	0.21	4.16	5.63	2.63	2.43	0.21	0.73	0.45	20.41	8.22	297.85	37.18
AG1007*	69.40	0.28	16.51	2.39	0.09	0.46	3.22	5.12	2.01	0.08	0.38	0.28	10.00	b.d.	635.00	7.70
AG1406	55.05	0.70	17.07	8.29	0.15	4.68	8.02	3.71	1.24	0.14	0.46	0.53	100.37	22.85	433.90	19.27

AG1402	59.65	0.68	16.25	7.03	0.16	2.96	6.70	3.24	1.89	0.18	0.37	0.45	21.62	6.09	405.26	24.60
HQ1402	52.16	0.57	21.78	6.76	0.17	2.36	9.24	4.31	1.03	0.27	0.57	0.41	12.11	5.10	1511.22	16.38
HQ1403	63.93	0.38	16.37	4.37	0.11	1.74	4.70	3.88	2.93	0.19	0.50	0.44	52.70	11.23	382.26	15.92
AG1308A1	47.37	1.06	19.73	8.77	0.23	3.81	8.63	4.09	3.25	0.67	1.61	0.46	47.40	17.22	1907.06	26.94
AG1308A	53.52	0.51	22.51	4.25	0.12	1.29	7.17	5.05	3.44	0.32	1.05	0.38	13.14	1.97	2891.82	18.76
VK1404	48.95	0.92	17.85	9.44	0.16	5.20	10.24	3.55	1.45	0.49	0.36	0.52	18.84	15.56	1371.15	21.51
VK1405	53.03	0.54	21.27	6.08	0.09	2.14	8.27	4.08	2.55	0.67	0.40	0.41	21.33	14.23	1534.67	20.80
MR1403	52.66	0.74	20.00	6.33	0.14	2.64	7.19	4.58	3.80	0.55	0.57	0.45	16.17	6.32	1469.97	25.11
LI1303A1	47.86	0.93	21.53	8.77	0.13	3.43	10.85	3.26	1.62	0.51	0.91	0.44	2.80	3.59	1332.91	22.62
LI1303	59.80	0.59	18.54	4.73	0.13	1.29	3.38	5.29	5.35	0.31	0.49	0.35	6.20	b.d.	665.43	27.37
MR1402/KJ1207*	41.69	1.46	19.04	11.89	0.21	6.84	12.89	2.30	0.69	1.23	0.53	0.53	14.06	b.d.	1816.68	34.15
KJ1316	60.26	0.50	17.54	5.35	0.13	1.77	5.09	4.37	3.57	0.40	0.34	0.40	13.99	2.76	1103.98	24.42
KJ1006A	57.09	0.82	18.62	5.29	0.12	2.02	4.00	4.28	6.05	0.41	0.71	0.43	8.00	5.28	692.00	21.93
KJ1002*	56.86	0.85	17.66	6.50	0.13	2.69	4.97	3.85	4.63	0.39	0.55	0.45	11.00	8.31	722.00	25.80
KJ1308	60.88	0.90	18.67	4.24	0.09	0.99	2.00	3.57	7.98	0.17	0.50	0.32	2.50	b.d.	512.01	19.69
KJ1508	47.48	0.97	18.27	10.28	0.15	5.97	10.45	2.90	1.02	0.56	1.09	0.53	54.00	37.00	1369.70	18.30
KJ1302A	58.41	0.64	14.20	4.70	0.12	1.72	4.39	0.23	6.73	0.44	6.48	0.42	74.30	39.96	225.79	10.48
KJ1303A1	46.93	1.06	13.68	7.52	0.14	7.13	8.56	2.84	2.44	0.56	8.76	0.65	397.90	143.68	2370.03	16.19
MR1401	61.43	0.60	15.49	4.47	0.08	2.29	4.11	3.66	3.85	0.27	2.97	0.50	44.51	19.92	801.97	13.21
KJ1307	50.95	0.78	14.13	6.72	0.11	7.82	7.18	3.17	2.01	0.37	6.59	0.70	279.10	200.54	759.34	14.66
LI1301	66.66	0.47	14.95	3.27	0.05	2.02	3.21	4.01	3.72	0.22	0.61	0.55	68.98	33.39	616.28	9.51
LI1003*	66.97	0.48	15.26	3.35	0.05	2.06	3.19	3.88	3.50	0.21	0.6	0.55	58.00	39.00	670.00	10.00
KJ1325A	61.25	0.42	14.35	3.24	0.06	2.09	4.23	1.46	4.02	0.20	8.6	0.56	35.10	26.29	404.38	9.44
KJ1324A	62.85	0.44	15.19	3.62	0.06	1.69	2.85	1.36	3.56	0.23	8.15	0.48	31.60	23.97	433.59	10.16
KJ1211A*	54.26	0.54	15.06	3.92	0.11	2.82	5.98	0.17	4.59	0.28	11.95	0.59	60.00	28.00	274.00	11.00
KJ1313	58.42	0.64	14.94	4.54	0.10	1.47	6.24	3.57	3.49	0.37	5.56	0.39	91.70	44.02	719.68	12.75

* data after Moritz et al. (2016a)

monzogabbro were emplaced at 28.3 ± 0.4 and 28.1 ± 0.4 Ma, respectively. The entire Late Eocene to Middle Oligocene intrusive suite comprises 9.7 ± 0.9 m.y. of episodic magmatism. In the Kadjaran ore field (Fig. 3), the post-subduction magmatism continued with the emplacement of Late Oligocene NNE-oriented adakitic shoshonitic trachybasaltic and trachyandesitic dikes between 26.6 ± 0.3 and 24.3 ± 0.3 Ma (Fig. 2a). These dikes contain significantly older zircons antecrysts reflecting recycling of Middle Eocene and Early Oligocene intrusions. A younger, voluminous Early Miocene adakitic high-K calc-alkaline porphyritic granodiorite dated at 22.8 ± 0.5 Ma is overlapping within error with EW-oriented porphyritic granodioritic and trachyandesitic dikes dated at 22.2 ± 0.3 and 21.2 ± 0.3 Ma, respectively (Figs. 2a and 3), and overlap with CA-ID-TIMS ages for similar samples (Fig. 2a; Table 1; Moritz et al., 2016). The entire Late Oligocene - Early Miocene magmatism represents a third magmatic episode lasting 5.4 ± 0.4 m.y. This latest magmatic suite is characterized by an adakitic signature, and also higher Mg#, Cr and Ni contents, distinct from the Late Eocene - Middle Oligocene high Sr/Y shoshonitic intrusive suite (Table 2).

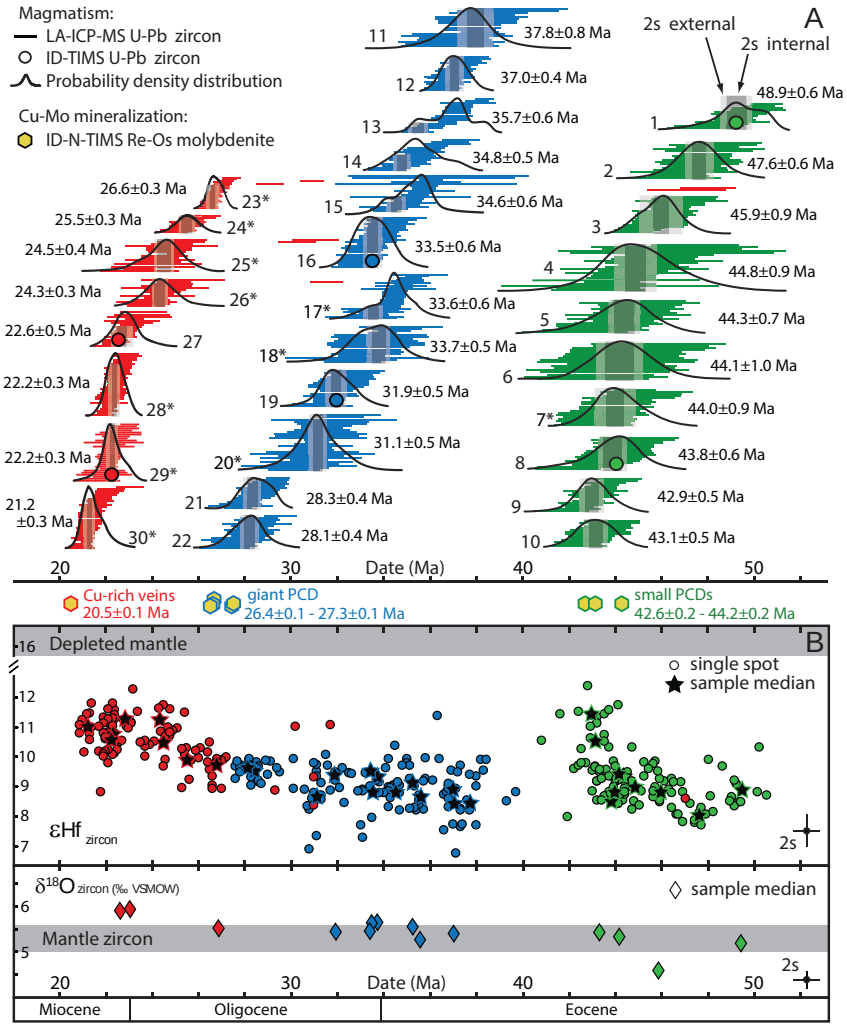

Figure 2: (a) Geochronology of the Meghri-Ordubad pluton and associated Cu-Mo mineralizations based on 601 concordant zircon U-Pb ages from thirty samples and nine molybdenite Re-Os ages. The Middle Eocene subduction-related calc-alkaline magmatism has a duration of 5.8 ± 0.8 m.y. (green), the Late Eocene Ð Middle Oligocene shoshonitic suite lasted 9.7 ± 0.9 m.y. (blue), and the Late Oligocene shoshonitic to Early Miocene high-K calc-alkaline adakitic magmas were emplaced within 5.4 ± 0.4 m.y. (red). The calculated mean age for each sample does not include antecryst ages (Miller et al., 2007; Appendix A and Supplementary Table B.1) and molybdenite Re-Os ages coincide with the end of each magmatic series (Table 1 and Supplementary Table B.2). Numbers 1 to 30 refer to the sample locations in Figure 3 and the descriptions in Table 1 and Supplementary Table B.1. Asterisks indicate dike samples. (b) Zircon in situ hafnium (Table 1 and Supplementary Table B.3) and oxygen isotopic data (Table 1 and Supplementary Table B.4) as a function of age. Hf isotope data are shown as individual analyses (n=365) and as sample median values while oxygen isotopic data are only shown as median $\delta^{18}O$ values (based on 280 analyses) due to limited inter- and intragrain variability.

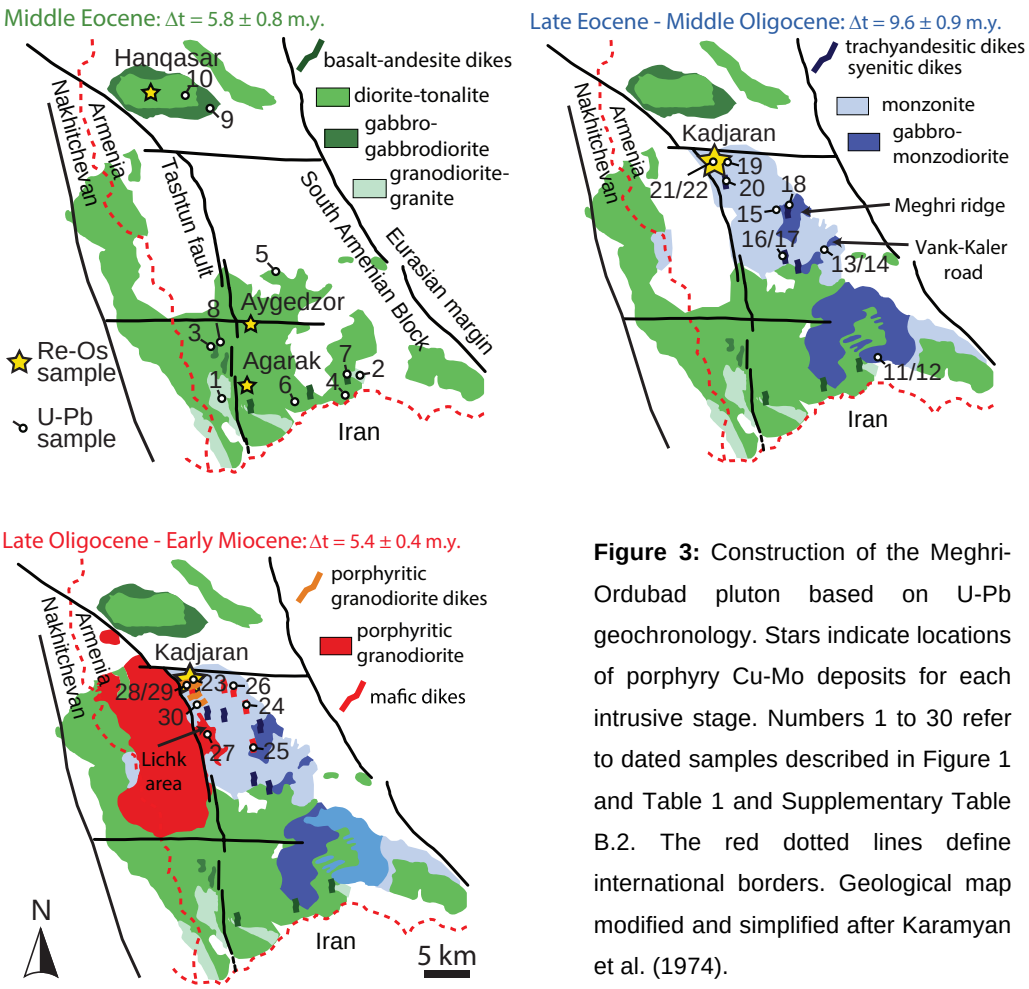

Figure 3: Construction of the Meghri-Ordubad pluton based on U-Pb geochronology. Stars indicate locations of porphyry Cu-Mo deposits for each intrusive stage. Numbers 1 to 30 refer to dated samples described in Figure 1 and Table 1 and Supplementary Table B.2. The red dotted lines define international borders. Geological map modified and simplified after Karamyan et al. (1974).

5. TIMING OF MINERALIZATION

The PCDs are aligned along the central N-S-oriented Tashtun fault (Fig. 3), but they were formed at different times during the MOP construction. The small tonnage PCDs (10 to 40 Mt at 0.2-0.5 % Cu and 0.03-0.04 % Mo) yield molybdenite Re-Os ages of 44.23 ± 0.22 and 42.62 ± 0.22 Ma in the southern part of the MOP at Agarak and Aygedzor, respectively, and 43.14 ± 0.22 Ma in the northern part at Hanqasar (Figs. 2a and 3; Supplementary Table B.2). These Re-Os ages are indistinguishable from the ages of the youngest Middle Eocene intrusions, which tightly constrain their formation to the end of subduction-related calc-alkaline magmatism (Fig. 2a). Molybdenite Re-Os dates reveal two distinct Cu-Mo mineralizing events in the giant Kadjaran PCD (2244 Mt at 0.2 % Cu and 0.02 % Mo). Molybdenite from the first mineralization event yields Re-Os ages between 27.28 ± 0.14 and 26.43 ± 0.13 Ma (Supplementary Table B.2). This mineralization is hosted by the youngest Late Eocene - Middle Oligocene shoshonitic high Sr/Y intrusions and is crosscut by the oldest Late Oligocene shoshonitic adakitic mafic dike (see Chapter 4 for details). Therefore, the first mineralizing event in Kadjaran is attributed to the very end of the Late Eocene - Middle Oligocene post-subduction shoshonitic high Sr/Y magmatism. These ages are in agreement with Re-Os ages reported from Mo mineralization hosted in the Iranian side of the MOP, namely the Qaradagh pluton (Simmonds and Moazzen, 2015). A younger molybdenite Re-Os age of 20.48 ± 0.10 Ma reveals a second ore-forming event in Kadjaran associated with a reopening of the structures hosting the 26-27 Ma-old Cu-Mo mineralization. It documents a genetic link with the Early Miocene adakitic high-K calc-alkaline porphyry granodiorite intrusion event (Fig. 2a; Supplementary Table B.2), and supports a cogenetic link with Cu-rich epithermal veins overprinting porphyritic granodioritic dikes dated at 22.2 ± 0.3 (see Chapter 4 for details). The Early Miocene hydrothermal event was already documented by a sericite K-Ar date of 22 ± 2 Ma in Kadjaran (Bagdasaryan et al., 1969), and it is consistent with a molybdenite Re-Os age of 21.01 ± 0.15 Ma reported from the Sungun PCD, located 70 km further south in northernmost Iran (e.g., Aghazadeh et al., 2015). Placing all these Re-Os ages into our comprehensive U-Pb geochronology framework of incremental pluton construction clearly links PCDs formation to the latest stage of each intrusive suite (Fig. 2a).

6. ASSESSING THE SOURCES OF ORE-FORMING MAGMAS USING HAFNIUM AND OXYGEN ISOTOPES

Combined hafnium and oxygen isotopic signatures are powerful tools to trace the sources of magmas and place constraints on mantle and crustal contributions. Zircons from the MOP intrusive suites display median initial εHf values between +8.0 and +11.3, which suggest an overall predominance of mantle-derived magmas with limited crustal assimilation (Fig. 2b;

Table 1 and Supplementary Table B.3). This limited range in Hf isotopic compositions is in marked contrast with the significant differences in whole-rock geochemistry over about 30 m.y. (Table 2). Interestingly, towards the end of the Middle Eocene calc-alkaline magmatism and throughout the Late Eocene to Early Miocene intrusive suites, Hf isotopic signatures become progressively more juvenile (Fig. 2b). Zircon oxygen isotope analyses reveal homogeneous $\delta^{18}O$ values in individual rocks and crystals (Table 1 and Supplementary Table B.4), but display a subtle $\delta^{18}O$ increase from +5.20 ± 0.19 ä to +5.97 ± 0.22 ä over 30 m.y. (Fig. 2b). These values and pattern imply very limited assimilation of supracrustal rocks (e.g., Lackey et al., 2005), and no crustal recycling of hydrothermally altered rocks (e.g., Bindeman, 2008). A single Middle Eocene sample with a median $\delta^{18}O$ value of +4.51 ± 0.69 ä may be attributed to minor assimilation of altered shallow crustal material (Fig. 2b). The slight, but systematic and coeval increase of $\delta^{18}O$ and εHf values over time together with the overall limited variations support a predominance of mantle-derived magmas with decreasing crustal contribution. It is consistent with a long-lived homogeneous deep reservoir in the lower crust or lithospheric mantle. Alternatively, this isotope pattern may be attributed to progressive cannibalization of young and juvenile lower crust, formed by mantle-derived magmas. However, this process cannot be quantified due to the limited isotopic contrast.

7. CONTROLLING FACTORS OF PORPHYRY COPPER DEPOSIT FORMATION

The MOP represents a unique place to investigate controlling factors leading to the formation of PCDs because all three intrusive suites share similar duration of magmatic activity, isotopic signatures and local structural setting (Figs. 2 and 3), but they were emplaced under different geodynamic settings (subduction vs. post-subduction), and they are distinct with respect to their magma composition (Table 2).

Our results suggest that protracted magmatism is a key pre-requisite for PCD genesis, and that differences in geodynamic setting and magma chemistry may account for modulating deposit tonnage. Caricchi et al. (2014) argued that for a similar magma flux, the duration of magmatism is one of the key differences between barren and ore-bearing plutons, but their dataset only included small-volume, short-lived barren plutons (Lago della Vacca and Torres del Paine). Meanwhile, long-lived plutonic systems with variable magma chemistry and related to different geodynamic settings are either barren at the present-day erosion level (e.g., Tuolumne intrusive suite; Coleman et al., 2004) or host variably sized PCDs, including giant deposits (e.g., Bingham vs. Corrocohuayco vs. El Abra; e.g., von Quadt et al., 2011; Chelle Michou et al., 2014; Correa et al., 2016).

In the MOP, Cu-Mo deposits of variable size were all formed at the end of long-lived magmatic episodes with durations between 5.4 and 9.7 m.y. (Fig. 2a). Therefore, we propose

that while long-lived magmatism is required for PCD formation, the size of the PCDs may be modulated by the frequency of repeated injections of hot, hydrous, oxidized, S-rich, and Cu-rich mafic magmas that rejuvenate the upper crustal reservoir, allowing for the accumulation of sulfur, metals and volatiles in the upper crust (e.g., Hattori & Keith, 2001; Scaillet, 2010; AudŽtat & Simon, 2012; Tapster et al., 2016).

8. SUMMARY AND CONCLUSIONS

This study documents 30 m.y. of incremental pluton construction in the central Tethyan metallogenic belt emplaced during a subduction to post-subduction geodynamic evolution. New comprehensive zircon U-Pb combined with molybdenite Re-Os geochronology in the MOP clearly links Cu-Mo mineralization to the late stages of three successive long-lived (5 to 10 m.y.) intrusive episodes. According to this study, various geodynamic settings and magmas of variable composition can produce PCDs, but the exploration challenge remains in identifying single long-lived and incrementally assembled magmatic suites associated with prospective ore zones. We conclude that protracted incremental crustal scale magmatism is a key requirement for the formation of PCDs in fertile magmatic belts, and that the frequency of upper crustal reservoir rejuvenation by mafic magmas may play a fundamental role for modulating PCD tonnage.

REFERENCES

Aghazadeh, M., Hou, Z., Badrzadeh, Z., and Zhou, L., 2015, TemporalÐspatial distribution and tectonic setting of porphyry copper deposits in Iran: Constraints from zircon UÐPb and molybdenite ReÐOs geochronology: Ore Geology Reviews, v. 70, p.385-406.

Albarede, F., Telouk, P., Blichert-Toft, J., Boyet, M., Agranier, A., and Nelson, B., 2004, Precise and accurate isotopic measurements using multiple-collector ICPMS: Geochimica and Cosmochimica Acta v. 68, p. 2725-2744.

AudŽtat, A., and Simon, A.C., 2012, Magmatic controls on porphyry Cu genesis, in Hedenquist, J.W., Harris, M., and Camus, F., eds, Geology and Genesis of Major Copper Deposits and Districts of the World: A Tribute to Richard Sillitoe: Society of Economic Geologists, Special Publication 16, p. 553-572.

Bagdasaryan, G.P., Gukasyan, R.Kh., and Karamyan, K.A., 1969, Absolute dating of Armenian ore formations: International Geology Review, v. 11, p. 1166Ð1172.

Bindeman, I., 2008, Oxygen isotopes in mantle and crustal magmas as revealed by single crystal analysis: Reviews in Mineralogy and Geochemistry, v. 69, p. 445-478.

Black, L. P., Kamo, S. L., Allen, C. M., Davis, D., Aleinikoff, J. N., Valley, J. W., Mundil, R., Campbell, I. H., Korsch, R. J., Williams, I. S., and Foudoulis, C., 2004, Improved $^{206}Pb/^{238}U$

microprobe geochronology by the monitoring of a trace-element-related matrix effect; SHRIMP, ID-TIMS, ELA-ICP-MS and oxygen isotope documentation for a series of zircon standards: Chemical Geology, v. 205, p. 115-140.

Boekhout F., Spikings R., Sempere T., Chiaradia M., Ulianov A. and Schaltegger U., 2012, Mesozoic arc magmatism along the southern Peruvian margin during Gondwana breakup and dispersal: Lithos, v. 146, p. 48-64.

Bouvier, A., Vervoort, J. D., and Patchett, P. J., 2008, The LuEHf and SmENd isotopic composition of CHUR: Constraints from unequilibrated chondrites and implications for the bulk composition of terrestrial planets: Earth and Planetary Science Letters, v. 273, p. 48-57.

d'Abzac, F.-X., Czaja, A. D., Beard, B. L., Schauer, J. J., and Johnson, C. M., 2014, Iron Distribution in Size-Resolved Aerosols Generated by UV-Femtosecond Laser Ablation: Influence of Cell Geometry and Implications for In Situ Isotopic Determination by LA-MC-ICP-MS: Geostandards and Geoanalytical Research, v.38, p. 293-309.

Caricchi, L., Simpson, G., and Schaltegger, U., 2014, Zircons reveal magma fluxes in the Earthõs crust: Nature, v. 511, p. 457-461.

Chelle-Michou, C., Chiaradia, M., Ovtcharova, M., Ulianov, A., and Wotzlaw, J.F., 2014, Zircon petrochronology reveals the temporal link between porphyry systems and the magmatic evolution of their hidden plutonic roots (the Eocene Coroccohuayco deposit, Peru): Lithos, v. 198, p. 129-140.

Chiaradia, M., Schaltegger, U., Spikings, R., Wotzlaw, J.F., and Ovtcharova, M., 2013, How accurately can we date the duration of magmatic-hydrothermal events in porphyry systems? - An invited paper: Economic Geology, v. 108, p. 565-584.

Coleman, D.S., Gray, W., and Glazner, A.F., 2004. Rethinking the emplacement and evolution of zoned plutons: Geochronologic evidence for incremental assembly of the Tuolumne Intrusive Suite, California: Geology, v. 32, p. 433-436.

Correa, K.J., Rabbia, O.M., Hern‡ndez, L.B., Selby, D., and Astengo, M., 2016, The timing of magmatism and ore formation in the El Abra porphyry copper deposit, northern Chile: Implications for long-lived multiple-event magmatic-hydrothermal porphyry systems: Economic Geology, v. 111, p. 1-28.

Fisher, C. M., Hanchar, J. M., Samson, S. D., Dhuime, B., Blichert-Toft, J., Vervoort, J. D., and Lam, R., 2011, Synthetic zircon doped with hafnium and rare earth elements: A reference material for in situ hafnium isotope analysis: Chemical Geology, v. 286, p. 32-47.

Hattori, K.H., and Keith, J.D., 2001, Contribution of mafic melt to porphyry copper mineralization: evidence from Mount Pinatubo, Philippines, and Bingham Canyon, Utah, USA: Mineralium Deposita, v. 36, p.799-806.

Hou, Z.Q., Duan, L.F., Lu, Y.J., Zheng, Y.C., Zhu, D.C., Yang, Z.M., Yang, Z.S., Wang, B.D., Pei, Y.R., Zhao, Z.D., McCuaig, T.C., 2015a, Lithospheric architecture of the Lhasa Terrane and its control on ore deposits in the Himalayan-Tibetan orogeny: Economic Geology, v. 110, p. 1541-1575.

Hou, Z.Q., Yang, Z.M., Lu, Y.J., Kemp, A.I.S., Zheng, Y.C., Li, Q.Y., Tang, J.X., Yang, Z.S., and Duan, L.F., 2015b, A genetic linkage between subduction- and collision-related porphyry Cu deposits in continental collision zones: Geology, v. 43, p. 247Ð250.

Iizuka, T. and Hirata, T., 2005, Improvements of precision and accuracy in in situ Hf isotope microanalysis of zircon using the laser ablation-MC-ICPMS technique: Chemical Geology, v. 220, p. 121-137.

Jackson, S., 2008, LAMTRACE data reduction software for LA-ICP-MS. Laser ablation ICP-MS in the Earth sciences: Current practices and outstanding issues: Mineralogical Association of Canada, Short Course Series 40, p. 305-307.

Karamyan, K.A., Tayan, R.N., and Guyumdjyan, O.P., 1974, The main features of intrusion magmatism Zangezur region of the Armenian SSR: Izvestia of Academy of Sciences of Armenian SSR, Nauki o Zemle v. 1, p. 54-65, (in Russian)

Lackey, J.S., Valley, J.W., and Saleeby, J.B., 2005, Supracrustal input to magmas in the deep crust of Sierra Nevada batholith: evidence from high-$\delta^{18}O$ zircon: Earth and Planetary Science Letters, v. 235, p. 315-330.

Ludwig, K.R., 2008, UserÕs Manual for Isoplot 3.70: A geochronological toolkit for Microsoft Excel: Berkeley Geochronology Center, Special Publication 4, 77 p.

Miller, J.S., Matzel, J.P., Miller, C.F., Burgess, S.D., and Miller, R.B., 2007, Zircon growth and recycling during the assembly of large, composite arc plutons: Journal of Volcanology and Geothermal Research, v. 167, p. 282Ð299.

Moritz, R., Rezeau, H., Ovtcharova, M., Tayan, R., Melkonyan, R., Hovakimyan, S., Ramazanov V., Selby, D., Ulianov, A., Chiaradia, M., and Putlitz, B., 2016, Long-lived, stationary magmatism and pulsed porphyry systems during Tethyan subduction to post-collision evolution in the southernmost Lesser Caucasus, Armenia and Nakhitchevan: Gondwana Research, v. 37, p. 465-503.

Mouthereau, F., Lacombe, O., VergŽs, J., 2012, Building the Zagros collisional orogen: timing, strain distribution and the dynamics of Arabia/Eurasia plate convergence. Tectonophysics, v. 532, p. 27-60.

Patchett, P. J. and Tatsumoto, M., 1981, A routine high-precision method for Lu-Hf isotope geochemistry and chronology: Contributions to Mineralogy and Petrology, v.75, p. 263-267.

Pearce, N.J., Perkins, W.T., Westgate, J.A., Gorton, M.P., Jackson, S.E., Neal, C.R., and Chenery, S.P., 1997, A compilation of new and published major and trace element data for

NIST SRM610 and NIST SRM612 glass reference materials: Geostandards, Newsletter 21, p. 115Ð144.

Richards, J.P., 2015, Tectonic, magmatic, and metallogenic evolution of the Tethyan orogen: from subduction to collision: Ore Geology Reviews, v. 70, p. 323-345.

Rohrlach, B.D., and Loucks, R.R., 2005, Multi-million-year cyclic ramp-up of volatiles in a lower crustal magma reservoir trapped below the Tampakan copper-gold deposit by Mio-Pliocene crustal compression in the Southern Philippines, in Porter, T.M. ed, Super porphyry copper and gold deposits Ða global perspective: PGC Publishing, v. 2, p. 369-407.

Scaillet, B., 2010, Economic geology: Volatile destruction: Nature Geoscience, v.3, p. 456Ð457.

Selby, D., and Creaser, R.A., 2004, Macroscale NTIMS and microscale LA-MC-ICP-MS Re-Os isotopic analysis of molybdenite: Testing spatial restrictions for reliable Re-Os age determinations, and implications for the decoupling of Re and Os within molybdenite: Geochimica et Cosmochimica Acta, v. 68, p. 3897-3908.

Selby, D., Creaser, R.A., Stein, H. J., Markey, R. J., and Hannah, J. L., 2007, Assessment of the ^{187}Re decay constant accuracy and precision: Cross calibration of the ^{187}Re-^{187}Os molybdenite and U-Pb zircon chronometers: Geochimica et Cosmochimica Acta, v. 71, p.1999Ð2013.

Sillitoe, R.H., 2010, Porphyry copper systems: Economic Geology, v. 105, p. 3Ð41.

Simmonds, V. and Moazzen, M., 2015, ReÐOs dating of molybdenites from Oligocene CuÐMoÐAu mineralized veins in the Qarachilar area, Qaradagh batholith (northwest Iran): implications for understanding Cenozoic mineralization in South Armenia, Nakhichivan, and Iran. International Geology Review, v. 57, p. 290Ð304.

Sl‡ma, J., Košler, J., Condon, D. J., Crowley, J. L., Gerdes, A., Hanchar, J. M., Horstwood, M. S. A., Morris, G. A., Nasdala, L., Norberg, N., Schaltegger, U., Schoene, B., Tubrett, M. N., and Whitehouse, M. J., 2008, Plešovice zircon - A new natural reference material for UÐPb and Hf isotopic microanalysis: Chemical Geology, v.249, p. 1-35.

Smoliar, M.I., Walker, R.J., and Morgan, J.W., 1996, Re-Os isotope constraints on the age of Group IIA, IIIA, IVA, and IVB iron meteorites: Science, v. 271, p. 1099Ð1102.

Sšderlund, U., Patchett, P. J., Vervoort, J. D., and Isachsen, C. E., 2004, The 176Lu decay constant determined by LuÐHf and UÐPb isotope systematics of Precambrian mafic intrusions: Earth and Planetary Science Letters, v. 219, p. 311-324.

Tapster, S., Condon, D.J., Naden, J., Noble, S.R., Petterson, M.G., Roberts, N.M.W., Saunders, A.D., and Smith, D.J., 2016, Rapid thermal rejuvenation of high-crystallinity magma linked to porphyry copper deposit formation: evidence from the Koloula porphyry prospect, Solomon Islands: Earth and Planetary Science Letters, v. 442, p. 206-217.

Tayan, R.N., 1998, On central magma-ore controlling zone of the Zangezur ore region: Proceedings of the National Academy of Sciences of the Republic of Armenia, v. 51, p. 20-27, (in Russian with English abstract).

Thirlwall, M. F. and Anczkiewicz, R., 2004, Multidynamic isotope ratio analysis using MC-ICP-MS and the causes of secular drift in Hf, Nd and Pb isotope ratios: International Journal of Mass Spectrometry, v.235, p.59-81.

Ulianov A., Muntener O., Schaltegger U. and Bussy F., 2012, The data treatment dependent variability of U-Pb zircon ages obtained using mono-collector, sector field, laser ablation ICP-MS: Journal of Analytical Atomic Spectrometry, v.27, p. 663-676.

Von Quadt, A., Erni, M., Martinek, K., Moll, M., Peytcheva, I., and Heinrich, C.A., 2011, Zircon crystallization and the lifetimes of ore-forming magmatic-hydrothermal systems: Geology, v. 39, p. 731-734.

Woodhead, J. D. and Hergt, J. M., 2005, A Preliminary Appraisal of Seven Natural Zircon Reference Materials for In Situ Hf Isotope Determination: Geostandards and Geoanalytical Research, v. 29, p. 183-195.

Yuan, H. L., Gao, S., Dai, M. N., Zong, C. L., GÜnther, D., Fontaine, G. H., Liu, X. M., and Diwu, C., 2008, Simultaneous determinations of U-Pb age, Hf isotopes and trace element compositions of zircon by excimer laser-ablation quadrupole and multiple-collector ICP-MS: Chemical Geology, v. 247, p. 100-118.

APPENDIX

Appendix A: Analytical methods procedures

In situ U-Pb zircon dating by LA-ICP-MS

The thirty igneous rock samples selected for dating were initially crushed, milled to <0.3 mm and processed using a gravity separation Wilfley table, a Frantz magnetic separator and a density separation in diiodomethane liquid at 3.32 $g.mL^{-1}$. Zircon grains were handpicked under a binocular microscope, and subsequently mounted in epoxy and polished. Zircon grains textures were revealed by cathodoluminescence images using a scanning electron microscope JEOL JSM7001F and CamScan MV2300 at the Institute of Earth Sciences of the University of Geneva and Lausanne, respectively. ***In-situ*** U-Pb dating of zircon by laser ablation inductively coupled plasma mass spectrometry (LA-ICP-MS) was carried out using an UP-193FX excimer laser ablation system interfaced to an ELEMENT XR sector field, single-collector ICP mass spectrometer at the Institute of Earth Sciences of the University of Lausanne. The operating conditions of the ablation system included a spot size of 35 µm, a repetition rate of 5 Hz, and an on-sample energy density of ~3 J/cm^2 per pulse. The measurement protocol and details related to the mass spectrometer optimisation are outlined in Ulianov et al. (2012). A GJ-1 standard zircon with an ID-TIMS $^{206}Pb/^{238}U$ age of 600.5±0.4 Ma (Schaltegger et al., unpublished; in Boekhout et al., 2012) was used for the standardisation of the relative sensitivity factor. For the accuracy control, the Plešovice standard was employed (Sl‡ma et al., 2008). Raw intensity vs. time data were reduced in LAMTRACE (Jackson, 2008). Only homogeneous time resolved $^{206}Pb/^{238}U$ and $^{207}Pb/^{235}U$ spectra corresponding to one single isotope abundance ratio per ablation are reported in this study. Weighted mean ages and concordia diagrams were obtained using Isoplot (Ludwig, 2008).

The mean age (i.e. crystallization age) is calculated from all concordant zircon population (Fig. 2a; Table 1 and Supplementary Table B.1). Reported errors (2 SD) in Figure 2a are named ÒinternalÓand ÒexternalÓerrors. Based on the probability density estimate curve and the mean square weighted deviation (MSWD), some samples exhibit subpopulations (Fig. 3a, samples n¡1, 13, 14, 15, 17, 21, 23, 27, 28 and 30; Supplementary Table B.1), and we only considered the younger subpopulation to represent the crystallization age, the older subpopulation interpreted as antecrystic or inherited zircons for adjacent rocks (Miller et al., 2007). The ÒinternalÓ error corresponds to the analytical uncertainties from the sample measurement, while the ÒexternalÓ error includes the propagation of analytical uncertainties from the sample measurement and the reproducibility of the measurements on the primary standard GJ-1 (Supplementary Figure A.1).

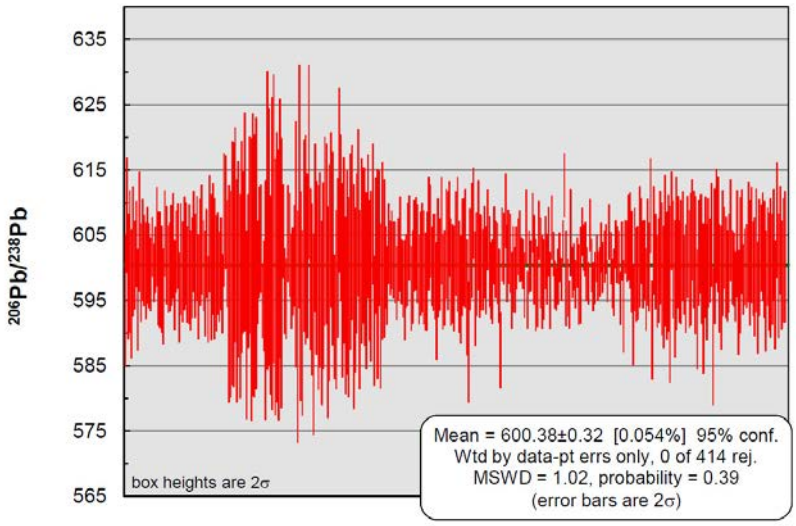

Supplementary Figure A.1: Reproducibility of the GJ1 standard including all analytical sessions carried out over 18 months.

Re-Os isotopes in molybdenite

Samples for Re-Os dating in molybdenite were selected from various Cu-Mo porphyry deposits throughout the Meghri-Ordubad pluton (Figs 2a and 3; Supplementary Table B.2). Sample RO280-2_N2 corresponds to a stockwork-like veinlet mainly filled by quartz-chalcopyrite-molybdenite from Agarak deposit, whereas samples RO812-3_Ankaser_N72p and RO812-7_Aigedzor_NRM-0560 were selected from quartz-molybdenite stockwork-like veinlets from Hanqasar and Aygedzor, respectively. Six samples from quartz-molybdenite (RO280-1_NI) and quartz-chalcopyrite-molybdenite (RO758-5_KJ1509, RO596-2_KJ-13-25A, RO612-10_KJ-13-25A, RO391-2_KJ-10-13A, and RO758-6_KJ15X1) stockwork-like veinlets were collected from the giant Kadjaran Cu-Mo deposit (Supplementary Table B.2). Grain size of molybdenite varies from 500µm to 2 mm.

Analyses were performed in the Laboratory for Sulfide and Source Rock Geochronology and Geochemistry in the Durham Geochemistry Center at the University of Durham (UK). The complete analytical procedure for Re-Os determinations is described in Selby and Creaser (2004) and Selby et al. (2007), and it is briefly described below. Molybdenite samples were dissolved and equilibrated with a known amount of ^{185}Re and isotopically normal Os in inverse aqua-regia (2:1 16 N HNO_3 and 12 N HCl, 3 mL) at 240¡C for 24 h in a Carius tube. Rhenium and Os were isolated and purified by solvent extraction, microdistillation, and anion exchange chromatography, and analyzed by negative thermal ionization mass spectrometry (N-TIMS) on a Fisher Scientific TRITON mass spectrometer using Faraday collectors. Total procedural blanks for Re and Os, are 2.2 ± 0.5 pg and 0.1 ± 0.03 pg, respectively, with an ^{187}Os/^{188}Os blank composition of 0.24 ± 0.05 (n = 3). Rhenium and Os

concentrations and Re-Os molybdenite date uncertainties are presented at the 2σ level, which includes the uncertainties in Re and Os mass spectrometer measurement, spike and standard Re and Os isotope compositions, and calibration uncertainties of ^{185}Re and ^{187}Os. Because a mixed ^{185}Re and Os tracer solution is used, uncertainties in weights of sample and tracer solution do not affect the calculated age, and are not considered. However, sample and tracer solution weight uncertainties are considered in determining the uncertainty in the Re and ^{187}Os concentrations. Uncertainty with and without the ^{187}Re decay constant (Smoliar et al., 1996; Selby et al., 2007) is also considered (Supplementary Table B.2).

In situ zircon Hf isotope analyses

Hf isotope analyses were carried out at the University of Geneva on a Teledyne - Photon Machines ÒAnalyte G2Ólaser system equipped with a two volume ÒHelEx-2Óablation cell (d'Abzac et al. 2014) and coupled to a Thermo Ç Neptune Plus È MC-ICP-MS. Ablation was performed over 35 µm spots at a fluence of ~6J.cm-2 and a repetition rate of 5Hz. Ablated particles were carried through a ~1.5 m PTFE tubing using a ~0.6 L.min-1 He gas flow (99.999% purity) and mixed with ~2.4 mL.min-1 N2 and ~1 L.min-1 Ar before entering the plasma torch. Measurements were performed at low mass resolution (~450) over 120 × 1s cycles using the following cup configuration: ^{171}Yb (L4), ^{173}Yb (L3), ^{174}(Yb+Hf) (L2), ^{175}Lu (L1), ^{176}(Hf+Yb+Lu) (C), ^{177}Hf (H1), ^{178}(Hf+Ta) (H2), ^{179}Hf (H3), ^{181}Ta (H4). Blanks were acquired following the same method as samples, without ablation, every ca. 10 analyses. Reference zircons Plešovice (Sl‡ma et al., 2008) and Temora-2 (Woodhead and Hergt, 2005) were measured after every 5 to 8 unknowns. Plešovice and Temora-2 zircons reach respective 0.282479±0.000027 (n=89) and 0.282670±0.000036 (n=98) over 10 months and 6 measurements sessions (see details in Table B.3). These values show a slight offset from the reference values to which the sample data are normalized. Instrument tuning is then performed so that this offset is (i) as small as possible (<1 εHf) and (ii) similar within uncertainty for all the different reference materials used (Supplementary Table B.3). This insures that the correction is accurately made for various trace elements concentrations potentially generating oxide species in the ICP torch and for different amounts of ^{176}Yb that need to be corrected (see below).

Data reduction was conducted after acquisition by proceeding to a blank subtraction, removing the isobaric interference of ^{176}Lu and ^{176}Yb on mass 176 (e.g. Fisher et al., 2011) and correcting the resulting ^{176}Hf/^{177}Hf ratio for mass bias using an exponential law (Albarede et al., 2004) (Supplementary Table B.3). The mass bias coefficients βYb and βHf were calculated from the measured ^{173}Yb/^{171}Yb and ^{179}Hf/^{177}Hf with the reference values ^{173}Yb/^{171}Yb=1.1234 (Thirlwall and Anczkiewicz, 2004) and ^{179}Hf/^{177}Hf=0.7325 (Patchett and Tatsumoto, 1981)

respectively. We used βYb to correct for Lu mass bias (Yuan et al., 2008) and the ^{176}Lu interference was corrected using ^{176}Lu/^{175}Lu=0.02645 (Thirlwall and Anczkiewicz, 2004). The isobaric interference of 176Yb is potentially high in zircons and was evaluated using ^{176}Yb/^{173}Yb=0.786954 (Thirlwall and Anczkiewicz, 2004). Correction for ^{176}Hf in-growth due to ^{176}Lu β--decay has been calculated (Iizuka and Hirata, 2005) using λ^{176}Lu=1.87×10-11 year-1 (Sš derlund et al., 2004) and the age determined in this study by U-Pb dating on zircon. The data are expressed as εHf units following:

$$\varepsilon Hf = [(^{176}Hf \acute{U}^{177}Hf)_{measured} / (^{176}Hf \acute{U}^{177}Hf)_{CHUR} - 1] \times 10000,$$

with the reference ÒCHURÓvalue of 0.282785 is taken from Bouvier et al. (2008).

3.4 In situ zircon O isotope analyses

Oxygen isotopes measurements were carried out on a different zircon sample set than those used for LA-ICPMS U-Pb zircon dating but their cathodoluminescence patterns are very consistent from one zircon sample set to another from the same crushed sample. The U-Pb weighted mean dates are considered to be representative enough to accurately trace the source evolution over 30 Ma.

Sample preparation and secondary ion mass spectrometry (SIMS) were carried out at the Canadian Centre for Isotopic Microanalysis (CCIM) at the University of Alberta. Polished zircon mid-sections of unknowns and zircon reference materials were exposed within a 25 mm diameter epoxy mount (M1323) using diamond grits. The mount was cleaned with a lab soap solution, and de-ionized H_2O. Prior to scanning electron microscopy (SEM), the mount was coated with 5 nm of high-purity Au. SEM characterization was carried out with a Zeiss EVO MA15 instrument equipped with a high-sensitivity, broadband cathodoluminescence (CL) detector. Beam conditions were 15kV and 2 nA sample current. A further 25 nm of Au was subsequently deposited on the mount prior to SIMS analysis.

Oxygen isotopes (^{18}O, ^{16}O) in zircon were analyzed using a Cameca IMS 1280 multicollector ion microprobe. A ^{133}Cs+ primary beam was operated with impact energy of 20 keV and beam current of ~ 2.5 nA. The ~12 μm diameter probe was rastered (18 x 18 μm) for 75 s prior to acquisition, and then 5 x 5 μm during acquisition, forming rectangular analyzed areas ~15 x 18 μm across and ~2 μm deep. The normal incidence electron gun was utilized for charge compensation. Negative secondary ions were extracted through 10 kV into the secondary (Transfer) column. Transfer conditions included a 122 μm entrance slit, a 5 x 5 mm pre-ESA (field) aperture, and 100x sample magnification at the field aperture, transmitting all regions of the sputtered area. No energy filtering was employed. The mass/charge separated

oxygen ions were detected simultaneously in Faraday cups LÕ2 (^{16}O-) and HÕ2 (^{18}O-) at mass resolutions (m/Δm at 10%) of 1950 and 2250, respectively. Secondary ion count rates for ^{16}O- and ^{18}O- were typically ~2.5 x 109 and 5 x 106 counts/s utilizing 1010 Ω and 1011 Ω amplifier circuits, respectively. Faraday cup baselines were measured at the start of the analytical session. A single analysis took 250 s, including pre-analysis rastering, automated secondary ion tuning, and 75 s of continuous peak counting.

Instrumental mass fractionation (IMF) was monitored by repeated analysis of a zircon primary reference material (RM), S0081 (UAMT1) with δ18O VSMOW = +4.87 (R. Stern, unpublished laser fluorination data from Ilya Bindeman, University of Oregon) and a secondary zircon RM, S0022 (TEM2) zircon with δ^{18}O VSMOW = +8.2 ä (Black et al., 2004). One analysis of the primary and secondary RM was taken after every 4 and 12 unknowns, respectively. Spot analyses of unknowns totalled 280 (Supplementary Table B.4). The data set of ^{18}O-/^{16}O- for S0081 zircon for each of two analytical sessions (N = 45, 51) was processed collectively for each session, yielding standard deviations of 0.10ä and 0.07ä , following correction for systematic within-session drift (≤0.4 ä). Overall IMF was +1.1 ä for both sessions. The individual spot uncertainties at 95% confidence for δ^{18}OVSMOW reported include errors relating to within-spot counting statistics, between-spot (geometric) effects, and correction for instrumental mass fractionation, and average ± 0.19 ä . Results for multiple spots on multiple grains of the secondary RM, S0022, gave session mean values for δ^{18}OVSMOW = +8.20 ±0.04 (MSWD = 0.79; N = 18, standard deviation = 0.08ä) and +8.19 ±0.05 (MSWD = 0.56; N = 15, standard deviation = 0.07ä).

Appendix B:

Supplementary Table B.1: Results of in situ LA-ICP-MS U-Pb dating. Shaded area indicates zircons used to calculate the weighted mean age for each individual sample.

Analysis (n=601)	Dates (Ma)				Isotopic ratios							
AG1304A (n°1 in Fig. 2)	**$^{206}Pb/^{238}U$**	**± 2 SD**	**$^{207}Pb/^{235}U$**	**± 2 SD**	**$^{206}Pb/^{238}U$**	**± SD %**	**$^{207}Pb/^{235}U$**	**± SD %**	**$^{207}Pb/^{206}Pb$**	**± SD %**	**Corr. Coef.**	**Comment**
de11f06	47.6	1.4	55.3	5.3	0.0074	1.46	0.0544	5.54	0.05335	5.34	0.2637	
de11f08	48	1.5	54.4	5.6	0.0075	1.53	0.0537	5.86	0.05193	5.66	0.2610	
de11e09	48.6	1.1	52.9	5.2	0.0076	1.17	0.0538	5.23	0.05141	5.1	0.2236	
de11f07	49	1.6	52	5.4	0.0076	1.59	0.0512	5.73	0.04884	5.5	0.2777	
de11f09	49.1	0.9	51.6	3.1	0.0077	0.88	0.0531	3.31	0.05002	3.19	0.2659	
de11f10	49.1	0.8	52.8	3.5	0.0077	0.78	0.0558	3.70	0.0526	3.62	0.2106	
de11e11	49.2	0.9	47.7	3.8	0.0077	0.94	0.0487	4.36	0.04591	4.26	0.2155	
de11f14	49.3	1.2	51.5	5.2	0.0077	1.2	0.0530	4.91	0.04994	4.76	0.2445	
de11e14	49.4	1.2	56.5	5.3	0.0077	1.19	0.0569	5.01	0.05363	4.87	0.2374	
de11e10	50.1	1.2	55.9	4.7	0.0078	1.17	0.0570	4.81	0.05304	4.67	0.2430	antecryst
de11e13	50.1	1.1	47.3	5	0.0078	1.06	0.0474	5.28	0.04406	5.17	0.2009	antecryst
de11f11	50.2	0.6	48.9	1.6	0.0078	0.61	0.0509	1.62	0.04734	1.5	0.3767	antecryst
de11f13	50.5	0.7	48.6	2.3	0.0079	0.7	0.0515	2.35	0.04727	2.24	0.2983	antecryst
Mean (n=9)	**48.94**	**0.36**										
2 SD propagated		**0.60**										

MA1501 (n°2 in Fig. 2)	**$^{206}Pb/^{238}U$**	**± 2 SD**	**$^{207}Pb/^{235}U$**	**± 2 SD**	**$^{206}Pb/^{238}U$**	**± SD %**	**$^{207}Pb/^{235}U$**	**± SD %**	**$^{207}Pb/^{206}Pb$**	**± SD %**	**Corr. Coef.**	**Comment**
jl10h11	46.4	2.1	47.9	4.4	0.0072	2.32	0.0481	6.13	0.04848	5.67	0.3787	
jl09k09	46.7	1.3	47.4	3.3	0.0073	1.39	0.0472	3.82	0.04687	3.56	0.3637	
jl09l12	46.7	1.2	48.7	4.7	0.0073	1.3	0.0493	5.05	0.049	4.88	0.2574	
jl09l11	46.9	2.3	45.8	3.9	0.0073	2.42	0.0460	5.25	0.04577	4.66	0.4609	

jl09l13	47.2	1.1	46.7	4.6	0.0074	1.17	0.0481	4.98	0.04714	4.84	0.2350
jl10h10	47.2	1.6	49.1	5.2	0.0074	1.69	0.0513	5.19	0.05035	4.91	0.3255
jl09k07	47.4	1.4	49.1	4.1	0.0074	1.47	0.0503	4.60	0.04932	4.36	0.3195
jl09l09	47.4	1.1	49	3.8	0.0074	1.13	0.0498	4.40	0.04884	4.25	0.2570
jl09k10	47.6	1.4	48.1	4.2	0.0074	1.51	0.0483	4.84	0.0474	4.6	0.3119
jl09k12	47.6	1.7	48.8	4.4	0.0074	1.79	0.0489	5.34	0.04795	5.03	0.3353
jl09l05	47.6	1.9	47.6	6	0.0074	1.99	0.0485	6.38	0.04759	6.06	0.3120
jl09k08	47.7	1.7	47.1	3.5	0.0074	1.77	0.0481	4.44	0.04719	4.07	0.3988
jl09l07	47.7	1.2	45.8	3.2	0.0074	1.29	0.0459	3.98	0.04499	3.76	0.3245
jl09l08	47.7	1.3	50.6	3.8	0.0074	1.39	0.0508	4.01	0.04981	3.76	0.3467
jl09l06	47.8	1.2	48.2	3.2	0.0074	1.28	0.0482	4.15	0.04723	3.95	0.3083
jl09k11	47.9	1.1	50.1	3.6	0.0075	1.19	0.0515	3.91	0.04984	3.72	0.3047
jl09k06	48	1.9	48.7	3.4	0.0075	1.99	0.0501	3.71	0.04851	3.13	0.5365
jl10h12	48	2.4	53.1	6.8	0.0075	2.52	0.0544	6.62	0.05263	6.12	0.3807
jl10h14	48	1.4	49.1	5.2	0.0075	1.46	0.0502	5.59	0.04859	5.4	0.2610
jl10h13	48.1	1.2	45.5	3.5	0.0075	1.29	0.0466	4.09	0.04508	3.88	0.3155
jl09l10	48.2	1.9	48	3.1	0.0075	2.02	0.0488	3.84	0.04721	3.27	0.5255
jl09k13	48.9	1.4	43.7	3.2	0.0076	1.46	0.0450	4.28	0.04292	4.02	0.3414
Mean (n=22)	**47.58**	**0.3**									
2 SD propagated		**0.61**									

AG1401 (n°3 in Fig. 2)	**$^{206}Pb/^{238}U$**	**± 2 SD**	**$^{207}Pb/^{235}U$**	**± 2 SD**	**$^{206}Pb/^{238}U$**	**± SD %**	**$^{207}Pb/^{235}U$**	**± SD %**	**$^{207}Pb/^{206}Pb$**	**± SD %**	**Corr. Coef.**	**Comment**
de10a08	44.7	0.9	48.7	9.5	0.007	1.04	0.0499	10.87	0.05176	10.82	0.0957	
de10b05	44.9	1	46	3.4	0.007	1.13	0.0469	4.16	0.04865	4	0.2719	
de10a09	45.1	1	45.3	3.4	0.007	1.11	0.0458	4.25	0.04749	4.1	0.2613	
de10a12	45.6	1.3	45.3	6.2	0.0071	1.39	0.0460	6.52	0.04701	6.37	0.2132	
de10b07	45.7	1.4	43.5	5.9	0.0071	1.56	0.0435	6.36	0.04448	6.17	0.2451	
de10a10	45.9	1.2	48.3	6.9	0.0072	1.36	0.0502	7.20	0.05062	7.07	0.1889	
de10a13	45.9	1.2	42.1	5.4	0.0072	1.34	0.0433	6.74	0.04364	6.61	0.1987	

de10b06	45.9	1.1	49.8	11	0.0071	1.18	0.0505	8.38	0.05156	8.3	0.1408	
de10a07	46	1.1	42.5	4.4	0.0072	1.18	0.0443	5.34	0.0446	5.21	0.2209	
de10a06	46.1	1.3	37.3	7.1	0.0072	1.39	0.0380	9.62	0.03826	9.52	0.1445	
de10b09	46.1	1.2	45.7	2.9	0.0072	1.35	0.0465	3.56	0.04687	3.29	0.3796	
de10b12	46.1	1.4	46.9	4.7	0.0072	1.58	0.0481	4.95	0.04845	4.69	0.3193	
de10a11	46.3	0.8	45.3	3.5	0.0072	0.86	0.0473	4.69	0.04765	4.61	0.1834	
de10a14	46.3	0.9	43.6	2.9	0.0072	0.93	0.0449	3.69	0.04525	3.57	0.2521	
de10b08	46.6	1.2	44.3	3.9	0.0073	1.31	0.0455	4.68	0.04527	4.49	0.2801	
de10b10	46.6	1.2	44.6	3.6	0.0072	1.25	0.0467	4.06	0.04708	3.86	0.3081	
de10b14	46.8	2	48	3.6	0.0073	2.11	0.0489	4.31	0.04864	3.76	0.4894	
de10b13	46.9	1.4	47.5	4	0.0073	1.52	0.0478	4.54	0.04754	4.28	0.3347	
de10b11	47.2	1.2	45.8	3.8	0.0073	1.27	0.0468	4.56	0.04656	4.38	0.2785	
Mean (n=19)	**45.94**	**0.33**										
2 SD propagated		**0.91**										

AG1404 (n°4 in Fig. 2)	**$^{206}Pb/^{238}U$**	**± 2 SD**	**$^{207}Pb/^{235}U$**	**± 2 SD**	**$^{206}Pb/^{238}U$**	**± SD %**	**$^{207}Pb/^{235}U$**	**± SD %**	**$^{207}Pb/^{206}Pb$**	**± SD %**	**Corr. Coef.**	**Comment**
de10d05	43.2	2	47.8	7.5	0.0067	2.37	0.0470	7.40	0.05086	7.01	0.3203	
de10d09	43.2	1.8	62.6	29.1	0.0067	2.12	0.0633	15.60	0.06857	15.46	0.1359	
de10c11	43.7	4.7	42.3	11.3	0.0068	5.38	0.0416	14.32	0.04441	13.27	0.3757	
de10d11	43.8	1.9	49.8	7.1	0.0068	2.21	0.0499	7.91	0.05321	7.59	0.2796	
de11n05	43.8	1.2	44.1	5.4	0.0068	1.4	0.0437	6.33	0.04662	6.17	0.2213	
de10c14	43.9	3.7	45	8	0.0068	4.22	0.0442	10.05	0.04718	9.12	0.4199	
de11n08	44.2	1.5	53.9	10	0.0069	1.68	0.0543	10.44	0.05708	10.3	0.1610	
de11n07	44.3	1.4	45	5.9	0.0069	1.58	0.0453	7.37	0.04765	7.2	0.2143	
de10d14	44.4	1.4	42.9	6.2	0.0069	1.53	0.0428	7.38	0.04502	7.22	0.2073	
de10d08	44.5	2.7	46.6	8.7	0.0069	3	0.0461	9.81	0.0485	9.34	0.3058	
de10d13	44.7	1.5	47.4	6.8	0.007	1.73	0.0470	7.67	0.04873	7.47	0.2256	
de10c09	44.8	3.2	44	10.1	0.007	3.56	0.0448	11.50	0.04646	10.94	0.3094	
de11n11	45.3	1.8	40.8	6.4	0.0071	1.98	0.0423	8.49	0.0432	8.26	0.2331	
de11n12	45.4	1.3	43.9	5.7	0.0071	1.42	0.0441	6.92	0.04511	6.77	0.2053	
de10d12	45.5	2	39.2	6.1	0.0071	2.17	0.0392	8.43	0.04008	8.15	0.2573	
de10c10	45.6	3	56.4	22.2	0.0071	3.29	0.0547	31.96	0.05587	31.79	0.1029	
de10d06	45.6	1.8	41.5	7.5	0.0071	1.95	0.0415	10.43	0.04238	10.25	0.1869	
de11n10	45.7	1.8	45.1	6	0.0071	1.93	0.0451	7.59	0.04614	7.34	0.2543	

de11n06	46.3	1.9	46.9	7.9	0.0072	2.11	0.0465	9.35	0.04686	9.11	0.2256	
de10c05	46.4	4.4	44.4	19.4	0.0072	4.78	0.0431	31.18	0.04347	30.81	0.1533	
de10c08	46.4	4.9	41.1	9.6	0.0072	5.26	0.0379	12.71	0.03823	11.57	0.4139	
de11n14	46.4	3	43.5	7.5	0.0072	3.24	0.0423	10.87	0.04266	10.38	0.2980	
de10c07	46.5	3.6	33.7	13.8	0.0072	3.89	0.0335	30.26	0.03377	30.01	0.1285	
de11n13	47.4	1.9	48.2	6.6	0.0074	2	0.0491	6.65	0.04819	6.34	0.3008	
Mean (n=24)	**44.82**	**0.45**										
2 SD propagated		**0.94**										

VK1403 (n°5 in Fig. 2)	**$^{206}Pb/^{238}U$**	**± 2 SD**	**$^{207}Pb/^{235}U$**	**± 2 SD**	**$^{206}Pb/^{238}U$**	**± SD %**	**$^{207}Pb/^{235}U$**	**± SD %**	**$^{207}Pb/^{206}Pb$**	**± SD %**	**Corr. Coef.**	**Comment**
de12n07	42.2	2.3	50.4	9.2	0.0066	2.7	0.0486	9.95	0.05343	9.58	0.2713	
de12o11	43.1	2.3	49.8	11	0.0067	2.63	0.0486	12.71	0.05263	12.44	0.2068	
de12o08	43.3	1.8	44.2	5.8	0.0067	2.05	0.0427	7.19	0.04626	6.89	0.2852	
de12n13	43.4	2	45.3	7.2	0.0068	2.26	0.0445	9.11	0.04752	8.83	0.2480	
de12o12	43.7	2.3	44.9	9.4	0.0068	2.62	0.0440	10.75	0.04698	10.43	0.2436	
de12o14	44	1.8	42.7	8.6	0.0069	2.01	0.0420	10.17	0.04413	9.97	0.1976	
de12o07	44.3	1.3	45.5	5.6	0.0069	1.52	0.0448	6.21	0.04706	6.02	0.2448	
de12n06	44.3	2.4	54.7	18	0.0069	2.75	0.0554	11.12	0.05827	10.77	0.2474	
de12o05	44.4	1.6	44.2	6.1	0.0069	1.82	0.0446	7.05	0.04689	6.81	0.2582	
de12n09	44.5	2.7	46.1	6.4	0.0069	2.99	0.0452	7.66	0.0475	7.05	0.3904	
de12o09	44.8	1.8	53.7	11.6	0.007	1.96	0.0530	15.26	0.05489	15.13	0.1285	
de12n10	44.8	1.5	41.5	5.8	0.007	1.72	0.0410	6.67	0.04255	6.44	0.2580	
de12o06	44.9	2	39.6	9.2	0.007	2.25	0.0395	13.09	0.04098	12.9	0.1718	
de12n12	44.9	1.6	42.5	6.8	0.007	1.76	0.0418	8.14	0.04336	7.95	0.2162	
de12o10	45	1.8	38.8	5.7	0.007	2.05	0.0384	7.46	0.03977	7.17	0.2749	
de12n05	45	2.6	49.2	8.1	0.007	2.91	0.0483	8.58	0.05004	8.07	0.3392	
de12n14	45.4	1.6	45.5	7.7	0.0071	1.79	0.0447	8.25	0.04565	8.05	0.2171	
Mean (n=17)	**44.34**	**0.44**										
2 SD propagated		**0.70**										

AG1403 (n°6 in Fig. 2)	**$^{206}Pb/^{238}U$**	**± 2 SD**	**$^{207}Pb/^{235}U$**	**± 2 SD**	**$^{206}Pb/^{238}U$**	**± SD %**	**$^{207}Pb/^{235}U$**	**± SD %**	**$^{207}Pb/^{206}Pb$**	**± SD %**	**Corr. Coef.**	**Comment**
de10i05	43.5	2.8	38.2	4.9	0.0068	3.22	0.0387	7.42	0.04134	6.69	0.4337	
de10i06	44.4	2.6	32	11.9	0.0069	2.91	0.0324	19.80	0.03404	19.59	0.1469	

de10i07	43	2.4	48.9	8.2	0.0067	2.83	0.0491	9.12	0.05313	8.67	0.3103
de10i08	44.2	2.7	53	14.1	0.0069	3.06	0.0515	14.95	0.05418	14.63	0.2047
de10i09	43.3	2.3	55.2	15.5	0.0067	2.64	0.0554	20.24	0.05999	20.07	0.1304
de10i10	44	2.1	46.3	6.9	0.0068	2.36	0.0462	7.83	0.04934	7.47	0.3013
de10i11	44.2	2.5	42	8.4	0.0069	2.83	0.0425	9.49	0.04467	9.06	0.2982
de10i12	44.4	2.4	44.9	8.1	0.0069	2.69	0.0452	12.32	0.04752	12.02	0.2184
de10i13	44.1	3.4	54.3	58.9	0.0069	3.89	0.0538	25.10	0.05657	24.8	0.1550
de10i14	45.2	3.1	47.2	9.8	0.007	3.46	0.0473	10.23	0.04904	9.63	0.3381
de10j05	44	3.4	46.6	10.2	0.0068	3.94	0.0470	11.99	0.05015	11.32	0.3287
de10j06	43.6	3.5	39.2	9.3	0.0068	4	0.0387	11.37	0.04133	10.64	0.3519
de10j07	45.5	2.5	53	24.6	0.0071	2.79	0.0533	14.92	0.05442	14.66	0.1870
de10j08	43.9	2.6	56.4	14.9	0.0068	2.95	0.0568	10.52	0.06066	10.1	0.2804
de10j09	43.9	2.7	40.7	9.2	0.0068	3.12	0.0406	10.61	0.04337	10.14	0.2941
de10j10	44.9	2.9	45.3	10.9	0.007	3.23	0.0457	11.68	0.04737	11.22	0.2766
de10j12	43.1	3.1	37	10.5	0.0067	3.58	0.0364	16.79	0.03941	16.4	0.2133
de10j13	45.8	2.9	40.6	10.3	0.0071	3.18	0.0397	14.36	0.04054	14	0.2215
Mean (n=18)	**44.14**	**0.62**									
2 SD propagated		**1.02**									

AG1406 (n°7 in Fig. 2)	**$^{206}Pb/^{238}U$**	**± 2 SD**	**$^{207}Pb/^{235}U$**	**± 2 SD**	**$^{206}Pb/^{238}U$**	**± SD %**	**$^{207}Pb/^{235}U$**	**± SD %**	**$^{207}Pb/^{206}Pb$**	**± SD %**	**Corr. Coef.**	**Comment**
de10e14	43	1.7	51.2	13.6	0.0067	2.04	0.0515	20.06	0.05574	19.96	0.1017	
de10f10	43.1	1.5	40.3	8.1	0.0067	1.73	0.0399	10.22	0.04326	10.07	0.1693	
de10f14	43.1	1.7	55.7	30	0.0067	2	0.0547	26.28	0.05928	26.2	0.0761	
de10e06	43.2	1.7	53.7	26.8	0.0067	1.96	0.0549	21.25	0.05942	21.16	0.0922	
de10f11	43.2	1.5	40.4	8	0.0067	1.72	0.0401	9.86	0.04347	9.71	0.1744	
de10f09	43.4	2	48.8	8.8	0.0068	2.35	0.0488	9.23	0.05207	8.93	0.2545	
de10f12	43.4	1.9	48.7	10.2	0.0068	2.17	0.0493	12.65	0.05258	12.46	0.1716	
de10e12	43.5	1.5	46	7	0.0068	1.75	0.0462	8.94	0.0493	8.77	0.1957	
de10f05	43.8	1.4	61.6	14.2	0.0068	1.55	0.0623	13.27	0.06643	13.18	0.1168	
de10e07	44	1.6	43.8	12.8	0.0068	1.88	0.0430	15.60	0.04593	15.49	0.1205	
de10e09	44	1.5	42.6	6	0.0069	1.74	0.0433	7.25	0.0455	7.04	0.2399	
de10e11	44.1	1.6	35.9	12.2	0.0069	1.8	0.0356	15.08	0.03748	14.97	0.1194	
de10e05	44.2	1.3	59.7	15.4	0.0069	1.49	0.0608	16.07	0.06393	16	0.0927	
de10f13	44.5	2	54.7	8.3	0.0069	2.27	0.0540	8.34	0.05674	8.03	0.2720	

de10e10	45.1	1.7	53.5	17	0.007	1.84	0.0543	21.30	0.0563	21.22	0.0864	
de10f07	45.2	1.6	54	15.4	0.007	1.79	0.0537	14.10	0.05569	13.99	0.1269	
de10e08	45.3	2	44.2	19.1	0.007	2.22	0.0444	19.47	0.04602	19.34	0.1140	
de10f08	45.7	1.8	52	14.6	0.0071	1.94	0.0518	13.36	0.05296	13.22	0.1452	
Mean (n=18)	**43.95**	**0.38**										
2 SD propagated		**0.89**										

AG1402 (n°8 in Fig. 2)	**$^{206}Pb/^{238}U$**	**± 2 SD**	**$^{207}Pb/^{235}U$**	**± 2 SD**	**$^{206}Pb/^{238}U$**	**± SD %**	**$^{207}Pb/^{235}U$**	**± SD %**	**$^{207}Pb/^{206}Pb$**	**± SD %**	**Corr. Coef.**	**Comment**
de11d09	41.9	1.4	45.9	7	0.0065	1.67	0.0453	8.22	0.05062	8.05	0.2031	
de11c09	42.2	1.6	42	8.7	0.0066	1.87	0.0407	10.95	0.04471	10.79	0.1708	
de11c11	43.2	1.1	58.5	13.2	0.0067	1.27	0.0575	11.85	0.06222	11.78	0.1072	
de11d10	43.4	1.3	49.3	8.8	0.0068	1.46	0.0498	9.38	0.05313	9.27	0.1556	
de11d12	43.4	1.6	45	7.6	0.0068	1.89	0.0452	9.04	0.04826	8.84	0.2091	
de11c06	43.7	1.4	44.6	7.2	0.0068	1.56	0.0448	8.65	0.0478	8.51	0.1803	
de11d11	43.7	1.5	42	6.1	0.0068	1.69	0.0420	7.59	0.04477	7.4	0.2226	
de11c13	44.1	1.6	47.9	8.4	0.0069	1.82	0.0489	9.41	0.05144	9.23	0.1935	
de11d06	44.1	1.5	46.6	5.5	0.0069	1.75	0.0473	6.61	0.04975	6.37	0.2649	
de11d08	44.1	1.4	40.3	8.3	0.0069	1.61	0.0401	10.09	0.04212	9.96	0.1596	
de11c07	44.3	1.2	51.8	7.1	0.0069	1.4	0.0515	6.81	0.05415	6.66	0.2057	
de11c08	44.3	1.3	53.2	10.7	0.0069	1.5	0.0536	11.05	0.05638	10.95	0.1357	
de11c12	44.4	1.2	53.8	16.9	0.0069	1.37	0.0521	21.64	0.05479	21.6	0.0633	
de11c10	44.5	1.5	50.7	7.3	0.0069	1.74	0.0505	8.41	0.05314	8.23	0.2068	
de11d07	44.6	1.4	38.5	6.6	0.0069	1.56	0.0381	9.23	0.04008	9.1	0.1690	
de11d05	44.7	1.8	40	7.3	0.007	1.97	0.0408	10.40	0.0423	10.21	0.1895	
de11d13	45	1.7	42.7	6.4	0.007	1.84	0.0420	8.30	0.0435	8.09	0.2218	
Mean (n=17)	**43.83**	**0.42**										
2 SD propagated		**0.62**										

HQ1402 (n°9 in Fig. 2)	**$^{206}Pb/^{238}U$**	**± 2 SD**	**$^{207}Pb/^{235}U$**	**± 2 SD**	**$^{206}Pb/^{238}U$**	**± SD %**	**$^{207}Pb/^{235}U$**	**± SD %**	**$^{207}Pb/^{206}Pb$**	**± SD %**	**Corr. Coef.**	**Comment**
de11g05	41.6	1.2	42.8	5.4	0.0065	1.46	0.0432	6.21	0.04819	6.04	0.2350	
de11h08	42.3	1	43.6	3.2	0.0066	1.22	0.0439	3.88	0.04824	3.68	0.3147	
de11h06	42.4	0.6	44.4	3.9	0.0066	0.77	0.0453	4.51	0.04978	4.44	0.1709	
de11g08	42.5	0.9	47.2	5.5	0.0066	1.03	0.0469	6.11	0.0516	6.02	0.1686	

de11h12	42.7	1.2	43.4	4.3	0.0066	1.38	0.0434	5.63	0.04769	5.46	0.2450	
de11g12	42.8	0.7	46	4.2	0.0067	0.85	0.0475	5.55	0.05143	5.48	0.1533	
de11g09	42.9	0.5	43.6	1.1	0.0067	0.58	0.0450	1.33	0.0487	1.2	0.4352	
de11g06	43	0.9	43.1	2.5	0.0067	1.04	0.0437	3.12	0.0473	2.94	0.3335	
de11g13	43	1.1	47.3	5.6	0.0067	1.34	0.0479	5.80	0.05185	5.64	0.2312	
de11h07	43	0.9	45	4.6	0.0067	1.08	0.0454	5.79	0.0492	5.69	0.1865	
de11h13	43.1	1.4	44.5	3.7	0.0067	1.65	0.0452	4.38	0.04893	4.06	0.3765	
de11g07	43.2	0.8	43.8	2.2	0.0067	0.95	0.0444	2.74	0.04811	2.57	0.3467	
de11g10	43.3	0.7	42.8	1.9	0.0067	0.83	0.0439	2.32	0.04758	2.17	0.3572	
de11g14	43.5	0.6	43.3	1.6	0.0068	0.73	0.0454	2.03	0.04841	1.89	0.3603	
de11h11	43.5	0.9	42.6	2.2	0.0068	1.08	0.0443	2.96	0.04726	2.76	0.3644	
de11g11	44.1	0.8	42.6	2.7	0.0069	0.9	0.0446	3.35	0.0469	3.23	0.2684	antecryst
de11h09	44.1	1	42.2	1.3	0.0069	1.13	0.0445	1.81	0.04679	1.41	0.6254	antecryst
Mean (n=15)	**42.92**	**0.25**										
2 SD propagated		**0.51**										

HQ1403 (n°10 in Fig. 2)	**$^{206}Pb/^{238}U$**	**± 2 SD**	**$^{207}Pb/^{235}U$**	**± 2 SD**	**$^{206}Pb/^{238}U$**	**± SD %**	**$^{207}Pb/^{235}U$**	**± SD %**	**$^{207}Pb/^{206}Pb$**	**± SD %**	**Corr. Coef.**	**Comment**
de11i08	42.4	1.2	38.5	5.2	0.0066	1.37	0.0382	7.28	0.04197	7.15	0.1882	
de11j08	42.4	0.9	45.7	3.8	0.0066	1.08	0.0456	4.52	0.05013	4.39	0.2389	
de11i06	42.5	1.2	46.7	5.2	0.0066	1.39	0.0475	5.72	0.05222	5.55	0.2429	
de11i12	42.7	1.1	40.1	7	0.0067	1.32	0.0399	9.97	0.04325	9.88	0.1324	
de11i09	42.9	0.9	44.5	4.2	0.0067	1.08	0.0452	5.31	0.04897	5.2	0.2034	
de11j07	42.9	1	41.9	5	0.0067	1.19	0.0415	6.53	0.04498	6.42	0.1823	
de11i11	43.2	1.4	42.7	6.1	0.0067	1.68	0.0433	8.01	0.04694	7.83	0.2098	
de11j06	43.2	1.4	43.8	5.3	0.0067	1.6	0.0440	6.55	0.04765	6.35	0.2443	
de11j09	43.2	1.2	45.1	5.1	0.0067	1.42	0.0439	5.75	0.04757	5.57	0.2470	
de11i13	43.5	1.2	44.5	6.2	0.0068	1.41	0.0441	6.94	0.04703	6.8	0.2030	
de11i07	43.6	1	50.1	4.3	0.0068	1.19	0.0507	4.58	0.05406	4.42	0.2600	
de11i10	43.7	0.9	45.6	3.8	0.0068	0.99	0.0466	4.62	0.04972	4.51	0.2144	
de11j13	43.7	1.3	43.7	4.5	0.0068	1.46	0.0427	5.60	0.04551	5.41	0.2605	
de11j10	43.8	1.2	44.7	5.4	0.0068	1.33	0.0447	6.14	0.04767	5.99	0.2168	
Mean (n=14)	**43.1**	**0.29**										
2 SD propagated		**0.53**										

AG1308A1 (n°11 in Fig. 2)	$^{206}Pb/^{238}U$	± 2 SD	$^{207}Pb/^{235}U$	± 2 SD	$^{206}Pb/^{238}U$	± SD %	$^{207}Pb/^{235}U$	± SD %	$^{207}Pb/^{206}Pb$	± SD %	Corr. Coef.	Comment
de10g08	36.8	2.1	34.9	4.3	0.0057	2.85	0.0371	6.23	0.04721	5.54	0.4575	
de10h06	36.8	1.9	37.6	4.7	0.0057	2.62	0.0386	6.67	0.04917	6.13	0.3930	
de10h08	36.9	2.3	33.9	2.8	0.0057	3.13	0.0345	4.81	0.04392	3.65	0.6510	
de10g09	37	1.6	36	4.2	0.0058	2.11	0.0374	5.38	0.04675	4.95	0.3921	
de10g12	37	1.5	36.7	2	0.0058	2.04	0.0391	3.15	0.04889	2.4	0.6476	
de10g05	37.1	2.4	36.7	3.6	0.0058	3.23	0.0388	5.11	0.04855	3.96	0.6321	
de10g06	37.2	2	33.4	3.2	0.0058	2.68	0.0348	5.19	0.04351	4.45	0.5159	
de10h10	37.3	1.6	37.1	3.1	0.0058	2.11	0.0391	4.22	0.04892	3.66	0.4994	
de10h14	37.7	1.1	38.4	4.2	0.0059	1.51	0.0404	5.91	0.04963	5.71	0.2557	
de10h12	37.8	1.2	38	4.1	0.0059	1.6	0.0399	6.03	0.04905	5.81	0.2655	
de10h13	37.9	1.1	36	3.2	0.0059	1.51	0.0381	4.79	0.04691	4.55	0.3150	
de10g07	38	1.7	39.4	3.1	0.0059	2.23	0.0422	4.59	0.05187	4.01	0.4860	
de10g11	38	1.7	36.1	3.8	0.0059	2.23	0.0372	5.23	0.04574	4.73	0.4264	
de10g13	38	1.8	35.4	3.5	0.0059	2.4	0.0378	5.41	0.04651	4.85	0.4435	
de10h09	38.2	2	38.4	5.3	0.0059	2.64	0.0404	6.00	0.04973	5.39	0.4399	
de10h11	38.4	1.2	38.6	6.3	0.006	1.56	0.0420	8.36	0.05075	8.21	0.1867	
de10g10	38.5	1.7	38.4	2.4	0.006	2.25	0.0413	4.19	0.04994	3.53	0.5375	
de10h07	39.3	2.2	36.1	2.8	0.0061	2.81	0.0386	3.95	0.04588	2.78	0.7109	
de10g14	39.7	2.2	35.9	3.3	0.0062	2.81	0.0379	5.25	0.04437	4.43	0.5356	
Mean (n=19)	**37.78**	**0.36**										
2 SD propagated		**0.78**										

AG1308A (n°12 in Fig. 2)	$^{206}Pb/^{238}U$	± 2 SD	$^{207}Pb/^{235}U$	± 2 SD	$^{206}Pb/^{238}U$	± SD %	$^{207}Pb/^{235}U$	± SD %	$^{207}Pb/^{206}Pb$	± SD %	Corr. Coef.	Comment
de11b05	36.4	0.8	36.9	2.6	0.0057	1.04	0.0383	3.75	0.04871	3.6	0.2775	
de11a08	36.5	0.8	35.1	2.4	0.0057	1.06	0.0367	3.55	0.04666	3.39	0.2984	
de11a06	36.6	0.6	34.5	1.7	0.0057	0.83	0.0366	2.68	0.04661	2.55	0.3095	
de11b08	36.6	0.8	36.7	1.5	0.0057	1.16	0.0377	2.33	0.04802	2.02	0.4980	
de11b09	36.7	1	34.7	3	0.0057	1.43	0.0368	4.84	0.04686	4.62	0.2957	
de11a05	36.8	0.5	36.9	1.9	0.0057	0.68	0.0379	2.52	0.04827	2.43	0.2695	
de11a11	36.8	1	36.1	3	0.0057	1.31	0.0371	4.58	0.04723	4.39	0.2859	
de11b10	36.8	1.1	36.3	3.2	0.0057	1.54	0.0375	4.63	0.04772	4.37	0.3324	
de11a14	36.9	0.9	33.9	2.5	0.0057	1.25	0.0354	3.85	0.04508	3.64	0.3248	

de11a07	37	0.7	35.8	1.3	0.0058	0.94	0.0381	2.17	0.04767	1.96	0.4324	
de11b14	37	0.8	35.3	1.6	0.0057	1.08	0.0365	2.48	0.04651	2.23	0.4359	
de11a12	37.1	0.8	35.7	1.5	0.0058	1.05	0.0376	2.15	0.0471	1.88	0.4876	
de11b07	37.2	0.5	36.3	1.4	0.0058	0.73	0.0377	2.09	0.04721	1.96	0.3490	
de11b06	37.4	0.6	37.7	1.7	0.0058	0.85	0.0389	2.41	0.04872	2.25	0.3534	
de11b11	37.4	1	37.3	2.3	0.0058	1.38	0.0393	3.78	0.04912	3.52	0.3650	
de11a13	37.5	0.7	35.4	1.3	0.0058	0.94	0.0372	2.25	0.04651	2.04	0.4185	
de11a09	37.7	0.9	36.2	2.3	0.0059	1.23	0.0381	3.37	0.04689	3.14	0.3647	
de11b12	37.7	0.8	36.6	2.9	0.0059	1.11	0.0389	3.99	0.04789	3.83	0.2784	
Mean (n=18)	**37.01**	**0.17**										
2 SD propagated		**0.42**										

VK1404 (n°13 in Fig. 2)	**$^{206}Pb/^{238}U$**	**± 2 SD**	**$^{207}Pb/^{235}U$**	**± 2 SD**	**$^{206}Pb/^{238}U$**	**± SD %**	**$^{207}Pb/^{235}U$**	**± SD %**	**$^{207}Pb/^{206}Pb$**	**± SD %**	**Corr. Coef.**	**Comment**
de12i06	35.4	0.7	32.5	1.8	0.0055	1.04	0.0356	3.04	0.04699	2.86	0.3417	
de12j05	35.4	0.5	33	1.5	0.0055	0.67	0.0349	2.57	0.04609	2.48	0.2608	
de12i05	35.7	0.8	32.4	1.4	0.0055	1.06	0.0353	2.41	0.04651	2.16	0.4406	
de12j06	36	0.6	32.1	1.7	0.0056	0.8	0.0349	2.68	0.04517	2.56	0.2983	
de12i10	36.3	0.8	33.9	1.5	0.0056	1.11	0.0372	2.63	0.04815	2.38	0.4227	
de12j09	36.7	0.4	31.1	1.3	0.0057	0.57	0.0349	2.15	0.04438	2.07	0.2655	antecryst
de12i07	36.8	0.8	31.6	1.4	0.0057	1.09	0.0357	2.35	0.0454	2.08	0.4642	antecryst
de12i08	36.8	0.8	33.2	2.5	0.0057	1.11	0.0370	3.96	0.04708	3.8	0.2804	antecryst
de12i11	37	0.8	32.4	1.7	0.0058	1.03	0.0372	2.96	0.04654	2.78	0.3474	antecryst
de12j07	37.1	0.6	33.2	1.3	0.0058	0.81	0.0372	2.24	0.04651	2.09	0.3614	antecryst
de12j14	37.1	0.6	32.5	1.1	0.0058	0.77	0.0373	1.91	0.04666	1.75	0.4027	antecryst
de12j12	37.2	0.5	32.5	1.5	0.0058	0.67	0.0367	2.52	0.04588	2.43	0.2658	antecryst
de12j13	37.2	0.6	33.3	1.5	0.0058	0.77	0.0380	2.42	0.04755	2.29	0.3187	antecryst
de12j10	37.3	0.5	32.3	1.2	0.0058	0.68	0.0367	2.17	0.04589	2.06	0.3135	antecryst
de12i09	37.6	1.2	32.2	1.8	0.0059	1.62	0.0369	2.99	0.04538	2.51	0.5423	antecryst
de12j11	38	0.5	32.8	1.3	0.0059	0.62	0.0377	2.10	0.04638	2.01	0.2948	antecryst
de12i12	38.3	0.4	33.5	1	0.006	0.57	0.0391	1.76	0.04726	1.67	0.3230	antecryst
Mean (n=5)	**35.7**	**0.47**										
2 SD propagated		**0.65**										

VK1405 (n°14 in Fig. 2)	$^{206}Pb/^{238}U$	± 2 SD	$^{207}Pb/^{235}U$	± 2 SD	$^{206}Pb/^{238}U$	± SD %	$^{207}Pb/^{235}U$	± SD %	$^{207}Pb/^{206}Pb$	± SD %	Corr. Coef.	Comment
de12m09	34.1	0.8	36.4	4.6	0.0053	1.17	0.0376	6.66	0.05148	6.56	0.1756	
de12l05	34.2	0.9	37.9	4.4	0.0053	1.27	0.0385	6.10	0.05272	5.97	0.2081	
de12m08	34.7	0.8	36.2	3.3	0.0054	1.22	0.0375	4.58	0.05045	4.41	0.2666	
de12l12	34.9	1.1	36.2	4.8	0.0054	1.51	0.0368	7.24	0.04941	7.08	0.2086	
de12m12	35.1	0.7	31.2	2.5	0.0055	0.94	0.0337	3.88	0.0445	3.76	0.2425	
de12l11	35.1	0.9	37.4	3.8	0.0055	1.27	0.0390	5.08	0.05143	4.92	0.2499	
de12m11	35.3	1.1	36.5	4.1	0.0055	1.51	0.0377	6.14	0.04971	5.95	0.2460	
de12l10	35.3	0.9	34.4	4	0.0055	1.3	0.0360	5.96	0.04753	5.82	0.2180	
de12m05	35.5	0.6	34.2	2.5	0.0055	0.89	0.0360	4.03	0.04754	3.93	0.2209	antecryst
de12l13	35.5	1.1	33.9	5.5	0.0055	1.62	0.0356	9.44	0.04693	9.3	0.1716	antecryst
de12m13	35.6	0.8	36.3	3.4	0.0055	1.1	0.0382	4.76	0.05043	4.63	0.2311	antecryst
de12l08	35.8	0.8	33.2	2.2	0.0056	1.18	0.0363	3.67	0.04697	3.48	0.3211	antecryst
de12m10	36.2	0.5	33.5	2.1	0.0056	0.74	0.0371	3.10	0.04804	3.01	0.2387	antecryst
de12l14	36.7	1	32.8	2	0.0057	1.42	0.0365	3.17	0.04641	2.83	0.4485	antecryst
de12m06	36.8	0.8	32.4	1.2	0.0057	1.04	0.0363	2.03	0.04625	1.74	0.5130	antecryst
de12l06	37.3	0.8	33.5	1.9	0.0058	1.01	0.0375	3.31	0.0469	3.15	0.3053	antecryst
Mean (n=8)	**34.81**	**0.3**										
2 SD propagated		**0.52**										

MR1403 (n°15 in Fig. 2)	$^{206}Pb/^{238}U$	± 2 SD	$^{207}Pb/^{235}U$	± 2 SD	$^{206}Pb/^{238}U$	± SD %	$^{207}Pb/^{235}U$	± SD %	$^{207}Pb/^{206}Pb$	± SD %	Corr. Coef.	Comment
de12f05	34	0.5	33.5	2.4	0.0053	0.79	0.0350	4.12	0.04798	4.04	0.1919	
de12f13	34.2	0.8	33.6	2.8	0.0053	1.24	0.0347	4.71	0.04746	4.54	0.2635	
de12e13	34.4	1.5	32.3	2.4	0.0054	2.18	0.0349	3.79	0.04687	3.1	0.5752	
de12f09	34.8	0.7	34.4	2.2	0.0054	1.06	0.0361	3.27	0.04847	3.09	0.3245	
de12e12	35	1.2	33.1	2.5	0.0054	1.79	0.0349	4.07	0.04694	3.65	0.4403	
de12f11	35	0.6	34.3	2.2	0.0054	0.88	0.0364	3.20	0.0489	3.08	0.2747	
de12f12	35	0.7	32.5	2	0.0054	1	0.0339	3.23	0.04558	3.07	0.3097	
de12e09	35.1	2.6	31.9	2	0.0055	3.7	0.0336	4.68	0.04433	2.87	0.7902	
de12f07	35.3	0.6	35.2	2.1	0.0055	0.8	0.0373	3.14	0.04927	3.04	0.2545	antecryst
de12e11	35.5	0.5	32.4	1.6	0.0055	0.76	0.0355	2.46	0.04677	2.34	0.3089	antecryst
de12e05	35.7	1.3	31.9	1.7	0.0056	1.87	0.0347	3.01	0.04492	2.36	0.6210	antecryst
de12f06	35.7	0.5	32.6	1.2	0.0056	0.64	0.0365	2.02	0.04727	1.92	0.3162	antecryst
de12f10	35.7	0.5	34.2	1.8	0.0055	0.68	0.0363	2.76	0.04792	2.68	0.2459	antecryst

de12f14	35.7	0.6	32.5	1.2	0.0056	0.79	0.0359	1.99	0.04654	1.83	0.3963	antecryst
de12e06	35.8	3.9	33.1	3	0.0056	5.42	0.0340	6.75	0.04401	4.02	0.8032	antecryst
de12e10	35.8	1.5	33.5	1.5	0.0056	2.13	0.0364	2.72	0.04711	1.69	0.7834	antecryst
de12e14	36	0.5	33.9	1.6	0.0056	0.68	0.0375	2.51	0.04864	2.42	0.2705	antecryst
de12e08	36.1	3.5	32	3.1	0.0056	4.86	0.0344	6.46	0.0446	4.26	0.7520	antecryst
de12e07	36.3	3.9	34.1	3	0.0056	5.44	0.0371	6.28	0.04802	3.13	0.8668	antecryst
Mean (n=8)	**34.57**	**0.4**										
2 SD propagated		**0.58**										

LI1303A1 (n°16 in Fig. 2)	**$^{206}Pb/^{238}U$**	**± 2 SD**	**$^{207}Pb/^{235}U$**	**± 2 SD**	**$^{206}Pb/^{238}U$**	**± SD %**	**$^{207}Pb/^{235}U$**	**± SD %**	**$^{207}Pb/^{206}Pb$**	**± SD %**	**Corr. Coef.**	**Comment**
jn22d06	32.6	0.9	34.6	2.8	0.0051	1.31	0.0356	4.50	0.05066	4.31	0.2908	
jn22d07	32.8	0.8	32	3.2	0.0051	1.15	0.0322	5.18	0.04588	5.05	0.2220	
jn22d12	32.8	0.9	33.2	3.6	0.0051	1.41	0.0330	6.11	0.04695	5.95	0.2306	
jn22e11	32.9	0.9	36.9	3.6	0.0051	1.44	0.0367	4.95	0.05216	4.74	0.2907	
jn22d10	33	0.9	33.2	3.3	0.0051	1.44	0.0323	6.01	0.04602	5.84	0.2394	
jn22d13	33	0.9	31	2.7	0.0051	1.3	0.0310	4.76	0.04414	4.58	0.2731	
jn22e10	33	1.1	35.3	4.5	0.0051	1.69	0.0356	6.83	0.05058	6.62	0.2474	
jn22d08	33.1	0.7	34.6	3	0.0051	1.07	0.0342	4.45	0.04864	4.32	0.2404	
jn22d11	33.1	0.8	35.9	3.8	0.0051	1.25	0.0355	5.81	0.05044	5.67	0.2153	
jn22e12	33.1	1	35.2	3.2	0.0051	1.47	0.0351	4.89	0.04998	4.66	0.3008	
jn22f10	33.2	0.9	33.7	3.5	0.0052	1.41	0.0342	5.99	0.04779	5.82	0.2355	
jn22d09	33.4	0.6	34.3	2.4	0.0052	0.95	0.0346	3.94	0.04828	3.82	0.2413	
jn22f08	33.4	1.1	34.8	4.9	0.0052	1.61	0.0357	7.43	0.04984	7.25	0.2168	
jn22e13	33.7	1.2	29.6	4.3	0.0052	1.78	0.0296	7.74	0.04124	7.53	0.2300	
jn22f06	33.7	0.8	34.7	3.6	0.0052	1.26	0.0350	5.29	0.0488	5.14	0.2381	
jn22e06	33.8	0.9	35	3.6	0.0053	1.29	0.0353	5.57	0.04838	5.42	0.2315	
jn22f11	33.8	0.7	33.3	2.4	0.0053	1.08	0.0342	3.83	0.04681	3.67	0.2823	
jn22f05	33.9	0.7	34.4	2.1	0.0053	1.1	0.0349	3.15	0.04776	2.95	0.3494	
jn22f09	33.9	1.1	36.2	4.9	0.0053	1.65	0.0371	7.00	0.05084	6.8	0.2358	
jn22e07	34	0.9	33.1	3.4	0.0053	1.36	0.0331	5.17	0.04525	4.99	0.2630	
jn22e08	34.1	0.8	33.2	3.2	0.0053	1.13	0.0334	4.87	0.04574	4.74	0.2319	
jn22e09	34.2	1.1	32.8	4.4	0.0053	1.54	0.0324	6.86	0.04439	6.68	0.2246	
jn22f12	34.2	0.8	33.9	2.2	0.0053	1.15	0.0343	3.49	0.04696	3.29	0.3300	
jn22f07	34.3	1.1	32.3	4.5	0.0053	1.57	0.0317	7.15	0.04336	6.98	0.2194	

jn22f13	34.6	1.2	35.8	4.1	0.0054	1.81	0.0365	7.09	0.04898	6.86	0.2551	
Mean (n=25)	**33.48**	**0.22**										
2 SD propagated		**0.55**										

LI1303 (n°17 in Fig. 2)	**$^{206}Pb/^{238}U$**	**± 2 SD**	**$^{207}Pb/^{235}U$**	**± 2 SD**	**$^{206}Pb/^{238}U$**	**± SD %**	**$^{207}Pb/^{235}U$**	**± SD %**	**$^{207}Pb/^{206}Pb$**	**± SD %**	**Corr. Coef.**	**Comment**
jn22b05	33.1	1.4	34.6	1.9	0.0052	2.18	0.0349	3.48	0.04872	2.71	0.6268	
jn22b07	33.1	1.7	33	2.1	0.0051	2.64	0.0329	3.57	0.04684	2.41	0.7385	
jn22c07	33.3	0.9	33.3	1.6	0.0052	1.29	0.0327	2.53	0.04566	2.18	0.5093	
jn22a05	33.5	0.6	33.2	1.8	0.0052	0.84	0.0329	3.10	0.04594	2.98	0.2713	
jn22a12	33.5	1.3	34.3	1.9	0.0052	1.92	0.0344	3.03	0.04807	2.34	0.6343	
jn22b08	33.5	1.1	34.5	2	0.0052	1.64	0.0349	3.01	0.04866	2.52	0.5455	
jn22b06	33.6	1.5	33.6	2.3	0.0052	2.19	0.0341	3.74	0.04759	3.03	0.5858	
de18a05	34	0.7	33.5	1.3	0.0053	1.06	0.0337	2.36	0.0462	2.11	0.4489	
jn22a11	34.2	0.5	34	1.6	0.0053	0.75	0.0338	2.49	0.04634	2.37	0.3017	antecryst
jn22a13	34.3	0.5	35	1.7	0.0053	0.74	0.0352	2.67	0.04815	2.57	0.2767	antecryst
jn22c06	34.3	0.5	33.8	1.7	0.0053	0.79	0.0340	2.77	0.0465	2.66	0.2847	antecryst
jn22c10	34.3	0.5	36.1	1.4	0.0053	0.67	0.0360	2.10	0.04924	1.99	0.3191	antecryst
de18a06	34.4	0.4	34.3	1.3	0.0053	0.52	0.0342	2.04	0.04683	1.97	0.2552	antecryst
jn22a10	34.4	0.5	33.8	1.5	0.0054	0.72	0.0338	2.34	0.04548	2.23	0.3073	antecryst
jn22b12	34.4	0.5	35.5	1.6	0.0054	0.78	0.0363	2.49	0.04872	2.36	0.3138	antecryst
jn22b13	34.4	0.5	35.2	1.4	0.0053	0.79	0.0349	2.33	0.04782	2.19	0.3393	antecryst
jn22c05	34.4	0.5	33.9	1.7	0.0054	0.78	0.0347	2.73	0.04661	2.62	0.2853	antecryst
jn22a09	34.5	0.5	34.8	1.4	0.0054	0.76	0.0351	2.22	0.04722	2.09	0.3417	antecryst
jn22c08	34.6	1.6	33.8	1.7	0.0054	2.25	0.0345	3.21	0.04636	2.29	0.7008	antecryst
jn22b11	34.7	0.5	34	1.3	0.0054	0.67	0.0341	2.27	0.04577	2.17	0.2950	antecryst
jn22c09	34.7	1.1	34.6	1.9	0.0054	1.6	0.0351	2.87	0.04717	2.38	0.5579	antecryst
jn22b10	34.8	0.4	34.8	1.5	0.0054	0.61	0.0356	2.27	0.04777	2.19	0.2683	antecryst
jn22c13	34.8	1.2	34.8	1.6	0.0054	1.75	0.0350	2.93	0.04708	2.35	0.5973	antecryst
jn22c11	35	0.7	35.3	1.6	0.0054	0.98	0.0355	2.54	0.04765	2.34	0.3863	antecryst
jn22a08	35.1	0.6	35	1.7	0.0055	0.8	0.0357	2.51	0.04712	2.38	0.3186	antecryst
jn22b09	35.1	0.5	35.8	1.4	0.0055	0.75	0.0361	2.23	0.0476	2.1	0.3363	antecryst
jn22a06	35.4	0.5	36.5	1.7	0.0055	0.71	0.0365	2.49	0.0482	2.39	0.2848	antecryst
jn22c12	35.5	1.2	34.9	2.2	0.0055	1.73	0.0354	3.76	0.04665	3.34	0.4599	antecryst
Mean (n=8)	**33.55**	**0.33**										

2 SD propagated		**0.60**										
KJ1316 (n°18 in Fig. 2)	**$^{206}Pb/^{238}U$**	**± 2 SD**	**$^{207}Pb/^{235}U$**	**± 2 SD**	**$^{206}Pb/^{238}U$**	**± SD %**	**$^{207}Pb/^{235}U$**	**± SD %**	**$^{207}Pb/^{206}Pb$**	**± SD %**	**Corr. Coef.**	**Comment**
de12r13	32.6	1.2	33.2	4.8	0.0051	1.78	0.0340	7.73	0.04836	7.52	0.2303	
de12r07	32.7	1.8	35.1	4.2	0.0051	2.69	0.0357	6.04	0.05076	5.41	0.4452	
de12s10	32.8	3.1	34	4.7	0.0051	4.74	0.0351	7.77	0.04999	6.16	0.6098	
de12r14	33	1	36.4	3.8	0.0051	1.55	0.0358	5.59	0.05093	5.37	0.2773	
de12r09	33.2	1.5	35	6.1	0.0052	2.21	0.0359	9.12	0.05014	8.85	0.2423	
de12r10	33.4	1.4	30.9	3	0.0052	2.15	0.0319	4.90	0.04447	4.4	0.4390	
de12s06	33.4	1.3	29.2	5	0.0052	1.97	0.0292	8.87	0.04072	8.65	0.2221	
de12s07	33.4	1.7	37.7	7.7	0.0052	2.49	0.0377	11.04	0.05267	10.76	0.2255	
de12r05	33.6	2.1	39.1	5	0.0052	3.15	0.0398	6.97	0.05549	6.22	0.4518	
de12r06	33.6	2.1	37.1	7.3	0.0052	3.11	0.0368	13.76	0.0513	13.4	0.2261	
de12s08	33.6	1.8	28.3	4.6	0.0052	2.63	0.0287	8.52	0.03999	8.1	0.3088	
de12s14	33.6	1.6	31	3.7	0.0052	2.37	0.0313	5.81	0.04363	5.31	0.4076	
de12s09	33.8	2.1	32.5	3.9	0.0053	3.16	0.0327	6.88	0.04476	6.11	0.4594	
de12s11	33.8	2	31.5	4.5	0.0053	2.9	0.0330	7.77	0.04518	7.21	0.3732	
de12r12	33.9	0.6	32.9	2.7	0.0053	0.95	0.0347	4.31	0.04751	4.2	0.2206	
de12s05	34.4	0.7	35.7	1.9	0.0053	1	0.0378	2.94	0.05175	2.76	0.3406	
de12r11	34.5	1.1	34.4	3.5	0.0054	1.65	0.0374	6.02	0.05019	5.79	0.2741	
de12r08	34.7	1.8	32.1	1.6	0.0054	2.67	0.0352	3.38	0.04731	2.07	0.7903	
Mean (n=18)	**33.73**	**0.29**										
2 SD propagated		**0.51**										

KJ1006A (n°19 in Fig. 2)	**$^{206}Pb/^{238}U$**	**± 2 SD**	**$^{207}Pb/^{235}U$**	**± 2 SD**	**$^{206}Pb/^{238}U$**	**± SD %**	**$^{207}Pb/^{235}U$**	**± SD %**	**$^{207}Pb/^{206}Pb$**	**± SD %**	**Corr. Coef.**	**Comment**
de12b06	31.1	1.5	31.6	4.5	0.0048	2.49	0.0304	7.21	0.04592	6.77	0.3452	
de12b07	31.1	1.1	36.4	12.7	0.0048	1.74	0.0365	15.86	0.05513	15.76	0.1097	
de12a08	31.5	0.6	33.2	2.4	0.0049	0.93	0.0336	3.97	0.04976	3.86	0.2342	
de12a05	31.6	0.7	31.4	3.2	0.0049	1.19	0.0318	5.59	0.04704	5.46	0.2129	
de12a06	31.6	0.7	32.3	2.3	0.0049	1.04	0.0329	3.80	0.04876	3.66	0.2733	
de12b12	31.7	1.2	31.9	2.5	0.0049	1.94	0.0321	4.57	0.04751	4.14	0.4243	
de12a10	31.8	1	31.6	1.7	0.0049	1.65	0.0325	3.47	0.04816	3.05	0.4758	
de12a07	31.9	0.7	31	2.9	0.005	1.12	0.0316	5.08	0.04584	4.96	0.2203	

de12a09	31.9	0.8	35.1	2.8	0.005	1.33	0.0365	4.07	0.05294	3.85	0.3265
de12a12	31.9	1.2	28.5	2.2	0.005	1.96	0.0298	4.43	0.04329	3.97	0.4427
de12b05	32	1.3	30.6	2.5	0.005	1.98	0.0311	4.79	0.04509	4.36	0.4135
de12b11	32.1	1.2	31.3	2.8	0.005	1.89	0.0319	4.34	0.04633	3.91	0.4352
de12b09	32.2	1.1	34.8	3.6	0.005	1.72	0.0349	5.58	0.05059	5.31	0.3082
de12a14	32.4	1.2	31.3	2	0.005	1.91	0.0322	3.93	0.04667	3.44	0.4854
de12b08	32.5	1	31.3	2.1	0.0051	1.52	0.0329	3.64	0.0468	3.31	0.4173
de12b10	32.6	0.9	32.3	2.1	0.0051	1.36	0.0341	3.43	0.04849	3.15	0.3964
de12b14	32.6	1.2	30.1	2.4	0.0051	1.82	0.0312	4.27	0.04438	3.86	0.4265
de12a13	32.8	1.2	30.9	1.7	0.0051	1.81	0.0322	3.05	0.04577	2.45	0.5942
Mean (n=18)	**31.89**	**0.22**									
2 SD propagated		**0.45**									

KJ1308 (n°20 in Fig. 2)	**$^{206}Pb/^{238}U$**	**± 2 SD**	**$^{207}Pb/^{235}U$**	**± 2 SD**	**$^{206}Pb/^{238}U$**	**± SD %**	**$^{207}Pb/^{235}U$**	**± SD %**	**$^{207}Pb/^{206}Pb$**	**± SD %**	**Corr. Coef.**	**Comment**
jn22l06	30.1	1.1	29.4	4.5	0.0047	1.84	0.0296	8.32	0.04575	8.11	0.2213	
jn22l07	30.1	1.5	32.6	3.6	0.0047	2.42	0.0326	6.49	0.05039	6.02	0.3730	
jn22l10	30.3	2.5	32.5	4.6	0.0047	4.17	0.0325	6.37	0.05023	4.82	0.6543	
jn22k07	30.6	1.4	34.1	5.3	0.0048	2.27	0.0340	7.80	0.05147	7.46	0.2911	
jn22k09	30.6	2	29.2	2.3	0.0048	3.29	0.0295	4.79	0.0446	3.48	0.6870	
jn22n07	30.7	0.8	29.9	3.3	0.0048	1.26	0.0301	5.54	0.04543	5.39	0.2276	
jn22l09	30.8	2.2	32.1	3.3	0.0048	3.58	0.0330	7.52	0.04984	6.61	0.4762	
jn22m07	30.8	1.4	30.9	3	0.0048	2.31	0.0317	4.86	0.04795	4.28	0.4750	
jn22k10	30.9	2.7	32.9	4.7	0.0048	4.35	0.0332	8.73	0.05024	7.57	0.4982	
jn22n06	30.9	2	31	5.9	0.0048	3.19	0.0312	8.58	0.04712	7.96	0.3720	
jn22n09	30.9	0.9	29.4	3.1	0.0048	1.48	0.0295	5.73	0.04461	5.54	0.2581	
jn22n12	30.9	0.8	28.7	2.3	0.0048	1.26	0.0290	4.24	0.04383	4.05	0.2971	
jn22l13	31	1.6	31.1	4.5	0.0048	2.61	0.0316	7.38	0.04771	6.9	0.3538	
jn22n11	31	0.9	34.4	3.7	0.0048	1.44	0.0345	5.63	0.05208	5.44	0.2559	
jn22k12	31.1	0.5	31.1	2.2	0.0048	0.8	0.0313	3.40	0.04737	3.3	0.2356	
jn22k13	31.1	0.6	33	2.5	0.0048	0.97	0.0334	3.99	0.05042	3.87	0.2431	
jn22l11	31.1	2.1	30.1	6	0.0048	3.39	0.0296	11.48	0.04479	10.97	0.2952	
jn22m05	31.1	1.8	33.7	4.7	0.0048	2.96	0.0327	7.30	0.0495	6.67	0.4056	
jn22k08	31.2	2	33.7	5.2	0.0049	3.26	0.0349	7.86	0.05165	7.15	0.4149	
jn22k11	31.3	1.5	32.8	3.7	0.0049	2.34	0.0323	5.97	0.04776	5.49	0.3921	

jn22m11	31.3	1.2	36.6	6	0.0049	1.95	0.0372	8.92	0.05503	8.7	0.2187	
jn22m13	31.3	0.9	31	3.5	0.0049	1.37	0.0311	6.34	0.04608	6.19	0.2161	
jn22m10	31.5	1.1	33.9	2.9	0.0049	1.69	0.0345	4.70	0.0511	4.39	0.3593	
jn22l08	31.7	1.5	32.4	2.6	0.0049	2.43	0.0331	4.49	0.04895	3.77	0.5418	
jn22m08	31.7	1.6	32	2.9	0.0049	2.55	0.0315	5.23	0.04661	4.57	0.4873	
jn22n05	31.8	2.7	30	2.5	0.0049	4.26	0.0302	5.64	0.04469	3.69	0.7559	
jn22n10	32.2	0.9	31	3.4	0.005	1.4	0.0314	5.76	0.04558	5.59	0.2429	
jn22m12	32.5	1.3	30.5	5	0.0051	1.98	0.0312	8.70	0.04434	8.47	0.2276	
Mean (n=28)	**31.11**	**0.21**										
2 SD propagated		**0.51**										

KJ1508 (n°21 in Fig. 2)	**$^{206}Pb/^{238}U$**	**± 2 SD**	**$^{207}Pb/^{235}U$**	**± 2 SD**	**$^{206}Pb/^{238}U$**	**± SD %**	**$^{207}Pb/^{235}U$**	**± SD %**	**$^{207}Pb/^{206}Pb$**	**± SD %**	**Corr. Coef.**	**Comment**
jl09e05	27.7	0.6	27.8	2	0.0043	1.05	0.0277	3.72	0.04678	3.57	0.2822	
jl09e08	27.8	0.6	28.5	2	0.0043	1.02	0.0283	3.66	0.04776	3.52	0.2783	
jl09f09	27.8	1.4	28	2.9	0.0043	2.46	0.0276	5.58	0.04662	5.01	0.4408	
jl10g05	27.8	0.9	28.1	1.8	0.0043	1.65	0.0279	3.46	0.04703	3.04	0.4770	
jl10f12	27.9	0.7	28.2	2.1	0.0043	1.31	0.0282	4.20	0.04765	3.99	0.3119	
jl10g06	28.1	0.6	28.3	1.8	0.0044	1.1	0.0289	3.22	0.0476	3.03	0.3412	
jl09e06	28.3	0.4	29.4	0.7	0.0044	0.71	0.0294	1.49	0.04845	1.31	0.4765	
jl09e07	28.3	0.8	27	2.5	0.0044	1.33	0.0271	4.82	0.04475	4.63	0.2761	
jl10f13	28.5	0.8	27.5	2.2	0.0044	1.35	0.0277	4.29	0.04573	4.07	0.3148	
jl09e12	28.6	0.8	29.5	2	0.0044	1.42	0.0297	3.59	0.04906	3.3	0.3953	
jl09f05	28.6	0.8	27.3	1.7	0.0044	1.34	0.0277	3.20	0.04564	2.91	0.4183	
jl09f13	28.6	0.9	29	1.7	0.0044	1.56	0.0290	3.35	0.04784	2.97	0.4650	
jl09e09	28.7	0.6	29.4	2	0.0045	1.09	0.0304	3.73	0.04901	3.57	0.2920	
jl09f07	28.7	1.1	29.2	2	0.0045	1.88	0.0303	3.83	0.04883	3.34	0.4905	
jl09f12	28.9	0.8	30.4	1.7	0.0045	1.4	0.0302	3.14	0.04874	2.81	0.4459	
jl09e13	29	0.9	29.5	1.3	0.0045	1.6	0.0293	2.60	0.04729	2.05	0.6153	antecryst
jl09f08	29	0.7	28.8	1.5	0.0045	1.27	0.0293	3.09	0.04719	2.82	0.4106	antecryst
jl09f06	29.1	0.7	29	1.9	0.0045	1.25	0.0289	3.67	0.04667	3.45	0.3406	antecryst
jl09f10	29.2	0.7	30.1	2	0.0045	1.18	0.0301	3.81	0.04858	3.62	0.3099	antecryst
jl09f11	29.4	0.5	28.5	1.7	0.0046	0.94	0.0291	3.36	0.04595	3.23	0.2794	antecryst
Mean (n=15)	**28.26**	**0.21**										
2 SD propagated		**0.38**										

KJ1509 (n°22 in Fig. 2)	$^{206}Pb/^{238}U$	± 2 SD	$^{207}Pb/^{235}U$	± 2 SD	$^{206}Pb/^{238}U$	± SD %	$^{207}Pb/^{235}U$	± SD %	$^{207}Pb/^{206}Pb$	± SD %	Corr. Coef.	Comment
jl09a05	27.1	1.1	27.5	4.1	0.0042	2.1	0.027153178	7.202923018	0.04691	6.89	0.291548305	
jl09a10	27.4	0.9	28.5	2.7	0.0043	1.63	0.028410078	5.249476164	0.04794	4.99	0.310507172	
jl10e10	27.5	1	30.6	3.6	0.0043	1.79	0.030750917	6.0412747	0.05189	5.77	0.296295085	
jl09a08	27.6	0.8	26.7	2.6	0.0043	1.53	0.026881125	5.892113373	0.04536	5.69	0.259669138	
jl09a09	27.6	1.1	29.7	3.8	0.0043	1.94	0.029672353	6.591934466	0.05007	6.3	0.294299042	
jl10f05	27.6	1.5	29.2	5.1	0.0043	2.8	0.029399749	7.734604062	0.04961	7.21	0.362009481	
jl09a07	27.7	1.2	27.6	3.6	0.0043	2.17	0.027633749	6.399164008	0.04663	6.02	0.339106795	
jl09b05	27.9	0.9	27.4	2.3	0.0043	1.53	0.026869273	4.49819964	0.04534	4.23	0.340136082	
jl09b12	28.2	0.8	28.1	2.9	0.0044	1.45	0.02875545	5.755640712	0.04742	5.57	0.251926775	
jl10e11	28.2	1	30.5	2.6	0.0044	1.8	0.030580712	5.257718136	0.05043	4.94	0.342353841	
jl10e13	28.2	1	27.9	3	0.0044	1.85	0.027712443	5.717569414	0.0457	5.41	0.323564065	
jl09a11	28.3	1.1	30.1	3.8	0.0044	1.95	0.030332088	6.709612507	0.05002	6.42	0.290627812	
jl09a13	28.3	1.2	28.1	3.7	0.0044	2.05	0.028015643	8.006878293	0.0462	7.74	0.256029869	
jl09b11	28.3	0.7	29.4	2.1	0.0044	1.27	0.029398233	3.713892836	0.04848	3.49	0.341959248	
jl10e12	28.3	0.9	29.4	3.5	0.0044	1.54	0.028803962	6.777285592	0.0475	6.6	0.227229616	
jl09a06	28.5	1.5	28.2	3.3	0.0044	2.6	0.028421931	6.621789788	0.04687	6.09	0.392643089	
jl09b07	28.5	0.7	29.3	2.6	0.0044	1.26	0.029604409	4.904610076	0.04882	4.74	0.256901156	
jl09b08	28.5	0.8	27.5	2.3	0.0044	1.35	0.027609356	4.421153696	0.04553	4.21	0.305350163	
jl09b13	28.5	1	28.4	3.2	0.0044	1.73	0.028227883	6.004614892	0.04655	5.75	0.288111733	
jl09b10	28.6	0.8	28	2.7	0.0044	1.42	0.027651804	4.747346627	0.0456	4.53	0.299114455	
jl09b06	29.5	0.7	29.3	1.5	0.0046	1.22	0.029498289	2.763837911	0.04653	2.48	0.441415177	inherited core
Mean (n=20)	**28.09**	**0.21**										
2 SD propagated		**0.38**										

KJ1302A (n°23 in Fig. 2)	$^{206}Pb/^{238}U$	± 2 SD	$^{207}Pb/^{235}U$	± 2 SD	$^{206}Pb/^{238}U$	± SD %	$^{207}Pb/^{235}U$	± SD %	$^{207}Pb/^{206}Pb$	± SD %	Corr. Coef.	Comment
de18d12	26.3	0.5	25.7	1.5	0.0041	0.89	0.0261	2.96	0.04626	2.82	0.3010	
de18d07	26.4	0.4	27.2	1.1	0.0041	0.69	0.0273	2.27	0.04824	2.16	0.3043	
de18d10	26.4	0.3	24.9	1.4	0.0041	0.64	0.0249	2.87	0.04408	2.8	0.2228	
de18d11	26.4	0.4	27.2	1.6	0.0041	0.8	0.0273	3.03	0.04833	2.92	0.2642	
de18c12	26.5	0.5	27.1	1.7	0.0041	0.94	0.0272	3.28	0.04817	3.14	0.2868	
de18e07	26.5	0.4	25.7	1.1	0.0041	0.79	0.0259	2.34	0.04576	2.2	0.3380	

de18e10	26.5	0.3	27.1	1.3	0.0041	0.61	0.0274	2.53	0.04852	2.46	0.2407	
de18d09	26.6	0.4	27.2	1.1	0.0041	0.71	0.0270	2.31	0.04787	2.2	0.3071	
de18d13	26.6	0.4	27	1.2	0.0041	0.83	0.0271	2.43	0.04791	2.28	0.3421	
de18e08	26.6	0.3	26.2	1.3	0.0041	0.64	0.0262	2.58	0.04632	2.5	0.2480	
de18c08	26.8	0.4	28	1.5	0.0042	0.68	0.0286	2.71	0.04946	2.62	0.2512	
de18e11	26.8	0.3	26.1	1.2	0.0042	0.65	0.0266	2.54	0.04595	2.46	0.2555	
de18c05	26.9	0.4	26.4	1.3	0.0042	0.84	0.0270	2.58	0.04657	2.44	0.3255	
de18d05	26.9	0.4	26.5	1.4	0.0042	0.68	0.0271	2.76	0.04682	2.67	0.2468	
de18d06	26.9	0.4	27.1	1.4	0.0042	0.69	0.0274	2.75	0.04728	2.66	0.2511	
de18c13	27	0.4	28.4	1.5	0.0042	0.72	0.0288	2.78	0.04967	2.69	0.2586	antecryst
de18e06	27	0.4	27.1	1.1	0.0042	0.81	0.0273	2.19	0.0472	2.04	0.3690	antecryst
de18d08	27.2	0.3	27	1.2	0.0042	0.6	0.0271	2.29	0.04679	2.21	0.2620	antecryst
de18e09	27.3	0.3	28	1	0.0042	0.62	0.0284	1.86	0.04898	1.75	0.3339	antecryst
de18c09	27.4	0.4	27.8	1.4	0.0043	0.72	0.0283	2.55	0.04774	2.45	0.2820	antecryst
de18c07	47.9	1.2	55.4	5.5	0.0075	1.28	0.0560	5.09	0.05303	5.35	0.2327	antecryst
de18c10	46.9	1.7	51.4	8.7	0.0073	1.82	0.0519	8.73	0.05061	9.14	0.1953	antecryst
de18c11	29.2	0.7	30	3.5	0.0045	1.22	0.0300	5.89	0.04875	5.34	0.2227	antecryst
de18e05	31	0.6	29.8	2.3	0.0048	0.91	0.0298	3.94	0.04501	3.86	0.2295	antecryst
Mean (n=15)	**26.61**	**0.09**										
2 SD propagated		**0.26**										

KJ1303A1 (n°24 in Fig. 2)	**$^{206}Pb/^{238}U$**	**± 2 SD**	**$^{207}Pb/^{235}U$**	**± 2 SD**	**$^{206}Pb/^{238}U$**	**± SD %**	**$^{207}Pb/^{235}U$**	**± SD %**	**$^{207}Pb/^{206}Pb$**	**± SD %**	**Corr. Coef.**	**Comment**
de18b10	24.8	0.7	23.9	2.6	0.0039	1.46	0.0244	5.84	0.04532	5.65	0.2502	
de18a11	25.1	0.8	25.1	3.9	0.0039	1.53	0.0250	7.76	0.04643	7.61	0.1971	
de18b11	25.3	0.5	25.6	2.6	0.0039	1.03	0.0254	5.50	0.04723	5.4	0.1874	
de18a12	25.4	0.7	29.5	3.4	0.0039	1.43	0.0290	6.02	0.05401	5.85	0.2375	
de18a10	25.5	0.7	31.4	4.4	0.004	1.38	0.0317	7.16	0.05753	7.03	0.1926	
de18b13	25.5	0.8	29	3.8	0.004	1.55	0.0295	6.87	0.05343	6.69	0.2257	
de18b08	25.7	0.5	26.3	1.8	0.004	0.94	0.0268	3.67	0.04867	3.55	0.2560	
de18b09	25.9	0.8	27.7	3.6	0.004	1.47	0.0276	6.80	0.05007	6.64	0.2162	
de18b07	26.1	0.8	24	4.2	0.0041	1.6	0.0240	9.19	0.04248	9.05	0.1741	
Mean (n=9)	**25.47**	**0.22**										
2 SD propagated		**0.32**										

MR1401 (n°25 in Fig. 2)	$^{206}Pb/^{238}U$	± 2 SD	$^{207}Pb/^{235}U$	± 2 SD	$^{206}Pb/^{238}U$	± SD %	$^{207}Pb/^{235}U$	± SD %	$^{207}Pb/^{206}Pb$	± SD %	Corr. Coef.	Comment
de12g09	23.4	1.7	22.1	1.8	0.0036	3.56	0.0233	5.04	0.04688	3.57	0.7061	
de12h13	23.4	0.7	21.2	3.2	0.0036	1.49	0.0210	8.73	0.04236	8.6	0.1707	
de12g10	24	1.8	27	3.9	0.0037	3.8	0.0265	8.47	0.05188	7.57	0.4486	
de12g07	24.2	1.9	21.7	3.7	0.0038	3.95	0.0215	9.33	0.041	8.45	0.4235	
de12h14	24.2	1	28.1	4.4	0.0038	2.12	0.0284	9.05	0.05418	8.8	0.2342	
de12g11	24.3	1.5	28.1	4.6	0.0038	3.02	0.0280	8.52	0.05347	7.97	0.3543	
de12h09	24.3	0.8	19.5	2.7	0.0038	1.65	0.0197	7.51	0.03756	7.33	0.2196	
de12h08	24.5	1	23	2.3	0.0038	1.98	0.0229	6.01	0.0438	5.67	0.3297	
de12h05	24.6	0.7	26.2	2.7	0.0038	1.38	0.0261	5.51	0.04983	5.33	0.2506	
de12h11	24.6	0.8	24.6	2.9	0.0038	1.55	0.0247	6.55	0.04707	6.36	0.2368	
de12h07	24.7	1	24	2.6	0.0038	1.94	0.0241	5.93	0.046	5.6	0.3273	
de12h10	24.7	1	23.4	3.6	0.0038	2.01	0.0233	7.85	0.04448	7.59	0.2560	
de12g08	24.8	2	25.5	3.9	0.0039	3.94	0.0255	8.79	0.04735	7.86	0.4481	
de12g14	24.8	0.9	26.8	3.9	0.0039	1.74	0.0275	8.07	0.05113	7.88	0.2156	
de12h12	25.2	1	26.4	4	0.0039	1.92	0.0261	8.30	0.04851	8.07	0.2315	
de12g12	25.4	0.9	25.7	4.7	0.0039	1.73	0.0255	9.39	0.04743	9.23	0.1842	
de12g13	30.2	0.8	30.5	2.6	0.0047	1.4	0.0313	4.63	0.04834	4.41	0.3026	antecryst
de12h06	31	1	27.9	3	0.0048	1.59	0.0280	5.40	0.04239	5.16	0.2945	antecryst
Mean (n=16)	**24.47**	**0.3**										
2 SD propagated		**0.42**										

KJ1307 (n°26 in Fig. 2)	$^{206}Pb/^{238}U$	± 2 SD	$^{207}Pb/^{235}U$	± 2 SD	$^{206}Pb/^{238}U$	± SD %	$^{207}Pb/^{235}U$	± SD %	$^{207}Pb/^{206}Pb$	± SD %	Corr. Coef.	Comment
de18f05	23.7	0.8	28.6	3.3	0.0037	1.6	0.0281	6.16	0.05508	5.95	0.2597	
de18g07	23.7	1	24.4	3.8	0.0037	2.12	0.0245	7.73	0.04814	7.43	0.2744	
de18g11	23.7	1.3	24.6	4.9	0.0037	2.68	0.0247	11.87	0.04835	11.56	0.2258	
de18f06	23.9	0.8	24.5	3.7	0.0037	1.67	0.0246	8.25	0.04819	8.08	0.2024	
de18g13	24.1	0.5	26.8	2.4	0.0037	1.11	0.0267	4.70	0.05228	4.57	0.2360	
de18g08	24.2	1.6	23.2	4.4	0.0038	3.33	0.0236	9.76	0.04501	9.17	0.3413	
de18f07	24.4	0.5	23.6	2.5	0.0038	1.1	0.0235	5.47	0.04493	5.36	0.2010	
de18f09	24.4	0.8	25	3	0.0038	1.57	0.0249	6.58	0.04761	6.39	0.2386	
de18f10	24.5	0.9	24.2	3.7	0.0038	1.76	0.0239	7.67	0.04562	7.47	0.2293	
de18g10	24.5	1.9	25.7	4.3	0.0038	3.81	0.0257	8.85	0.04912	7.99	0.4304	

de18f13	24.6	1.1	24.9	3.7	0.0038	2.26	0.0250	8.30	0.04771	7.99	0.2722	
de18f12	24.8	0.9	27.2	4.4	0.0039	1.8	0.0275	8.51	0.0512	8.32	0.2115	
de18e12	24.9	0.7	23.1	3.8	0.0039	1.38	0.0232	8.46	0.04321	8.35	0.1631	
de18g09	25.3	1.8	25.5	3.8	0.0039	3.48	0.0250	8.65	0.04646	7.92	0.4023	
de18g06	31.7	0.9	32.4	3.5	0.0049	1.5	0.0324	5.49	0.0487	5.31	0.2718	antecryst
Mean (n=14)	**24.3**	**0.22**										
2 SD propagated		**0.31**										

LI1301 (n°27 in Fig. 2)	**$^{206}Pb/^{238}U$**	**± 2 SD**	**$^{207}Pb/^{235}U$**	**± 2 SD**	**$^{206}Pb/^{238}U$**	**± SD %**	**$^{207}Pb/^{235}U$**	**± SD %**	**$^{207}Pb/^{206}Pb$**	**± SD %**	**Corr. Coef.**	**Comment**
de11m05	22	0.6	23.1	1.7	0.0034	1.33	0.0230	3.78	0.04906	3.54	0.3517	
de10k07	22.3	0.5	23.3	2.2	0.0035	1.21	0.0241	4.93	0.04999	4.78	0.2454	
de10k06	22.4	0.6	21.9	2.2	0.0035	1.35	0.0224	5.17	0.04653	4.99	0.2612	
de10k08	22.4	0.5	20.5	2.3	0.0035	1.04	0.0208	5.91	0.04309	5.82	0.1759	
de10k11	22.6	0.7	23.4	5.6	0.0035	1.51	0.0237	14.36	0.04904	14.28	0.1052	
de10k09	22.7	0.5	21	1.9	0.0035	1.1	0.0209	5.05	0.04343	4.93	0.2178	
de10k14	22.7	0.5	22.3	1.6	0.0035	1.15	0.0232	3.71	0.04819	3.53	0.3098	
de11m14	22.8	0.5	22.7	2	0.0035	1.11	0.0228	4.85	0.04736	4.72	0.2289	
de10k10	22.9	0.5	24.3	2.1	0.0036	1.16	0.0255	4.83	0.05132	4.69	0.2401	
de10k13	22.9	0.6	24.6	4.6	0.0036	1.35	0.0263	9.13	0.05301	9.03	0.1479	
de11m06	23.1	0.5	23.4	1.6	0.0036	1.14	0.0239	3.71	0.04826	3.53	0.3073	antecryst
de11m08	23.1	0.9	22.7	1.6	0.0036	1.86	0.0231	4.34	0.0465	3.92	0.4287	antecryst
de11m11	23.1	1.2	22.7	2.3	0.0036	2.53	0.0233	6.55	0.04704	6.04	0.3863	antecryst
de11m07	23.2	0.4	22	1.1	0.0036	0.88	0.0223	3.02	0.04485	2.89	0.2913	antecryst
de11m12	23.4	1.4	23.1	1.5	0.0036	2.91	0.0234	4.26	0.04714	3.11	0.6832	antecryst
de11m09	23.5	1.2	24	1.6	0.0037	2.46	0.0249	4.39	0.04883	3.64	0.5599	antecryst
de11m10	23.6	1	23.2	1.8	0.0037	2.21	0.0236	4.28	0.04625	3.67	0.5159	antecryst
Mean (n=10)	**22.58**	**0.17**										
2 SD propagated		**0.45**										

KJ1325A (n°28 in Fig. 2)	**$^{206}Pb/^{238}U$**	**± 2 SD**	**$^{207}Pb/^{235}U$**	**± 2 SD**	**$^{206}Pb/^{238}U$**	**± SD %**	**$^{207}Pb/^{235}U$**	**± SD %**	**$^{207}Pb/^{206}Pb$**	**± SD %**	**Corr. Coef.**	**Comment**
de17f05	21.7	0.6	23	1.3	0.0034	1.31	0.0234	3.57	0.04988	3.32	0.3670	
de17f07	21.9	0.3	22.3	1.2	0.0034	0.72	0.0226	2.91	0.04818	2.82	0.2474	
de17f06	22	0.5	21.6	1.4	0.0034	1.15	0.0217	3.49	0.04629	3.29	0.3300	

de17h12	22	0.3	24.6	1.4	0.0036	0.97	0.0223	3.96	0.0533	2.95	0.2449	
de17e05	22.1	0.3	21.5	1.3	0.0034	0.71	0.0217	3.01	0.0464	2.93	0.2355	
de17e06	22.1	0.3	21.8	0.7	0.0034	0.67	0.0222	1.94	0.04736	1.82	0.3455	
de17e11	22.1	0.8	22.2	1.7	0.0034	1.73	0.0220	4.36	0.04701	4	0.3970	
de17f09	22.1	0.4	21.6	1.6	0.0034	1.14	0.0218	3.75	0.04585	3.85	0.3042	
de17g09	22.1	0.6	22.6	1.3	0.0034	1.37	0.0225	3.33	0.04793	3.04	0.4109	
de17g11	22.1	0.6	21.6	1.4	0.0034	1.44	0.0217	3.67	0.04637	3.38	0.3919	
de17h08	22.2	0.6	22.5	1.4	0.0036	0.97	0.0223	3.96	0.04784	3.17	0.2449	
de17e07	22.3	0.6	20.8	2	0.0035	1.24	0.0213	5.31	0.04406	5.16	0.2337	
de17e10	22.3	0.5	21.9	1.3	0.0035	1.09	0.0225	3.30	0.04659	3.11	0.3308	
de17g12	22.3	0.6	23.9	1.5	0.0035	1.43	0.0243	3.45	0.05034	3.14	0.4145	
de17h11	22.3	0.4	22.8	1.1	0.0036	0.97	0.0223	3.96	0.04848	2.4	0.2449	
de17e08	22.4	0.4	22.5	1.5	0.0035	1	0.0229	3.52	0.04747	3.37	0.2845	
de17f08	22.4	0.3	22.5	1.2	0.0035	0.72	0.0232	2.70	0.04814	2.6	0.2669	
de17f10	22.4	0.4	23.2	1.3	0.0035	0.93	0.0235	3.26	0.0487	3.12	0.2857	
de17h06	22.4	0.4	21.4	1.6	0.0035	0.99	0.0218	3.88	0.04529	3.75	0.2553	
de17h07	22.4	0.5	23.4	1.3	0.0036	0.97	0.0223	3.96	0.04954	2.83	0.2449	
de17h10	22.4	0.4	22.3	1.3	0.0036	0.97	0.0223	3.96	0.04704	2.99	0.2449	
de17e12	22.5	0.6	22	1.4	0.0035	1.43	0.0222	3.51	0.04612	3.21	0.4069	
de17g05	22.5	0.5	22.6	1.7	0.0035	1.1	0.0226	4.10	0.04687	3.95	0.2683	
de17g06	22.5	0.5	21.9	1.1	0.0035	1.03	0.0224	2.50	0.04635	2.28	0.4117	
de17g08	22.5	0.6	22.4	1.4	0.0035	1.3	0.0225	3.44	0.04663	3.19	0.3774	
de17e09	22.6	0.5	22.2	1.2	0.0035	1.19	0.0225	3.13	0.04662	2.89	0.3807	
de17g07	22.7	0.5	27.4	1.3	0.0035	2.06	0.0243	3.86	0.05758	2.45	0.5330	antecryst
de17g10	22.7	0.4	22.9	1.2	0.0035	0.98	0.0231	2.89	0.04781	2.72	0.3390	antecryst
de17f11	22.8	0.5	21.6	1.3	0.0035	1.03	0.0220	3.13	0.04554	2.96	0.3286	antecryst
de17e13	22.9	0.4	22.7	1	0.0036	0.92	0.0235	2.31	0.0474	2.12	0.3981	antecryst
de17g13	22.9	0.6	21.9	1.4	0.0035	1.61	0.0224	2.87	0.04577	3.12	0.5603	antecryst
de17h09	22.9	0.5	23.4	1.5	0.0036	0.97	0.0223	3.96	0.04805	3.31	0.2449	antecryst
Mean (n=26)	**22.23**	**0.08**										
2 SD propagated		**0.25**										

KJ1324A (n°29 in Fig. 2)	**$^{206}Pb/^{238}U$**	**± 2 SD**	**$^{207}Pb/^{235}U$**	**± 2 SD**	**$^{206}Pb/^{238}U$**	**± SD %**	**$^{207}Pb/^{235}U$**	**± SD %**	**$^{207}Pb/^{206}Pb$**	**± SD %**	**Corr. Coef.**	**Comment**
de17a07	21.6	1	21.7	1.3	0.0034	2.42	0.0222	3.53	0.0474	2.57	0.6855	

de17c07	21.7	0.7	21.4	1.3	0.0034	1.53	0.0221	3.61	0.04712	3.27	0.4238
de17a06	21.9	0.5	21.6	1.7	0.0034	1.08	0.0217	4.14	0.04624	4	0.2607
de17a09	21.9	1.2	22.3	1.4	0.0034	2.64	0.0221	4.50	0.04724	3.64	0.5871
de17a10	21.9	1	22.3	1.5	0.0034	2.35	0.0226	3.94	0.04824	3.16	0.5967
de17c10	21.9	0.9	22.4	1.4	0.0034	2.17	0.0229	3.63	0.04889	2.91	0.5978
de17a05	22	0.3	21.4	1.2	0.0034	0.73	0.0216	3.24	0.04601	3.16	0.2251
de17b13	22	0.5	21.9	1.5	0.0034	1.15	0.0221	3.55	0.04716	3.36	0.3238
de17c13	22	0.4	21.6	1.7	0.0034	1	0.0218	3.87	0.0465	3.74	0.2583
de17b10	22.1	0.4	22.2	1.4	0.0034	0.93	0.0222	3.40	0.04734	3.27	0.2736
de17c05	22.1	0.4	21.4	1.2	0.0034	1.02	0.0218	3.00	0.04653	2.82	0.3401
de17c06	22.1	0.5	21.3	1.4	0.0034	1.21	0.0214	3.43	0.04566	3.21	0.3527
de17c12	22.1	0.6	21.2	1.2	0.0034	1.3	0.0216	3.27	0.04616	3	0.3976
de17d07	22.1	0.5	21.8	1.7	0.0034	1.14	0.0218	3.75	0.04653	3.57	0.3042
de17b11	22.2	0.4	21.5	1.2	0.0034	0.93	0.0215	3.04	0.0458	2.89	0.3063
de17b12	22.2	0.4	23.6	1.4	0.0034	0.9	0.0234	3.22	0.05002	3.09	0.2796
de17d09	22.2	0.4	21.2	1.1	0.0035	0.87	0.0218	2.76	0.04512	2.62	0.3151
de17a11	22.3	0.9	22	1.5	0.0035	2.1	0.0224	3.52	0.04645	2.83	0.5959
de17c08	22.3	0.5	21.2	1.1	0.0035	1.11	0.0218	3.11	0.04524	2.91	0.3564
de17c09	22.3	1.3	22.5	1.6	0.0035	2.9	0.0229	4.34	0.04739	3.23	0.6681
de17b06	22.4	0.9	23.7	1.6	0.0035	2.06	0.0243	3.86	0.05046	3.27	0.5330
de17d05	22.4	0.5	23.4	1.7	0.0035	1.02	0.0238	3.79	0.04939	3.65	0.2691
de17d12	22.4	0.6	21	1.2	0.0035	1.26	0.0217	3.06	0.04509	2.79	0.4116
de17a12	22.5	1	22.4	1.2	0.0035	2.13	0.0226	3.38	0.04677	2.63	0.6294
de17a08	22.6	0.9	23.1	1.4	0.0035	1.96	0.0237	3.26	0.04916	2.6	0.6020
de17d06	22.6	0.5	22.3	1.8	0.0035	1.03	0.0223	4.29	0.04623	4.16	0.2403
de17a13	22.7	0.7	22.1	1.1	0.0035	1.61	0.0224	2.87	0.04637	2.38	0.5603
de17d11	22.8	0.5	23.3	1.3	0.0035	1.18	0.0236	2.98	0.04891	2.74	0.3955
de17b08	23	0.4	22	1.7	0.0036	0.97	0.0223	3.96	0.04497	3.84	0.2449
Mean (n=29)	**22.23**	**0.12**									
2 SD propagated		**0.27**									

KJ1313 (n°30 in Fig. 2)	**$^{206}Pb/^{238}U$**	**± 2 SD**	**$^{207}Pb/^{235}U$**	**± 2 SD**	**$^{206}Pb/^{238}U$**	**± SD %**	**$^{207}Pb/^{235}U$**	**± SD %**	**$^{207}Pb/^{206}Pb$**	**± SD %**	**Corr. Coef.**	**Comment**
jn22g06	20.9	0.6	21.4	2.5	0.0032	1.35	0.0208	6.41	0.04725	6.27	0.2105	
jn22g10	20.9	0.5	20.7	1.5	0.0032	1.09	0.0206	3.77	0.04664	3.61	0.2891	

jn22h09	20.9	0.4	21.7	1.1	0.0033	0.94	0.0220	2.82	0.04829	2.66	0.3332	
jn22i07	20.9	0.5	23.9	3	0.0032	1.29	0.0238	6.54	0.05403	6.41	0.1973	
jn22i05	21	0.4	21.4	1.3	0.0033	0.95	0.0218	3.32	0.04795	3.18	0.2862	
jn22j07	21	0.5	21.6	2	0.0033	1.29	0.0218	5.04	0.04803	4.87	0.2561	
jn22g07	21.1	0.3	20.3	1.4	0.0033	0.81	0.0208	3.63	0.04566	3.54	0.2230	
jn22h11	21.1	0.4	21.4	1.9	0.0033	1.04	0.0214	4.78	0.04707	4.67	0.2174	
jn22h13	21.1	0.4	21.6	1.7	0.0033	1.02	0.0218	3.93	0.04803	3.8	0.2592	
jn22i10	21.2	0.4	22.3	1.9	0.0033	0.98	0.0223	4.56	0.049	4.45	0.2151	
jn22j06	21.2	0.5	21.2	1.7	0.0033	1.15	0.0215	4.17	0.04725	4.01	0.2757	
jn22j08	21.2	0.4	23.9	2	0.0033	1.01	0.0239	4.45	0.05253	4.33	0.2272	
jn22g05	21.3	0.5	20.3	2.1	0.0033	1.11	0.0199	5.36	0.04366	5.24	0.2072	
jn22g08	21.3	0.5	22.4	1.9	0.0033	1.12	0.0223	4.40	0.04908	4.26	0.2543	
jn22g09	21.3	0.5	21.7	1.9	0.0033	1.12	0.0216	4.53	0.04743	4.39	0.2472	
jn22h10	21.3	0.5	21	1.9	0.0033	1.21	0.0212	4.64	0.04668	4.48	0.2607	
jn22j09	21.3	0.5	20.9	2	0.0033	1.18	0.0205	4.97	0.04518	4.83	0.2373	
jn22j12	21.3	0.5	22.2	2.5	0.0033	1.29	0.0218	5.69	0.04787	5.54	0.2268	
jn22g13	21.4	0.5	22.3	1.9	0.0033	1.09	0.0221	4.54	0.0486	4.41	0.2399	
jn22h07	21.4	0.4	22.8	1.4	0.0033	1	0.0227	3.45	0.04989	3.3	0.2900	
jn22i11	21.5	0.5	22.6	1.6	0.0033	1.21	0.0225	3.66	0.04944	3.45	0.3310	
jn22j10	21.5	0.7	22.2	2.3	0.0033	1.58	0.0220	5.59	0.04839	5.36	0.2827	
jn22h12	21.6	0.4	21.8	1.8	0.0034	0.86	0.0221	4.00	0.04707	3.91	0.2148	
jn22i09	21.7	0.6	22	2.1	0.0034	1.41	0.0220	5.07	0.04686	4.87	0.2781	
jn22i12	21.7	0.5	21.5	2	0.0034	1.19	0.0219	5.00	0.04664	4.86	0.2378	
jn22h06	21.8	0.4	22.1	1.5	0.0034	1.02	0.0220	3.75	0.04697	3.61	0.2719	antecryst
jn22g12	21.9	0.5	22.7	1.7	0.0034	1.12	0.0228	4.25	0.04872	4.1	0.2635	antecryst
jn22g11	22	0.5	22.6	1.9	0.0034	1.24	0.0224	4.25	0.04779	4.06	0.2921	antecryst
jn22i06	22.1	0.6	23.4	2	0.0034	1.32	0.0231	4.24	0.04935	4.03	0.3113	antecryst
jn22i08	22.2	0.6	22.9	1.9	0.0034	1.29	0.0226	4.52	0.04821	4.33	0.2855	antecryst
jn22j13	23	0.6	24.1	1.7	0.0036	1.23	0.0244	3.91	0.04922	3.71	0.3147	antecryst
Mean (n=25)	**21.22**	**0.09**										
2 SD propagated		**0.33**										

Supplementary Table B.2: Re-Os data for molybdenite from various PCDs in the Meghri-Ordubad pluton.

Sample	Location	wt (g)	Re (ppm)	±	^{187}Re (ppm)	±	^{187}Os (ppb)	±	Age (Ma)	±[a]	±[b]	Description
RO280-2_N2[d]	Agarak	0.024	538.8	1.9	338.7	1.2	249.6	0.7	44.23	0.18	0.22	stockwork-like veins (quartz-molybdenite-chalcopyrite)
RO812-3_Ankaser_N72p[d]	Hanqasar	0.022	76.3	0.3	47.9	0.2	34.5	0.1	43.14	0.17	0.22	stockwork-like veins (quartz-molybdenite)
RO812-7_Aigedzor_NRM-0560[d]	Aygedzor	0.011	1141.0	5.5	717.2	3.5	509.5	2.3	42.62	0.17	0.22	stockwork-like veins (quartz-molybdenite)
RO758-5_KJ1509	Kadjaran	0.020	238.6	0.9	150.0	0.6	68.2	0.2	27.28	0.11	0.14	stockwork-like veins (quartz-molybdenite-chalcopyrite)
RO280-1_Ni[d]	Kadjaran	0.042	368.3	1.2	231.5	0.8	104.9	0.3	27.19	0.11	0.14	stockwork-like veins (quartz-molybdenite)
RO596-2_KJ-13-25A	Kadjaran	0.015	350.8	1.4	220.5	0.9	97.9	0.4	26.65	0.11	0.14	sheared stockwork-like veins (quartz-molybdenite-chalcopyrite)
RO612-10_KJ-13-25A[c]	Kadjaran	0.027	365.4	1.3	229.6	0.8	101.9	0.3	26.64	0.11	0.14	sheared stockwork-like veins (quartz-molybdenite-chalcopyrite)
RO391-2_KJ-10-13A[d]	Kadjaran	0.050	160.4	0.5	100.8	0.3	44.4	0.1	26.43	0.11	0.13	stockwork-like veins (quartz-molybdenite-chalcopyrite)
RO758-6_KJ15X1	Kadjaran	0.020	360.6	1.3	226.6	0.8	77.4	0.2	20.48	0.08	0.10	reopening of moly stockwork-like veins (quartz-molybdenite-chalcopyrite)

[a] age uncertainty includes all analytical sources of uncertainty

[b] age uncertainty includes all analytical sources of uncertainty and the uncertainty in the ^{187}Re decay constant

[c] repeat analysis. Aliquot analyzed comes from one mineral separate.

[d] Re-Os ages cited in Moritz et al. (2016)

Supplementary Table B.3: Results of in situ Hf isotope MC-ICP-MS analyses.

Samples

Analysis (n=365)	# cycles integrated	176Hf/177Hf	176Hf/177Hf std corrected	2se	176Lu/177Hf	2se	173Yb/177Hf	1se	174Hf177Hf	2se	178Hf/177Hf	2se	U-Pb Age (Ma)[a]	176Hf/177Hf (t) CHUR[b]	176Hf/177Hf (t)	εHf (t)	2se
AG1304A (s080515) n=11																	
AG1304A_1.dat	80	0.283003	0.283000	1.9E-05	0.003034	3.0E-04	0.149593	9.6E-03	0.008679	2.4E-05	1.467268	1.3E-04	50.5	0.282753	0.282997	8.6	1.3
AG1304A_2.dat	60	0.282996	0.282993	1.5E-05	0.001209	4.2E-05	0.056566	1.9E-03	0.008655	1.4E-05	1.467249	1.6E-04	49.3	0.282754	0.282991	8.4	1.0
AG1304A_3.dat	100	0.283055	0.283052	2.8E-05	0.009890	7.4E-05	0.417537	5.1E-03	0.008741	3.6E-05	1.467267	1.1E-04	50.2	0.282753	0.283043	10.2	2.0
AG1304A_4.dat	70	0.282994	0.282991	1.6E-05	0.003402	1.3E-04	0.159420	4.2E-03	0.008686	2.1E-05	1.467285	1.4E-04	49.1	0.282754	0.282988	8.3	1.1
AG1304A_5.dat	60	0.283001	0.282997	1.7E-05	0.000922	1.1E-05	0.041956	9.2E-04	0.008665	1.3E-05	1.467278	1.5E-04	49	0.282754	0.282997	8.6	1.2

AG1304A_6.dat	50	0.283037	0.283034	2.4E-05	0.001793	3.0E-05	0.072572	1.9E-03	0.008675	2.4E-05	1.467385	2.2E-04	48	0.282755	0.283032	9.8	1.7
AG1304A_7.dat	90	0.282996	0.282992	1.5E-05	0.001019	2.6E-05	0.043738	2.8E-04	0.008667	1.1E-05	1.467227	1.2E-04	49.4	0.282754	0.282991	8.4	1.0
AG1304A_8.dat	120	0.283014	0.283010	1.2E-05	0.001317	3.6E-05	0.053413	4.8E-04	0.008668	1.1E-05	1.467277	9.4E-05	49.2	0.282754	0.283009	9.0	0.8
AG1304A 9.dat	100	0.283030	0.283026	1.6E-05	0.000971	7.4E-06	0.042508	7.7E-04	0.008672	1.1E-05	1.467245	1.2E-04	48.6	0.282754	0.283025	9.6	1.1
AG1304A_11.dat	70	0.283016	0.283013	1.4E-05	0.001040	1.4E-05	0.043985	9.4E-04	0.008658	1.2E-05	1.467229	1.3E-04	49.1	0.282754	0.283012	9.1	1.0
AG1304A_12.dat	70	0.283005	0.283002	1.5E-05	0.001327	4.7E-05	0.056823	9.5E-04	0.008655	1.2E-05	1.467268	1.3E-04	50.1	0.282754	0.283000	8.7	1.0
Median ± 2SD																**8.7**	**1.3**
MA1501 (s07-081015) n=13																	
MA1501_01	110	0.282958	0.282974	9.8E-06	0.001256	5.2E-05	0.049253	1.0E-03	0.008658	7.3E-06	1.467266	1.1E-04	47.4	0.282755	0.282973	7.7	0.7
MA1501_02	120	0.282967	0.282983	8.6E-06	0.001364	7.5E-05	0.056342	1.9E-03	0.008675	7.1E-06	1.467258	7.8E-05	47.6	0.282755	0.282982	8.0	0.6
MA1501_03	120	0.282967	0.282983	7.4E-06	0.001352	2.3E-05	0.053815	7.8E-04	0.008659	7.1E-06	1.467255	9.1E-05	46.7	0.282756	0.282981	8.0	0.5
MA1501_04	90	0.282973	0.282988	1.1E-05	0.001508	2.5E-05	0.060278	6.8E-04	0.008666	8.4E-06	1.467236	9.2E-05	47.7	0.282755	0.282987	8.2	0.8
MA1501_05	100	0.282974	0.282989	9.6E-06	0.001596	1.9E-05	0.065849	6.6E-04	0.008665	7.8E-06	1.467253	1.0E-04	46.4	0.282756	0.282988	8.2	0.7
MA1501_06	120	0.282983	0.282999	8.9E-06	0.001151	1.2E-05	0.045856	3.8E-04	0.008657	6.7E-06	1.467247	8.1E-05	48.1	0.282755	0.282998	8.6	0.6
MA1501 07	120	0.282966	0.282982	8.1E-06	0.001537	6.9E-05	0.058773	1.3E-03	0.008661	7.9E-06	1.467282	6.8E-05	47.9	0.282755	0.282981	8.0	0.6
MA1501_08	120	0.282978	0.282994	7.5E-06	0.001591	4.8E-05	0.062274	6.7E-04	0.008657	7.1E-06	1.467246	7.6E-05	48.9	0.282754	0.282992	8.4	0.5
MA1501_09	120	0.282968	0.282984	8.3E-06	0.001367	1.7E-05	0.052438	5.9E-04	0.008660	6.3E-06	1.467247	9.9E-05	48.2	0.282755	0.282983	8.1	0.6
MA1501_10	120	0.282961	0.282977	8.3E-06	0.001603	6.0E-05	0.060294	1.1E-03	0.008668	7.6E-06	1.467280	7.3E-05	47.4	0.282755	0.282975	7.8	0.6
MA1501_11	120	0.282977	0.282992	7.7E-06	0.001417	2.1E-05	0.053355	3.8E-04	0.008674	6.7E-06	1.467242	7.8E-05	47.2	0.282755	0.282991	8.3	0.5
MA1501_12	120	0.282959	0.282975	7.8E-06	0.001455	4.6E-05	0.056207	8.0E-04	0.008667	6.6E-06	1.467251	8.2E-05	46.9	0.282756	0.282974	7.7	0.5
MA1501 13	120	0.282956	0.282971	8.1E-06	0.001530	8.5E-05	0.058721	1.8E-03	0.008652	7.0E-06	1.467258	7.8E-05	47.7	0.282755	0.282970	7.6	0.6
Median ± 2SD																**8.0**	**0.6**
AG1401 (s080515) n=10																	
AG1401_1.dat	90	0.283018	0.283015	1.5E-05	0.003241	1.0E-04	0.138299	2.5E-03	0.008677	2.2E-05	1.467263	1.0E-04	46.8	0.282756	0.283012	9.1	1.1
AG1401_2.dat	110	0.283007	0.283004	1.4E-05	0.001694	2.5E-05	0.063874	5.5E-04	0.008665	1.3E-05	1.467314	9.8E-05	46.9	0.282756	0.283002	8.7	1.0
AG1401_3.dat	110	0.283019	0.283016	1.4E-05	0.002534	8.1E-05	0.097771	1.3E-03	0.008675	1.5E-05	1.467284	1.0E-04	46.1	0.282756	0.283013	9.1	1.0
AG1401_4.dat	110	0.282987	0.282984	1.4E-05	0.002684	1.2E-04	0.106953	3.1E-03	0.008670	1.5E-05	1.467292	1.0E-04	46.6	0.282756	0.282981	8.0	1.0
AG1401 5.dat	110	0.283038	0.283034	1.3E-05	0.002511	2.1E-04	0.097452	4.2E-03	0.008688	1.7E-05	1.467278	1.1E-04	45.7	0.282756	0.283032	9.8	0.9
AG1401_6.dat	110	0.282998	0.282995	1.4E-05	0.001853	5.5E-05	0.076193	2.0E-03	0.008664	1.4E-05	1.467297	1.1E-04	45.9	0.282756	0.282993	8.4	1.0
AG1401_7.dat	90	0.283000	0.282996	1.5E-05	0.001565	4.7E-05	0.064399	2.0E-03	0.008658	1.3E-05	1.467264	1.2E-04	45.9	0.282756	0.282995	8.4	1.0
AG1401_8.dat	110	0.283011	0.283007	1.4E-05	0.002660	2.0E-04	0.112226	4.8E-03	0.008669	1.6E-05	1.467307	1.0E-04	46.3	0.282756	0.283005	8.8	1.0

AG1401_9.dat	110	0.283021	0.283018	1.4E-05	0.002409	1.2E-04	0.098998	2.1E-03	0.008688	1.5E-05	1.467266	1.1E-04	45.9	0.282756	0.283016	9.2	1.0
AG1401_10.dat	110	0.283004	0.283001	1.5E-05	0.002540	1.8E-04	0.104073	3.7E-03	0.008674	1.4E-05	1.467274	1.1E-04	45.6	0.282756	0.282999	8.6	1.1
Median ± 2SD																**8.8**	**1.0**
AG1404 (s080515) n=12																	
AG1404_1.dat	120	0.283019	0.283015	1.2E-05	0.001403	4.6E-05	0.066975	1.2E-03	0.008671	1.2E-05	1.467264	9.1E-05	44.7	0.282757	0.283014	9.1	0.9
AG1404_2.dat	110	0.283012	0.283009	1.3E-05	0.001814	6.1E-05	0.084014	1.7E-03	0.008662	1.5E-05	1.467310	1.5E-04	44.4	0.282757	0.283007	8.9	0.9
AG1404_3.dat	120	0.283008	0.283004	1.7E-05	0.001814	4.7E-05	0.081269	1.5E-03	0.008677	1.5E-05	1.467347	1.2E-04	43.8	0.282757	0.283003	8.7	1.2
AG1404_4.dat	35	0.283034	0.283031	1.9E-05	0.000916	4.0E-05	0.048791	2.0E-03	0.008693	1.9E-05	1.467425	2.9E-04	45.6	0.282756	0.283030	9.7	1.3
AG1404_5.dat	110	0.283019	0.283016	1.3E-05	0.001448	2.0E-05	0.068346	1.3E-03	0.008679	1.2E-05	1.467236	1.1E-04	43.2	0.282758	0.283015	9.1	0.9
AG1404_5bis.da	80	0.282991	0.282988	1.3E-05	0.001163	4.0E-05	0.052753	5.1E-04	0.008649	1.1E-05	1.467248	1.5E-04	44.7	0.282757	0.282987	8.1	0.9
AG1404 6.dat	120	0.283013	0.283010	1.3E-05	0.001282	4.1E-05	0.057093	1.5E-03	0.008666	1.2E-05	1.467194	1.1E-04	43.9	0.282757	0.283009	8.9	0.9
AG1404_7.dat	120	0.283024	0.283021	1.1E-05	0.001303	3.4E-05	0.055913	9.4E-04	0.008678	1.2E-05	1.467240	1.1E-04	43.7	0.282758	0.283020	9.3	0.8
AG1404_8.dat	100	0.283008	0.283005	1.2E-05	0.001455	7.6E-05	0.066207	2.7E-03	0.008660	1.1E-05	1.467244	1.2E-04	45.6	0.282756	0.283004	8.8	0.9
AG1404_9.dat	60	0.283020	0.283016	1.5E-05	0.001292	3.4E-05	0.062955	1.9E-03	0.008665	1.3E-05	1.467225	1.5E-04	46.4	0.282756	0.283015	9.2	1.0
AG1404_10.dat	100	0.283016	0.283013	1.2E-05	0.001160	3.7E-05	0.053469	1.7E-03	0.008656	1.0E-05	1.467218	1.2E-04	46.5	0.282756	0.283012	9.1	0.8
AG1404_11.dat	110	0.283006	0.283003	1.3E-05	0.001180	3.1E-05	0.054368	1.7E-03	0.008651	1.0E-05	1.467239	1.1E-04	46.4	0.282756	0.283002	8.7	0.9
Median ± 2SD																**9.0**	**0.8**
VK1403 (s050215) n=10																	
VK1403_01.dat	120	0.283026	0.283030	1.1E-05	0.001158	4.7E-05	0.049072	1.2E-03	0.008681	8.8E-06	1.467323	1.1E-04	44	0.282757	0.283029	9.6	0.8
VK1403_02.dat	120	0.283023	0.283027	1.2E-05	0.001397	8.0E-05	0.060613	1.7E-03	0.008673	1.4E-05	1.467308	1.3E-04	43.3	0.282758	0.283026	9.5	0.8
VK1403_03.dat	100	0.283022	0.283026	1.2E-05	0.000838	1.2E-05	0.035341	3.0E-04	0.008668	8.7E-06	1.467306	1.3E-04	45.4	0.282756	0.283025	9.5	0.9
VK1403_04.dat	120	0.283001	0.283005	1.4E-05	0.001270	1.9E-05	0.056495	4.7E-04	0.008660	1.4E-05	1.467310	1.2E-04	44.4	0.282757	0.283004	8.7	1.0
VK1403_05.dat	120	0.283014	0.283018	1.3E-05	0.001264	1.9E-05	0.054698	6.4E-04	0.008667	1.1E-05	1.467337	1.4E-04	43.4	0.282758	0.283017	9.2	0.9
VK1403 06.dat	55	0.282992	0.282996	1.7E-05	0.001561	3.1E-05	0.072153	2.5E-04	0.008655	1.6E-05	1.467301	1.5E-04	44.8	0.282757	0.282995	8.4	1.2
VK1403_07.dat	120	0.283024	0.283028	1.1E-05	0.001195	2.3E-05	0.053725	5.5E-04	0.008670	1.0E-05	1.467323	1.3E-04	42.2	0.282758	0.283027	9.5	0.8
VK1403_08.dat	80	0.283014	0.283017	1.9E-05	0.000856	6.2E-06	0.035171	1.6E-04	0.008650	1.2E-05	1.467333	1.6E-04	44.03	0.282757	0.283016	9.2	1.3
VK1403_09.dat	120	0.282989	0.282992	1.8E-05	0.001802	1.1E-04	0.080490	2.3E-03	0.008657	1.8E-05	1.467333	1.3E-04	45	0.282757	0.282991	8.3	1.2
VK1403_10.dat	120	0.283020	0.283024	1.2E-05	0.001145	1.2E-05	0.050849	3.5E-04	0.008671	9.1E-06	1.467311	1.2E-04	44.5	0.282757	0.283023	9.4	0.9
Median ± 2SD																**9.3**	**1.0**
AG1403 (s080515) n=11																	
AG1403_1.dat	120	0.283018	0.283015	1.2E-05	0.000762	3.5E-06	0.035838	3.8E-04	0.008666	1.3E-05	1.467248	1.1E-04	44.4	0.282757	0.283014	9.1	0.8

AG1403_2.dat	120	0.283030	0.283026	1.3E-05	0.001361	1.2E-05	0.063821	6.3E-04	0.008670	1.6E-05	1.467269	1.1E-04	43	0.282758	0.283025	9.4	0.9
AG1403_3.dat	120	0.283033	0.283029	1.1E-05	0.001008	3.7E-05	0.046551	5.5E-04	0.008676	1.2E-05	1.467192	8.5E-05	43.1	0.282758	0.283028	9.6	0.8
AG1403_4.dat	120	0.283027	0.283024	1.3E-05	0.001509	2.9E-05	0.071004	7.8E-04	0.008685	1.5E-05	1.467238	1.1E-04	45.8	0.282756	0.283023	9.4	0.9
AG1403 5.dat	120	0.283038	0.283035	1.2E-05	0.001225	2.7E-05	0.058243	9.9E-04	0.008682	1.3E-05	1.467239	8.5E-05	43.9	0.282757	0.283034	9.8	0.8
AG1403_6.dat	120	0.283028	0.283025	1.2E-05	0.001658	4.3E-05	0.075674	9.4E-04	0.008671	1.1E-05	1.467267	1.0E-04	43.3	0.282758	0.283024	9.4	0.9
AG1403_7.dat	70	0.283006	0.283002	1.4E-05	0.001169	4.1E-05	0.054738	1.3E-03	0.008652	1.0E-05	1.467254	1.3E-04	44.2	0.282757	0.283001	8.6	1.0
AG1403_8.dat	120	0.283023	0.283020	1.2E-05	0.001286	1.0E-04	0.057704	2.5E-03	0.008668	8.9E-06	1.467238	9.7E-05	44.1	0.282757	0.283019	9.3	0.9
AG1403_9.dat	40	0.283030	0.283026	2.3E-05	0.001143	5.3E-05	0.050157	1.7E-03	0.008681	1.6E-05	1.467522	2.6E-04	43.6	0.282758	0.283025	9.5	1.7
AG1403_10.dat	100	0.283023	0.283019	1.1E-05	0.001056	1.3E-05	0.046736	4.1E-04	0.008671	1.0E-05	1.467269	9.7E-05	45.2	0.282757	0.283019	9.3	0.8
AG1403_11.dat	80	0.283019	0.283016	1.5E-05	0.001355	8.4E-05	0.063832	2.7E-03	0.008674	1.0E-05	1.467223	1.2E-04	44	0.282757	0.283015	9.1	1.0
Median ± 2SD																**9.4**	**0.6**
AG1406 (s080515) n=10																	
AG1406_1.dat	120	0.283010	0.283007	1.2E-05	0.001342	2.5E-05	0.061993	1.4E-03	0.008659	1.1E-05	1.467273	1.2E-04	43	0.282758	0.283006	8.8	0.8
AG1406_2.dat	120	0.283005	0.283002	1.1E-05	0.001271	6.8E-05	0.059201	2.3E-03	0.008664	1.1E-05	1.467271	1.0E-04	43.5	0.282758	0.283001	8.6	0.8
AG1406_3.dat	120	0.282998	0.282994	1.3E-05	0.001352	4.8E-05	0.060517	1.0E-03	0.008659	1.2E-05	1.467303	9.9E-05	44.1	0.282757	0.282993	8.3	0.9
AG1406_4.dat	120	0.283009	0.283005	1.3E-05	0.001187	3.1E-05	0.050593	1.1E-03	0.008666	1.1E-05	1.467284	1.1E-04	45.1	0.282757	0.283004	8.8	0.9
AG1406 5.dat	120	0.283022	0.283019	1.4E-05	0.003034	1.3E-04	0.139088	2.8E-03	0.008672	1.7E-05	1.467281	1.1E-04	44.2	0.282757	0.283016	9.2	1.0
AG1406_6.dat	120	0.283034	0.283031	1.3E-05	0.001346	7.3E-05	0.060033	1.4E-03	0.008671	9.1E-06	1.467273	1.2E-04	43.1	0.282758	0.283030	9.6	0.9
AG1406_7.dat	70	0.283001	0.282998	1.4E-05	0.001385	9.2E-05	0.064106	1.3E-03	0.008652	1.4E-05	1.467285	1.3E-04	43.4	0.282758	0.282997	8.5	1.0
AG1406_8.dat	120	0.283019	0.283016	1.3E-05	0.001536	4.7E-05	0.060323	1.1E-03	0.008659	1.2E-05	1.467267	1.1E-04	43.2	0.282758	0.283015	9.1	0.9
AG1406_9.dat	120	0.283012	0.283009	1.2E-05	0.001351	6.2E-05	0.061242	1.3E-03	0.008675	1.3E-05	1.467308	9.6E-05	45.7	0.282756	0.283008	8.9	0.9
AG1406_10.dat	120	0.283037	0.283033	1.2E-05	0.001387	1.5E-05	0.059123	7.6E-04	0.008669	1.0E-05	1.467273	1.1E-04	45.2	0.282757	0.283032	9.7	0.9
Median ± 2SD																**8.8**	**0.9**
AG1402 (s040215) n=10																	
AG1402_10.dat	90	0.282980	0.283001	1.6E-05	0.000846	1.4E-05	0.036209	4.7E-04	0.008682	1.1E-05	1.467247	1.4E-04	43.7	0.282758	0.283001	8.6	1.1
AG1402_09.dat	120	0.282972	0.282994	1.4E-05	0.001057	6.0E-05	0.042792	1.1E-03	0.008690	1.4E-05	1.467331	1.2E-04	44.1	0.282757	0.282993	8.3	1.0
AG1402_08.dat	120	0.282962	0.282984	1.3E-05	0.001798	1.5E-04	0.073767	2.8E-03	0.008656	1.3E-05	1.467295	1.2E-04	41.9	0.282759	0.282982	7.9	0.9
AG1402_07.dat	120	0.282976	0.282997	1.3E-05	0.000938	2.1E-05	0.039453	6.6E-04	0.008669	1.0E-05	1.467303	1.0E-04	44.1	0.282757	0.282996	8.5	0.9
AG1402_06.dat	120	0.282988	0.283009	1.3E-05	0.001226	2.6E-05	0.050655	5.2E-04	0.008675	1.2E-05	1.467292	1.3E-04	44.7	0.282757	0.283008	8.9	0.9
AG1402_05.dat	120	0.282979	0.283001	1.3E-05	0.002104	2.4E-04	0.089494	5.3E-03	0.008673	1.3E-05	1.467299	1.1E-04	44.3	0.282757	0.282999	8.6	0.9
AG1402_04.dat	120	0.282976	0.282997	1.5E-05	0.000974	1.7E-05	0.040007	3.0E-04	0.008659	1.4E-05	1.467307	1.2E-04	44.3	0.282757	0.282996	8.5	1.0

AG1402_03.dat	80	0.282977	0.282998	1.5E-05	0.001179	5.5E-05	0.053625	1.4E-03	0.008671	1.6E-05	1.467276	1.5E-04	43.2	0.282758	0.282997	8.5	1.1
AG1402_02.dat	120	0.282981	0.283002	1.2E-05	0.000951	1.9E-05	0.038703	3.2E-04	0.008663	1.0E-05	1.467310	1.2E-04	44.4	0.282757	0.283002	8.6	0.8
AG1402_01.dat	120	0.282984	0.283005	1.1E-05	0.000984	4.5E-05	0.039133	8.4E-04	0.008680	8.7E-06	1.467272	9.8E-05	43.7	0.282758	0.283005	8.7	0.8
Median ± 2SD																**8.5**	**0.5**
HQ1402 (s080515) n=9																	
HQ1402_1.dat	120	0.283063	0.283060	1.2E-05	0.000948	4.0E-05	0.040428	1.1E-03	0.008649	1.0E-05	1.467248	9.3E-05	43.5	0.282758	0.283059	10.7	0.9
HQ1402_2.dat	120	0.283086	0.283083	1.2E-05	0.000973	2.4E-05	0.042335	4.6E-04	0.008677	9.4E-06	1.467260	1.0E-04	42.4	0.282758	0.283082	11.4	0.8
HQ1402_3.dat	80	0.283112	0.283108	1.7E-05	0.002616	2.4E-04	0.120061	5.2E-03	0.008711	1.8E-05	1.467324	1.3E-04	42.8	0.282758	0.283106	12.3	1.2
HQ1402_4.dat	120	0.283083	0.283080	1.3E-05	0.001494	7.8E-06	0.065621	5.8E-04	0.008670	1.2E-05	1.467256	1.0E-04	43.5	0.282758	0.283079	11.3	0.9
HQ1402_5.dat	100	0.283091	0.283088	1.5E-05	0.001700	5.2E-05	0.077012	1.9E-03	0.008688	1.2E-05	1.467261	1.2E-04	44.1	0.282757	0.283087	11.6	1.0
HQ1402 8.dat	30	0.283050	0.283047	2.0E-05	0.001299	1.6E-04	0.055903	5.2E-03	0.008693	2.0E-05	1.467385	2.6E-04	42.5	0.282758	0.283046	10.2	1.4
HQ1402_9.dat	60	0.283079	0.283076	1.7E-05	0.000860	3.1E-05	0.044407	1.4E-03	0.008659	1.1E-05	1.467191	1.5E-04	43.2	0.282758	0.283075	11.2	1.2
HQ1402_10.dat	120	0.283081	0.283078	1.2E-05	0.001187	2.7E-05	0.053019	7.2E-04	0.008660	9.9E-06	1.467241	9.7E-05	43	0.282758	0.283077	11.3	0.8
HQ1402_11.dat	80	0.283084	0.283081	1.6E-05	0.000767	3.6E-05	0.033401	5.8E-04	0.008664	1.2E-05	1.467241	1.3E-04	41.6	0.282759	0.283080	11.4	1.1
Median ± 2SD																**11.3**	**1.2**
HQ1403 (s080515) n=11																	
HQ1403_1.dat	120	0.283050	0.283047	1.4E-05	0.000743	4.1E-05	0.033480	1.3E-03	0.008676	9.0E-06	1.467228	1.1E-04	44.7	0.282757	0.283046	10.2	1.0
HQ1403_2.dat	120	0.283051	0.283048	1.2E-05	0.000556	1.3E-05	0.022285	4.4E-04	0.008673	8.7E-06	1.467251	8.8E-05	43.7	0.282758	0.283047	10.2	0.8
HQ1403_3.dat	120	0.283074	0.283071	1.0E-05	0.000967	4.0E-05	0.037780	7.6E-04	0.008676	1.0E-05	1.467258	9.8E-05	43.2	0.282758	0.283070	11.0	0.7
HQ1403_4.dat	70	0.283035	0.283032	1.5E-05	0.001147	6.7E-05	0.049779	2.6E-03	0.008679	1.3E-05	1.467295	1.3E-04	42.4	0.282758	0.283031	9.6	1.1
HQ1403_5.dat	120	0.283061	0.283057	1.2E-05	0.001027	6.0E-05	0.040240	1.1E-03	0.008673	9.3E-06	1.467230	9.5E-05	42.9	0.282758	0.283056	10.6	0.8
HQ1403_6.dat	90	0.283057	0.283053	1.6E-05	0.000860	3.2E-05	0.034898	7.1E-04	0.008663	1.0E-05	1.467239	1.3E-04	43.5	0.282758	0.283053	10.4	1.1
HQ1403_7.dat	100	0.283036	0.283033	1.3E-05	0.000775	3.6E-05	0.029640	5.9E-04	0.008655	1.0E-05	1.467236	1.0E-04	42.7	0.282758	0.283032	9.7	0.9
HQ1403 9.dat	100	0.283087	0.283083	1.3E-05	0.001134	3.3E-05	0.047810	5.8E-04	0.008674	1.1E-05	1.467230	1.2E-04	43.7	0.282758	0.283082	11.5	0.9
HQ1403_10.dat	100	0.283072	0.283068	1.4E-05	0.001084	7.6E-05	0.044115	1.7E-03	0.008676	1.0E-05	1.467162	1.0E-04	42.9	0.282758	0.283067	10.9	1.0
HQ1403_11.dat	70	0.283036	0.283033	1.4E-05	0.000780	3.2E-05	0.030807	1.1E-03	0.008664	1.1E-05	1.467228	1.3E-04	42.5	0.282758	0.283032	9.7	1.0
HQ1403_12.dat	60	0.283059	0.283056	1.8E-05	0.001063	4.1E-05	0.047855	1.7E-03	0.008671	1.3E-05	1.467231	1.7E-04	40.8	0.282759	0.283055	10.5	1.3
Median ± 2SD																**10.4**	**1.2**
AG1308A1 (s040215) n=12																	
AG1308A1_10.da	120	0.282956	0.282977	1.2E-05	0.001086	1.9E-05	0.051618	3.1E-04	0.008678	1.5E-05	1.467365	1.1E-04	38	0.282761	0.282976	7.6	0.9
AG1308A1_09bis	120	0.282930	0.282951	1.6E-05	0.001665	4.3E-05	0.079308	2.0E-03	0.008650	1.8E-05	1.467331	1.4E-04	37.1	0.282762	0.282950	6.7	1.1

AG1308A1_09	120	0.282818	0.282839	1.8E-05	0.001627	4.8E-05	0.078975	2.5E-03	0.008627	2.4E-05	1.467558	1.6E-04	37.1	0.282762	0.282838	2.7	1.3
AG1308A1_08.da	120	0.283002	0.283024	2.2E-05	0.001298	3.5E-05	0.059887	1.1E-03	0.008731	2.3E-05	1.467295	1.3E-04	38	0.282761	0.283023	9.3	1.5
AG1308A1_07.da	120	0.282987	0.283008	1.2E-05	0.000960	2.6E-06	0.045471	2.2E-04	0.008678	1.2E-05	1.467277	1.1E-04	39.7	0.282760	0.283007	8.7	0.9
AG1308A1_06.da	80	0.282994	0.283015	2.3E-05	0.001243	3.3E-06	0.059373	2.1E-04	0.008697	3.0E-05	1.467347	1.2E-04	36.8	0.282762	0.283014	8.9	1.7
AG1308A1_05.da	120	0.282978	0.282999	1.4E-05	0.000612	3.7E-06	0.030874	1.9E-04	0.008656	1.0E-05	1.467286	1.1E-04	39.3	0.282760	0.282999	8.4	1.0
AG1308A1_04.da	120	0.282980	0.283001	1.8E-05	0.000744	1.3E-05	0.035329	3.2E-04	0.008673	1.7E-05	1.467290	1.4E-04	36.9	0.282762	0.283000	8.4	1.3
AG1308A1_03.da	120	0.283018	0.283039	2.1E-05	0.000625	1.6E-06	0.030884	2.5E-04	0.008709	1.6E-05	1.467290	1.2E-04	38.2	0.282761	0.283038	9.8	1.5
AG1308A1_02_ri	120	0.282956	0.282977	2.0E-05	0.002330	4.1E-06	0.115043	8.8E-04	0.008675	2.6E-05	1.467333	1.4E-04	37.3	0.282762	0.282976	7.6	1.4
AG1308A1_02.da	120	0.282974	0.282995	2.1E-05	0.002947	1.2E-05	0.151099	1.4E-03	0.008670	2.5E-05	1.467305	1.3E-04	37.3	0.282762	0.282993	8.2	1.5
AG1308A1_01.da	120	0.283018	0.283039	1.9E-05	0.000937	3.2E-06	0.045250	4.5E-04	0.008735	2.2E-05	1.467316	1.3E-04	38.4	0.282761	0.283039	9.8	1.3
Median ± 2SD																**8.4**	**3.8**
AG1308A (s080515) n=10																	
AG1308A_1.dat	110	0.282977	0.282973	1.9E-05	0.001245	6.0E-05	0.055552	1.5E-03	0.008659	1.7E-05	1.467313	9.5E-05	36.6	0.282762	0.282972	7.4	1.3
AG1308A_2.dat	110	0.282984	0.282981	1.8E-05	0.004264	3.7E-05	0.198092	1.5E-03	0.008657	2.6E-05	1.467279	9.5E-05	37	0.282762	0.282978	7.6	1.3
AG1308A_3.dat	110	0.282995	0.282992	1.7E-05	0.001475	3.9E-05	0.064136	6.8E-04	0.008672	1.8E-05	1.467291	9.4E-05	37.7	0.282761	0.282991	8.1	1.2
AG1308A_4.dat	110	0.282998	0.282995	1.9E-05	0.000684	1.7E-05	0.029171	2.7E-04	0.008660	1.5E-05	1.467306	1.0E-04	36.8	0.282762	0.282994	8.2	1.3
AG1308A_5.dat	70	0.283028	0.283025	2.1E-05	0.001019	1.0E-05	0.046824	4.9E-04	0.008698	2.1E-05	1.467286	1.1E-04	37.7	0.282761	0.283024	9.3	1.5
AG1308A_6.dat	80	0.282982	0.282979	2.0E-05	0.002005	1.2E-05	0.092870	6.5E-04	0.008668	2.1E-05	1.467296	1.2E-04	37.4	0.282761	0.282977	7.6	1.4
AG1308A_7.dat	110	0.283011	0.283008	1.6E-05	0.002375	7.1E-06	0.100085	2.8E-04	0.008664	1.9E-05	1.467304	1.0E-04	36.6	0.282762	0.283006	8.6	1.1
AG1308A_8.dat	110	0.283013	0.283010	1.7E-05	0.001374	3.3E-05	0.060755	6.4E-04	0.008692	1.7E-05	1.467254	9.6E-05	36.7	0.282762	0.283009	8.7	1.2
AG1308A_9.dat	110	0.283034	0.283030	1.8E-05	0.001875	9.3E-05	0.083363	1.9E-03	0.008686	2.1E-05	1.467278	1.0E-04	36.9	0.282762	0.283029	9.4	1.2
AG1308A_10.dat	110	0.283045	0.283042	1.9E-05	0.002509	1.8E-04	0.110198	3.8E-03	0.008700	2.1E-05	1.467287	9.6E-05	36.4	0.282762	0.283040	9.8	1.4
Median ± 2SD																**8.4**	**1.7**
VK1404 (s050215) n=10																	
VK1404_01.dat	120	0.283031	0.283034	1.3E-05	0.000516	3.3E-06	0.021464	9.6E-05	0.008672	9.5E-06	1.467289	6.7E-05	37.3	0.282762	0.283034	9.6	0.9
VK1404_02.dat	120	0.283011	0.283015	1.3E-05	0.001637	4.2E-05	0.069495	8.1E-04	0.008670	1.5E-05	1.467318	7.5E-05	38	0.282761	0.283014	8.9	0.9
VK1404_03.dat	120	0.283024	0.283028	1.4E-05	0.000508	1.2E-05	0.021766	3.6E-04	0.008683	1.1E-05	1.467343	1.1E-04	37.2	0.282762	0.283028	9.4	1.0
VK1404_04.dat	120	0.283009	0.283013	1.4E-05	0.000713	1.3E-05	0.032404	3.1E-04	0.008652	1.4E-05	1.467365	1.2E-04	37.1	0.282762	0.283012	8.9	1.0
VK1404_05.dat	70	0.282990	0.282994	1.5E-05	0.001119	5.0E-05	0.050618	1.1E-03	0.008644	2.0E-05	1.467358	1.2E-04	35.7	0.282763	0.282993	8.2	1.1
VK1404_06.dat	120	0.282989	0.282993	1.4E-05	0.000342	6.3E-06	0.014964	1.5E-04	0.008673	1.3E-05	1.467325	1.1E-04	35.4	0.282763	0.282992	8.1	1.0
VK1404_07.dat	80	0.283008	0.283012	1.7E-05	0.000696	2.4E-05	0.029341	5.5E-04	0.008656	1.3E-05	1.467348	1.4E-04	36.8	0.282762	0.283012	8.8	1.2

VK1404_08.dat	80	0.283013	0.283017	1.8E-05	0.000385	1.6E-05	0.016653	3.4E-04	0.008664	1.1E-05	1.467331	1.3E-04	36.8	0.282762	0.283017	9.0	1.2
VK1404_09.dat	120	0.282997	0.283000	1.4E-05	0.000651	1.3E-05	0.031204	3.1E-04	0.008661	1.2E-05	1.467314	1.1E-04	37.6	0.282761	0.283000	8.4	1.0
VK1404_10.dat	75	0.283025	0.283028	1.4E-05	0.000531	3.7E-06	0.023233	8.0E-05	0.008680	1.4E-05	1.467317	1.4E-04	38.3	0.282761	0.283028	9.4	1.0
Median ± 2SD																**8.9**	**1.0**
VK1405 (s050215) n=10																	
VK1405_01.dat	60	0.283030	0.283034	2.6E-05	0.000742	2.6E-05	0.031617	8.0E-04	0.008703	1.8E-05	1.467347	2.2E-04	34.1	0.282764	0.283033	9.5	1.8
VK1405_02.dat	120	0.283014	0.283017	1.5E-05	0.001017	5.8E-05	0.040581	1.3E-03	0.008671	1.2E-05	1.467326	1.3E-04	34.7	0.282763	0.283017	9.0	1.0
VK1405_03.dat	100	0.283000	0.283003	1.5E-05	0.001592	3.0E-05	0.065062	7.2E-04	0.008660	1.6E-05	1.467342	1.3E-04	36.8	0.282762	0.283002	8.5	1.1
VK1405_04.dat	40	0.282995	0.282998	1.9E-05	0.001328	2.5E-05	0.055425	5.9E-04	0.008687	2.6E-05	1.467295	1.8E-04	35.5	0.282763	0.282998	8.3	1.4
VK1405_05.dat	120	0.282991	0.282995	1.5E-05	0.000812	9.6E-06	0.033629	1.4E-04	0.008670	1.4E-05	1.467326	1.2E-04	35.3	0.282763	0.282994	8.2	1.1
VK1405 06.dat	120	0.283019	0.283023	1.6E-05	0.000940	1.9E-05	0.040832	4.8E-04	0.008694	1.5E-05	1.467334	1.4E-04	35.8	0.282762	0.283022	9.2	1.1
VK1405_07.dat	120	0.283006	0.283010	1.7E-05	0.000594	8.8E-06	0.023284	2.3E-04	0.008674	1.1E-05	1.467317	1.3E-04	34.2	0.282764	0.283010	8.7	1.2
VK1405_08.dat	80	0.282989	0.282993	1.8E-05	0.002104	1.1E-04	0.086123	2.5E-03	0.008661	1.9E-05	1.467280	1.5E-04	37.3	0.282762	0.282991	8.1	1.3
VK1405_09bis.d	50	0.282991	0.282995	2.9E-05	0.000796	5.3E-05	0.035052	1.2E-03	0.008678	1.9E-05	1.467285	1.6E-04	35.1	0.282763	0.282994	8.2	2.0
VK1405_10.dat	100	0.283012	0.283015	1.4E-05	0.000867	1.2E-05	0.034446	2.4E-04	0.008663	1.1E-05	1.467316	1.3E-04	35.3	0.282763	0.283015	8.9	1.0
Median ± 2SD																**8.6**	**1.0**
MR1403 (s050215) n=10																	
MR1403_01.dat	100	0.283012	0.283016	1.8E-05	0.000954	1.1E-05	0.039360	2.5E-04	0.008663	1.8E-05	1.467341	1.2E-04	34.2	0.282764	0.283015	8.9	1.3
MR1403_02.dat	120	0.282999	0.283002	1.9E-05	0.000813	7.7E-06	0.032203	1.1E-04	0.008656	1.8E-05	1.467295	1.3E-04	35.5	0.282763	0.283002	8.5	1.3
MR1403_03.dat	115	0.283038	0.283042	1.7E-05	0.000650	2.4E-06	0.025774	1.9E-05	0.008672	1.6E-05	1.467311	1.2E-04	35	0.282763	0.283042	9.9	1.2
MR1403_04.dat	115	0.283017	0.283021	1.9E-05	0.001675	6.1E-05	0.067886	1.4E-03	0.008689	2.8E-05	1.467288	1.1E-04	35.7	0.282763	0.283020	9.1	1.3
MR1403_05.dat	115	0.283034	0.283038	2.4E-05	0.000983	3.7E-05	0.040822	9.4E-04	0.008691	2.6E-05	1.467348	1.2E-04	35	0.282763	0.283037	9.7	1.7
MR1403_06.dat	115	0.283020	0.283023	2.0E-05	0.001719	1.1E-04	0.071029	2.6E-03	0.008707	2.3E-05	1.467313	1.5E-04	35.1	0.282763	0.283022	9.2	1.4
MR1403 07.dat	115	0.283017	0.283021	1.7E-05	0.000678	1.4E-05	0.027510	2.8E-04	0.008666	1.6E-05	1.467303	9.2E-05	36.1	0.282762	0.283020	9.1	1.2
MR1403_08.dat	65	0.283078	0.283082	3.2E-05	0.000972	2.9E-05	0.038390	2.6E-04	0.008730	2.8E-05	1.467506	2.3E-04	36.3	0.282762	0.283081	11.3	2.3
MR1403_09.dat	115	0.283039	0.283042	1.7E-05	0.001043	6.7E-05	0.040492	1.2E-03	0.008660	1.8E-05	1.467347	8.0E-05	35.8	0.282762	0.283042	9.9	1.2
MR1403_10.dat	120	0.283013	0.283017	1.8E-05	0.001175	1.3E-06	0.049094	2.3E-04	0.008662	2.5E-05	1.467310	1.3E-04	34.4	0.282763	0.283016	8.9	1.3
Median ± 2SD																**9.1**	**1.6**
LI1303A1 (s081214) n=13																	
LI1303a1_25_1.	110	0.283010	0.283020	1.4E-05	0.000329	3.6E-06	0.011358	1.1E-04	0.008649	1.2E-05	1.467290	1.0E-04	34.6	0.282763	0.283020	9.1	1.0
LI1303a1_20.da	120	0.282996	0.283005	1.4E-05	0.000471	5.8E-06	0.018634	8.9E-05	0.008647	1.2E-05	1.467248	1.2E-04	34.3	0.282763	0.283005	8.5	1.0

LI1303a1_13.da	100	0.282988	0.282997	1.5E-05	0.001519	7.5E-05	0.056714	1.2E-03	0.008616	1.8E-05	1.467270	1.3E-04	34.2	0.282764	0.282996	8.2	1.0
LI1303a1_24.da	110	0.283034	0.283043	1.3E-05	0.001886	1.4E-04	0.063721	2.5E-03	0.008675	1.2E-05	1.467233	1.2E-04	34.2	0.282764	0.283042	9.9	0.9
LI1303a1_11.da	80	0.283011	0.283021	1.4E-05	0.000743	2.8E-05	0.024469	4.2E-04	0.008644	1.2E-05	1.467285	1.2E-04	33.8	0.282764	0.283020	9.1	1.0
LI1303a1_23.da	120	0.283002	0.283011	1.4E-05	0.002694	1.6E-05	0.092634	4.8E-04	0.008651	1.6E-05	1.467260	1.0E-04	33.8	0.282764	0.283010	8.7	1.0
LI1303a1_19.da	120	0.283013	0.283022	1.1E-05	0.000654	1.6E-05	0.020855	2.9E-04	0.008649	1.0E-05	1.467275	1.0E-04	33.7	0.282764	0.283022	9.1	0.8
LI1303a1_21.da	120	0.283009	0.283018	1.4E-05	0.002411	5.2E-05	0.082889	9.7E-04	0.008658	1.5E-05	1.467265	1.1E-04	33.4	0.282764	0.283016	8.9	1.0
LI1303a1_22.da	90	0.283021	0.283030	1.7E-05	0.000833	5.9E-05	0.035735	1.2E-03	0.008667	1.8E-05	1.467295	1.3E-04	33.2	0.282764	0.283029	9.4	1.2
LI1303a1_03.da	120	0.283003	0.283012	1.3E-05	0.001061	8.2E-06	0.037445	2.8E-04	0.008636	1.2E-05	1.467234	9.1E-05	33.1	0.282764	0.283012	8.8	0.9
LI1303a1_16.da	95	0.282959	0.282968	2.2E-05	0.000925	3.2E-05	0.050632	9.8E-04	0.008589	2.9E-05	1.467230	2.0E-04	33.1	0.282764	0.282968	7.2	1.6
LI1303a1_14.da	85	0.282970	0.282980	2.5E-05	0.000593	9.2E-06	0.032929	1.8E-04	0.008610	3.1E-05	1.467286	2.6E-04	33.0	0.282764	0.282979	7.6	1.8
LI1303a1_15.da	85	0.283004	0.283013	1.5E-05	0.001641	9.1E-05	0.055710	1.7E-03	0.008648	1.5E-05	1.467317	1.3E-04	32.9	0.282764	0.283012	8.8	1.1
Median ± 2SD																**8.8**	**1.4**
LI1303 (s081214) n=13																	
LI1303_35.dat	120	0.283001	0.283010	1.7E-05	0.005064	5.0E-04	0.178688	9.2E-03	0.008670	2.4E-05	1.467230	1.0E-04	35.5	0.282763	0.283006	8.6	1.2
LI1303_23.dat	40	0.283028	0.283038	2.4E-05	0.004513	6.6E-04	0.155935	1.2E-02	0.008698	4.3E-05	1.467239	1.7E-04	35.1	0.282763	0.283035	9.6	1.7
LI1303_24.dat	120	0.283031	0.283040	2.5E-05	0.008542	2.7E-04	0.305513	4.4E-03	0.008711	3.6E-05	1.467264	1.0E-04	34.8	0.282763	0.283035	9.6	1.7
LI1303_25.dat	115	0.282988	0.282997	2.3E-05	0.006708	3.3E-04	0.252212	7.5E-03	0.008660	3.7E-05	1.467256	9.6E-05	34.7	0.282763	0.282993	8.1	1.6
LI1303_32.dat	45	0.283002	0.283011	2.0E-05	0.002533	2.6E-04	0.091593	5.1E-03	0.008648	3.3E-05	1.467160	2.4E-04	34.7	0.282763	0.283009	8.7	1.4
LI1303_10.dat	100	0.283047	0.283056	2.2E-05	0.003170	1.3E-04	0.115242	2.6E-03	0.008704	2.4E-05	1.467295	1.1E-04	34.5	0.282763	0.283054	10.3	1.6
LI1303_04.dat	80	0.283005	0.283014	1.5E-05	0.001788	1.9E-04	0.073825	4.7E-03	0.008675	1.9E-05	1.467234	1.2E-04	34.4	0.282763	0.283013	8.8	1.1
LI1303_11.dat	80	0.283008	0.283017	2.2E-05	0.002320	3.4E-04	0.082534	7.0E-03	0.008663	3.0E-05	1.467280	1.3E-04	34.4	0.282763	0.283016	8.9	1.5
LI1303_33.dat	110	0.283010	0.283019	2.6E-05	0.007232	7.1E-05	0.277616	2.3E-03	0.008681	3.5E-05	1.467213	1.1E-04	34.3	0.282763	0.283014	8.9	1.9
LI1303_12.dat	120	0.283006	0.283015	2.2E-05	0.006518	5.1E-05	0.222869	1.4E-03	0.008684	2.5E-05	1.467221	1.0E-04	34.2	0.282764	0.283011	8.8	1.5
LI1303_01.dat	70	0.283001	0.283010	1.3E-05	0.001366	2.3E-05	0.054430	3.0E-04	0.008652	1.8E-05	1.467233	1.6E-04	34.0	0.282764	0.283009	8.7	0.9
LI1303_22.dat	60	0.282979	0.282988	2.4E-05	0.002791	3.3E-04	0.096277	6.4E-03	0.008635	2.9E-05	1.467330	2.3E-04	33.5	0.282764	0.282986	7.9	1.7
LI1303_21.dat	110	0.283007	0.283016	1.6E-05	0.004598	3.6E-04	0.158238	6.6E-03	0.008678	2.2E-05	1.467239	1.0E-04	33.1	0.282764	0.283013	8.8	1.1
Median ± 2SD																**8.8**	**1.3**
KJ1207[d] (s07-081015) n=13																	
KJ1207_01	120	0.283019	0.283035	9.0E-06	0.000492	3.2E-05	0.021321	5.3E-04	0.008658	4.7E-06	1.467291	8.2E-05	33.43	0.282764	0.283035	9.6	0.6
KJ1207_02	120	0.283013	0.283028	6.8E-06	0.000315	9.1E-06	0.017143	2.5E-04	0.008657	3.6E-06	1.467242	9.0E-05	33.43	0.282764	0.283028	9.3	0.5
KJ1207_03	90	0.283017	0.283033	1.0E-05	0.001723	3.7E-05	0.072216	1.3E-03	0.008663	6.3E-06	1.467256	9.9E-05	33.43	0.282764	0.283032	9.5	0.7

KJ1207_04	45	0.283020	0.283036	1.0E-05	0.001560	9.9E-05	0.063412	1.1E-03	0.008659	8.2E-06	1.467440	1.3E-04	33.43	0.282764	0.283035	9.6	0.7
KJ1207_05	20	0.283006	0.283022	1.7E-05	0.000931	3.3E-05	0.034840	6.6E-04	0.008652	1.5E-05	1.467582	1.6E-04	33.43	0.282764	0.283022	9.1	1.2
KJ1207_06	50	0.283024	0.283040	1.1E-05	0.001766	4.9E-05	0.071936	1.4E-03	0.008673	8.0E-06	1.467417	1.5E-04	33.43	0.282764	0.283039	9.7	0.8
KJ1207_07	50	0.283012	0.283028	1.4E-05	0.000838	5.6E-05	0.030668	7.1E-04	0.008661	8.8E-06	1.467430	1.5E-04	33.43	0.282764	0.283028	9.3	1.0
KJ1207_08	100	0.283018	0.283034	7.8E-06	0.000977	3.3E-05	0.038085	6.6E-04	0.008654	4.5E-06	1.467253	1.1E-04	33.43	0.282764	0.283033	9.5	0.6
KJ1207_09	60	0.283019	0.283034	9.8E-06	0.000345	1.2E-05	0.015311	3.2E-04	0.008665	3.8E-06	1.467185	1.6E-04	33.43	0.282764	0.283034	9.6	0.7
KJ1207_10	100	0.283018	0.283033	9.1E-06	0.000655	1.3E-05	0.026389	1.4E-04	0.008660	4.5E-06	1.467130	1.7E-04	33.43	0.282764	0.283033	9.5	0.6
KJ1207_11	120	0.283019	0.283035	6.6E-06	0.000821	4.6E-06	0.031024	1.4E-04	0.008663	3.6E-06	1.466922	2.4E-04	33.43	0.282764	0.283035	9.6	0.5
KJ1207_12	120	0.283018	0.283033	6.7E-06	0.000914	5.7E-06	0.036126	1.1E-04	0.008661	4.0E-06	1.467178	1.1E-04	33.43	0.282764	0.283033	9.5	0.5
KJ1207_13	120	0.283023	0.283038	6.6E-06	0.000368	9.0E-06	0.016497	2.0E-04	0.008659	3.4E-06	1.467080	1.3E-04	33.43	0.282764	0.283038	9.7	0.5
Median ± 2SD																**9.5**	**0.3**
KJ1316[d] (s07-081015) n=12																	
KJ1316_01	110	0.283011	0.283026	6.7E-06	0.000740	1.2E-05	0.035653	3.7E-04	0.008653	4.7E-06	1.467231	8.1E-05	33.7	0.282764	0.283026	9.3	0.5
KJ1316_02	110	0.283017	0.283032	6.9E-06	0.001078	4.6E-06	0.051934	1.7E-04	0.008660	5.4E-06	1.467234	8.1E-05	33.7	0.282764	0.283032	9.5	0.5
KJ1316_03	120	0.283014	0.283030	7.1E-06	0.000707	5.8E-06	0.033040	2.0E-04	0.008655	4.1E-06	1.467244	8.0E-05	33.7	0.282764	0.283029	9.4	0.5
KJ1316_04	120	0.283014	0.283030	6.5E-06	0.000639	9.4E-06	0.031089	3.4E-04	0.008659	4.6E-06	1.467256	8.7E-05	33.7	0.282764	0.283030	9.4	0.5
KJ1316_05	120	0.283012	0.283028	5.9E-06	0.001472	2.8E-05	0.070196	6.0E-04	0.008654	5.7E-06	1.467234	5.6E-05	33.7	0.282764	0.283027	9.3	0.4
KJ1316_06	80	0.283016	0.283032	7.5E-06	0.000690	1.6E-05	0.033116	2.4E-04	0.008661	5.8E-06	1.467259	9.2E-05	33.7	0.282764	0.283031	9.5	0.5
KJ1316_07	120	0.283010	0.283026	7.0E-06	0.000694	1.4E-05	0.032878	3.6E-04	0.008655	4.4E-06	1.467229	9.6E-05	33.7	0.282764	0.283025	9.2	0.5
KJ1316_08	120	0.283017	0.283033	7.0E-06	0.000811	1.2E-05	0.037328	2.7E-04	0.008661	4.5E-06	1.467227	8.2E-05	33.7	0.282764	0.283032	9.5	0.5
KJ1316_09	120	0.282999	0.283014	6.2E-06	0.000730	5.8E-06	0.036417	3.0E-04	0.008655	4.4E-06	1.467206	7.7E-05	33.7	0.282764	0.283014	8.8	0.4
KJ1316_10	120	0.283020	0.283036	7.1E-06	0.001163	4.3E-05	0.054378	8.6E-04	0.008657	5.7E-06	1.467242	8.2E-05	33.7	0.282764	0.283035	9.6	0.5
KJ1316_11	120	0.283009	0.283025	6.2E-06	0.000647	6.9E-06	0.029988	2.4E-04	0.008651	3.8E-06	1.467228	8.6E-05	33.7	0.282764	0.283024	9.2	0.4
KJ1316_12	70	0.283012	0.283028	7.8E-06	0.000978	3.0E-05	0.045049	6.9E-04	0.008660	5.0E-06	1.467266	1.1E-04	33.7	0.282764	0.283027	9.3	0.6
Median ± 2SD																**9.4**	**0.4**
KJ1006A (s050215) n=10																	
KJ1006A_01.dat	120	0.283034	0.283038	9.3E-06	0.000339	6.1E-06	0.013866	9.1E-05	0.008666	6.8E-06	1.467292	6.8E-05	31.6	0.282765	0.283037	9.6	0.7
KJ1006A_02.dat	120	0.283019	0.283023	1.3E-05	0.000472	1.3E-05	0.019278	1.5E-04	0.008666	9.1E-06	1.467339	1.1E-04	31.9	0.282765	0.283023	9.1	0.9
KJ1006A_03.dat	120	0.283045	0.283048	1.3E-05	0.001496	1.2E-04	0.055433	2.1E-03	0.008692	1.2E-05	1.467274	9.6E-05	31.5	0.282765	0.283048	10.0	0.9
KJ1006A_04.dat	120	0.283027	0.283031	9.8E-06	0.000540	6.7E-06	0.022515	1.0E-04	0.008661	7.4E-06	1.467330	8.0E-05	31.9	0.282765	0.283031	9.4	0.7
KJ1006A_05.dat	120	0.283029	0.283032	9.6E-06	0.000596	3.6E-05	0.023579	7.9E-04	0.008672	8.4E-06	1.467313	9.5E-05	31.1	0.282765	0.283032	9.4	0.7

KJ1006A_06.dat	120	0.283026	0.283030	1.2E-05	0.000559	2.8E-05	0.023825	6.2E-04	0.008672	8.4E-06	1.467330	1.1E-04	32.5	0.282765	0.283029	9.4	0.9
KJ1006A_07.dat	120	0.283025	0.283029	1.2E-05	0.000498	1.3E-05	0.021769	1.4E-04	0.008676	7.8E-06	1.467312	1.1E-04	32.6	0.282765	0.283029	9.3	0.9
KJ1006A_08.dat	120	0.283031	0.283035	1.1E-05	0.000367	7.0E-06	0.015646	2.2E-04	0.008665	7.4E-06	1.467305	1.1E-04	32.2	0.282765	0.283035	9.5	0.8
KJ1006A 09.dat	120	0.283012	0.283016	1.2E-05	0.001071	1.4E-05	0.045553	1.8E-04	0.008668	1.0E-05	1.467321	9.9E-05	32.1	0.282765	0.283015	8.9	0.9
KJ1006A_10.dat	120	0.283010	0.283014	1.2E-05	0.000982	6.3E-06	0.039697	6.6E-05	0.008660	9.9E-06	1.467321	1.1E-04	31.7	0.282765	0.283013	8.8	0.8
Median ± 2SD																**9.4**	**0.7**
KJ1308 (s081214) n=16																	
KJ1308_22.dat	90	0.282993	0.283002	1.4E-05	0.001814	1.0E-04	0.067962	2.2E-03	0.008636	1.4E-05	1.467320	1.2E-04	32.3	0.282765	0.283001	8.4	1.0
KJ1308_05.dat	80	0.283000	0.283009	1.3E-05	0.000687	3.7E-05	0.024336	7.1E-04	0.008641	1.1E-05	1.467223	9.2E-05	31.3	0.282765	0.283009	8.6	0.9
KJ1308_28.dat	120	0.283012	0.283021	1.4E-05	0.000445	1.8E-05	0.016220	2.8E-04	0.008634	1.1E-05	1.467214	1.1E-04	31.3	0.282765	0.283021	9.0	1.0
KJ1308 29.dat	120	0.282997	0.283006	1.1E-05	0.000998	2.7E-05	0.033836	4.8E-04	0.008642	1.3E-05	1.467245	8.9E-05	31.3	0.282765	0.283005	8.5	0.7
KJ1308_08.dat	60	0.283020	0.283029	1.7E-05	0.002331	1.2E-04	0.081137	2.2E-03	0.008643	1.7E-05	1.467314	1.6E-04	31.1	0.282765	0.283028	9.3	1.2
KJ1308_16.dat	120	0.282962	0.282971	1.9E-05	0.000847	2.8E-05	0.038221	6.9E-04	0.008619	2.1E-05	1.467229	1.7E-04	31.1	0.282765	0.282970	7.2	1.4
KJ1308_21.dat	80	0.283030	0.283039	1.2E-05	0.000760	2.0E-05	0.027190	3.2E-04	0.008661	9.9E-06	1.467225	1.4E-04	31.1	0.282765	0.283039	9.7	0.9
KJ1308_20.dat	55	0.283031	0.283040	1.6E-05	0.000473	1.2E-05	0.015255	1.8E-04	0.008660	9.7E-06	1.467360	1.7E-04	31.0	0.282766	0.283040	9.7	1.1
KJ1308_38.dat	50	0.283003	0.283012	1.6E-05	0.000804	2.5E-05	0.031670	4.2E-04	0.008650	2.0E-05	1.467227	1.6E-04	31.0	0.282766	0.283011	8.7	1.1
KJ1308 37.dat	120	0.282997	0.283007	1.3E-05	0.000586	2.4E-05	0.025403	9.9E-04	0.008632	1.1E-05	1.467238	9.1E-05	30.9	0.282766	0.283006	8.5	0.9
KJ1308_14.dat	70	0.282949	0.282959	1.4E-05	0.001185	1.2E-04	0.039891	2.1E-03	0.008606	1.6E-05	1.467475	1.7E-04	30.8	0.282766	0.282958	6.8	1.0
KJ1308_23.dat	80	0.282987	0.282996	1.4E-05	0.001231	4.2E-05	0.044055	1.1E-03	0.008643	1.5E-05	1.467262	1.4E-04	30.8	0.282766	0.282996	8.1	1.0
KJ1308_35.dat	100	0.282990	0.282999	1.7E-05	0.000515	1.2E-05	0.022781	6.5E-04	0.008637	1.5E-05	1.467216	1.4E-04	30.7	0.282766	0.282999	8.2	1.2
KJ1308_01.dat	120	0.283006	0.283015	1.2E-05	0.000535	1.3E-05	0.019536	3.7E-04	0.008648	9.2E-06	1.467271	1.3E-04	30.6	0.282766	0.283015	8.8	0.9
KJ1308_10.dat	120	0.283035	0.283044	1.0E-05	0.000553	1.2E-05	0.018309	1.8E-04	0.008649	1.0E-05	1.467231	9.5E-05	30.1	0.282766	0.283044	9.8	0.7
KJ1308_13.dat	65	0.283007	0.283017	1.5E-05	0.001032	1.6E-05	0.037846	1.8E-04	0.008637	1.9E-05	1.467228	1.4E-04	30.1	0.282766	0.283016	8.8	1.1
Median ± 2SD																**8.7**	**1.6**
KJ1508 (s07-081015) n=15																	
KJ1508_01	120	0.283023	0.283039	1.0E-05	0.000948	2.8E-05	0.042395	4.8E-04	0.008665	8.0E-06	1.467305	9.6E-05	28.3	0.282767	0.283038	9.6	0.7
KJ1508_02	120	0.283010	0.283026	9.0E-06	0.001731	3.9E-05	0.074265	7.2E-04	0.008658	8.2E-06	1.467231	8.2E-05	28.6	0.282767	0.283025	9.1	0.6
KJ1508 03	120	0.283015	0.283031	6.7E-06	0.001402	5.4E-05	0.061989	1.5E-03	0.008655	5.9E-06	1.467266	7.6E-05	29	0.282767	0.283030	9.3	0.5
KJ1508_04	120	0.283021	0.283037	9.4E-06	0.000596	2.1E-05	0.025482	6.6E-04	0.008658	5.2E-06	1.467233	8.9E-05	29.4	0.282767	0.283036	9.5	0.7
KJ1508_05	120	0.283022	0.283038	7.9E-06	0.000981	2.7E-05	0.042397	8.2E-04	0.008663	6.7E-06	1.467254	7.6E-05	27.8	0.282768	0.283038	9.6	0.6
KJ1508_06	120	0.283028	0.283044	8.5E-06	0.001019	5.5E-05	0.044000	9.3E-04	0.008670	6.6E-06	1.467233	7.6E-05	27.7	0.282768	0.283043	9.8	0.6

KJ1508_07	120	0.283028	0.283043	8.0E-06	0.000820	2.8E-05	0.036165	9.7E-04	0.008666	5.9E-06	1.467238	8.3E-05	29.1	0.282767	0.283043	9.8	0.6
KJ1508_08	120	0.283007	0.283023	1.2E-05	0.002487	2.9E-05	0.117715	1.5E-03	0.008663	1.0E-05	1.467221	9.0E-05	28.7	0.282767	0.283022	9.0	0.8
KJ1508_09	45	0.283013	0.283029	1.3E-05	0.001570	4.9E-05	0.084285	2.3E-03	0.008665	1.5E-05	1.467318	1.7E-04	28.3	0.282767	0.283028	9.2	0.9
KJ1508_10	120	0.283021	0.283037	8.3E-06	0.001914	5.1E-05	0.088201	4.1E-04	0.008668	8.1E-06	1.467247	7.8E-05	28.5	0.282767	0.283036	9.5	0.6
KJ1508_11	120	0.283018	0.283034	8.2E-06	0.001039	3.7E-05	0.045495	5.9E-04	0.008655	5.8E-06	1.467203	7.6E-05	27.8	0.282768	0.283033	9.4	0.6
KJ1508_12	120	0.283028	0.283044	9.0E-06	0.000903	2.4E-05	0.040592	3.8E-04	0.008663	6.0E-06	1.467261	7.7E-05	28.9	0.282767	0.283044	9.8	0.6
KJ1508_13	120	0.283023	0.283039	8.5E-06	0.000617	2.8E-05	0.027944	1.0E-03	0.008661	5.5E-06	1.467205	8.0E-05	28.6	0.282767	0.283038	9.6	0.6
KJ1508_14	120	0.283021	0.283037	7.4E-06	0.000995	1.7E-05	0.044906	9.4E-04	0.008652	6.5E-06	1.467259	9.6E-05	28.1	0.282767	0.283036	9.5	0.5
KJ1508_15	120	0.283021	0.283037	7.3E-06	0.000787	8.8E-06	0.034582	4.0E-04	0.008656	5.1E-06	1.467233	7.9E-05	28.5	0.282767	0.283036	9.5	0.5
Median ± 2SD																**9.5**	**0.5**
KJ1509 (s07-081015) n=13																	
KJ1509_01	120	0.283024	0.283039	8.0E-06	0.000805	1.4E-05	0.034059	2.3E-04	0.008662	6.5E-06	1.467266	8.3E-05	27.6	0.282768	0.283039	9.6	0.6
KJ1509_02	120	0.283030	0.283045	7.2E-06	0.000590	8.2E-06	0.026040	3.4E-04	0.008663	5.3E-06	1.467253	7.0E-05	28.2	0.282767	0.283045	9.8	0.5
KJ1509_03	120	0.283024	0.283040	7.1E-06	0.000593	9.4E-06	0.026037	1.3E-04	0.008657	5.4E-06	1.467264	8.3E-05	28.3	0.282767	0.283039	9.6	0.5
KJ1509_04	120	0.283005	0.283021	8.8E-06	0.000957	1.8E-05	0.041008	2.5E-04	0.008654	8.0E-06	1.467258	8.1E-05	28.3	0.282767	0.283021	9.0	0.6
KJ1509_05	120	0.283008	0.283024	6.8E-06	0.001028	2.5E-05	0.042317	7.9E-04	0.008665	6.3E-06	1.467252	7.3E-05	28.6	0.282767	0.283023	9.1	0.5
KJ1509_06	120	0.283017	0.283032	7.2E-06	0.000468	3.7E-06	0.019836	2.0E-04	0.008660	4.5E-06	1.467246	8.2E-05	29.5	0.282766	0.283032	9.4	0.5
KJ1509_07	120	0.283027	0.283043	6.1E-06	0.000438	1.6E-05	0.018432	4.4E-04	0.008664	4.5E-06	1.467249	7.9E-05	28.5	0.282767	0.283042	9.7	0.4
KJ1509_08	120	0.283031	0.283046	8.1E-06	0.000727	4.6E-06	0.032632	1.6E-04	0.008670	5.6E-06	1.467248	8.6E-05	28.2	0.282767	0.283046	9.9	0.6
KJ1509_09	120	0.283030	0.283046	8.7E-06	0.000726	1.1E-05	0.032567	3.1E-04	0.008660	6.0E-06	1.467238	8.5E-05	27.1	0.282768	0.283046	9.8	0.6
KJ1509_10	120	0.283011	0.283027	8.5E-06	0.000534	1.0E-05	0.023966	1.9E-04	0.008658	5.6E-06	1.467219	7.7E-05	27.6	0.282768	0.283027	9.2	0.6
KJ1509_11	120	0.283024	0.283040	7.7E-06	0.000812	2.6E-05	0.038700	9.4E-04	0.008665	6.1E-06	1.467234	9.2E-05	27.9	0.282767	0.283040	9.6	0.5
KJ1509_12	120	0.283022	0.283037	7.8E-06	0.000759	6.0E-06	0.034436	2.6E-04	0.008666	5.6E-06	1.467257	7.2E-05	28.5	0.282767	0.283037	9.5	0.5
KJ1509_13	120	0.283024	0.283040	7.9E-06	0.000880	4.3E-05	0.038791	7.5E-04	0.008667	6.5E-06	1.467251	8.2E-05	28.3	0.282767	0.283039	9.6	0.6
Median ± 2SD																**9.6**	**0.6**
KJ1302A (s081214) n=13																	
KJ1302A_07a.da	120	0.282988	0.282997	1.1E-05	0.001027	1.9E-05	0.032642	3.8E-04	0.008662	1.2E-05	1.467222	9.8E-05	47.0	0.282755	0.282996	8.5	0.8
KJ1302A_21.dat	60	0.282991	0.283000	1.8E-05	0.000367	1.3E-05	0.012225	2.7E-04	0.008638	1.3E-05	1.467232	1.3E-04	31.0	0.282766	0.283000	8.3	1.3
KJ1302A_07b.da	120	0.283006	0.283015	1.4E-05	0.001308	1.6E-04	0.039701	2.5E-03	0.008651	1.2E-05	1.467208	9.7E-05	29.3	0.282767	0.283015	8.8	1.0
KJ1302A_15.dat	120	0.283039	0.283048	1.0E-05	0.000626	1.5E-05	0.016111	2.4E-04	0.008662	8.4E-06	1.467223	8.6E-05	27.2	0.282768	0.283048	9.9	0.7
KJ1302A_22.dat	100	0.283036	0.283045	1.3E-05	0.000802	3.2E-05	0.022251	3.1E-04	0.008656	1.0E-05	1.467251	1.1E-04	27.0	0.282768	0.283045	9.8	0.9

KJ1302A_10.dat	80	0.283009	0.283018	2.0E-05	0.000782	1.5E-05	0.026725	3.3E-04	0.008655	2.1E-05	1.467199	1.5E-04	27.0	0.282768	0.283018	8.8	1.4
KJ1302A_13.dat	120	0.283038	0.283047	1.2E-05	0.000914	3.2E-05	0.024755	4.8E-04	0.008668	1.1E-05	1.467239	9.6E-05	26.8	0.282768	0.283047	9.8	0.8
KJ1302A_05.dat	80	0.283035	0.283044	1.6E-05	0.000795	4.3E-05	0.025165	8.5E-04	0.008652	1.8E-05	1.467394	1.5E-04	26.8	0.282768	0.283044	9.7	1.1
KJ1302A 20.dat	70	0.283012	0.283022	2.8E-05	0.000696	2.5E-05	0.029390	5.8E-04	0.008648	3.5E-05	1.467317	2.8E-04	26.6	0.282768	0.283021	8.9	2.0
KJ1302A_09.dat	120	0.283027	0.283037	1.0E-05	0.000663	1.7E-05	0.020051	3.9E-04	0.008655	7.4E-06	1.467219	9.0E-05	26.5	0.282768	0.283036	9.5	0.7
KJ1302A_23.dat	105	0.283054	0.283063	1.3E-05	0.000956	3.7E-05	0.025559	5.7E-04	0.008661	9.9E-06	1.467314	1.5E-04	26.5	0.282768	0.283063	10.4	0.9
KJ1302A_18.dat	120	0.283035	0.283044	1.2E-05	0.000816	1.3E-05	0.020741	1.4E-04	0.008645	1.0E-05	1.467225	9.1E-05	26.4	0.282768	0.283044	9.7	0.8
KJ1302A_17.dat	85	0.283044	0.283054	2.1E-05	0.001193	1.1E-04	0.045559	2.7E-03	0.008662	2.1E-05	1.467355	1.4E-04	26.4	0.282768	0.283053	10.1	1.5
Median ± 2SD																**9.7**	**1.3**
KJ1303A1 (s081214) n=12																	
KJ1303A2_03.da	90	0.283021	0.283031	1.3E-05	0.001056	4.3E-05	0.035436	1.0E-03	0.008670	1.0E-05	1.467340	9.5E-05	26.6	0.282768	0.283030	9.3	0.9
KJ1303A2_05.da	60	0.283010	0.283019	2.0E-05	0.001426	4.7E-05	0.062021	2.2E-03	0.008662	2.5E-05	1.467389	2.5E-04	26.6	0.282768	0.283019	8.9	1.4
KJ1303A1_09.da	90	0.283048	0.283057	1.5E-05	0.000526	1.5E-05	0.021635	4.0E-04	0.008660	1.5E-05	1.467209	1.2E-04	26.1	0.282769	0.283057	10.2	1.1
KJ1303A2_04.da	50	0.283039	0.283048	2.1E-05	0.000400	7.6E-06	0.014109	1.5E-04	0.008668	2.2E-05	1.467511	2.7E-04	26.0	0.282769	0.283048	9.9	1.5
KJ1303A1 11.da	120	0.283046	0.283055	1.3E-05	0.000333	3.0E-06	0.011651	3.5E-05	0.008658	9.1E-06	1.467241	9.7E-05	25.9	0.282769	0.283055	10.1	0.9
KJ1303A1_10.da	80	0.283036	0.283046	2.4E-05	0.000465	1.1E-05	0.017467	2.7E-04	0.008662	1.9E-05	1.467314	1.5E-04	25.7	0.282769	0.283045	9.8	1.7
KJ1303A1_08.da	120	0.283019	0.283028	1.6E-05	0.001139	1.0E-04	0.045309	2.1E-03	0.008650	1.5E-05	1.467266	1.0E-04	25.6	0.282769	0.283027	9.1	1.1
KJ1303A1_03.da	120	0.283048	0.283058	1.2E-05	0.000876	2.3E-05	0.030438	2.3E-04	0.008658	9.3E-06	1.467230	9.4E-05	25.5	0.282769	0.283057	10.2	0.8
KJ1303A1_15.da	60	0.283039	0.283048	1.9E-05	0.000419	7.9E-06	0.015942	2.7E-04	0.008654	1.3E-05	1.467290	1.6E-04	25.5	0.282769	0.283048	9.9	1.4
KJ1303A1_05.da	120	0.283043	0.283052	1.4E-05	0.000469	7.6E-06	0.017257	2.5E-04	0.008657	9.3E-06	1.467241	1.2E-04	25.4	0.282769	0.283052	10.0	1.0
KJ1303A1 13.da	100	0.283011	0.283021	1.4E-05	0.000932	5.0E-05	0.033658	8.7E-04	0.008637	1.3E-05	1.467239	1.2E-04	25.3	0.282769	0.283020	8.9	1.0
KJ1303A1_07.da	60	0.283067	0.283077	1.6E-05	0.000388	9.3E-06	0.015072	1.4E-04	0.008676	1.2E-05	1.467206	1.7E-04	25.1	0.282769	0.283077	10.9	1.1
Median ± 2SD																**9.9**	**1.2**
MR1401 (s050215) n=10																	
MR1401_01.dat	110	0.283075	0.283078	2.0E-05	0.000704	1.8E-05	0.028046	3.1E-04	0.008685	1.5E-05	1.467509	3.4E-04	24.7	0.282769	0.283078	10.9	1.4
MR1401_02.dat	110	0.283023	0.283027	1.3E-05	0.000739	7.1E-05	0.026438	1.4E-03	0.008663	1.3E-05	1.467297	9.3E-05	31	0.282766	0.283026	9.2	0.9
MR1401_03.dat	110	0.283066	0.283070	1.4E-05	0.000580	2.6E-05	0.020800	4.8E-04	0.008676	1.1E-05	1.467320	9.5E-05	24.6	0.282770	0.283069	10.6	1.0
MR1401 04.dat	120	0.283069	0.283073	1.2E-05	0.000369	5.3E-06	0.014321	1.0E-04	0.008668	8.5E-06	1.467283	6.6E-05	24.8	0.282769	0.283073	10.7	0.9
MR1401_05.dat	120	0.283092	0.283095	1.6E-05	0.000430	1.4E-05	0.016383	3.3E-04	0.008677	1.5E-05	1.467324	1.2E-04	24.8	0.282769	0.283095	11.5	1.2
MR1401_06.dat	120	0.283090	0.283094	1.1E-05	0.000624	2.2E-05	0.022931	4.0E-04	0.008660	8.6E-06	1.467242	6.8E-05	23.4	0.282770	0.283093	11.4	0.8
MR1401_07.dat	120	0.283088	0.283092	1.1E-05	0.000718	9.2E-06	0.029250	2.1E-04	0.008674	1.1E-05	1.467259	7.8E-05	25.4	0.282769	0.283092	11.4	0.8

MR1401_08.dat	120	0.283072	0.283076	1.2E-05	0.000746	1.7E-05	0.027955	3.0E-04	0.008684	1.0E-05	1.467249	6.4E-05	30.2	0.282766	0.283075	10.9	0.8
MR1401_09.dat	80	0.283096	0.283099	1.3E-05	0.000682	3.9E-05	0.028020	8.2E-04	0.008689	1.2E-05	1.467230	7.6E-05	24.5	0.282770	0.283099	11.6	0.9
MR1401_10.dat	90	0.283093	0.283097	1.3E-05	0.000436	2.3E-05	0.017786	5.4E-04	0.008672	9.8E-06	1.467264	6.5E-05	24.3	0.282770	0.283097	11.6	0.9
Median ± 2SD																**11.2**	**1.5**
KJ1307 (s081214) n=13																	
KJ1307_13.dat	120	0.283067	0.283076	1.2E-05	0.000703	1.3E-05	0.022559	2.0E-04	0.008651	9.7E-06	1.467225	8.8E-05	31.7	0.282765	0.283076	11.0	0.9
KJ1307_17.dat	120	0.283048	0.283057	1.2E-05	0.000339	1.2E-06	0.011071	4.9E-05	0.008645	8.3E-06	1.467242	8.7E-05	25.3	0.282769	0.283057	10.2	0.8
KJ1307_01.dat	80	0.283066	0.283075	1.3E-05	0.000829	3.7E-05	0.033677	9.3E-04	0.008665	1.1E-05	1.467212	1.1E-04	24.9	0.282769	0.283075	10.8	0.9
KJ1307_10.dat	75	0.283061	0.283070	1.5E-05	0.000465	4.7E-06	0.016917	9.3E-05	0.008658	8.7E-06	1.467253	1.3E-04	24.8	0.282769	0.283070	10.6	1.0
KJ1307_11.dat	120	0.283038	0.283047	1.1E-05	0.000622	2.6E-05	0.022438	4.8E-04	0.008645	1.1E-05	1.467270	9.7E-05	24.6	0.282770	0.283047	9.8	0.8
KJ1307 08.dat	50	0.283032	0.283041	2.0E-05	0.000468	2.7E-05	0.017476	4.6E-04	0.008646	1.4E-05	1.467411	1.7E-04	24.5	0.282770	0.283041	9.6	1.4
KJ1307_18.dat	120	0.283055	0.283064	1.1E-05	0.000557	1.4E-05	0.018194	2.1E-04	0.008656	9.4E-06	1.467254	1.0E-04	24.5	0.282770	0.283064	10.4	0.8
KJ1307_07.dat	120	0.283065	0.283074	1.0E-05	0.000417	2.3E-05	0.014480	3.8E-04	0.008643	8.8E-06	1.467237	1.0E-04	24.4	0.282770	0.283074	10.8	0.7
KJ1307_22.dat	120	0.283056	0.283065	1.2E-05	0.000497	2.2E-06	0.016492	7.1E-05	0.008650	7.7E-06	1.467260	9.2E-05	24.1	0.282770	0.283065	10.4	0.9
KJ1307_04.dat	120	0.283052	0.283062	9.9E-06	0.000425	3.2E-06	0.014800	1.3E-04	0.008652	8.2E-06	1.467240	9.3E-05	23.9	0.282770	0.283062	10.3	0.7
KJ1307_03.dat	120	0.283051	0.283060	1.1E-05	0.000616	1.6E-05	0.022523	3.7E-04	0.008656	8.2E-06	1.467250	1.1E-04	23.7	0.282770	0.283060	10.3	0.7
KJ1307 14.dat	120	0.283042	0.283051	1.1E-05	0.000489	1.3E-05	0.017768	2.7E-04	0.008649	1.0E-05	1.467243	9.2E-05	23.7	0.282770	0.283051	9.9	0.8
KJ1307_19.dat	60	0.283057	0.283066	1.4E-05	0.000524	1.4E-05	0.017748	2.9E-04	0.008646	1.1E-05	1.467347	1.4E-04	23.7	0.282770	0.283066	10.5	1.0
Median ± 2SD																**10.4**	**0.8**
LI1301 (s040215) n=10																	
LI1301_10.dat	120	0.283065	0.283086	1.8E-05	0.000846	3.5E-05	0.030299	6.6E-04	0.008677	1.2E-05	1.467247	1.2E-04	22.9	0.282771	0.283086	11.1	1.3
LI1301_09.dat	120	0.283063	0.283084	1.4E-05	0.001034	5.3E-05	0.038022	9.2E-04	0.008680	1.3E-05	1.467267	1.1E-04	23.1	0.282770	0.283083	11.1	1.0
LI1301_08.dat	120	0.283094	0.283116	1.9E-05	0.001044	3.1E-05	0.038417	5.6E-04	0.008721	2.2E-05	1.467262	1.2E-04	23.2	0.282770	0.283115	12.2	1.3
LI1301 07.dat	100	0.283062	0.283083	1.7E-05	0.001008	6.4E-05	0.036454	1.2E-03	0.008690	1.5E-05	1.467304	1.4E-04	23.1	0.282770	0.283082	11.0	1.2
LI1301_06.dat	100	0.283043	0.283065	1.4E-05	0.000600	2.2E-05	0.021302	4.0E-04	0.008677	1.4E-05	1.467295	1.2E-04	23.5	0.282770	0.283064	10.4	1.0
LI1301_05.dat	100	0.283065	0.283086	1.6E-05	0.001103	5.6E-05	0.041147	1.1E-03	0.008696	1.6E-05	1.467271	1.5E-04	22.8	0.282771	0.283086	11.1	1.2
LI1301_04.dat	110	0.283075	0.283096	1.5E-05	0.000803	3.6E-05	0.028468	6.7E-04	0.008676	1.3E-05	1.467321	1.3E-04	22.4	0.282771	0.283096	11.5	1.0
LI1301_03.dat	110	0.283081	0.283103	1.7E-05	0.000959	3.4E-05	0.035194	6.3E-04	0.008707	2.2E-05	1.467326	1.2E-04	22.3	0.282771	0.283102	11.7	1.2
LI1301_02.dat	110	0.283066	0.283088	1.9E-05	0.000954	3.8E-05	0.035543	7.7E-04	0.008676	1.6E-05	1.467348	1.7E-04	22.9	0.282771	0.283087	11.2	1.3
LI1301_01.dat	110	0.283070	0.283092	1.2E-05	0.001111	8.1E-05	0.042228	1.6E-03	0.008667	1.4E-05	1.467323	9.5E-05	22.4	0.282771	0.283091	11.3	0.9
Median ± 2SD																**11.2**	**0.9**

KJ1325A (s081214) n=14

KJ1325A_12.dat	120	0.283071	0.283080	1.0E-05	0.001319	8.1E-05	0.042104	1.6E-03	0.008655	8.4E-06	1.467246	9.7E-05	22.9	0.282771	0.283080	10.9	0.7
KJ1325A_05.dat	120	0.283056	0.283066	1.1E-05	0.001151	6.0E-05	0.037001	1.0E-03	0.008656	9.9E-06	1.467256	1.2E-04	22.6	0.282771	0.283065	10.4	0.8
KJ1325A_09.dat	120	0.283056	0.283065	1.3E-05	0.001150	1.6E-05	0.040420	3.6E-04	0.008655	1.0E-05	1.467240	1.1E-04	22.5	0.282771	0.283064	10.4	0.9
KJ1325A_04.dat	120	0.283046	0.283055	1.1E-05	0.000929	2.1E-05	0.032225	2.7E-04	0.008659	1.2E-05	1.467271	9.8E-05	22.4	0.282771	0.283055	10.0	0.8
KJ1325A_19	90	0.283079	0.283088	1.1E-05	0.001054	7.8E-05	0.033481	1.6E-03	0.008664	1.3E-05	1.467346	1.5E-04	22.4	0.282771	0.283087	11.2	0.8
KJ1325A_21.dat	120	0.283065	0.283074	1.1E-05	0.000948	2.6E-05	0.027940	4.9E-04	0.008652	8.1E-06	1.467290	1.1E-04	22.4	0.282771	0.283074	10.7	0.8
KJ1325A_03.dat	80	0.283079	0.283089	1.5E-05	0.001482	7.5E-05	0.048756	1.3E-03	0.008676	1.2E-05	1.467285	1.3E-04	22.3	0.282771	0.283088	11.2	1.1
KJ1325A_01.dat	80	0.283047	0.283056	1.4E-05	0.001087	3.9E-05	0.035041	8.2E-04	0.008652	1.3E-05	1.467274	1.3E-04	22.1	0.282771	0.283056	10.1	1.0
KJ1325A 02.dat	80	0.283037	0.283046	1.6E-05	0.001022	2.3E-05	0.041427	8.6E-04	0.008662	1.5E-05	1.467197	1.5E-04	22.1	0.282771	0.283046	9.7	1.1
KJ1325A_07.dat	120	0.283075	0.283084	1.1E-05	0.000971	2.3E-05	0.034488	4.7E-04	0.008669	1.1E-05	1.467281	1.0E-04	22.1	0.282771	0.283084	11.1	0.8
KJ1325A_20.dat	120	0.283066	0.283075	1.0E-05	0.000708	5.2E-05	0.023270	8.5E-04	0.008665	9.0E-06	1.467279	9.3E-05	22.1	0.282771	0.283075	10.7	0.7
KJ1325A_15.dat	120	0.283065	0.283074	1.1E-05	0.001165	6.5E-05	0.035517	9.7E-04	0.008658	9.5E-06	1.467255	1.2E-04	22.0	0.282771	0.283073	10.7	0.8
KJ1325A_18.dat	100	0.283080	0.283089	1.2E-05	0.001089	4.7E-05	0.033715	7.4E-04	0.008673	1.1E-05	1.467270	1.3E-04	21.9	0.282771	0.283089	11.2	0.9
KJ1325A_14.dat	120	0.283048	0.283058	1.1E-05	0.001308	9.2E-05	0.040307	1.5E-03	0.008641	8.7E-06	1.467251	9.7E-05	21.7	0.282771	0.283057	10.1	0.8
Median ± 2SD																**10.7**	**1.0**

KJ1324A (s081214) n=16

KJ1324A_16.dat	100	0.283069	0.283078	1.2E-05	0.000632	1.9E-05	0.018742	3.2E-04	0.008658	1.0E-05	1.467249	1.1E-04	23.0	0.282771	0.283078	10.9	0.9
KJ1324A_10.dat	100	0.283058	0.283067	1.5E-05	0.000929	1.6E-05	0.027847	2.6E-04	0.008666	1.1E-05	1.467254	1.2E-04	22.7	0.282771	0.283067	10.5	1.1
KJ1324A_09.dat	100	0.283049	0.283058	1.2E-05	0.001091	2.5E-05	0.033073	4.0E-04	0.008649	1.1E-05	1.467282	1.2E-04	22.5	0.282771	0.283058	10.1	0.8
KJ1324A_14.dat	100	0.283056	0.283066	1.4E-05	0.000884	2.2E-05	0.026881	3.5E-04	0.008666	1.1E-05	1.467239	1.1E-04	22.4	0.282771	0.283065	10.4	1.0
KJ1324A_08.dat	100	0.283044	0.283053	1.3E-05	0.001046	4.5E-05	0.031670	7.9E-04	0.008652	1.0E-05	1.467250	1.2E-04	22.3	0.282771	0.283053	10.0	0.9
KJ1324A 27.dat	120	0.283072	0.283081	1.0E-05	0.000929	2.4E-05	0.026761	3.9E-04	0.008654	9.9E-06	1.467224	9.4E-05	22.3	0.282771	0.283081	11.0	0.7
KJ1324A_18.dat	90	0.283059	0.283068	1.6E-05	0.001286	6.8E-05	0.041005	1.2E-03	0.008656	1.4E-05	1.467254	1.2E-04	22.2	0.282771	0.283068	10.5	1.1
KJ1324A_17.dat	100	0.283049	0.283059	1.4E-05	0.000845	4.5E-05	0.026969	7.8E-04	0.008664	1.2E-05	1.467216	1.3E-04	22.1	0.282771	0.283058	10.2	1.0
KJ1324A_24.dat	120	0.283079	0.283088	1.3E-05	0.001126	4.2E-05	0.036604	7.7E-04	0.008677	1.2E-05	1.467242	8.5E-05	22.1	0.282771	0.283088	11.2	0.9
KJ1324A_32.dat	60	0.283088	0.283097	1.7E-05	0.001186	8.6E-05	0.035955	1.5E-03	0.008666	1.3E-05	1.467196	1.7E-04	22.1	0.282771	0.283097	11.5	1.2
KJ1324A_01.dat	100	0.283048	0.283057	4.2E-05	0.001229	9.3E-05	0.065670	2.0E-03	0.008668	4.2E-05	1.467134	5.1E-04	22.0	0.282771	0.283057	10.1	3.0
KJ1324A_23.dat	75	0.283059	0.283069	1.5E-05	0.000966	3.5E-05	0.028675	6.8E-04	0.008643	1.3E-05	1.467228	1.4E-04	22.0	0.282771	0.283068	10.5	1.1
KJ1324A_02.dat	100	0.283065	0.283075	2.1E-05	0.000710	4.2E-05	0.033684	9.6E-04	0.008682	2.7E-05	1.467197	2.4E-04	21.9	0.282771	0.283074	10.7	1.5
KJ1324A_05.dat	110	0.283045	0.283055	1.3E-05	0.000927	4.4E-05	0.029054	7.5E-04	0.008652	1.1E-05	1.467248	1.1E-04	21.9	0.282771	0.283054	10.0	0.9
KJ1324A_06.dat	100	0.283043	0.283053	1.4E-	0.000972	3.5E-	0.031680	7.4E-	0.008652	1.3E-	1.467290	1.1E-	21.9	0.282771	0.283052	9.9	1.0

				05		05		04		05		04				
KJ1324A_28.dat	120	0.283075	0.283084	1.1E-05	0.001065	4.5E-05	0.030874	6.5E-04	0.008648	9.6E-06	1.467231	9.5E-05	21.9	0.282771	0.283084	11.1	0.8
Median ± 2SD																**10.5**	**1.0**
KJ1313 (s081214) n=13																	
KJ1313_07.dat	120	0.283061	0.283070	1.1E-05	0.001362	3.4E-05	0.046880	7.6E-04	0.008653	1.1E-05	1.467197	9.8E-05	22.0	0.282771	0.283070	10.6	0.8
KJ1313_11.dat	50	0.283009	0.283018	2.4E-05	0.001095	7.5E-05	0.054728	2.7E-03	0.008610	2.5E-05	1.467236	1.7E-04	21.8	0.282771	0.283018	8.7	1.7
KJ1313_31.dat	120	0.283072	0.283081	1.1E-05	0.001077	3.0E-05	0.040594	1.0E-03	0.008664	9.6E-06	1.467188	8.1E-05	21.7	0.282771	0.283080	10.9	0.8
KJ1313_09.dat	120	0.283094	0.283103	1.0E-05	0.001311	2.2E-05	0.046533	3.7E-04	0.008661	1.0E-05	1.467233	7.5E-05	21.4	0.282772	0.283103	11.7	0.7
KJ1313_13.dat	100	0.283071	0.283081	9.6E-06	0.001119	2.4E-05	0.038575	6.5E-04	0.008660	8.9E-06	1.467217	1.0E-04	21.4	0.282772	0.283080	10.9	0.7
KJ1313_01.dat	120	0.283065	0.283074	1.0E-05	0.000685	8.3E-06	0.026083	5.0E-04	0.008665	8.1E-06	1.467267	9.2E-05	21.3	0.282772	0.283074	10.7	0.7
KJ1313_04.dat	120	0.283085	0.283094	1.0E-05	0.000987	3.4E-05	0.032918	4.6E-04	0.008668	8.2E-06	1.467274	9.3E-05	21.3	0.282772	0.283094	11.4	0.7
KJ1313_05.dat	120	0.283060	0.283069	1.1E-05	0.001702	8.7E-05	0.061424	1.6E-03	0.008648	9.5E-06	1.467231	8.8E-05	21.3	0.282772	0.283068	10.5	0.8
KJ1313_33.dat	90	0.283084	0.283093	1.2E-05	0.002062	1.6E-04	0.076523	3.2E-03	0.008677	1.5E-05	1.467250	1.1E-04	21.2	0.282772	0.283093	11.3	0.9
KJ1313_03.dat	90	0.283048	0.283057	1.1E-05	0.001185	2.8E-05	0.041062	7.8E-04	0.008647	1.0E-05	1.467252	8.6E-05	21.1	0.282772	0.283057	10.1	0.8
KJ1313_34.dat	70	0.283079	0.283088	1.1E-05	0.000996	5.2E-05	0.035855	1.3E-03	0.008661	1.2E-05	1.467322	1.6E-04	21.0	0.282772	0.283088	11.2	0.8
KJ1313_06.dat	120	0.283073	0.283083	1.1E-05	0.001355	4.8E-05	0.044450	1.1E-03	0.008653	9.8E-06	1.467250	9.0E-05	20.9	0.282772	0.283082	11.0	0.8
KJ1313_16.dat	100	0.283066	0.283075	1.3E-05	0.001260	7.3E-05	0.044331	1.1E-03	0.008655	9.5E-06	1.467215	9.2E-05	20.9	0.282772	0.283074	10.7	0.9
Median ± 2SD																**10.9**	**1.5**

Standards

Analysis PL: n=89)	(TM: n=98;	# cycles integrated	176Hf/177Hf	2se	176Lu/177Hf	2se	173Yb/177Hf	1se	178Hf/177Hf	2se	Age (Ma)[c]	176Hf/177Hf (t) CHUR*	176Hf/177Hf (t)	εHf (t)	2se	εHf offset from ref
s081214																
TEMORA-2 (n=11)																
TM_10-1.dat		120	0.282695	0.000011	0.001104	0.000008	0.039679	0.000157	1.467264	0.000083	417	0.282522	0.282687	5.8	0.8	0.0
TM_10-3.dat		120	0.282704	0.000013	0.001344	0.000005	0.047713	0.000187	1.467244	0.000083	417	0.282522	0.282693	6.1	0.9	0.2
TM_10-4.dat		120	0.282684	0.000012	0.000682	0.000007	0.021606	0.000136	1.467224	0.000095	417	0.282522	0.282679	5.5	0.9	-0.2
TM_10-5.dat		80	0.282689	0.000015	0.000646	0.000018	0.020646	0.000242	1.467281	0.000102	417	0.282522	0.282684	5.7	1.0	-0.1
TM_10-6.dat		120	0.282666	0.000013	0.001221	0.000050	0.042481	0.000973	1.467261	0.000086	417	0.282522	0.282657	4.7	0.9	-1.0
TM_10-7.dat		110	0.282685	0.000013	0.001410	0.000030	0.049623	0.000453	1.467309	0.000094	417	0.282522	0.282674	5.4	0.9	-0.4
TM_10-9.dat		120	0.282682	0.000013	0.001830	0.000029	0.062679	0.000593	1.467313	0.000115	417	0.282522	0.282667	5.1	0.9	-0.6
TM_10-11.dat		120	0.282671	0.000014	0.002196	0.000030	0.074988	0.000421	1.467246	0.000092	417	0.282522	0.282654	4.7	1.0	-1.1
TM_10-12.dat		120	0.282676	0.000014	0.000500	0.000002	0.017410	0.000152	1.467229	0.000082	417	0.282522	0.282672	5.3	1.0	-0.5

TM_10-13.dat	110	0.282671	0.000012	0.000531	0.000005	0.018070	0.000155	1.467236	0.000082	417	0.282522	0.282667	5.1	0.9	-0.6
TM_10-14.dat	90	0.282694	0.000013	0.000540	0.000007	0.018364	0.000156	1.467276	0.000081	417	0.282522	0.282690	5.9	0.9	0.1
Mean												**0.282675**	**5.4**		**-0.4**
2SD												**0.000026**	**0.9**		
Normalization factor												**1.000040**			
PLESOVICE (n=12)															
PL_10-2.dat	120	0.282493	0.000012	0.000116	0.000002	0.006596	0.000043	1.467241	0.000132	337	0.282573	0.282492	-2.8	0.8	0.3
PL_10-3.dat	120	0.282485	0.000011	0.000091	0.000001	0.004919	0.000038	1.467252	0.000092	337	0.282573	0.282485	-3.1	0.8	0.1
PL_10-4.dat	120	0.282472	0.000013	0.000091	0.000000	0.004619	0.000033	1.467239	0.000087	337	0.282573	0.282471	-3.6	0.9	-0.4
PL_10-5.dat	120	0.282473	0.000011	0.000133	0.000002	0.006504	0.000026	1.467268	0.000099	337	0.282573	0.282473	-3.6	0.8	-0.3
PL_10-6.dat	120	0.282471	0.000011	0.000091	0.000000	0.004554	0.000023	1.467281	0.000100	337	0.282573	0.282471	-3.6	0.8	-0.4
PL_10-7.dat	120	0.282467	0.000012	0.000132	0.000002	0.006406	0.000025	1.467274	0.000101	337	0.282573	0.282466	-3.8	0.8	-0.5
PL_10-8.dat	120	0.282477	0.000011	0.000128	0.000002	0.006284	0.000021	1.467292	0.000087	337	0.282573	0.282477	-3.4	0.8	-0.2
PL_10-9.dat	120	0.282470	0.000012	0.000126	0.000001	0.006186	0.000016	1.467297	0.000085	337	0.282573	0.282469	-3.7	0.9	-0.4
PL_10-10.dat	120	0.282475	0.000012	0.000128	0.000001	0.006189	0.000018	1.467290	0.000094	337	0.282573	0.282475	-3.5	0.8	-0.2
PL_10-11.dat	120	0.282467	0.000010	0.000128	0.000001	0.006250	0.000018	1.467237	0.000086	337	0.282573	0.282466	-3.8	0.7	-0.5
PL_10-12.dat	120	0.282468	0.000012	0.000130	0.000001	0.006340	0.000019	1.467257	0.000088	337	0.282573	0.282468	-3.7	0.8	-0.5
PL_10-13.dat	120	0.282484	0.000010	0.000128	0.000001	0.006283	0.000022	1.467273	0.000077	337	0.282573	0.282483	-3.2	0.7	0.0
Mean												**0.282475**	**-3.5**		**-0.2**
2SD												**0.000016**	**0.6**		
Normalization factor												**1.000026**			
Average Normalization factor (TM + PL)												**1.000033**			
s020315															
TEMORA-2 (n=6)															
TM 14-06.dat	120	0.282661	0.000010	0.001286	0.000042	0.051175	0.000713	1.467281	0.000074	417	0.282522	0.282651	4.6	0.7	-1.2
TM_14-05.dat	90	0.282671	0.000011	0.000641	0.000010	0.027281	0.000298	1.467286	0.000086	417	0.282522	0.282666	5.1	0.8	-0.7
TM 14-04.dat	120	0.282671	0.000010	0.000684	0.000015	0.028029	0.000266	1.467273	0.000067	417	0.282522	0.282666	5.1	0.7	-0.7
TM_14-03.dat	120	0.282659	0.000010	0.001376	0.000013	0.056426	0.000316	1.467291	0.000075	417	0.282522	0.282648	4.4	0.7	-1.3
TM 14-02.dat	120	0.282673	0.000010	0.001028	0.000020	0.043901	0.000507	1.467275	0.000061	417	0.282522	0.282665	5.0	0.7	-0.7
TM_14-01.dat	120	0.282657	0.000011	0.001038	0.000024	0.042986	0.000634	1.467294	0.000071	417	0.282522	0.282649	4.5	0.7	-1.2
Mean												**0.282657**	**4.8**		**-1.0**
2SD												**0.000018**	**0.6**		
Normalization factor												**1.000101**			
PLESOVICE (n=6)															
PL_14-06.dat	120	0.282472	0.000009	0.000127	0.000001	0.008157	0.000019	1.467284	0.000064	337	0.282573	0.282472	-3.6	0.6	-0.3
PL_14-05.dat	120	0.282472	0.000010	0.000128	0.000001	0.007959	0.000019	1.467283	0.000076	337	0.282573	0.282472	-3.6	0.7	-0.3
PL_14-04.dat	120	0.282479	0.000009	0.000128	0.000001	0.007993	0.000021	1.467294	0.000093	337	0.282573	0.282478	-3.4	0.6	-0.1
PL_14-03.dat	120	0.282468	0.000009	0.000128	0.000001	0.007981	0.000019	1.467325	0.000073	337	0.282573	0.282468	-3.7	0.7	-0.5
PL_14-02.dat	120	0.282465	0.000010	0.000129	0.000001	0.008005	0.000023	1.467294	0.000085	337	0.282573	0.282465	-3.8	0.7	-0.6
PL_14-01.dat	120	0.282478	0.000010	0.000112	0.000002	0.007527	0.000054	1.467305	0.000074	337	0.282573	0.282477	-3.4	0.7	-0.2
Mean												**0.282472**	**-3.6**		**-0.3**
2SD												**0.000011**	**0.4**		
Normalization factor												**1.000036**			
Average Normalization factor (TM +												**1.000069**			

PL)															
s040215															
TEMORA-2 (n=8)															
TM_6-4.dat	120	0.282677	0.000011	0.001612	0.000016	0.064218	0.000263	1.467288	0.000091	417	0.282522	0.282664	5.0	0.8	-0.7
TM_6-3.dat	100	0.282657	0.000011	0.001360	0.000032	0.050297	0.000592	1.467284	0.000085	417	0.282522	0.282647	4.4	0.8	-1.3
TM_6-2.dat	100	0.282669	0.000012	0.001453	0.000052	0.056158	0.000870	1.467304	0.000088	417	0.282522	0.282658	4.8	0.8	-0.9
TM_6-1.dat	100	0.282675	0.000011	0.001566	0.000027	0.057178	0.000592	1.467302	0.000077	417	0.282522	0.282662	5.0	0.8	-0.8
TM_5-4.dat	120	0.282666	0.000012	0.000669	0.000005	0.027633	0.000214	1.467287	0.000112	417	0.282522	0.282661	4.9	0.9	-0.8
TM_5-3.dat	120	0.282668	0.000012	0.001351	0.000020	0.058949	0.000635	1.467294	0.000083	417	0.282522	0.282657	4.8	0.9	-1.0
TM_5-2.dat	120	0.282662	0.000013	0.001084	0.000011	0.045966	0.000350	1.467321	0.000091	417	0.282522	0.282654	4.7	0.9	-1.1
TM_5-1.dat	120	0.282663	0.000015	0.001598	0.000016	0.072868	0.000438	1.467284	0.000114	417	0.282522	0.282650	4.5	1.1	-1.2
Mean												**0.282657**	**4.8**		**-1.0**
2SD												**0.000012**	**0.4**		
Normalization factor												**1.000104**			
PLESOVICE (n=10)															
PL_6-5.dat	120	0.282464	0.000011	0.000163	0.000001	0.011833	0.000095	1.467292	0.000103	337	0.282573	0.282463	-3.9	0.8	-0.6
PL_6-4.dat	120	0.282464	0.000011	0.000097	0.000001	0.006162	0.000055	1.467268	0.000083	337	0.282573	0.282464	-3.9	0.8	-0.6
PL 6-3.dat	120	0.282475	0.000013	0.000092	0.000001	0.005649	0.000030	1.467303	0.000086	337	0.282573	0.282475	-3.5	0.9	-0.2
PL_6-2.dat	120	0.282478	0.000010	0.000074	0.000002	0.004248	0.000055	1.467292	0.000070	337	0.282573	0.282477	-3.4	0.7	-0.2
PL 6-1.dat	120	0.282480	0.000011	0.000076	0.000001	0.004447	0.000030	1.467267	0.000075	337	0.282573	0.282479	-3.3	0.8	-0.1
PL_5-5.dat	120	0.282470	0.000013	0.000067	0.000002	0.004327	0.000040	1.467294	0.000082	337	0.282573	0.282470	-3.6	0.9	-0.4
PL 5-4.dat	120	0.282482	0.000012	0.000070	0.000001	0.004889	0.000041	1.467295	0.000080	337	0.282573	0.282482	-3.2	0.8	0.0
PL_5-3.dat	120	0.282447	0.000012	0.000090	0.000001	0.006988	0.000081	1.467358	0.000090	337	0.282573	0.282446	-4.5	0.8	-1.2
PL 5-2.dat	120	0.282456	0.000013	0.000076	0.000000	0.004911	0.000016	1.467298	0.000069	337	0.282573	0.282456	-4.2	0.9	-0.9
PL_5-1.dat	120	0.282478	0.000014	0.000069	0.000000	0.004456	0.000021	1.467297	0.000095	337	0.282573	0.282478	-3.4	1.0	-0.1
Mean												**0.282469**	**-3.7**		**-0.4**
2SD												**0.000023**	**0.8**		
Normalization factor												**1.000046**			
Average Normalization factor (TM + PL)												**1.000075**			
s080515															
TEMORA-2 (n=24)															
TM-NW 13 1.dat	90	0.282698	0.000012	0.001226	0.000022	0.065550	0.001703	1.467234	0.000127	417	0.282522	0.282688	5.9	0.9	0.1
TM-NW_13_2.dat	120	0.282713	0.000018	0.001328	0.000031	0.073036	0.001563	1.467294	0.000100	417	0.282522	0.282703	6.4	1.3	0.6
TM-NW 13 3.dat	110	0.282670	0.000017	0.001449	0.000048	0.076968	0.000589	1.467305	0.000095	417	0.282522	0.282658	4.8	1.2	-0.9
TM-NW_13_4.dat	110	0.282716	0.000018	0.001059	0.000050	0.056145	0.001525	1.467296	0.000112	417	0.282522	0.282708	6.6	1.3	0.7
TM-NW_13_5.dat	110	0.282680	0.000018	0.001375	0.000013	0.078925	0.000957	1.467296	0.000115	417	0.282522	0.282669	5.2	1.3	-0.6
TM-NW_13_6.dat	110	0.282673	0.000015	0.001369	0.000012	0.076764	0.000926	1.467307	0.000121	417	0.282522	0.282662	4.9	1.0	-0.8
TM-NW_13_7.dat	110	0.282644	0.000017	*0.001449*	0.000010	0.069119	0.000401	1.467288	0.000090	417	0.282522	0.282633	3.9	1.2	-1.8
TM-NW_13_8.dat	110	0.282674	0.000014	0.001454	0.000012	0.069566	0.000325	1.467340	0.000103	417	0.282522	0.282663	5.0	1.0	-0.8
TM-NW_13_9.dat	110	0.282704	0.000016	0.001485	0.000013	0.071653	0.000480	1.467280	0.000089	417	0.282522	0.282692	6.0	1.1	0.2
TM-NW_13_10.da	120	0.282685	0.000018	0.001470	0.000012	0.072129	0.000598	1.467278	0.000094	417	0.282522	0.282673	5.3	1.2	-0.4
TM-NW_13_11.da	120	0.282680	0.000015	0.001383	0.000039	0.065565	0.000668	1.467281	0.000086	417	0.282522	0.282669	5.2	1.1	-0.6
TM-NW_13_12.da	120	0.282707	0.000015	0.001408	0.000039	0.067239	0.000647	1.467265	0.000080	417	0.282522	0.282696	6.1	1.1	0.3
TM-NW_13_13.da	120	0.282655	0.000019	0.001622	0.000092	0.082488	0.003417	1.467254	0.000079	417	0.282522	0.282642	4.2	1.4	-1.5

TM-NW_13_14.da	120	0.282681	0.000017	0.001622	0.000099	0.079273	0.003326	1.467254	0.000083	417	0.282522	0.282669	5.2	1.2	-0.6
TM-NW_13_15.da	120	0.282704	0.000016	0.001624	0.000015	0.078641	0.001211	1.467194	0.000095	417	0.282522	0.282691	6.0	1.1	0.2
TM-NW_13_16.da	120	0.282687	0.000018	0.001400	0.000010	0.067765	0.000678	1.467281	0.000090	417	0.282522	0.282676	5.4	1.3	-0.3
TM-NW_13_17.da	120	0.282717	0.000017	0.001313	0.000009	0.064649	0.000678	1.467286	0.000094	417	0.282522	0.282707	6.5	1.2	0.7
TM-NW_13_18.da	120	0.282679	0.000018	0.001880	0.000016	0.090096	0.001507	1.467244	0.000108	417	0.282522	0.282664	5.0	1.3	-0.7
TM-NW_13_19.da	120	0.282705	0.000019	0.002452	0.000069	0.118372	0.002990	1.467251	0.000103	417	0.282522	0.282686	5.8	1.3	0.0
TM-NW_13_20.da	120	0.282709	0.000017	0.000542	0.000003	0.025273	0.000395	1.467265	0.000101	417	0.282522	0.282705	6.5	1.2	0.6
TM-NW_13_21.da	120	0.282718	0.000016	0.000627	0.000025	0.028989	0.000887	1.467266	0.000099	417	0.282522	0.282714	6.8	1.1	0.9
TM-NW_13_22.da	120	0.282713	0.000015	0.000568	0.000005	0.025435	0.000252	1.467286	0.000103	417	0.282522	0.282709	6.6	1.0	0.8
TM-NW_13_23.da	120	0.282707	0.000015	0.000525	0.000001	0.023168	0.000200	1.467285	0.000109	417	0.282522	0.282703	6.4	1.1	0.6
TM-NW_13_24.da	120	0.282721	0.000015	0.000549	0.000001	0.023970	0.000234	1.467219	0.000110	417	0.282522	0.282717	6.9	1.0	1.0
Mean												**0.282683**	**5.7**		**-0.1**
2SD												**0.000046**	**1.6**		
Normalization factor												**1.000010**			
PLESOVICE (n=18)															
PL-NW_13_1.dat	110	0.282479	0.000014	0.000130	0.000004	0.008208	0.000098	1.467289	0.000116	337	0.282573	0.282478	-3.3	1.0	-0.1
PL-NW_13_2.dat	110	0.282488	0.000013	0.000074	0.000004	0.004805	0.000105	1.467333	0.000098	337	0.282573	0.282487	-3.0	0.9	0.2
PL-NW_13_3.dat	110	0.282494	0.000013	0.000068	0.000004	0.004441	0.000095	1.467318	0.000099	337	0.282573	0.282494	-2.8	0.9	0.4
PL-NW 13 4.dat	110	0.282475	0.000014	0.000070	0.000005	0.004558	0.000116	1.467304	0.000109	337	0.282573	0.282474	-3.5	1.0	-0.3
PL-NW_13_5.dat	110	0.282482	0.000013	0.000064	0.000003	0.004244	0.000077	1.467281	0.000094	337	0.282573	0.282482	-3.2	0.9	0.0
PL-NW 13 6.dat	110	0.282472	0.000015	0.000063	0.000002	0.004202	0.000054	1.467273	0.000082	337	0.282573	0.282472	-3.6	1.0	-0.3
PL-NW_13_7.dat	120	0.282476	0.000013	0.000065	0.000003	0.004375	0.000084	1.467257	0.000095	337	0.282573	0.282476	-3.4	0.9	-0.2
PL-NW 13 8.dat	120	0.282483	0.000013	0.000065	0.000003	0.004481	0.000076	1.467266	0.000093	337	0.282573	0.282483	-3.2	0.9	0.0
PL-NW_13_9.dat	120	0.282490	0.000013	0.000065	0.000003	0.004260	0.000082	1.467286	0.000119	337	0.282573	0.282489	-3.0	0.9	0.2
PL-NW 13 10.da	120	0.282479	0.000015	0.000067	0.000003	0.004430	0.000071	1.467287	0.000090	337	0.282573	0.282479	-3.3	1.0	-0.1
PL-NW_13_11.da	120	0.282489	0.000014	0.000086	0.000005	0.005489	0.000124	1.467240	0.000100	337	0.282573	0.282489	-3.0	1.0	0.2
PL-NW 13 12.da	120	0.282484	0.000014	0.000117	0.000007	0.007390	0.000167	1.467281	0.000118	337	0.282573	0.282483	-3.2	1.0	0.0
PL-NW_13_13.da	120	0.282506	0.000013	0.000128	0.000004	0.008131	0.000078	1.467253	0.000099	337	0.282573	0.282506	-2.4	0.9	0.8
PL-NW 13 14.da	120	0.282509	0.000013	0.000134	0.000002	0.008618	0.000156	1.467267	0.000094	337	0.282573	0.282508	-2.3	1.0	0.9
PL-NW_13_15.da	120	0.282499	0.000014	0.000142	0.000003	0.009013	0.000153	1.467267	0.000098	337	0.282573	0.282498	-2.7	1.0	0.5
PL-NW 13 16.da	120	0.282505	0.000012	0.000144	0.000001	0.009191	0.000074	1.467242	0.000102	337	0.282573	0.282504	-2.4	0.9	0.7
PL-NW_13_17.da	120	0.282521	0.000012	0.000130	0.000002	0.008651	0.000150	1.467231	0.000103	337	0.282573	0.282520	-1.9	0.8	1.3
PL-NW 13 18.da	120	0.282525	0.000013	0.000121	0.000005	0.007835	0.000107	1.467243	0.000102	337	0.282573	0.282524	-1.7	0.9	1.4
Mean												**0.282491**	**-2.9**		**0.3**
2SD												**0.000031**	**1.1**		
Normalization factor												**0.999966**			
Average Normalization factor (TM + PL)												**0.999988**			
s050215															
TEMORA-2 (n=19)															
TM_12-1.dat	120	0.282668	0.000014	0.001882	0.000008	0.088149	0.000499	1.467330	0.000101	417	0.282522	0.282653	4.6	1.0	-1.1
TM_12-2.dat	120	0.282669	0.000012	0.001500	0.000006	0.068077	0.000415	1.467316	0.000100	417	0.282522	0.282657	4.8	0.9	-1.0
TM_12-3.dat	110	0.282663	0.000015	0.001536	0.000006	0.068777	0.000150	1.467354	0.000106	417	0.282522	0.282651	4.6	1.0	-1.2
TM_12-4.dat	120	0.282659	0.000014	0.001601	0.000024	0.072411	0.000862	1.467320	0.000099	417	0.282522	0.282646	4.4	1.0	-1.3
TM_12-5.dat	95	0.282684	0.000016	0.002507	0.000031	0.119238	0.001033	1.467348	0.000111	417	0.282522	0.282664	5.0	1.1	-0.7
TM_12-6.dat	115	0.282692	0.000015	0.001463	0.000017	0.063440	0.000243	1.467334	0.000139	417	0.282522	0.282680	5.6	1.1	-0.2

TM_12-7.dat	120	0.282685	0.000014	0.000821	0.000014	0.030791	0.000265	1.467324	0.000081	417	0.282522	0.282679	5.5	1.0	-0.2
TM_12-8.dat	120	0.282696	0.000014	0.000879	0.000018	0.034481	0.000413	1.467298	0.000124	417	0.282522	0.282689	5.9	1.0	0.1
TM_12-9.dat	120	0.282696	0.000012	0.000664	0.000021	0.026938	0.000377	1.467295	0.000093	417	0.282522	0.282691	6.0	0.8	0.2
TM_12-10.dat	120	0.282666	0.000015	0.001332	0.000037	0.056532	0.000859	1.467323	0.000105	417	0.282522	0.282655	4.7	1.1	-1.0
TM_12-11.dat	120	0.282707	0.000019	0.001501	0.000029	0.062704	0.000545	1.467260	0.000170	417	0.282522	0.282695	6.1	1.3	0.3
TM_12-12.dat	120	0.282663	0.000012	0.001182	0.000046	0.052922	0.001185	1.467325	0.000090	417	0.282522	0.282654	4.7	0.9	-1.1
TM_12-13.dat	120	0.282657	0.000014	0.001643	0.000079	0.075052	0.002043	1.467318	0.000100	417	0.282522	0.282644	4.3	1.0	-1.4
TM_12-14.dat	120	0.282677	0.000014	0.001513	0.000015	0.068160	0.000427	1.467287	0.000086	417	0.282522	0.282665	5.0	1.0	-0.7
TM_12-15.dat	120	0.282707	0.000011	0.001202	0.000045	0.050403	0.001209	1.467243	0.000081	417	0.282522	0.282697	6.2	0.8	0.4
TM_12-16.dat	120	0.282683	0.000010	0.001002	0.000034	0.041891	0.000882	1.467320	0.000074	417	0.282522	0.282675	5.4	0.7	-0.4
TM_12-17.dat	120	0.282705	0.000013	0.001276	0.000027	0.052820	0.000746	1.467306	0.000087	417	0.282522	0.282695	6.1	0.9	0.3
TM_12-18.dat	120	0.282679	0.000012	0.000879	0.000034	0.037778	0.000862	1.467276	0.000076	417	0.282522	0.282672	5.3	0.8	-0.5
TM_12-19.dat	120	0.282708	0.000011	0.000780	0.000028	0.032910	0.000728	1.467277	0.000067	417	0.282522	0.282701	6.3	0.8	0.5
Mean												**0.282672**	**5.3**		**-0.5**
2SD												**0.000038**	**1.3**		
Normalization factor												**1.000050**			
PLESOVICE (n=15)															
PL_12-1.dat	120	0.282473	0.000017	0.000070	0.000000	0.004347	0.000022	1.467334	0.000146	337	0.282573	0.282473	-3.5	1.2	-0.3
PL 12-2.dat	120	0.282485	0.000016	0.000069	0.000001	0.003956	0.000020	1.467322	0.000133	337	0.282573	0.282484	-3.1	1.1	0.1
PL_12-3.dat	120	0.282474	0.000015	0.000069	0.000000	0.004186	0.000010	1.467301	0.000130	337	0.282573	0.282474	-3.5	1.1	-0.3
PL 12-4.dat	120	0.282480	0.000015	0.000059	0.000001	0.003527	0.000013	1.467318	0.000140	337	0.282573	0.282479	-3.3	1.1	-0.1
PL_12-5.dat	120	0.282480	0.000014	0.000076	0.000000	0.004819	0.000028	1.467320	0.000132	337	0.282573	0.282479	-3.3	1.0	-0.1
PL 12-6.dat	120	0.282490	0.000014	0.000061	0.000001	0.003809	0.000046	1.467277	0.000114	337	0.282573	0.282489	-3.0	1.0	0.2
PL_12-7.dat	120	0.282496	0.000012	0.000104	0.000001	0.006359	0.000020	1.467288	0.000110	337	0.282573	0.282495	-2.8	0.8	0.4
PL 12-8.dat	120	0.282485	0.000014	0.000110	0.000000	0.006826	0.000020	1.467315	0.000140	337	0.282573	0.282484	-3.1	1.0	0.1
PL_12-9.dat	120	0.282495	0.000011	0.000107	0.000001	0.006625	0.000027	1.467298	0.000091	337	0.282573	0.282494	-2.8	0.8	0.4
PL 12-10.dat	120	0.282471	0.000013	0.000103	0.000002	0.006297	0.000015	1.467309	0.000093	337	0.282573	0.282471	-3.6	0.9	-0.4
PL_12-11.dat	120	0.282499	0.000014	0.000103	0.000000	0.006466	0.000038	1.467274	0.000121	337	0.282573	0.282498	-2.7	1.0	0.5
PL 12-12.dat	120	0.282506	0.000013	0.000087	0.000002	0.005607	0.000077	1.467317	0.000127	337	0.282573	0.282505	-2.4	0.9	0.8
PL_12-13.dat	120	0.282496	0.000013	0.000097	0.000001	0.006076	0.000023	1.467308	0.000141	337	0.282573	0.282495	-2.7	0.9	0.4
PL 12-14.dat	120	0.282496	0.000011	0.000081	0.000001	0.004961	0.000025	1.467288	0.000093	337	0.282573	0.282496	-2.7	0.8	0.5
PL_12-15.dat	120	0.282517	0.000012	0.000074	0.000001	0.004648	0.000022	1.467286	0.000116	337	0.282573	0.282517	-2.0	0.8	1.2
Mean												**0.282489**	**-3.0**		**0.2**
2SD												**0.000026**	**0.9**		
Normalization factor												**0.999976**			
Average Normalization factor (TM + PL)												**1.000013**			
s07-081015															
TEMORA-2 (n=30)															
run1\TEM_2-1.d	120	0.282677	0.000009	0.001264	0.000024	0.053438	0.000374	1.467225	0.000066	417	0.282522	0.282667	5.1	0.6	-0.6
run1\TEM_2-2.d	110	0.282674	0.000009	0.001328	0.000006	0.056682	0.000218	1.467251	0.000062	417	0.282522	0.282664	5.0	0.6	-0.7
run1\TEM_2-3.d	120	0.282659	0.000008	0.001023	0.000046	0.045373	0.001074	1.467262	0.000074	417	0.282522	0.282651	4.5	0.6	-1.2
run1\TEM_2-4.d	120	0.282669	0.000009	0.000825	0.000016	0.034147	0.000305	1.467260	0.000100	417	0.282522	0.282663	5.0	0.7	-0.8
run1\TEM_2-5.d	120	0.282658	0.000008	0.000870	0.000007	0.036936	0.000041	1.467225	0.000085	417	0.282522	0.282651	4.6	0.6	-1.2
run1\TEM_2-6.d	120	0.282674	0.000009	0.001354	0.000016	0.057213	0.000470	1.467282	0.000095	417	0.282522	0.282663	5.0	0.7	-0.8
run1\TEM_2-7.d	120	0.282674	0.000010	0.001472	0.000030	0.062047	0.000813	1.467246	0.000102	417	0.282522	0.282662	4.9	0.7	-0.8

run1\TEM_2-8.d	120	0.282662	0.000009	0.000973	0.000023	0.040791	0.000543	1.467241	0.000108	417	0.282522	0.282654	4.7	0.6	-1.1
run1\TEM_2-9.d	120	0.282677	0.000009	0.001264	0.000018	0.051923	0.000340	1.467252	0.000090	417	0.282522	0.282667	5.1	0.7	-0.6
run1\TEM_2-10.	120	0.282673	0.000010	0.000747	0.000022	0.032328	0.000520	1.467245	0.000095	417	0.282522	0.282668	5.1	0.7	-0.6
run1\TEM_2-11.	120	0.282660	0.000009	0.000840	0.000005	0.035376	0.000199	1.467239	0.000088	417	0.282522	0.282654	4.6	0.6	-1.1
run1\TEM_2-12.	120	0.282668	0.000009	0.000728	0.000020	0.031715	0.000757	1.467273	0.000099	417	0.282522	0.282662	4.9	0.6	-0.8
run1\TEM_2-13.	120	0.282677	0.000009	0.000721	0.000010	0.030220	0.000355	1.467295	0.000087	417	0.282522	0.282671	5.3	0.6	-0.5
run1\TEM_2-14.	120	0.282659	0.000008	0.000892	0.000032	0.036987	0.000749	1.467297	0.000091	417	0.282522	0.282652	4.6	0.6	-1.1
run1\TEM_2-15.	120	0.282685	0.000010	0.000498	0.000010	0.021882	0.000262	1.467245	0.000117	417	0.282522	0.282681	5.6	0.7	-0.2
run2\TEM_2-1.d	120	0.282680	0.000007	0.001502	0.000011	0.073530	0.000141	1.467242	0.000097	417	0.282522	0.282668	5.2	0.5	-0.6
run2\TEM_2-2.d	100	0.282666	0.000006	0.001143	0.000037	0.049711	0.000394	1.467269	0.000063	417	0.282522	0.282657	4.8	0.5	-1.0
run2\TEM_2-3.d	120	0.282678	0.000008	0.001254	0.000028	0.060069	0.001237	1.467265	0.000069	417	0.282522	0.282668	5.2	0.6	-0.6
run2\TEM_2-4.d	120	0.282683	0.000006	0.000935	0.000010	0.041663	0.000322	1.467236	0.000094	417	0.282522	0.282676	5.4	0.4	-0.3
run2\TEM_2-5.d	80	0.282663	0.000007	0.000645	0.000024	0.027874	0.000321	1.467286	0.000113	417	0.282522	0.282658	4.8	0.5	-0.9
run2\TEM_2-6.d	120	0.282666	0.000007	0.000552	0.000009	0.024530	0.000258	1.467299	0.000095	417	0.282522	0.282661	4.9	0.5	-0.8
run2\TEM_2-7.d	120	0.282695	0.000007	0.001470	0.000009	0.072567	0.000430	1.467226	0.000078	417	0.282522	0.282683	5.7	0.5	-0.1
run2\TEM_2-8.d	80	0.282676	0.000008	0.001432	0.000021	0.072343	0.000437	1.467283	0.000107	417	0.282522	0.282664	5.0	0.6	-0.7
run2\TEM_2-9.d	120	0.282675	0.000006	0.001213	0.000037	0.052784	0.001177	1.467335	0.000089	417	0.282522	0.282666	5.1	0.4	-0.7
run2\TEM_2-10.	120	0.282658	0.000006	0.001360	0.000040	0.063015	0.000995	1.467234	0.000069	417	0.282522	0.282647	4.4	0.4	-1.3
run2\TEM_2-11.	120	0.282675	0.000006	0.001210	0.000033	0.054882	0.001092	1.467215	0.000083	417	0.282522	0.282666	5.1	0.4	-0.7
run2\TEM 2-12.	120	0.282675	0.000006	0.000945	0.000050	0.044138	0.000981	1.467228	0.000086	417	0.282522	0.282668	5.2	0.4	-0.6
run2\TEM_1-2.d	120	0.282668	0.000013	0.000882	0.000002	0.052809	0.000612	1.467225	0.000105	417	0.282522	0.282661	4.9	0.9	-0.8
run2\TEM 1-3.d	120	0.282661	0.000010	0.001368	0.000013	0.067717	0.000414	1.467253	0.000080	417	0.282522	0.282651	4.5	0.7	-1.2
run2\TEM_1-4.d	120	0.282656	0.000009	0.001108	0.000005	0.057979	0.000508	1.467251	0.000079	417	0.282522	0.282647	4.4	0.7	-1.3
Mean												**0.282662**	**5.0**		**-0.8**
2SD												**0.000018**	**0.6**		
Normalization factor												**1.000083**			
PLESOVICE (n=28)															
run1\PL_2-1.da	120	0.282474	0.000006	0.000112	0.000001	0.008151	0.000026	1.467235	0.000078	337	0.282573	0.282473	-3.5	0.5	-0.3
run1\PL 2-2.da	120	0.282469	0.000007	0.000062	0.000000	0.004473	0.000006	1.467255	0.000074	337	0.282573	0.282468	-3.7	0.5	-0.5
run1\PL_2-3.da	120	0.282480	0.000007	0.000062	0.000000	0.004484	0.000017	1.467259	0.000077	337	0.282573	0.282480	-3.3	0.5	-0.1
run1\PL 2-4.da	120	0.282464	0.000007	0.000072	0.000001	0.005121	0.000050	1.467209	0.000074	337	0.282573	0.282463	-3.9	0.5	-0.6
run1\PL_2-5.da	120	0.282472	0.000007	0.000096	0.000000	0.006961	0.000039	1.467229	0.000089	337	0.282573	0.282472	-3.6	0.5	-0.3
run1\PL 2-6.da	120	0.282487	0.000007	0.000090	0.000001	0.006455	0.000049	1.467254	0.000081	337	0.282573	0.282486	-3.1	0.5	0.1
run1\PL_2-7.da	120	0.282486	0.000006	0.000083	0.000001	0.005903	0.000057	1.467246	0.000069	337	0.282573	0.282486	-3.1	0.5	0.1
run1\PL 2-8.da	120	0.282485	0.000008	0.000081	0.000003	0.005827	0.000120	1.467218	0.000077	337	0.282573	0.282485	-3.1	0.6	0.1
run1\PL_2-9.da	120	0.282478	0.000008	0.000103	0.000000	0.007416	0.000024	1.467233	0.000066	337	0.282573	0.282477	-3.4	0.5	-0.2
run1\PL 2-10.d	120	0.282478	0.000007	0.000103	0.000000	0.007321	0.000024	1.467234	0.000076	337	0.282573	0.282478	-3.4	0.5	-0.1
run1\PL_2-11.d	120	0.282478	0.000007	0.000105	0.000000	0.007641	0.000022	1.467241	0.000082	337	0.282573	0.282478	-3.4	0.5	-0.1
run1\PL 2-12.d	120	0.282478	0.000007	0.000105	0.000000	0.007703	0.000014	1.467253	0.000075	337	0.282573	0.282477	-3.4	0.5	-0.2
run1\PL_2-13.d	120	0.282469	0.000007	0.000111	0.000002	0.007784	0.000047	1.467245	0.000087	337	0.282573	0.282468	-3.7	0.5	-0.5
run1\PL 2-14.d	120	0.282480	0.000007	0.000116	0.000002	0.008378	0.000080	1.467265	0.000078	337	0.282573	0.282479	-3.3	0.5	-0.1
run1\PL_2-15.d	120	0.282485	0.000007	0.000100	0.000002	0.006892	0.000058	1.467243	0.000079	337	0.282573	0.282485	-3.1	0.5	0.1
run2\PL 2-1 da	120	0.282472	0.000006	0.000117	0.000001	0.009016	0.000030	1.467225	0.000106	337	0.282573	0.282471	-3.6	0.4	-0.4
run2\PL_2-2.da	120	0.282473	0.000008	0.000114	0.000000	0.008864	0.000032	1.467167	0.000256	337	0.282573	0.282473	-3.5	0.6	-0.3
run2\PL_2-3.da	120	0.282472	0.000007	0.000101	0.000000	0.007772	0.000072	1.467215	0.000178	337	0.282573	0.282471	-3.6	0.5	-0.4
run2\PL_2-4.da	120	0.282476	0.000005	0.000126	0.000000	0.008610	0.000020	1.467226	0.000080	337	0.282573	0.282475	-3.5	0.4	-0.2
run2\PL_2-5.da	120	0.282469	0.000006	0.000126	0.000000	0.008917	0.000042	1.467218	0.000144	337	0.282573	0.282468	-3.7	0.4	-0.5

run2\PL_2-6.da	120	0.282469	0.000005	0.000130	0.000000	0.008824	0.000038	1.466837	0.000289	337	0.282573	0.282468	-3.7	0.4	-0.5
run2\PL_2-7.da	120	0.282475	0.000004	0.000148	0.000001	0.010291	0.000041	1.467230	0.000069	337	0.282573	0.282474	-3.5	0.3	-0.3
run2\PL_2-8.da	120	0.282470	0.000007	0.000130	0.000000	0.008729	0.000032	1.465661	0.000732	337	0.282573	0.282469	-3.7	0.5	-0.4
run2\PL_1-1.da	120	0.282468	0.000008	0.000068	0.000002	0.004627	0.000080	1.467236	0.000068	337	0.282573	0.282468	-3.7	0.6	-0.5
run2\PL_1-2.da	120	0.282475	0.000007	0.000068	0.000002	0.004540	0.000075	1.467219	0.000077	337	0.282573	0.282475	-3.5	0.5	-0.2
run2\PL_1-3.da	120	0.282466	0.000008	0.000070	0.000002	0.004803	0.000068	1.467246	0.000082	337	0.282573	0.282465	-3.8	0.5	-0.6
run2\PL_1-4.da	120	0.282475	0.000007	0.000062	0.000002	0.004260	0.000052	1.467250	0.000073	337	0.282573	0.282475	-3.5	0.5	-0.2
run2\PL_1-5.da	75	0.282471	0.000008	0.000058	0.000002	0.004035	0.000052	1.467245	0.000086	337	0.282573	0.282470	-3.6	0.6	-0.4
Mean												**0.282474**	**-3.5**		**-0.3**
2SD												**0.000012**	**0.4**		
Normalization factor												**1.000028**			
Average Normalization factor (TM + PL)												**1.000056**			

[a] Using the age obtained by LA-ICPMS in this study (Table B.1)
[b] Using CHUR values of Bouvier et al. (2008)
[c] Plesovice age from Sláma et al. (2008) and Temora-2 from Woodhead and Hergt (2005)
[d] A mean age is shown because we measured on a zircon batch used for oxygen isotopes, where LA-ICPMS has not been performed

Session dd/mm/yy	**2SD TEMORA**	**176Hf/177Hf TEMORA**
s081214	0.000026	0.282675
s020315	0.000018	0.282657
s040215	0.000012	0.282657
s080515	0.000046	0.282683
s050215	0.000038	0.282672
s07-081015	0.000018	0.282662

Over 10 months

TEMORA n=98

	176Hf/177Hf (t)	eps Hf (t)
Mean	0.282670	
2SD	0.000036	**1.3**

PLESOVICE n=89

Mean	0.282479	
2SD	0.000027	1.0

Supplementary Table B.4: Results of in situ oxygene isotope SIMS analyses.

Analysis (n=280)	Spot location single grain	$^{18}O/^{16}O$	1σ (%) Inter-session	$\delta^{18}O$ (SMOW)	2σ (‰) Inter-session
AG1304A (n=20)					
AG1304A_1/1	Core	0.00201580	0.0099	5.28	0.20
AG1304A_11/1	Core	0.00201578	0.0095	5.28	0.19
AG1304A_11/2	Rim	0.00201589	0.0094	5.33	0.19
AG1304A_12/1	Core	0.00201546	0.0111	5.12	0.22
AG1304A_12/2	Rim	0.00201546	0.0094	5.12	0.19
AG1304A_13/1	Core	0.00201557	0.0076	5.17	0.15
AG1304A_13/2	Rim	0.00201548	0.0107	5.13	0.21
AG1304A_18/1	Core	0.00201566	0.0118	5.21	0.24
AG1304A_18/2	Rim	0.00201586	0.0114	5.32	0.23
AG1304A_25/1	Core	0.00201583	0.0099	5.30	0.20
AG1304A_25/2	Rim	0.00201533	0.0106	5.05	0.21
AG1304A_30/1	Core	0.00201556	0.0108	5.16	0.22
AG1304A_4/1	Core	0.00201511	0.0084	4.94	0.17
AG1304A_4/2	Intermediate	0.00201552	0.0085	5.15	0.17
AG1304A_4/3	Rim	0.00201579	0.0077	5.28	0.15
AG1304A_17/1	Core	0.00201571	0.0081	5.24	0.16
AG1304A_17/2	Rim	0.00201558	0.0108	5.18	0.22
AG1304A_32/1	Core	0.00201576	0.0097	5.26	0.19
AG1304A_32/2	Rim	0.00201573	0.0080	5.25	0.16
AG1304A_5/1	Core	0.00201560	0.0079	5.19	0.16
Median ± 2SD				**5.20**	**0.19**

AG1401 (n=20)					
AG1401_1/1	Core	0.00201376	0.0122	4.27	0.24
AG1401_1/2	Rim	0.00201358	0.0079	4.18	0.16
AG1401_11/1	Core	0.00201396	0.0118	4.37	0.24
AG1401_11/2	Intermediate	0.00201368	0.0089	4.23	0.18
AG1401_11/3	Rim	0.00201444	0.0098	4.61	0.20
AG1401_16/1	Core	0.00201361	0.0114	4.20	0.23
AG1401_17/1	Core	0.00201559	0.0076	5.18	0.15
AG1401_17/2	Intermediate	0.00201550	0.0113	5.13	0.23
AG1401_17/3	Rim	0.00201509	0.0082	4.93	0.16
AG1401_3/1	Core	0.00201384	0.0096	4.31	0.19
AG1401_3/2	Rim	0.00201499	0.0101	4.88	0.20
AG1401_7/1	Core	0.00201491	0.0098	4.84	0.20
AG1401_10/1	Core	0.00201394	0.0104	4.36	0.21
AG1401_13/1	Core	0.00201406	0.0081	4.42	0.16
AG1401_13/2	Rim	0.00201452	0.0084	4.65	0.17
AG1401_18/1	Core	0.00201374	0.0083	4.26	0.17
AG1401_22/1	Core	0.00201373	0.0090	4.25	0.18
AG1401_22/2	Rim	0.00201472	0.0112	4.75	0.22
AG1401_6/1	Core	0.00201547	0.0102	5.12	0.20
AG1401_6/2	Rim	0.00201494	0.0083	4.86	0.17
Median ± 2SD				**4.51**	**0.69**
AG1402 (n=20)					

AG1402_1/1	Core	0.00201614	0.0077	5.46	0.15
AG1402_1/2	Rim	0.00201561	0.0113	5.19	0.23
AG1402_18/1	Core	0.00201634	0.0098	5.56	0.20
AG1402_18/2	Rim	0.00201600	0.0095	5.39	0.19
AG1402_3/1	Core	0.00201598	0.0104	5.38	0.21
AG1402_3/2	Rim	0.00201583	0.0101	5.30	0.20
AG1402_6/1	Core	0.00201576	0.0096	5.27	0.19
AG1402_6/2	Rim	0.00201586	0.0107	5.32	0.21
AG1402_9/1	Core	0.00201609	0.0078	5.43	0.16
AG1402_9/2	Intermediate	0.00201578	0.0101	5.28	0.20
AG1402_9/3	Rim	0.00201589	0.0101	5.33	0.20
AG1402_10/1	Core	0.00201593	0.0089	5.35	0.18
AG1402_14/1	Core	0.00201587	0.0085	5.32	0.17
AG1402_16/1	Core	0.00201587	0.0075	5.32	0.15
AG1402_19/1	Core	0.00201580	0.0102	5.29	0.20
AG1402_19/2	Intermediate	0.00201597	0.0079	5.37	0.16
AG1402_19/3	Rim	0.00201572	0.0088	5.24	0.18
AG1402_22/1	Core	0.00201584	0.0099	5.30	0.20
AG1402_8/1	Core	0.00201585	0.0087	5.31	0.17
AG1402_8/2	Rim	0.00201592	0.0096	5.35	0.19
Median ± 2SD				**5.32**	**0.16**
HQ1403 (n=20)					
HQ1403_1/1	Core	0.00201615	0.0086	5.46	0.17
HQ1403_1/2	Rim	0.00201553	0.0117	5.15	0.23

HQ1403_11/1	Core	0.00201611	0.0106	5.44	0.21
HQ1403_11/2	Rim	0.00201605	0.0106	5.41	0.21
HQ1403_12/1	Core	0.00201643	0.0108	5.60	0.22
HQ1403_17/1	Core	0.00201606	0.0133	5.42	0.27
HQ1403_17/2	Rim	0.00201604	0.0076	5.41	0.15
HQ1403_2/1	Core	0.00201600	0.0106	5.39	0.21
HQ1403_2/2	Rim	0.00201575	0.0113	5.26	0.23
HQ1403_22/1	Core	0.00201574	0.0112	5.25	0.22
HQ1403_3/1	Core	0.00201595	0.0112	5.36	0.22
HQ1403_4/1	Core	0.00201614	0.0104	5.46	0.21
HQ1403_7/1	Core	0.00201632	0.0099	5.55	0.20
HQ1403_15/1	Core	0.00201698	0.0098	5.87	0.20
HQ1403_15/2	Rim	0.00201581	0.0093	5.29	0.19
HQ1403_16/1	Core	0.00201616	0.0082	5.47	0.16
HQ1403_16/2	Rim	0.00201631	0.0098	5.54	0.20
HQ1403_18/1	Core	0.00201601	0.0075	5.39	0.15
HQ1403_20/1	Core	0.00201609	0.0119	5.43	0.24
HQ1403_22/2	Rim	0.00201595	0.0089	5.36	0.18
Median ± 2SD				**5.42**	**0.30**
AG1308A (n=20)					
AG1308A_10/1	Core	0.00201590	0.0097	5.34	0.19
AG1308A_10/2	Rim	0.00201598	0.0103	5.38	0.21
AG1308A_17/1	Core	0.00201600	0.0077	5.39	0.15
AG1308A_17/2	Rim	0.00201626	0.0088	5.51	0.18

AG1308A_18/1	Core	0.00201613	0.0110	5.45	0.22
AG1308A_18/2	Rim	0.00201629	0.0086	5.53	0.17
AG1308A_2/1	Core	0.00201574	0.0086	5.26	0.17
AG1308A_2/2	Rim	0.00201582	0.0095	5.29	0.19
AG1308A_20/1	Core	0.00201581	0.0103	5.29	0.21
AG1308A_20/2	Rim	0.00201631	0.0096	5.54	0.19
AG1308A_3/1	Core	0.00201588	0.0111	5.33	0.22
AG1308A_3/2	Rim	0.00201589	0.0094	5.33	0.19
AG1308A_4/1	Core	0.00201597	0.0087	5.37	0.17
AG1308A_9/1	Core	0.00201558	0.0115	5.18	0.23
AG1308A_9/2	Rim	0.00201579	0.0089	5.28	0.18
AG1308A_5/1	Core	0.00201592	0.0090	5.35	0.18
AG1308A_6/1	Core	0.00201629	0.0073	5.53	0.15
AG1308A_6/2	Rim	0.00201630	0.0110	5.54	0.22
AG1308A_7/1	Core	0.00201653	0.0107	5.65	0.21
AG1308A_7/2	Rim	0.00201633	0.0095	5.55	0.19
Median ± 2SD				**5.37**	**0.25**
VK1405 (n=20)					
VK1405_10/1	Core	0.00201584	0.0085	5.31	0.17
VK1405_11/1	Core	0.00201592	0.0088	5.35	0.18
VK1405_11/2	Rim	0.00201581	0.0120	5.29	0.24
VK1405_16/1	Core	0.00201535	0.0095	5.06	0.19
VK1405_4/1	Core	0.00201566	0.0093	5.21	0.19
VK1405_4/2	Rim	0.00201564	0.0091	5.20	0.18

VK1405_5/1	Core	0.00201598	0.0084	5.38	0.17
VK1405_5/2	Intermediate	0.00201560	0.0101	5.19	0.20
VK1405_5/3	Rim	0.00201527	0.0136	5.02	0.27
VK1405_8/1	Core	0.00201569	0.0090	5.23	0.18
VK1405_9/1	Core	0.00201589	0.0108	5.33	0.22
VK1405_9/2	Rim	0.00201577	0.0099	5.27	0.20
VK1405_1/1	Core	0.00201571	0.0099	5.24	0.20
VK1405_23/1	Core	0.00201571	0.0095	5.24	0.19
VK1405_23/2	Rim	0.00201636	0.0114	5.57	0.23
VK1405_14/1	Core	0.00201562	0.0093	5.20	0.19
VK1405_15/1	Core	0.00201603	0.0081	5.40	0.16
VK1405_20/1	Core	0.00201574	0.0128	5.26	0.26
VK1405_13/1	Core	0.00201596	0.0128	5.37	0.26
VK1405_27/1	Core	0.00201592	0.0096	5.35	0.19
Median ± 2SD				**5.26**	**0.24**
MR1403 (n=20)					
MR1403_1/1	Core	0.00201637	0.0090	5.57	0.18
MR1403_1/2	Rim	0.00201610	0.0082	5.44	0.16
MR1403_10/1	Core	0.00201655	0.0092	5.66	0.18
MR1403_11/1	Core	0.00201628	0.0090	5.53	0.18
MR1403_11/2	Rim	0.00201632	0.0092	5.54	0.18
MR1403_12/1	Core	0.00201655	0.0114	5.66	0.23
MR1403_12/2	Rim	0.00201671	0.0090	5.74	0.18
MR1403_13/1	Core	0.00201640	0.0092	5.59	0.18

MR1403_13/2	Rim	0.00201623	0.0084	5.50	0.17
MR1403_19/1	Core	0.00201611	0.0090	5.44	0.18
MR1403_2/1	Core	0.00201622	0.0090	5.50	0.18
MR1403_2/2	Rim	0.00201610	0.0103	5.44	0.21
MR1403_3/1	Core	0.00201635	0.0084	5.56	0.17
MR1403_21/1	Core	0.00201647	0.0100	5.62	0.20
MR1403_21/2	Rim	0.00201639	0.0085	5.58	0.17
MR1403_6/1	Core	0.00201641	0.0094	5.59	0.19
MR1403_6/2	Rim	0.00201645	0.0077	5.61	0.15
MR1403_7/1	Core	0.00201613	0.0093	5.45	0.19
MR1403_8/1	Core	0.00201664	0.0088	5.71	0.18
MR1403_9/1	Core	0.00201661	0.0076	5.69	0.15
Median ± 2SD				**5.58**	**0.18**
LI1303A1 (n=20)					
LI1303A1_2/1	Core	0.00201650	0.0079	5.63	0.16
LI1303A1_2/2	Intermediate	0.00201634	0.0109	5.56	0.22
LI1303A1_2/3	Rim	0.00201648	0.0088	5.62	0.18
LI1303A1_3/1	Core	0.00201639	0.0094	5.58	0.19
LI1303A1_3/2	Rim	0.00201634	0.0084	5.55	0.17
LI1303A1_5/1	Core	0.00201657	0.0119	5.67	0.24
LI1303A1_5/2	Rim	0.00201640	0.0086	5.58	0.17
LI1303A1_6/1	Core	0.00201655	0.0107	5.66	0.21
LI1303A1_6/2	Rim	0.00201652	0.0099	5.64	0.20
LI1303A1_7/1	Core	0.00201668	0.0091	5.73	0.18

LI1303A1_7/2	Rim	0.00201668	0.0088	5.73	0.18
LI1303A1_8/1	Core	0.00201639	0.0118	5.58	0.24
LI1303A1_12/1	Core	0.00201658	0.0104	5.67	0.21
LI1303A1_12/2	Rim	0.00201647	0.0090	5.62	0.18
LI1303A1_15/1	Core	0.00201633	0.0073	5.55	0.15
LI1303A1_16/1	Core	0.00201671	0.0090	5.74	0.18
LI1303A1_17/1	Core	0.00201639	0.0108	5.58	0.22
LI1303A1_18/1	Core	0.00201655	0.0073	5.66	0.15
LI1303A1_19/1	Core	0.00201680	0.0081	5.79	0.16
LI1303A1_19/2	Rim	0.00201657	0.0114	5.67	0.23
Median ± 2SD				**5.64**	**0.14**
KJ1207 (n=20)					
KJ1207_1/1	Core	0.00201657	0.0113	5.67	0.23
KJ1207_1/2	Intermediate	0.00201647	0.0089	5.62	0.18
KJ1207_1/3	Rim	0.00201631	0.0078	5.54	0.16
KJ1207_10/1	Core	0.00201597	0.0120	5.37	0.24
KJ1207_10/2	Rim	0.00201574	0.0103	5.26	0.21
KJ1207_2/1	Core	0.00201597	0.0100	5.37	0.20
KJ1207_2/2	Rim	0.00201638	0.0086	5.58	0.17
KJ1207_3/1	Core	0.00201630	0.0107	5.53	0.21
KJ1207_3/2	Rim	0.00201629	0.0077	5.53	0.15
KJ1207_5/1	Core	0.00201609	0.0090	5.43	0.18
KJ1207_5/2	Rim	0.00201580	0.0088	5.28	0.18
KJ1207_7/1	Core	0.00201637	0.0080	5.57	0.16

KJ1207_12/1	Core	0.00201589	0.0100	5.33	0.20
KJ1207_14/1	Core	0.00201624	0.0085	5.50	0.17
KJ1207_16/1	Core	0.00201635	0.0089	5.56	0.18
KJ1207_17/1	Core	0.00201605	0.0097	5.41	0.19
KJ1207_17/2	Rim	0.00201561	0.0082	5.19	0.16
KJ1207_4/1	Core	0.00201619	0.0073	5.48	0.15
KJ1207_9/1	Core	0.00201654	0.0091	5.66	0.18
KJ1207_9/2	Rim	0.00201627	0.0097	5.52	0.19
Median ± 2SD				**5.51**	**0.27**
KJ1002 (n=21)					
KJ1002_1/1	Core	0.00201635	0.0095	5.56	0.19
KJ1002_1/2	Rim	0.00201594	0.0092	5.35	0.18
KJ1002_11/1	Core	0.00201569	0.0087	5.23	0.17
KJ1002_11/2	Rim	0.00201557	0.0089	5.17	0.18
KJ1002_16/1	Core	0.00201572	0.0098	5.24	0.20
KJ1002_16/2	Intermediate	0.00201615	0.0086	5.46	0.17
KJ1002_16/3	Rim	0.00201607	0.0100	5.42	0.20
KJ1002_2/1	Core	0.00201639	0.0092	5.58	0.18
KJ1002_2/2	Rim	0.00201616	0.0078	5.47	0.16
KJ1002_3/1	Core	0.00201663	0.0101	5.70	0.20
KJ1002_3/2	Rim	0.00201632	0.0093	5.55	0.19
KJ1002_6/1	Core	0.00201576	0.0098	5.27	0.20
KJ1002_6/2	Intermediate	0.00201573	0.0130	5.25	0.26
KJ1002_6/3	Rim	0.00201604	0.0093	5.41	0.19

KJ1002_9/1	Core	0.00201650	0.0086	5.64	0.17
KJ1002_9/2	Rim	0.00201625	0.0095	5.51	0.19
KJ1002_18/1	Core	0.00201653	0.0083	5.65	0.17
KJ1002_18/2	Rim	0.00201612	0.0094	5.45	0.19
KJ1002_24/1	Core	0.00201649	0.0092	5.63	0.18
KJ1002_24/2	Intermediate	0.00201617	0.0094	5.47	0.19
KJ1002_24/3	Rim	0.00201631	0.0093	5.54	0.19
Median ± 2SD				**5.47**	**0.31**
KJ1316 (n=19)					
KJ1316_1/1	Core	0.00201653	0.0078	5.65	0.16
KJ1316_13/1	Core	0.00201642	0.0093	5.59	0.19
KJ1316_14/1	Core	0.00201654	0.0121	5.66	0.24
KJ1316_14/2	Rim	0.00201644	0.0085	5.61	0.17
KJ1316_16/1	Core	0.00201666	0.0081	5.71	0.16
KJ1316_2/1	Core	0.00201602	0.0113	5.40	0.23
KJ1316_2/2	Rim	0.00201635	0.0108	5.56	0.22
KJ1316_4/1	Core	0.00201676	0.0102	5.76	0.20
KJ1316_4/2	Rim	0.00201647	0.0087	5.62	0.17
KJ1316_5/1	Core	0.00201638	0.0092	5.58	0.18
KJ1316_9/1	Core	0.00201696	0.0095	5.86	0.19
KJ1316_9/2	Rim	0.00201672	0.0084	5.75	0.17
KJ1316_18/1	Core	0.00201689	0.0082	5.83	0.16
KJ1316_18/2	Rim	0.00201648	0.0095	5.62	0.19
KJ1316_20/1	Core	0.00201673	0.0086	5.75	0.17

KJ1316_21/1	Core	0.00201659	0.0086	5.68	0.17
KJ1316_23/1	Core	0.00201634	0.0098	5.56	0.20
KJ1316_6/1	Core	0.00201640	0.0090	5.58	0.18
KJ1316_7/1	Core	0.00201643	0.0089	5.60	0.18
Median ± 2SD				**5.62**	**0.22**
KJ1302A (n=20)					
KJ1302A_13/1	Core	0.00201648	0.0125	5.63	0.25
KJ1302A_13/2	Rim	0.00201663	0.0097	5.70	0.19
KJ1302A_2/1	Core	0.00201640	0.0107	5.58	0.21
KJ1302A_2/2	Rim	0.00201651	0.0091	5.64	0.18
KJ1302A_3/1	Core	0.00201631	0.0075	5.54	0.15
KJ1302A_3/2	Rim	0.00201607	0.0089	5.42	0.18
KJ1302A_4/1	Core	0.00201635	0.0085	5.56	0.17
KJ1302A_4/2	Rim	0.00201618	0.0116	5.48	0.23
KJ1302A_5/1	Core	0.00201640	0.0111	5.58	0.22
KJ1302A_5/2	Rim	0.00201628	0.0089	5.52	0.18
KJ1302A_6/1	Core	0.00201623	0.0087	5.50	0.17
KJ1302A_7/1	Core	0.00201637	0.0102	5.57	0.20
KJ1302A_14/1	Core	0.00201630	0.0087	5.53	0.17
KJ1302A_16/1	Core	0.00201643	0.0097	5.60	0.19
KJ1302A_17/1	Core	0.00201636	0.0106	5.57	0.21
KJ1302A_19/1	Core	0.00201583	0.0087	5.30	0.17
KJ1302A_19/2	Rim	0.00201582	0.0086	5.29	0.17
KJ1302A_8/1	Core	0.00201627	0.0101	5.52	0.20

KJ1302A_9/1	Core	0.00201620	0.0092	5.49	0.18
KJ1302A_9/2	Rim	0.00201620	0.0099	5.49	0.20
Median ± 2SD				**5.54**	**0.20**
KJ1324A (n=20)					
KJ1324A_1/1	Core	0.00201712	0.0097	5.94	0.19
KJ1324A_1/2	Rim	0.00201689	0.0075	5.83	0.15
KJ1324A_10/1	Core	0.00201709	0.0122	5.93	0.24
KJ1324A_10/2	Rim	0.00201701	0.0105	5.89	0.21
KJ1324A_17/1	Core	0.00201686	0.0092	5.82	0.18
KJ1324A_17/2	Intermediate	0.00201713	0.0095	5.95	0.19
KJ1324A_17/3	Rim	0.00201689	0.0101	5.83	0.20
KJ1324A_4/1	Core	0.00201729	0.0084	6.03	0.17
KJ1324A_4/2	Rim	0.00201692	0.0095	5.84	0.19
KJ1324A_5/1	Core	0.00201741	0.0089	6.09	0.18
KJ1324A_5/2	Rim	0.00201708	0.0076	5.92	0.15
KJ1324A_8/1	Core	0.00201694	0.0115	5.86	0.23
KJ1324A_8/2	Rim	0.00201692	0.0093	5.84	0.19
KJ1324A_9/1	Core	0.00201692	0.0086	5.84	0.17
KJ1324A_16/1	Core	0.00201719	0.0110	5.98	0.22
KJ1324A_16/2	Rim	0.00201714	0.0086	5.95	0.17
KJ1324A_18/1	Core	0.00201708	0.0082	5.92	0.16
KJ1324A_18/2	Rim	0.00201698	0.0085	5.88	0.17
KJ1324A_22/1	Core	0.00201719	0.0103	5.98	0.21
KJ1324A_22/2	Rim	0.00201727	0.0098	6.02	0.20

Median ± 2SD				**5.92**	**0.15**
LI1301 (n=20)					
LI1301_11/1	Core	0.00201661	0.0082	5.69	0.16
LI1301_2/1	Core	0.00201725	0.0106	6.01	0.21
LI1301_2/2	Intermediate	0.00201732	0.0097	6.04	0.19
LI1301_2/3	Rim	0.00201684	0.0075	5.81	0.15
LI1301_3/1	Core	0.00201682	0.0086	5.79	0.17
LI1301_3/2	Rim	0.00201706	0.0100	5.91	0.20
LI1301_4/1	Core	0.00201735	0.0095	6.06	0.19
LI1301_4/2	Rim	0.00201744	0.0094	6.10	0.19
LI1301_5/1	Core	0.00201719	0.0090	5.98	0.18
LI1301_5/2	Rim	0.00201684	0.0085	5.81	0.17
LI1301_8/1	Core	0.00201708	0.0099	5.93	0.20
LI1301_15/1	Core	0.00201732	0.0117	6.04	0.23
LI1301_16/1	Core	0.00201716	0.0088	5.96	0.18
LI1301_16/2	Intermediate	0.00201708	0.0102	5.93	0.20
LI1301_16/3	Rim	0.00201697	0.0076	5.87	0.15
LI1301_17/1	Core	0.00201740	0.0094	6.08	0.19
LI1301_21/1	Core	0.00201712	0.0092	5.94	0.18
LI1301_21/2	Rim	0.00201721	0.0104	5.99	0.21
LI1301_6/1	Core	0.00201722	0.0090	6.00	0.18
LI1301_6/2	Rim	0.00201728	0.0095	6.03	0.19
Median ± 2SD				**5.97**	**0.22**
Standard	S0081_UAMT	0.00201497		4.87	

Appendix C: Zircon cathodoluminescence imaging and U-Pb, Hf and O isotope spot analysis

In situ U-Pb and Hf isotope spot analysis

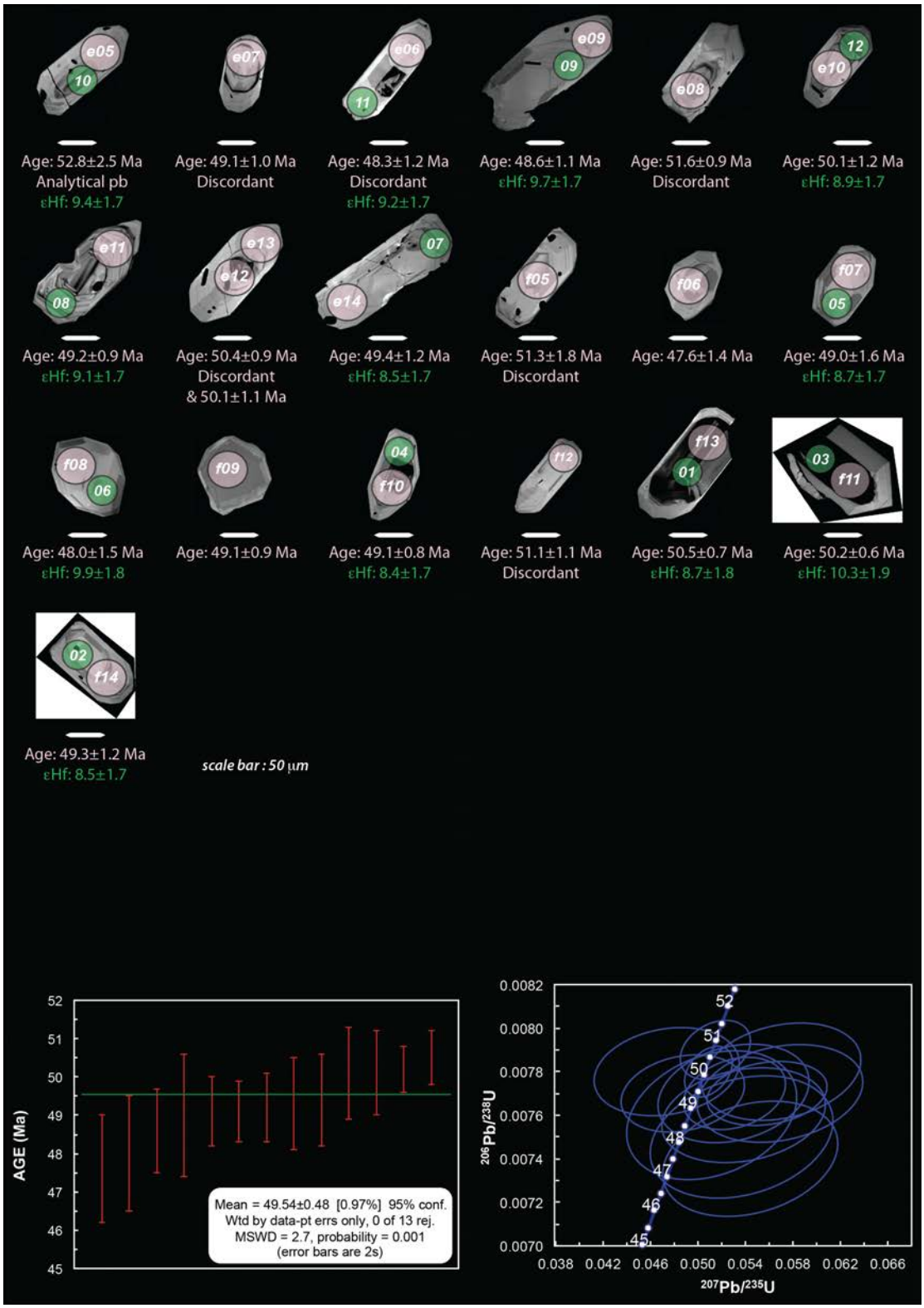

AG1402A

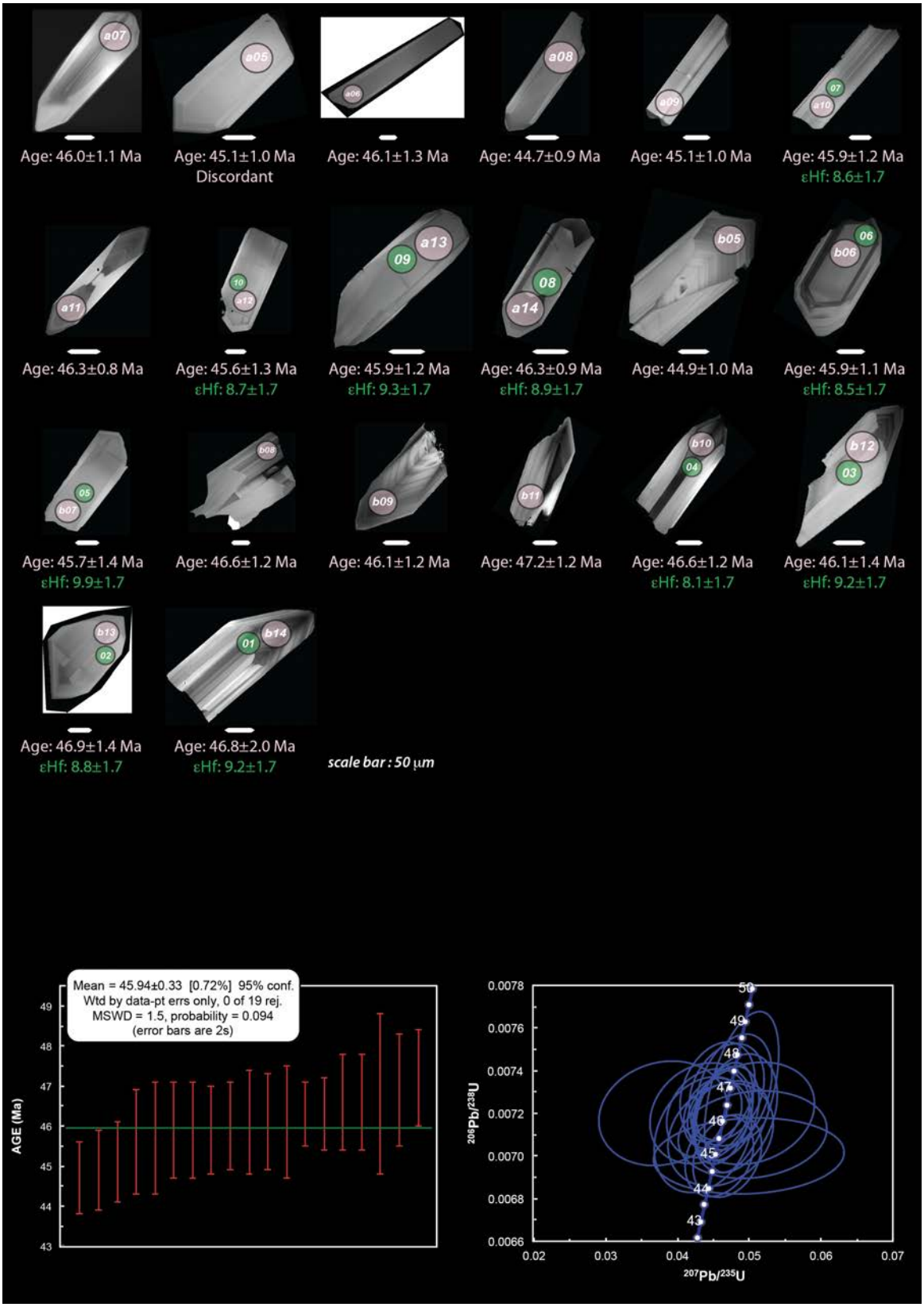
Age: 46.0±1.1 Ma
Age: 45.1±1.0 Ma
Discordant
Age: 46.1±1.3 Ma
Age: 44.7±0.9 Ma
Age: 45.1±1.0 Ma
Age: 45.9±1.2 Ma
εHf: 8.6±1.7
Age: 46.3±0.8 Ma
Age: 45.6±1.3 Ma
εHf: 8.7±1.7
Age: 45.9±1.2 Ma
εHf: 9.3±1.7
Age: 46.3±0.9 Ma
εHf: 8.9±1.7
Age: 44.9±1.0 Ma
Age: 45.9±1.1 Ma
εHf: 8.5±1.7
Age: 45.7±1.4 Ma
εHf: 9.9±1.7
Age: 46.6±1.2 Ma
Age: 46.1±1.2 Ma
Age: 47.2±1.2 Ma
Age: 46.6±1.2 Ma
εHf: 8.1±1.7
Age: 46.1±1.4 Ma
εHf: 9.2±1.7
Age: 46.9±1.4 Ma
εHf: 8.8±1.7
Age: 46.8±2.0 Ma
εHf: 9.2±1.7
scale bar : 50 μm
Mean = 45.94±0.33 [0.72%] 95% conf.
Wtd by data-pt errs only, 0 of 19 rej.
MSWD = 1.5, probability = 0.094
(error bars are 2s)
AGE (Ma)
206Pb/238U
207Pb/235U

AG1401

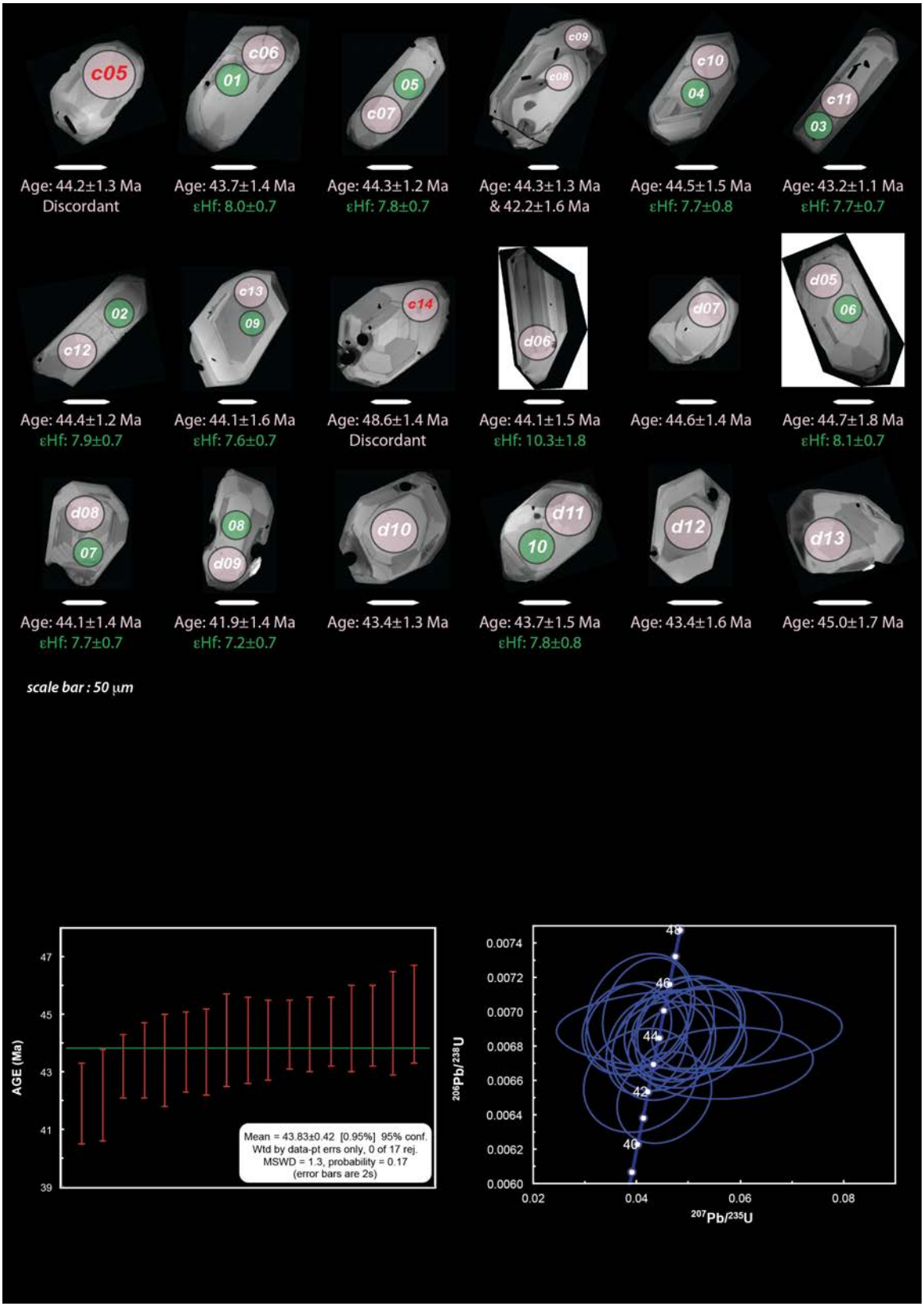
c05
Age: 44.2±1.3 Ma
Discordant
c06
01
Age: 43.7±1.4 Ma
εHf: 8.0±0.7
05
c07
Age: 44.3±1.2 Ma
εHf: 7.8±0.7
c09
c08
Age: 44.3±1.3 Ma
& 42.2±1.6 Ma
c10
04
Age: 44.5±1.5 Ma
εHf: 7.7±0.8
c11
03
Age: 43.2±1.1 Ma
εHf: 7.7±0.7
02
c12
Age: 44.4±1.2 Ma
εHf: 7.9±0.7
c13
09
Age: 44.1±1.6 Ma
εHf: 7.6±0.7
c14
Age: 48.6±1.4 Ma
Discordant
d06
Age: 44.1±1.5 Ma
εHf: 10.3±1.8
d07
Age: 44.6±1.4 Ma
d05
06
Age: 44.7±1.8 Ma
εHf: 8.1±0.7
d08
07
Age: 44.1±1.4 Ma
εHf: 7.7±0.7
08
d09
Age: 41.9±1.4 Ma
εHf: 7.2±0.7
d10
Age: 43.4±1.3 Ma
d11
10
Age: 43.7±1.5 Ma
εHf: 7.8±0.8
d12
Age: 43.4±1.6 Ma
d13
Age: 45.0±1.7 Ma
scale bar : 50 μm
AGE (Ma)
47
45
43
41
39
Mean = 43.83±0.42 [0.95%] 95% conf.
Wtd by data-pt errs only, 0 of 17 rej.
MSWD = 1.3, probability = 0.17
(error bars are 2s)
206Pb/238U
0.0074
0.0072
0.0070
0.0068
0.0066
0.0064
0.0062
0.0060
46
44
42
40
0.02
0.04
0.06
0.08
207Pb/235U

AG1402

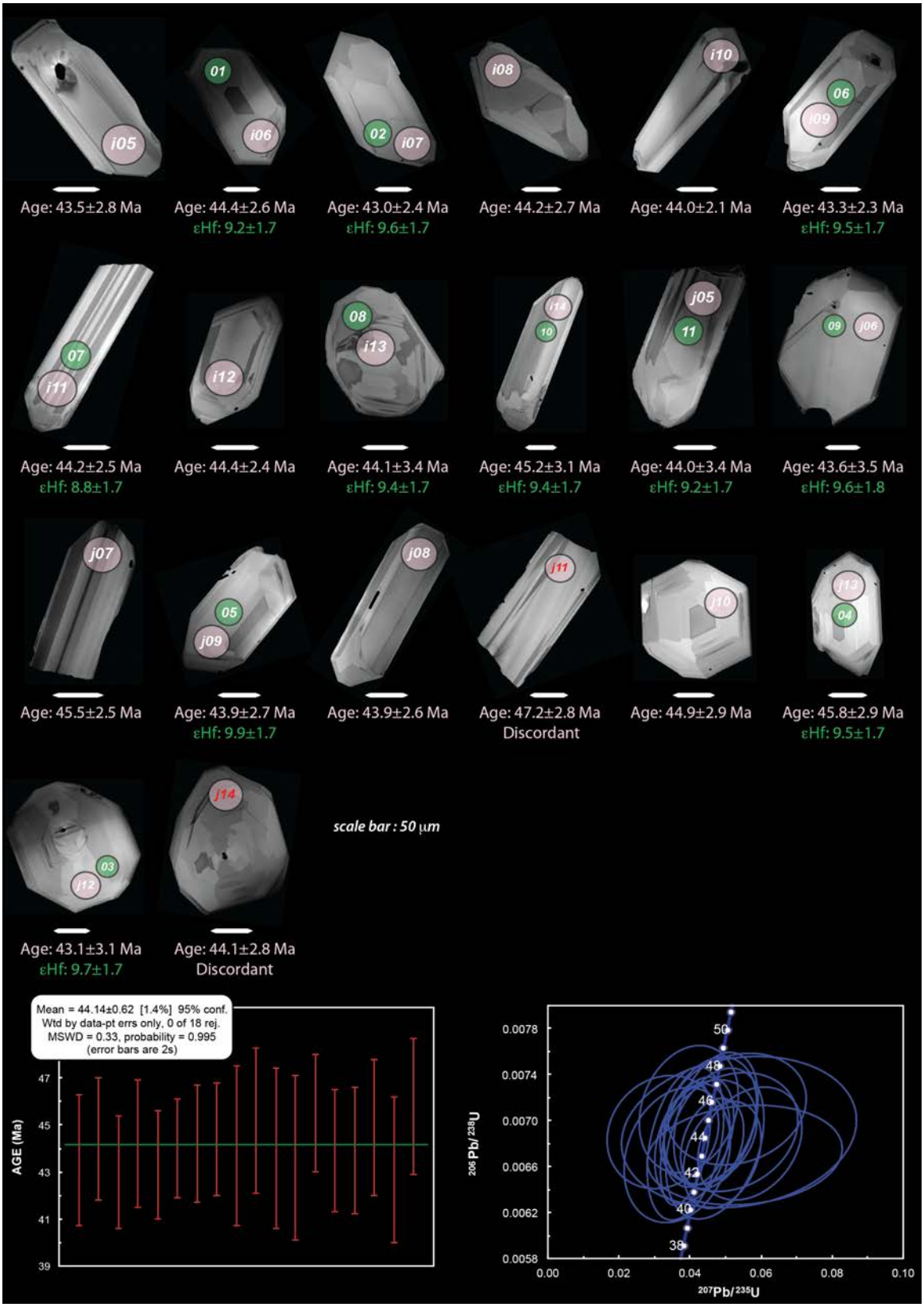
Age: 43.5±2.8 Ma
Age: 44.4±2.6 Ma
εHf: 9.2±1.7
Age: 43.0±2.4 Ma
εHf: 9.6±1.7
Age: 44.2±2.7 Ma
Age: 44.0±2.1 Ma
Age: 43.3±2.3 Ma
εHf: 9.5±1.7
Age: 44.2±2.5 Ma
εHf: 8.8±1.7
Age: 44.4±2.4 Ma
Age: 44.1±3.4 Ma
εHf: 9.4±1.7
Age: 45.2±3.1 Ma
εHf: 9.4±1.7
Age: 44.0±3.4 Ma
εHf: 9.2±1.7
Age: 43.6±3.5 Ma
εHf: 9.6±1.8
Age: 45.5±2.5 Ma
Age: 43.9±2.7 Ma
εHf: 9.9±1.7
Age: 43.9±2.6 Ma
Age: 47.2±2.8 Ma
Discordant
Age: 44.9±2.9 Ma
Age: 45.8±2.9 Ma
εHf: 9.5±1.7
scale bar : 50 μm
Age: 43.1±3.1 Ma
εHf: 9.7±1.7
Age: 44.1±2.8 Ma
Discordant
Mean = 44.14±0.62 [1.4%] 95% conf.
Wtd by data-pt errs only, 0 of 18 rej.
MSWD = 0.33, probability = 0.995
(error bars are 2s)
AGE (Ma)
206Pb/238U
207Pb/235U

AG1403


Age: 46.4±4.4 Ma
εHf: 8.8±1.7
Age: 46.0±4.2 Ma
Discordant
Age: 46.4±4.9 Ma
εHf: 9.3±1.7
Age: 46.5±3.6 Ma
εHf: 9.2±1.8
Age: 46.4±3.0 Ma
Age: 47.4±1.9 Ma
Age: 44.8±3.2 Ma
Age: 45.4±1.3 Ma
Age: 45.6±3.0 Ma
εHf: 8.9±1.7
Age: 43.7±4.7 Ma
εHf: 9.4±1.7
Age: 44.1±3.8 Ma
Discordant
Age: 44.7±4.1 Ma
Discordant
εHf: 8.2±1.7
Age: 43.9±3.7 Ma
εHf: 9.0±1.7
Age: 45.6±1.8 Ma
εHf: 9.8±1.8
Age: 43.2±2.0 Ma
εHf: 9.2±1.7
Age: 44.3±1.6 Ma
Discordant
Age: 44.5±2.7 Ma
Age: 43.2±1.8 Ma
Age: 45.1±2.1 Ma
Discordant
Age: 43.8±1.9 Ma
εHf: 8.8±1.7
Age: 46.3±1.9 Ma
Age: 43.8±1.2 Ma
Age: 44.3±1.4 Ma
Age: 44.2±1.5 Ma
Age: 45.7±1.8 Ma
Age: 47.3±2.3 Ma
Discordant
Age: 45.3±1.8 Ma
Age: 45.5±2.0 Ma
Age: 44.7±1.5 Ma
εHf: 9.2±1.7
Age: 44.4±1.4 Ma
εHf: 9.0±1.7
scale bar : 50 μm
AGE (Ma)
Mean = 44.82±0.45 [1.0%] 95% conf.
Wtd by data-pt errs only, 0 of 24 rej.
MSWD = 1.2, probability = 0.20
(error bars are 2s)
$^{206}Pb/^{238}U$
$^{207}Pb/^{235}U$

AG1404

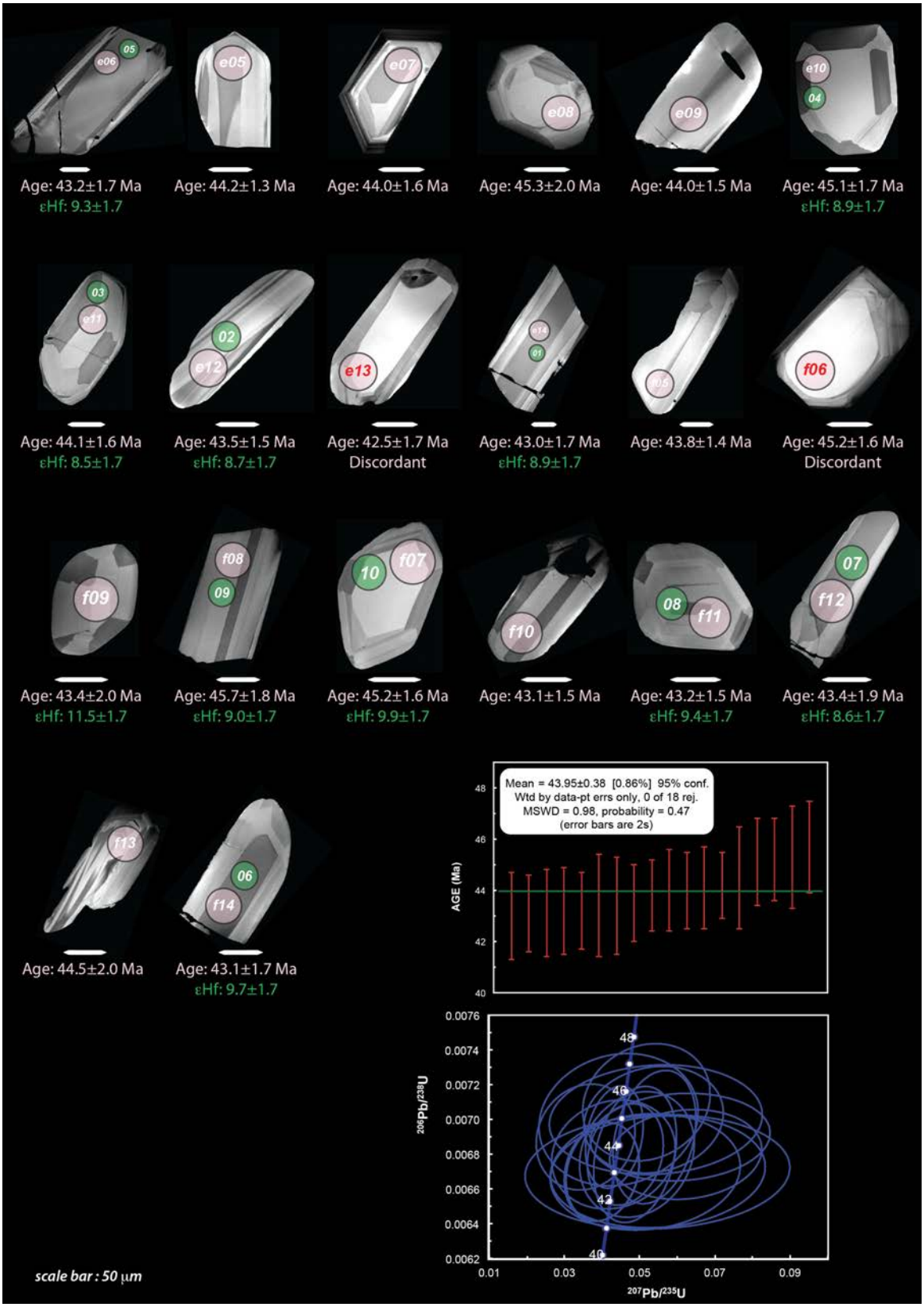
Age: 43.2±1.7 Ma
εHf: 9.3±1.7
Age: 44.2±1.3 Ma
Age: 44.0±1.6 Ma
Age: 45.3±2.0 Ma
Age: 44.0±1.5 Ma
Age: 45.1±1.7 Ma
εHf: 8.9±1.7
Age: 44.1±1.6 Ma
εHf: 8.5±1.7
Age: 43.5±1.5 Ma
εHf: 8.7±1.7
Age: 42.5±1.7 Ma
Discordant
Age: 43.0±1.7 Ma
εHf: 8.9±1.7
Age: 43.8±1.4 Ma
Age: 45.2±1.6 Ma
Discordant
Age: 43.4±2.0 Ma
εHf: 11.5±1.7
Age: 45.7±1.8 Ma
εHf: 9.0±1.7
Age: 45.2±1.6 Ma
εHf: 9.9±1.7
Age: 43.1±1.5 Ma
Age: 43.2±1.5 Ma
εHf: 9.4±1.7
Age: 43.4±1.9 Ma
εHf: 8.6±1.7
Age: 44.5±2.0 Ma
Age: 43.1±1.7 Ma
εHf: 9.7±1.7
Mean = 43.95±0.38 [0.86%] 95% conf.
Wtd by data-pt errs only, 0 of 18 rej.
MSWD = 0.98, probability = 0.47
(error bars are 2s)
AGE (Ma)
48
46
44
42
40
0.0076
0.0074
0.0072
0.0070
0.0068
0.0066
0.0064
0.0062
206Pb/238U
0.01
0.03
0.05
0.07
0.09
207Pb/235U
scale bar : 50 µm

AG1406

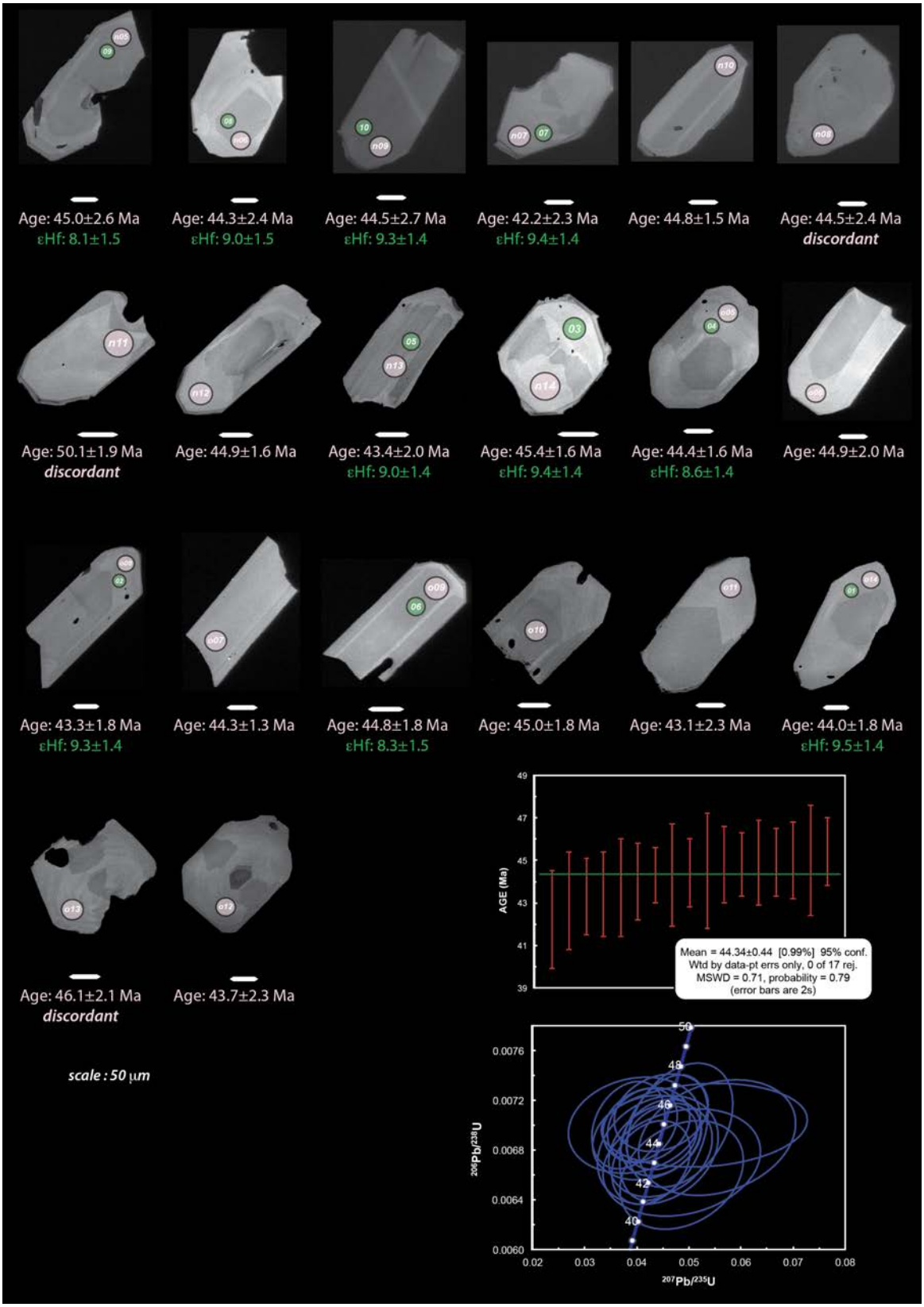
Age: 45.0±2.6 Ma
εHf: 8.1±1.5
Age: 44.3±2.4 Ma
εHf: 9.0±1.5
Age: 44.5±2.7 Ma
εHf: 9.3±1.4
Age: 42.2±2.3 Ma
εHf: 9.4±1.4
Age: 44.8±1.5 Ma
Age: 44.5±2.4 Ma
discordant
Age: 50.1±1.9 Ma
discordant
Age: 44.9±1.6 Ma
Age: 43.4±2.0 Ma
εHf: 9.0±1.4
Age: 45.4±1.6 Ma
εHf: 9.4±1.4
Age: 44.4±1.6 Ma
εHf: 8.6±1.4
Age: 44.9±2.0 Ma
Age: 43.3±1.8 Ma
εHf: 9.3±1.4
Age: 44.3±1.3 Ma
Age: 44.8±1.8 Ma
εHf: 8.3±1.5
Age: 45.0±1.8 Ma
Age: 43.1±2.3 Ma
Age: 44.0±1.8 Ma
εHf: 9.5±1.4
Age: 46.1±2.1 Ma
discordant
Age: 43.7±2.3 Ma
scale : 50 μm
AGE (Ma)
Mean = 44.34±0.44 [0.99%] 95% conf.
Wtd by data-pt errs only, 0 of 17 rej.
MSWD = 0.71, probability = 0.79
(error bars are 2s)
206Pb/238U
207Pb/235U

VK1403

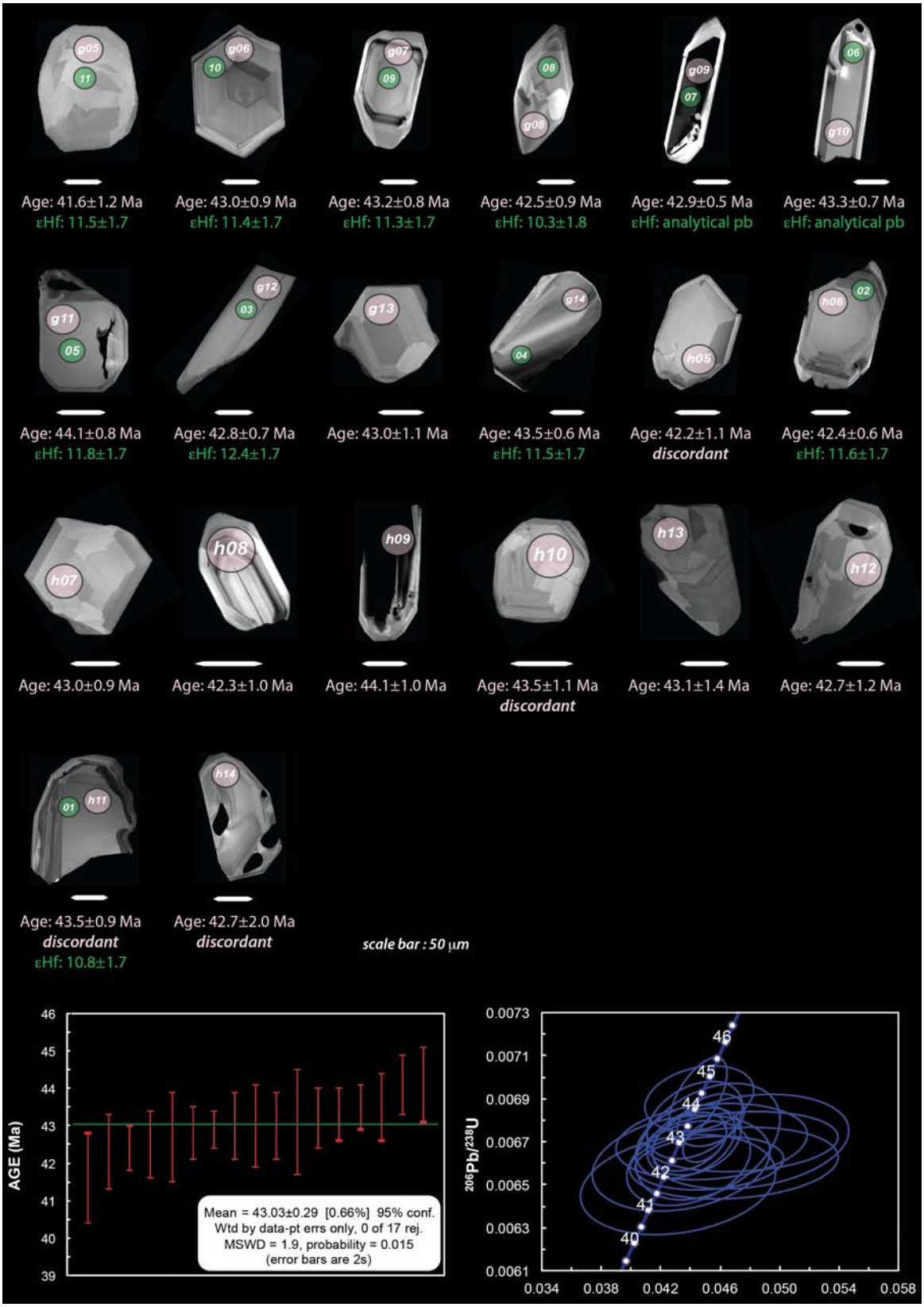
g05
11
Age: 41.6±1.2 Ma
εHf: 11.5±1.7
g06
10
Age: 43.0±0.9 Ma
εHf: 11.4±1.7
g07
09
Age: 43.2±0.8 Ma
εHf: 11.3±1.7
08
g08
Age: 42.5±0.9 Ma
εHf: 10.3±1.8
g09
07
Age: 42.9±0.5 Ma
εHf: analytical pb
06
g10
Age: 43.3±0.7 Ma
εHf: analytical pb
g11
05
Age: 44.1±0.8 Ma
εHf: 11.8±1.7
g12
03
Age: 42.8±0.7 Ma
εHf: 12.4±1.7
g13
Age: 43.0±1.1 Ma
g14
04
Age: 43.5±0.6 Ma
εHf: 11.5±1.7
h05
Age: 42.2±1.1 Ma
discordant
h06
02
Age: 42.4±0.6 Ma
εHf: 11.6±1.7
h07
Age: 43.0±0.9 Ma
h08
Age: 42.3±1.0 Ma
h09
Age: 44.1±1.0 Ma
h10
Age: 43.5±1.1 Ma
discordant
h13
Age: 43.1±1.4 Ma
h12
Age: 42.7±1.2 Ma
01
h11
Age: 43.5±0.9 Ma
discordant
εHf: 10.8±1.7
h14
Age: 42.7±2.0 Ma
discordant
scale bar : 50 μm
AGE (Ma)
46
45
44
43
42
41
40
39
Mean = 43.03±0.29 [0.66%] 95% conf.
Wtd by data-pt errs only, 0 of 17 rej.
MSWD = 1.9, probability = 0.015
(error bars are 2s)
206Pb/238U
0.0073
0.0071
0.0069
0.0067
0.0065
0.0063
0.0061
0.034
0.038
0.042
0.046
0.050
0.054
0.058

HQ1402

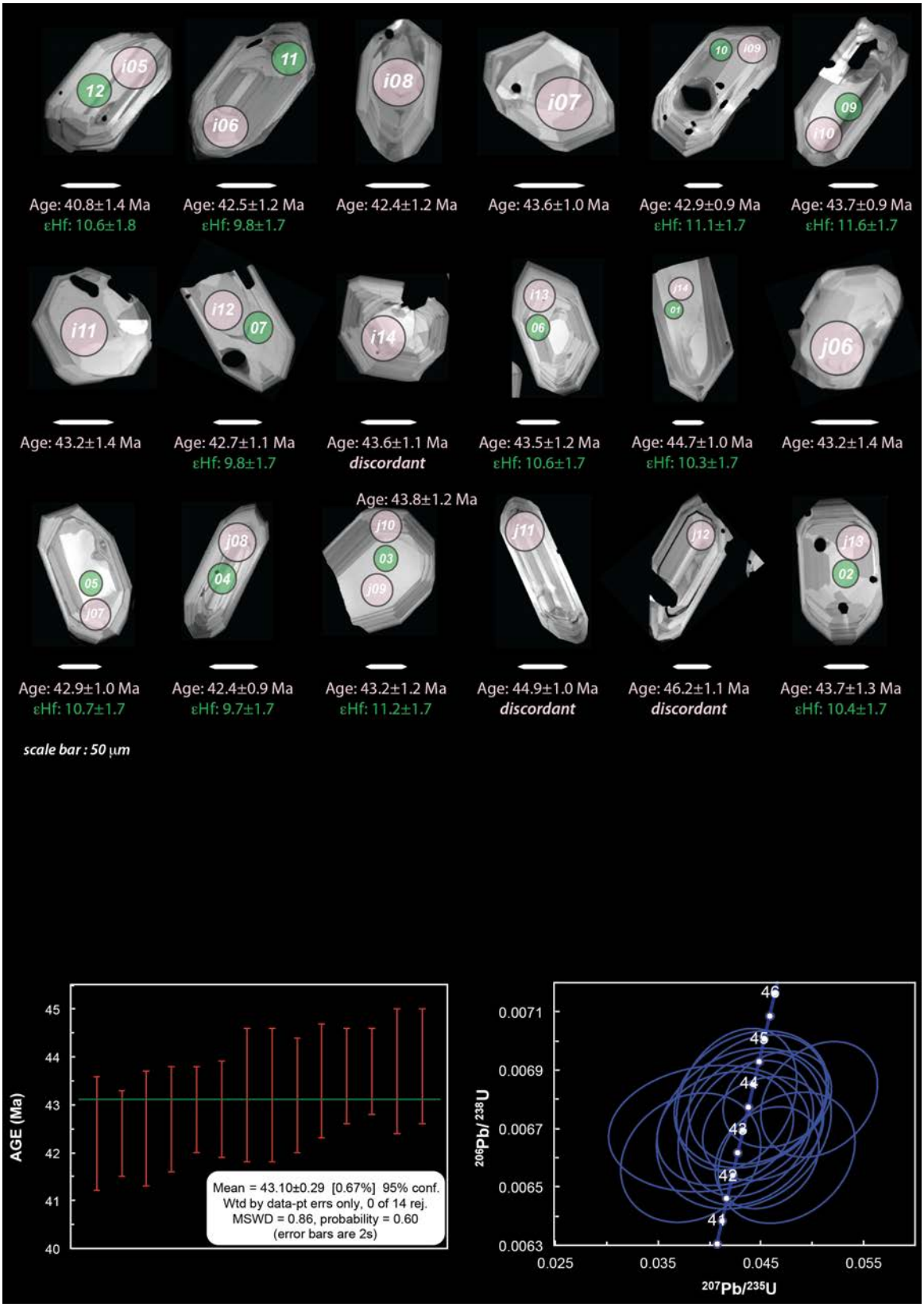
Age: 40.8±1.4 Ma
εHf: 10.6±1.8
Age: 42.5±1.2 Ma
εHf: 9.8±1.7
Age: 42.4±1.2 Ma
Age: 43.6±1.0 Ma
Age: 42.9±0.9 Ma
εHf: 11.1±1.7
Age: 43.7±0.9 Ma
εHf: 11.6±1.7
Age: 43.2±1.4 Ma
Age: 42.7±1.1 Ma
εHf: 9.8±1.7
Age: 43.6±1.1 Ma
discordant
Age: 43.5±1.2 Ma
εHf: 10.6±1.7
Age: 44.7±1.0 Ma
εHf: 10.3±1.7
Age: 43.2±1.4 Ma
Age: 42.9±1.0 Ma
εHf: 10.7±1.7
Age: 42.4±0.9 Ma
εHf: 9.7±1.7
Age: 43.8±1.2 Ma
Age: 43.2±1.2 Ma
εHf: 11.2±1.7
Age: 44.9±1.0 Ma
discordant
Age: 46.2±1.1 Ma
discordant
Age: 43.7±1.3 Ma
εHf: 10.4±1.7
scale bar : 50 μm
AGE (Ma)
Mean = 43.10±0.29 [0.67%] 95% conf.
Wtd by data-pt errs only, 0 of 14 rej.
MSWD = 0.86, probability = 0.60
(error bars are 2s)
206Pb/238U
207Pb/235U

HQ1403

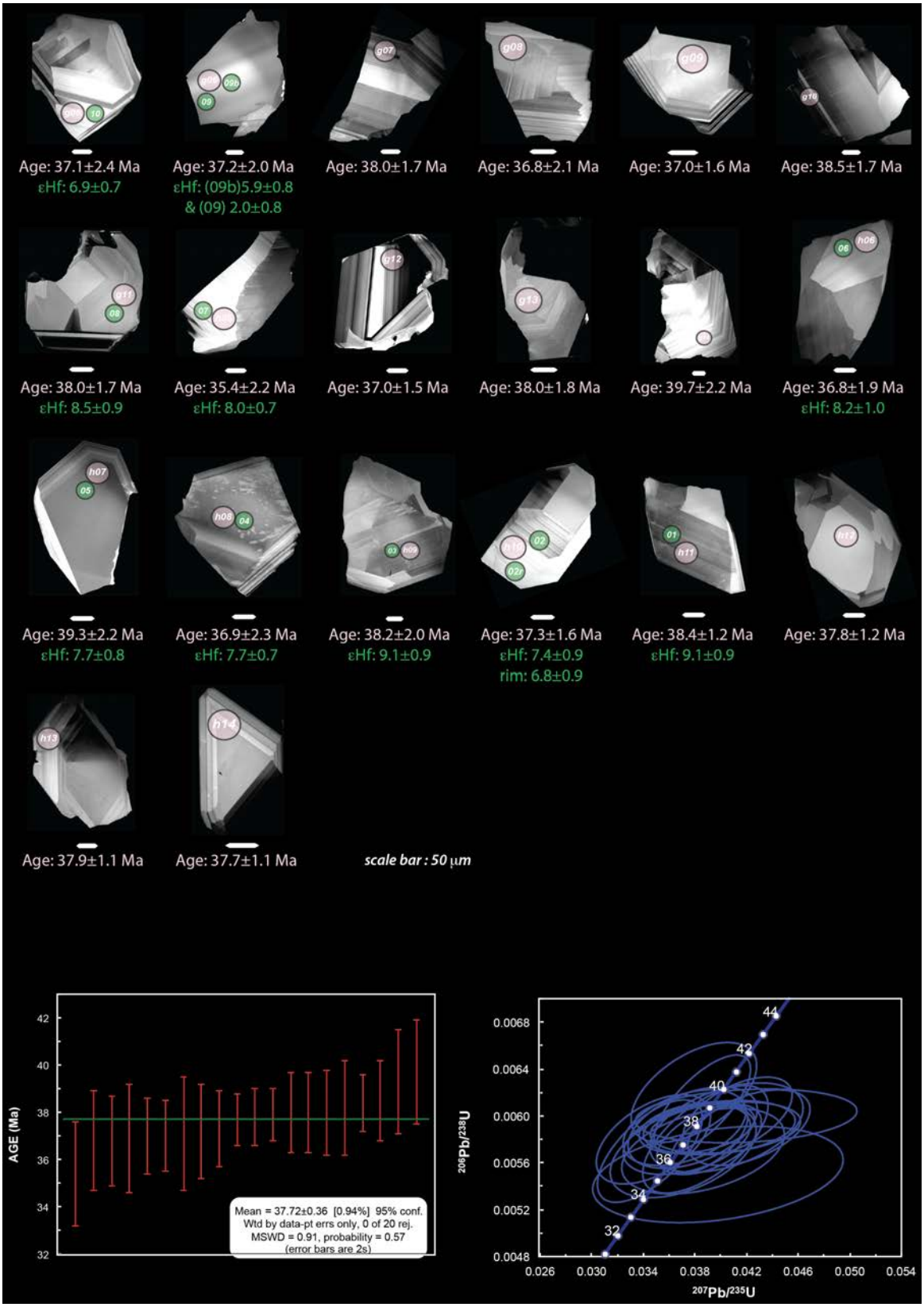
Age: 37.1±2.4 Ma
εHf: 6.9±0.7
Age: 37.2±2.0 Ma
εHf: (09b)5.9±0.8
& (09) 2.0±0.8
Age: 38.0±1.7 Ma
Age: 36.8±2.1 Ma
Age: 37.0±1.6 Ma
Age: 38.5±1.7 Ma
Age: 38.0±1.7 Ma
εHf: 8.5±0.9
Age: 35.4±2.2 Ma
εHf: 8.0±0.7
Age: 37.0±1.5 Ma
Age: 38.0±1.8 Ma
Age: 39.7±2.2 Ma
Age: 36.8±1.9 Ma
εHf: 8.2±1.0
Age: 39.3±2.2 Ma
εHf: 7.7±0.8
Age: 36.9±2.3 Ma
εHf: 7.7±0.7
Age: 38.2±2.0 Ma
εHf: 9.1±0.9
Age: 37.3±1.6 Ma
εHf: 7.4±0.9
rim: 6.8±0.9
Age: 38.4±1.2 Ma
εHf: 9.1±0.9
Age: 37.8±1.2 Ma
Age: 37.9±1.1 Ma
Age: 37.7±1.1 Ma
scale bar : 50 μm
AGE (Ma)
Mean = 37.72±0.36 [0.94%] 95% conf.
Wtd by data-pt errs only, 0 of 20 rej.
MSWD = 0.91, probability = 0.57
(error bars are 2s)
206Pb/238U
207Pb/235U

AG1408A1

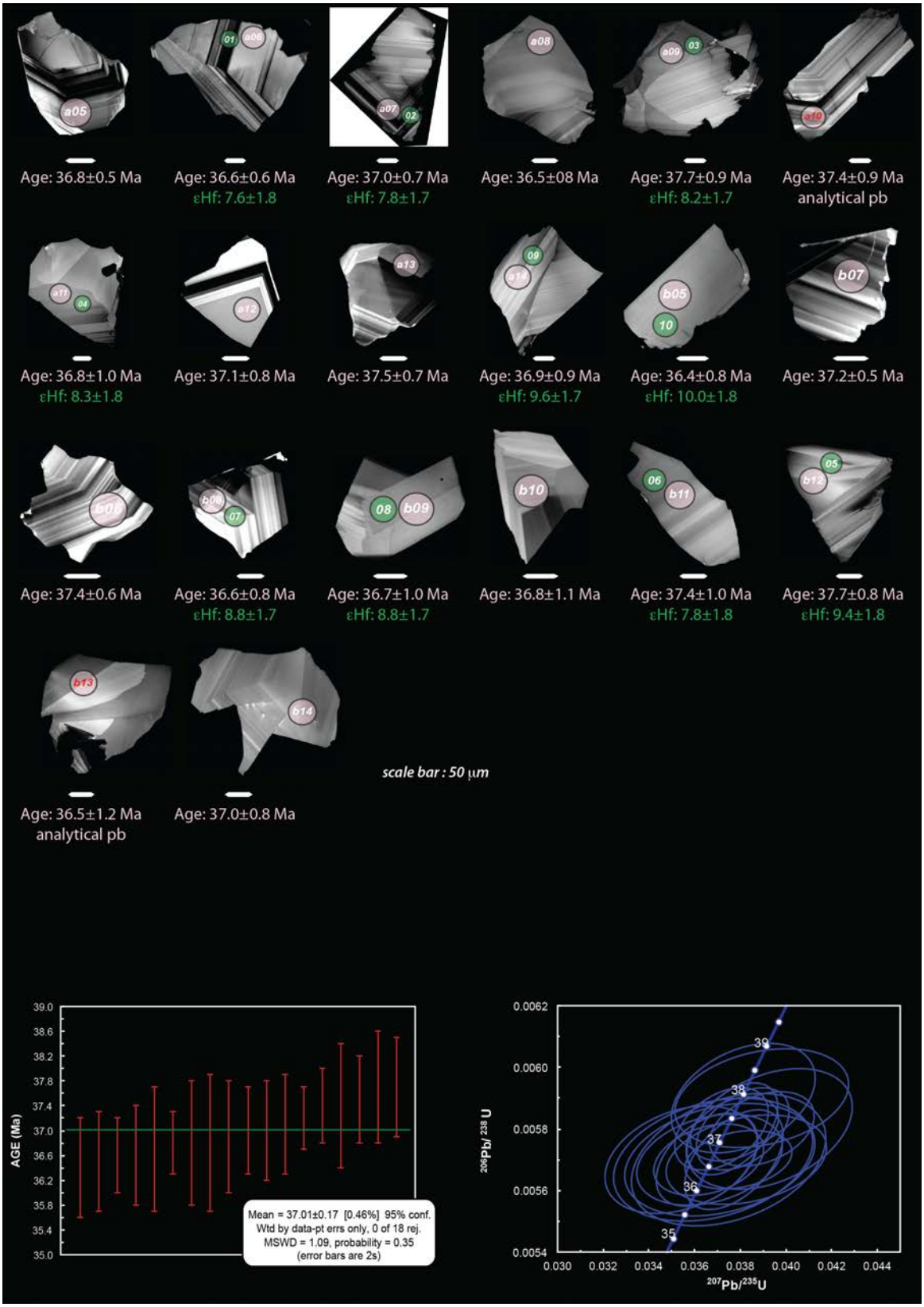
a05
Age: 36.8±0.5 Ma
01
a06
Age: 36.6±0.6 Ma
εHf: 7.6±1.8
a07
02
Age: 37.0±0.7 Ma
εHf: 7.8±1.7
a08
Age: 36.5±08 Ma
a09
03
Age: 37.7±0.9 Ma
εHf: 8.2±1.7
a10
Age: 37.4±0.9 Ma
analytical pb
a11
04
Age: 36.8±1.0 Ma
εHf: 8.3±1.8
a12
Age: 37.1±0.8 Ma
a13
Age: 37.5±0.7 Ma
09
a14
Age: 36.9±0.9 Ma
εHf: 9.6±1.7
b05
10
Age: 36.4±0.8 Ma
εHf: 10.0±1.8
b07
Age: 37.2±0.5 Ma
b01
Age: 37.4±0.6 Ma
b06
07
Age: 36.6±0.8 Ma
εHf: 8.8±1.7
08
b09
Age: 36.7±1.0 Ma
εHf: 8.8±1.7
b10
Age: 36.8±1.1 Ma
06
b11
Age: 37.4±1.0 Ma
εHf: 7.8±1.8
05
b12
Age: 37.7±0.8 Ma
εHf: 9.4±1.8
b13
Age: 36.5±1.2 Ma
analytical pb
b14
Age: 37.0±0.8 Ma
scale bar : 50 μm
AGE (Ma)
Mean = 37.01±0.17 [0.46%] 95% conf.
Wtd by data-pt errs only, 0 of 18 rej.
MSWD = 1.09, probability = 0.35
(error bars are 2s)
206Pb/238U
207Pb/235U

AG1408A

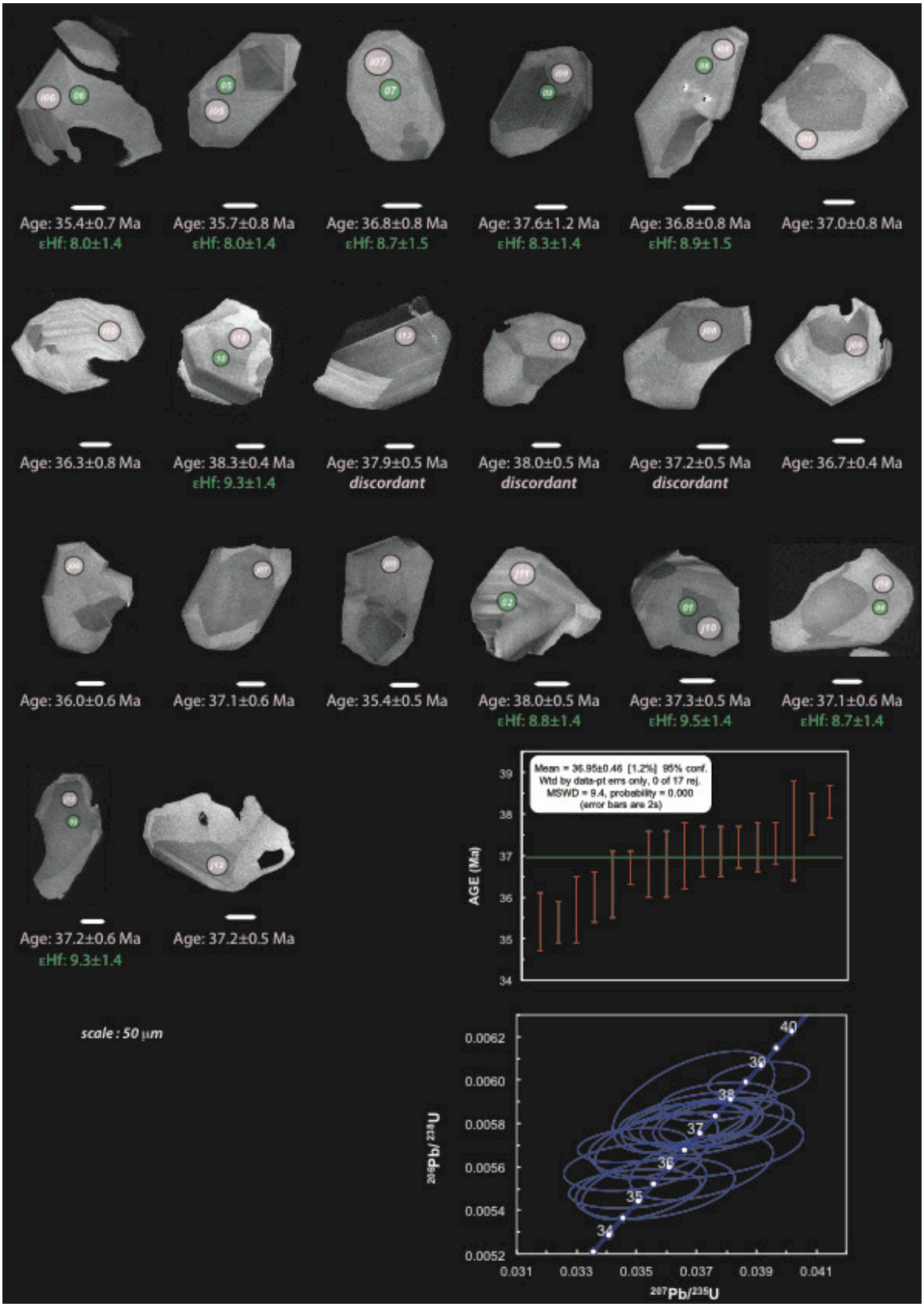
Age: 35.4±0.7 Ma
εHf: 8.0±1.4
Age: 35.7±0.8 Ma
εHf: 8.0±1.4
Age: 36.8±0.8 Ma
εHf: 8.7±1.5
Age: 37.6±1.2 Ma
εHf: 8.3±1.4
Age: 36.8±0.8 Ma
εHf: 8.9±1.5
Age: 37.0±0.8 Ma
Age: 36.3±0.8 Ma
Age: 38.3±0.4 Ma
εHf: 9.3±1.4
Age: 37.9±0.5 Ma
discordant
Age: 38.0±0.5 Ma
discordant
Age: 37.2±0.5 Ma
discordant
Age: 36.7±0.4 Ma
Age: 36.0±0.6 Ma
Age: 37.1±0.6 Ma
Age: 35.4±0.5 Ma
Age: 38.0±0.5 Ma
εHf: 8.8±1.4
Age: 37.3±0.5 Ma
εHf: 9.5±1.4
Age: 37.1±0.6 Ma
εHf: 8.7±1.4
Age: 37.2±0.6 Ma
εHf: 9.3±1.4
Age: 37.2±0.5 Ma
scale : 50 µm
Mean = 36.95±0.46 [1.2%] 95% conf.
Wtd by data-pt errs only, 0 of 17 rej.
MSWD = 9.4, probability = 0.000
(error bars are 2s)
AGE (Ma)
39
38
37
36
35
34
0.0062
0.0060
0.0058
0.0056
0.0054
0.0052
206Pb/238U
0.031
0.033
0.035
0.037
0.039
0.041
207Pb/235U
40
39
38
37
36
35
34

VK1404

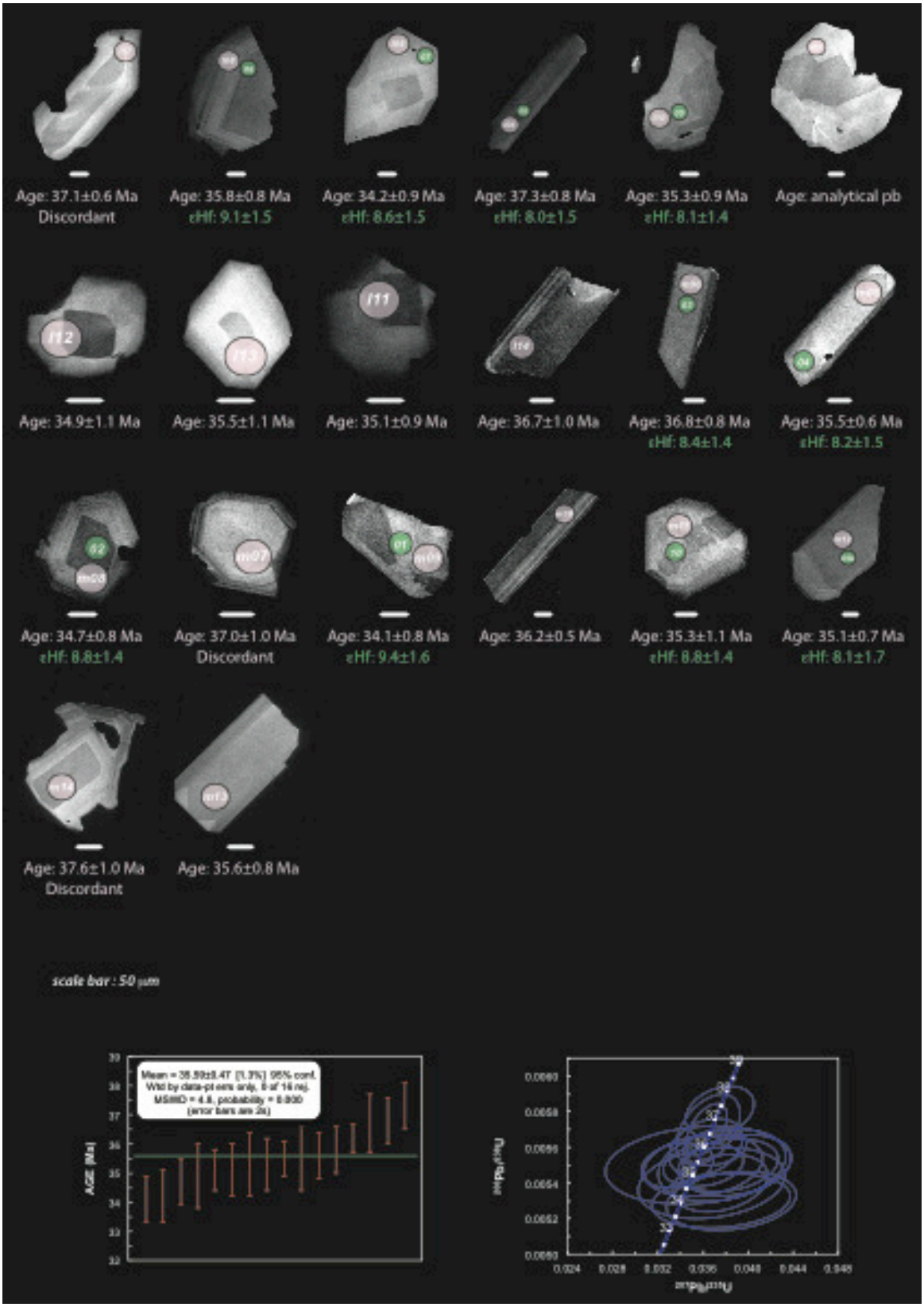
Age: 37.1±0.6 Ma
Discordant
Age: 35.8±0.8 Ma
εHf: 9.1±1.5
Age: 34.2±0.9 Ma
εHf: 8.6±1.5
Age: 37.3±0.8 Ma
εHf: 8.0±1.5
Age: 35.3±0.9 Ma
εHf: 8.1±1.4
Age: analytical pb
Age: 34.9±1.1 Ma
Age: 35.5±1.1 Ma
Age: 35.1±0.9 Ma
Age: 36.7±1.0 Ma
Age: 36.8±0.8 Ma
εHf: 8.4±1.4
Age: 35.5±0.6 Ma
εHf: 8.2±1.5
Age: 34.7±0.8 Ma
εHf: 8.8±1.4
Age: 37.0±1.0 Ma
Discordant
Age: 34.1±0.8 Ma
εHf: 9.4±1.6
Age: 36.2±0.5 Ma
Age: 35.3±1.1 Ma
εHf: 8.8±1.4
Age: 35.1±0.7 Ma
εHf: 8.1±1.7
Age: 37.6±1.0 Ma
Discordant
Age: 35.6±0.8 Ma
scale bar : 50 μm

VK1405

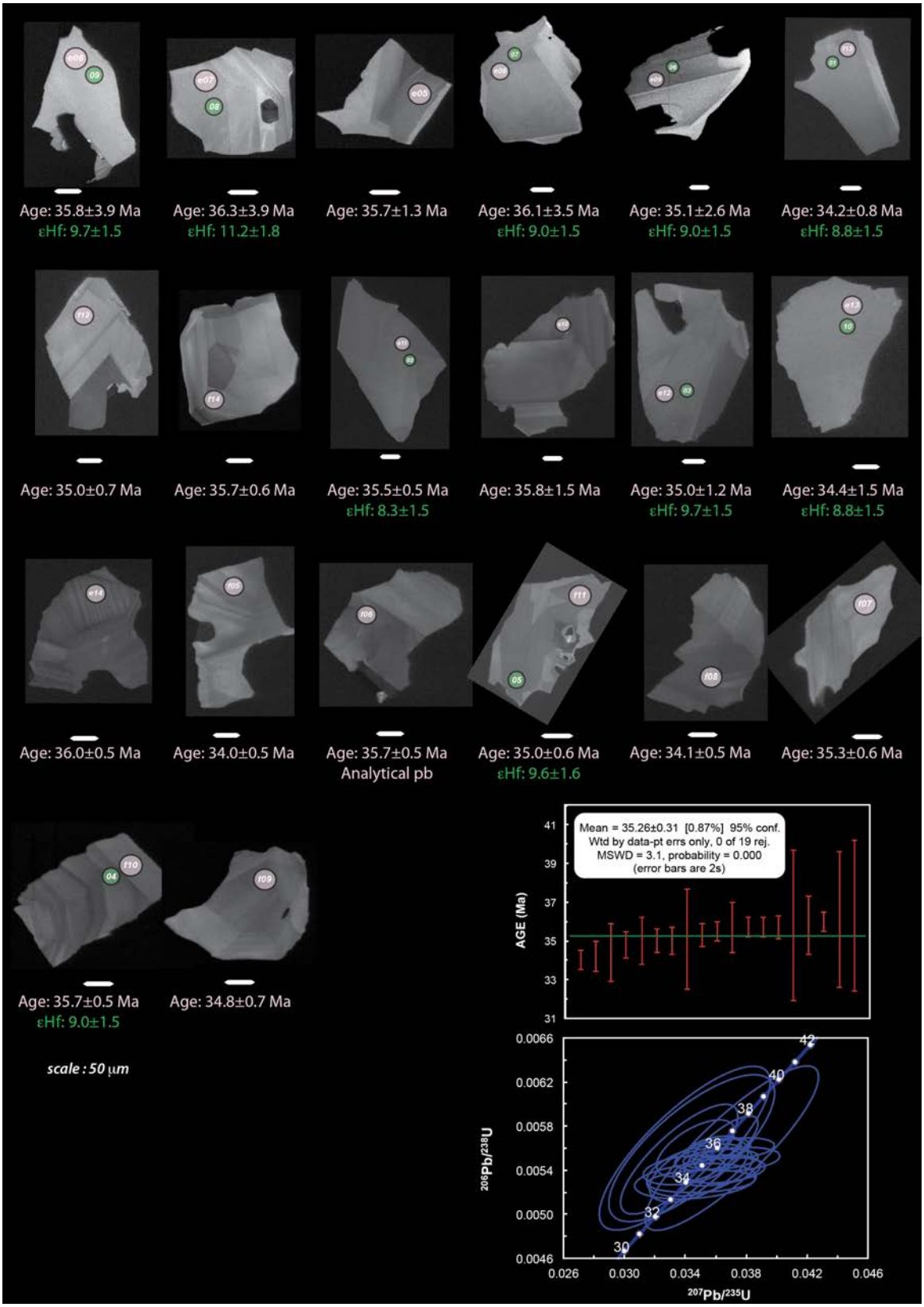
Age: 35.8±3.9 Ma
εHf: 9.7±1.5
Age: 36.3±3.9 Ma
εHf: 11.2±1.8
Age: 35.7±1.3 Ma
Age: 36.1±3.5 Ma
εHf: 9.0±1.5
Age: 35.1±2.6 Ma
εHf: 9.0±1.5
Age: 34.2±0.8 Ma
εHf: 8.8±1.5
Age: 35.0±0.7 Ma
Age: 35.7±0.6 Ma
Age: 35.5±0.5 Ma
εHf: 8.3±1.5
Age: 35.8±1.5 Ma
Age: 35.0±1.2 Ma
εHf: 9.7±1.5
Age: 34.4±1.5 Ma
εHf: 8.8±1.5
Age: 36.0±0.5 Ma
Age: 34.0±0.5 Ma
Age: 35.7±0.5 Ma
Analytical pb
Age: 35.0±0.6 Ma
εHf: 9.6±1.6
Age: 34.1±0.5 Ma
Age: 35.3±0.6 Ma
Age: 35.7±0.5 Ma
εHf: 9.0±1.5
Age: 34.8±0.7 Ma
scale : 50 μm
Mean = 35.26±0.31 [0.87%] 95% conf.
Wtd by data-pt errs only, 0 of 19 rej.
MSWD = 3.1, probability = 0.000
(error bars are 2s)
AGE (Ma)
41
39
37
35
33
31
0.0066
0.0062
0.0058
0.0054
0.0050
0.0046
206Pb/238U
42
40
38
36
34
32
30
0.026
0.030
0.034
0.038
0.042
0.046
207Pb/235U

MR1403


Age: 29.0±0.7 Ma
Contamination?
Age: 32.6±0.9 Ma
Age: 32.8±0.8 Ma
εHf: 8.4±1.0
Age: 33.4±1.1 Ma
Age: 33.0±0.9 Ma
Age: 33.1±0.8 Ma
Age: 33.0±0.9 Ma
Age: 28.8±1.3 Ma
Contamination?
Age: 33.8±0.9 Ma
εHf: 8.7±1.1
Age: 34.1±0.8 Ma
Age: 34.2±1.1 Ma
εHf: 7.9±1.1
Age: 33.0±1.1 Ma
εHf: 7.3±1.3
Age: 32.9±0.9 Ma
εHf: 8.4±1.1
Age: 33.1±1.0 Ma
εHf: 6.9±1.2
Age: 33.9±0.7 Ma
Age: 33.7±0.8 Ma
εHf: 8.8±1.0
Age: 34.3±1.1 Ma
εHf: 8.2±1.0
Age: 33.4±1.1 Ma
εHf: 8.6±1.0
Age: 33.2±0.9 Ma
εHf: 9.1±1.1
Age: 33.8±0.7 Ma
εHf: 8.4±1.1
Age: 34.2±0.8 Ma
εHf: 9.5±1.0
Age: 34.6±1.2 Ma
εHf: 8.7±1.0
Scale bar:
100 μm

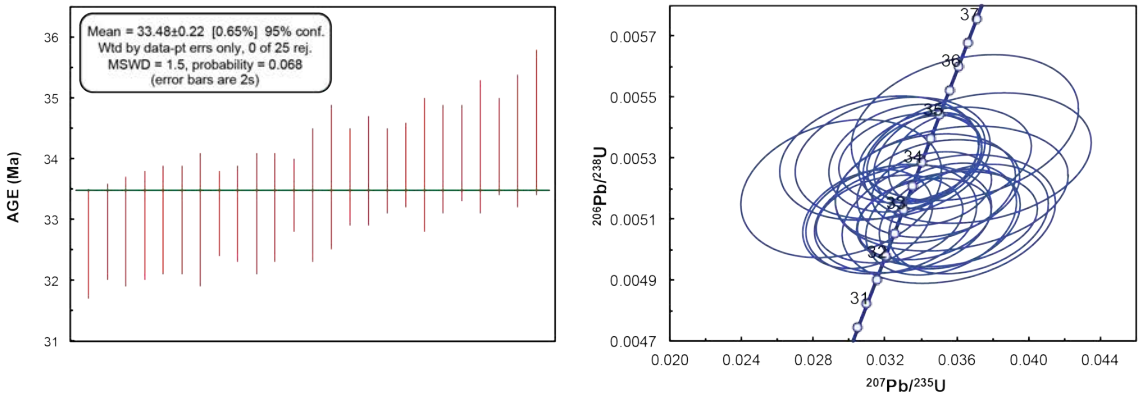
Mean = 33.48±0.22 [0.65%] 95% conf.
Wtd by data-pt errs only, 0 of 25 rej.
MSWD = 1.5, probability = 0.068
(error bars are 2s)
AGE (Ma)
36
35
34
33
32
31
0.0057
0.0055
0.0053
0.0051
0.0049
0.0047
206Pb/238U
0.020
0.024
0.028
0.032
0.036
0.040
0.044
207Pb/235U

LI1303A1


01
a05
Age: 34.0±0.7 Ma
εHf: 8.4±1.0
a06
04
Age: 34.4±0.4 Ma
εHf: 8.5±1.1
a05
Age: 33.5±0.6 Ma
a06
Age: 35.4±0.5 Ma
a07
Age: 22.0±0.5 Ma
Contamination?
a08
Age: 35.1±0.6 Ma
10
a09
Age: 34.5±0.5 Ma
εHf: 10.0±1.2
11
a10
Age: 34.4±0.5 Ma
εHf: 8.6±1.2
a11
12
Age: 34.2±0.5 Ma
εHf: 8.4±1.2
a12
Age: 33.5±1.3 Ma
a13
Age: 34.3±0.5 Ma
b05
Age: 33.1±1.4 Ma
b06
Age: 33.6±1.5 Ma
b07
21
Age: 33.1±1.7 Ma
εHf: 8.5±1.1
b08
22
Age: 33.5±1.1 Ma
εHf: 7.5±1.3
23
b09
Age: 35.1±0.5 Ma
εHf: 9.3±1.3
24
b10
Age: 34.8±0.4 Ma
εHf: 9.3±1.3
b11
25
Age: 34.7±0.5 Ma
εHf: 7.8±1.2
b12
Age: 34.4±0.5 Ma
b13
Age: 34.4±0.5 Ma
c05
Age: 34.4±0.5 Ma
c10
Age: 34.3±0.5 Ma
c11
Age: 35.0±0.7 Ma
c06
Age: 34.3±0.5 Ma
c07
32
Age: 33.3±0.9 Ma
εHf: 8.4±1.2
33
c08
Age: 34.6±1.6 Ma
εHf: 8.5±1.3
c09
Age: 34.7±1.1 Ma
c13
35
Age: 34.8±1.2 Ma
εHf: 8.3±1.1
c12
Age: 35.5±1.2 Ma
Scale bar:
50μm

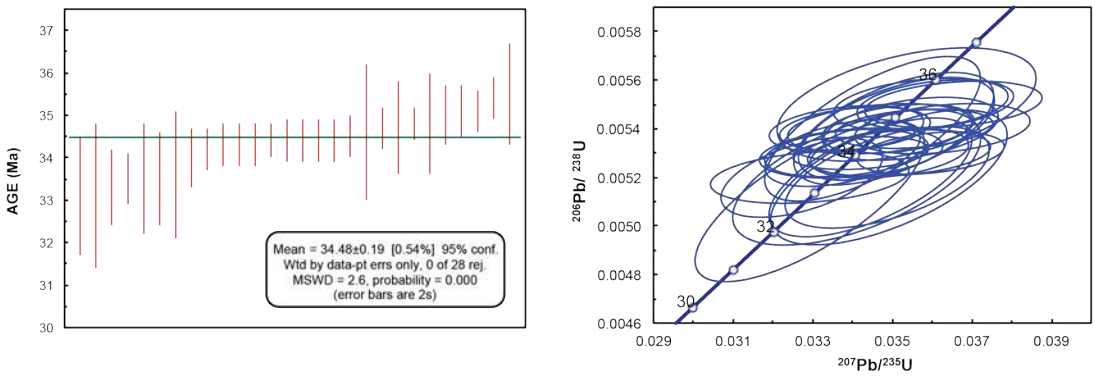
AGE (Ma)
37
36
35
34
33
32
31
30
Mean = 34.48±0.19 [0.54%] 95% conf.
Wtd by data-pt errs only, 0 of 28 rej.
MSWD = 2.6, probability = 0.000
(error bars are 2s)
206Pb/238U
0.0058
0.0056
0.0054
0.0052
0.0050
0.0048
0.0046
0.029
0.031
0.033
0.035
0.037
0.039
207Pb/235U
36
34
32
30

LI1303

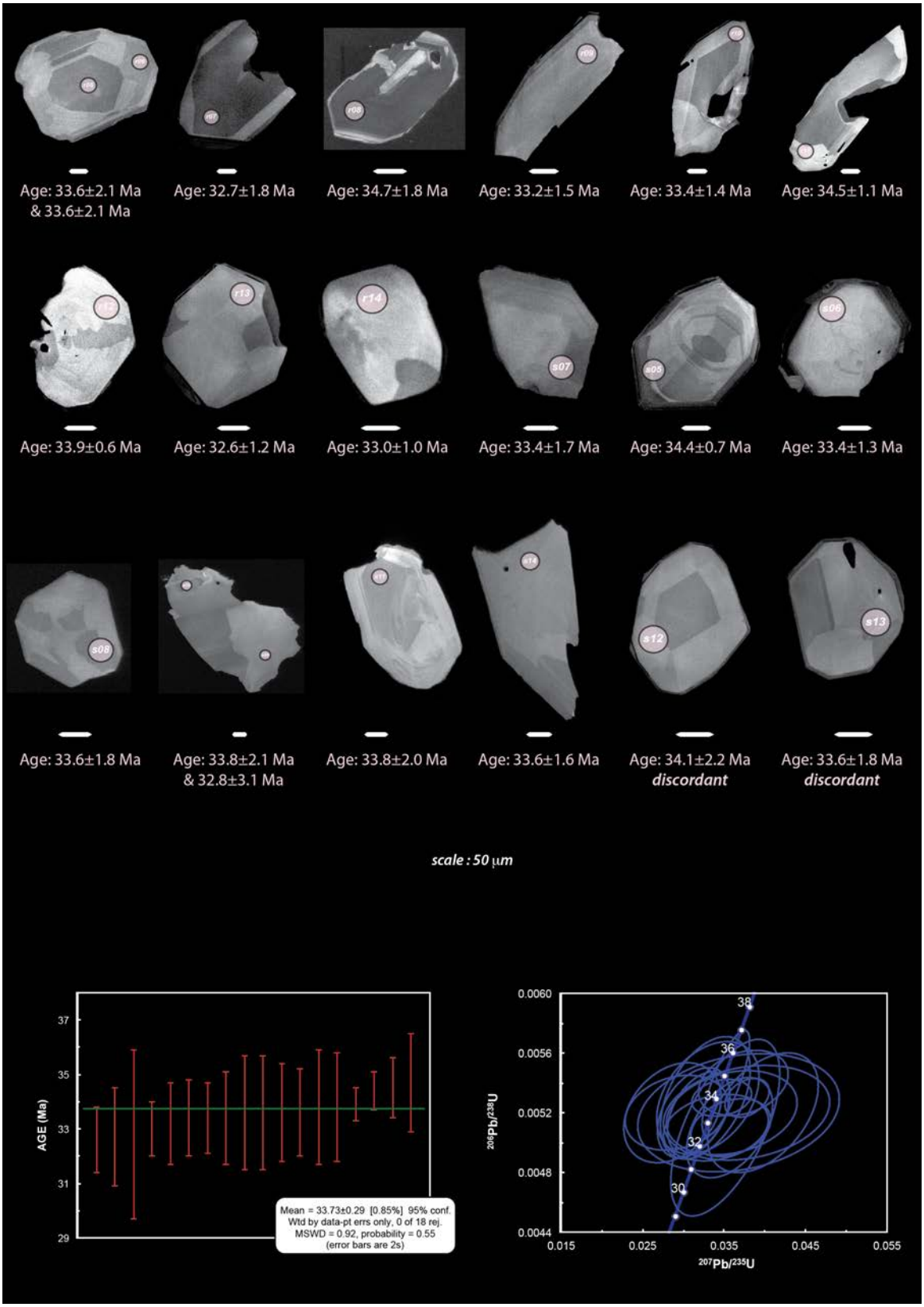
Age: 33.6±2.1 Ma & 33.6±2.1 Ma
Age: 32.7±1.8 Ma
Age: 34.7±1.8 Ma
Age: 33.2±1.5 Ma
Age: 33.4±1.4 Ma
Age: 34.5±1.1 Ma
Age: 33.9±0.6 Ma
Age: 32.6±1.2 Ma
Age: 33.0±1.0 Ma
Age: 33.4±1.7 Ma
Age: 34.4±0.7 Ma
Age: 33.4±1.3 Ma
Age: 33.6±1.8 Ma
Age: 33.8±2.1 Ma & 32.8±3.1 Ma
Age: 33.8±2.0 Ma
Age: 33.6±1.6 Ma
Age: 34.1±2.2 Ma discordant
Age: 33.6±1.8 Ma discordant
scale : 50 μm
AGE (Ma)
Mean = 33.73±0.29 [0.85%] 95% conf.
Wtd by data-pt errs only, 0 of 18 rej.
MSWD = 0.92, probability = 0.55
(error bars are 2s)
206Pb/238U
207Pb/235U

KJ1316

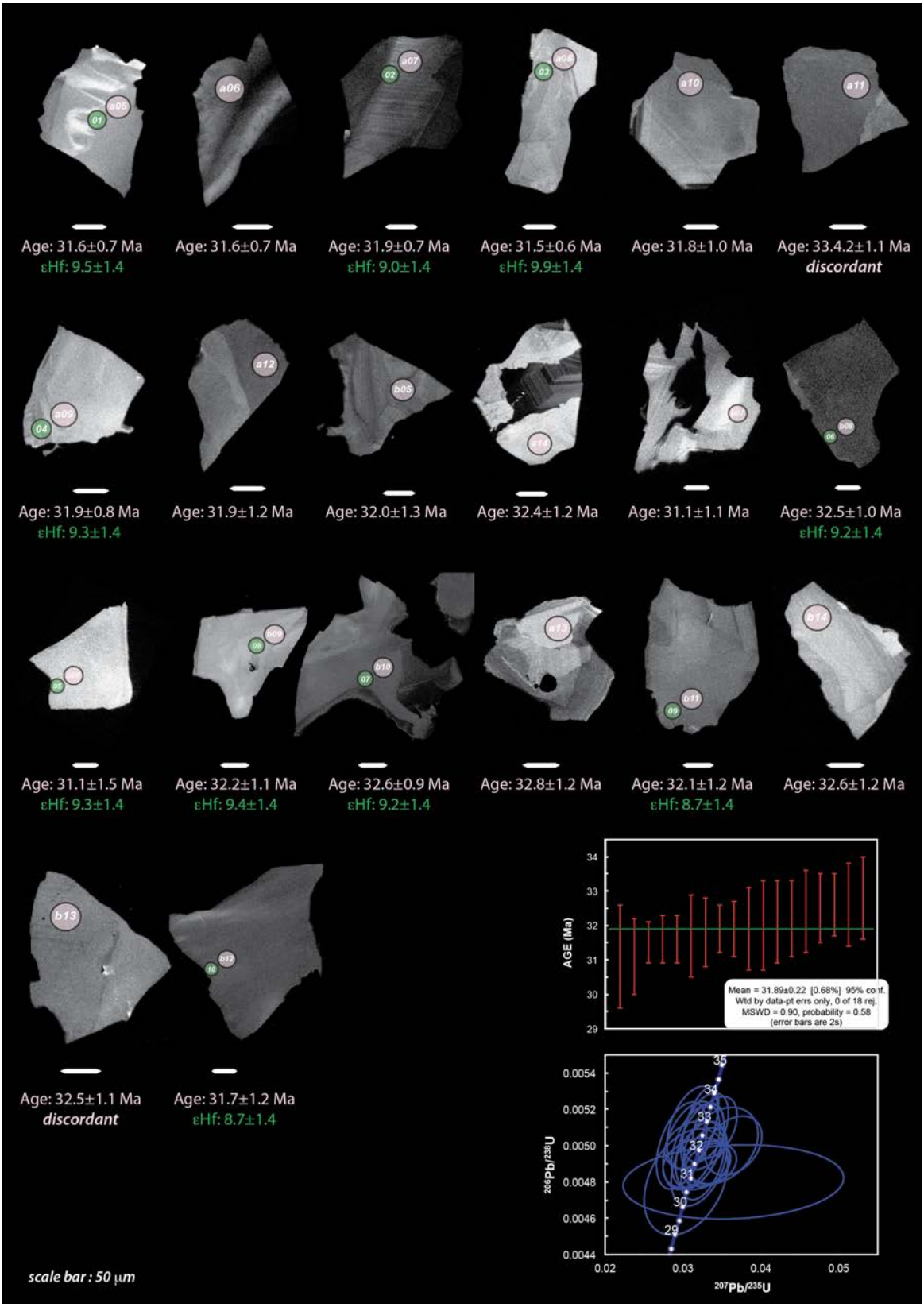
Age: 31.6±0.7 Ma
εHf: 9.5±1.4
Age: 31.6±0.7 Ma
Age: 31.9±0.7 Ma
εHf: 9.0±1.4
Age: 31.5±0.6 Ma
εHf: 9.9±1.4
Age: 31.8±1.0 Ma
Age: 33.4.2±1.1 Ma
discordant
Age: 31.9±0.8 Ma
εHf: 9.3±1.4
Age: 31.9±1.2 Ma
Age: 32.0±1.3 Ma
Age: 32.4±1.2 Ma
Age: 31.1±1.1 Ma
Age: 32.5±1.0 Ma
εHf: 9.2±1.4
Age: 31.1±1.5 Ma
εHf: 9.3±1.4
Age: 32.2±1.1 Ma
εHf: 9.4±1.4
Age: 32.6±0.9 Ma
εHf: 9.2±1.4
Age: 32.8±1.2 Ma
Age: 32.1±1.2 Ma
εHf: 8.7±1.4
Age: 32.6±1.2 Ma
Age: 32.5±1.1 Ma
discordant
Age: 31.7±1.2 Ma
εHf: 8.7±1.4
scale bar : 50 μm
AGE (Ma)
Mean = 31.89±0.22 [0.68%] 95% conf.
Wtd by data-pt errs only, 0 of 18 rej.
MSWD = 0.90, probability = 0.58
(error bars are 2s)
206Pb/238U
207Pb/235U

KJ1006A


k07
01
k08
k09
k10
05
k11
k13
k12
08
Age: 30.6±1.4 Ma
εHf: 8.8±0.9
Age: 31.2±2 Ma
Age: 30.6±2 Ma
Age: 30.9±2.7 Ma
Age: 31.3±1.5 Ma
εHf: 8.6±0.9
Age: 31.1±0.5 Ma
Age: 31.1±0.6 Ma
εHf: 9.3±1.2
l06
10
13
l07
l08
14
l09
l10
l11
16
l13
20
Age: 30.1±1.1 Ma
εHf: 9.8±0.7
Age: 30.1±1.5 Ma
εHf: 8.8±1.1
Age: 31.7±1.5 Ma
Age: 30.8±2.2 Ma
εHf: 6.8±1.0
Age: 30.3±2.5 Ma
Age: 31.1±2.1 Ma
εHf: 7.2±1.4
Age: 31.0±1.6 Ma
εHf: 9.7±1.1
21
m05
22
m07
m08
23
m10
m11
28
m12
m13
29
Age: 31.1±1.8 Ma
εHf: 9.7±0.9
εHf: 8.4±1.0
Age: 30.8±1.4 Ma
Age: 31.7±1.6 Ma
εHf: 8.1±1.0
Age: 31.5±1.1 Ma
Age: 31.3±1.2 Ma
Age: 32.5±1.3 Ma
εHf: 9.0±1.0
Age: 31.3±0.9 Ma
εHf: 8.5±0.7
n05
n09
n07
35
n06
37
n10
n11
38
n12
Scale bar:
50μm
Age: 31.8±2.7 Ma
Age: 30.9±0.9 Ma
Age: 30.7±0.8 Ma
εHf: 8.2±1.2
Age: 30.9±2.0 Ma
Age: 32.2±0.9 Ma
εHf: 8.5±0.9
Age: 31.0±0.9 Ma
Age: 30.9±0.8 Ma
εHf: 8.7±1.1

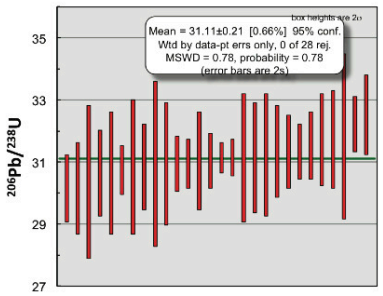
box heights are 2σ
Mean = 31.11±0.21 [0.66%] 95% conf.
Wtd by data-pt errs only, 0 of 28 rej.
MSWD = 0.78, probability = 0.78
(error bars are 2s)
35
33
31
29
27
206Pb/238U

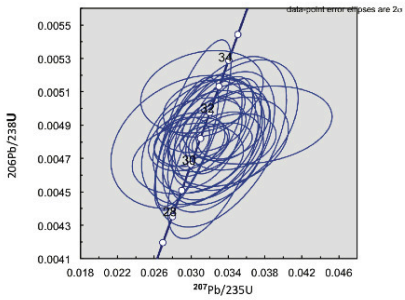
data-point error ellipses are 2σ
0.0055
0.0053
0.0051
0.0049
0.0047
0.0045
0.0043
0.0041
206Pb/238U
34
33
32
31
29
0.018
0.022
0.026
0.030
0.034
0.038
0.042
0.046
207Pb/235U

KJ1308

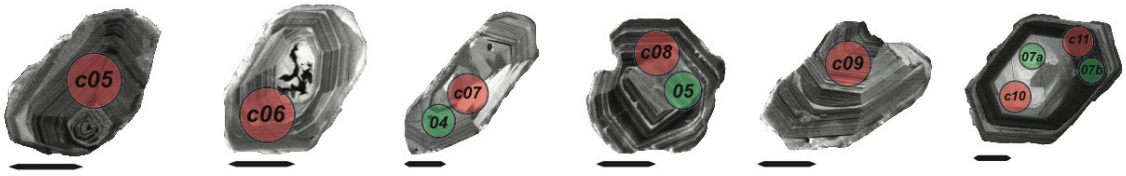

Age: 26.9±0.4 Ma | Analytical pb. | Age: 47.9±1.2 Ma analytical pb | Age: 26.8±0.4 Ma εHf: 9.7±1.1 | Age: 27.4±0.4 Ma | Age: 46.9±1.7 Ma Age: 29.2±0.7 Ma εHf: 8.5±0.8 analytical pb

Age: 26.5±0.5 Ma εHf: 9.5±0.07 | Age: 27.0±0.4 Ma εHf: 8.8±1.4 | Age:26.9±0.4 Ma | Age:26.9±0.4 Ma | Age:26.4±0.4 Ma | Age: 27.2±0.3 Ma εHf: 9.9±0.7

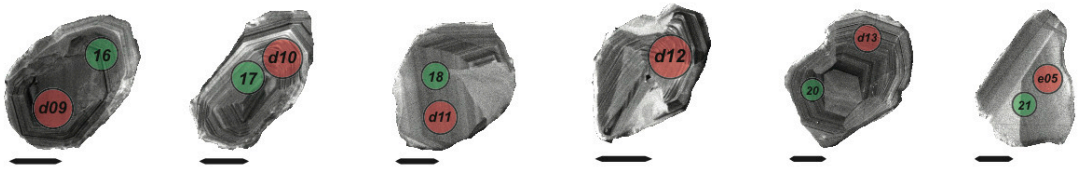

Age: 26.6±0.4 Ma analytical pb | Age: 26.4±0.3 Ma εHf: 10.1±1.5 | Age: 26.4±0.4 Ma εHf: 9.7±0.8 | Age: 26.3±0.5 Ma | Age: 26.6±0.4 Ma εHf: 8.9±2.0 | Age: 31.0±0.6 Ma εHf: 8.3±1.3

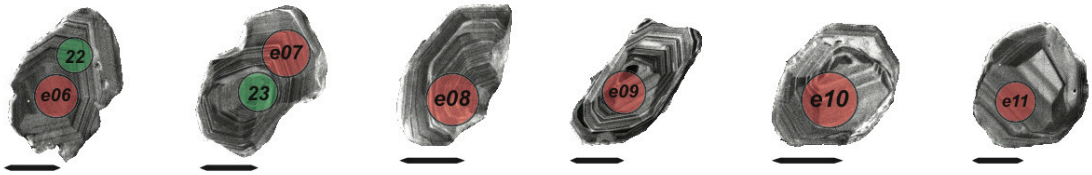

Age: 27.0±0.4 Ma εHf: 9.8±0.9 | Age: 26.5±0.4 Ma εHf: 10.4±0.9 | Age: 26.6±0.3 Ma | Age: 27.3±0.3 Ma | Age: 26.5±0.3 Ma | Age: 26.8±0.3 Ma

Scale bar: 50μm

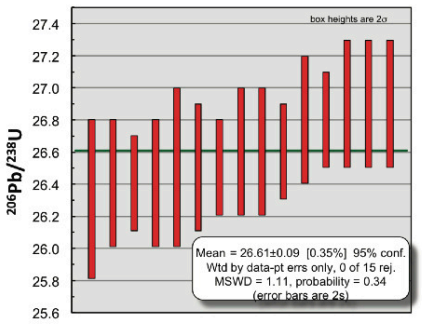

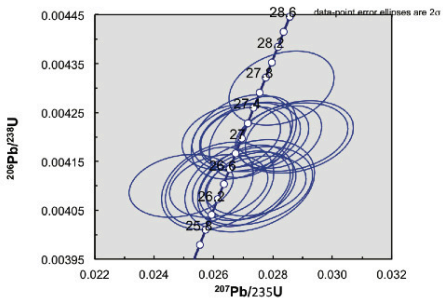

KJ1302A

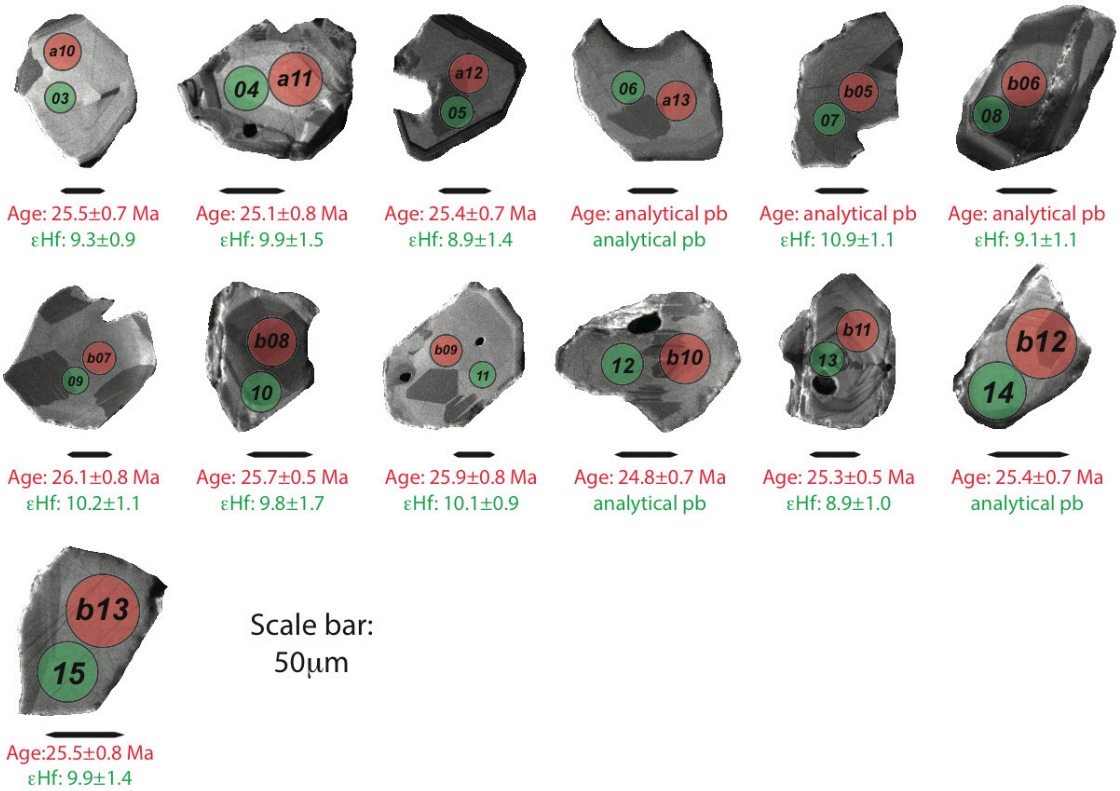
a10
03
Age: 25.5±0.7 Ma
εHf: 9.3±0.9
04
a11
Age: 25.1±0.8 Ma
εHf: 9.9±1.5
a12
05
Age: 25.4±0.7 Ma
εHf: 8.9±1.4
06
a13
Age: analytical pb
analytical pb
b05
07
Age: analytical pb
εHf: 10.9±1.1
b06
08
Age: analytical pb
εHf: 9.1±1.1
b07
09
Age: 26.1±0.8 Ma
εHf: 10.2±1.1
b08
10
Age: 25.7±0.5 Ma
εHf: 9.8±1.7
b09
11
Age: 25.9±0.8 Ma
εHf: 10.1±0.9
12
b10
Age: 24.8±0.7 Ma
analytical pb
b11
13
Age: 25.3±0.5 Ma
εHf: 8.9±1.0
b12
14
Age: 25.4±0.7 Ma
analytical pb
b13
15
Age:25.5±0.8 Ma
εHf: 9.9±1.4
Scale bar:
50μm

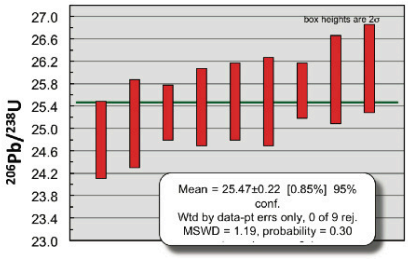
box heights are 2σ
206Pb/238U
27.0
26.6
26.2
25.8
25.4
25.0
24.6
24.2
23.8
23.4
23.0
Mean = 25.47±0.22 [0.85%] 95% conf.
Wtd by data-pt errs only, 0 of 9 rej.
MSWD = 1.19, probability = 0.30

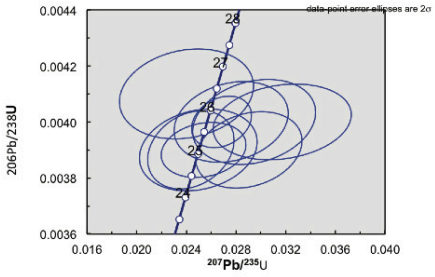
data-point error ellipses are 2σ
206Pb/238U
0.0044
0.0042
0.0040
0.0038
0.0036
0.016
0.020
0.024
0.028
0.032
0.036
0.040
207Pb/235U
28
27
26
25
24

KJ1303A1

Age: 24.9±0.7 Ma
εHf: 10.8±0.9

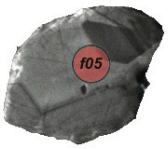

Age: 23.7±0.8 Ma

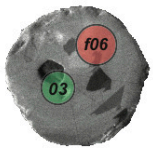

Age: 23.9±0.8 Ma
εHf: 10.3±0.7

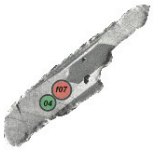

Age: 24.4±0.5 Ma
εHf: 10.3±0.7

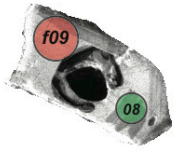

Age: 24.4±08 Ma
εHf: 9.6±1.4

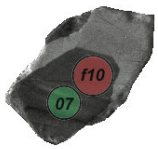

Age: 24.5±0.9 Ma
εHf: 10.8±0.7

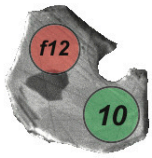

Age: 24.8±0.9 Ma
εHf: 10.6±1.0

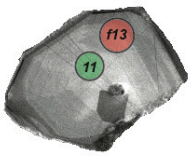

Age: 24.6±1.1 Ma
εHf: 9.8±0.8

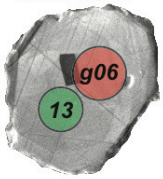

Age: 31.7±0.9 Ma
εHf: 11.0±0.9

Age: 23.7±1.0 Ma
Age: 24.2±1.6 Ma
εHf: 9.9±0.8

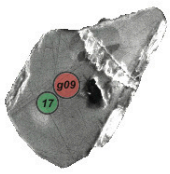

Age: 25.3±1.8 Ma
εHf: 10.2±0.8

Age: 24.5±1.9 Ma
εHf: 10.4±0.8

Age: 23.7±1.3 Ma
εHf: 10.5±1.0

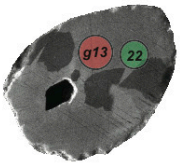

Age: 24.1±0.5 Ma
εHf: 10.4±0.9

Scale bar:
50μm

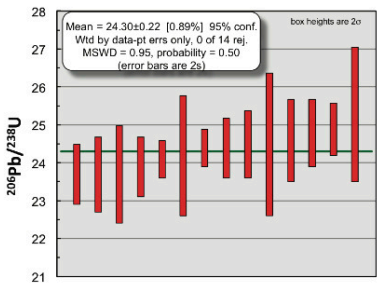

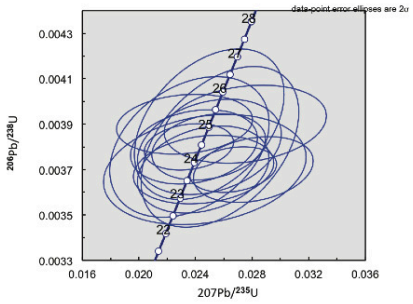

KJ1307

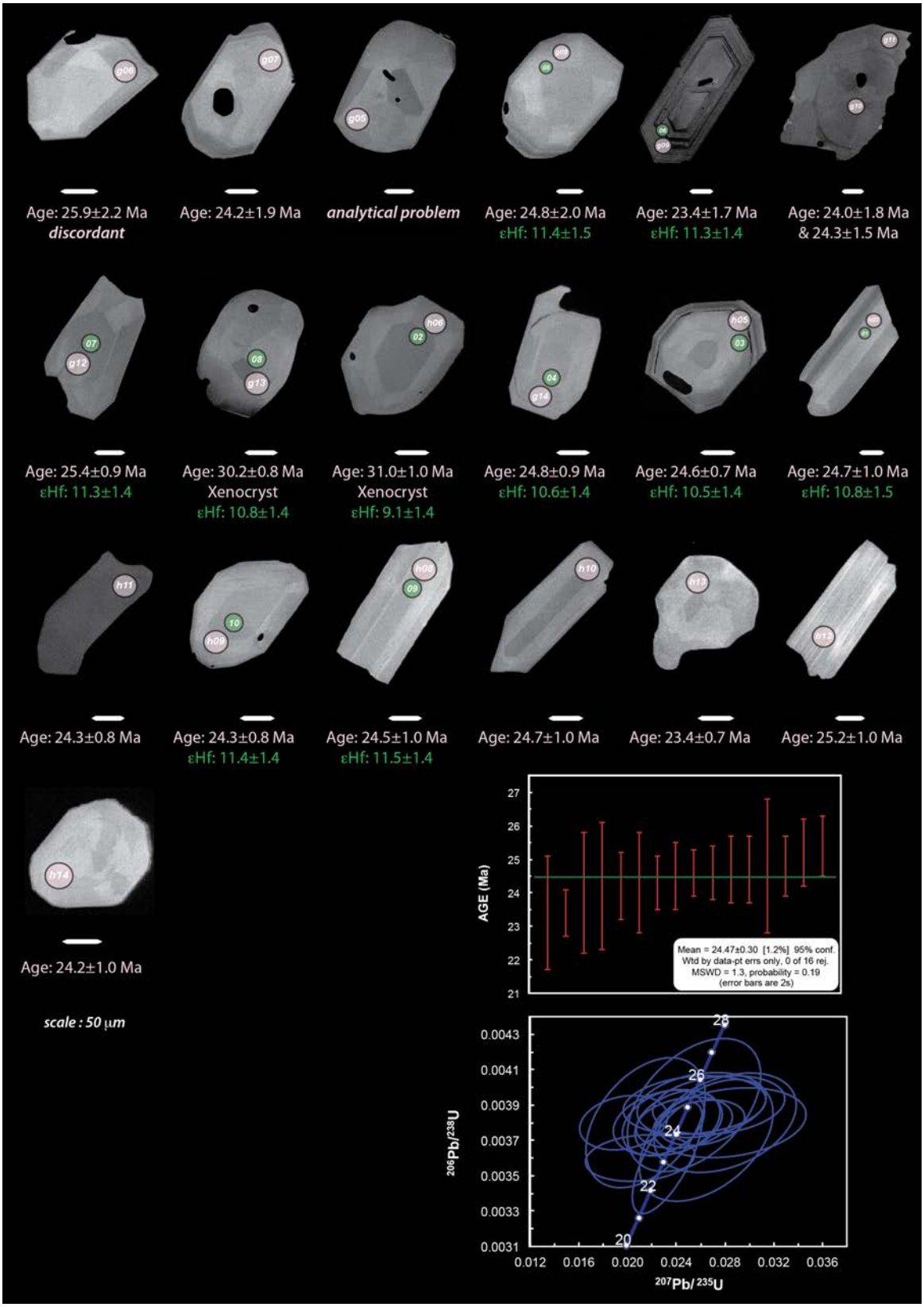
Age: 25.9±2.2 Ma
discordant
Age: 24.2±1.9 Ma
analytical problem
Age: 24.8±2.0 Ma
εHf: 11.4±1.5
Age: 23.4±1.7 Ma
εHf: 11.3±1.4
Age: 24.0±1.8 Ma
& 24.3±1.5 Ma
Age: 25.4±0.9 Ma
εHf: 11.3±1.4
Age: 30.2±0.8 Ma
Xenocryst
εHf: 10.8±1.4
Age: 31.0±1.0 Ma
Xenocryst
εHf: 9.1±1.4
Age: 24.8±0.9 Ma
εHf: 10.6±1.4
Age: 24.6±0.7 Ma
εHf: 10.5±1.4
Age: 24.7±1.0 Ma
εHf: 10.8±1.5
Age: 24.3±0.8 Ma
Age: 24.3±0.8 Ma
εHf: 11.4±1.4
Age: 24.5±1.0 Ma
εHf: 11.5±1.4
Age: 24.7±1.0 Ma
Age: 23.4±0.7 Ma
Age: 25.2±1.0 Ma
Age: 24.2±1.0 Ma
scale : 50 μm
AGE (Ma)
Mean = 24.47±0.30 [1.2%] 95% conf.
Wtd by data-pt errs only, 0 of 16 rej.
MSWD = 1.3, probability = 0.19
(error bars are 2s)
206Pb/238U
207Pb/235U

MR1401

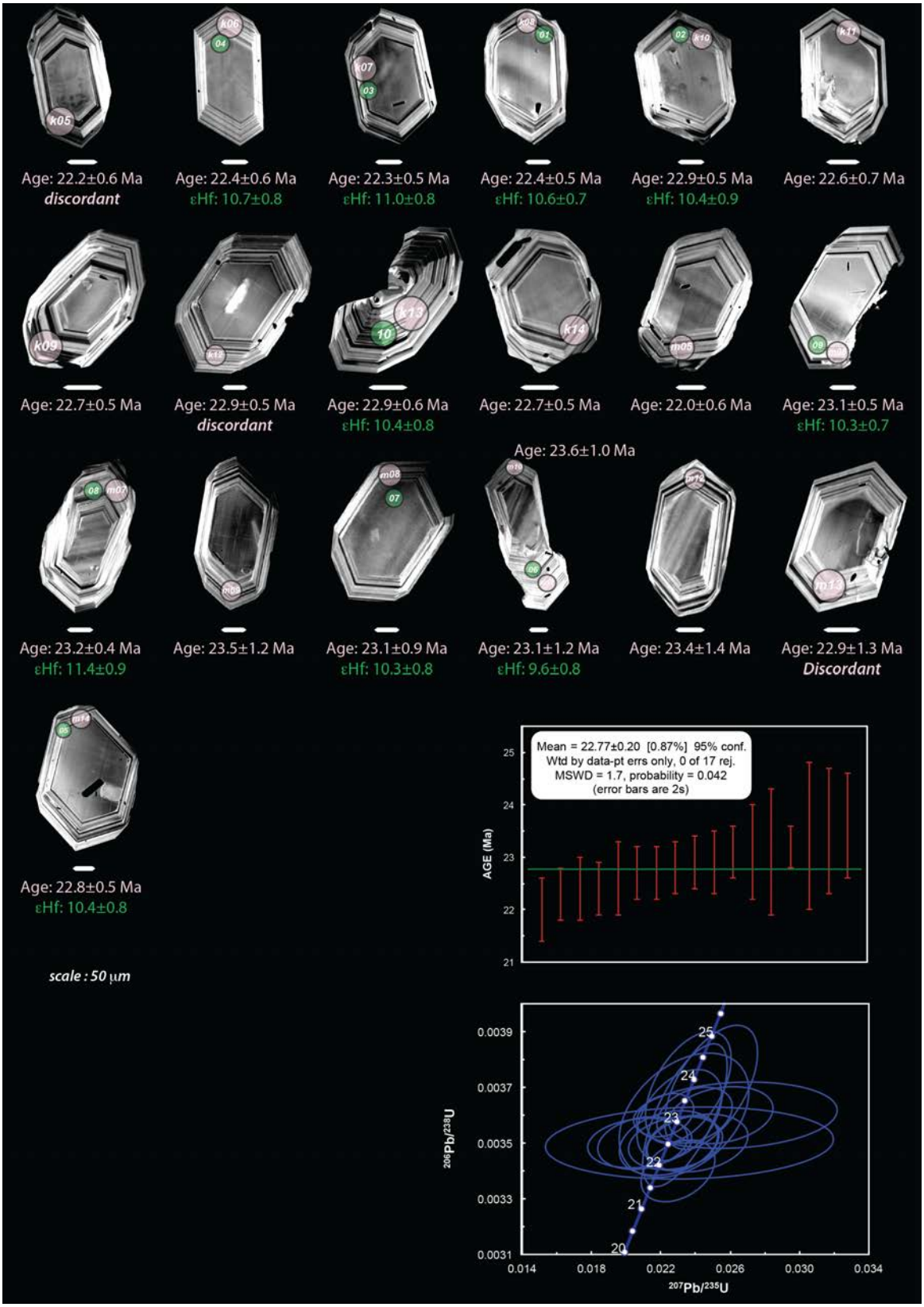
Age: 22.2±0.6 Ma
discordant
Age: 22.4±0.6 Ma
εHf: 10.7±0.8
Age: 22.3±0.5 Ma
εHf: 11.0±0.8
Age: 22.4±0.5 Ma
εHf: 10.6±0.7
Age: 22.9±0.5 Ma
εHf: 10.4±0.9
Age: 22.6±0.7 Ma
Age: 22.7±0.5 Ma
Age: 22.9±0.5 Ma
discordant
Age: 22.9±0.6 Ma
εHf: 10.4±0.8
Age: 22.7±0.5 Ma
Age: 22.0±0.6 Ma
Age: 23.1±0.5 Ma
εHf: 10.3±0.7
Age: 23.6±1.0 Ma
Age: 23.2±0.4 Ma
εHf: 11.4±0.9
Age: 23.5±1.2 Ma
Age: 23.1±0.9 Ma
εHf: 10.3±0.8
Age: 23.1±1.2 Ma
εHf: 9.6±0.8
Age: 23.4±1.4 Ma
Age: 22.9±1.3 Ma
Discordant
Age: 22.8±0.5 Ma
εHf: 10.4±0.8
scale : 50 μm
Mean = 22.77±0.20 [0.87%] 95% conf.
Wtd by data-pt errs only, 0 of 17 rej.
MSWD = 1.7, probability = 0.042
(error bars are 2s)
AGE (Ma)
25
24
23
22
21
0.0039
0.0037
0.0035
0.0033
0.0031
206Pb/238U
0.014
0.018
0.022
0.026
0.030
0.034
207Pb/235U

LI1301


01
a05
Age: 22.0±0.3 Ma
εHf: 10.1±3
02
a06
Age: 21.9±0.5 Ma
εHf: 10.7±1.5
a07
Age: 21.6±1.0 Ma
a09
a08
05
Age: 22.6±0.9 Ma
Age: 21.9±1.2 Ma
εHf: 10.0±0.9
a10
06
Age: 21.9±1.0 Ma
εHf: 9.9±1.0
a11
08
Age: 22.3±0.9 Ma
εHf: 10.0±0.9
a12
09
Age: 22.5±1.0 Ma
εHf: 10.1±0.8
a13
10
Age: 22.7±0.7 Ma
εHf: 10.5±1.1
b06
14
Age: 22.4±0.9 Ma
εHf: 10.4±1.0
16
Age: 23.0±0.4 Ma
εHf: 10.9±0.9
b08
17
b10
Age: 22.1±0.4 Ma
εHf: 10.2±1.0
b11
18
Age: 22.2±0.4 Ma
εHf: 10.5±1.1
b12
Age: 22.2±0.4 Ma
b13
23
Age: 22.0±0.5 Ma
εHf: 10.5±1.1
c05
c06
24
Age: 22.1±0.4 Ma
Age: 22.1±0.5 Ma
εHf: 11.2±0.9
c08
c07
Age: 21.7±0.7 Ma
Age: 22.3±0.5 Ma
c09
27
Age: 22.3±1.3 Ma
εHf: 11.0±0.7
25
c10
Age: 21.9±0.9 Ma
εHf: 11.1±0.8
c12
32
Age: 22.1±0.6 Ma
εHf: 11.5±1.2
d09
Age: 22.2±0.4 Ma
d11
Age: 22.8±0.5 Ma
d12
Age: 22.4±0.6 Ma
Scale bar:
50μm

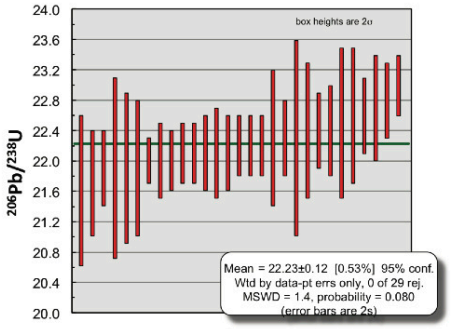
box heights are 2σ
206Pb/238U
24.0
23.6
23.2
22.8
22.4
22.0
21.6
21.2
20.8
20.4
20.0
Mean = 22.23±0.12 [0.53%] 95% conf.
Wtd by data-pt errs only, 0 of 29 rej.
MSWD = 1.4, probability = 0.080
(error bars are 2s)

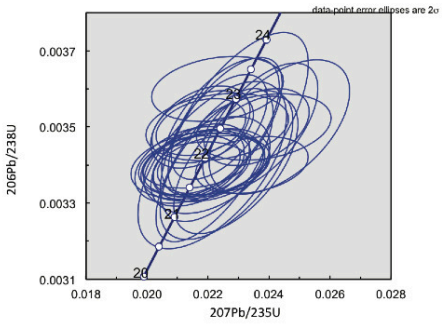
data-point error ellipses are 2σ
206Pb/238U
0.0037
0.0035
0.0033
0.0031
0.018
0.020
0.022
0.024
0.026
0.028
207Pb/235U
24
28
21

KJ1324A


e05
01
Age: 22.1±0.3 Ma
εHf: 10.1±1.0
e06
02
Age: 22.1±0.3 Ma
εHf: 9.7±1.1
e07
03
Age: 22.3±0.6 Ma
εHf: 11.2±1.1
e08
04
Age: 22.4±0.4 Ma
εHf: 10.0±0.8
e09
05
Age: 22.6±0.5 Ma
εHf: 10.4±0.8
e10
06
Age: 22.3±0.5 Ma
analytical pb
e11
07
Age: 22.1±0.8 Ma
εHf:11.1±0.8
e12
09
Age: 22.5±0.6 Ma
εHf: 10.4±0.9
e13
12
Age: 22.9±0.4 Ma
εHf: 10.9±0.7
f05
14
Age: 21.7±0.6 Ma
εHf: 10.1±0.8
f06
15
Age: 22.0±0.5 Ma
εHf: 10.7±0.8
f08
19
Age: 22.4±0.3 Ma
εHf: 11.2±0.8
f09
20
Age: 22.1±0.4 Ma
εHf: 10.7±0.7
f10
21
Age: 22.4±0.4 Ma
εHf: 10.7±0.8
f11
Age: 22.8±0.5 Ma
g13
h06
Age: 22.9±0.6 Ma
Age: 22.4±0.4 Ma
g06
g05
Age: 22.5±0.5 Ma
Age: 22.5±0.5 Ma
g07
Age: 22.7±0.5 Ma
g08
Age: 22.5±0.6 Ma
g09
Age: 22.1±0.6 Ma
g10
Age: 22.7±0.4 Ma
g12
g11
Age: 22.1±0.6 Ma
Age: 22.3±0.6 Ma
h09
Age: 22.9±0.5 Ma
h10
Age: 22.4±0.4 Ma
h07
Age: 22.4±0.5 Ma
h08
Age: 22.2±0.6 Ma
h11
Age: 22.3±0.4 Ma
h12
Age: 22.0±0.3 Ma
Scale bar:
50μm

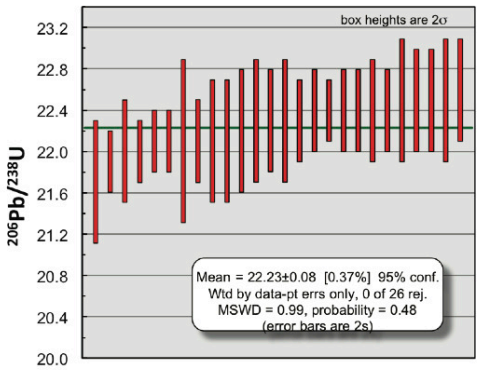
box heights are 2σ
206Pb/238U
23.2
22.8
22.4
22.0
21.6
21.2
20.8
20.4
20.0
Mean = 22.23±0.08 [0.37%] 95% conf.
Wtd by data-pt errs only, 0 of 26 rej.
MSWD = 0.99, probability = 0.48
(error bars are 2s)

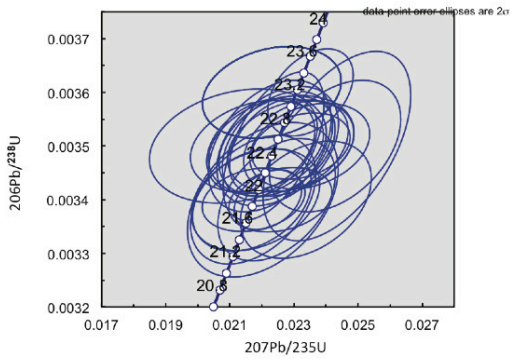
data-point error ellipses are 2σ
206Pb/238U
0.0037
0.0036
0.0035
0.0034
0.0033
0.0032
0.017
0.019
0.021
0.023
0.025
0.027
207Pb/235U
24
23.6
23.2
22.8
22.4
22
21.6
21.2
20.8

KJ1325A


g05
01
Age: 21.3±0.5 Ma
εHf: 10.7±0.7
g06
Age: 20.9±0.6 Ma
g07
03
Age: 21.1±0.3 Ma
εHf: 10.1±0.8
g08
04
Age: 21.3±0.5 Ma
εHf: 11.4±0.7
g09
05
Age: 21.3±0.5 Ma
εHf: 10.5±0.8
g10
06
Age: 20.9±0.5 Ma
εHf: 11.0±0.8
g11
07
Age: 22.0±0.5 Ma
εHf: 10.6±0.8
g12
Age: 21.9±0.5 Ma
g13
09
Age: 21.4±0.5 Ma
εHf: 11.7±0.7
h06
10
Age: 21.8±0.4 Ma
εHf: analytical pb
h07
13
Age: 21.4±0.4 Ma
εHf: analytical pb
h09
16
Age: 20.9±0.4 Ma
εHf: 10.7±0.9
h10
11
Age: 21.3±0.5 Ma
εHf: 8.7±1.7
h11
Age: 21.1±0.4 Ma
h12
Age: 21.6±0.4 Ma
h13
Age: 21.1±0.4 Ma
i05
Age: 21.0±0.4 Ma
εHf: 8.4±1.0
i06
Age: 22.1±0.6 Ma
εHf: 8.5±1.1
i07
Age: 20.9±0.5 Ma
i08
Age: 22.2±0.6 Ma
i09
Age: 21.7±0.6 Ma
i10
Age: 21.2±0.4 Ma
i11
Age: 21.5±0.5 Ma
εHf: 8.4±1.0
j06
33
Age: 21.2±0.5 Ma
εHf: 11.3±0.9
j07
Age: 21.0±0.5 Ma
j09
31
Age: 21.3±0.5 Ma
εHf: 10.9±0.8
32
j10
Age: 21.5±0.7 Ma
analytical pb
j12
Age: 21.3±0.5 Ma
j13
45
Age: 23.0±0.6 Ma
analytical pb
Scale bar:
50μm

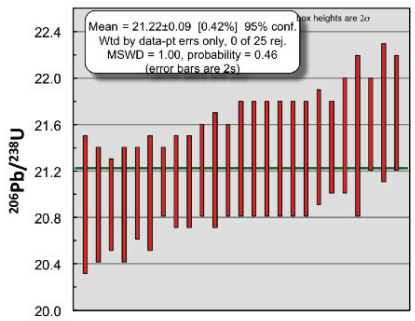
Mean = 21.22±0.09 [0.42%] 95% conf.
Wtd by data-pt errs only, 0 of 25 rej.
MSWD = 1.00, probability = 0.46
(error bars are 2s)
206Pb/238U
22.4
22.0
21.6
21.2
20.8
20.4
20.0

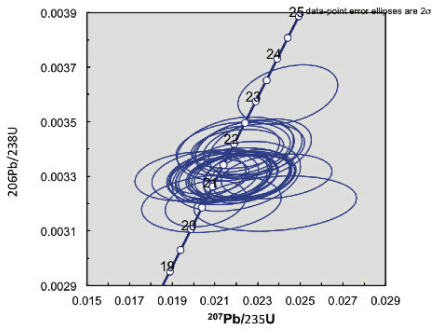
25 data-point error ellipses are 2σ
206Pb/238U
0.0039
0.0037
0.0035
0.0033
0.0031
0.0029
0.015
0.017
0.019
0.021
0.023
0.025
0.027
0.029
207Pb/235U

KJ1313

In situ Oxygene isotope spot analysis

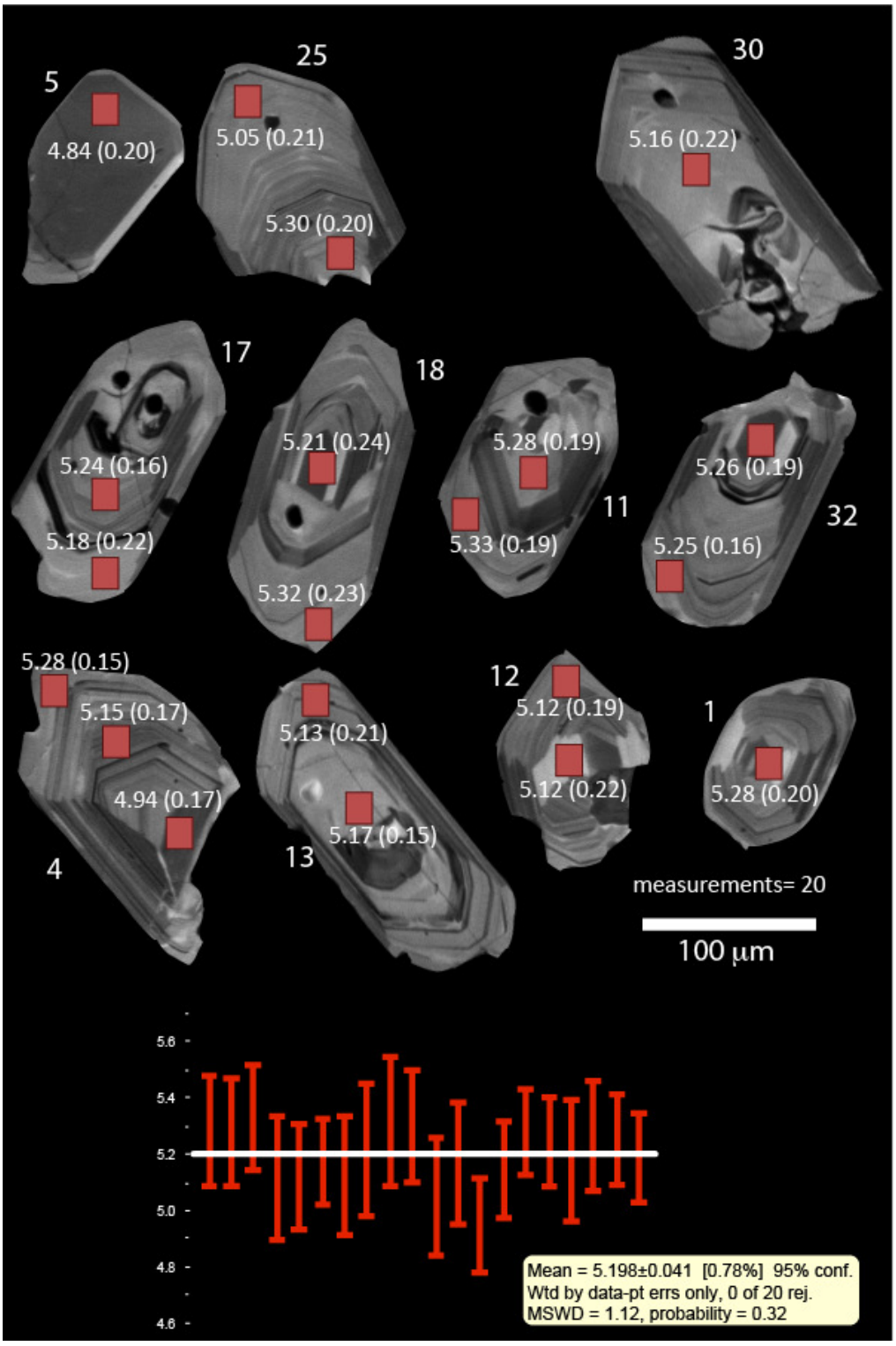

AG1304A

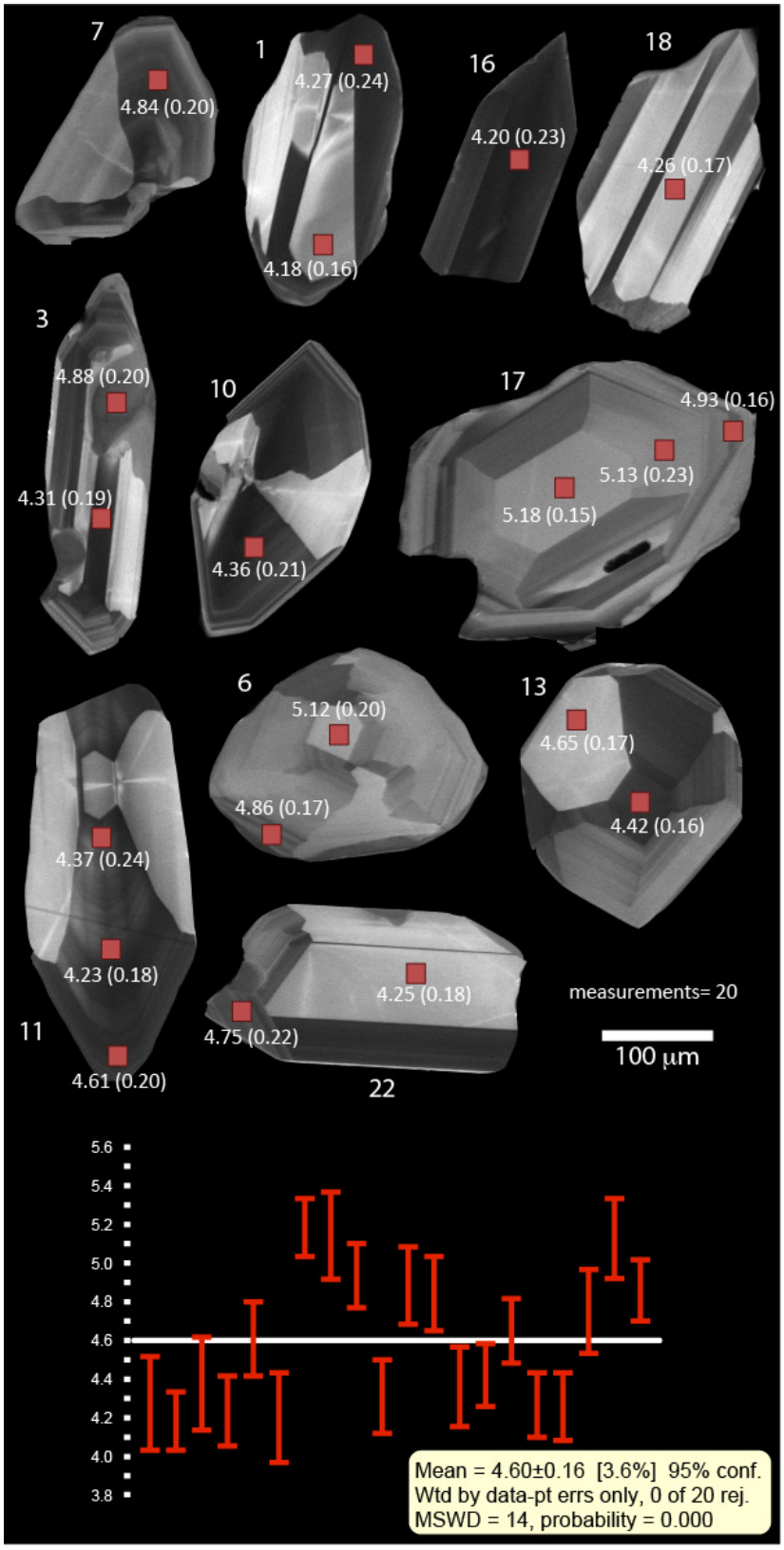
7
4.84 (0.20)
1
4.27 (0.24)
4.18 (0.16)
16
4.20 (0.23)
18
4.26 (0.17)
3
4.88 (0.20)
4.31 (0.19)
10
4.36 (0.21)
17
4.93 (0.16)
5.13 (0.23)
5.18 (0.15)
6
5.12 (0.20)
4.86 (0.17)
13
4.65 (0.17)
4.42 (0.16)
4.37 (0.24)
4.23 (0.18)
11
4.61 (0.20)
4.25 (0.18)
4.75 (0.22)
22
measurements= 20
100 µm
5.6
5.4
5.2
5.0
4.8
4.6
4.4
4.2
4.0
3.8
Mean = 4.60±0.16 [3.6%] 95% conf.
Wtd by data-pt errs only, 0 of 20 rej.
MSWD = 14, probability = 0.000

AG1401

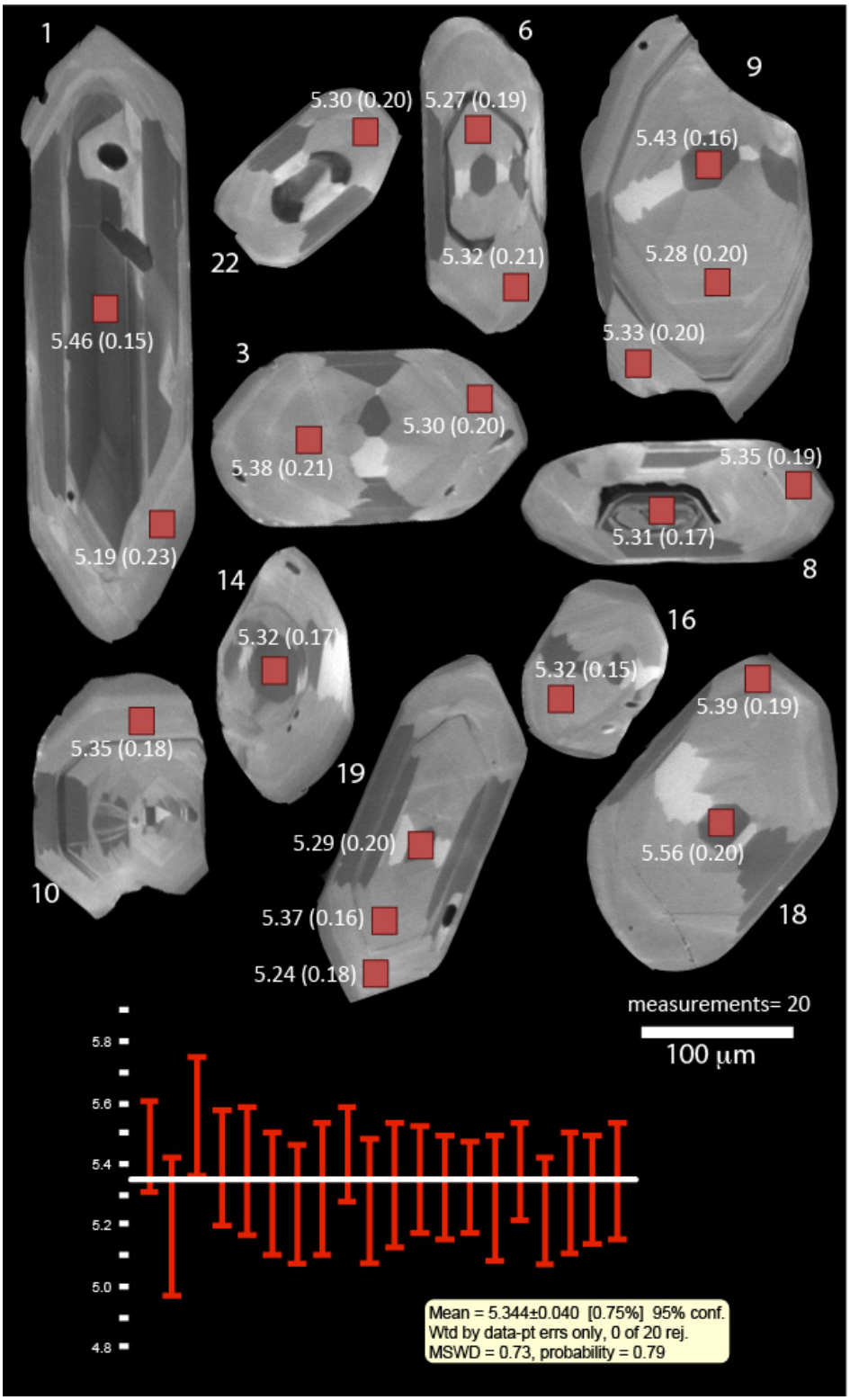
1
5.46 (0.15)
5.19 (0.23)
6
5.30 (0.20)
5.27 (0.19)
22
5.32 (0.21)
9
5.43 (0.16)
5.28 (0.20)
5.33 (0.20)
3
5.30 (0.20)
5.38 (0.21)
5.35 (0.19)
5.31 (0.17)
8
14
5.32 (0.17)
16
5.32 (0.15)
5.39 (0.19)
5.35 (0.18)
19
5.29 (0.20)
5.37 (0.16)
5.24 (0.18)
10
5.56 (0.20)
18
measurements= 20
100 µm
5.8
5.6
5.4
5.2
5.0
4.8
Mean = 5.344±0.040 [0.75%] 95% conf.
Wtd by data-pt errs only, 0 of 20 rej.
MSWD = 0.73, probability = 0.79

AG1402

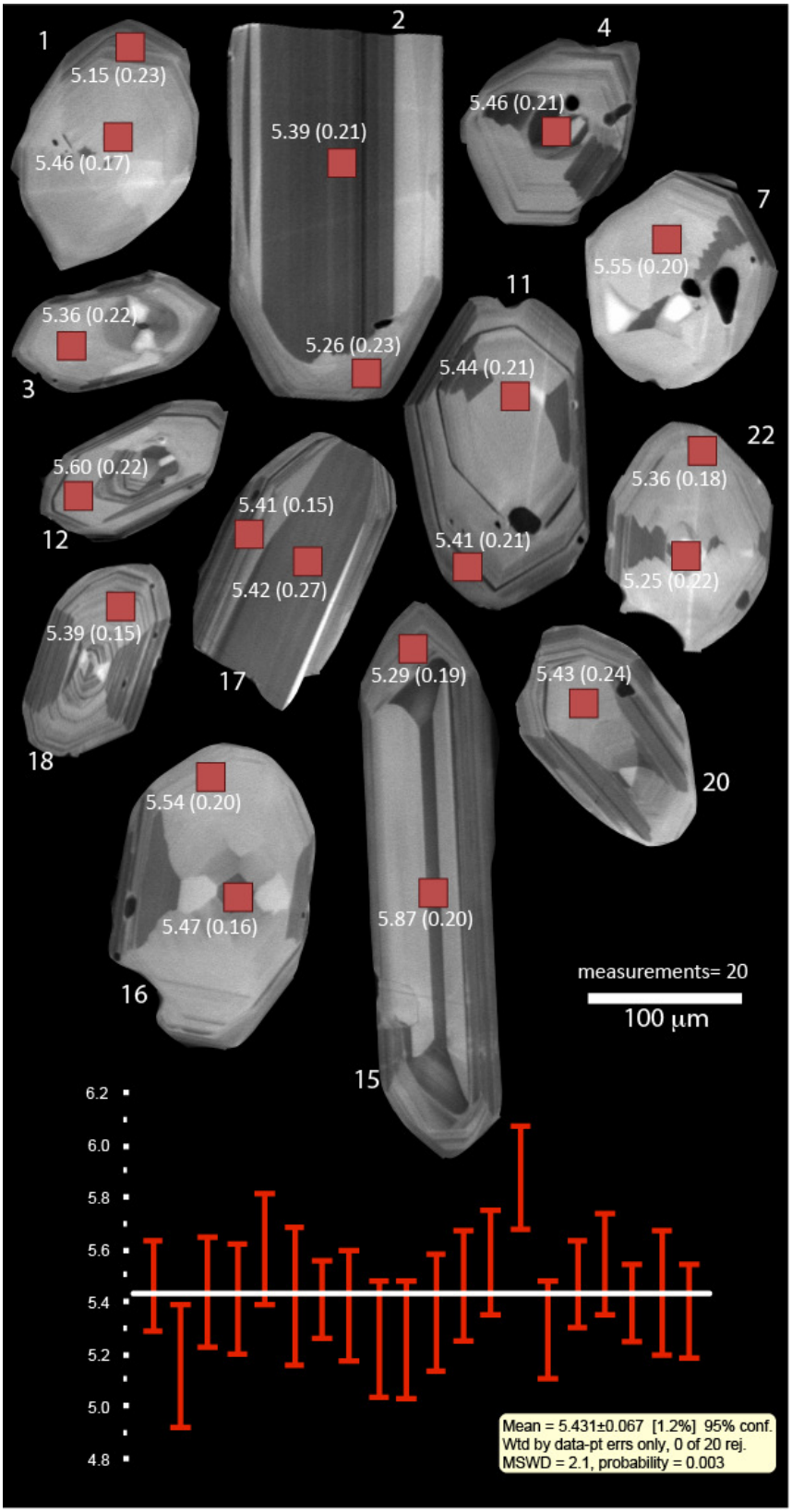
1
5.15 (0.23)
5.46 (0.17)
2
5.39 (0.21)
4
5.46 (0.21)
7
5.55 (0.20)
11
5.44 (0.21)
5.26 (0.23)
3
5.36 (0.22)
22
5.36 (0.18)
5.25 (0.22)
12
5.60 (0.22)
17
5.41 (0.15)
5.42 (0.27)
5.41 (0.21)
18
5.39 (0.15)
5.29 (0.19)
5.43 (0.24)
20
16
5.54 (0.20)
5.47 (0.16)
15
5.87 (0.20)
measurements= 20
100 µm
6.2
6.0
5.8
5.6
5.4
5.2
5.0
4.8
Mean = 5.431±0.067 [1.2%] 95% conf.
Wtd by data-pt errs only, 0 of 20 rej.
MSWD = 2.1, probability = 0.003

HQ1403

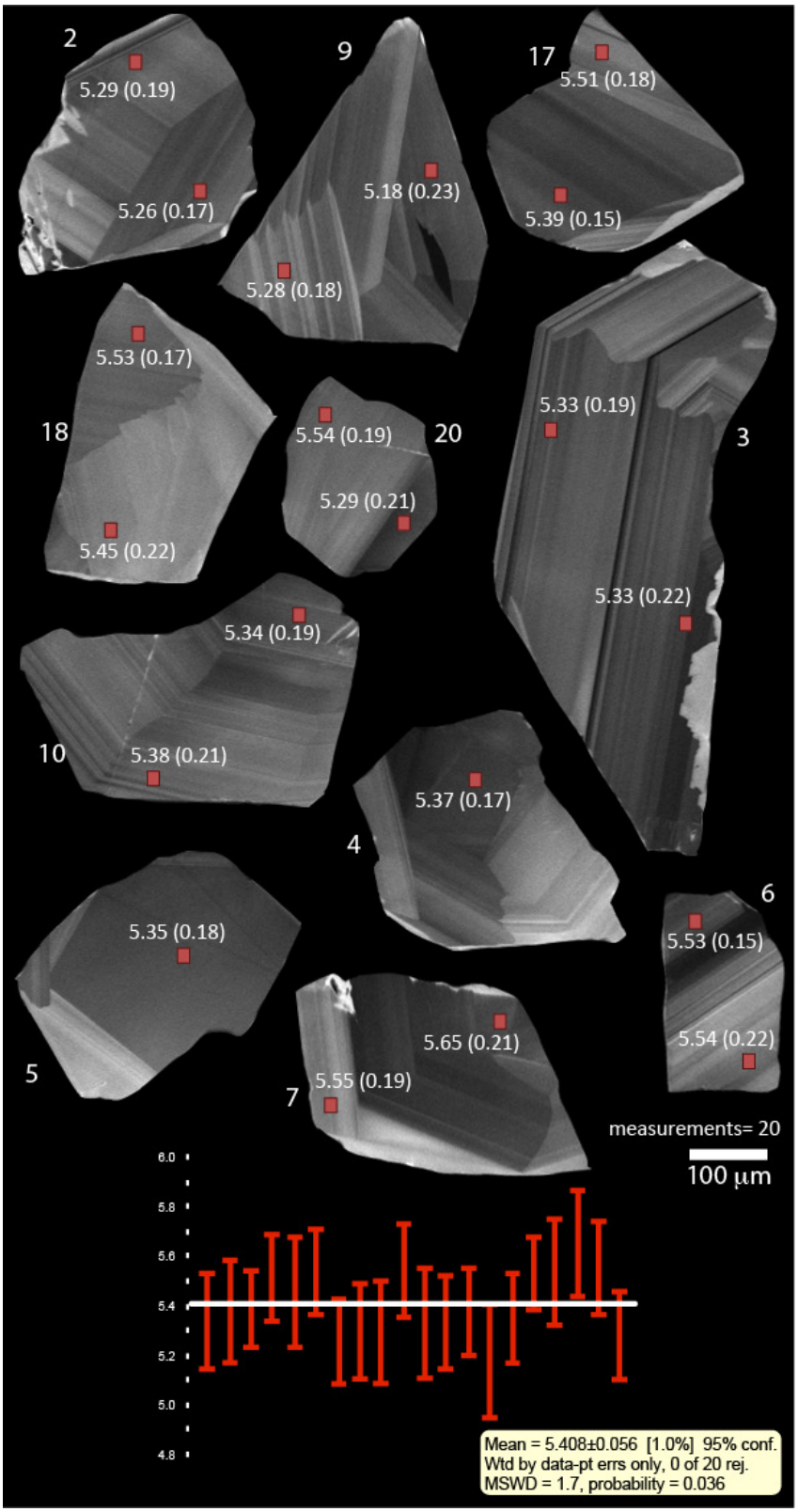
2
5.29 (0.19)
5.26 (0.17)
9
5.18 (0.23)
5.28 (0.18)
17
5.51 (0.18)
5.39 (0.15)
5.53 (0.17)
18
5.45 (0.22)
5.54 (0.19)
20
5.29 (0.21)
5.33 (0.19)
3
5.33 (0.22)
5.34 (0.19)
10
5.38 (0.21)
5.37 (0.17)
4
5.35 (0.18)
5
6
5.53 (0.15)
5.54 (0.22)
5.65 (0.21)
7
5.55 (0.19)
measurements= 20
100 µm
6.0
5.8
5.6
5.4
5.2
5.0
4.8
Mean = 5.408±0.056 [1.0%] 95% conf.
Wtd by data-pt errs only, 0 of 20 rej.
MSWD = 1.7, probability = 0.036

AG1308A

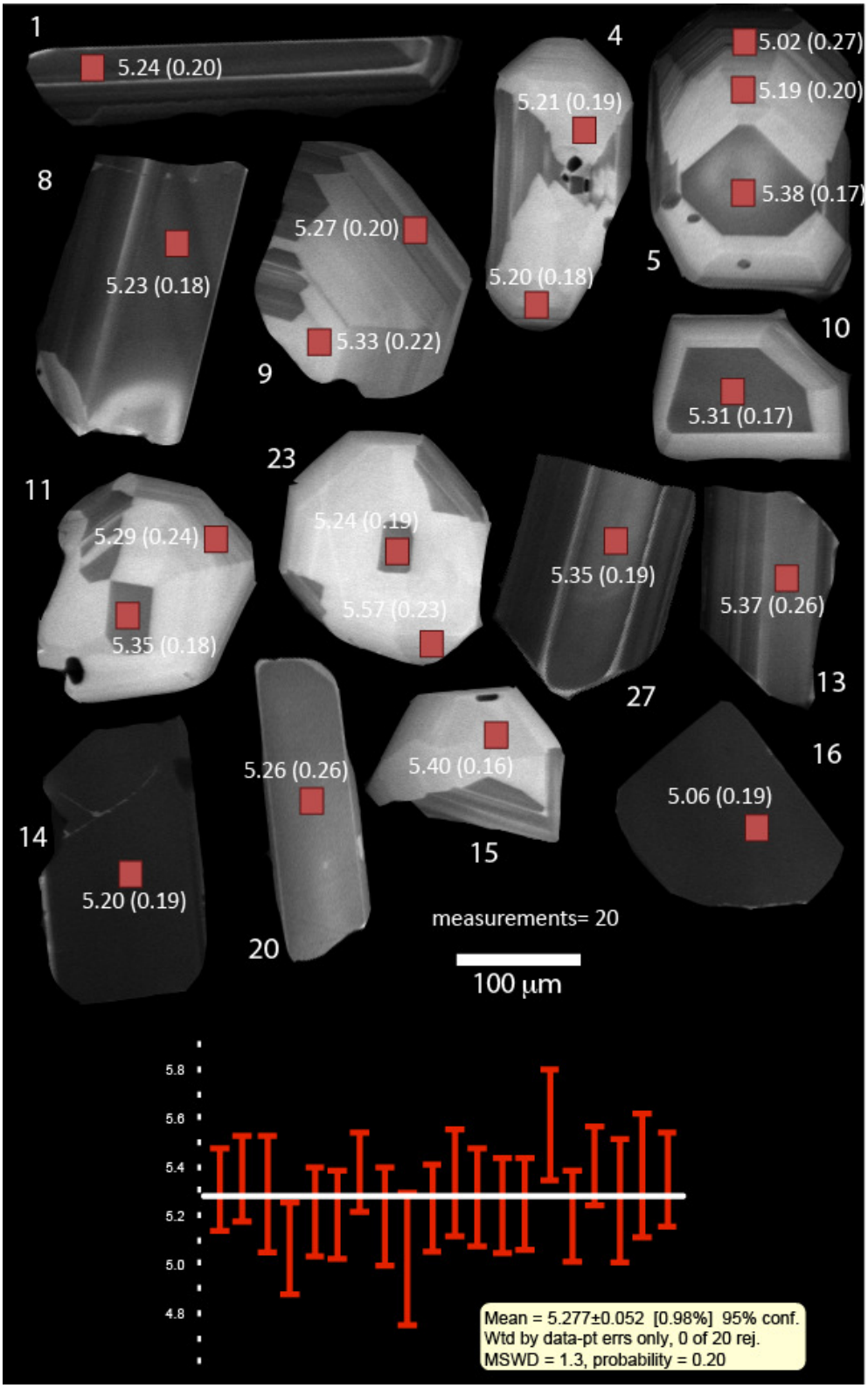
1
5.24 (0.20)
4
5.21 (0.19)
5.02 (0.27)
5.19 (0.20)
5.38 (0.17)
5
8
5.23 (0.18)
5.27 (0.20)
5.33 (0.22)
9
5.20 (0.18)
10
5.31 (0.17)
23
5.24 (0.19)
5.57 (0.23)
11
5.29 (0.24)
5.35 (0.18)
5.35 (0.19)
27
5.37 (0.26)
13
16
5.06 (0.19)
5.40 (0.16)
15
5.26 (0.26)
20
14
5.20 (0.19)
measurements= 20
100 µm
5.8
5.6
5.4
5.2
5.0
4.8
Mean = 5.277±0.052 [0.98%] 95% conf.
Wtd by data-pt errs only, 0 of 20 rej.
MSWD = 1.3, probability = 0.20

VK1405

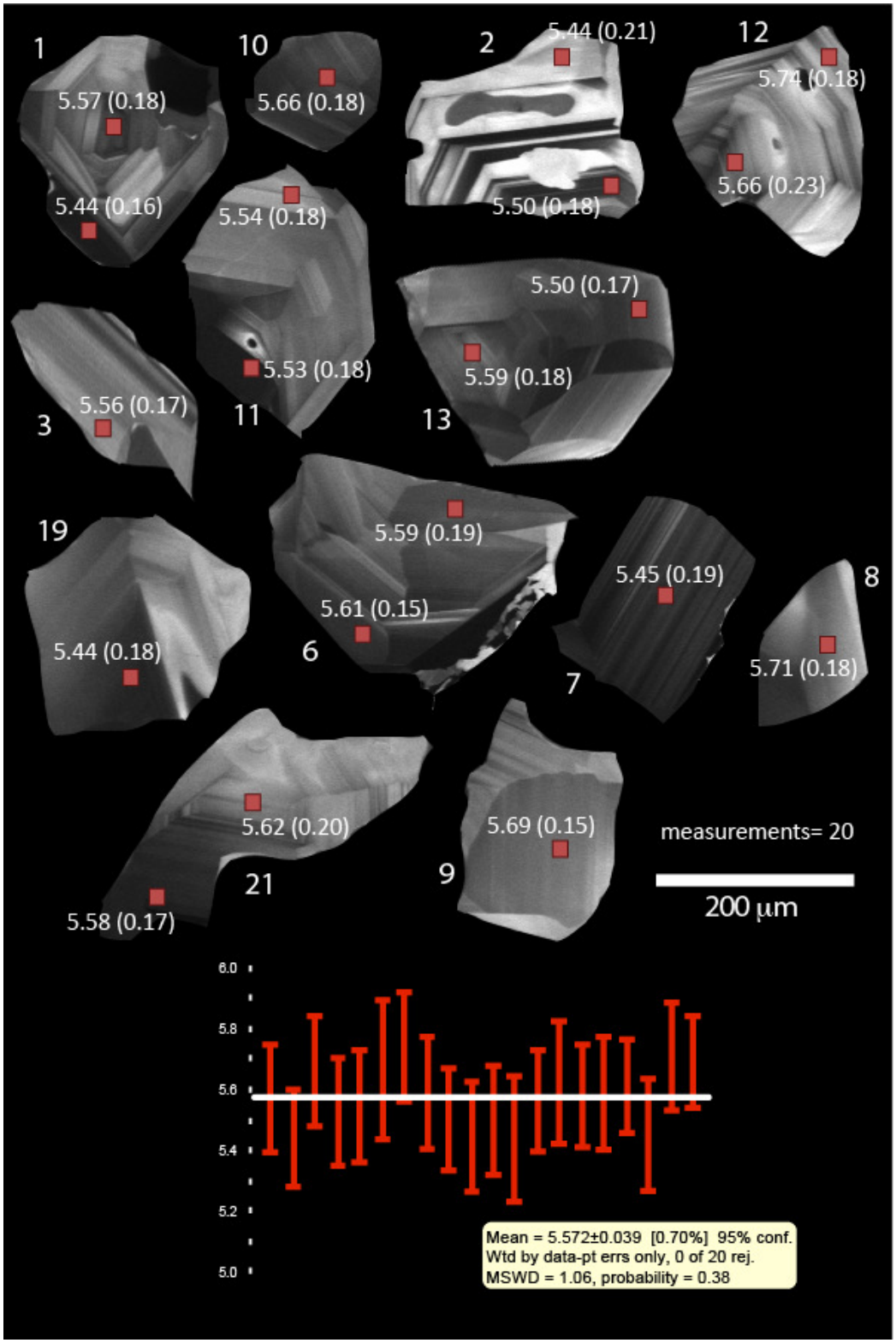
1
5.57 (0.18)
5.44 (0.16)
10
5.66 (0.18)
2
5.44 (0.21)
5.50 (0.18)
12
5.74 (0.18)
5.66 (0.23)
5.54 (0.18)
5.53 (0.18)
11
5.50 (0.17)
5.59 (0.18)
13
3
5.56 (0.17)
19
5.44 (0.18)
5.59 (0.19)
5.61 (0.15)
6
5.45 (0.19)
7
8
5.71 (0.18)
5.62 (0.20)
21
5.58 (0.17)
9
5.69 (0.15)
measurements= 20
200 µm
6.0
5.8
5.6
5.4
5.2
5.0
Mean = 5.572±0.039 [0.70%] 95% conf.
Wtd by data-pt errs only, 0 of 20 rej.
MSWD = 1.06, probability = 0.38

MR1403

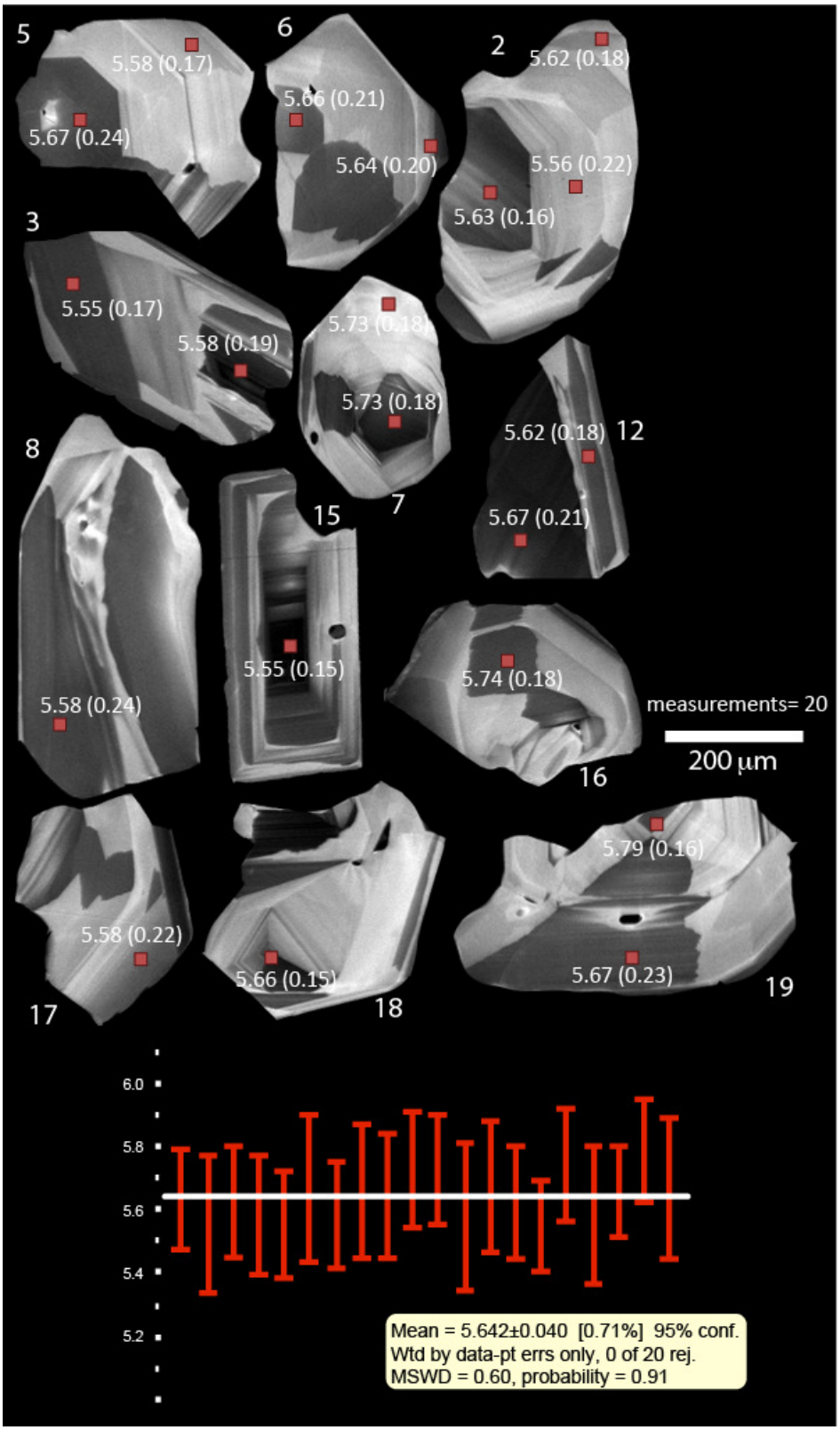
5
5.58 (0.17)
5.67 (0.24)
6
5.66 (0.21)
5.64 (0.20)
2
5.62 (0.18)
5.56 (0.22)
5.63 (0.16)
3
5.55 (0.17)
5.58 (0.19)
5.73 (0.18)
5.73 (0.18)
8
5.58 (0.24)
15
7
5.55 (0.15)
5.62 (0.18)
12
5.67 (0.21)
5.74 (0.18)
16
measurements= 20
200 µm
17
5.58 (0.22)
18
5.66 (0.15)
5.79 (0.16)
5.67 (0.23)
19
6.0
5.8
5.6
5.4
5.2
Mean = 5.642±0.040 [0.71%] 95% conf.
Wtd by data-pt errs only, 0 of 20 rej.
MSWD = 0.60, probability = 0.91

LI1303A1

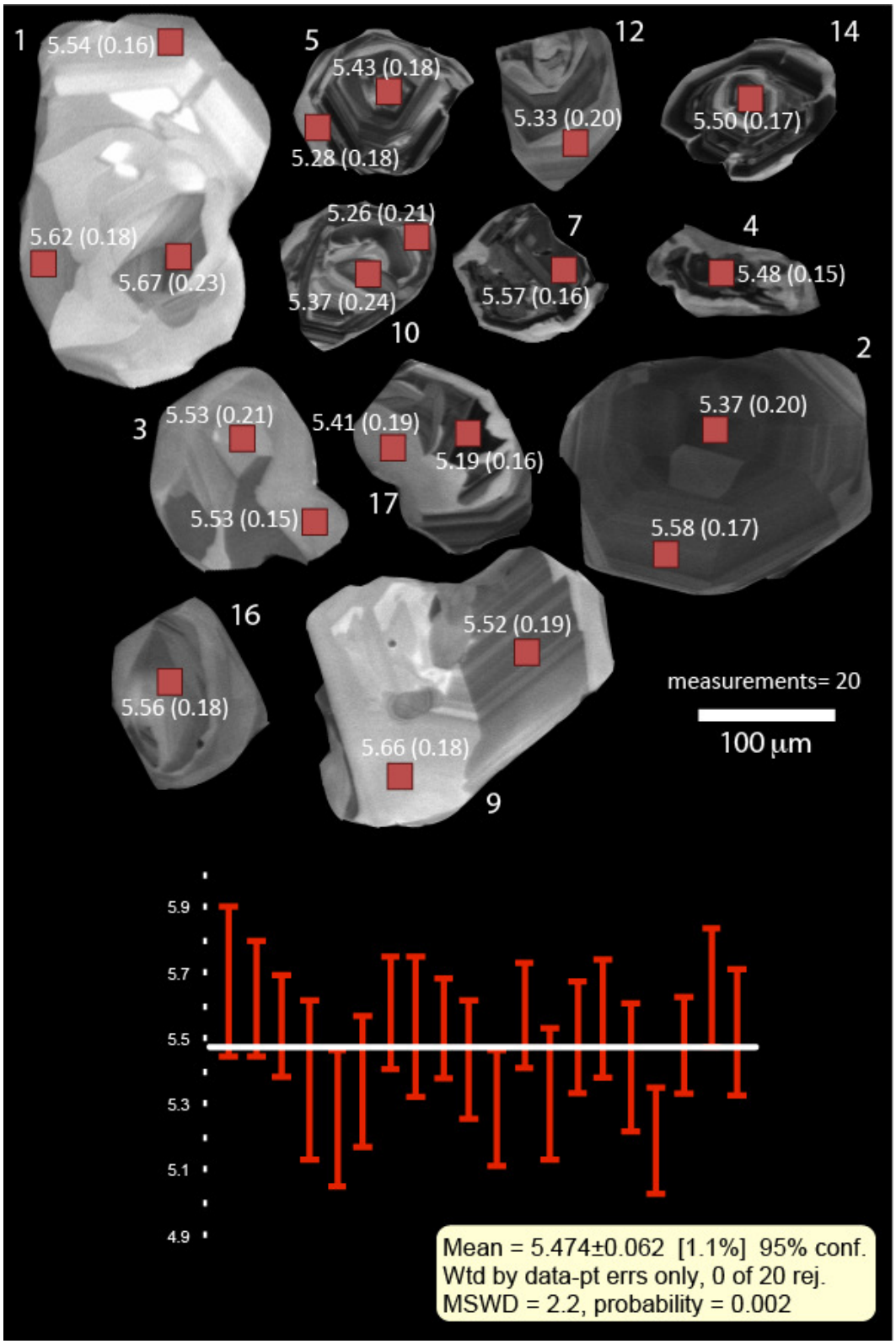
1
5.54 (0.16)
5
5.43 (0.18)
5.28 (0.18)
12
5.33 (0.20)
14
5.50 (0.17)
5.62 (0.18)
5.67 (0.23)
5.26 (0.21)
5.37 (0.24)
10
7
5.57 (0.16)
4
5.48 (0.15)
2
5.37 (0.20)
3
5.53 (0.21)
5.53 (0.15)
5.41 (0.19)
5.19 (0.16)
17
5.58 (0.17)
16
5.56 (0.18)
5.52 (0.19)
5.66 (0.18)
9
measurements= 20
100 µm
5.9
5.7
5.5
5.3
5.1
4.9
Mean = 5.474±0.062 [1.1%] 95% conf.
Wtd by data-pt errs only, 0 of 20 rej.
MSWD = 2.2, probability = 0.002

MR1402

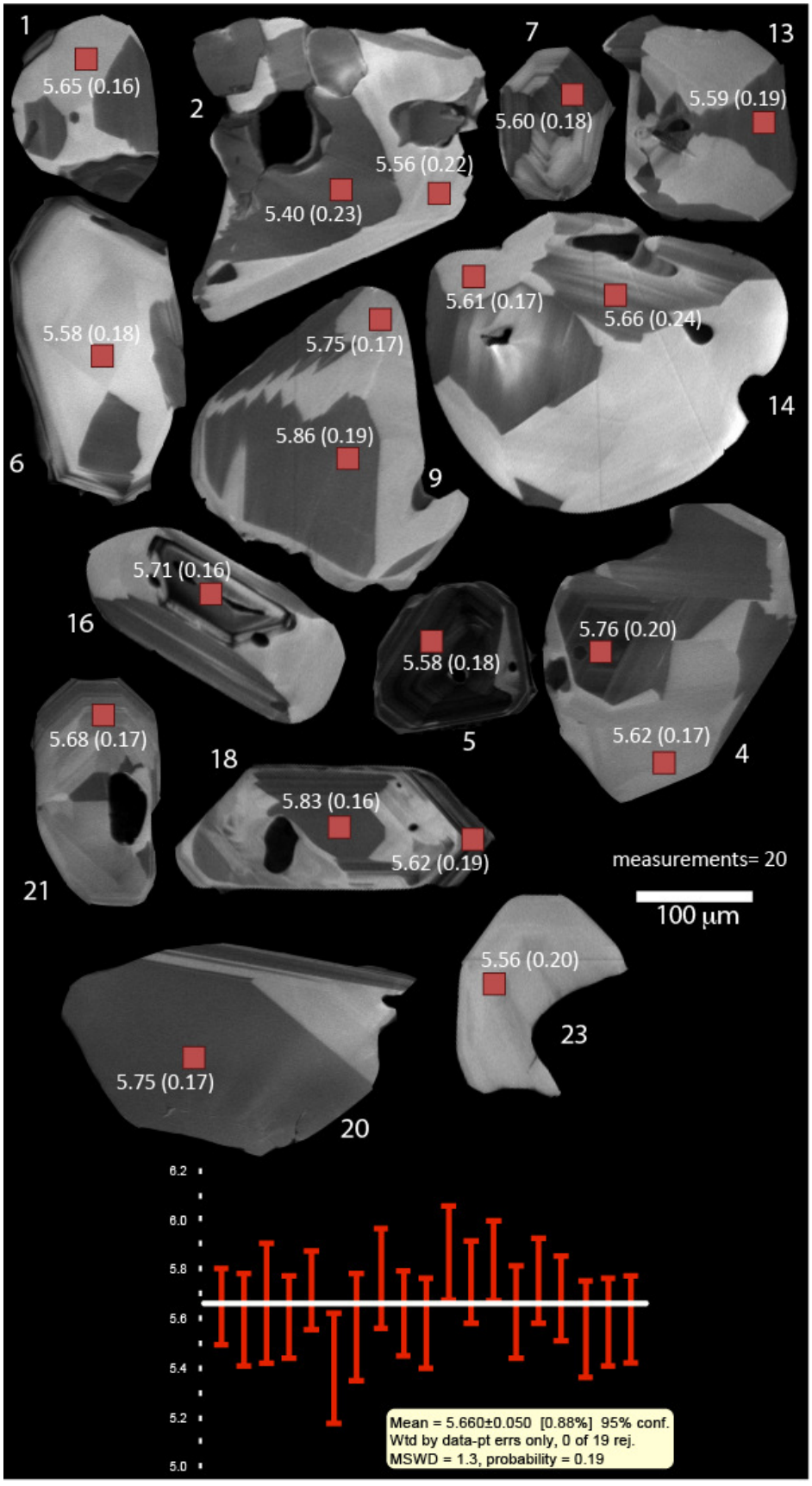
1
5.65 (0.16)
2
5.40 (0.23)
5.56 (0.22)
7
5.60 (0.18)
13
5.59 (0.19)
5.58 (0.18)
6
5.75 (0.17)
5.86 (0.19)
9
5.61 (0.17)
5.66 (0.24)
14
5.71 (0.16)
16
5.58 (0.18)
5
5.76 (0.20)
5.62 (0.17)
4
5.68 (0.17)
21
18
5.83 (0.16)
5.62 (0.19)
measurements= 20
100 µm
5.56 (0.20)
23
5.75 (0.17)
20
6.2
6.0
5.8
5.6
5.4
5.2
5.0
Mean = 5.660±0.050 [0.88%] 95% conf.
Wtd by data-pt errs only, 0 of 19 rej.
MSWD = 1.3, probability = 0.19

KJ1316

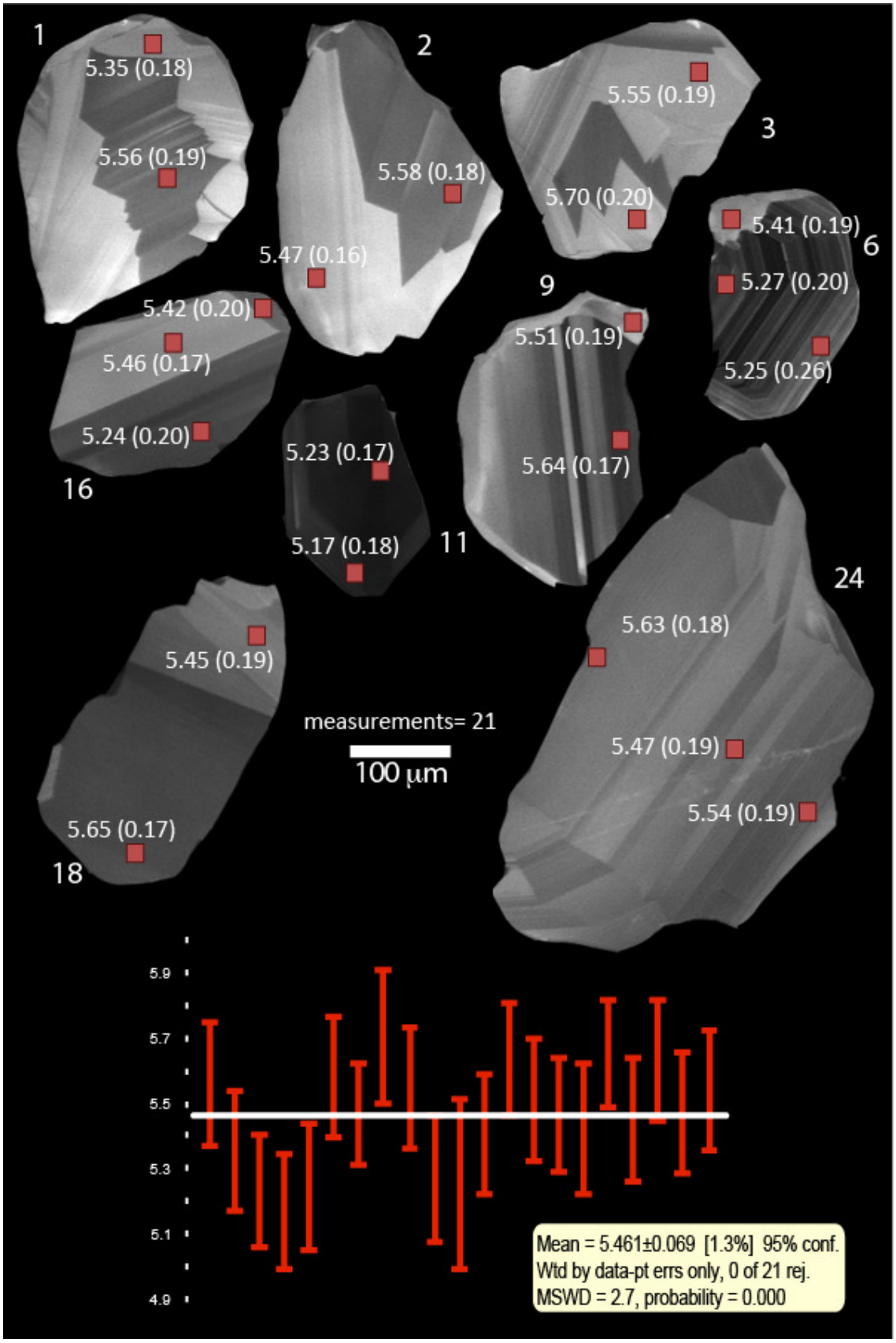
1
5.35 (0.18)
5.56 (0.19)
2
5.58 (0.18)
5.47 (0.16)
3
5.55 (0.19)
5.70 (0.20)
6
5.41 (0.19)
5.27 (0.20)
5.25 (0.26)
9
5.51 (0.19)
5.64 (0.17)
16
5.42 (0.20)
5.46 (0.17)
5.24 (0.20)
5.23 (0.17)
5.17 (0.18)
11
24
5.63 (0.18)
5.47 (0.19)
5.54 (0.19)
5.45 (0.19)
measurements= 21
100 μm
18
5.65 (0.17)
5.9
5.7
5.5
5.3
5.1
4.9
Mean = 5.461±0.069 [1.3%] 95% conf.
Wtd by data-pt errs only, 0 of 21 rej.
MSWD = 2.7, probability = 0.000

KJ1006A

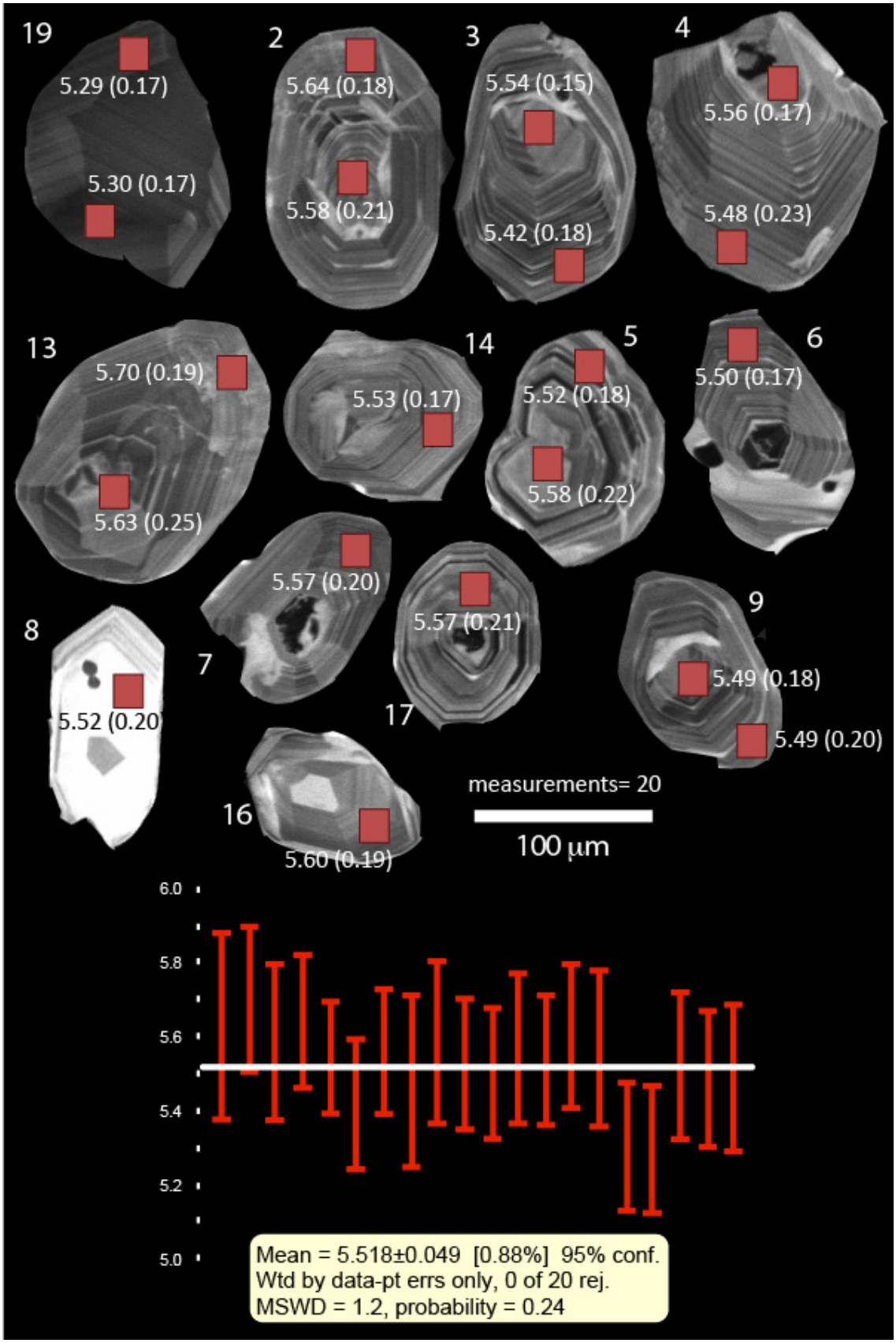
19
5.29 (0.17)
5.30 (0.17)
2
5.64 (0.18)
5.58 (0.21)
3
5.54 (0.15)
5.42 (0.18)
4
5.56 (0.17)
5.48 (0.23)
13
5.70 (0.19)
5.63 (0.25)
14
5.53 (0.17)
5
5.52 (0.18)
5.58 (0.22)
6
5.50 (0.17)
8
5.52 (0.20
7
5.57 (0.20)
17
5.57 (0.21)
9
5.49 (0.18)
5.49 (0.20)
16
5.60 (0.19)
measurements= 20
100 μm
6.0
5.8
5.6
5.4
5.2
5.0
Mean = 5.518±0.049 [0.88%] 95% conf.
Wtd by data-pt errs only, 0 of 20 rej.
MSWD = 1.2, probability = 0.24

KJ1302A

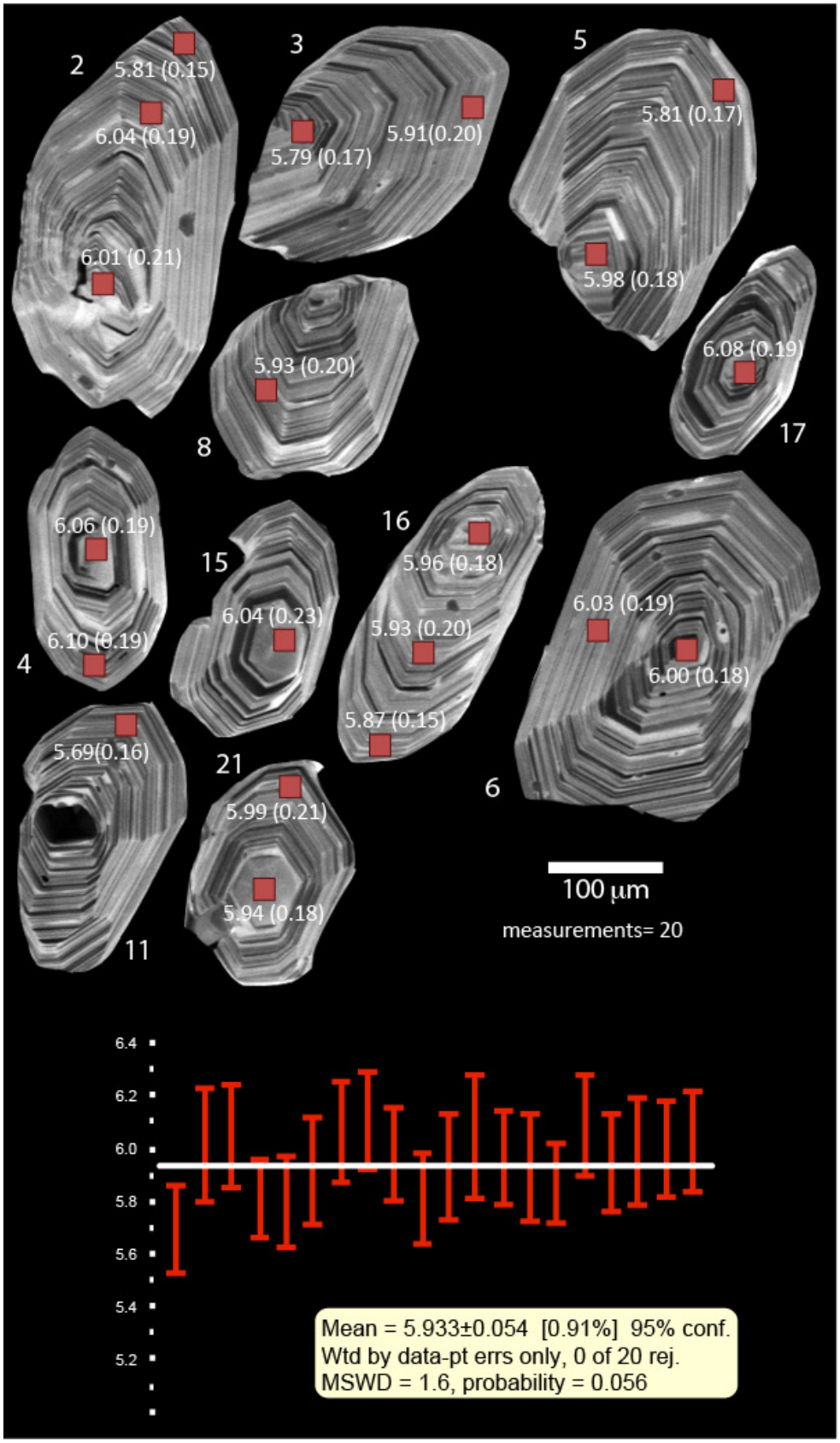
2
5.81 (0.15)
6.04 (0.19)
6.01 (0.21)
3
5.79 (0.17)
5.91(0.20)
5
5.81 (0.17)
5.98 (0.18)
6.08 (0.19)
17
5.93 (0.20)
8
6.06 (0.19)
4
6.10 (0.19)
15
6.04 (0.23)
16
5.96 (0.18)
5.93 (0.20)
5.87 (0.15)
6.03 (0.19)
6.00 (0.18)
6
5.69(0.16)
11
21
5.99 (0.21)
5.94 (0.18)
100 µm
measurements= 20
6.4
6.2
6.0
5.8
5.6
5.4
5.2
Mean = 5.933±0.054 [0.91%] 95% conf.
Wtd by data-pt errs only, 0 of 20 rej.
MSWD = 1.6, probability = 0.056

LI1301

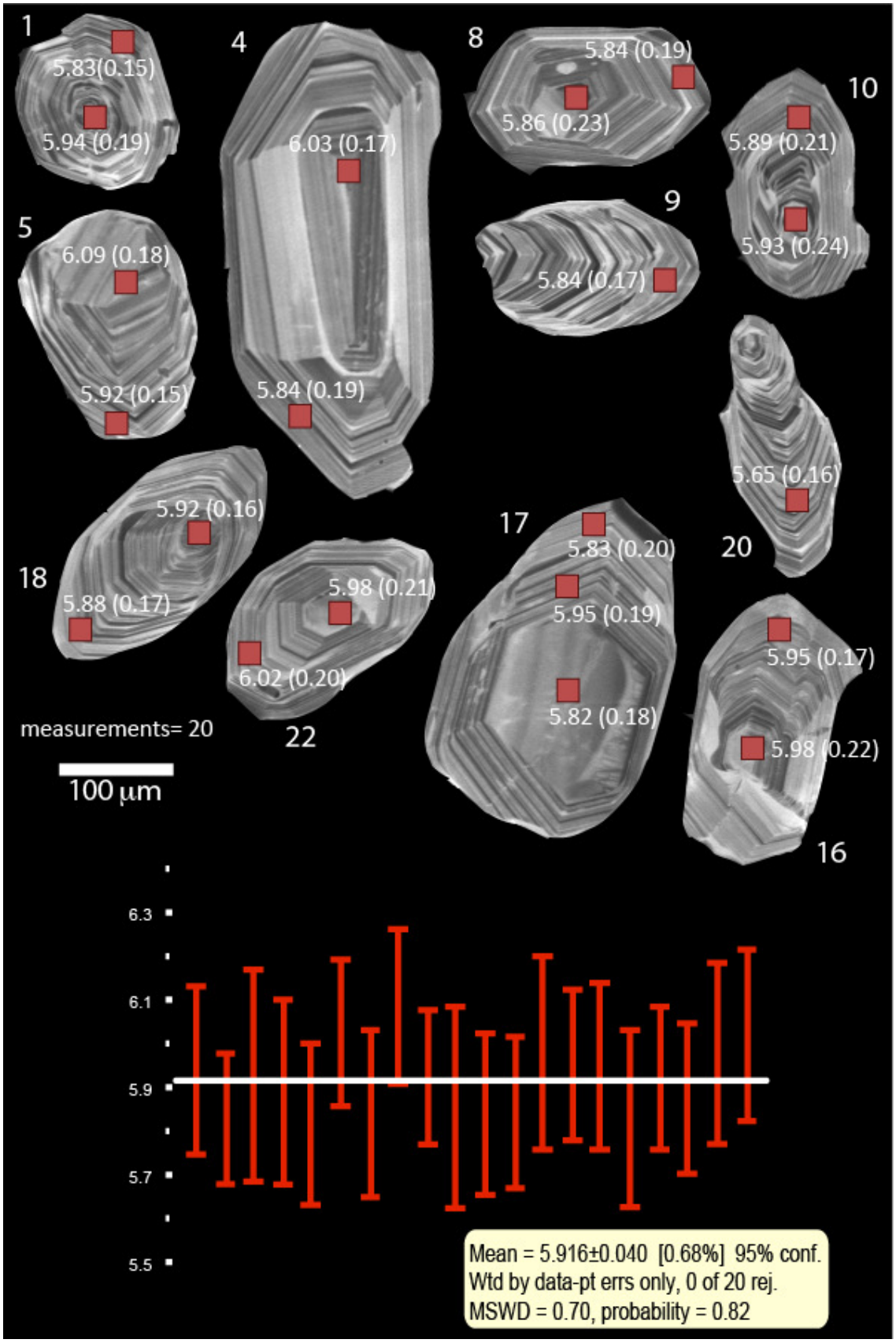
1
5.83(0.15)
5.94 (0.19)
4
6.03 (0.17)
5.84 (0.19)
8
5.84 (0.19)
5.86 (0.23)
10
5.89 (0.21)
5.93 (0.24)
9
5.84 (0.17)
5
6.09 (0.18)
5.92 (0.15)
5.65 (0.16)
20
5.92 (0.16)
18
5.88 (0.17)
5.98 (0.21)
6.02 (0.20)
22
17
5.83 (0.20)
5.95 (0.19)
5.82 (0.18)
5.95 (0.17)
5.98 (0.22)
16
measurements= 20
100 µm
6.3
6.1
5.9
5.7
5.5
Mean = 5.916±0.040 [0.68%] 95% conf.
Wtd by data-pt errs only, 0 of 20 rej.
MSWD = 0.70, probability = 0.82

KJ1324A

CHAPTER 2

30 m.y. of Cenozoic magmatism along the Tethyan margin during Arabia-Eurasia accretionary orogenesis (Meghri-Ordubad pluton, southernmost Lesser Caucasus)

HervŽ Rezeau[1], Robert Moritz[1], Julien Leuthold[2], Samvel Hovakimyan[1,3], Rodrik Tayan[3], and Massimo Chiaradia[1]

[1]Department of Earth Sciences, University of Geneva, 1205 Geneva, Switzerland; [2]Institute of Geochemistry and Petrology, ETH ZŸrich, 8092 ZŸrich, Switzerland; [3]Institute of Geological Sciences, National Academy of Sciences, 0019 Yerevan, Armenia

ABSTRACT

Three magmatic series of substantially different ages and compositions were successively emplaced to form the composite Meghri-Ordubab pluton (MOP) in the southernmost Lesser Caucasus. The protracted incremental assembly during 30 m.y., from Middle Eocene to Early Miocene, renders this location particularly suitable to characterize the petrogenetic evolution of Cenozoic magmatism during the final stage of the Neotethyan subduction. Based on whole-rock geochemistry, two main transitions tightly constrained in time are recognized. The first transition from Middle Eocene medium- to high-K calc-alkaline to Late Eocene - Middle Oligocene shoshonitic magmatism corresponds to a marked increase in LREE and MREE and more juvenile $^{87}Sr/^{86}Sr$ and $^{143}Nd/^{144}Nd$ ratios. The second transition to Late Oligocene - Early Miocene high-K calc-alkaline "adakite-like" magmatism is coeval with a marked increase in Mg#, and Ni and Cr contents together with a depletion in MREE and HREE. Although the three differentiation series are derived from lower to mid-crustal hydrous magma fractionation, temporal variations of the magmatic source conditions are required to explain the contrasting chemistry of the parental magmas over time. Medium- to high-K calc-alkaline parental magmas were generated by high degree of partial melting (~15%) of a garnet lherzolite. The shoshonitic and adakitic magmatic series represent magmas produced by low degree of partial melting (1-5%) of a garnet lherzolite, but a higher amount of residual garnet is required to reproduce the "adakite-like" signature. The timing of the two main geochemical transitions in the MOP is correlated with a progressive evolution from a compressional to an extensional stress regime linked to (1) the final stage of the Neotethyan subduction followed by the Arabia-Eurasia continental collision during the Eocene-Oligocene, and (2) the transition toward post-collisional magmatism, combined with a switch toward transcurrent tectonics during the Late Oligocene - Early Miocene.

Keywords: Tethyan orogenic belt; Arabia-Eurasia collision; crustal growth; calc-alkaline, shoshonitic and adakitic series; geochemical modeling; Lesser Caucasus

1. INTRODUCTION

Magmatic arcs display chemically diverse suites of magmas along an orogenic belt, including tholeiitic, calc-alkaline and alkaline magmas (e.g., Foley, 1992; Hochstaedter et al., 1996; Straub et al., 2015). The geochemistry of subduction-related primary magmas is inferred from the enrichments of large ion lithophile elements (LILE) relative to high-field strength elements (HFSE) and/or rare-earth elements (REE) (e.g., Kelemen et al., 2003). The variety of geochemical characteristics of primary magmas is generally inherited from the mantle source and reflects processes such as fluid-fluxed melting in response to the dehydration of the subducted oceanic crust (e.g., McCulloch & Gamble, 1991; Elliott et al., 1997) or decompression melting (e.g., Concei•ao & Green, 2004; Castro et al., 2013). The degree of mantle partial melting has also a significant effect on the trace element composition of primary magmas (e.g., Ringwood, 1975; Barragan et al., 1998). During magma ascent to the upper crust, assimilation and fractional crystallization crustal processes impact the geochemical characteristics of the hydrous primary magmas (Jagoutz, 2010; Nandedkar et al., 2014). Crustal interactions make it difficult to identify the primary composition of fractionated arc magmas, and the recognition of these processes remains crucial to assess the petrogenesis of arc magmas through space and time along an orogenic belt.

The southernmost Lesser Caucasus is located along the central segment of the Alpine-Himalayan orogenic belt and belongs to the Turkish-Iranian plateau. The temporal geodynamic evolution from a subduction to collision to post-collisional setting is controversial along the Turkish-Iranian plateau, as well as the petrogenesis of its magmatic rocks. The Lesser Caucasus segment results from repeated micro-plate accretion and collision events during the successive closure of the Paleotethys ocean in the Late Paleozoic - Early Mesozoic and the Neotethys ocean in the Late Cretaceous - Cenozoic (e.g., Barrier & Vrielynck, 2008; Sosson et al., 2010; Rolland, 2017). The exact timing for the onset of the Arabia-Eurasia collision is unclear and occurred either during the Late Cretaceous (Mohajjel & Fergusson, 2000), Late Eocene to Oligocene (Vincent et al., 2007; Allen & Armstrong, 2008; Agard et al., 2011; Ballato et al., 2011; Van Hunen & Allen, 2011; Rolland et al., 2012; Moritz et al., 2016a), or Early to Middle Miocene (McQuarrie et al., 2003; Okay et al., 2010).

The Cenozoic Meghri-Ordubad pluton (MOP) is located in the southernmost Lesser Caucasus and displays three temporally and chemically distinct intrusive suites assembled over 30 m.y. (Rezeau et al., 2016). They are interpreted to record an evolution from subduction-related to post-collisional magmatism (Moritz et al., 2016a). However, the magmatic source

evolution and subsequent crustal processes remain poorly constrained. This study aims at precisely documenting and interpreting the temporal compositional evolution of Cenozoic magmatism revealed in the MOP, based on whole-rock major, trace and radiogenic isotope geochemistry on a representative sample suite timely-constrained by detailed zircon U-Pb geochronology (Rezeau et al., 2016). The contrasting chemistry of the least differentiated rocks from each magmatic series highlights two major geochemical transitions during the Middle to Late Eocene and the Middle to Late Oligocene. Geochemical modeling was carried out to characterize the temporal evolution of the magmatic source partial melting and composition, as well as crustal differentiation processes over time. These new temporal and geochemical constraints, combined with tectonic features, allow us to refine the tectono-magmatic evolution model for the MOP within the regional geodynamic framework of the Cenozoic Arabia-Eurasia accretionary orogeny, from subduction to post-collisional settings.

2. REGIONAL GEOTECTONIC SETTING OF THE LESSER CAUCASUS

The Lesser Caucasus extends over the territories of Armenia, Azerbaijan and Georgia. From SW to NE, the Lesser Caucasus consists of three main tectonic domains (Fig. 1; Sosson et al., 2010 and references therein): (1) the Gondwana-derived South Armenian Block (SAB), (2) the Amasia-Sevan-Hakari ophiolite suture zone, also known as Sevan-Akera suture zone, and (3) the Southern Eurasian plate margin consisting of the Somkheto-Karabagh belt and the Kapan block. The Lesser Caucasus is a Jurassic to Quaternary orogenic belt formed during NNE-verging convergence of the SAB toward the Eurasian margin. The progressive closure of the northern branch of the Neotethys ended at 88-83 Ma ($^{40}Ar/^{39}Ar$ dating; Rolland et al., 2009; HŠssig et al., 2015). It includes a phase of oceanic obduction over the SAB and the Tauride-Anatolian block (TAB) (Fig. 1; HŠssig et al., 2013 2015, 2016), followed by Late Cretaceous-Paleogene collision (Sosson et al., 2010; Rolland et al., 2012). As a consequence of the SAB-Eurasian margin collision, the subduction jumped SW of the Turkish Bitlis-PŸturge massif (BPM) and SAB-TAB (Fig. 1; Rolland et al., 2012). The southwestern limit of the SAB coincides with the accretionary boundary with the Bitlis-PŸturge terrane dated at 74-71 Ma ($^{40}Ar/^{39}Ar$ dating; OberhŠnsli et al., 2010; Rolland et al., 2012). The Cenozoic evolution is characterized by the northward diachronous convergence of Arabia towards Eurasia closing the southern branch of the Neotethys ocean and illustrated by Cenozoic magmatism along the Turkish - Iranian plateau (Agard et al., 2011; Chiu et al., 2013; Neill et al., 2015; Moritz et al., 2016a). Important to note that Eyuboglu et al. (2012, 2016a, b) have contended this geodynamic evolution and have suggested an alternative interpretation, based essentially on their studies along the Eastern Pontides, with a Jurassic to Cenozoic south-verging subduction along its northern boundary. For a review of the regional geodynamic setting evolution in the Caucasus

from the Mesozoic to Cenozoic, the reader is referred to Sosson et al. (2010), Rolland et al. (2012, 2016), Moritz et al. (2016a,b) and Rolland (2017).

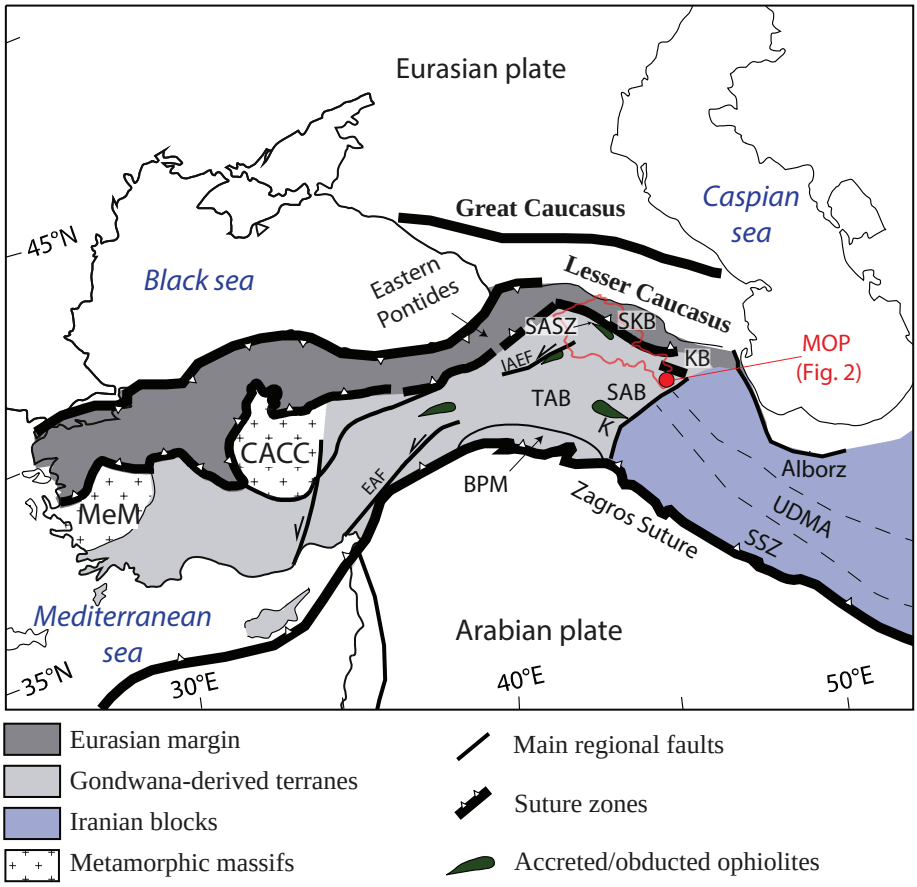

Figure 1: Regional map of Turkish-Caucasus-Iranian belts showing the main tectonic features, suture zones and volcanic belts. The red dot indicates the study area: the Meghri-Ordubad pluton (MOP). BPM: Bitlis-PŸturge massif, CACC: Central Anatolian Crystalline Complex, EAF: East Anatolian fault, K: Khoy ophiolites, KB: Kapan block, IAEF: Izmir Ankara-Erzinkan fault, MeM: Menderes massif, SAB: South Armenian block, SASZ: Sevan-Akera suture zone, SSZ: Sanandaj-Sirjan zone, SKB: Somkheto-Karabagh belt, TAB: Tauride-Anatolian block; UDMA: Urumieh-Dokhtar magmatic arc. Modified after Sosson et al. (2010).

3. STRUCTURAL SETTING, GEOLOGY AND GEOCHRONOLOGY OF THE MEGHRI-ORDUBAD PLUTON

The MOP was incrementally emplaced over 30 m.y. during final convergence and collision of the Arabian and Eurasian plates (Moritz et al., 2016a; Rezeau et al., 2016). The MOP outcrops within the territories of southern Armenia, Nakhitchevan, and NW Iran (Fig. 2; Karamyan et al., 1974). In the southernmost Lesser Caucasus, the MOP is emplaced in the Zangezur-Ordubad region and is mainly exposed in the eastern uplifted Zangezur block, accompanied by subsidiary

intrusions in the western downthrown Nakhitchevan block (Tayan et al., 1976). These two blocks are separated by the NW-trending dextral strike-slip Ordubad–Salvard fault, which is active since the Eocene (Fig. 2; Karamyan et al., 1974; Tayan et al., 1976; Hovakimyan et al., 2016). On the eastern side of the MOP, the NW-trending, dextral strike-slip Khustup-Giratakh fault separates the Zangezur block from the Eurasian margin (Fig. 2; Tayan et al., 1976; Hovakimyan et al., 2016). Magma ascended to upper crustal levels along regional NS- and subsidiary EW- and SW-oriented faults, displaying vertical and strike-slip movements (Mkrtchyan et al., 1969; Tayan et al., 1976; Karamyan, 1978). The faults are Eocene in age and were reactivated during the Neogene (Tayan, 1998). The parallel N-S-trending dextral strike-slip Tashtun fault extends through the central part of the Zangezur block and controls ore deposits and magma emplacement (Fig. 2; Tayan, 1998; Hovakimyan and Tayan, 2008; Hovakimyan et al., 2016).

Half of the uplifted Zangezur block is composed of the MOP and the remaining part includes a succession of Mesozoic, Cenozoic and Quaternary sedimentary and volcanic rocks (Fig. 2; Karamyan et al., 1974; Tayan et al., 1976; Karamyan, 1978). The MOP outcrops over ~1000 km^2 and is well-defined by three long-lived intrusive magmatic suites including, (1) Middle Eocene medium- to high-K calc-alkaline magmatism (hereafter referred to as series 1) from 48.9 to 43.1 Ma, including the emplacement of an early granite at 48.9 Ma and a tonalite at 47.6 Ma, followed by the emplacement of gabbro-diorite-tonalite intrusions (45.9-43.1 Ma); (2) Late Eocene - Middle Oligocene episodic shoshonitic to high-K calc-alkaline magmatism (hereafter referred to as series 2) from 37.8 to 28.1 Ma, characterized by the successive emplacement of alkaline gabbroids, monzogabbro, monzonite and syenite; and (3) Late Oligocene - Early Miocene high-K calc-alkaline "adakite-like" magmatism (hereafter referred to as series 3) from 26.6 to 21.2 Ma including an early generation of lamprophyre dikes followed by the emplacement of porphyritic granodioritic intrusions and dikes (Fig. 2; Table 1; Karamyan et al., 1974; Karamyan, 1978; Melkonyan, et al., 2008, 2010; Rezeau et al., 2016). Petrographic characteristics of the different rock types of the MOP can be found in Moritz et al. (2016a) and extensive descriptions are provided in Chapter 3. Based on this detailed framework, we use temporal geochemical variations observed in the MOP to (1) compare the three successive magmatic series, (2) study the variations in the mantle source partial melting that can explain the distinct geochemical composition of the parental magmas, and (3) link the incremental assembly of the MOP with the regional geodynamic evolution.

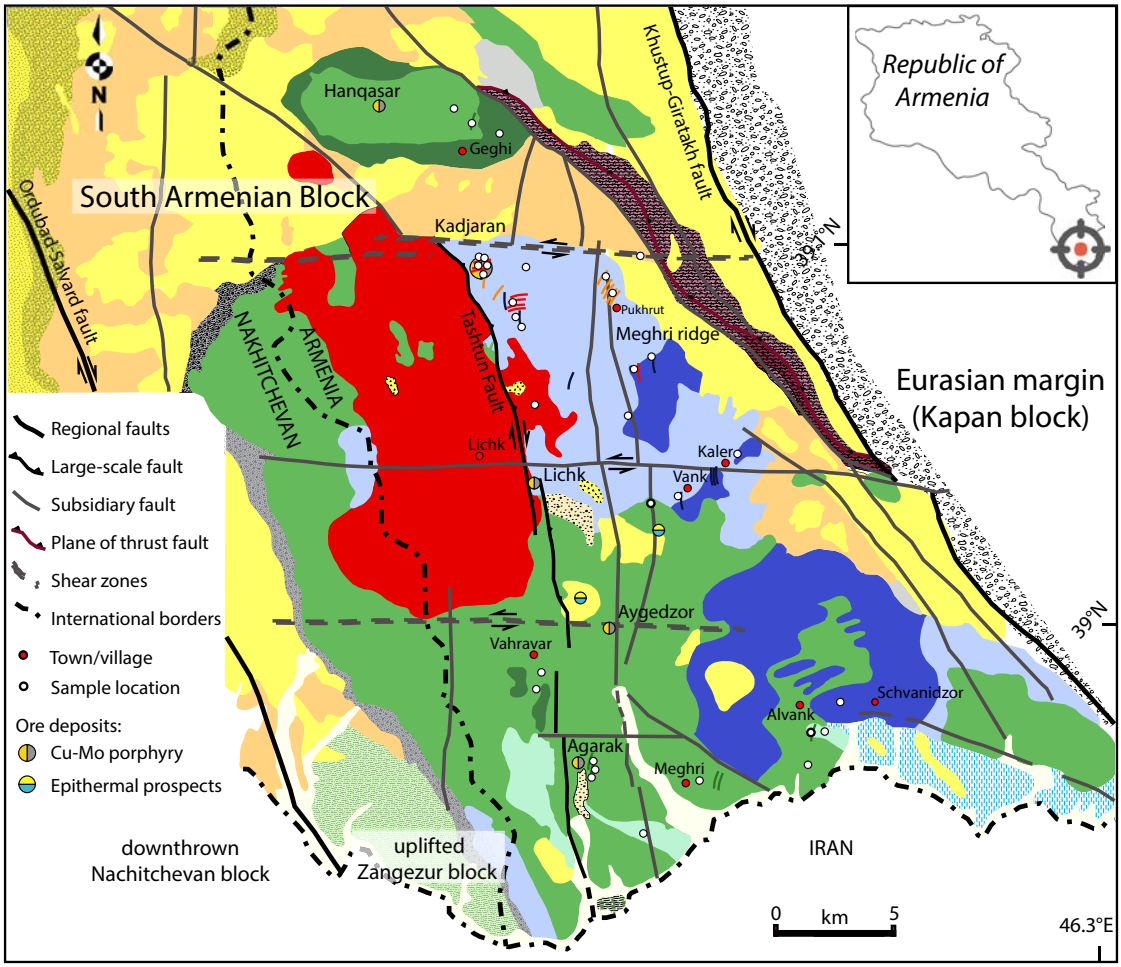

Intrusive rocks (Meghri-Ordubad Pluton)

Late Oligocene - Early Miocene (26.6 - 21.2 Ma)

- E-W porphyritic granodioritic dike
- Porphyritic granodiorite
- NNE calc-alkaline lamprophyres

Late Eocene - Middle Oligocene (37.8 - 28.1 Ma)

- NNE trachyandesitic and syenitic dike
- Monzonite - Quartz-monzonite
- Gabbro - Monzogabbro - Monzodiorite

Middle Eocene (49.9 - 43.1 Ma)

- NNE basaltic-andesitic dike
- Diorite to Tonalite
- Gabbro - Monzodiorite
- Tonalite - Granite

Volcano-sedimentary rocks

- Alluvial sediments (Quaternary)
- Sisian and Nor Arevik suites: terrigenous lacustrine sediments (Late Pliocene)
- Andesite - dacite (EarlyMiocene - Early Pliocene)
- Limestone, sandstone and ophiolitoclastic conglomerate (Oligocene - Early Miocene)
- Geghakar suite: basalt - andesite and tuffaceous sandstone (Middle Eocene)
- Hornfels with pyroxene-epidote (Middle Eocene)
- Kaputjugh suite: basalt - andesitic breccia and tuff (Middle Eocene)
- Piramsar suite: flysch - terrigeneous carbonate (Late Cretaceous - Middle Eocene)
- Organic-rich limestone with chert (Early Cretaceous)
- Shvanidzor suite: silicified limestone and andesite-rhyolite (Late Jurassic - Early Cretaceous)
- Khustup suite: basalt-andesite, tuffaceous sandstone and limestone (Late Jurassic)
- Bitumous limestone with corals and foraminifera (Middle Devonian - Late Permian)

Figure 2: Geological map of the Zangezur-Ordubad area showing the composite Meghri-Ordubad pluton and surrounding volcano-sedimentary rocks, the main structural features and the location of major porphyry Cu-Mo and epithermal deposits and prospects. Modified after Karamyan et al. (1974) and the updated version of Djrbashyan & Tayan (2008). The top right inset shows the location of the MOP in the southern Republic of Armenia.

Table 1: Sample descriptions of the Meghri-Ordubad pluton

Samples	Dates (Ma)*	Location (see Fig. 2)	Longitude	Latitude	Rock type		Mineralogical assemblage
AG1304A	48.9 ± 0.6	Agarak area	E46 11.734	N38 53.804	Granite	coarse	*Main phases:* quartz, plagioclase, K-feldspar,amphibole and biotite. *Accessory:* zircon and oxide.
MA1501	47.6 ± 0.6	Alvank area	E46 19.892	N38 56.303	Tonalite	coarse	*Main phases:* plagioclase, amphibole, K-feldspar, biotite and quartz. *Accessory:* zircon, apatite, and oxide.
AG1401	45.9 ± 0.9	Vahravar area	E46 10.329	N38 57.179	Hornblende Gabbro	cumulate	*Main phases:* plagioclase and amphibole ± clinopyroxene. *Accessory:* zircon, apatite, and titanite.
AG1404	44.8 ± 0.9	Alvank area	E46 17.324	N38 55.012	Diorite	coarse	*Main phases:* plagioclase, amphibole, biotite, quartz and K-feldspar. *Accessory:* zircon, apatite, titanite and oxide.
VK1403	44.3 ± 0.7	Vank-Kaler road	E46 13.036	N39 02.034	Quartz Monzonite	coarse	*Main phases:* plagioclase phenocryssts, K-feldspar, quartz, biotite and amphibole. *Accessory:* zircon, apatite, titanite and oxide.
AG1403	44.1 ± 1	Agarak area	E46 17.324	N38 55.012	Diorite	coarse	*Main phases:* plagioclase, amphibole ± clinopyroxene, biotite, quartz and K-feldspar. *Accessory:* zircon, apatite, titanite and oxide.
AG1406	44 ± 0.9	Alvank area	E46 19.892	N38 56.303	Basalt-andesite	dike (NNE-oriented)	*Main phases:* plagioclase phenocrysts, amphibole, biotite, quartz and K-feldspar. *Accessory:* zircon, apatite and oxide.
AG1402	43.8 ± 0.6	Vahravar area	E46 10.329	N38 57.179	Diorite	coarse	*Main phases:* plagioclase, amphibole ± clinopyroxene, biotite, quartz and K-feldspar. *Accessory:* zircon, apatite and oxide.
HQ1402	42.9 ± 0.5	Hanqasar/Geghi area	E46 08.393	N39 13.702	Monzodiorite	coarse	*Main phases:* plagioclase and amphibole ± biotite, quartz and K-feldspar. *Accessory:* zircon, apatite and oxide.
HQ1403	43.1 ± 0.5	Hanqasar/Geghi area	E46 07.348	N39 13.805	Tonalite	coarse	*Main phases:* plagioclase, amphibole, biotite, quartz and K-feldspar. *Accessory:* zircon, apatite and oxide.
AG1302A	-	Agarak area	E46 11.733	N38 53.804	Trachybasalt	enclave	*Main phases:* plagioclase phenocrysts and plagioclase, pyroxene, amphibole. *Accessory:* mineral: oxide
HQ1404	-	Hanqasar/Geghi area	E46 07.948	N39 13.743	Granite	dike (NNE-oriented)	*Main phases:* plagioclase, quartz, K-feldspar and minor amphiboles. *Accessory:* zircon, apatite and oxide.
AG1308A1	37.8 ± 0.8	Schvanidzor area	E46 22.594	N38 56.873	Monzogabbro	coarse	*Main phases:* plagioclase, clinopyroxene, amphibole, biotite and K-feldspar. *Accessory:* zircons, apatite and oxide.
AG1308A	37 ± 0.4	Schvanidzor area	E46 22.594	N38 56.873	Monzodiorite	coarse	
VK1404	35.7 ± 0.6	Near Kaler	E46 16.975	N39 03.411	Monzogabbro	coarse	*Main phases:* plagioclase, clinopyroxene, biotite, and K-feldspar. *Accessory:* zircon, apatite and oxide.
VK1405	34.8 ± 0.5	Near Kaler	E46 16.975	N39 03.411	Monzodiorite	coarse	*Main phases:* plagioclase, clinopyroxene, biotite, and K-feldspar. *Accessory:* zircon, apatite and oxide.
MR1403	34.6 ± 0.6	Meghri ridge	E46 14.495	N39 05.877	Monzodiorite	coarse	*Main phases:* plagioclase, clinopyroxene, olivine, biotite, and K-feldspar. *Accessory:* zircon, baddeleyite, apatite and oxide.
LI1303A1	33.5 ± 0.6	Vank.Kaler road	E46 15.578	N39 03.458	Monzogabbro	coarse	*Main phases:* plagioclase, clinopyroxene, and biotite. *Accessory:* zircon, apatite and oxide.
LI1303	33.6 ± 0.6	Vank-Kaler road	E46 15.578	N39 03.458	Syenite	dike (NNE-oriented)	*Main phases:* plagioclase, K-feldspar, clinopyroxene, biotite and quartz. *Accessory:* zircon, apatite and oxide.
MR1402	33.49 ± 0.02	Meghri ridge	E46 13.287	N39 06.159	Hornblende Gabbro	cumulate	*Main phases:* plagioclase, amphibole, clinopyroxene and biotite. *Accessory:* zircon, apatite and oxide.

KJ1316	33.7 ± 0.5	Meghri ridge	E46 13.287	N39 06.159	Trachyandesite	Dike (NNE-oriented)	*Main phases:* plagioclase, amphibole, clinopyroxene, biotite, K-feldspar and quartz. *Accessory:* zircon, apatite and oxide.
KJ1006A	31.9 ± 0.5	Kadjaran ore field	E46 12.745	N39 09.076	Monzonite	coarse	*Main phases:* plagioclase, amphibole, clinopyroxene, biotite, and K-feldspar. *Accessory:* zircon, apatite and oxide.
KJ1308	31.1 ± 0.5	Road to Meghri	E46 11.134	N39 08.656	Syenite	sill	*Main phases:* K-feldspar, plagioclase, quartz, amphibole and biotite. *Accessory:* zircon, apatite and oxide.
KJ1508	28.3 ± 0.4	Kadjaran open pit	E46 08.416	N39 08.840	Gabbro (weakly altered)	coarse	*Main phases:* plagioclase, amphibole and clinopyroxene + alteration minerals. *Accessory:* zircon, apatite and oxide.
KJ1318	-	Meghri ridge	E46 13.287	N39 06.159	Trachyandesite	Dike (NNE-oriented)	*Main phases:* plagioclase, amphibole, clinopyroxene, biotite, K-feldspar and quartz. *Accessory:* zircon, apatite and oxide.
KJ1319	-	Meghri ridge	E46 13.287	N39 06.159	hornblende gabbro	enclaves	*Main phases:* plagioclase, amphibole, clinopyroxene, biotite. *Accessory:* zircon, apatite and oxide.
VK1406	-	Vank-Kaler road	E46 15.894	N39 03.981	Trachyandesitic dike	dike (NNE-oriented)	*Main phases:* plagioclase phenocrysts, plagioclase and minor biotite minerals. *Accessory:* zircon, apatite and oxide.
MR1404	-	Meghri ridge	E46 14.495	N39 05.877	Essexite	dike (NNE-oriented)	*Main phases:* clinopyroxene, amphibole, biotite and nepheline. *Accessory:* sulfide and oxide.
KJ1302A	26.6 ± 0.3	Kadjaran Open pit	E46 08.414	N39 08.757	Trachyandesite	altered dike (NNE-oriented)	*Main phases:* clinopyroxene, amphibole and plagioclase phenocrysts, and sanidine matrix. *Accessory:* zircon, apatite and oxide.
KJ1303A	25.5 ± 0.3	Near Pukhrut	E46 12.629	N39 07.513	Trachybasalt	lamprophyre dike (NNE-oriented)	*Main phases:* olivine pseudomorph phenocrysts, amphibole, phlogopite and sanidine. *Accessory:* zircon, apatite and oxide.
MR1401	24.5 ± 0.4	Meghri Ridge	E46 12.808	N39 06.430	Porphyritic trachyandesite	dike (NNE-oriented)	*Main phases:* plagioclase and biotite phenocrysts, amphibole pseudomorph, pyroxene pseudomorph, and K-feldspar matrix. *Accessory:* zircon, apatite and oxide.
KJ1307	24.3 ± 0.3	Road to Pukhrut	E46 12.907	N39 08.182	Trachybasalt	lamprophyre dike (NNE-oriented)	*Main phases:* clinopyroxene, amphibole and plagioclase phenocrysts, and sanidine matrix. *Accessory:* zircon, apatite and oxide.
LI1301	22.6 ± 0.5	Lichk area	E46 10.368	N39 01.780	Porphyritic granodiorite	coarse	*Main phases:* plagioclase, K-feldspar, amphibole, biotite and quartz. *Accessory:* zircon, apatite, titanite and oxide.
KJ1324A	22.2 ± 0.3	Kadjaran Open pit	E46 08.026	N39 08.972	Porphyritic granodioritic	altered dike (EW-oriented)	*Main phases:* plagioclase, biotite and amphibole phenocrysts and fine-grained matrix. *Accessory:* zircon, apatite and oxide.
KJ1325A	22.2 ± 0.3	Kadjaran Open pit	E46 08.026	N39 08.972	Porphyritic granodioritic	altered dike (EW-oriented)	*Main phases:* plagioclase, biotite and amphibole phenocrysts and fine-grained matrix. *Accessory:* zircon, apatite and oxide.
KJ1313	21.2 ± 0.3	Road to Meghri	E46 11.054	N39 08.547	Porphyritic dioritic	dike (EW-oriented)	*Main phases:* plagioclase, biotite and amphibole phenocrysts and fine-grained matrix. *Accessory:* zircon, apatite and oxide.
LI1401	-	Road to Meghri	E46 13.590	N39 02.126	Trachybasalt-trachyandesite	dike (NNE-oriented)	*Main phases:* K-feldspar, biotite and clinopyroxene. *Accessory:* zircon, apatite and oxide.

* From Rezeau et al. (2016) except for sample MR1402 from Moritz et al. (2016a).

4. ANALYTICAL METHODS

Thirty-seven whole-rock samples from the MeghriÐOrdubad pluton were analyzed for major and trace element composition (Table 2), of which thirty samples were analyzed previously by isotope dilution - thermal ionization mass spectrometry (ID-TIMS) and laser ablation Ð inductively coupled plasma Ðmass spectrometer (LA-ICP-MS) for zircon U-Pb dating (Table 1; Moritz et al., 2016a; Rezeau et al., 2016). We also use the data set of Moritz et al. (2016a) in some of the geochemical diagrams. Elevated loss of ignition (LOI > 2) is observed for lamprophyre and porphyritic granodioritic dike samples of magmatic series 3 (Table 2). Lamprophyre ferromagnesian phenocrysts or its groundmass are generally replaced by carbonates, due to the high volatile content of such rocks, also called deuteric alteration of primary minerals (e.g., Rock, 1991; Prelević et al., 2004), whereas porphyritic granodioritc dikes suffered late hydrothermal alteration, but their geochemical composition (K, Na, Ba, Rb, Th, Sr) remains consistent with respect to the data set of Moritz et al. (2016a) for similar unaltered dikes. Samples were crushed using a steel jaw crusher and a hydraulic press to finally be powdered to <70 µm using a mortar agate mill at the University of Geneva, Switzerland. Major elements were analyzed on fused sample powder mixed (5:1) with lithium tetraborate ($Li_2B_4O_7$) glass beads by X-ray fluorescence (XRF) using a Philips PW 2400 spectrometer at the University of Lausanne, Switzerland. The 2σ uncertainties are <1%, except for MgO and K_2O <3%, based on repeated measurements of the BHVO-1, NIM-N and NIM-G standards. Loss on ignition (LOI) was determined based on the mass difference of 2Ð3 g of dried (110¡C) powdered rock before and after heating to 1050 ¡C. Trace element concentrations were determined by LA- ICP-MS at the University of Lausanne on the same glass beads as used for major element analysis, using a sector-field Element XR ICP mass spectrometer interfaced to an UP-193FX 193 nm Excimer ablation system. The spectrometer was operated at low resolution; it was optimized for a maximum sensitivity at ThO^+/Th^+ and $Ba^{2+/}Ba^+$ ratios of ~0.10% and <2.9%, respectively. The on-sample laser beam fluence was set at 5 J/cm^2 at a laser pulse repetition rate of 10 Hz; the pit size was 100 µm. Helium was used as a carrier gas. Background and signal were measured for 90s and 50s, respectively. Three points were measured on each sample and the results were averaged. The NIST 612 glass standard was used as external standard to calibrate the instrument mass fractionation and the spectrometer drift. Concentration values were taken from Pearce et al. (1997). The raw data were reduced using LAMTRACE (Jackson, 2008) and calcium concentration previously obtained by XRF was used as internal standard.

Twenty-nine samples were analyzed for whole-rock Pb, Sr and Nd isotopic compositions following the method described by BŽguelin et al. (2015) at the University of Geneva, Switzerland. Results are given in Table 3. Strontium, neodymium and lead isotope

separation was carried out using cascade columns with Sr-spec, TRU-spec and Ln-spec resins following a modified method after Pin et al. (1994). The analyses were carried out in static mode using a Thermo Triton thermal ionization mass spectrometer on Faraday cups. Lead was loaded on Re filaments using the silica gel technique. Samples and standards were measured at a pyrometer-controlled temperature of 1220 ¡C. Lead isotope ratios were corrected for instrumental fractionation by a factor of 0.07% per a.m.u. based on the SRM981 standard and using the standard values of Todt et al. (1996). External reproducibility of the standard ratios are 0.08% for $^{206}Pb/^{204}Pb$, 0.11% for $^{207}Pb/^{204}Pb$ and 0.15% for $^{208}Pb/^{204}Pb$. Strontium was loaded on single Re filaments with a Ta oxide solution and measured at a pyrometer-controlled temperature of 1480 ¡C in static mode. $^{87}Sr/^{86}Sr$ ratios were internally corrected for fractionation using a $^{88}Sr/^{86}Sr$ ratio of 8.375209. Raw values were further corrected for external fractionation by a value of +0.03%, determined by repeated measurements of the SRM987 standard ($^{87}Sr/^{86}Sr$ = 0.710250). External reproducibility of the $^{87}Sr/^{86}Sr$ ratio for the SRM987 standard is 7 ppm. Neodymium was loaded on double Re filaments with 1 M HNO_3 and measured in static mode. $^{143}Nd/^{144}Nd$ ratios were internally corrected for fractionation using a $^{146}Nd/^{144}Nd$ ratio of 0.7219 and the ^{144}Sm interference on ^{144}Nd was monitored on the mass ^{147}Sm and corrected by using a $^{144}Sm/^{147}Sm$ ratio of 0.206700. External reproducibility of the JNdi-1 standard from Tanaka et al. (2000) is <5 ppm. Corrections for time-integrated decay of radioactive parents to radiogenic daughters were carried out for the samples using parent and daughter element concentrations determined by LA-ICP-MS and appropriate LA-ICP-MS zircon U-Pb age.

5. RESULTS

5.1 Whole-rock major and trace elements geochemistry

Three differentiation magmatic series were recognized in the MOP: series 1 is characterized by medium-K to high-K calc-alkaline gabbro to granite, series 2 is composed of high-K calc-alkaline to shoshonitic gabbro to syenite, and series 3 is defined by high-K calc-alkaline lamprophyre and porphyritic granodiorite (Figs. 3a,b; Peccerillo & Taylor, 1976; Middlemost, 1994). All three intrusive suites display negative correlations of TiO_2, CaO, MgO, FeO_{tot}, P_2O_5 with increasing SiO_2, whereas Na_2O and K_2O are positively correlated with the latter (Figs. 3b-f; Table 2). Series 1 and 2 display negative trends of Al_2O_3 through differentiation, reflecting the effect of plagioclase fractionation (Fig. 3d). By contrast, the Al_2O_3 content in series 3 is positively correlated with SiO_2 and is attributed to limited plagioclase fractionation during differentiation (Fig. 3d). The P_2O_5 content is higher for series 2

Table 2. Samples whole-rock major (XRF) and trace elements (LA-ICP-MS, XRF) geochemistry.

Samples	AG1406	AG1302A	HQ1402	AG1401	AG1304A	MA1501	AG1404	VK1403	AG1403	AG1402	HQ1403	HQ1404	AG1308A1	VK1404	VK1405	MR1403	LI1303A1	KJ1319
Rock type	Basalt-Andesite	Trachybasalt	Monzodiorite	Hornblende Gabbro	Granite	Tonalite	Diorite	Quartz Monzonite	Diorite	Diorite	Tonalite	Granite	Monzogabbro	Monzogabbro	Monzodiorite	Monzodiorite	Monzogabbro	Hornblende gabbro
Dates (Ma)	**44**	-	**42.9**	**45.9**	48.9	47.6	44.8	44.3	44.1	43.8	43.1	-	**37.8**	**35.7**	**34.8**	**34.6**	**33.5**	-
Major elements (wt%)																		
SiO_2	**55.1**	**55.9**	**52.2**	**45.8**	70.3	64.9	60.6	65.9	58.3	59.6	63.9	66.0	**47.4**	**49.0**	**53.0**	**52.7**	**47.9**	**54.2**
TiO_2	**0.7**	**0.8**	**0.6**	**0.9**	0.3	0.5	0.6	0.6	0.9	0.7	0.4	0.3	**1.1**	**0.9**	**0.5**	**0.7**	**0.9**	**0.7**
Al_2O_3	**17.1**	**16.6**	**21.8**	**20.2**	15.3	15.8	16.4	15.0	13.9	16.2	16.4	15.7	**19.7**	**17.9**	**21.3**	**20.0**	**21.5**	**17.7**
Fetot	**7.5**	**10.2**	**6.1**	**9.5**	2.3	4.7	6.0	4.2	9.0	6.3	3.9	3.1	**7.9**	**8.5**	**5.5**	**5.7**	**7.9**	**7.5**
MnO	**0.1**	**0.1**	**0.2**	**0.2**	0.0	0.1	0.1	0.1	0.2	0.2	0.1	0.1	**0.2**	**0.2**	**0.1**	**0.1**	**0.1**	**0.2**
MgO	**4.7**	**3.6**	**2.4**	**5.4**	0.5	1.9	2.8	1.1	4.2	3.0	1.7	1.0	**3.8**	**5.2**	**2.1**	**2.6**	**3.4**	**3.7**
CaO	**8.0**	**2.7**	**9.2**	**11.5**	2.4	5.0	5.9	3.4	5.6	6.7	4.7	2.7	**8.6**	**10.2**	**8.3**	**7.2**	**10.9**	**7.6**
Na_2O	**3.7**	**4.1**	**4.3**	**2.3**	5.8	3.5	3.4	3.2	2.6	3.2	3.9	3.7	**4.1**	**3.5**	**4.1**	**4.6**	**3.3**	**4.7**
K_2O	**1.2**	**2.8**	**1.0**	**1.1**	0.5	2.1	2.3	4.5	2.4	1.9	2.9	4.6	**3.3**	**1.5**	**2.5**	**3.8**	**1.6**	**1.2**
P_2O_5	**0.1**	**0.2**	**0.3**	**0.4**	0.1	0.2	0.2	0.2	0.2	0.2	0.2	0.1	**0.7**	**0.5**	**0.7**	**0.5**	**0.5**	**0.4**
Mg#	**0.5**	**0.4**	**0.4**	**0.5**	0.3	0.4	0.5	0.3	0.5	0.5	0.4	0.4	**0.5**	**0.5**	**0.4**	**0.5**	**0.4**	**0.5**
LOI	**0.46**	**0.83**	**0.57**	**0.65**	0.86	0.33	0.48	0.57	0.73	0.37	0.5	1.37	**1.61**	**0.36**	**0.4**	**0.57**	**0.91**	**0.63**
Trace elements (ppm)																		
Rb	**34.6**	**73.0**	**17.4**	**52.7**	13.2	*44.1*	53.7	145.9	57.0	38.1	72.6	106.9	**86.7**	**41.9**	**68.8**	**94.3**	**40.6**	**22.6**
Ba	**575.3**	**562.2**	**703.5**	**210.6**	159.9	*475.9*	695.1	736.1	668.4	646.2	857.4	1168.5	**1223.3**	**741.0**	**947.4**	**1185.7**	**469.8**	**560.0**
Sr	**433.9**	**203.9**	**1511.2**	**467.7**	332.4	*268.5*	407.4	179.9	297.9	405.3	652.4	382.3	**1907.1**	**1371.1**	**1534.7**	**1470.0**	**1332.9**	**809.3**
Th	**3.6**	**5.7**	**0.9**	**2.2**	12.1	*5.9*	5.9	11.1	6.4	4.0	7.4	12.9	**10.8**	**16.1**	**25.9**	**26.7**	**8.1**	**8.0**
U	**1.0**	**1.8**	**0.4**	**1.0**	2.9	*1.7*	1.3	3.4	1.7	1.0	2.3	2.6	**2.4**	**3.4**	**4.6**	**6.9**	**1.9**	**1.7**
Nb	**4.0**	**3.5**	**3.5**	**2.8**	6.5	*6.3*	6.4	12.7	9.3	6.9	5.9	6.0	**43.0**	**9.8**	**23.7**	**23.9**	**13.7**	**9.8**
Ta	**0.3**	**0.3**	**0.1**	**0.2**	0.6	-	0.4	0.8	0.5	0.5	0.4	0.4	**1.8**	**0.5**	**1.1**	**1.0**	**0.5**	**0.6**
K	**10328.9**	**23048.8**	**8584.0**	**9154.2**	4526.0	-	19166.5	36976.9	20188.8	15714.0	24283.3	37904.3	**26983.1**	**12076.0**	**21166.1**	**31529.6**	**13436.3**	**9981.0**
Pb	**6.8**	**4.4**	**9.2**	**5.4**	2.2	*2.5*	10.0	21.7	9.2	9.0	11.3	11.2	**8.9**	**9.6**	**11.6**	**19.8**	**11.1**	**19.8**

Zr	**78.2**	**79.2**	**83.9**	**46.9**	200.0	*100.3*	128.2	354.2	167.1	139.0	123.5	195.2	**294.5**	**139.1**	**250.2**	**257.7**	**151.1**	**113.2**
Hf	**2.3**	**2.5**	**2.0**	**1.4**	5.1	-	3.7	9.7	4.8	3.8	3.4	5.3	**7.0**	**3.6**	**5.5**	**5.7**	**3.6**	**3.0**
Ti	**4953.7**	**5835.0**	**3986.6**	**6420.5**	2395.9	-	4488.1	4526.1	6380.5	4743.9	2845.6	2288.0	**7549.5**	**6488.4**	**3782.7**	**5161.6**	**5595.5**	**5229.5**
La	**11.5**	**13.9**	**12.4**	**9.4**	18.0	*18.8*	17.5	23.4	20.6	18.3	19.4	24.5	**105.5**	**60.8**	**67.1**	**87.4**	**45.4**	**33.4**
Ce	**23.9**	**27.3**	**25.6**	**21.0**	32.6	*22.7*	35.3	52.3	46.5	37.3	36.7	42.9	**187.9**	**111.1**	**122.5**	**157.0**	**86.7**	**56.7**
Nd	**12.8**	**14.5**	**14.3**	**12.9**	12.6	*10.8*	17.4	27.2	26.2	19.0	16.3	16.9	**64.3**	**49.0**	**47.2**	**60.9**	**40.9**	**23.0**
Sm	**3.1**	**3.4**	**3.2**	**3.4**	2.4	-	3.9	6.1	6.1	4.3	3.2	3.0	**10.4**	**8.8**	**7.8**	**9.8**	**7.6**	**4.4**
Eu	**0.8**	**1.1**	**1.2**	**1.1**	0.6	-	1.0	1.0	1.0	1.2	0.9	0.8	**2.7**	**2.4**	**2.1**	**2.6**	**1.9**	**1.3**
Gd	**3.2**	**3.6**	**3.1**	**3.8**	2.3	-	3.8	6.0	5.8	4.2	2.8	2.8	**7.6**	**6.9**	**6.0**	**7.3**	**6.1**	**3.9**
Tb	**0.5**	**0.5**	**0.5**	**0.6**	0.3	-	0.6	1.0	0.9	0.6	0.4	0.4	**0.9**	**0.8**	**0.7**	**0.9**	**0.8**	**0.5**
Dy	**3.5**	**3.7**	**3.0**	**4.0**	2.4	-	4.1	6.6	6.4	4.4	2.5	2.8	**5.3**	**4.5**	**4.2**	**4.9**	**4.6**	**3.3**
Y	**19.3**	**20.2**	**16.4**	**20.4**	14.7	*15.9*	22.8	37.9	37.2	24.6	14.5	15.9	**26.9**	**21.5**	**20.8**	**25.1**	**22.6**	**17.4**
Ho	**0.7**	**0.7**	**0.6**	**0.8**	0.5	-	0.8	1.3	1.3	0.9	0.5	0.6	**1.0**	**0.8**	**0.8**	**0.9**	**0.8**	**0.6**
Er	**2.1**	**2.2**	**1.7**	**2.3**	1.6	-	2.4	4.2	4.1	2.7	1.5	1.7	**2.6**	**2.2**	**2.0**	**2.5**	**2.2**	**1.8**
Yb	**2.3**	**2.3**	**1.8**	**2.1**	2.2	-	2.7	4.5	4.4	2.9	1.7	1.8	**2.6**	**1.9**	**1.9**	**2.4**	**2.0**	**1.8**
Lu	**0.4**	**0.4**	**0.3**	**0.3**	0.4	-	0.4	0.7	0.7	0.4	0.3	0.3	**0.4**	**0.3**	**0.3**	**0.4**	**0.3**	**0.3**
Pr	**3.0**	**3.4**	**3.2**	**2.7**	3.5	-	4.2	6.5	6.0	4.5	4.2	4.6	**18.7**	**12.4**	**12.9**	**16.6**	**10.0**	**6.0**
Cr	**100.4**	**17.8**	**12.1**	**10.3**	26.7	*16.4*	21.7	15.7	20.4	21.6	52.7	15.2	**47.4**	**18.8**	**21.3**	**16.2**	**2.8**	**23.6**
Ni	**22.8**	**6.5**	**5.1**	**14.2**	2.0	*3.1*	5.6	3.0	8.2	6.1	11.2	2.8	**17.2**	**15.6**	**14.2**	**6.3**	**3.6**	**14.9**

in bold: least differentiated (i.e., assumed parental magmas and cumulates)

in italic: trace elements values analyzed by XRF.

Table 2. continued.

Samples	KJ1508	MR1402	MR1404	AG1308A	LI1303	KJ1316	KJ1006A	KJ1308	KJ1318	VK1406	LI1401	KJ1303A1	KJ1307	MR1401	KJ1302A	LI1301	KJ1325A	KJ1324A	KJ1313
Rock type	Gabbro	Hornblende gabbro	Essexite	Monzodiorite	Syenite	Trachyandesite	Monzonite	Syenite	Trachyandesite	Trachyandesite	Trachybasalt	Trachybasalt	Trachybasalt	Trachyandesite	Trachyandesite	Granodiorite	Granodiorite	Granodiorite	Granodiorite
Dates (Ma)	**28.3**	**33.49**	**34**	37	33.6	33.7	31.9	31.1	-	34.8	**-**	**25.5**	**24.3**	24.5	26.6	22.6	22.2	22.2	21.2
Major elements (wt%)																			
SiO_2	**47.5**	**41.7**	**41.9**	53.5	59.8	60.3	57.1	60.9	57.9	57.8	**51.0**	**46.9**	**51.0**	61.4	58.4	66.7	61.3	62.9	58.4
TiO_2	**1.0**	**1.5**	**1.2**	0.5	0.6	0.5	0.8	0.9	0.5	0.7	**1.1**	**1.1**	**0.8**	0.6	0.6	0.5	0.4	0.4	0.6
Al_2O_3	**18.3**	**19.0**	**17.0**	22.5	18.5	17.5	18.6	18.7	17.7	18.6	**13.7**	**13.7**	**14.1**	15.5	14.2	14.9	14.3	15.2	14.9
Fetot	**9.3**	**10.7**	**9.9**	3.8	4.3	4.8	4.8	3.8	5.7	5.2	**7.7**	**6.8**	**6.0**	4.0	4.2	2.9	2.9	3.3	4.1
MnO	**0.2**	**0.2**	**0.2**	0.1	0.1	0.1	0.1	0.1	0.1	0.1	**0.2**	**0.1**	**0.1**	0.1	0.1	0.0	0.1	0.1	0.1
MgO	**6.0**	**6.8**	**5.7**	1.3	1.3	1.8	2.0	1.0	2.2	2.2	**8.3**	**7.1**	**7.8**	2.3	1.7	2.0	2.1	1.7	1.5
CaO	**10.5**	**12.9**	**12.4**	7.2	3.4	5.1	4.0	2.0	6.0	3.3	**8.0**	**8.6**	**7.2**	4.1	4.4	3.2	4.2	2.8	6.2
Na_2O	**2.9**	**2.3**	**5.3**	5.0	5.3	4.4	4.3	3.6	4.3	4.9	**4.0**	**2.8**	**3.2**	3.7	0.2	4.0	1.5	1.4	3.6
K_2O	**1.0**	**0.7**	**2.0**	3.4	5.4	3.6	6.0	8.0	3.1	4.0	**2.2**	**2.4**	**2.0**	3.9	6.7	3.7	4.0	3.6	3.5
P_2O_5	**0.6**	**1.2**	**0.8**	0.3	0.3	0.4	0.4	0.2	0.5	0.4	**0.6**	**0.6**	**0.4**	0.3	0.4	0.2	0.2	0.2	0.4
Mg#	**0.5**	**0.5**	**0.5**	0.4	0.4	0.4	0.4	0.3	0.4	0.4	**0.7**	**0.7**	**0.7**	0.5	0.4	0.6	0.6	0.5	0.4
LOI	**1.09**	**0.53**	**0.87**	1.05	0.49	0.34	0.71	0.5	0.52	1.22	**1.41**	**8.76**	**6.59**	2.97	6.48	0.61	8.6	8.15	5.56
Trace elements (ppm)																			
Rb	***54.5***	**11.6**	**39.4**	78.3	125.9	100.3	179.3	185.8	82.3	82.6	**63.4**	**46.4**	**46.2**	102.9	191.2	93.0	133.6	108.7	77.9
Ba	***483.9***	**455.1**	**1464.1**	1221.9	1142.3	1263.0	834.7	1843.1	1259.1	1159.1	**792.4**	**1293.4**	**566.2**	901.7	1261.3	649.4	752.8	779.2	937.0
Sr	***1369.7***	**1816.7**	**2188.0**	2891.8	665.4	1104.0	692.0	512.0	1181.4	732.0	**1071.9**	**2370.0**	**759.3**	802.0	225.8	616.3	404.4	433.6	719.7
Th	***3.4***	**4.4**	**10.4**	13.6	33.4	23.7	19.6	16.0	19.7	37.6	**8.8**	**6.9**	**11.8**	20.8	17.3	23.2	16.8	14.6	15.5
U	***8.3***	**1.1**	**1.4**	3.6	6.7	4.0	5.3	4.9	3.7	11.2	**3.4**	**2.3**	**3.8**	7.8	6.9	3.4	6.1	3.6	4.4
Nb	***4.3***	**11.9**	**8.5**	27.0	28.7	23.7	38.1	31.3	16.2	31.2	**12.2**	**12.6**	**10.5**	13.2	10.1	11.5	10.3	9.6	12.2
Ta	-	**0.5**	**0.4**	1.2	1.4	1.5	1.8	1.8	1.0	1.5	**0.7**	**0.7**	**0.7**	1.0	0.6	0.9	0.8	0.7	0.8
K	-	**5697.3**	**16703.2**	28593.3	44487.6	29655.9	50195.1	66258.4	25537.4	33043.1	**18167.1**	**20282.0**	**16687.6**	31970.7	56999.1	30857.3	33403.5	29579.4	29178.1
Pb	***1.5***	**5.6**	**7.5**	12.5	17.7	10.4	24.2	13.2	11.0	12.6	**8.3**	**11.8**	**13.0**		133.5	9.7	13.4	17.7	
Zr	***31.6***	**71.8**	**95.8**	214.1	387.8	213.3	200.7	1000.6	183.6	348.8	**117.3**	**138.2**	**124.7**	167.3	176.7	131.8	114.1	123.4	134.9

Hf	-	**2.5**	**2.9**	4.7	7.4	5.4	5.3	23.6	4.5	7.6	**3.2**	**3.3**	**2.9**	4.5	4.4	3.6	2.9	3.3	3.4
Ti	-	**10391.1**	**8202.9**	3634.9	3523.1	3495.0	4940.2	5369.5	3872.7	4909.8	**7905.2**	**6363.3**	**4708.2**	4204.4	3882.1	3253.2	2521.8	2642.5	3872.4
La	***28.4***	**68.2**	**103.5**	86.0	79.5	63.8	77.1	25.8	64.7	85.5	**35.8**	**37.1**	**43.2**	39.8	64.3	36.1	32.2	32.5	45.5
Ce	***45.6***	**146.7**	**195.4**	144.2	141.6	119.9	129.3	47.2	111.7	154.6	**70.7**	**71.4**	**79.5**	70.8	109.7	58.7	51.4	54.5	76.9
Nd	***26.5***	**76.5**	**85.7**	49.6	51.5	47.2	49.6	18.6	43.6	57.4	**33.7**	**32.7**	**33.8**	27.6	43.3	20.3	18.2	19.0	28.4
Sm	***5.1***	**14.3**	**14.1**	7.9	8.5	7.8	7.9	3.7	7.4	9.0	**6.4**	**6.1**	**5.9**	4.7	6.5	3.2	2.8	3.0	4.2
Eu	-	**4.1**	**3.6**	2.7	1.9	1.9	2.1	1.5	1.9	2.2	**1.8**	**1.8**	**1.5**	1.2	1.5	0.9	0.7	0.9	1.1
Gd	-	**11.4**	**9.5**	5.7	6.2	5.9	5.6	3.1	5.6	6.8	**5.0**	**4.8**	**4.4**	3.5	4.2	2.4	2.3	2.4	3.1
Tb	-	**1.3**	**1.1**	0.7	0.8	0.8	0.7	0.5	0.7	0.8	**0.6**	**0.6**	**0.5**	0.4	0.4	0.3	0.3	0.3	0.4
Dy	-	**7.3**	**5.6**	3.8	5.0	4.5	4.4	3.0	4.1	5.1	**3.3**	**3.4**	**2.9**	2.7	2.2	1.9	1.7	2.0	2.3
Y	***18.3***	**34.1**	**26.0**	18.8	27.4	24.4	21.9	19.7	20.8	27.9	**15.3**	**16.2**	**14.7**	13.2	10.5	9.5	9.4	10.2	12.8
Ho	-	**1.3**	**1.0**	0.7	0.9	0.9	0.8	0.7	0.8	1.0	**0.6**	**0.6**	**0.5**	0.5	0.3	0.3	0.3	0.4	0.5
Er	-	**3.3**	**2.6**	1.8	2.8	2.6	2.2	2.2	2.1	2.9	**1.5**	**1.5**	**1.4**	1.4	0.9	0.9	0.9	1.0	1.2
Yb	-	**2.7**	**2.2**	1.8	2.9	2.8	2.4	2.8	2.2	3.1	**1.3**	**1.4**	**1.3**	1.4	0.9	1.0	1.0	1.1	1.2
Lu	-	**0.4**	**0.3**	0.3	0.5	0.4	0.4	0.5	0.3	0.5	**0.2**	**0.2**	**0.2**	0.2	0.1	0.2	0.2	0.2	0.2
Pr	-	**18.1**	**22.0**	14.4	14.6	12.9	13.4	5.0	11.7	16.0	**8.4**	**8.1**	**8.6**	7.6	11.7	5.8	5.2	5.4	7.6
Cr	***53.8***	**14.1**	**35.8**	13.1	6.2	14.0	8.0	2.5	11.9	9.1	**450.9**	**397.9**	**279.1**	44.5	74.3	69.0	35.1	31.6	91.7
Ni	***37.2***	-	**9.2**	2.0		2.8	5.3		3.2	2.3	**159.0**	**143.7**	**200.5**	19.9	40.0	33.4	26.3	24.0	44.0

in bold: least differentiated (i.e., assumed parental magmas and cumulates)

in italic: trace elements values analyzed by XRF.

and 3, likely related to the occurrence of apatite crystals (Fig. 3f). Mg# (calculating all Fe as FeO_{tot}), Cr and Ni contents are the highest in series 3 (Mg#=0.7; Cr=279-451 ppm; Ni=144-200 ppm) compared to series 1 (Mg#=0.6-0.4; Cr=3-183 ppm; Ni=6.5-72 ppm) and series 2 (Mg#=0.6-0.4; Cr=2.8-47 ppm; Ni=3.6-18 ppm) (Figs. 3g-h). Intrusions displaying a SiO_2 content >55 wt% are interpreted as differentiated rocks. Among the least differentiated rocks (SiO_2 <55 wt%), three samples are interpreted as cumulates due to their very low SiO_2 content and their cumulate texture, whereas the others are assumed to represent parental melt composition for each differentiation series (Table 2). They are further used to discuss the evolution of the magmatic source over time and avoid major effect of crustal fractionation.

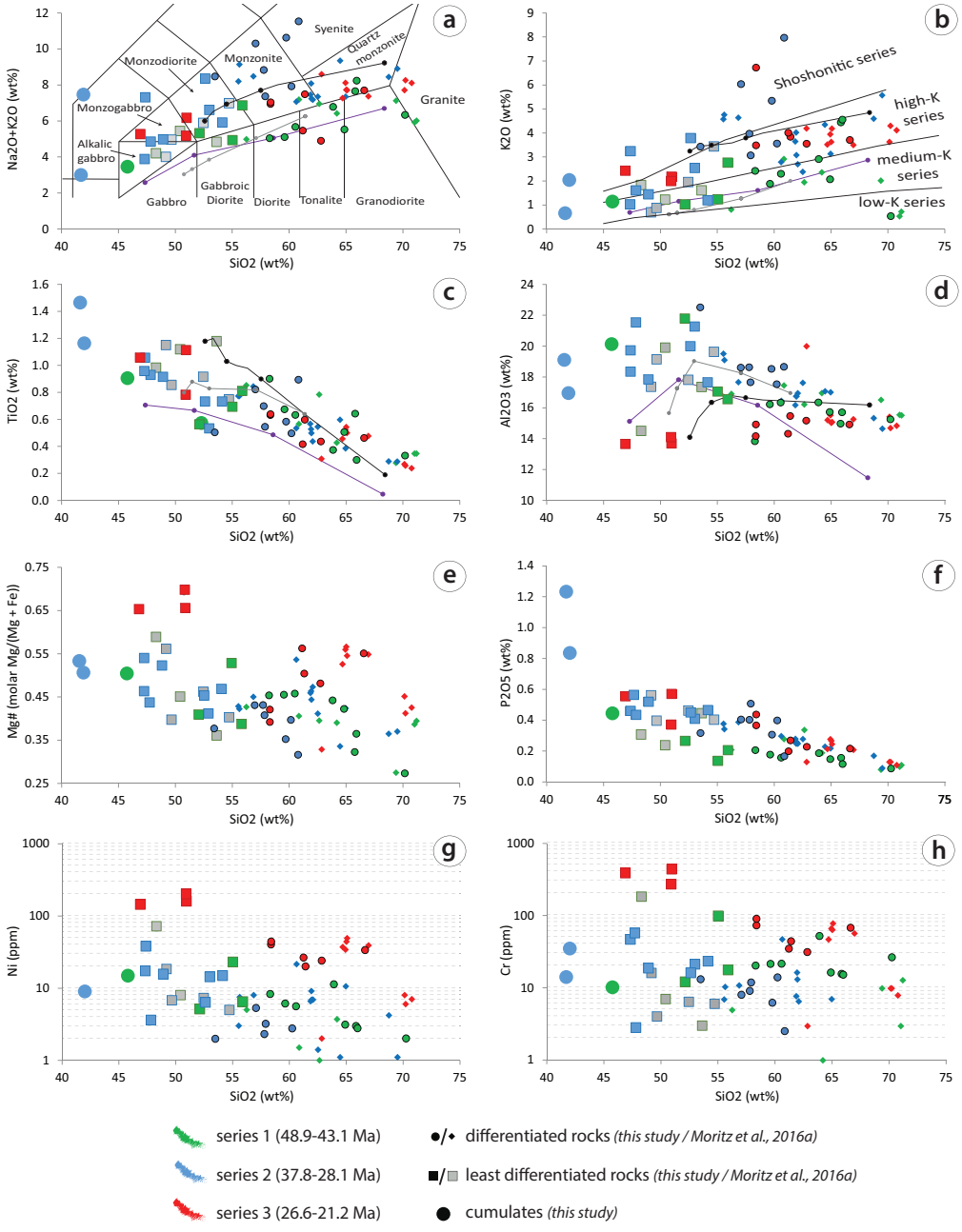

Figure 3: a) TAS diagram (Middlemost, 1994), b-f) Major elements vs. SiO_2 Harker diagrams. g-h) Ni and Cr contents vs. SiO_2. Fields in b from Peccerillo and Taylor (1976) and Mg# calculated as molar Mg/(Mg + Fe). Liquid line of descent (LLD) in a-d are from fractional crystallization experiments conducted on a primitive hydrous arc magmas at 0.7 GPa and temperatures ranging from 1170 to 700¡C (purple line; Nandedkar et al., 2014), and from field-based mass-balance fractionation models in the Kohistan arc exposed in Northern Pakistan (gray line; Jagoutz, 2010) and the Dariv igneous complex exposed in Western Mongolia (black line; Bucholz et al., 2014). Dots on LLD indicate the melt composition at 10%, 30%, 60% and 90% of melt remaining.

On multi-element plots normalized to a primitive mantle (McDonough & Sun, 1995) and a chondritic composition (C1; Sun & McDonough, 1989), all three magmatic series are characterized by marked Nb, Ta, and Ti negative anomalies (Fig. 4). The Ti negative anomaly becomes generally stronger as one progresses from mafic to felsic samples. In the magmatic series 1, felsic samples from the southern part of the MOP display negative Eu anomalies revealing plagioclase fractionation. By contrast, felsic rocks from the series 1 sampled in the northern part, together with magmatic series 2 and 3, display a concave-up shaped pattern pointing to amphibole-dominated fractionation. Least differentiated rocks from series 1 display high Ba/La (20-60) and Ba/Nb (120-200) together with low Th/Yb (<2.5) and high Pb/Ce (0.15-0.35) ratios (Figs. 5a,b). By contrast, magmatic series 2 and 3 display low Ba/La (10-20), low Ba/Nb (20-100), high Th/Yb (2.5-20) and low Pb/Ce (<2) ratios (Figs. 5a,b). Higher Sr/Y ratios (24-84 and 22-70 with one sample from each series at 154 and 146, respectively) are observed for series 2 and 3, whereas series 1 displays lower Sr/Y ratios (4.8-45 with one sample at 92 ppm; Figs. 4 and 5c). A higher range of REE ratios is observed for both series 2 and 3 (La/Yb=9.1-48 and 27-68; La/Sm=4.8-11 and 6.1-11; Dy/Yb=1.1-2.7 and 1.7-2.5, respectively) compared to series 1 (La/Yb=2.9-14; La/Sm=2.2-8.1; Dy/Yb=1.1-1.9; Figs. 4 and 5d-f). Each intrusive suite displays a positive correlation of La/Yb and La/Sm ratios with SiO_2, whereas Dy/Yb ratios are negatively correlated (Figs. 5b-f). These ratios increase significantly over time (Fig. 5b-f). According to Sr/Y vs. Y and La/Yb vs. Yb plots, the magmatic series 1 belongs to Ònormal volcanic arcÓ whereas the magmatic series 3 fall in the Òadakite-likeÓ field (Figs. 5g,h). Rocks from the magmatic series 2 plot outside these two fields (Figs. 5g,h).

5.2 Whole-rock radiogenic isotope geochemistry

In the $^{143}Nd/^{144}Nd_i$ vs. $^{87}Sr/^{86}Sr_i$ isotope diagram, all plutonic rocks plot along the mantle array, between the Depleted MORB Mantle (DMM) and Bulk Silicate Earth (BSE) reservoirs (Fig. 6a). The overall variations are very small (Figs. 6a,b; Table 3). Intrusions from series 1 display the most radiogenic $^{87}Sr/^{86}Sr_i$ ratios (0.70419-0.70435) and the lowest $^{143}Nd/^{144}Nd_i$ ratios (0.51270-0.51278), whereas series 2 shows the least radiogenic $^{87}Sr/^{86}Sr_i$ ratios (0.70387-

0.70409) with higher $^{143}Nd/^{144}Nd_i$ ratios (0.51280-0.51283), and series 3 is transitional ($^{87}Sr/^{86}Sr_i$: 0.70407 to 0.70433 and $^{143}Nd/^{144}Nd_i$: 0.51275 to 0.51286; Figs. 6a,b). $^{207}Pb/^{204}Pb_i$ ratios have limited variations ranging between 15.55 and 15.62 over 30 m.y. (Fig. 6c), and display a small but systematic increase from series 1 to 3 (Table 3). By contrast, $^{206}Pb/^{204}Pb_i$ and $^{208}Pb/^{204}Pb_i$ ratios increase over time and within a single magmatic series, with ranges of 18.26-18.76 and 38.15-38.9 for series 1, 18.72-18.86 and 38.75-38.83 for series 2, and 18.87-18.97 and 38.84-38.95 for series 3 (Fig. 6d). These ratios fall along the orogen curve defined by Zartman & Doe (1981) and are in good agreement with isotopic compositions reported regionally for magmatic rocks (Figs. 6c,d).

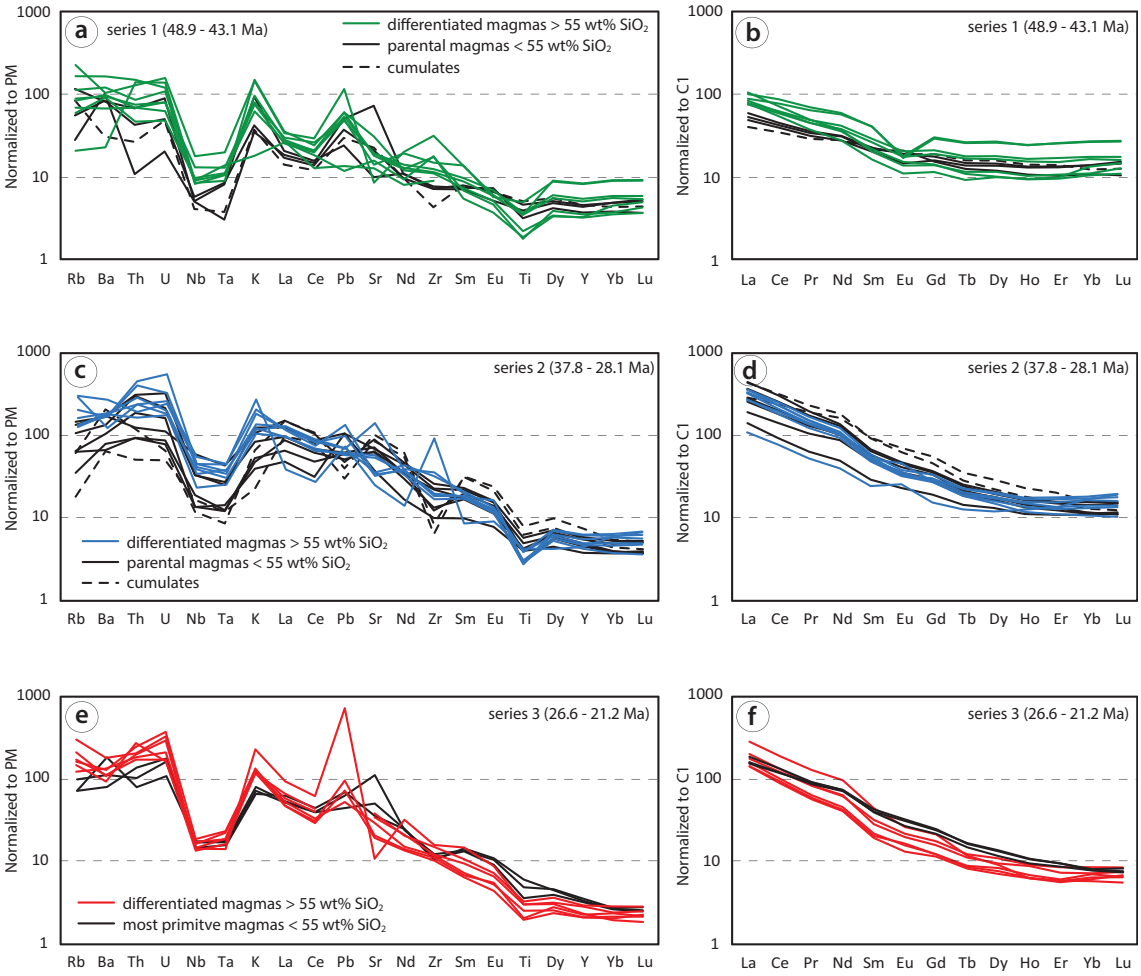

Figure 4: Multi-element and rare earth element plots are, respectively, normalized to the primitive mantle (PM; McDonough & Sun, 1995) and chondrite compositions (C1; Sun & McDonough, 1989) for each intrusive suite of the MOP.

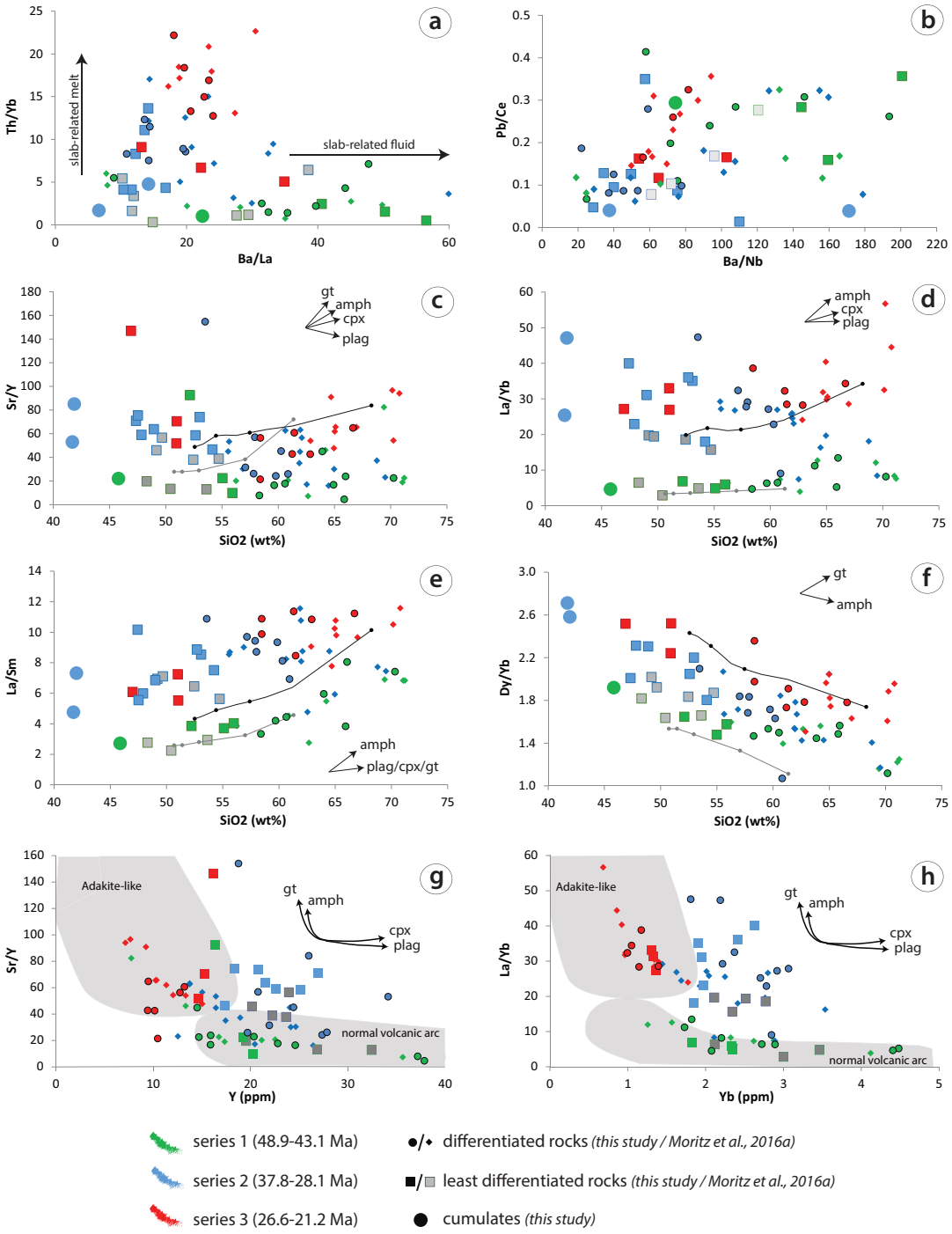

Figure 5: a) Th/Yb vs. Ba/La, b) Pb/Ce vs. Ba/Nb, c-f) REE ratios vs. SiO_2, g-h) Sr/Y vs. Y (ppm) and La/Yb vs. Yb (ppm) plots showing adakite-like and normal arc volcanic rocks fields after Moyen (2009). Liquid line of descent (LLD) are from mass-balance fractionation models in the Kohistan arc exposed in Northern Pakistan (gray line; Jagoutz, 2010) and the Dariv igneous complex exposed in Western Mongolia (black line; Bucholz et al., 2014). Numbers along LLDs are melt remaining fraction. Dots on LLD indicate the melt composition at 10%, 30%, 60% and 90% of melt remaining on the gray and black lines, whereas it corresponds to melt compositions from 1170 to 700¡C on the blue line. Arrows in c-f indicate the influence of plagioclase (plag), clinopyroxene (cpx), amphibole (amph), and garnet (gt) fractionation.

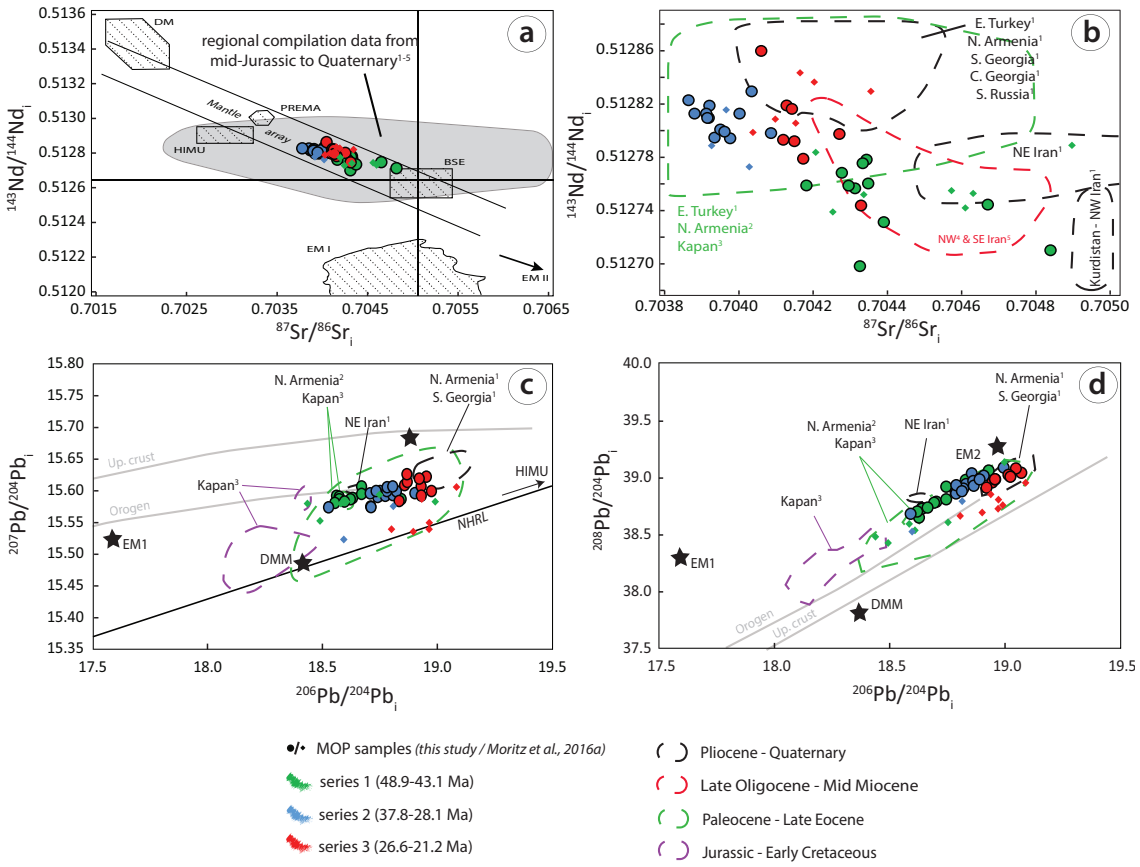

Figure 6: a) $^{143}Nd/^{144}Nd_i$ vs. $^{87}Sr/^{86}Sr_i$ with fields of the DMM (Depleted MORB Mantle), BSE (Bulk Silicate Earth), HIMU (high μ), EM1 (Enriched Mantle 1) and EM2 (Enriched Mantle 2) end-members are from Zindler & Hart (1986), b) Zoom in from a), c-d) $^{208}Pb/^{204}Pb_i$ and $^{207}Pb/^{204}Pb_i$ vs. $^{206}Pb/^{204}Pb_i$ plots. Lead isotopic evolution curves for the orogene and upper crust correspond to the plumbotectonics model (version II) from Zartman & Doe (1981). Mantle end-members are from Saal et al. (2005), respectively. Northern Hemisphere Reference Line (NHRL) is from Hart (1984). Exponent numbers refers to 1- Neill et al. (2015) and references therein, 2- Sahakyan et al. (2016), 3- Mederer et al. (2013), 4- Aghazadeh et al. (2011), and 5- Shafiei et al. (2009).

Table 3. Radiogenic Sr, Nd and Pb isotope geochemistry.

Samples	Dates (Ma)	$^{87}Sr/^{86}Sr_i$	$^{87}Sr/^{86}Sr$	$^{143}Nd/^{144}Nd_i$	$^{143}Nd/^{144}Nd$	$^{206}Pb/^{204}Pb_i$	$^{207}Pb/^{204}Pb_i$	$^{208}Pb/^{204}Pb_i$	$^{206}Pb/^{204}Pb$	$^{207}Pb/^{204}Pb$	$^{208}Pb/^{204}Pb$
series 1											
AG1304A	48.9 ± 0.6	0.70466	0.70474	0.51275	0.51278	18.26	15.55	38.15	18.93	15.58	39.05
AG1401	45.9 ± 0.9	0.70428	0.70449	0.51277	0.51282	18.55	15.59	38.58	18.63	15.59	38.64
AG1404	44.8 ± 0.9	0.70431	0.70456	0.51276	0.51280	18.58	15.59	38.64	18.64	15.59	38.72
VK1403	44.3 ± 0.7	0.70434	0.70582	0.51278	0.51282	18.76	15.59	38.90	18.83	15.59	38.97
AG1403	44.1 ± 1	0.70435	0.70470	0.51276	0.51280	18.56	15.58	38.62	18.64	15.58	38.72
AG1406	44 ± 0.9	0.70433	0.70448	0.51278	0.51282	18.64	15.58	38.70	18.70	15.59	38.78
AG1402	43.8 ± 0.6	0.70430	0.70447	0.51276	0.51280	18.57	15.58	38.63	18.62	15.58	38.69
HQ1402	42.9 ± 0.5	0.70419	0.70421	0.51276	0.51280	18.68	15.58	38.76	18.70	15.58	38.77

HQ1403	43.1 ± 0.5	0.70433	0.70452	0.51270	0.51274	18.58	15.58	38.64	18.67	15.58	38.73
AG1302A	43.00	0.70483	0.70556	0.51271	0.51276	18.54	15.59	38.59	18.75	15.60	38.80
HQ1404	43.00	0.70439	0.70488	0.51273	0.51276	18.65	15.59	38.75	18.75	15.59	38.91
series 2											
AG1308A1	37.8 ± 0.8	0.70389	0.70396	0.51281	0.51284	18.73	15.59	38.78	18.83	15.60	38.93
AG1308A	37 ± 0.4	0.70387	0.70392	0.51282	0.51285	18.72	15.58	38.76	18.82	15.59	38.90
VK1404	35.7 ± 0.6	0.70398	0.70403	0.51280	0.51282	18.73	15.58	38.83	18.86	15.59	39.03
VK1405	34.8 ± 0.5	0.70409	0.70416	0.51280	0.51282	18.86	15.59	38.82	19.00	15.59	39.08
MR1403	34.6 ± 0.6	0.70394	0.70404	0.51280	0.51282	18.77	15.59	38.83	18.89	15.59	38.98
LI1303A1	33.5 ± 0.6	0.70393	0.70397	0.51282	0.51284	18.73	15.59	38.78	18.79	15.59	38.86
LI1303	33.6 ± 0.6	0.70393	0.70420	0.51281	0.51283	18.73	15.59	38.75	18.86	15.60	38.96
MR1402	33.49 ± 0.02	0.70392	0.70393	0.51281	0.51284	18.73	15.57	38.77	18.79	15.57	38.85
KJ1316	33.7 ± 0.5	0.70396	0.70408	0.51280	0.51282	18.78	15.59	38.75	18.91	15.60	39.01
KJ1308	31.1 ± 0.5	0.70404	0.70450	0.51283	0.51285	18.75	15.60	38.79	18.87	15.60	38.92
MR1404	35.00	0.70380	0.70383	0.51282	0.51285	18.73	15.57	38.77	18.79	15.57	38.93
KJ1318	33.70	0.70392	0.70402	0.51281	0.51283	18.78	15.60	38.78	18.89	15.60	38.97
KJ1319	33.70	0.70401	0.70405	0.51281	0.51284	18.79	15.60	38.83	18.82	15.60	38.87
VK1406	34.50	0.70397	0.70413	0.51280	0.51282	18.29	15.56	38.34	18.59	15.57	38.67
series 3											
KJ1303A1	25.5 ± 0.3	-	-	0.51280	0.51282	18.90	15.60	38.90	18.95	15.61	38.95
KJ1303A2	25.5 ± 0.3	0.70427	0.70433	0.51280	0.51282	18.87	15.58	38.84	18.92	15.58	38.90
MR1401	24.5 ± 0.4	0.70412	0.70425	0.51279	0.51281	18.95	15.59	38.93	19.07	15.60	39.03
KJ1307	24.3 ± 0.3	0.70407	0.70432	0.51286	0.51279	18.95	15.60	38.93	19.05	15.62	39.07
LI1301	22.6 ± 0.5	0.70418	0.70413	0.51278	0.51288	18.97	15.62	38.89	19.03	15.60	39.00
KJ1325A	22.2 ± 0.3	0.70413	0.70438	0.51282	0.51283	18.91	15.61	38.92	18.96	15.61	38.98
KJ1324A	22.2 ± 0.3	0.70415	0.70444	0.51282	0.51283	18.92	15.61	38.92	19.02	15.62	39.02
KJ1313	21.2 ± 0.3	0.70433	0.70442	0.51275	0.51276	18.94	15.62	38.95	18.96	15.62	38.98
LI1401	26.00	0.70417	0.70424	0.51280	0.51282	18.92	15.58	38.91	19.03	15.59	39.00

6. DISCUSSION

6.1 Isotopic constraints on the magmatic source

Magmatic rocks from the MOP display radiogenic isotopic compositions overlapping with regional isotope trends reported for Mesozoic and Cenozoic magmatic rocks in surrounding areas (Fig. 6). The decrease in the $^{87}Sr/^{86}Sr$ ratio together with the concomitant increase in $^{143}Nd/^{144}Nd$ from the magmatic series 1 to 2 reveals an increase of the mantle-dominated source over time. This can be interpreted as a consequence of a decreasing contribution of slab-related components in the mantle source (Figs. 6a,b; McCulloch & Gamble, 1991; Hawkesworth et al., 1993). This would be consistent with the decreasing LILE/HFSE and LILE/LREE ratios observed over time in the MOP (Figs. 5a,b; Elliott et al., 1997; Barragan et al., 1998). Complementary zircon εHf values (+8 to +11) support a predominance of mantle-derived

magmas with limited crustal contribution, although the limited isotopic contrast between each magmatic series cannot rule out a progressive cannibalization of young and juvenile lower crust (Rezeau et al., 2016). The absence of inherited zircons in our samples advocates for little to no crustal contamination (Rezeau et al., 2016). By contrast, the Pb isotopic compositions display more radiogenic signatures over time (Figs. 6c,d), with $^{207}Pb/^{204}Pb$ and $^{206}Pb/^{204}Pb$ ratios increasing parallel to the North Hemisphere Reference Line toward the HIMU component (Fig. 6c). The decoupling between the Pb and Sr-Nd isotope systems is difficult to reconcile with a scenario involving slab-related fluid. It could rather suggest the involvement of a HIMU-type mantle component, which potentially corresponds to a mantle previously metasomatized during the closure of the northern branch of the Neotethys ocean (Rolland et al., 2009; Mederer et al., 2013). To our knowledge and as pointed out by Neill et al. (2015), there are no appropriate isotopic studies for the Caucasian segment along the Tethyan margin and no reported Armenian mantle xenoliths, which makes this hypothesis difficult to test. The transition from the magmatic series 2 to 3 is characterized by a subtle decrease in $^{143}Nd/^{144}Nd$ ratios and an increase in $^{87}Sr/^{86}Sr$ and $^{207}Pb/^{204}Pb$ ratios, which may indicate a cryptic sediment contribution likely released from the slab (e.g., Marschall and Schumacher, 2012). This correlates with zircon $\delta^{18}O$ values, which slightly increase toward higher values (~6 ä) in the Early Miocene (Rezeau et al., 2016), although such slight increase may be ascribed to fractional crystallization (e.g., Bucholz et al., 2017) or supracrustal assimilation (e.g., Lackey et al., 2005).

6.2 Partial melting models for each magmatic series

The least differentiated rocks of the magmatic series 1 and 2 display Mg# < 0.6 and certainly represent parental magmas derived from primitive melts via crustal differentiation, whereas mafic dikes from the magmatic series 3 display Mg# > 0.6 and could potentially approach primitive melts (e.g., Kelemen et al., 2003). Here, we quantitatively constrain the mantle source partial melting using the mineral proportions in the range of natural garnet lherzolite (e.g., Walter, 1998) together with the non-modal batch melting equilibrium equation $C_{liq}/C_i = 1/(D+F(1-P))$ of Shaw (1979), where C_{liq} is the concentration of a given element in the residual melt, C_i is the initial concentration of an element i in the parental melt, F is the fraction of melt produced, D is the bulk partition coefficient, and P is the bulk partition coefficient of the trace elements entering the melt from the melting minerals. Detailed calculations and partition coefficients from the literature are provided in Appendix A. The Primitive mantle (McDonough & Sun, 1995) was selected as the starting composition and mixed with various amounts of E-MORB component (Sun & McDonough, 1989) to simulate mantle fertilization by slab-related fluids over time. We modeled a selected range of REE for 1 to 30 % partial melting along the best-fit models for each magmatic series (Figs. 7a-c; Appendix A). Early ultramafic

fractionation was also modeled through Rayleigh fractionation in order to reproduce an early primitive melt fractionation leading to parental melt compositions corresponding to those observed in the MOP (Figs. 7a-c; Appendix A).

The REE average composition for parental magmas of the magmatic series 1 is best reproduced by high degree partial melting (F=0.15) of a garnet lherzolite (2% garnet) using a Primitive mantle starting composition mixed with 2% of E-MORB, and followed by 20-40% early fractionation of olivine-rich ultramafic cumulates (Fig. 7a; Supplementary Table A.1). The latter does not fractionate LREE over MREE or HREE and consequently the REE ratios remain constant at the first stage of lower crustal fractional crystallization (Fig. 7a). However, early olivine fractionation decreases Mg# values of the fractionated basaltic-andesitic liquids (Kelemen et al., 2003; Jagoutz, 2010; Bucholz et al., 2014; Nandedkar et al., 2014), similar to Mg# values displayed by the series 1 (Fig. 3e). By contrast, the average REE pattern of the parental magmas from the magmatic series 2 is best reproduced by a low degree of partial melting (F=0.02) of a garnet lherzolite (7% garnet) using a Primitive mantle starting composition mixed with 10% of E-MORB (Fig. 7b; Supplementary Table A.2). Following the generation of primitive melts, 30-50% early fractionation of ultramafic cumulates in the lower crust is proposed to match the average parental magma composition displayed by the magmatic series 2 (Fig. 7b). The average REE pattern of the magmatic series 3 is best reproduced by a relatively low degree of partial melting (F=0.05) of a garnet lherzolite (12% garnet) using identical starting composition as for the magmatic series 2, followed by the 30-50% early fractionation of ultramafic cumulates (Fig. 7c; Supplementary Table A.3).

According to our modeling, it could be argued that the transition from the magmatic series 1 to 2 is reasonably explained by lowering the degree of partial melting, whereas the transition between the magmatic series 2 and 3 displays a similar low degree of partial melting and is rather controlled by a higher residual garnet content (Figs. 7a-c). The residual garnet could either correspond to higher initial garnet component in the lherzolite or be related to newly formed garnet through metasomatic reactions. The decreasing degree of partial melting is capable of significantly increase the LREE contents without affecting HREE concentrations (Ringwood, 1975; Barragan et al., 1998), and therefore argues for the marked increase of LREE/HREE and MREE/HREE ratios in the magmatic series 2 (Figs. 5d-f and 7a,b). By contrast, the increase of residual garnet will deplete the HREE contents and consequently increase LREE/HREE and MREE/HREE ratios, which corresponds to the geochemical characteristics displayed by the magmatic series 3 (Figs. 5d-f and 7c).

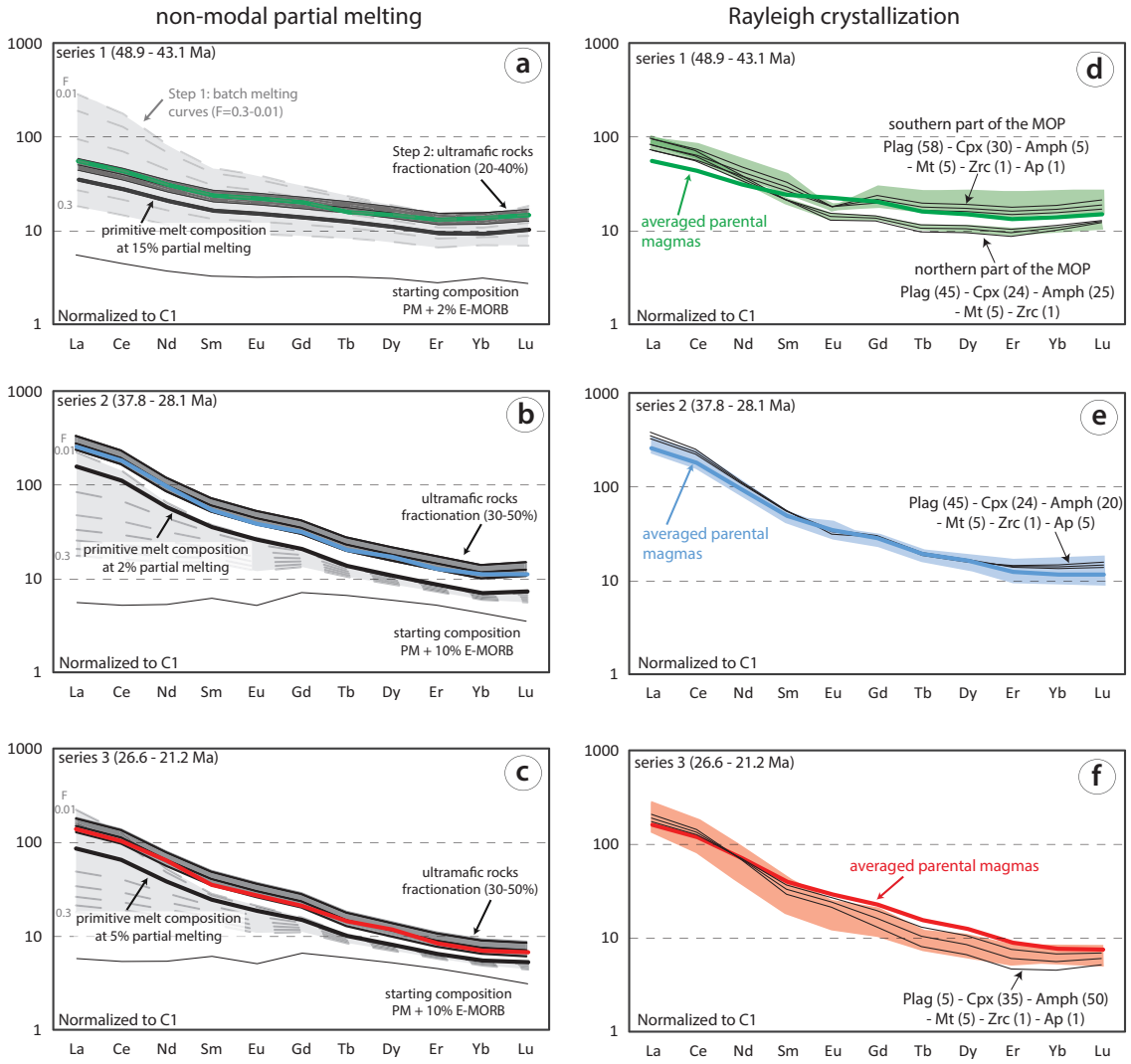

Figure 7: Chondrite normalized REE plots (C1; Sun & McDonough, 1989) for each intrusive suite of the MOP. The color scheme is the same as previous figures. Non-modal partial melting models are shown on the left side of the figure compared with the average composition of parental magmas represented by the colored bold line. These models start from Primitive Mantle with 2% and 10% EMORB with different modal proportions of residual garnet (a-c). Partial melting of 1 to 30% from the starting composition is shown as a gray shaded region with dotted thick black lines, with the thick black line indicating the best-fit model (a-c). Dunite is fractionally removed (thin black lines and black shaded region) from this composition to reach a composition overlapping with the average composition of parental magmas from the MOP. Model curves for fractional crystallisation are shown by the thin black lines on the right side of the figure (d-e). The magmatic series 1, 2 and 3 are reproduced by 30-50%, 20-40% and 10-30% fractionation of plagioclase (plag), clinopyroxene (cpx), amphibole (amph), magnetite (mt), zircon (zrc) and apatite (ap). The average composition of parental magmas is represented by the coloured bold line, whereas the coloured shaded region reflects the more differentiated samples in the magmatic series. See text for discussion and Appendix A and B for calculations.

The increase of initial residual garnet in the lherzolite from 2% to 7% required by the modeling could be explained by the presence of a heterogeneous garnet lherzolite, which is in

agreement with natural range of examples for garnet lherzolite (e.g., Walter, 1998). The presence of garnet in lherzolite during fluid-fluxed melting has been experimentally documented (Sen and Dunn, 1994; Rapp and Watson, 1995). Although the magmatic series 2 and 3 display similar LREE/HREE and MREE/HREE ratios, the magmatic series 3 is characterized by significantly higher Mg#, Ni and Cr contents together with an "adakite-like" geochemical signature and modeled with 12% residual garnet (Figs. 3e,g,h, 5g,h, 7c). Such characteristics have been experimentally reproduced through the generation of a hybridized partial melt in the mantle wedge by effective interactions between slab-related silicic melts and peridotite (Rapp et al., 1999). The reaction initiates the breakdown of olivine and promotes the formation of pyrope-rich garnet and low Mg# orthopyroxene (Rapp et al., 1999). This would explain the geochemical characteristics of the "adakite-like" magmatic series 3. Alternatively, high LREE/MREE and LREE/HREE ratios can also be promoted by high-pressure mineral (gt ± amph) fractionation in a thickened lower crust (MacPherson et al., 2006; Davidson et al., 2007; Moyen, 2009). Although it will be discussed in the next section, the distinction between high-pressure partial melting and high-pressure fractionation remains very challenging since both scenarios involve melt generation in equilibrium with garnet-rich lithologies that provide favorable conditions to generate "adakite-like" melts.

Finally, the reason for the marked K-rich signature of the magmatic series 2 and 3 is difficult to assess based on our modeling, but it is generally considered that partial melting of a metasomatized mantle source; i.e., amphibole and/or phlogopite, generates high-K to shoshonitic rocks (e.g., Menzies and Hawkesworth, 1987; Foley, 1992; Concei•ao and Green, 2004).

6.3 Magmatic differentiation series dominated by fractional crystallization

For each differentiation series, high- to medium-pressure hydrous magma crustal differentiation is the dominant process to produce coeval SiO_2-rich magmas. Major and trace element differentiation trends recognized in the MOP (Figs. 3a-d and 5b-f) tend to follow liquid lines of descent (LLD) obtained from fractional crystallization experiments conducted at 0.7 GPa for hydrous, calc-alkaline to arc tholeiitic magmas (Nandedkar et al., 2014), and from field-based mass-balance fractionation in the lower crust derived for the Kohistan arc, Pakistan (Jagoutz, 2010) and the Dariv igneous complex, Mongolia (Bucholz et al., 2014). These LLD represent early fractionation of ultramafic plutonic rocks and subsequent gabbroic cumulates from calc-alkaline to alkaline primitive melts. The recognition of sparse cumulates in the MOP, however, does not allow us to model the LLD for major elements by mass-balance calculation following Jagoutz (2010). Consequently, we carried out standard trace element modeling to evaluate crystallizing mineral assemblages from a starting average composition of parental magmas

using the Rayleigh fractionation equation $C_{liq}/C_i = F^{(D-1)}$ (Figs. 7d-f), where C_{liq} is the concentration of a given element in the residual melt, C_i is the initial concentration of an element i in the parental melt, F is the fraction of remaining melt, and D is the bulk partition coefficient. Detailed calculations and the used mineral partition coefficients are summarized in Appendix B.

The magmatic series 1 is characterized by the emplacement of diorite and tonalite both in the southern and the northern parts of the MOP (Fig. 2). Southern intrusions display marked Eu negative anomalies, whereas the northern ones lack any Eu negative anomalies and exhibit concave-up REE patterns (Fig. 7d). Eu and Sr negative anomalies and low Sr/Y are characteristic of plagioclase fractionation, whereas amphibole fractionation depletes the residual melt in Y, MREE and HREE, and consequently results in increasing Sr/Y and La/Yb ratios combined with a typical REE concave-up shape (Figs. 5g,h and 7d; e.g., Moyen, 2009). Geochemical differences between evolved rocks sampled in the northern and southern parts of the MOP are modeled by the 30-50% fractionation of plagioclase, clinopyroxene, amphibole, magnetite, zircon and apatite with the following proportions 58/30/5/5/1/1 and 45/23/25/5/1/0, respectively (Fig. 7d; Supplementary Table B.1). Such mineral assemblages are in agreement with experimental results (e.g., Nandedkar et al., 2014). The negative correlation of the Dy/Yb ratio with SiO_2 increase indicates the involvement of amphibole fractionation during crustal differentiation (Fig. 5d; Davidson et al., 2007). Various sequences of crystallization from a common parental melt may reproduce trace element patterns respectively displayed in the southern and northern parts of the MOP, which emphasize the cogenetic link between mafic and SiO_2-rich intrusions in the magmatic series 1.

Differentiated rocks from the magmatic series 2 are exclusively characterized by a concave-up REE pattern together with slightly positive or no Eu negative anomalies (Fig. 7e). This pattern resembles the one displayed by the intrusions in the northern part of the MOP from the magmatic series 1. The negative Dy/Yb correlation with the increase of SiO_2 also indicates amphibole fractionation (Fig. 5d; Davidson et al., 2007). Series 2 differentiated samples are best reproduced by 20-40% fractionation of plagioclase, clinopyroxene, amphibole, magnetite, zircon and apatite in the proportions 45/24/20/5/1/5, similar to the northern magmatic rocks from the series 1 (Fig. 7e; Supplementary Table B.2). In the Sr/Y vs. Y and La/Yb vs. Yb diagrams, the data plot outside the "normal volcanic arc" and "adakite-like" fields and display significant scatter (Figs. 5g,h). The series 2 characterized by high Sr/Y and La/Yb ratios and high Y and Yb contents may reflect different sequences of crystallization dominated by clinopyroxene, amphibole, and/or plagioclase fractionation in various proportions over time. Alternatively, it could correspond to the melting of a metasomatized lithospheric mantle source initially more enriched in Sr and La compared to series 1. This highlights the limits of whole-

rock geochemistry to characterize accurately magma petrogenesis and sequence of mineral crystallization.

Granodiorite and granite from the "adakite-like" magmatic series 3 are characterized by a marked concave-up REE pattern along with HREE depletion (Figs. 5g,h and 7f). According to our modeling, geochemical features are reproduced by 10-30% fractionation of plagioclase, clinopyroxene, amphibole, magnetite, zircon and apatite with the following proportions: 5/35/50/5/1/1 (Fig. 7f; Supplementary Table B.3). An early fractionation of amphibole ± garnet is generally proposed to drive geochemical characteristics toward an "adakite-like" signature (e.g., Moyen, 2009). In the MOP, the geochemical modeling does not necessarily require garnet fractionation for the magmatic series 3, which is also in agreement with the lack of positive correlation of Dy/Yb ratios with SiO_2, which argues against garnet fractionation (Fig. 5d; MacPherson et al., 2006; Davidson et al., 2007). The modeling and geochemical trends clearly indicate an amphibole-dominated crustal fractionation process, which explains high Sr/Y and La/Yb ratios concomitant with decreasing Y and Yb concentrations, respectively (Figs. 5g,h,).

6.4 Summary of geochemical modeling

According to our non-modal batch melting modeling, the first geochemical transition between the magmatic series 1 and 2 reflects a decreasing degree of partial melting of a garnet lherzolite, whereas the second transition between the magmatic series 2 and 3 is controlled by a higher residual garnet content for a similar low degree of partial melting (Figs. 7a-c). Crustal differentiation processes are overall characterized by fractional crystallization sequences with variable fractionated proportions of plagioclase, clinopyroxene, amphibole, magnetite, zircon and apatite. However, the differentiation series of the MOP evolved from plagioclase- and clinopyroxene-dominated to amphibole-dominated fractional crystallization over time (Figs. 7d-f). This evolution indicates a progressive early appearance of amphibole fractionation at the expense of plagioclase crystallization, which is generally promoted by higher water contents in parental magmas and/or crystallization at higher pressure potentially leading to an "adakite-like" signature (Moyen, 2009; Krawczynski et al., 2012). The lack of any geochemical evidence for garnet fractionation argues against significant crustal thickening over time. However, we believe that the amphibole-dominated fractionation modeled for the magmatic series 3 points toward a generation of magmas at deeper crustal levels, i.e., mid- to lower crustal levels, and therefore suggests a progressive thickening of the crust over time. The latter would corroborate the progressive increase of the Sr/Y ratio, generally proposed to reflect thickened crust (Mamani et al., 2010; Chapman et al., 2015; Chiaradia, 2015). This would also be in good agreement with modeled compositions of primitive melts that are in the range of average primitive oceanic arc basalt compositions (i.e., Lesser Antilles) for the magmatic series 1, and progressively evolve

toward the range of average primitive continental arc basalt-andesite (i.e., Andean-type) for the magmatic series 2 and 3 (Appendix A; Kelemen et al., 2003). This temporal evolution together with mantle-like isotopic compositions reflect the construction of a Cenozoic juvenile arc, where the MOP is a product of subduction- and collision-related magmatism, which has contributed to a net continental crustal growth over 30 m.y. along the Tethyan margin (e.g., Moyen et al., 2017). In conclusion, the distinct geochemical compositions displayed by parental magmas for each magmatic series are mainly inherited from mantle source-related processes (degree of partial melting, initial garnet content), with substantial contributions of crustal fractional crystallization processes (plagioclase- and clinopyroxene-dominated vs. amphibole-dominated fractional crystallization).

6.5 Linking the temporal evolution of the MOP to the regional geodynamic framework of the Arabia-Eurasia accretionary orogeny

6.5.1 Plate kinematics and regional stress regime

The Arabia-Eurasia accretionary orogeny arised from a complex geotectonic evolution with the successive closure of the northern and southern branches of the Neotethys oceans during the Mesozoic and Cenozoic, respectively (e.g., Barrier & Vrielynck, 2008). The latter is of particular interest to this study, since it correlates with the age of the incremental assembly of the MOP from ~50 to 20 Ma (Rezeau et al., 2016). Kinematic reconstructions for the motions of the Arabian plate reveal variations in convergence rates characterized by a rapid convergence in the EoceneÐOligocene followed by a period of slower convergence since the Early Miocene (Fig. 8a; Rosenbaum et al., 2002; McQuarrie et al., 2003; Bertrand et al., 2014). The rapid convergence rate of the Arabian plate induced a period of regional compression and shortening in the overriding (SAB-Eurasia) continental lithosphere (Fig. 8a; Agard et al., 2011; Mouthereau et al., 2012; Bertrand et al., 2014). The highest rate of convergence was coeval with the long-lived magmatic series 2 from 37.8 to 28.1 Ma and may reflect the progressive onset of compression (transpression in the MOP) as a consequence of the Arabian-Eurasian collision. If we consider the Late Eocene 5.3 m.y.-long magmatic lull, the duration of the compressional stage and collision-related magmatism lasted ~15 m.y. (Fig. 8b). Such a duration is in line with the lag time of 15-20 m.y. between the two-stage "soft" to "hard" collision evolution proposed by Ballato et al. (2011) based on their investigation in the Alborz, northern Iran, and dynamic numerical modeling by Van Hunen & Allen (2011) predicting slab break-off 20Ð25 m.y. after the onset of the Arabia-Eurasia collision during the Oligocene.

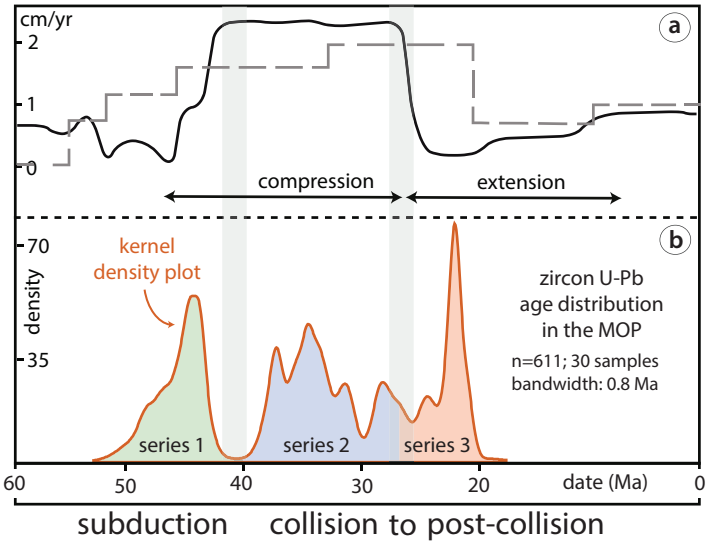

Figure 8: a) Rates of convergence versus time of the Africa plate. Black and gray dashed lines correspond to calculations after Bertrand et al. (2014) and Rosenbaum et al. (2002), respectively. The compressional and extensional stress regimes are inferred from Bertrand et al. (2014). b) Zircon U-Pb age distribution in the MOP compiled after Rezeau et al. (2016) showing Kernel density distribution using Vermeesch (2012).

The marked decrease of the Arabian plate convergence rate during the Late Oligocene - Early Miocene is associated with a regional extensional or transtensional stress regime in the overriding continental lithosphere (Fig. 8a; Agard et al., 2011; Mouthereau et al., 2012; Bertrand et al., 2014) and also a change of the plate convergence angle from NE-SW to N-S (e.g., Avagyan et al., 2010). The switch from a collisional/transpressional to an extensional/transtensional regime in the MOP would have facilitated fast ascent of magmas stored at the base of the crust or within the lithospheric mantle and could also explain the emplacement of the shoshonite to Òadakite-like" lamprophyre dikes with a near-primitive melt geochemistry (Mg# > 0.6, high Ni "nd Cr) (Glazner, 1991; Turner et al., 1999; Prelević et al., 2004; Campbell et al., 2014). The normal, strike-slip Tashtun fault and the formation of the Meghri-Tey graben are evidence for Late Oligocene - Early Miocene extension to transtension in the MOP (Tayan, 1998; Hovakimyan & Tayan, 2008; Hovakimyan et al., 2016). The Cenozoic uplift/exhumation of the Zangezur block described by Tayan et al. (1976) is confirmed by the Late Oligocene porphyry-style mineralization overprint by Early Miocene epithermal mineralization within ~5-6 Myr in the world-class Kadjaran porphyry Cu-Mo deposit (Rezeau et al., 2016, see also Chapter 4). Similar sequences of overprinting ore-forming events attributed to exhumation are recognized worldwide (e.g., Sillitoe, 2010). Therefore, we interpret the second transition to reflect the initiation of the post-collisional magmatism along with transcurrent tectonics.

The overall regional geodynamic evolution during the Cenozoic proposed follows a general consensus for a north-verging subduction setting based on regional tectonic (e.g., Sosson et al., 2010; HŠssig et al., 2016; Rolland et al., 2016), magmatic (e.g., Pearce et al., 1990; Keskin, 2003; Omrani et al., 2008; Agard et al., 2011; Mouthereau et al., 2012; Chiu et al., 2013; Moritz et al., 2016a) and tomographic studies (e.g., Mouthereau et al., 2012; Skobeltsyn et al., 2014). However, this interpretation is challenged by Eyuboglu et al. (2012, 2016a, b) who favor a Jurassic to Cenozoic south-verging subduction along the northern part of the Eastern Pontides. The north to south succession of tholeiitic gabbro, calc-alkaline to high-K calc-alkaline granodiorite, and adakitic-like granodiorite along the Eastern Pontides is interpreted as a Cenozoic southward subduction including an episode of slab break-off during the Pliocene-Quaternary. A south-verging subduction below the Lesser Caucasus is also proposed during the Neogene (Rolland, 2017), but the lack of evidence remains a matter of debate. In the following section, we assume a regional north-verging subduction to collision evolution responsible for the incremental emplacement of the MOP.

6.5.2 MOP multi-stage emplacement

Gabbro to granite from the magmatic series 1 crystallized mainly from medium-K calc-alkaline magmas over 5.8 m.y. at Middle Eocene time (48.9 - 43.1 Ma). The magma emplacement was facilitated by three main N-S-oriented faults, which were subsequently reactivated over time (Fig. 2 and 9a; Karamyan, 1978; Tayan, 1998; Hovakimyan et al., 2016). The marked Nb, Ta and Ti depletions together with high HFSE/LREE, LILE/LREE and $^{87}Sr/^{86}Sr$ ratios are characteristic of arc magmatism dominated by slab-derived fluids. We propose that dehydration of the slab triggered the high fluid-fluxed partial melting of a garnet lherzolite, which generated primitive melts that subsequently underwent crustal fractional crystallization (Fig. 9a). As previously proposed by Moritz et al. (2016a), the magmatic series 1 represents a typical calc-alkaline subduction-related intrusive suite linked to the closure of the Neotethys ocean during the Middle Eocene. This corroborates the widespread subduction-related calc-alkaline magmatism reported southeastward along the Iranian Urumieh-Dokhtar belt (e.g., Agard et al., 2011; Mouthereau et al., 2012; Chiu et al., 2013).

After an apparent 5.3 m.y.-long magmatic lull (Fig. 8b; Rezeau et al., 2016), gabbro to syenite from the magmatic series 2 crystallized from high-K calc-alkaline to shoshonitic magmas over 9.3 m.y. during the Late Eocene - Middle Oligocene (37.8 - 28.1 Ma). The geochemical transition from calc-alkaline to shoshonitic between magmatic series 1 and 2 is characterized by a decrease of slab-related fluid input, which is interpreted to be linked to a decrease of garnet lherzolite partial melting. We also propose a low partial melting of a pre-enriched mantle source in the stability field of K-bearing minerals to generate the shoshonitic magmatic series 2 (Fig.

9b). In the Western Mexican Volcanic Belt, a similar geochemical transition was generated through re-melting of a previously metasomatized mantle during the late stage of the subduction, when the input of slab-derived fluids was limited (e.g., Hochstaedter et al. 1996). It is also important to note that the decoupling between the Pb and Sr-Nd isotope systematics suggests mantle heterogeneities and the potential presence of a second mantle component HIMU ascending through mantle asthenospheric flow (Fig. 9b). In the MOP, the magmatic series 2 was emplaced during the onset of regional collision and the new temporal constraints allow us to propose the initiation of the Arabia-Eurasia continental collision between 43 and 38 Ma, followed by the progressive onset of collision until ~28-26 Ma. This temporal range for the collision event is in agreement with previous regional studies (Vincent et al., 2007; Allen & Armstrong, 2008; Agard et al., 2011; Ballato et al., 2011; Van Hunen & Allen, 2011; Mouthereau et al., 2012; Moritz et al., 2016a).

Lamprophyre dikes and porphyritic granodiorite from the magmatic series 3 crystallized from "adakite-like" magmas over 5.4 m.y. during the Late Oligocene - Early Miocene (26.6 - 21.2 Ma). The magmatism was coeval with extensional tectonics facilitating the ascent of mafic magmas to the upper continental crust. The magmatism is characterized by a dominant mantle-related isotopic signature, however, the increase of whole rock $^{86}Sr/^{87}Sr$ ratios (Fig. 6b) and zircon $\delta^{18}O$ values (Rezeau et al., 2016) points toward a minor contribution of subducted sediments or altered oceanic crust to magmas generated in the mantle wedge. Several scenarios may contribute to such tectono-magmatic features during the Late Oligocene to Miocene (Fig. 9c), including a reorganization of the plate kinematics induced by a temporal change of the Arabian-Eurasian plate convergence angle from NE-SW to N-S (e.g., Avagyan et al., 2010) combined with slab roll-back (e.g., Zagros orogeny, Agard et al., 2011; Mouthereau et al., 2012), slab break-off (e.g., NW Iran, Aghazadeh et al., 2011; SE Iran, Shafiei et al., 2009; E. Anatolia, Keskin, 2003) or delamination (e.g., central Iran, Haschke et al., 2010; southernmost Lesser Caucasus, Moritz et al., 2016a; E. Anatolia, Pearce et al., 1990). Although these scenarios would certainly initiate decompression melting and/or promote (slab?) silicic melt reactions in the mantle wedge generating "adakite-like" melts (Rapp et al. 1999; Aghazadeh et al., 2011; Castro et al., 2013), the data presented in this study do not allow us to constrain any of these geodynamic settings during post-collision magmatism. In addition to mantle-related processes, crustal differentiation dominated by amphibole in a thickened lower crust is also a favorable process to generate high Sr/Y and MREE-HREE depletion (e.g., Mamani et al., 2010; Chapmann et al., 2015; Chiaradia, 2015) and have certainly played a role during the incremental growth of the MOP, especially within this collisional context.

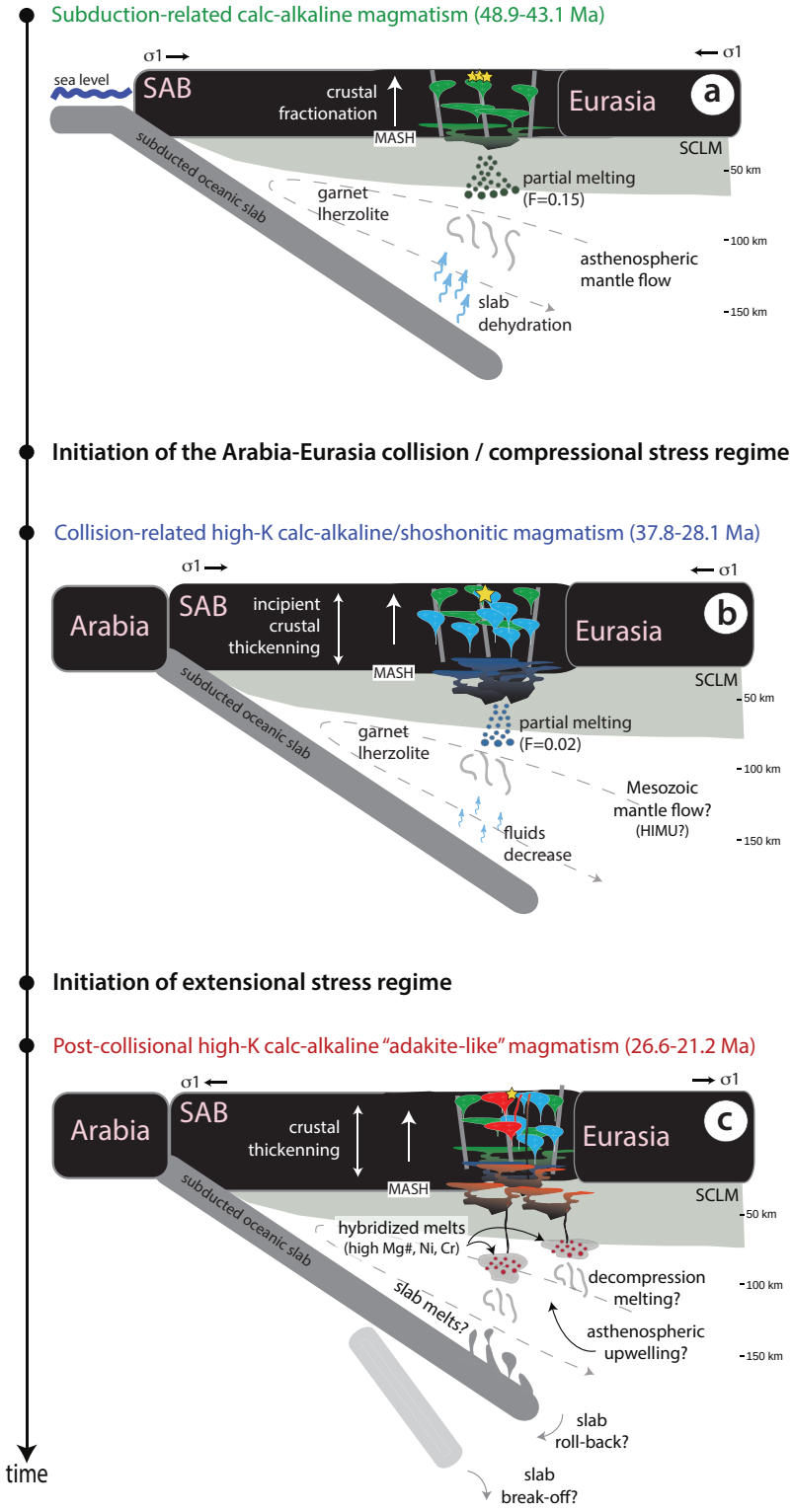

Figure 9: Schematic regional geodynamic evolution model describing the successive emplacement of the three magmatic suites forming the MOP intrusive complex in subduction-related (a), collision-related (b) and post-collisional settings (c). Yellow stars represent porphyry Cu-Mo deposits formation associated with each intrusive event (Rezeau et al., 2016). MASH: melting-assimilation-storage-hybridization zone (Hildreth & Moorbath, 1988), SAB: South Armenian block, SCLM: subcontinental lithospheric mantle. See text for discussion.

Finally, Neogene volcanism is extensively documented along the Turkish-Iranian plateau and displays an ÒOIB-likeÓ geochemical signature explained by sublithospheric small-scale convective removal as a result of delamination and/or slab break-off during the Miocene (Kaislaniemi et al., 2014; Neill et al., 2015). The post-collisional magmatism is in line with the marked orogenic uplift across the Arabia-Eurasia collision zone during the Neogene (e.g., Austermann & Iaffaldano, 2013) and corroborates the unusual thin lithosphere imaged at the present day below the Turkish-Iranian plateau (e.g., Robert et al., 2015).

7. CONCLUSIONS

The above data set and interpretations provide detailed temporal, geochemical and tectonic constraints on the incrementally assembled MOP. The nearly 30 m.y.-long continuous Cenozoic magmatism is characterized by three distinct geochemical magmatic series and represents an evolution from subduction-related calc-alkaline, to collision-related high-K-shoshonitic, to post-collisional "adakite-like" magmatism (Fig. 9). Partial melting geochemical modeling reveals that the calc-alkaline to shoshonitic transition is mainly related to a progressive decrease of degree of partial melting of a garnet lherzolite, whereas the second transition to "adakite-like" magmatism seems to be controlled by a higher content of garnet in the mantle source. The latter is interpreted in terms of primitive hybridized melts generated through an effective interaction of silicic melts and peridotite in the mantle wedge. Complementary trace element geochemical modeling confirms crustal hydrous magma fractionation and indicates progressive crustal thickening over time. The latter is evidenced by the predominant amphibole fractionation and the limited plagioclase crystallization characterizing the magmatic series 3, without any evidence of garnet fractionation. Tectono-magmatic features observed in the MOP are linked to the regional Cenozoic geodynamic evolution of the Arabia-Eurasia accretionary orogeny. We conclude that the initiation of the Arabia-Eurasia collision ~40 Ma was followed by the progressive increase of the compressional stress regime until the onset of collision at ~28 Ma. Then, the stress regime switched to extensional and/or transcurrent tectonics, which mark the transition toward post-collisional magmatism. It remains unclear which geodynamic scenarios might have triggered extensional tectonics in the southernmost Lesser Caucasus and could potentially be related to slab roll-back, slab break-off and/or delamination, as suggested by previous studies for different segments of the Turkish-Iranian plateau. In conclusion, the 30 m.y.-long subduction to post-collisional mantle-dominated magmatism in the MOP documents the construction of a Cenozoic juvenile arc that contributed to a net continental crustal growth along the Tethyan margin during the Arabia-Eurasia accretionary orogenesis.

REFERENCES

Agard, P., Omrani, J., Jolivet, L., Whitechurch, H., Vrielynck, B., Spakman, W., MoniŽ, P., Meyer, B., Wortel, R., 2011. Zagros orogeny: a subduction-dominated process. Geological Magazine 148, 692Ð725.

Aghazadeh, M., Castro, A., Badrzadeh, Z., Vogt, K., 2011. Post-collisional polycyclic plutonism from the Zagros hinterland: the Shaivar Dagh plutonic complex, Alborz belt, Iran. Geological Magazine 148, 980Ð1008.

Aignertorres, M., Blundy, J., Ulmer, P., Pettke, T., 2007. Laser Ablation ICPMS study of trace element partitioning between plagioclase and basaltic melts: an experimental approach. Contributions to Mineralogy and Petrology 153, 647-667.

Allen, M.B., Armstrong, H.A., 2008. ArabiaÐEurasia collision and the forcing of mid-Cenozoic global cooling. Palaeogeography, Palaeoclimatology, Palaeoecology 265, 52Ð58.

Austermann, J., Iaffaldano, G., 2013. The role of the Zagros orogeny in slowing down Arabia-Eurasia convergence since ~5 Ma, Tectonics 32, 351Ð363.

Avagyan, A., Sosson, M., Karakhanian, A., Philip, H., Rebai, S., Rolland, Y., Melkonyan, R., Davtyan, V., 2010. Recent tectonic stress evolution in the Lesser Caucasus and adjacent regions. Geological Society London Special Publications 340, 393-408.

Ballato, P., Uba, C.E., Landgraf, A., Strecker, M.R., Sudo, M., Stockli, D.F., Friedrich, A., Tabatabaei, S.H., 2011. ArabiaÐEurasia continental collision: insights from late Tertiary foreland-basin evolution in the Alborz Mountains, northern Iran. Geological Society of America Bulletin 123, 106Ð131.

Barragan, R., Geist, D., Hall, M., Larsen, P., Kurz, M., 1998. Subduction controls on the compositions of lavas from the Ecuadorian Andes. Earth and Planetary Science Letters 154, 153Ð166.

Barrier, E., Vrielynck, B. (Eds.), 2008. Palaeotectonic Maps of the Middle East. CGMW.

BŽguelin, P., Chiaradia, M., Beate, B., Spikings, R., 2015. The Yanaurcu volcano (Western Cordillera, Ecuador): A field, petrographic, geochemical, isotopic and geochronological study. Lithos 218, 37-53.

Bertrand, G., Guillou-Frottier, L., Loiselet, C., 2014. Distribution of porphyry copper deposits along the western Tethyan and Andean subduction zones: Insights from a paleotectonic approach. Ore Geology Reviews 60, 174-190.

Bucholz, C. E., Jagoutz, O., VanTongeren, J. A., Setera, J., Wang, Z., 2017. Oxygen isotope trajectories of crystallizing melts: Insights from modeling and the plutonic record. Geochimica et Cosmochimica Acta 207, 154-184.

Bucholz, C. E., Jagoutz, O., Schmidt, M. W., Sambuu, O., 2014. Fractional crystallization of high-K arc magmas: biotite- versus amphibole-dominated fractionation series in the Dariv Igneous complex, Western Mongolia. Contributions to Mineralogy and Petrology 168, 1-28.

Campbell, I. H., Stepanov, A. S., Liang, H. Y., Allen, C. M., Norman, M. D., Zhang, Y. Q., Xie, Y. W. 2014. The origin of shoshonites: new insights from the Tertiary high-potassium intrusions of eastern Tibet. Contributions to Mineralogy and Petrology 167(3), 1-22.

Castro, A., Aghazadeh, M., Badrzadeh, Z., Chichorro, M., 2013. Late EoceneÐOligocene post-collisional monzonitic intrusions from the Alborz magmatic belt, NW Iran. An example of monzonite magma generation from a metasomatized mantle source. Lithos 180-181, 109Ð127.

Chapman, J. B., Ducea, M. N., DeCelles, P. G., Profeta, L., 2015. Tracking changes in crustal thickness during orogenic evolution with Sr/Y: An example from the North American Cordillera. Geology 43(10), 919-922.

Chiaradia, M., 2015. Crustal thickness control on Sr/Y signatures of recent arc magmas: an Earth scale perspective. Scientific reports, 5, 8115.

Chiu, H.-Y., Chung, S.-L., Zarrinkoub, M.H., Mohammadi, S.S., Khatib, M.M., Iizuka, Y., 2013. Zircon UÐPb age constraints from Iran on the magmatic evolution related to Neotethyan subduction and Zagros orogeny. Lithos 162-163, 70Ð87.

Concei•‹o, R.V., Green, D.H., 2004. Derivation of potassic (shoshonitic) magmas by decompression melting of phlogopite + pargasite lherzolite. Lithos 72, 209Ð229.

Davidson, J., Turner, S., Handley, H., Macpherson, C., Dosseto, A., 2007. Amphibole ÒspongeÓ in arc crust? Geology 35, 787-790.

Djrbashyan, R. T., and Tayan, R. N., 2008. Geological Map of the Southern Zangezur, Armenia, Lesser Caucasus. Institute of Geological Sciences, Armenian National Academy of Sciences. Based on the "Geological map of the Zangezur mining district", Scale 1: 50 000. Authors: Karamyan K.A., Guyumdjyan H.P., Djrbashyan R.T., Tayan R.N., 1974.

Elkins, L., Gaetani, G., Sims, K., 2008. Partitioning of U and Th during garnet pyroxenite partial melting: Constraints on the source of alkaline ocean island basalts. Earth and Planetary Science Letters 265, 270-286.

Elliott, T., Plank, T., Zindler, A., White, W., Bourdon, B., 1997. Element transport from slab to volcanic front at the Mariana arc. Journal of Geophysical Research: Solid Earth 102, 14991-15019.

Eyuboglu, Y., Santosh, M., Yi, K., Bektaş, O., Kwon, S., 2012. Discovery of Miocene adakitic dacite from the Eastern Pontides Belt (NE Turkey) and a revised geodynamic model for the late Cenozoic evolution of the Eastern Mediterranean region. Lithos, 146, 218-232.

Eyuboglu, Y., Dudas, F.O., Santosh, M., Xiao, Y., Yi, K., Chatterjee, N., Wu, F.Y., Bektaş, O., 2016a. Where are the remnants of a Jurassic ocean in the eastern Mediterranean region? Gondwana Research 33, 63-91.

Eyuboglu, Y., Dudas, F. O., Santosh, M., Zhu, D. C., Yi, K., Chatterjee, N., Jeong, Y. J., Akaryali, E., Liu, Z. 2016b. Cenozoic forearc gabbros from the northern zone of the Eastern Pontides Orogenic Belt, NE Turkey: implications for slab window magmatism and convergent margin tectonics. Gondwana Research, 33, 160-189.

Foley, S., 1992. Vein-plus-wall-rock melting mechanisms in the lithosphere and the origin of potassic alkaline magmas. Lithos 28, 435-453.

Fujimaki, H., 1986. Partition-Coefficients of Hf, Zr, and Ree between Zircon, Apatite, and Liquid. Contributions to Mineralogy and Petrology 94, 42-45.

Glazner, A. F., 1991. Plutonism, oblique subduction, and continental growth: An example from the Mesozoic of California. Geology 19, 784-786.

Green, T., Blundy, J., Adam, J., Yaxley, G., 2000. SIMS determination of trace element partition coefficients between garnet, clinopyroxene and hydrous basaltic liquids at 2-7.5 GPa and 1080-1200¡C. Lithos 53, 165-187.

Hart, S. R., 1984. A large-scale isotope anomaly in the southern hemisphere mantle. Nature 309, 753-757.

Haschke, M., Ahmadian, J., Murata, M., McDonald, I., 2010. Copper mineralization prevented by arc-root delamination during AlpineÐHimalayan collision in Central Iran. Economic Geology 105, 855Ð865.

HŠssig, M., Duretz, T., Rolland, Y., Sosson, M. 2016. Obduction of old oceanic lithosphere due to reheating and plate reorganization: Insights from numerical modeling and the NE Anatolia-Lesser Caucasus case example. Journal of Geodynamics 96, 35-49.

HŠssig, M., Rolland, Y., Sosson, M. 2015. From seafloor spreading to obduction: Jurassic-Cretaceous evolution of the northern branch of the Neotethys in the Northeastern Anatolian and Lesser Caucasus regions. Geological Society, London, Special Publications, 428, SP428-10.

HŠssig, M., Rolland, Y., Sosson, M., Galoyan, G., Sahakyan, L., Topuz, G., , elik, …F., Avagyan, A., MŸller, C., 2013. Linking the NE Anatolian and Lesser Caucasus ophiolites: evidence for large-scale obduction of oceanic crust and implications for the formation of the Lesser Caucasus-Pontides Arc. Geodinamica acta 26, 311-330.

Hawkesworth, C. J., Gallagher, K., Hergt, J. M., McDermott, F., 1993. Mantle and slab contribution in arc magmas. Annual Review of Earth and Planetary Sciences 21, 175-204.

Hildreth, W., Moorbath, S., 1988. Crustal contributions to arc magmatism in the Andes of central Chile. Contributions to mineralogy and petrology 98, 455-489.

Hochstaedter, A. G., Ryan, J. G., Luhr, J. F., Hasenaka, T., 1996. On B/Be ratios in the Mexican volcanic belt. Geochimica et Cosmochimica Acta 60, 613-628.

Hovakimyan, S.E., Tayan, R.N., 2008. Fractures of the Lichk-Ayguedzor ore field and mineralization controls. Proceedings of the National Academy of Sciences of the Republic of Armenia, Earth Sciences 61, 3Ð12 (in Russian with English abstract).

Hovakimyan, S., Moritz, R., Tayan, R., Melkonyan, R., Harutyunyan, M., 2016. Regional strike-slip tectonics and porphyry Cu-Mo and epithermal ore deposit formation during Cenozoic subduction to post-collisional evolution of the southernmost Lesser Caucasus, Tethyan belt. 14th Swiss Geoscience Meeting, 18-19 November 2016, Geneva, p. 61 (abstract volume).

Jackson, S.E., 2008. Lamtrace data reduction software for LA-ICP-MS. In: Sylvester, P. (Ed.), Laser Ablation ICP-MS in the Earth Sciences: Current Practices and Out- standing Issues. Short Course series, Mineralogical Association of Canada vol. 40, 305Ð307.

Jagoutz, O. E., 2010. Construction of the granitoid crust of an island arc. Part II: a quantitative petrogenetic model. Contributions to Mineralogy and Petrology 160, 359-381.

Kaislaniemi, L., Van Hunen, J., Allen, M. B., Neill, I., 2014. Sublithospheric small-scale convection - A mechanism for collision zone magmatism. Geology 42, 291-294.

Karamyan, K.A., 1978. Geology, structure and condition of formation copperÐmolybdenum deposits of Zangezour ore region. Publishing House of the Academy of Sciences Armenian SSR, Yerevan, 179 p. (in Russian).

Karamyan, K.A., Tayan, R.N., Guyumdjyan, O.P., 1974. The main features of intrusion magmatism Zangezur region of the Armenian SSR. Proceedings of the National Academy of Sciences of the Republic of Armenia, 27, 54-65 (in Russian).

Kelemen, P. B., Hangh¿f, K., Greene, A. R., 2003, One view of the geochemistry of subduction- related magmatic arcs, with an emphasis on primitive andesite and lower crust, in The Crust, edited by R. L. Rudnick, Elsevier, Oxford

Keskin, M., 2003. Magma generation by slab steepening and breakoff beneath a sub- ductionÐ accretion complex: an alternative model for collision-related volcanism in Eastern Anatolia, Turkey. Geophysical Research Letters 30, 8046-8050.

Krawczynski, M. J., Grove, T. L., Behrens, H., 2012. Amphibole stability in primitive arc magmas: effects of temperature, H2O content, and oxygen fugacity. Contribution to Mineralogy and Petrology 164, 317Ð339.

Lackey, J. S., Valley, J. W., Saleeby, J. B., 2005. Supracrustal input to magmas in the deep crust of Sierra Nevada batholith: evidence from high $\delta^{18}O$ zircon. Earth and Planetary Science Letters 235, 315-330.

Luhr, J.F., Carmichael, I.S.E., 1980. The Colima volcanic complex, Mexico. I: post-caldera andesites from Volcan Colima. Contributions to Mineralogy and Petrology 71, 343-372.

Macpherson, C. G., Dreher, S. T., Thirlwall, M. F., 2006. Adakites without slab melting: high pressure differentiation of island arc magma, Mindanao, the Philippines. Earth and Planetary Science Letters 243, 581-593.

Mamani, M., Wšrner, G., Sempere, T., 2010. Geochemical variations in igneous rocks of the Central Andean orocline (13 S to 18 S): Tracing crustal thickening and magma generation through time and space. Geological Society of America Bulletin 122, 162-182.

Marschall, H. R., Schumacher, J. C., 2012. Arc magmas sourced from mŽlange diapirs in subduction zones. Nature Geoscience 5, 862-867.

McCulloch, M. T., Gamble, J. A., 1991. Geochemical and geodynamical constraints on subduction zone magmatism. Earth and Planetary Science Letters 102, 358-374.

McDonough, W. F., Sun, S. S., 1995. The composition of the Earth. Chemical Geology 120, 223-253.

McKenzie, D., O'Nions, R. K., 1991. Partial melt distributions from inversion of rare Earth element concentrations. Journal of Petrology 32, 1021-1091.

McQuarrie, N., Stock, J.M., Verdel, C., Wernicke, B.P., 2003. Cenozoic evolution of the Neotethys and implications for the causes of plate motions. Geophysical Research Letters 30, 1Ð6.

Mederer, J., Moritz, R., Ulianov, A., Chiaradia, M., 2013. Middle Jurassic to Cenozoic evolution of arc magmatism during Neotethys subduction and arc-continent collision in the Kapan Zone, southern Armenia. Lithos 177, 61Ð78.

Melkonyan, R.L., Ghukasian, R.Kh., Tayan, R.N., Haruntunyan, M.A., 2008. Geochronometry of the Meghri pluton monzonites (Armenia) - results and consequences. Proceedings of the National Academy of Sciences of the Republic of Armenia 61, 3Ð9 (in Russian with English abstract).

Melkonyan, R.L., Ghukasian, R.Kh., Tayan, R.N., Khorenyan, R.A., Hovakimyan, S.E., 2010. The stages of copperÐmolybdenum ore formation in Southern Armenia (by the results of RbÐSr isotope age estimations). Proceedings of the National Academy of Sciences of the Republic of Armenia 63, 21Ð32 (in Russian with English abstract).

Menzies, M.A., Hawkesworth, C.J., 1987. Upper mantle processes and composition. In: Nixon PH (ed) Mantle xenoliths, Wiley, Chichester, 725-738.

Middlemost, E.A.K., 1994. Naming materials in the magma/igneous rock system. Earth-Science Reviews 37, 215Ð224.

Mkrtchyan, S.S., Karamyan, K.A., Arevshaytan, T.A., 1969. The Kadjaran copperÐ molybdenum deposit. Publishing House of the Academy of Sciences Armenian SSR, Yerevan, 326 pp. (in Russian).

Mohajjel, M., Fergusson, C.L., 2000. Dextral transpression in Late Cretaceous continental collision, SanandajÐSirjan zone, western Iran. Journal of Structural Geology 22, 1125Ð1139.

Moritz, R., Rezeau, H., Ovtcharova, M., Tayan, R., Melkonyan, R., Hovakimyan, S., Ramazanov, V., Selby, D., Ulianov, A., Chiaradia, M., Putlitz, B., 2016a. Long-lived, stationary magmatism and pulsed porphyry systems during Tethyan subduction to post-collision evolution in the southernmost Lesser Caucasus, Armenia and Nakhitchevan. Gondwana Research 37, 465-503.

Moritz, R., Melkonyan, R., Selby, D., Popkhadze, N., Gugushvili, V., Tayan, R., Ramazanov, V., 2016b. Metallogeny of the Lesser Caucasus: From arc construction to post-collision evolution. In : Richards, J. (ed), Tethyan Tectonics and Metallogeny, Special Publication of the Society of Economic Geology vol. 19, 157-192.

Mouthereau, F., Lacombe, O., VergÞs, J., 2012. Building the Zagros collisional orogen: timing, strain distribution and the dynamics of Arabia/Eurasia plate convergence. Tectonophysics 532, 27-60.

Moyen, J. F., 2009. High Sr/Y and La/Yb ratios: the meaning of the Òadakite-like signatureÓ Lithos 112, 556-574.

Moyen, J.F., Laurent, O., Chelle-Michou, C., CouziniÞ, S., Vanderhaeghe, O., Zeh, A., Villaros, A., Gardien, V., 2017. Collision vs. subduction-related magmatism: two contrasting sites of granite formation and implications for crustal growth. Lithos 277, 154-177.

Nandedkar, R. H., Ulmer, P., MŸntener, O., 2014. Fractional crystallization of primitive, hydrous arc magmas: an experimental study at 0.7 GPa. Contributions to Mineralogy and Petrology 167, 1-27.

Nandedkar, R.H., HŸrlimann, N., Ulmer, P., MŸntener, O., 2016. AmphiboleÐmelt trace element partitioning of fractionating calc-alkaline magmas in the lower crust: an experimental study. Contributions to Mineralogy and Petrology 171, 71. doi:10.1007/s00410-016-1278-0

Neill, I., Meliksetian, K., Allen, M. B., Navasardyan, G., Kuiper, K., 2015. Petrogenesis of mafic collision zone magmatism: The Armenian sector of the TurkishÐIranian Plateau. Chemical Geology 403, 24-41.

OberhŠnsli, R., Candan, O., Bousquet, R., Rimmele, G., Okay, A., Goff, J., 2010. Alpine HP evolution of the eastern Bitlis complex, SE Turkey. In: Sosson, M., Kaymakci, N., Stephenson, R.A., Bergerat, F., Starostenko, V. (Eds.), Sedimentary Basin Tectonics from

the Black Sea and Caucasus to the Arabian Platform. Geological Society London, Special publication vol. 340, 461-483.

Okay, A.I., Zattin, M., Cavazza, W., 2010. Apatite fission-track data for the Miocene ArabiaÐ Eurasia collision. Geology 38, 35Ð38.

Omrani J., Agard P., Whitechurch H., Benoit M., Prouteau G. and Jolivet, L., 2008. Arc magmatism and subduction history beneath the Zagros Mountains, Iran: a new report of adakites and geodynamic consequences, Lithos 106, 380Ð398.

Pearce, J., Bender, J., De Long, S., Kidd, W., Low, P., Guner, Y., Saroglu, F., Yilmaz, Y., Moorbath, S., Mitchell, J., 1990. Genesis of collision volcanism in Eastern Anatolia, Turkey. Journal of Volcanology and Geothermal Research 44, 189-229.

Pearce, N.J., Perkins, W.T., Westgate, J.A., Gorton, M.P., Jackson, S.E., Neal, C.R., Chenery, S.P., 1997. A compilation of new and published major and trace element data for NIST SRM610 and NIST SRM612 glass reference materials. Geostandards Newsletter 21, 115Ð 144.

Peccerillo, A., Taylor, S.R., 1976. Geochemistry of Eocene calc-alkaline volcanic rocks from the Kastamanou area, northern Turkey. Contributions to Mineralogy and Petrology 58, 63Ð 81.

Pin, C., Briot, D., Bassin, C., Poitrasson, F., 1994. Concomitant separation of strontium and samariumÐneodymium for isotopic analysis in silicate samples, based on specific extraction chromatography. Analytica Chimica Acta 298, 209Ð217.

Prelević, D., Foley, S. F., Cvetković, V., Romer, R. L., 2004. Origin of minette by mixing of lamproite and dacite magmas in Veliki Majdan, Serbia. Journal of Petrology 45, 759-792.

Rapp, R.P., Watson, E.B., 1995. Dehydration melting of metabasalt at 8Ð32 kbar: implications for continental growth and crustÐmantle recycling. Journal of Petrology 36, 891Ð931.

Rapp, R.P., Shimizu, N., Norman, M.D., Applegate, G.S., 1999. Reaction between slab derived melts and peridotite in the mantle wedge: experimental constraints at 3.8 GPa. Chemical Geology 160, 335- 356.

Rezeau, H., Moritz, R., Wotzlaw, J. F., Tayan, R., Melkonyan, R., Ulianov, A., Selby, D., d'Abzac F. X. Stern, R. A., 2016. Temporal and genetic link between incremental pluton assembly and pulsed porphyry Cu-Mo formation in accretionary orogens. Geology 44, 627-630.

Ringwood, A. E., 1975. Composition and petrology of the earth's mantle, McGraw Hill, New York.

Robert, A. M., Fernˆndez, M., JimŽnez-Munt, I., VergŽs, J., 2015. Lithospheric structure in Central Eurasia derived from elevation, geoid anomaly and thermal analysis. Geological Society, London, Special Publications 427, http://doi.org/10.1144/SP427.10.

Rock, N. M. S., 1991. Lamprophyres. Glasgow, Blackie, 285 pp.

Rolland, Y. (2017). Caucasus collisional history: Review of data from East Anatolia to West Iran. Gondwana Research. doi: 10.1016/j.gr.2017.05.005

Rolland, Y., Billo, S., Corsini, M., Sosson, M., Galoyan, G., 2009. Blueschists of the Amassia-Stepanavan suture zone (Armenia): linking Tethys subduction history from E-Turkey to W-Iran. International Journal of Earth Sciences 98(3), 533-550.

Rolland, Y., Perincek, D., Kaymakci, N., Sosson, M., Barrier, E., Avagyan, A., 2012. Evidence for ~80–75 Ma subduction jump during Anatolide–Tauride–Armenian block accretion and ~48 Ma Arabia–Eurasia collision in Lesser Caucasus–East Anatolia. Journal of Geodynamics 56–57, 76–85.

Rolland, Y., HŠssig, M., Bosch, D., Meijers, M.J.M., Sosson, M., Bruguier, O., Adamia, Sh., and Sadradze, N., 2016. A review of the plate convergence history of the East Anatolia-Transcaucasus region during the Variscan: Insights from the Georgian basement and its connection to the Eastern Pontides. Journal of Geodynamics 96, 131–145.

Rosenbaum, G., Lister, G. S., Duboz, C., 2002. Relative motions of Africa, Iberia and Europe during Alpine orogeny. Tectonophysics 359, 117-129.

Saal, A.E., Hart, S.R., Shimizu, N., Hauri, E.H., Layne, G.D., Eiler, J.M., 2005. Pb isotopic variability in melt inclusions from the EMI–EMII–HIMU mantle end-members and the role of the oceanic lithosphere. Earth and Planetary Science Letters 240, 605–620.

Sahakyan, L., Bosch, D., Sosson, M., Avagyan, A., Galoyan, Gh., Rolland, Y., Bruguier, O., Stepanyan, Zh., Galland, B., Vardanyan, S., 2016. Geochemistry of the Eocene magmatic rocks from the Lesser Caucasus area (Armenia): evidence of a subduction geodynamic environment. Geological Society, London, Special Publications 428, http://doi.org/10.1144/SP428.12

Sen, C., Dunn, T., 1994 Dehydration melting of a basaltic composition amphibolite at 1.5 and 2.0 GPa: implications for the origin of adakites. Contributions to Mineralogy and Petrology 117, 394–409.

Shafiei, B., Haschke, M., Shahabpour, J., 2009. Recycling of orogenic arc crust triggers porphyry Cu mineralization in Kerman Cenozoic arc rocks, southeastern Iran. Mineralium Deposita 44, 265– 283.

Shaw, D. M., 1979. Trace element melting models. Physics and Chemistry of the Earth 11, 577-586.

Sillitoe, R. H., 2010. Porphyry copper systems. Economic Geology 105, 3-41.

Skobeltsyn, G., Mellors, R., Gšk, R., TŸrkelli, N., Yetirmishli, G., Sandvol, E., 2014. Upper mantle S wave velocity structure of the East Anatolian-Caucasus region. Tectonics 33, 207-221.

Sosson, M., Rolland, Y., MŸller, C., Danelian, T., Melkonyan, R., Kekelia, S., Adamia, S., Babzadeh, V., Kangarli, T., Avagyan, A., Galoyan, G., Mosar, J., 2010. Subductions, obduction and collision in the Lesser Caucasus (Armenia, Azerbaijan, Georgia), new insights. In: Sosson, M., Kaymakci, N., Stephenson, R.A., Bergerat, F., Starostenko, V. (Eds.), Sedimentary basin tectonics from the Black Sea and Caucasus to the Arabian platform. Geological Society London, Special publication 340, 329Ð352.

Straub, S. M., Woodhead, J. D., Arculus, R. J., 2015. Temporal evolution of the Mariana Arc: Mantle wedge and subducted slab controls revealed with a tephra perspective. Journal of Petrology 56, 409-439.

Sun, S.-S., McDonough, W.F., 1989. Chemical and isotopic systematics of oceanic basalts: Implications for mantle composition and processes. Geological Society of London, Special Publication 42, 313Ð345.

Tanaka, T., Togashi, S., Kamioka, H., Amakawa, H., Kagami, H., Hamamoto, T., Yuhara, M., Orihashi, Y., Yoneda, S., Shimizu, H., Kunimaru, T., Takahashi, K., Yanagi, Y., Nakano, T., Fujimaki, H., Shinjo, R., Asahara, Y., Tanimizu, M., Dragusanu, C., 2000. JNdi-1: a neodymium isotopic reference in consistency with La Jolla neodymium. Chemical Geology 168, 279Ð281.

Tayan, R.N., 1998. On central magma-ore controlling zone of the Zangezour ore region. Proceedings of the National Academy of Sciences of the Republic of Armenia 51, 20Ð26 (in Russian with English abstract).

Tayan, R.N., Plotnikov, E.P., Abdurakhmanov, R.U., 1976. Some features of emplacement of geological structure of the ZangezourÐNakhichevan region of Lesser Caucasus. Proceedings of the National Academy of Sciences of the Republic of Armenia 29, 12Ð20 (in Russian).

Todt, W., Cliff, R.A., Hanser, A., Hofmann, A.W., 1996. Evaluation of a 202Pb−205Pb double spike for high-precision lead isotope analysis. In: Basu, A., Hart, S. (Eds.), Earth Processes: Reading the Isotopic Code. American Geophysical Union, Washington, Geophysical Monograph vol. 95, 429Ð437.

Turner, S. P., Platt, J. P., George, R. M. M., Kelley, S. P., Pearson, D. G., Nowell, G. M., 1999. Magmatism associated with orogenic collapse of the BeticÐAlboran domain, SE Spain. Journal of Petrology 40, 1011-1036.

Van Hunen, J., Allen, M.B., 2011. Continental collision and slab break-off: A comparison of 3-D numerical models with observations. Earth and Planetary Science Letters 302, 27Ð37.

Vermeesch, P., 2012. On the visualisation of detrital age distributions. Chemical Geology 312-313, 190-194.

Vincent, S. J., Morton, A. C., Carter, A., Gibbs, S., Barabadze, T. G., 2007. Oligocene uplift of the Western Greater Caucasus: an effect of initial ArabiaÐEurasia collision. Terra Nova 19, 160-166.

Walter, M.J., 1998. Melting of garnet peridotite and the origin of komatiite and depleted lithosphere. Journal of Petrology 39, 29Ð60.

Watson, E.B., Green, T.H., 1981. Apatite/liquid partition coefficients for the rare earth elements and strontium. Earth and Planetary Science Letters 56, 405Ð421.

Zack, T., Foley, S.F., Jenner, G.A., 1997. A consistent partition coefficient set for clinopyroxene, amphibole and garnet from laser ablation microprobe analysis of garnet pyroxenites from Kakanui, New Zealand. Neues Jahrbuch fur Mineralogie, Abhirchen 172, 23-41.

Zartman, R.E., Doe, B.R., 1981. Plumbotectonics - the model. Tectonophysics 75, 135Ð162.

Zindler, A., Hart, S., 1986. Chemical geodynamics. Annual Review of Earth and Planetary Sciences 14, 493Ð571.

APPENDIX

Appendix A: Non-modal batch melting after Shaw (1979) and Rayleigh fractionation of dunite modeling. Starting compositions for partial melting correspond to Primitive Mantle mixed with 2% and 10% E-MORB (Sun and McDonough, 1989; McDonough and Sun, 1995). The primitive melt composition generated from partial melting (5 - 15%) is subsequently modified during the fractional crystallization of dunite in order to reach the average composition of the parental magmas for each magmatic series. Starting composition in the non-modal batch melting modeling is modified for few elements to have a better fit and highlighted in yellow. Partition coefficients and associated references are given in the Table. Primitive melt compositions from oceanic and continental arc magmas are provided for comparison (Kelemen et al., 2003). See text for discussion.

Supplementary Table A.1: Series 1: Middle Eocene

Step 1: non modal batch melting

	Olivine	Orthopyroxene	Clinopyroxene	Garnet	Amphibole	Sum
Source mode	0.5	0.3	0.18	0.02	0	1
Melt mode	0.3	0.2	0.5	0	0	1

	La	Ce	Nd	Sm	Eu	Gd	Tb	Dy	Er	Yb	Lu	Sr	Y
Starting composition (ppm)													
Primitive Mantle + 2% EMORB	1.3	2.7	1.7	0.5	0.2	0.6	0.1	0.7	0.5	0.5	0.1	22.6	4.7
Non-modal batch melting													
F=0.3	4.3	8.9	5.4	1.5	0.5	1.8	0.3	1.9	1.2	1.2	0.2	74.3	11.9
F=0.2	6.4	13.0	7.6	2.0	0.7	2.4	0.4	2.4	1.5	1.4	0.2	107.3	14.8
F=0.15	**8.3**	**16.9**	**9.6**	**2.5**	**0.9**	**2.8**	**0.5**	**2.8**	**1.7**	**1.6**	**0.3**	138.0	**16.8**
F=0.1	12.1	24.2	13.1	3.2	1.1	3.5	0.6	3.3	1.9	1.8	0.3	193.2	19.5
F=0.05	22.2	42.3	20.4	4.6	1.5	4.5	0.7	3.9	2.3	2.1	0.4	321.9	23.2
F=0.02	44.1	76.8	30.8	6.1	2.0	5.5	0.8	4.5	2.6	2.3	0.5	536.3	26.1
F=0.01	65.8	105.6	37.0	6.9	2.2	5.9	0.9	4.7	2.7	2.4	0.5	689.4	27.3

Step 2: Rayleigh fractionation of ultramafic rocks

	Olivine	Orthopyroxene	Clinopyroxene
Fractionation mode (Dunite)	0.9	0.05	0.05

Starting composition (ppm)	La	Ce	Nd	Sm	Eu	Gd	Tb	Dy	Er	Yb	Lu	Sr	Y
From 15% partial melting	**8.3**	**16.9**	**9.6**	**2.5**	**0.9**	**2.8**	**0.5**	**2.8**	**1.7**	**1.6**	**0.3**	**138.0**	**16.8**
F=0.9	9.3	18.8	10.7	2.8	1.0	3.1	0.5	3.1	1.8	1.8	0.3	**153.2**	18.7
F=0.8	**10.4**	**21.1**	**12.0**	**3.1**	**1.1**	**3.5**	**0.6**	**3.5**	**2.1**	**2.0**	**0.3**	**172.2**	**20.9**
F=0.7	**11.9**	**24.1**	**13.7**	**3.5**	**1.2**	**4.0**	**0.7**	**3.9**	**2.4**	**2.3**	**0.4**	**196.7**	**23.8**
F=0.6	**13.9**	**28.1**	**16.0**	**4.1**	**1.4**	**4.6**	**0.8**	**4.6**	**2.7**	**2.7**	**0.4**	**229.2**	**27.7**
F=0.5	16.6	33.7	19.1	4.9	1.7	5.5	0.9	5.5	3.3	3.2	0.5	274.7	33.1

F=0.4	20.8	42.1	23.8	6.1	2.1	6.9	1.1	6.8	4.1	3.9	0.7	342.9	41.1
F=0.3	27.7	56.1	31.7	8.1	2.8	9.1	1.5	9.0	5.4	5.2	0.9	456.3	54.4

Kd values	La	Ce	Nd	Sm	Eu	Gd	Tb	Dy	Er	Yb	Lu	Sr	Y
Olivine (McKenzie & O'Nions, 1991)	0.0004	0.0005	0.001	0.0013	0.0016	0.0015	0.0015	0.0017	0.0015	0.0015	0.0015	0	0
Orthopyroxene (Green et al., 2000)	0.00055	0.0009	0.00305	0.0084	0.01695	0.023	0.0296	0.0406	0.0633	0.133	0.1185	0.001	0.049
Clinopyroxene (McKenzie & O'Nions, 1991; Elkins et al., 2008)	0.0536	0.0858	0.1873	0.291	0.32	0.4	0.42	0.442	0.387	0.43	0.4	0.128	0
Garnet (Zack et al., 1997; Green et al., 2000)	0.0003	0.0022	0.02	0.14	0.26	0.6	1.7	2.7	4	4.5	6	0.001	3.2
Amphibole (Nandedkar et al., 2016)	0.279	0.656	1.827	3.312	3.345	4.792	5.307	5.212	5.396	4.685	4.147	0.339	5.012

References Composition	La	Ce	Nd	Sm	Eu	Gd	Tb	Dy	Er	Yb	Lu	Sr	Y
Primitive mantle (McDonough and Sun, 1995)	0.7	1.7	1.3	0.4	0.2	0.5	0.1	0.7	0.4	0.4	0.1	19.9	4.3
EMORB (Sun and McDonough, 1989)	6.3	15.0	9.0	2.6	0.9	3.0	0.5	3.6	2.3	2.4	0.4	155.0	22.0
Primitive Mantle + 2% EMORB	0.8	1.9	1.4	0.5	0.2	0.6	0.1	0.7	0.5	0.5	0.1	22.6	4.7

Average primitive arc basalts (Kelemen et al, 2003)	La	Ce	Nd	Sm	Eu	Gd	Tb	Dy	Er	Yb	Lu	Sr	Y
av. oceanic	7.01	15.67	10.14	2.7	0.95	3.1	0.52	3.31	2	1.86	0.27	-	-
av. continental	11.85	25.87	14.88	3.43	1.07	3.55	0.51	3.32	1.95	1.82	0.28	-	-
Lesser Antilles	8.72	18.94	10.93	2.68	0.91	3.47	0.43	3.86	2.38	1.59	0.25	-	-
Marianas	5	11.73	9.1	2.72	1.01	2.86	0.55	2.77	1.65	2.29	0.37	-	-
Andean	18.79	41.23	20.6	4.37	1.24	3.37	0.6	2.93	1.79	1.83	0.28	-	-
Cascades	11.29	24.22	13.74	3.16	1.02	3.46	0.49	3.29	1.88	1.88	0.27	-	-

Average primitive andesites (Kelemen et al., 2003)	La	Ce	Nd	Sm	Eu	Gd	Tb	Dy	Er	Yb	Lu	Sr	Y
av. continental	18.89	37.44	20.89	3.92	1.08	3.92	0.51	3.09	1.63	1.54	0.23	-	-
av. oceanic	-	-	-	-	-	-	-	-	-	-	-	-	-

Supplementary Table A.2: Series 2: Late Eocene - Middle Oligocene

Step 1: non modal batch melting

	Olivine	Orthopyroxene	Clinopyroxene	Garnet	Amphibole	Sum
Source mode	0.5	0.24	0.18	0.07	0.01	1
Melt mode	0.3	0.2	0.4	0	0.1	1

	La	Ce	Nd	Sm	Eu	Gd	Tb	Dy	Er	Yb	Lu	Sr	Y
Starting composition (ppm)													
Primitive Mantle + 10% EMORB	1.3	3.0	2.0	0.6	0.2	0.8	0.1	1.0	0.6	0.6	0.1	33.4	6.1
Non-modal batch melting													
F=0.3	4.4	10.3	7.3	2.4	0.7	2.9	0.4	2.3	1.2	1.0	0.1	110.9	13.2
F=0.2	6.4	14.8	10.0	3.0	0.9	3.3	0.4	2.5	1.3	1.1	0.2	159.3	14.1
F=0.15	8.4	19.1	12.2	3.5	1.0	3.6	0.5	2.6	1.4	1.1	0.2	203.7	14.6
F=0.1	12.1	26.7	15.7	4.1	1.2	3.9	0.5	2.7	1.4	1.2	0.2	282.5	15.2

F=0.05	21.6	44.5	22.1	5.0	1.4	4.2	0.5	2.8	1.5	1.2	0.2	460.6	15.8
F=0.02	**40.9**	**74.0**	**29.2**	**5.8**	**1.6**	**4.5**	**0.5**	**2.8**	**1.5**	**1.2**	**0.2**	**740.9**	**16.1**
F=0.01	58.3	95.1	32.6	6.1	1.7	4.6	0.5	2.9	1.5	1.2	0.2	929.4	16.3

Step 2: Rayleigh fractionation of ultramafic rocks

	Olivine	Orthopyroxene	Clinopyroxene
Fractionation mode (Dunite)	0.9	0.05	0.05

Starting composition (ppm)	La	Ce	Nd	Sm	Eu	Gd	Tb	Dy	Er	Yb	Lu	Sr	Y
From 2% partial melting	40.9	74.0	29.2	5.8	1.6	4.5	0.5	2.8	1.5	1.2	0.2	740.9	16.1
F=0.9	45.4	82.2	32.4	6.4	1.8	5.0	0.6	3.2	1.6	1.4	0.2	822.7	17.9
F=0.8	51.1	92.5	36.4	7.2	2.0	5.6	0.7	3.5	1.8	1.5	0.2	924.8	20.1
F=0.7	**58.3**	**105.6**	**41.5**	**8.2**	**2.3**	**6.4**	**0.8**	**4.0**	**2.1**	**1.7**	**0.3**	**1056.0**	**22.9**
F=0.6	**68.0**	**123.1**	**48.3**	**9.6**	**2.6**	**7.4**	**0.9**	**4.7**	**2.4**	**2.0**	**0.3**	**1230.7**	**26.6**
F=0.5	**81.6**	**147.6**	**57.9**	**11.4**	**3.2**	**8.8**	**1.1**	**5.6**	**2.9**	**2.4**	**0.4**	**1475.1**	**31.7**
F=0.4	101.9	184.3	72.2	14.2	3.9	11.0	1.3	7.0	3.6	3.0	0.5	1841.1	39.4
F=0.3	135.8	245.4	96.0	18.9	5.2	14.6	1.7	9.2	4.8	3.9	0.6	2450.1	52.2

Kd values	La	Ce	Nd	Sm	Eu	Gd	Tb	Dy	Er	Yb	Lu	Sr	Y
Olivine (McKenzie & O'Nions, 1991)	0.0004	0.0005	0.001	0.0013	0.0016	0.0015	0.0015	0.0017	0.0015	0.0015	0.0015	0	0
Orthopyroxene (Green et al., 2000)	0.00055	0.0009	0.00305	0.0084	0.01695	0.023	0.0296	0.0406	0.0633	0.133	0.1185	0.001	0.049
Clinopyroxene (McKenzie & O'Nions, 1991; Elkins et al., 2008)	0.0536	0.0858	0.1873	0.291	0.32	0.4	0.42	0.442	0.387	0.43	0.4	0.128	0
Garnet (Zack et al., 1997; Green et al., 2000)	0.0003	0.0022	0.02	0.14	0.26	0.6	1.7	2.7	4	4.5	6	0.001	3.2
Amphibole (Nandedkar et al., 2016)	0.279	0.656	1.827	3.312	3.345	4.792	5.307	5.212	5.396	4.685	4.147	0.339	5.012

References Composition	La	Ce	Nd	Sm	Eu	Gd	Tb	Dy	Er	Yb	Lu	Sr	Y
Primitive mantle (McDonough and Sun, 1995)	0.7	1.7	1.3	0.4	0.2	0.5	0.1	0.7	0.4	0.4	0.1	19.9	4.3
EMORB (Sun and McDonough, 1989)	6.3	15.0	9.0	2.6	0.9	3.0	0.5	3.6	2.3	2.4	0.4	155.0	22.0
Primitive Mantle + 10% EMORB	1.2	3.0	2.0	0.6	0.2	0.8	0.1	1.0	0.6	0.6	0.1	33.4	6.1

Average primitive arc basalts (Kelemen et al, 2003)	La	Ce	Nd	Sm	Eu	Gd	Tb	Dy	Er	Yb	Lu	Sr	Y
av. oceanic	7.01	15.67	10.14	2.7	0.95	3.1	0.52	3.31	2	1.86	0.27	-	-
av. continental	11.85	25.87	14.88	3.43	1.07	3.55	0.51	3.32	1.95	1.82	0.28	-	-
Lesser Antilles	8.72	18.94	10.93	2.68	0.91	3.47	0.43	3.86	2.38	1.59	0.25	-	-
Marianas	5	11.73	9.1	2.72	1.01	2.86	0.55	2.77	1.65	2.29	0.37	-	-
Andean	18.79	41.23	20.6	4.37	1.24	3.37	0.6	2.93	1.79	1.83	0.28	-	-
Cascades	11.29	24.22	13.74	3.16	1.02	3.46	0.49	3.29	1.88	1.88	0.27	-	-

Average primitive andesites (Kelemen et al., 2003)	La	Ce	Nd	Sm	Eu	Gd	Tb	Dy	Er	Yb	Lu	Sr	Y
av. continental	18.89	37.44	20.89	3.92	1.08	3.92	0.51	3.09	1.63	1.54	0.23	-	-
av. oceanic	-	-	-	-	-	-	-	-	-	-	-	-	-

Supplementary Table A.3: Series 3: Late Oligocene - Early Miocene

Step 1: non modal batch melting													
	Olivine	Orthopyroxene	Clinopyroxene	Garnet	Amphibole	Sum							
Source mode	0.45	0.27	0.13	0.12	0.03	1							
Melt mode	0.3	0.2	0.4	0	0.1	1							
Starting composition (ppm)	La	Ce	Nd	Sm	Eu	Gd	Tb	Dy	Er	Yb	Lu	Sr	Y
Primitive Mantle + 10% EMORB	1.3	3.0	2.0	0.6	0.2	0.8	0.1	1.0	0.6	0.6	0.1	33.4	6.1
Non-modal batch melting													
F=0.3	4.3	10.1	6.8	2.1	0.6	2.2	0.3	1.6	0.8	0.7	0.1	111.4	9.0
F=0.2	6.4	14.4	9.1	2.5	0.7	2.4	0.3	1.6	0.8	0.7	0.1	160.2	9.4
F=0.15	8.3	18.4	10.9	2.8	0.8	2.6	0.3	1.7	0.9	0.7	0.1	205.2	9.6
F=0.1	11.9	25.4	13.7	3.2	0.9	2.7	0.3	1.7	0.9	0.8	0.1	285.3	9.8
F=0.05	**21.0**	**41.0**	**18.2**	**3.7**	**1.1**	**2.9**	**0.3**	**1.8**	**0.9**	**0.8**	**0.1**	**468.1**	**10.1**
F=0.02	38.9	64.8	22.8	4.1	1.2	3.0	0.3	1.8	0.9	0.8	0.1	760.5	10.2
F=0.01	54.4	80.4	24.9	4.3	1.2	3.1	0.3	1.8	0.9	0.8	0.1	960.4	10.3

Step 2: Rayleigh fractionation of ultramafic rocks													
	Olivine	Orthopyroxene	Clinopyroxene										
Fractionation mode (Dunite)	0.9	0.05	0.05										
Starting composition (ppm)	La	Ce	Nd	Sm	Eu	Gd	Tb	Dy	Er	Yb	Lu	Sr	Y
From 5% partial melting	21.0	41.0	18.2	3.7	1.1	2.9	0.3	1.8	0.9	0.8	0.1	468.1	10.1
F=0.9	23.3	45.5	20.2	4.1	1.2	3.2	0.4	2.0	1.0	0.9	0.1	519.8	11.2
F=0.8	26.2	51.2	22.7	4.7	1.3	3.6	0.4	2.2	1.1	1.0	0.1	584.3	12.5
F=0.7	**30.0**	**58.4**	**25.9**	**5.3**	**1.5**	**4.1**	**0.5**	**2.5**	**1.3**	**1.1**	**0.2**	**667.2**	**14.3**
F=0.6	**34.9**	**68.1**	**30.2**	**6.2**	**1.7**	**4.8**	**0.6**	**2.9**	**1.5**	**1.3**	**0.2**	**777.6**	**16.6**
F=0.5	**41.9**	**81.7**	**36.2**	**7.4**	**2.1**	**5.7**	**0.7**	**3.5**	**1.8**	**1.5**	**0.2**	**931.9**	**19.8**
F=0.4	52.4	102.0	45.1	9.2	2.6	7.1	0.8	4.3	2.2	1.9	0.3	1163.2	24.6
F=0.3	69.7	135.8	60.0	12.2	3.4	9.5	1.1	5.7	2.9	2.5	0.4	1548.0	32.6

Kd values	La	Ce	Nd	Sm	Eu	Gd	Tb	Dy	Er	Yb	Lu	Sr	Y
Olivine (McKenzie & O'Nions, 1991)	0.0004	0.0005	0.001	0.0013	0.0016	0.0015	0.0015	0.0017	0.0015	0.0015	0.0015	0	0
Orthopyroxene (Green et al., 2000)	0.00055	0.0009	0.00305	0.0084	0.01695	0.023	0.0296	0.0406	0.0633	0.133	0.1185	0.001	0.049
Clinopyroxene (McKenzie & O'Nions, 1991; Elkins et al., 2008)	0.0536	0.0858	0.1873	0.291	0.32	0.4	0.42	0.442	0.387	0.43	0.4	0.128	0
Garnet (Zack et al., 1997; Green et al., 2000)	0.0003	0.0022	0.02	0.14	0.26	0.6	1.7	2.7	4	4.5	6	0.001	3.2
Amphibole (Nandedkar et al., 2016)	0.279	0.656	1.827	3.312	3.345	4.792	5.307	5.212	5.396	4.685	4.147	0.339	5.012
References Composition	La	Ce	Nd	Sm	Eu	Gd	Tb	Dy	Er	Yb	Lu	Sr	Y
Primitive mantle (McDonough and Sun, 1995)	0.7	1.7	1.3	0.4	0.2	0.5	0.1	0.7	0.4	0.4	0.1	19.9	4.3
EMORB (Sun and McDonough, 1989)	6.3	15.0	9.0	2.6	0.9	3.0	0.5	3.6	2.3	2.4	0.4	155.0	22.0

Primitive Mantle + 10% EMORB	1.2	3.0	2.0	0.6	0.2	0.8	0.1	1.0	0.6	0.6	0.1	33.4	6.1
Average primitive arc basalts (Kelemen et al, 2003)	La	Ce	Nd	Sm	Eu	Gd	Tb	Dy	Er	Yb	Lu	Sr	Y
av. oceanic	7.01	15.67	10.14	2.7	0.95	3.1	0.52	3.31	2	1.86	0.27	-	-
av. continental	11.85	25.87	14.88	3.43	1.07	3.55	0.51	3.32	1.95	1.82	0.28	-	-
Lesser Antilles	8.72	18.94	10.93	2.68	0.91	3.47	0.43	3.86	2.38	1.59	0.25	-	-
Marianas	5	11.73	9.1	2.72	1.01	2.86	0.55	2.77	1.65	2.29	0.37	-	-
Andean	18.79	41.23	20.6	4.37	1.24	3.37	0.6	2.93	1.79	1.83	0.28	-	-
Cascades	11.29	24.22	13.74	3.16	1.02	3.46	0.49	3.29	1.88	1.88	0.27	-	-
Average primitive andesites (Kelemen et al., 2003)	La	Ce	Nd	Sm	Eu	Gd	Tb	Dy	Er	Yb	Lu	Sr	Y
av. continental	18.89	37.44	20.89	3.92	1.08	3.92	0.51	3.09	1.63	1.54	0.23	-	-
av. oceanic	-	-	-	-	-	-	-	-	-	-	-	-	-

Appendix B: Rayleigh fractionation modeling using a starting composition of the average composition of the parental magmas for each magmatic series. Partition coefficients and associated references are given in the Table. See text for discussion.

Supplementary Table B.1: Series 1: Middle Eocene

Rayleigh fractionation - crustal processes	Clinopyroxene	Plagioclase	Amphibole	Magnetite	Zircon	Apatite	Sum						
Fractionation mode - southern part of the MOP	0.3	0.58	0.05	0.05	0.01	0.01	1						
Fractionation mode - northern part of the MOP	0.24	0.45	0.25	0.05	0.01	0	1						
Starting composition (ppm)	La	Ce	Nd	Sm	Eu	Gd	Tb	Dy	Er	Yb	Lu	Sr	Y
Average composition of parental magmas in MOP (SiO2<55 wt.%)	12.6	25.6	13.9	3.2	1.0	3.3	0.5	3.4	2.0	2.2	0.3	716.3	18.6
Rayleigh fractionation - southern part of the MOP													
F=0.9	13.7	27.8	14.8	3.4	1.0	3.4	0.5	3.5	2.1	2.3	0.4	719.0	19.9
F=0.8	15.1	30.5	15.8	3.6	1.0	3.5	0.5	3.6	2.2	2.4	0.4	722.0	21.3
F=0.7	**16.8**	**33.8**	**17.1**	**3.8**	**1.0**	**3.7**	**0.6**	**3.8**	**2.3**	**2.5**	**0.4**	**725.4**	**23.1**
F=0.6	**19.1**	**38.1**	**18.8**	**4.1**	**1.0**	**3.9**	**0.6**	**4.0**	**2.5**	**2.7**	**0.5**	**729.3**	**25.4**
F=0.5	**22.2**	**43.9**	**20.9**	**4.4**	**1.0**	**4.1**	**0.7**	**4.3**	**2.7**	**2.9**	**0.5**	**734.0**	**28.3**
F=0.4	26.6	52.2	23.9	4.9	1.0	4.4	0.7	4.7	2.9	3.2	0.6	739.8	32.4
F=0.3	33.7	65.3	28.3	5.5	1.0	4.8	0.8	5.2	3.3	3.6	0.7	747.3	38.5
F=0.2	46.9	89.5	36.0	6.7	1.0	5.5	0.9	6.0	3.9	4.3	0.8	758.0	49.2
F=0.1	82.7	153.5	54.4	9.1	1.0	6.8	1.2	7.6	5.2	5.8	1.2	776.7	74.9
Rayleigh fractionation - northern part of the MOP													
F=0.9	13.7	27.7	14.4	3.2	1.0	3.2	0.5	3.2	1.9	2.1	0.3	729.4	17.9
F=0.8	15.2	30.3	15.1	3.2	0.9	3.0	0.5	3.0	1.8	2.0	0.3	744.3	17.1
F=0.7	**17.0**	**33.4**	**15.9**	**3.2**	**0.9**	**2.8**	**0.4**	**2.8**	**1.7**	**1.9**	**0.3**	**761.6**	**16.3**

F=0.6	**19.3**	**37.5**	**16.9**	**3.2**	**0.8**	**2.6**	**0.4**	**2.6**	**1.5**	**1.8**	**0.3**	**782.1**	**15.4**
F=0.5	**22.5**	**42.9**	**18.2**	**3.2**	**0.7**	**2.4**	**0.4**	**2.4**	**1.4**	**1.7**	**0.3**	**806.9**	**14.3**
F=0.4	27.1	50.7	19.8	3.2	0.7	2.2	0.3	2.1	1.3	1.5	0.3	838.5	13.2
F=0.3	34.5	62.8	22.1	3.2	0.6	2.0	0.3	1.8	1.1	1.4	0.3	881.0	11.8
F=0.2	48.4	85.0	25.9	3.2	0.5	1.6	0.2	1.5	0.9	1.2	0.3	944.6	10.1
F=0.1	86.5	142.4	34.0	3.2	0.3	1.2	0.2	1.1	0.6	0.9	0.2	1064.1	7.8

Kd values	La	Ce	Nd	Sm	Eu	Gd	Tb	Dy	Er	Yb	Lu	Sr	Y
Plagioclase (Aignertorres et al., 2007)	0.071	0.045	0.104	0.065	1.2	0.153	0.102	0.128	0.137	0.141	0.19	1.568	0.009
Clinopyroxene (McKenzie & O'Nions, 1991; Elkins et al., 2008)	0.0536	0.0858	0.1873	0.291	0.32	0.4	0.42	0.442	0.387	0.43	0.4	0.128	-
Amphibole (Nandedkar et al., 2016)	0.279	0.656	1.827	3.312	3.345	4.792	5.307	5.212	5.396	4.685	4.147	0.339	5.012
Garnet (Zack et al., 1997; Green et al., 2000)	0.0003	0.0022	0.02	0.14	0.26	0.6	1.7	2.7	4	4.5	6	0.001	3.2
Magnetite (Luhr & Carmichael 1980)	0.325	0.27	0.4	0.42	0.31	0	0.52	0.51	-	0.355	0.38	-	-
Zircon (Fujimaki 1986)	3.11	3.49	3.8	4.72	2.39	6.41	-	-	-	-	-	-	-
Apatite (Watson and Green, 1981)	6.4	8.94	14.02	19.1	2	17.15	16.175	15.2	12.36	10.94	9.52	-	-

Supplementary Table B.2: Series 2: Late Eocene - Middle Oligocene

Rayleigh fractionation - crustal processes

	Clinopyroxene	Plagioclase	Amphibole	Magnetite	Zircon	Apatite	Sum
Fractionation mode	0.24	0.45	0.2	0.05	0.01	0.05	1

Starting composition (ppm)	La	Ce	Nd	Sm	Eu	Gd	Tb	Dy	Er	Yb	Lu	Sr	Y
Average compostition of parental magmas in MOP (SiO2<55 wt.%)	66.6	120.3	47.6	8.1	2.2	6.3	0.8	4.5	2.2	2.1	0.3	1404.2	22.4

Rayleigh fractionation - southern part of the MOP

F=0.9	72.3	129.2	49.2	8.1	2.1	6.0	0.7	4.3	2.2	2.2	0.3	1428.4	22.0
F=0.8	**79.3**	**139.9**	**51.0**	**8.0**	**2.0**	**5.7**	**0.7**	**4.0**	**2.2**	**2.2**	**0.3**	**1456.0**	**21.6**
F=0.7	**87.9**	**153.2**	**53.3**	**8.0**	**1.9**	**5.4**	**0.7**	**3.8**	**2.2**	**2.3**	**0.4**	**1487.9**	**21.1**
F=0.6	**99.2**	**170.0**	**55.9**	**7.9**	**1.8**	**5.1**	**0.6**	**3.6**	**2.2**	**2.3**	**0.4**	**1525.6**	**20.6**
F=0.5	114.3	192.4	59.3	7.8	1.6	4.7	0.6	3.3	2.2	2.4	0.4	1571.4	20.0
F=0.4	136.0	223.8	63.6	7.7	1.5	4.3	0.5	3.0	2.2	2.5	0.4	1629.3	19.2
F=0.3	170.2	271.9	69.7	7.5	1.3	3.8	0.4	2.6	2.2	2.6	0.5	1707.2	18.4
F=0.2	233.4	357.8	79.2	7.4	1.1	3.2	0.4	2.2	2.1	2.8	0.5	1823.3	17.2
F=0.1	400.6	572.1	98.7	7.0	0.9	2.4	0.3	1.6	2.1	3.2	0.7	2040.4	15.3

Kd values	La	Ce	Nd	Sm	Eu	Gd	Tb	Dy	Er	Yb	Lu	Sr	Y
Plagioclase (Aignertorres et al., 2007)	0.071	0.045	0.104	0.065	1.2	0.153	0.102	0.128	0.137	0.141	0.19	1.568	0.009
Clinopyroxene (McKenzie & O'Nions, 1991; Elkins et al., 2008)	0.0536	0.0858	0.1873	0.291	0.32	0.4	0.42	0.442	0.387	0.43	0.4	0.128	-
Amphibole (Nandedkar et al., 2016)	0.279	0.656	1.827	3.312	3.345	4.792	5.307	5.212	5.396	4.685	4.147	0.339	5.012
Garnet (Zack et al., 1997; Green et al., 2000)	0.0003	0.0022	0.02	0.14	0.26	0.6	1.7	2.7	4	4.5	6	0.001	3.2
Magnetite (Luhr & Carmichael 1980)	0.325	0.27	0.4	0.42	0.31	0	0.52	0.51	-	0.355	0.38	-	-
Zircon (Fujimaki 1986)	3.11	3.49	3.8	4.72	2.39	6.41	-	-	-	-	-	-	-
Apatite (Watson and Green, 1981)	6.4	8.94	14.02	19.1	2	17.15	16.175	15.2	12.36	10.94	9.52	-	-

Supplementary Table B.3: Series 3: Late Oligocene - Early Miocene

Rayleigh fractionation - crustal processes

	Clinopyroxene	Plagioclase	Amphibole	Magnetite	Zircon	Apatite	Sum
Fractionation mode	0.35	0.08	0.5	0.05	0.01	0.01	1

Starting composition (ppm)	La	Ce	Nd	Sm	Eu	Gd	Tb	Dy	Er	Yb	Lu	Sr	Y
Average compostition of parental magmas in MOP (SiO2<55 wt.%)	38.7	73.9	33.4	6.2	1.7	4.7	0.6	3.2	1.5	1.3	0.2	1400.4	15.4
Rayleigh fractionation - southern part of the MOP													
F=0.9	**41.8**	**77.9**	**32.8**	**5.5**	**1.6**	**3.9**	**0.5**	**2.6**	**1.2**	**1.1**	**0.2**	**1501.3**	**12.9**
F=0.8	**45.5**	**82.6**	**32.0**	**4.9**	**1.4**	**3.2**	**0.4**	**2.1**	**1.0**	**0.9**	**0.1**	**1622.7**	**10.6**
F=0.7	**50.1**	**88.3**	**31.3**	**4.3**	**1.2**	**2.5**	**0.3**	**1.6**	**0.7**	**0.7**	**0.1**	**1772.2**	**8.5**
F=0.6	56.0	95.4	30.4	3.7	1.1	1.9	0.2	1.2	0.5	0.6	0.1	1962.1	6.5
F=0.5	64.0	104.5	29.4	3.0	0.9	1.4	0.1	0.8	0.4	0.4	0.1	2213.0	4.8
F=0.4	75.2	116.8	28.2	2.4	0.7	0.9	0.1	0.5	0.2	0.3	0.1	2564.2	3.3
F=0.3	92.6	134.9	26.7	1.8	0.6	0.6	0.1	0.3	0.1	0.2	0.0	3100.5	2.1
F=0.2	124.2	165.3	24.8	1.2	0.4	0.3	0.0	0.1	0.1	0.1	0.0	4052.1	1.0
F=0.1	205.3	233.9	21.8	0.6	0.2	0.1	0.0	0.0	0.0	0.0	0.0	6403.4	0.3

Kd values	La	Ce	Nd	Sm	Eu	Gd	Tb	Dy	Er	Yb	Lu	Sr	Y
Plagioclase (Aignertorres et al., 2007)	0.071	0.045	0.104	0.065	1.2	0.153	0.102	0.128	0.137	0.141	0.19	1.568	0.009
Clinopyroxene (McKenzie & O'Nions, 1991; Elkins et al., 2008)	0.0536	0.0858	0.1873	0.291	0.32	0.4	0.42	0.442	0.387	0.43	0.4	0.128	-
Amphibole (Nandedkar et al., 2016)	0.279	0.656	1.827	3.312	3.345	4.792	5.307	5.212	5.396	4.685	4.147	0.339	5.012
Garnet (Zack et al., 1997; Green et al., 2000)	0.0003	0.0022	0.02	0.14	0.26	0.6	1.7	2.7	4	4.5	6	0.001	3.2
Magnetite (Luhr & Carmichael 1980)	0.325	0.27	0.4	0.42	0.31	0	0.52	0.51	-	0.355	0.38	-	-
Zircon (Fujimaki 1986)	3.11	3.49	3.8	4.72	2.39	6.41	-	-	-	-	-	-	-
Apatite (Watson and Green, 1981)	6.4	8.94	14.02	19.1	2	17.15	16.175	15.2	12.36	10.94	9.52	-	-

CHAPTER 3

Petrological characterization of subduction- and collision-related magmatism in the composite Meghri-Ordubad pluton, southernmost Lesser Caucasus (Tethyan Orogenic Belt)

HervŽ Rezeau[1], Julien Leuthold[2], Robert Moritz[1], Rodrik Tayan[3], Samvel Hovakimyan[1,3], Alexey Ulianov[4] and Kalin Kouzmanov[1]

[1]Department of Earth Sciences, University of Geneva, 1205 Geneva, Switzerland; [2]Institute of Geochemistry and Petrology, ETH ZŸrich, 8092 ZŸrich, Switzerland; [3]Institute of Geological Sciences, National Academy of Sciences, 0019 Yerevan, Armenia; [4]Institute of Earth Sciences, University of Lausanne, 1015 Lausanne, Switzerland

ABSTRACT

The composite Meghri-Ordubad pluton belongs to the southernmost Lesser Caucasus located in the central segment of the Tethyan orogenic belt. It is characterized by nested intrusions incrementally emplaced from Middle Eocene to Early Miocene coeval to the closure of the Neotethyan ocean and the regional Arabia-Eurasia continental collision. The recognition of three compositionally distinct magmatic series includes the early emplacement of subduction-related medium- to high-K calc-alkaline series 1, followed by syn-collisional shoshonitic to high-K calc-alkaline series 2, and post-collisional high-K calc-alkaline adakitic series 3. This study presents detailed petrography and mineral chemistry on representative dated intrusions for each differentiation series to shed light on the complex magmatic plumbing system that generated the composite Meghri-Ordubad pluton. The Middle Eocene magmatic series 1 is dominated by dioritic to tonalitic intrusions characterized by early plagioclase fractionation indicative of shallow crystallization (<200-350 MPa), and by the presence of hornblende gabbro displaying early amphibole crystallized at higher pressure (>200-350 MPa). The Late Eocene - Middle Oligocene K-rich magmatic series 2 is dominated by gabbro - monzogabbro - monzodiorite - monzonite - syenite intrusions and dikes characterized by a contrasting mineral assemblage, including crystallization of biotite at the expense of amphibole and the occurrence of abundant poikilitic K-felspar and occasionally nepheline. Based on the sequence of mineral crystallization and mineral chemistry, intrusions and dikes display crystallization at relatively high (>200-350 MPa) and low (<200-350 MPa) pressure representative of storage at various crustal levels. Subsidiary hornblende gabbro shows early amphibole fractionation suggesting crystallization in the mid- to lower crust. The Late Oligocene - Early Miocene high-K calc-alkaline adakitic magmatic series 3 includes early emplacement of lamprophyres followed by porphyritic granodioritic intrusions and dikes. Calc-alkaline lamprophyres are composed of high Mg# phlogopite, and clinopyroxene and amphibole

phenocrysts characterized by reverse chemical zoning characterized by high Mg#, high Cr and Ni contents together with the lowest REE contents and a lack Eu negative anomalies. This suggests ascent of primitive-like melt to the upper crust and host-rock assimilation and hybridization. Younger porphyritic granodioritic magmas indicate crystallization at shallower crustal levels (<200 MPa). Plagioclase textures and *in-situ* mineral chemistry reveal magma interactions indicative of open-system magmatic processes and crystallization dominated by cooling. Reverse chemical zoning displayed by amphibole and clinopyroxene phenocrysts combined with dendritic amphibole and phlogopite in the groundmass of calc-alkaline lamprophyres indicate hybridization in the upper crust and fast crystallization through rapid decompression and/or cooling, respectively. Such detailed petrological characterization allows us to identify various crustal levels of magma crystallization and to reveal interactions between magmas reservoirs through mafic resplenishment and recycling of crystal mushes. Although magmatic source processes control the liquid line of descent and consequently the sequence of mineral crystallization, each magmatic differentiation series is dominated by fractional crystallization ± crustal assimilation. In conclusion, we propose the first temporal and spatial petrogenetic model for the composite Meghri-Ordubad pluton encompassing three long-lived magmatic series incrementally emplaced over 30 million years.

Keywords: Arabia-Eurasia collision zone; incremental pluton growth; Lesser Caucasus; mineral chemistry; magmatic open-system processes

1. INTRODUCTION

Understanding the growth of composite batholiths that shape the continental crust represents one of the main scientific challenges for petrologists since decades. The characterization of intrusive complexes along an orogenic belt allows us to understand the cyclic evolution of an orogeny and incremental growth of the continental crust linked to a specific geodynamic evolution (e.g., DeCelles et al., 2009; DeCelles & Graham, 2015; Paterson & Ducea, 2015). Recent advances in geochronology together with thermal modelling revealed relatively fast pulses of magma batches in composite pluton complexes (from ~20 to ~500 ka), which helps to place new quantitative constraints on rates of melt emplacement and time scales of magmatic differentiation mechanisms (e.g., Lipman, 2007; Leuthold et al., 2012; Schoene et al., 2012; Carrichi et al., 2014; Annen et al., 2015; Barboni et al., 2015; Broderick et al., 2015; Samperton et al., 2015; Bucholz et al., 2016). Complementary experiments and field-based petrological studies on exposed crustal sections emphasized the role of fractional crystallization (± assimilation) as the main magmatic differentiation process (e.g., Grove et al., 2003; Sisson et al., 2005; Jagoutz, 2010; Bucholz et al., 2014; Nandedkar et al., 2014; Walker et al., 2015). Upper crustal magmatic systems are generally represented by silicic crystal-mush magma reservoirs, which are subject to chemical modification through episodic magma rejuvenation by

magma mixing and/or mingling, and ultimately may trigger large volcanic eruptions (e.g., Wotzlaw et al., 2013, 2015; Leuthold et al., 2014; Bachmann & Huber, 2016; Buret et al., 2017; Cashman et al., 2017).

The Lesser Caucasus belongs to the central segment of the Alpine-Himalayan orogenic belt and consists of three main tectonic domains (e.g., Sosson et al., 2010), including the Gondwana-derived South Armenian Block, the Sevan-Akera suture zone, and the Eurasian plate margin (Fig. 1a). The Lesser Caucasus records a complex orogenic evolution from Jurassic to Quaternary related to the successive closure of the northern and southern branch of the Neotethys ocean (e.g., Barrier & Vrielynck, 2008). The last major orogenic event corresponds to the Arabia-Eurasia continental collision evidenced by widespread Eocene to Quaternary magmatism along the Turkish-Iranian plateau (Fig. 1b). According to recent studies, the onset of collision occurred during the Late Eocene to Oligocene followed by post-collisional magmatism from Miocene to Quaternary (e.g., Allen & Armstrong, 2008; Agard et al., 2011; Ballato et al., 2011; Chiu et al., 2013; Kaislaniemi et al., 2014; Moritz et al., 2016; Rezeau et al., 2017). The composite Meghri-Ordubad pluton (MOP) represents the largest Cenozoic intrusive complex (~1000 km^2) in the Lesser Caucasus characterized by three distinct magmatic series (medium-K calc-alkaline, shoshonitic to high-K calc-alkaline) forming nested intrusions incrementally assembled over 30 m.y. from Middle Eocene to Early Miocene in subduction to post-subduction settings (Fig. 2; Karamyan et al., 1974; Moritz et al., 2016; Rezeau et al., 2016, 2017).

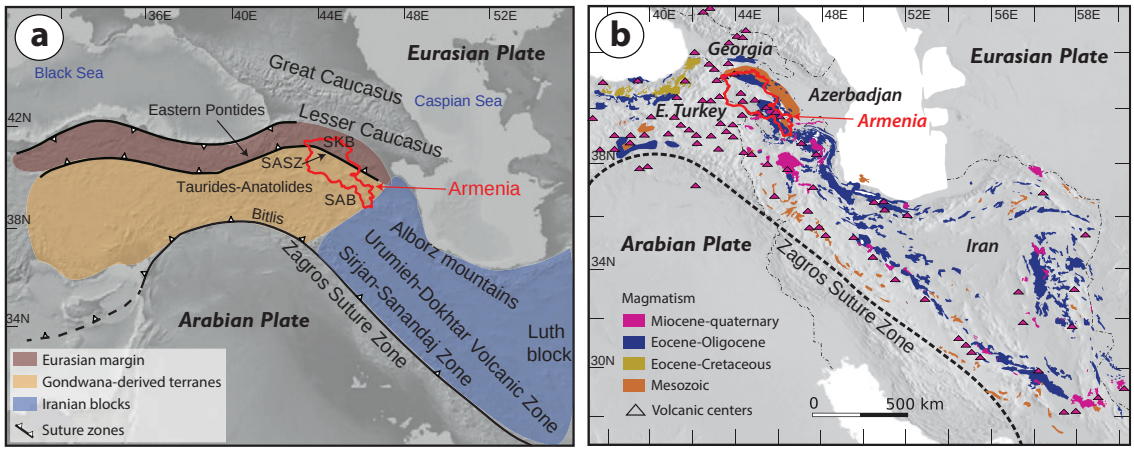

Figure 1: a) Regional map of the Turkish-Caucasus-Iranian collision zone showing the main tectonic units, suture zones and volcanic belts. SAB: South Armenian block, SASZ: Sevan-Akera suture zone, SKB: Somkheto-Karabagh belt. Modified after Sosson et al. (2010). b) Compilation of magmatism along the Turkish-Caucasus-Iranian collision zone after Chiu et al. (2013), Kuşcu et al. (2013), Mederer et al. (2013), Kaislaniemi et al. (2014), Delibaş et al. (2016) and Rezeau et al. (2016).

This study represents the first detailed petrological investigation of the composite MOP and aims at characterizing the crustal magmatic plumbing system for each magmatic series. Field and petrographic observations combined with *in-situ* major and trace element mineral chemistry help in (1) identifying various sequences of mineral crystallization representative of the parental melts composition, (2) placing quantitative constraints on pressure and temperature of magma crystallization, and (3) revealing crustal magmatic open-system processes. In conclusion, we propose a conceptual petrogenetic model for each magmatic series aiming at summarizing the incremental growth of the composite MOP in space and time.

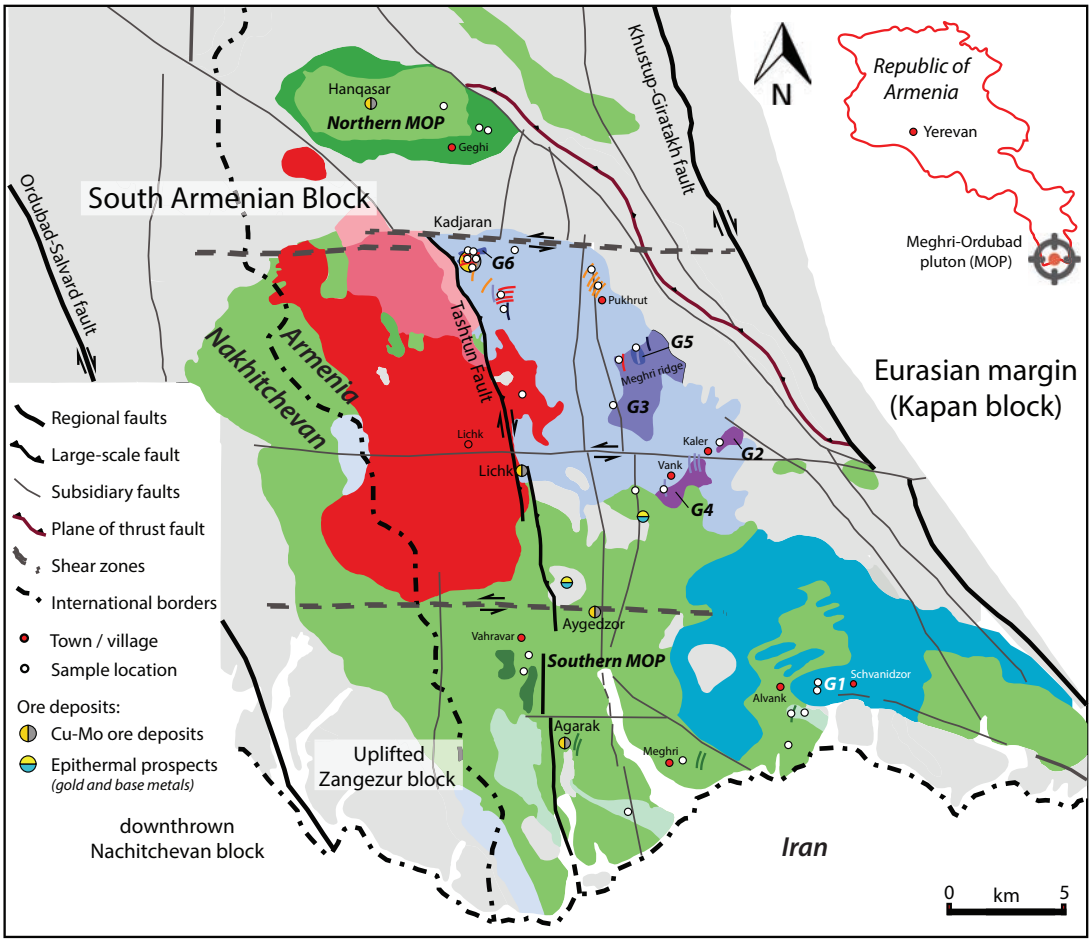

Intrusive Rocks of the Meghri-Ordubad Pluton

Late Oligocene - Early Miocene (26.6 - 21.2 Ma)

- Porphyry andesitic dike
- Porphyry granodiorite (3 sub-facies)
- Calc-alkaline lamprophyre (minette, vogesite, spessartite)

Late Eocene - Middle Oligocene (37.8 - 28.1 Ma)

- Dioritic to syenitic dike
- Nepheline-monzogabbro dike (Essexite)
- Monzonite
- Hornblende gabbro (G5,6)
- Monzodiorite (G3)
- Gabbros (G2,4)
- Monzogabbro/Monzodiorite (G1)

Middle Eocene (49.9 - 43.1 Ma)

- Andesitic dike
- Diorite to Tonalite
- Monzodiorite
- Hornblende gabbro
- Early granite / tonalite

Volcano-sedimentary rocks

- See Rezeau et al. (2017) for details

Figure 2: Simplified geological map of the composite Meghri-Ordubad pluton together with the main structural features and the location of major porphyry Cu-Mo ore deposits and epithermal prospects. Modified after Karamyan et al. (1974) and the updated version of Djrbashyan & Tayan (2008). The top right inset shows the location of the Meghri-Ordubad pluton in southern Armenia. G1 to G6 stand for gabbroids 1 to 6. See text for details.

2. FIELD OBSERVATIONS AND PETROGRAPHY

Recent geochronological and whole-rock geochemical studies have reassessed the sequence of intrusions and identified the emplacement of three successive magmatic series (Fig. 3; Moritz et al., 2016; Rezeau et al., 2016, 2017): 1) the middle Eocene medium- to high-K calc-alkaline series 1 (45.9 - 43.1 Ma), 2) late Eocene - Middle Oligocene shoshonitic series 2 (37.8 - 28.1 Ma), and 3) the late Oligocene - Early Miocene high-K calc-alkaline adakitic series 3 (26.6 - 21.2 Ma). In the following sections, we will describe representative samples from each individual differentiation series from a field-based perspective (Fig. 4) combined with petrographic observations, mainly carried out under optical microscopy (Fig. 5), QEMSCAN image analysis (Figs. 6 and 7; Appendix A) and backscattered images (Fig. 8). Sample descriptions including modal mineral proportions are provided in Table 1 and Appendix A.

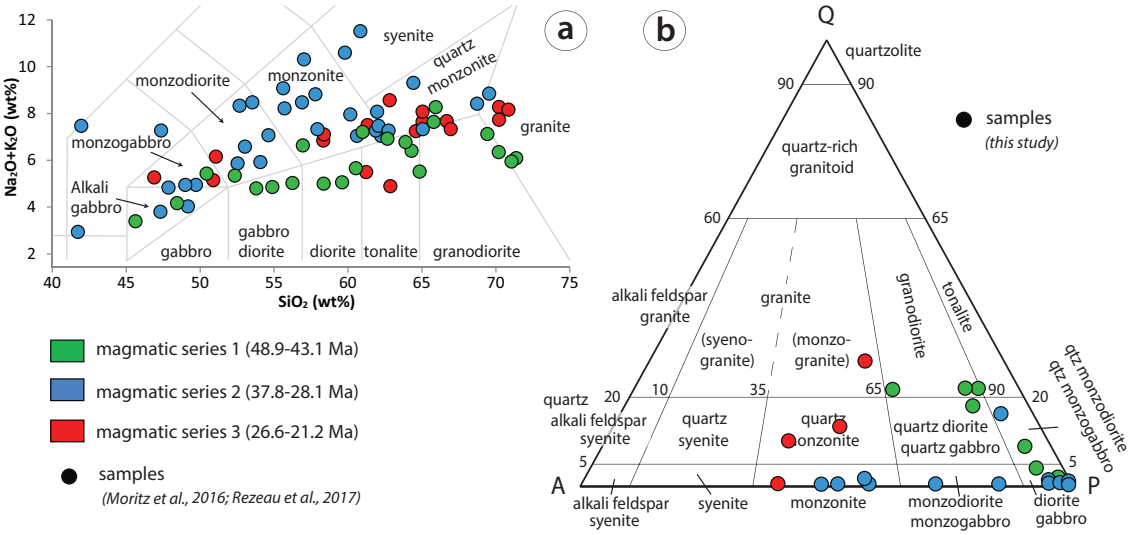

Figure 3: a) TAS diagram after Middlemost (1994), b) QAP modal classification of plutonic rocks after Le Ma"tre et al. (2002). End-members are Q=quartz, A=alkali feldspar and P=plagioclase. Modal proportions are from quantitative mineral QEMSCAN analyses of representative samples (see Fig. 7 and Table 1)

2.1 Middle Eocene intrusive series 1 (48.9 - 43.1 Ma)

Granite (48.9 ± 0.6 Ma) and tonalite (47.6 ± 0.6 Ma) are respectively emplaced in the southwestern and southeastern parts of the MOP and correspond to the oldest intrusions (Fig. 2).

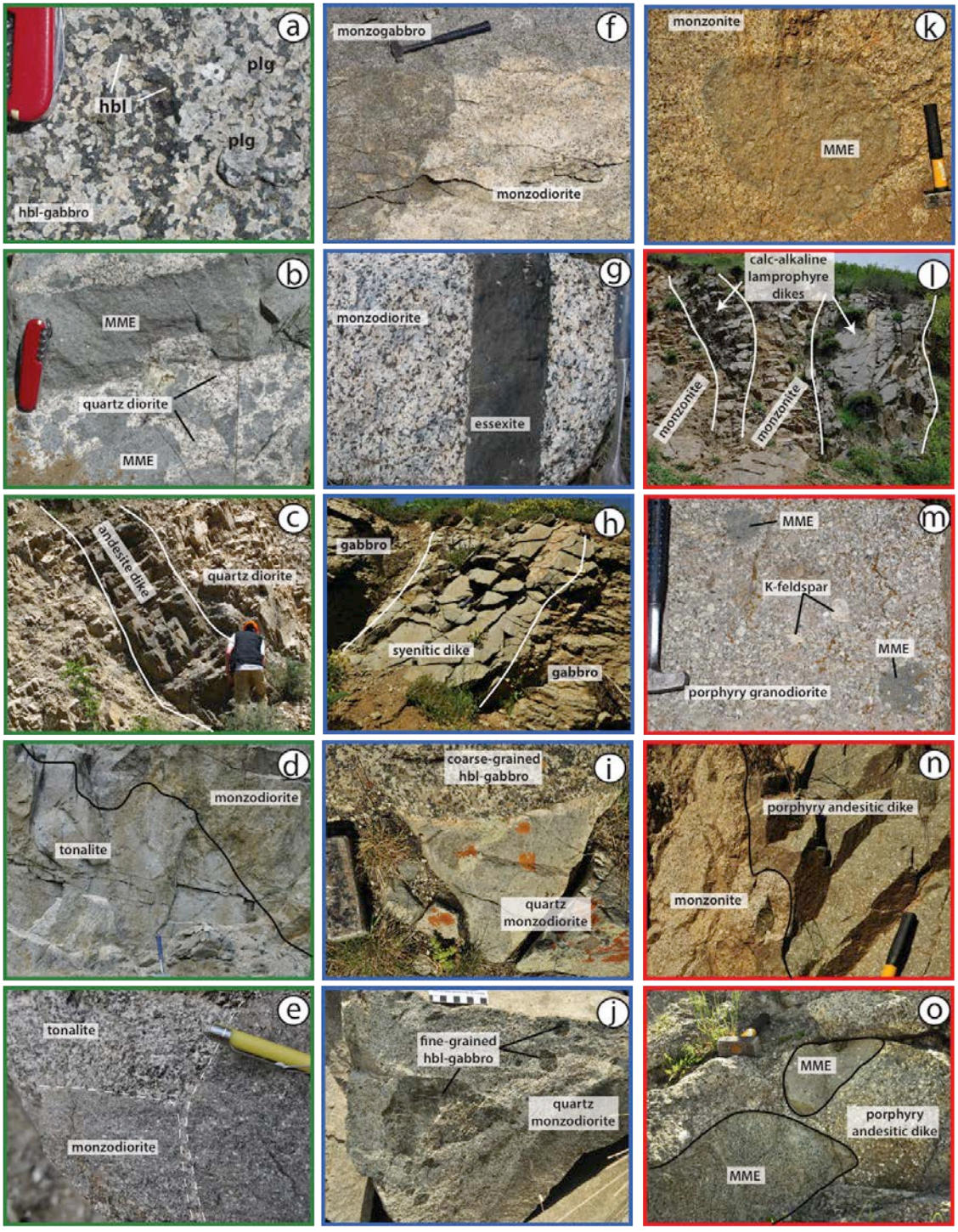

Figure 4: a) Coarse-grained hornblende gabbro with hornblende-plagioclase intergrowth near Vahravar village (Fig. 2). b) Magmatic breccia and/or mingling between diorite - tonalite and magmatic mafic enclaves near Vahravar village (Fig. 2). c) NNE-oriented andesitic dike crosscutting diorite - tonalite with sharp contact near Meghri town (Fig. 2). d) Ductile contact between tonalite and monzodiorite in the northern part of the MOP near Geghi village (Fig. 2). e) Close up with ductile tonalite apophysis penetrating the monzodiorite. f) Ductile contact between monzogabbro and monzodiorite near Schvanidzor village (Fig. 2). g) Essexite dike crosscutting monzodiorite with a sharp contact and carrying some plagioclase xenocrysts at Meghri ridge (Fig. 2). h) Syenitic dike crosscutting gabbro along the road to Vank

village (Fig. 2). i) Sharp contact between coeval coarse-grained hornblende gabbro and quartz monzodiorite at Meghri ridge (Fig. 2). j) Fine-grained hornblende gabbro enclaves in quartz monzodiorite dike at Meghri ridge (Fig. 2). k) Monzonite in Kadjaran area (Fig. 2) hosting magmatic mafic enclave. l) Parallel NNE-oriented calc-alkaline lamprophyre dikes crosscutting monzonite near Phukrut village (Fig. 2). m) Porphyry granodiorite (1st sub-facies) near Lichk (Fig. 2) showing assimilation of magmatic mafic enclaves. n) Sharp contact between a porphyry andesitic dike and the host monzonite near Kadjaran town (Fig. 2). o) Magmatic mafic enclaves showing different stages of assimilation within a porphyry andesitic dike near Kadjaran town (Fig. 2). See text for discussion. Abbreviations: hbl hornblende, MME mafic magmatic enclave, plg plagioclase.

The former is hydrothermally altered, whereas the latter displays a mineral assemblage dominated by plagioclase, quartz and K-feldspar together with subsidiary amphibole, biotite and magnetite. Accessory minerals mainly consist of titanite, zircon and apatite. They are not further considered in this study.

Hornblende gabbro (45.9 ± 0.9 Ma) represents the oldest mafic cumulates and occurs as small outcrops in the southwestern part of the MOP in the vicinity of Vahravar village (Fig. 2). It is almost exclusively composed of large amphibole and plagioclase intergrowth suggesting co-crystallization (Figs. 4a, 5a, 6a and 7). Amphibole displays large brown cores overgrown by a late green rim, which could reflect either crystallization from different magmas at various depths or sub-solidus reequilibration (Fig. 5a). K-feldspar occurs in late thin veinlets. Magnetite is abundant with ilmenite exsolutions (Figs. 5a and 6a). Titanite, zircon and apatite are accessory minerals.

Intermediate to felsic intrusions of dioritic to tonalitic composition (44.8 ± 0.9 to 43.8 ± 0.6 Ma) are mapped over a large area in the southern part of the MOP (Fig. 2). They are dominantly characterized by euhedral plagioclase and subsidiary late green amphibole hosting inclusions of plagioclase (Figs. 5b, 6b and 7). Quartz, K-feldspar and biotite are interstitial late mineral phases (Figs. 5b and 6b). Resorbed clinopyroxene is overgrown by amphibole and plagioclase exhibits sieved cores (Fig. 6b). Biotite is partially replaced by chlorite and epidote. Accessory minerals consist of magnetite, titanite, apatite, ilmenite and zircon. Noteworthy is that abundant magmatic mafic enclaves (MMEs) with sinuous borders illustrate interactions between a molten differentiated melt and a syn-magmatic mafic magma (Fig. 4b).

Andesitic dikes (44.0 ± 0.9 Ma) outcrop in the southern part of the MOP crosscutting diorite - tonalite with either sinuous or sharp contacts (Fig. 4c). The mineral assemblage is dominated by plagioclase and dark to light green amphibole together with minor quartz, biotite and K-feldspar (Figs. 5c, 6c and 7). Dark green amphibole macrocrysts host plagioclase inclusions and are overgrown by light green amphibole rims as illustrated by backscattered images showing resorption of early crystallized amphibole (Figs. 5c and 8a). Light green

amphibole also occurs as a late interstitial phase (Fig. 5c). Plagioclase displays optical zoning including sieved cores and/or successive zoning (Figs. 5c, 6c and 8b). Rare relicts of clinopyroxene are observed. Accessory minerals include titanite, zircon, apatite, and magnetite with ilmenite exsolution.

Monzodiorite (42.9 ± 0.5 Ma) and tonalite (43.1 ± 0.5 Ma) located in the northern part in the vicinity of the Geghi village (Fig. 2) are characterized by tonalite apophyses into the monzodiorite indicative of co-existence in the ductile regime (Figs. 4d,e). Monzodiorite is dominated by plagioclase and interstitial green amphibole together with subsidiary biotite, quartz, and K-feldspar (Figs. 5d, 6d and 7). Plagioclase commonly displays three optically distinct zones and outer rims are associated with green amphibole and biotite (Fig. 8c). Relicts of clinopyroxene surrounded by amphibole are observed. Magnetite, apatite, titanite, ilmenite and zircon are accessory minerals. Tonalite is composed of euhedral plagioclase, green amphibole and late interstitial quartz, K-feldspar and biotite similar to those emplaced in the southern part (Figs. 6e and 7). Locally, plagioclase exhibits optical zoning. Biotite is partially chloritized. Accessory minerals are magnetite, titanite, apatite, ilmenite and zircon.

2.2 Late Eocene - Middle Oligocene intrusive series 2 (37.8 - 28.1 Ma)

The magmatic series 2 is characterized by intrusions of similar compositions emplaced over ~10 m.y. from SE to NW in the MOP, but they are distinct in age and location (Fig. 2; Table 1). For the sake of clarity, they are grouped as follows: Schvanidzor monzogabbro-monzodiorite (hereafter referred to as Gabbroids 1), Kaler gabbro-monzogabbro (Gabbroids 2), Meghri ridge monzodiorite (Gabbroid 3), Vank gabbro-monzogabbro (Gabbroids 4), Meghri ridge hornblende gabbro (Gabbroid 5) and Kadjaran hornblende gabbro (Gabbroids 6) (Fig. 2).

Gabbroids 1 (G1 on Fig. 2) consist of monzogabbro and monzodiorite of similar age (37.8 ± 0.8 Ma and 37 ± 0.4 Ma) showing a mutual ductile contact (Fig. 4f). Monzogabbro is mainly composed of plagioclase and brown amphibole with subsidiary biotite and interstitial K-feldspar (Figs. 5e, 6f and 7). Euhedral plagioclase and biotite are optically homogeneous and occur as inclusions in amphibole, which suggests early plagioclase and biotite crystallization (Figs. 5e and 6f). Amphibole surrounds relicts of clinopyroxene as a mineral phase. Abundant large crystals of apatite inclusions (up to 2 vol%) occur in all mineral phases illustrating early apatite fractionation (Figs. 5e, 6f and 7). Zeolite group minerals are observed as late open-space filling minerals and document late magmatic metasomatic process. As this unit was formerly described as nepheline-bearing syenogranite, zeolites may also correspond to the alteration of former feldspathoid minerals (Deer et al., 2004). The monzodiorite displays a similar mineral assemblage, however the abundance of ferromagnesian minerals decreases at the expense of feldspars (Table 1). Accessory minerals are zircon, titanite and magnetite.

Table 1: Samples descriptions

					modal proportion of major mineral phases (%)**								
Sample name	**Rock type**	**Dates (Ma)***	**Longitude**	**Latitude**	**ol**	**cpx**	**amph**	**plg**	**bt**	**ksp**	**qtz**	**ksp-qtz matrix**	**neph**
AG1401	Hornblende Gabbro	45.9 ± 0.9	E46 10.329	N38 57.179	-	0	51	38	0	1	0	-	-
AG1406	Andesite	44 ± 0.9	E46 19.892	N38 56.303	-	1	22	60	5	4	6	-	-
AG1402	Quartz diorite	43.8 ± 0.6	E46 10.329	N38 57.179	-	0	12	54	5	9	17	-	-
AG1403	Quartz diorite	44.1 ± 1	E46 17.324	N38 55.012	-	-	-	-	-	-	-	-	-
AG1404	Quartz diorite	44.8 ± 0.9	E46 17.324	N38 55.012	-	0	11	55	7	7	17	-	-
HQ1402	Monzodiorite	42.9 ± 0.5	E46 08.393	N39 13.702	-	0	14	74	2	5	3	-	-
HQ1403	Tonalite	43.1 ± 0.5	E46 07.348	N39 13.805	-	0	9	45	1	22	18	-	-
AG1308A1	Monzogabbro	37.8 ± 0.8	E46 22.594	N38 56.873	-	2	28	36	7	14	0	-	-
AG1308A	Monzodiorite	37 ± 0.4	E46 22.594	N38 56.873	-	-	-	-	-	-	-	-	-
VK1404	Gabbro	35.7 ± 0.6	E46 16.975	N39 03.411	-	22	0	62	10	1	0	-	-
VK1405	Monzogabbro	34.8 ± 0.5	E46 16.975	N39 03.411	-	-	-	-	-	-	-	-	-
MR1403	Monzodiorite	34.6 ± 0.6	E46 14.495	N39 05.877	1	12	0	38	7	35	0	-	2
LI1303A1	Gabbro	33.5 ± 0.6	E46 15.578	N39 03.458	-	9	0	68	10	3	0	-	-
MR1402	Hornblende Gabbro	33.49 ± 0.02	E46 13.287	N39 06.159	-	1	43	42	1	1	0	-	-
KJ1317_mafic	Hornblende Gabbro	*33.5 ± 0.7*	E46 13.287	N39 06.159	-	0.1	21	72	-	1	-	-	-
KJ1317_felsic	quartz monzodiorite	33.7 ± 0.5	E46 13.287	N39 06.159	-	1.5	7	69	-	6	14	-	-
KJ0901A	Monzonite	31.9 ± 0.5	E46 10.532	N39 08.954	-	2	2	51	3	37	1	-	-
KJ1006A	Monzonite	31.9 ± 0.5	E46 12.745	N39 09.076	-	1	7	40	7	42	0	-	-
KJ1508	Hornblende Gabbro	28.3 ± 0.4	E46 08.416	N39 08.840	-	1	39	46	2	2	0	-	-
MR1404	Essexite	-	E46 14.495	N39 05.877	-	-	-	-	-	-	-	-	-
KJ1303A	Vogesite	25.5 ± 0.3	E46 12.629	N39 07.513	-	0	11	19	6	27	5	-	-
KJ1307	Spessartite	24.3 ± 0.3	E46 12.907	N39 08.182	-	-	-	-	-	-	-	-	-
MR1401	Porphyry andesitic dike	24.5 ± 0.4	E46 12.808	N39 06.430	-	0	0	35	1	31	10	14	-
LI1301	Porphyry granodiorite	22.6 ± 0.5	E46 10.368	N39 01.780	-	0	11	35	6	23	22	-	-
KJ1313	Porphyry andesitic dike	21.2 ± 0.5	E46 10.368	N39 01.780	-	0	0.2	24	5	21	5	31	-

* From Rezeau et al. (2016) except for sample MR1402 from Moritz et al. (2016a) - The date in italic represent an unpublished age.

** Modal compositions have been calculated using QEMSCAN image analysis.

Abbreviations: Ol Olivine, Cpx Clinopyroxene, Amph Amphibole Plg Plagioclase Bt Biotite Ksp K-feldspar, Qtz Quartz, Neph Nepheline

Gabbroids 2 (G2 on Fig. 2) include gabbro and monzogabbro of overlapping age (35.7 ± 0.6 Ma and 34.8 ± 0.5 Ma). Gabbro is dominated by plagioclase and weathered clinopyroxene with subsidiary biotite, magnetite and apatite (Figs. 5f, 6g and 7). Plagioclase is generally characterized by distinct core and rim (Fig. 6g). Apatite inclusions occur in both plagioclase and clinopyroxene as an early fractionating phase, whereas biotite was formed by reaction along clinopyroxene and magnetite grains (Fig. 5f and 6g). Zircon, magnetite and titanite are accessory minerals. Monzogabbro represents a coeval differentiated melt displaying rare relicts

of clinopyroxene together with variably sized plagioclase, and higher proportion of poikilitic K-feldspar and late interstitial biotite.

Gabbroid 3 consists of a large monzodiorite in area dated at 34.6 ± 0.6 Ma (G3 on Fig. 2). It is essentially composed of clusters of clinopyroxene and altered olivine rimmed by biotite and magnetite, plagioclase phenocrysts and poikilitic K-feldspar displaying late nepheline wormy exsolutions (Figs. 5g, 6h and 7). Apatite inclusions occur in olivine, clinopyroxene and plagioclase indicative of their early crystallization (Fig. 6g), whereas plagioclase and biotite are only observed in and/or along clinopyroxene grains (Fig. 7h). Accessory minerals are magnetite, baddeleyite and zircon. Olivine-rich MMEs (troctolite) are also observed and discussed further below in the mineral chemistry section.

An essexite dike, also known as nepheline monzogabbro (Le Ma'tre et al., 2002), crosscuts Gabbroid 3 at the Meghri ridge and displays crystal assimilation of the host rock (Fig. 4g). The mineral assemblage is dominated by clinopyroxene with co-crystallizing biotite, magnetite, Cu-Fe sulfides and late poikilitic nepheline (Figs. 5h and 8f). The studied sample was devoid of zircon and its age remains unconstrained. However, the presence of nepheline suggests that this rock type likely belongs to the shoshonitic Si-undersaturated to Si-critically saturated magmatic series 2.

Gabbroid 4 (G4 on Fig. 2) is a small outcrop of gabbro dated at 33.5 ± 0.6 Ma and spatially close to Gabbroids 2. It is mainly composed of plagioclase, clinopyroxene and biotite with late interstitial K-feldspar (Figs. 5i, 6i and 7). Plagioclase displays distinct cores and rims and poikilitic biotite crystals are reaction phases to clinopyroxene and magnetite (Figs. 6i and 8e). Apatite and plagioclase inclusions in clinopyroxene represent the earliest phase to crystallize (Fig. 6i). Accessory minerals are zircon, titanite and ilmenite. Important to note that a coeval syenitic dike dated at 33.6 ± 0.6 Ma crosscuts the intrusion and likely represent a syn-magmatic differentiated melt (Fig. 4h).

Gabbroid 5 (G5 on Fig. 2) is emplaced within G3 and consists of a coarse-grained cumulate hornblende gabbro dated at 33.49 ± 0.02 Ma. It is essentially composed of large brown amphibole and plagioclase with subordinate clinopyroxene relicts and biotite (Figs. 5j, 6j and 7). Amphibole inclusions in plagioclase indicate early amphibole fractionation (Fig. 6j). Apatite and magnetite are abundant (up to 3 vol%) and their occurrence in amphibole and rarely in plagioclase suggests an early crystallization (Figs. 5j and 7). Additionally, field observations and zircon U-Pb geochronology reveal that a coeval quartz monzodiorite dike dated at 33.7 ± 0.5 Ma and MMEs-hosted fine-grained hornblende gabbro (Fig. 4j) dated at 33.5 ± 0.6 Ma (unpublished data) crosscut the coarse-grained hornblende gabbro (Fig. 4i). The quartz monzodiorite dike and MMEs exhibit rare plagioclase sieved cores overgrown by optically

homogeneous rims associated with late interstitial green amphibole, quartz and K-feldspar. Accessory minerals are zircon, titanite and ilmenite.

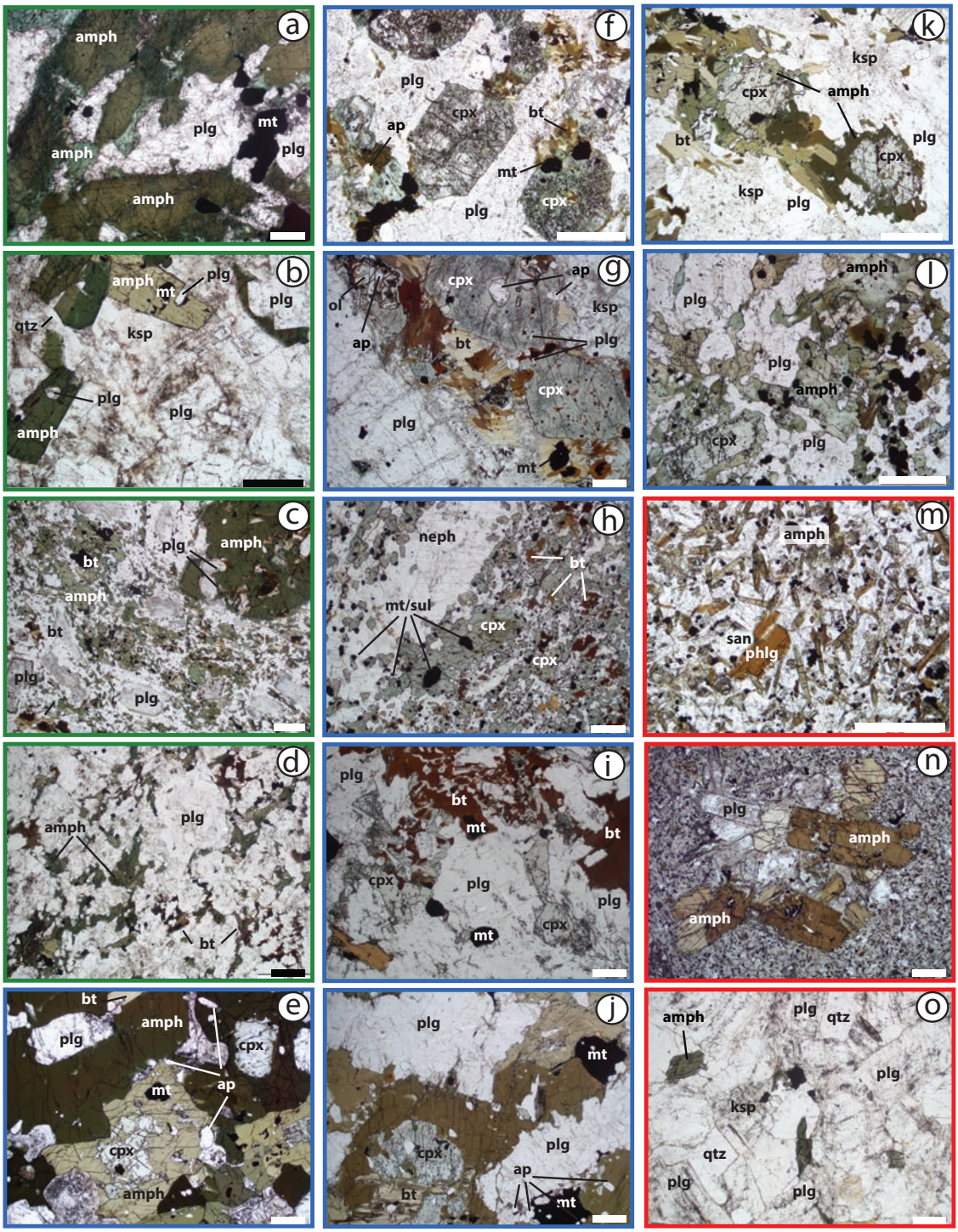

Figure 5: Summary of representative mineral textures observed in the MOP. a) Hornblende gabbro with subhedral brown amphibole (amph) with green overgrowths and co-crystallizing plagioclase (plg) and magnetite (mt). b) Tonalite with plagioclase inclusions in amphibole with interstitial K-feldspar (ksp) and quartz (qtz). c) Andesitic dike with subhedral brown amphibole with plagioclase inclusions rimmed and surrounded by late green amphibole and biotite (bt). Note the visible zoning in plagioclase. d) Monzodiorite

emplaced in the northern part of the MOP displaying plagioclase with interstitial green amphibole and biotite. e) Highly pleochroic brown amphibole with clinopyroxene (cpx), plagioclase, biotite and apatite (ap) inclusions in monzogabbro (Gabbroids 1). f) Gabbro with altered clinopyroxene and euhedral plagioclase with magnetite, biotite and apatite (gabbroids 2). g) Monzodiorite (Gabbroid 3) hosting olivine, clinopyroxene and plagioclase phenocrysts surrounded by large poikilitic K-feldspar in monzodiorite. Biotite occurs as reaction along the clinopyroxene and magnetite grain margins. Note apatite inclusions in olivine and clinopyroxene, and plagioclase inclusions in clinopyroxene. h) Essexite with clinopyroxene along with biotite, magnetite and primary Fe-Cu sulfides surrounded by late nepheline. i) Gabbro (Gabbroid 4) with plagioclase and clinopyroxene together with reddish biotite and magnetite. j) Hornblende gabbro (Gabbroid 5) showing clinopyroxene surrounded by brown amphibole with apatite and magnetite inclusions and large plagioclase in contact. Biotite occurs as late mineral phase. k) Monzonite with plagioclase phenocrysts and clinpyroxene clusters surrounded by brown amphibole and biotite within poikilitic K-feldspar. l) Hornblende gabbro (Gabbroid 6) showing hydrothermally altered brown to green amphibole surrounding clinopyroxene together with interstitial plagioclase. m) Calc-alkaline lamprophyre (vogesite) showing fine-grained acicular brown amphibole, phlogopite (phlg) and sanidine (san). n) Calc-alkaline lamprophyre (spessartite) with phenocrysts of brown amphibole and plagioclase surrounded by feldspar microlites. o) Porphyry granodiorite showing plagioclase, quartz, K-feldspar and interstitial green amphibole.

Monzonite (31.9 ± 0.5 and 31.83 ± 0.02 Ma) was emplaced in the MOP over a large area (Fig. 2). Monzonite is characterized by large plagioclase phenocrysts and clinopyroxene clusters overgrown by brown amphibole surrounded by biotite and late poikilitic K-feldspar (Figs. 5k, 6k and 7). Apatite occurs in both clinopyroxene and amphibole illustrating its early fractionation (Figs. 5k and 6k). Accessory minerals are characterized by zircon, titanite and magnetite. We also report abundant MMEs, which are not further investigated (Fig. 4k).

Gabbroid 6 consists of coeval fine-grained hornblende gabbro (28.3 ± 0.5) coevally emplaced to an heavily altered monzonite (28.1 ± 0.5 Ma) outcropping in and around the large Kadjaran Cu-Mo porphyry-epithermal deposit (G6 on Fig. 2). The hornblende gabbro is composed of plagioclase and patchy green to brown amphibole replacing clinopyroxene relicts, combined with subordinate biotite and late K-feldspar (Figs. 5l, 6l and 7). Although relatively well preserved, amphibole and plagioclase experienced hydrothermal alteration evidenced by the presence of shreddy biotite, chlorite and epidote (Figs. 5l and 6l). This indicates hydrothermal alteration certainly related to the formation of the Kadjaran Cu-Mo porphyry-epithermal deposit. Zircon, apatite, and titanite represent accessory phases.

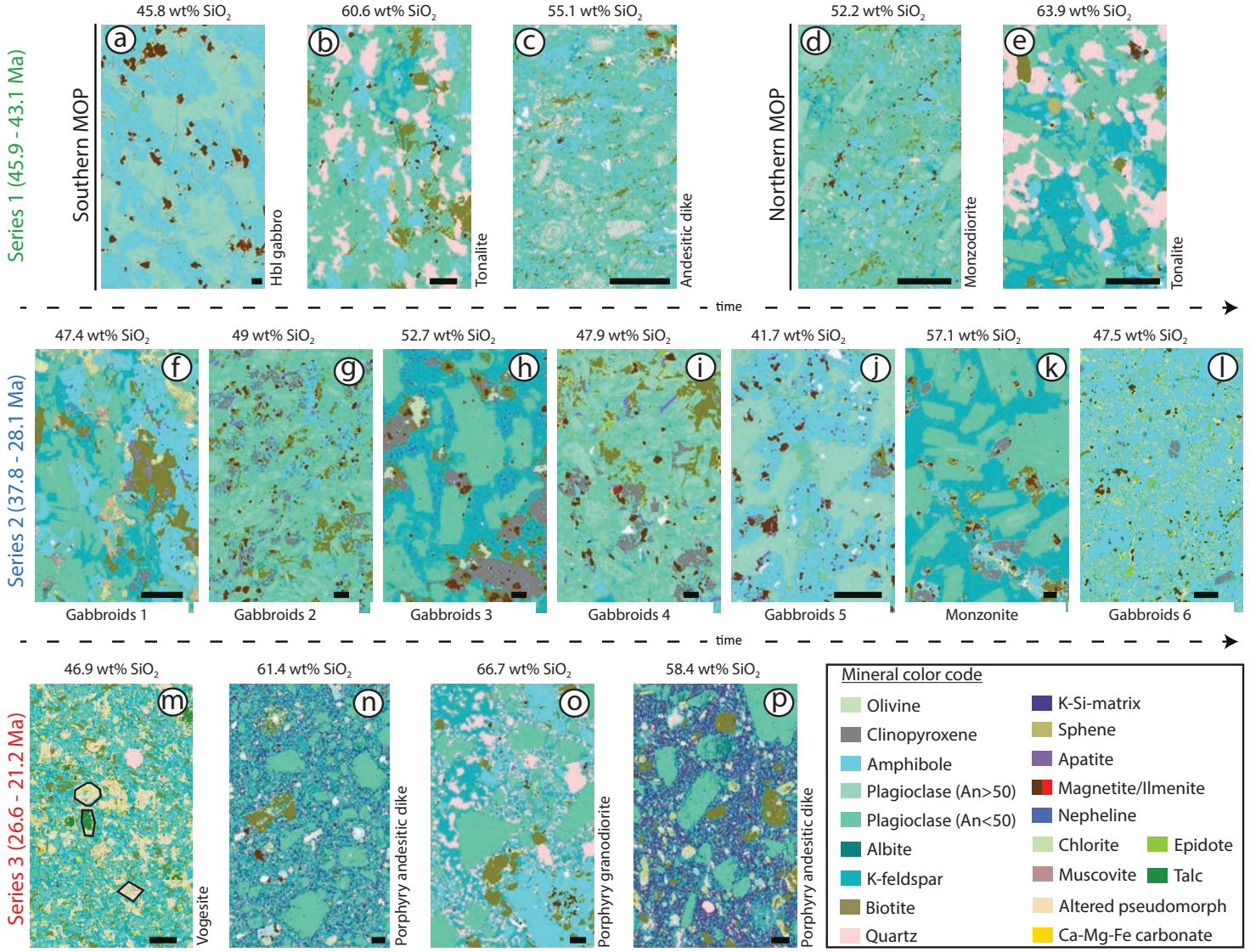
Series 1 (45.9 - 43.1 Ma)
Southern MOP
Northern MOP
45.8 wt% SiO2
60.6 wt% SiO2
55.1 wt% SiO2
52.2 wt% SiO2
63.9 wt% SiO2
a
b
c
d
e
Hbl gabbro
Tonalite
Andesitic dike
Monzodiorite
Tonalite
time
Series 2 (37.8 - 28.1 Ma)
47.4 wt% SiO2
49 wt% SiO2
52.7 wt% SiO2
47.9 wt% SiO2
41.7 wt% SiO2
57.1 wt% SiO2
47.5 wt% SiO2
f
g
h
i
j
k
l
Gabbroids 1
Gabbroids 2
Gabbroids 3
Gabbroids 4
Gabbroids 5
Monzonite
Gabbroids 6
time
Series 3 (26.6 - 21.2 Ma)
46.9 wt% SiO2
61.4 wt% SiO2
66.7 wt% SiO2
58.4 wt% SiO2
m
n
o
p
Vogesite
Porphyry andesitic dike
Porphyry granodiorite
Porphyry andesitic dike
Mineral color code
Olivine
Clinopyroxene
Amphibole
Plagioclase (An>50)
Plagioclase (An<50)
Albite
K-feldspar
Biotite
Quartz
K-Si-matrix
Sphene
Apatite
Magnetite/Ilmenite
Nepheline
Chlorite
Epidote
Muscovite
Talc
Altered pseudomorph
Ca-Mg-Fe carbonate

Figure 6: QEMSCAN false-color images of representative samples for each individual magmatic series emplaced in the MOP with whole-rock SiO_2 weight percent indicated. Scale bar is 2 millimeters. See text for discussion.

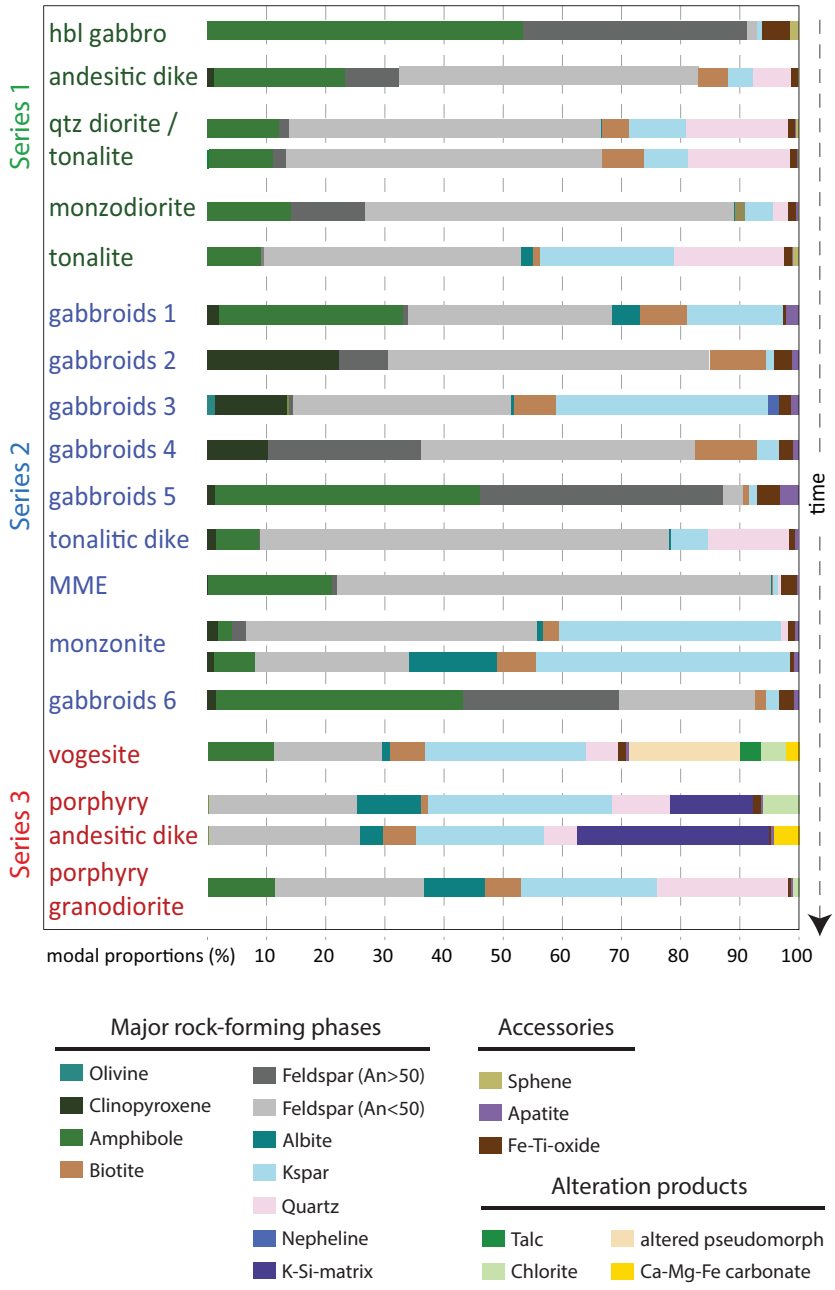

Figure 7: Modal proportions of rock-forming minerals (>1%) for representative samples of each individual magmatic series emplaced in the MOP. See QEMSCAN images in Figure 6 and associated details in Supplementary Tables A.1-3.

2.3 Late Oligocene - Early Miocene intrusive series 3 (26.6 - 21.2 Ma)

Calc-alkaline lamprophyre dikes (26.6 ± 0.3 Ma to 24.3 ± 0.3Ma) are located near Pukhrut village and in the Kadjaran ore field area (Fig. 2). They are intruding diorite to tonalite and monzonite from the Series 1 and 2, respectively (Figs. 2 and 4l). According to Le Ma'tre et al. (2002), calc-alkaline lamprophyres composed of higher proportions of biotite compared to

hornblende are classified as minette (K-feldspar > plagioclase) and kersantite (plagioclase > K-feldspar), whereas dikes dominated by hornblende and/or clinopyroxene are named vogesite (K-feldspar > plagioclase) and spessartite (plagioclase > K-feldspar). Earlier studies in the MOP reported and mapped these lamprophyre dikes as kersantite, minette and spessartite (Karamyan et al., 1974; Djrbashyan & Tayan, 2008), however, calc-alkaline lamprophyre dikes investigated in this study either display a groundmass dominated by K-feldspar over plagioclase and by acicular brown amphibole over strongly pleochroic yellow-brown biotite, or are characterized by a groundmass dominated by plagioclase combined with clinopyroxene and amphibole phenocrysts, which allow us to classify them as vogesite and spessartite, respectively (Figs. 5m,n, 6m and 7, Table 1). Spessartite hosts reversely zoned clinopyroxene and amphibole phenocrysts together with resorbed quartz macrocrysts, which likely indicate assimilation of the host-rock (Figs. 8g,h). Carbonate and talc commonly replace former primary mineral phases such as clinopyroxene and/or amphibole pseudomorphs (Fig. 6m). Such alteration features are interpreted as a late autometasomatic stage due to the volatile-rich character of lamprophyre magmatism, also known as deuteric alteration (Rock, 1991; Prelević et al., 2004). Alternatively, it might be due to hydrothermal alteration in the vicinity of ore deposits (Prelević et al., 2004).

Porphyritic granodiorite (22.6 ± 0.5 Ma) is emplaced to the west of the N-S-oriented Tashtun fault from Lichk village to Kadjaran town (Fig. 2). Three sub-facies have been identified based on the abundance of K-feldspar phenocrysts (Fig. 2; Tayan et al., 1976). Magmatic mafic enclaves are common and contain K-feldspar xenocrysts, which illustrate host-rock assimilation and chemical interaction between two co-existing magmas of variable composition (Fig. 4m). Porphyritic granodiorite is composed of K-feldspar, plagioclase, quartz and subsidiary green amphibole and biotite (Figs. 5o, 6o and 7). Few plagioclase phenocrysts display sieved cores overgrown by complex oscillatory zoning (Fig. 8i). Accessory minerals are zircon, apatite, titanite and magnetite.

Syn-magmatic porphyritic andesitic dikes (24.5 ± 0.3 Ma, 22.2 ± 0.3 Ma and 21.2 ± 0.3Ma) crosscut monzonite in the Kadjaran ore field and Gabbroid 3 in the Meghri ridge (Figs. 2 and 4n). We also report MMEs showing partial to advanced assimilation of the host porphyryitic ganodiorite (Fig. 4). The mineral assemblage is dominated by plagioclase, biotite and altered amphibole phenocrysts surrounded by a weathered groundmass composed of altered fine-grained K-feldspar and plagioclase together with resorbed quartz, which is further characterized as a Si-K-rich matrix (Figs. 6n,p and 7). Rare plagioclase exhibits optical zoning and accessory minerals are zircon, apatite, titanite and magnetite.

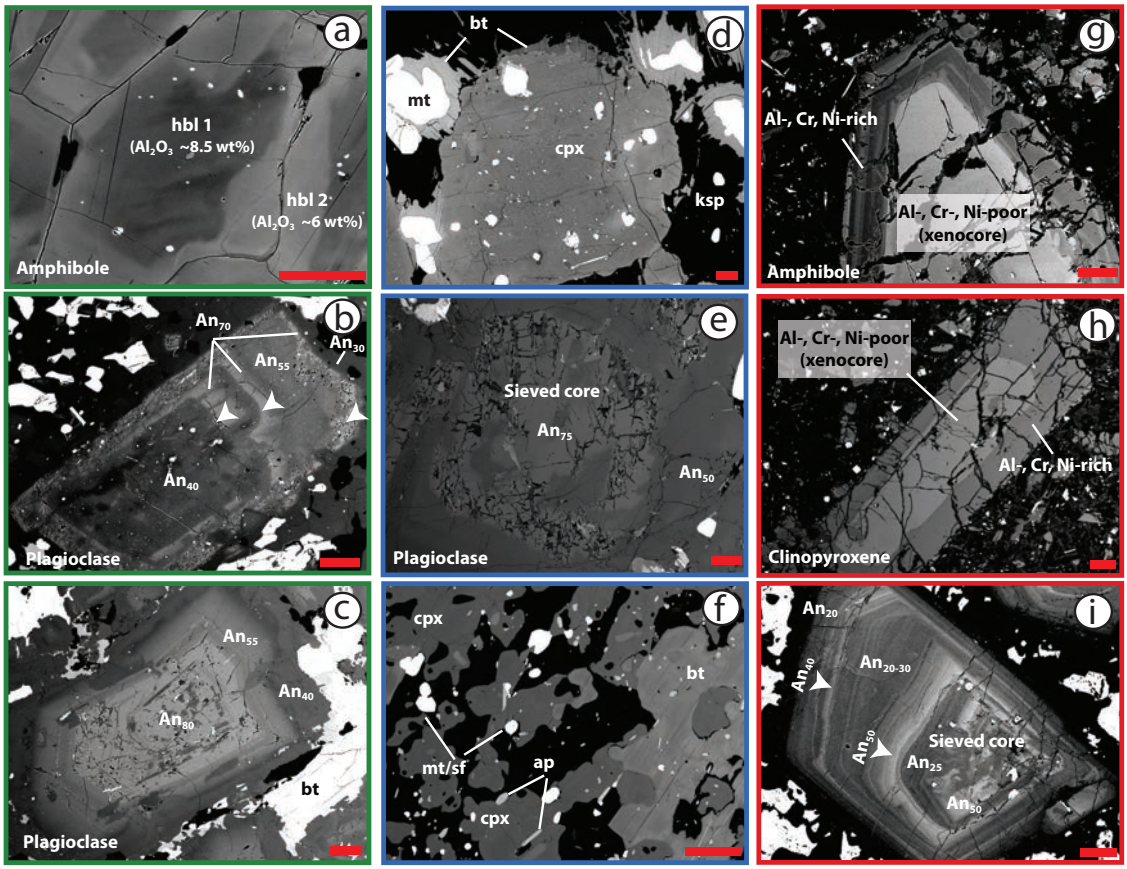

Figure 8: Back-scattered images showing a) Al-rich amphibole resorbed at the expense of Al-poor amphibole in andesitic dikes, b) Complex zoning in plagioclase with several An-rich to An-poor resorbed zones (white arrows) in andesitic dikes, c) Normally zoned plagioclase with three distinct zones from An-rich to An-poor in monzodiorite, d) Fairly homogeneous clinopyroxene (cpx) together with magnetite (mt), biotite (bt) and poikilitic K-feldspar (ksp) in Gabbroid 3, e) Plagioclase with An-rich sieved core and An-poor overgrowth in gabbroids 4, f) Clinopyroxene with biotite and a large amount of magnetite, Cu-Fe-sulfides (sf) and apatite (ap) inclusions occurring in essexite dike g, h) Amphibole and clinopyroxene phenocrysts hosted in spessartite showing reverse zoning and revealing Al-, Cr-, and Ni-poor xenocores surrounded by Al-, Cr-, and Ni-rich rim, i) Complex plagioclase textures showing An-rich sieved core and oscillatory zoning sequences from An-rich (white arrows) to An-poor. Scale bar is 50 µm. See text for discussion.

3. ANALYTICAL METHODS

Petrographic observations were carried out under petrographic microscope combined with automated mineral analysis and textural imaging of the studied samples using an FEI QEMSCAN¨ Quanta 650F facility at the Department of Earth Sciences, University of Geneva, Switzerland. The system is equipped with two Bruker QUANTAX light-element energy dispersive X-ray spectrometer (EDS) detectors. Analyses were conducted at a high vacuum, accelerating voltage of 25 kV, and a beam current of 10 nA on carbon-coated polished thin sections. The field image operating mode (Pirrie et al., 2004) was used for analyses. In total,

221 individual fields were measured per sample, with 1500 μm^2 per field, and a point spacing of 5 µm or 10 µm. One thousand counts per point were acquired, yielding a limit of detection of approximately 2wt% per element for mineral classification. Measurements were performed using the iMeasure v5.3.2 software, and the iDiscover¨ v5.3.2 software package was used for data processing. Electronic results consist of: i) high-quality spatially resolved and fully quantified mineralogical maps, ii) BSE images with identical resolution as the mineralogical maps, and iii) X-ray element distribution maps.

Major element compositions of minerals were measured *in-situ* on thin sections using a five-spectrometer JEOL JXA-8200 Superprobe (hereafter referred as to electron probe micro-analyzer, EPMA) at the Institute of Earth Sciences, University of Lausanne, Switzerland. Natural and synthetic silicate and oxide phases were used as standards. Operating conditions were 15 kV, 15 nA and a 3 µm beam. Depending on the nature of the analysed elements (i.e. alkali and non-alkali), counting times were 10s-30s on peak and 5s-15s on the respective background.

In-situ mineral trace element analyses were carried out on 100 µm-thick sections by laser ablation inductively coupled plasma mass spectrometry (LA-ICP-MS) using an ELEMENT XR system interfaced to a NewWave UP-193 ArF excimer ablation system at the Institute of Earth Sciences, University of Lausanne, Switzerland. The laser was operated with a spot size between 30 and 75 µm combined with repetition rate frequencies between 9 and 15 Hz according to the spot size. We measured NIST SRM612 standard twice at the beginning and twice at the end of an analytical sequence for external standardization of plagioclase, clinopyroxene, hornblende, and biotite. Background and ablation interval acquisition times were about 100 s and 50 s, respectively. Electron microprobe data were used as an internal standard for all analysed minerals. Raw data were reduced off-line using the LAMTRACE software (Jackson, 2008), and a minimum of 30 s signal intervals were manually set to have a representative signal and to avoid contribution from mineral inclusions.

4. MINERAL CHEMISTRY

4.1 Olivine

Olivine crystals are only occurring in Gabbroid 3 and their hosted MMEs. Olivine within the former has an average low Forsterite content of Fo_{51} compared to the latter yielding Fo_{75} (Supplementary Table B.1 and Electronic Appendix E.1). Concentrations in Cr and Ni were only detected by EPMA in the olivine-bearing MME with average values of 500 ppm and 200 ppm, respectively (Supplementary Table B.1 and Electronic Appendix E.1). No LA-ICP-MS trace element measurements were performed for olivine.

4.2 Clinopyroxene

Clinopyroxene crystals are diopside in composition for all investigated samples. In the magmatic series 1, three samples contained clinopyroxene suitable for EPMA measurements, but they were not suitable for satisfactory LA-ICP-MS trace element analyses, due to their small size and occurrence of inclusions. Clinopyroxene is devoid of core to rim chemical zoning, and has an average Mg# ranging from 0.64 to 0.76 together with low Al_2O_3 (0.2-3 wt%) and low Ti (0.001-0.01 a.p.f.u) (Figs. 9a,b; Supplementary Table B.1 and Electronic Appendix E.2). Clinopyroxene-bearing intrusions from the magmatic series 2 display resorbed relicts of clinoyproxene with overgrowth of amphibole (G1, G5, G6, monzonite) or biotite (G2, G3, G4, essexite). Clinopyroxene crystals display on average higher Al_2O_3 concentrations (1-6 wt%) and a large range of Mg# (0.63-0.87) (Figs. 9a,b). Overall clinopyroxene displays higher Ti content (0.01-0.04) (Supplementary Table B.1 and Electronic Appendix E.2). In the magmatic series 3, only spessartite contains clinopyroxene with xenocrystic cores displaying low Mg# (0.75-0.80), low Al_2O_3 content (0.9-1.5 wt%) and low Ti (0.003-0.008 a.p.f.u) compared to the overgrowth characterized by the highest Mg # (up to 0.89), and moderate Al_2O_3 (2-4 wt%) and Ti (0.01-0.02) content (Figs. 9a,b). The negative correlation observed between Al_2O_3 and Mg# for almost each individual sample is attributed to sub-solidus exchange during cooling (e.g., MŸntener et al., 2001; Dessimoz et al., 2012; Bucholz et al., 2014).

In terms of trace elements composition, clinopyroxene crystals are dominantly characterized by average Eu negative anomalies ($Eu_N/Eu^*=Eu_N/((Sm_N+Gd_N)/2)$) ranging from 0.92 to 0.24 coeval with a decrease of Sr concentrations from 237 to 28 ppm indicative of progressive plagioclase co-crystallization (Figs. 9c,d; Supplementary Table B.1 and Electronic Appendix E.2). The essexite dike is composed of clinopyroxene significantly enriched in Sr (229 to 337 ppm) lacking Eu negative anomalies (0.76-0.92) pointing toward crystallization before late poikilitic nepheline (Figs. 9c,d). Clinopyroxene from magmatic series 2 systematically has low Cr (< 50 ppm) and Ni (< 15 ppm) contents (Supplementary Table B.1 and Electronic Appendix E.2). Xenocores observed in spessartite present marked Eu negative anomalies (~ 0.45) and low Sr (30-50 ppm), Cr (19-176 ppm) and Ni (39-65 ppm). By contrast, overgrowth rims exhibit slight to no Eu negative anomalies (~0.9) and contain on average higher concentrations of Sr (~100 ppm), Cr (4073-4586 ppm) and Ni (187-205 ppm) (Figs. 9c,d; Tables 2 and 3). The absence of visible Eu negative anomalies indicates that clinopyroxene crystallized prior to plagioclase, whereas samples characterized by marked Eu negative anomalies suggest co-crystallization of plagioclase and clinopyroxene. Noteworthy is that high Mg# and Al content of clinopyroxene overgrowth rims observed in spessartite display composition close to primitive clinopyroxene reported from high pressure experiment (Fig. 9a;

MŸntener et al., 2001) and 10 times less enriched in REE than clinopyroxene analysed from other intrusions (Fig. 9d).

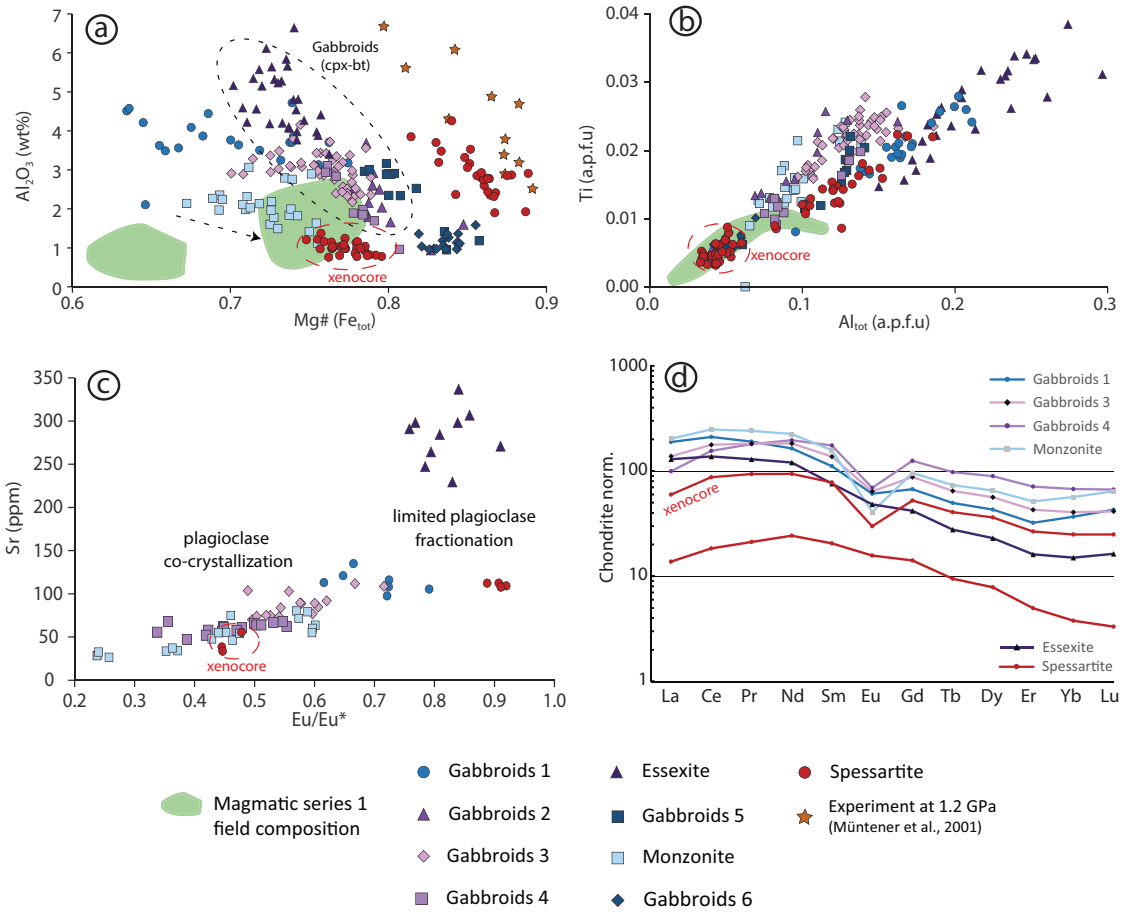

Figure 9: Clinopyroxene mineral chemistry. a) Al_2O_3 (wt% vs. Mg# showing the large range of compositional evolution through time. The dashed black arrow indicates effect of cooling and sub-solidus reequilibration occurring in most samples, b) Al^{IV} (a.p.f.u) vs. Ti^{4+} (a.p.f.u), c) Cr (ppm) vs. Eu/Eu*, and d) Average REE patterns for clinopyroxene normalized to C1-chondrite (McDonough & Sun, 1995).

4.3 Plagioclase

The average core to rim anorthite content (An) within the magmatic series 1 varies from bytownite to andesine (An_{86} to An_{33}; Fig. 10a, Supplementary Table B.2 and Electronic Appendix E.3). In the southern part of the MOP, hornblende gabbro contains large homogeneous bytownite with an average An_{86-87} composition, whereas it ranges from labradorite cores to andesine rims (An_{58} to An_{33}), with rare bytwonite cores (An_{70-80}) in diorite - tonalite (Fig. 10a). Basaltic-andesitic dikes also display a large range of plagioclase composition from labradorite cores to andesine rims (An_{60} to An_{35}), with resorption embayments filled with microinclusions within An-rich plagioclase overgrowth (An_{65-85}; Figs. 8b and 10a). In the northern part of the MOP, monzodiorite hosts plagioclase with systematic three sharp zones

from core to rim (Figs. 8c and 10a), including bytwonite to labradorite cores (An_{90} to An_{60}), a labradorite to andesine intermediate zones (An_{60} to An_{45}), and andesine rims (An_{40} to An_{30}). The coeval tonalite contains normally zoned plagioclase with andesine cores (An_{50}) and oligoclase rims (An_{20}; Fig. 10a).

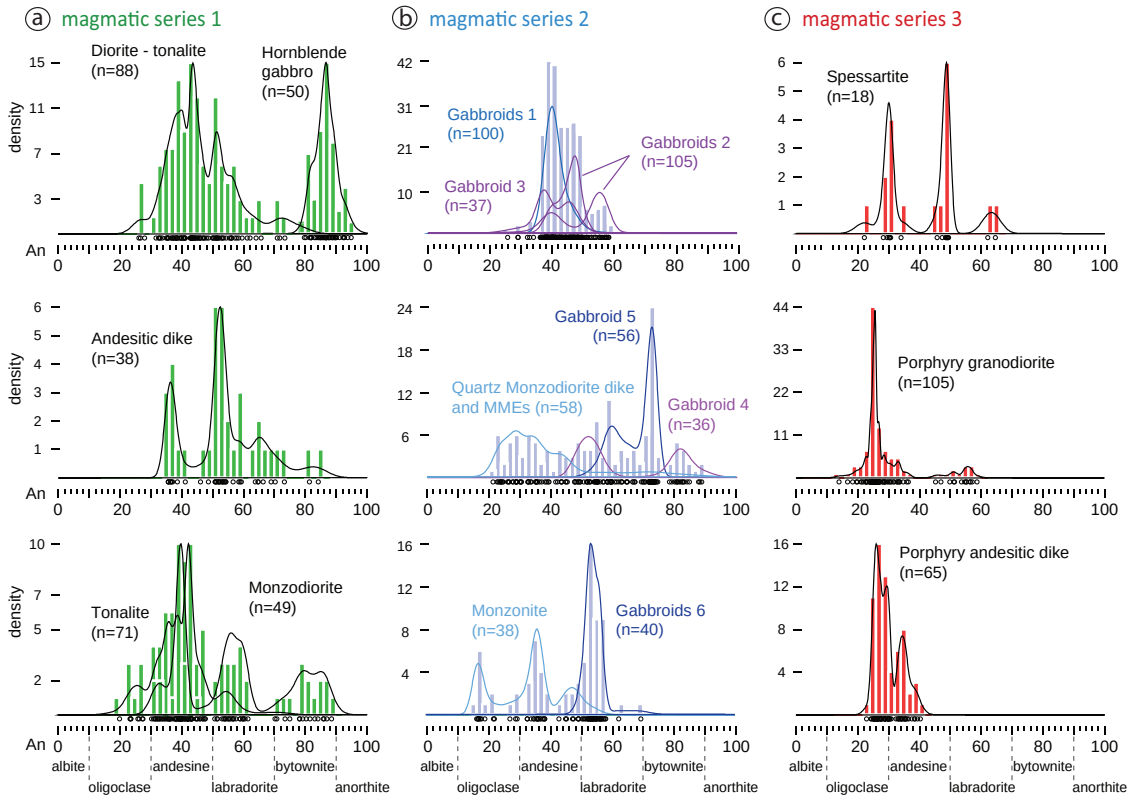

Figure 10: Histograms showing the An-content distribution in plagioclase for representative samples for each magmatic series 1 (a), 2 (b), and 3 (c). Curves represent Kernel density distribution and circles along the x-axis indicate the data density using Vermeesch (2012). For the sake of clarity, names of samples and associated number of analyses are reported on each diagram. MMEs stand for mafic magmatic enclaves, i.e., fine-grained hornblende gabbro. See Supplementary Table B.2 for summary and Electronic Appendix E.3 for detailed analyses.

The average An content within the entire magmatic series 2 ranges from labradorite to andesine (An_{70} to An_{20}; Fig. 10a, Supplementary Table B.2 and Electronic Appendix E.3). Gabbroids 1, 2 and 3 plagioclase grains display andesine composition (An_{50} to An_{30}), with few labradorite cores ($An_{60\text{-}50}$) in gabbroids 2 (Fig. 10b). Gabbroid 4 contains plagioclase with a bytownite ($An_{70\text{-}80}$) core overgrown by labradorite plagioclase ($An_{55\text{-}50}$; Fig. 8e), whereas Gabbroid 5 contains normally zoned plagioclase from bytownite to labradorite (An_{75} to An_{60}; Fig. 10b). Younger monzonite consists of normally zoned andesine-oligoclase crystals showing a wide range of compositions from An_{55} to An_{20} compared to gabbroids 6, which contain normally zoned

labradorite (An_{60-50}; Fig. 10b). The average An content within the entire magmatic series 3 ranges also from labradorite to oligoclase (An_{53} to An_{25}; Fig. 10c, Supplementary Table B.2 and Electronic Appendix E.3). Three types of plagioclase phenocrysts with variable compositions were recognized in spessartite, including two homogeneous andesine crystals of An_{48} and An_{34}, and a reversely zoned plagioclase with a large oligoclase core (An_{35}) and a thin resorption labradorite rim (An_{62-64}; Fig. 10c). Porphyritic andesitic dikes host normally zoned plagioclase with andesine cores (An_{34}) to oligoclase rims (An_{27}), similar to plagioclase in porphyritic granodiorite, which is predominantly composed of normally zoned oligoclase (An_{27-25}) together with rare sieved andesine to labradorite core (Figs. 8i and 10c). The overall compositional variation associated with sieved textures and Ca-rich growth zones for each magmatic series indicate interactions between differentiated and more juvenile magmas. By contrast, the lack of marked zonation rather indicate cooling and/or decompression.

Chondrite normalized plagioclase REE patterns display lower LREE and MREE in the magmatic series 1 compared to the series 2 and 3 (Fig. 11; Supplementary Table B.3 and Electronic Appendix E.3). Plagioclase in porphyritic granodiorite is the most depleted in HREE (Fig. 11), which corroborate whole-rock REE element pattern (Rezeau et al., 2017).

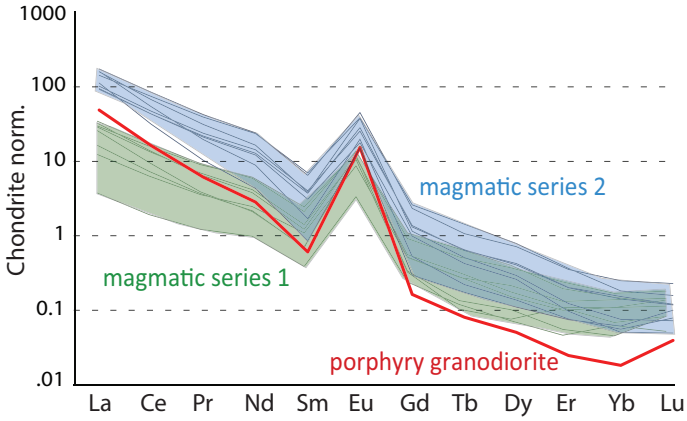

Figure 11: Plagioclase REE patterns for samples from magmatic series 1, series 2, and series 3.

4.4 Amphibole

In the MOP, the entire spectrum of amphibole compositions varies from Mg-hastingsite to Mg-hornblende (Fig. 12a; Supplementary Table B.4 and Electronic Appendix E.4). In magmatic series 1, hornblende gabbro hosts hastingsite characterized by core composition displaying Mg# of 0.6-0.8, low Si of 6-6.3 apfu, high Al_{tot} of 2.1-2.3 apfu, high Ti of 0.2-0.3 apfu, and $(Na + K)_A$ of 0.5-0.6 apfu, whereas rim composition consists of Mg# of 0.65, high Si of 6.5-7.1 apfu, low Al_{tot} of 1.2-17 apfu, low Ti of 0.05-0.2 apfu, and $(Na + K)_A$ of 0.2-0.4 apfu (Figs. 12a-d).

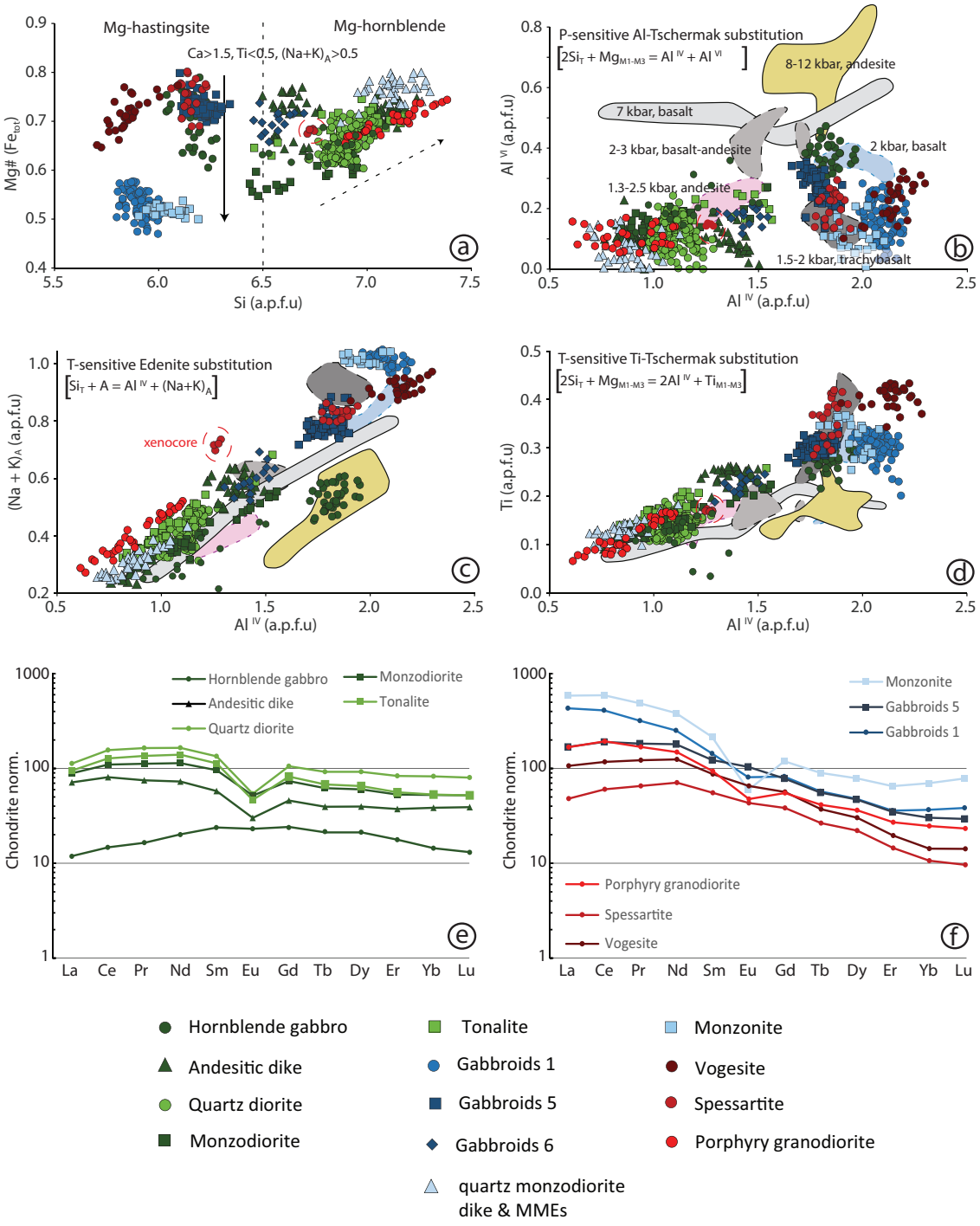

Figure 12: a) Amphibole classification scheme from Leake et al. (1997) of representative amphibole-bearing samples from each magmatic series. Filled black arrow indicates trend of magmatic differentiation, whereas black dotted arrow indicates trend for sub-solidus re-equilibration. b) Pressure-sensitive Al-Tschermak exchange. c, d) Temperature-sensitive edenite and Ti-Tschermak substitution, respectively. e, f) Average REE patterns of amphiboles for magmatic series 1 and 2 normalized to chondrite (McDonough & Sun, 1995). Data for comparison in b), c) and d): hydrous andesite fractionation at 8Ð12 kbar (Alonso-Perez et al., 2009); hydrous olivine-tholeiite at 7 kbar (Nandekar et al., 2014); high-Al basalt at 2 kbar (Sisson & Grove, 1993); hydrous basaltic andesite and andesite at 2Ð3 kbar (Moore & Carmichael, 1998);

hydrous andesite at 1.3Ð2.5 kbar (Rutherford & Devine, 2003); trachybasalt at 1.5Ð2 kbar (Barclay & Carmichael, 2004).

Amphibole crystallized in diorite - tonalite displays low Mg# of 0.7-0.6, high Si of 7-6.7 apfu, low Al_{tot} of 1.1-1.3 apfu, Ti of 0.1-0.2 apfu, and $(Na + K)_A$ of 0.3-0.5 apfu (Figs. 12a-d). Basaltic-andesitic dikes contain early Mg-hornblende characterized by Mg# of 0.7, Si of 6.6 apfu, Al_{tot} of 1.5 apfu, Ti of 0.25 apfu, and $(Na + K)_A$ of 0.55, and late sub-solidus Mg-hornblende characterized by Mg# of 0.7, Si of 7.1 apfu, Al_{tot} of 1.0 apfu, Ti of 0.1 apfu, $(Na + K)_A$ of 0.25 apfu (Figs. 12a-d). Intrusions of the northern part of the MOP, characterized by a compositional evolution from monzodiorite to tonalite, host amphibole with Mg# of 0.5-0.7, Si of 6.4-7.2 apfu, Al_{tot} of 0.9-1.8 apfu, Ti of 0.1-0.3 apfu, and $(Na + K)_A$ of 0.3-0.7 apfu (Figs. 12a-d).

In magmatic series 2, amphiboles from Gabbroids 1 and monzonite have similar compositions including low Mg# of 0.5-0.6, low Si of 5.8-6.1 apfu, high Ti of 0.2-0.4 apfu, high Al_{tot} of 2-2.4 apfu, and high $(Na + K)_A$ of 0.9-1.04 apfu (Figs. 12a-d). Owing to uncertainties of individual microprobe analyses, $(Na+K)_A$ sums up to 1.04 and violates the A-site cation allowance of $(Na+K)_A = 1$ (Supplementary Table B.4 and Electronic Table E.4; Leake et al., 1997; Hawthorne et al., 2012). Amphibole of Gabbroid 5 has a fairly narrow compositional range with high Mg# of 0.7-0.8, low Si of 6.1-6.3 apfu, high Al_{tot} of 2-2.4 apfu, high Ti of 0.3 apfu and high $(Na + K)_A$ of 0.8-0.9, whereas a crosscutting quartz monzodiorite dike and its MMEs contain a Mg-hornblende similar to sub-solidus amphibole reported above from andesitic dikes (Figs. 12a-d). Amphibole in Gabbroids 6 is characterized by Mg# of 0.7, Si of 6.5-6.7 apfu, Al_{tot} of 1.5-1.7 apfu, Ti of 0.2 and $(Na + K)_A$ of 0.5-0.7 (Figs. 12a-d).

In magmatic series 3, vogesite dikes host acicular Mg-hastingsite in the groundmass, which is characterized by high Mg# of 0.7-0.8, low Si of 5.8-6 apfu, high Al_{tot} of 2.2-2.5 apfu, high Ti of 0.4 apfu and high $(Na + K)_A$ of 0.9-1 apfu (Figs. 12a-d). In spessartite, amphibole displays reverse zoning with resorbed Mg-hornblende yielding Mg# of 0.7, high Si of 6.7 apfu, low Ti of 0.2 apfu, low Al_{tot} of 1.4 apfu, and $(Na + K)_A$ of 0.7 apfu, overgrown by Mg-hastingsite characterized by high Mg# of 0.7-0.8, low Si of 6.1-6.2 apfu, high Al_{tot} of 1.9-2.1 apfu, high Ti of 0.3-0.4 apfu, and high $(Na + K)_A$ of 0.8-0.9 apfu (Figs. 12a-d). Porphyry granodiorite contains Mg-hornblende with a low Mg# of 0.66-0.74, high Si of 6.9-7.3 apfu, low Ti of 0.1-0.2 apfu, low Al_{tot} of 0.8-1.3 apfu, and low $(Na + K)_A$ of 0.3-0.5 apfu (Figs. 12a-d). For each individual sample, amphibole compositions exhibit a positive correlation with the T-sensitive Edenite and Ti-Tschermak exchanges within and among individual samples, whereas there is no correlation with respect to the P-sensitive Al-Tschermak substitution within individual samples, but a broad positive correlation among samples (Figs. 12b-d).

Amphibole from magmatic series 1 is characterized by a relatively flat REE pattern, which contrasts with LREE (± MREE) rich patterns displayed by younger magmatic series 2 and 3 for similar Mg# or SiO_2 (Figs. 12e,f; Supplementary Table B.4 and Electronic Appendix E.4). Mg-hastingsite from calc-alkaline lamprophyres tends to be less enriched in REE compared to Mg-hastingsite of series 2 (Fig. 12f). For each magmatic series, REE patterns from the most mafic to the more evolved rocks display progressive enrichments, combined with the progressive development of negative Eu anomalies and a concomitant depletion in Sr (Figs. 12e,f). This reflects the progressive onset of plagioclase crystallization together with amphibole. Amphibole from magmatic series 3 has systematically higher Ni (100-500 ppm) and Cr (100-300 ppm) concentrations (except xenocrysts) compared to older igneous rocks (Ni and Cr: 0-100 ppm) for similar Mg# or SiO_2 (Supplementary Table B.4 and Electronic Appendix E.4). Only andesitic dikes from magmatic series 1 contain amphibole with a large range of Cr concentrations (0-500 ppm).

4.5 Biotite

Biotite from magmatic series 1 is annite with low Mg# values of 0.4-0.6 and Al^{IV} of 2.3-2.5 a.p.f.u (Fig. 13a; Supplementary Table B.5 and Electronic Appendix E.5). By contrast, biotite in magmatic series 2 and 3 has variable compositions, ranging from annite to phlogopite, including a tendency towards siderophyllite and eastonite in some samples, and display a large range of Mg# values of 0.5-0.8 and Al^{IV} of 2.2-2.7 a.p.f.u (Fig. 13a). In magmatic series 3, biotite yields systematically higher Ni ± Cr contents for a similar Mg# values compared to older intrusive suites, which could indicate a cogenetic link between mafic and felsic end-members (Fig. 13b). Strontium contents in biotite are negatively correlated with decreasing Mg# values from 0.8 to 0.5 reflecting progressive influence of plagioclase co-crystallization (Figs. 13c,d).

5. SEQUENCE OF CRYSTALLIZATION FOR EACH MAGMATIC SERIES

Petrography and mineral chemistry yield complementary pieces of information to establish a representative sequence of mineral crystallization for each individual magmatic series emplaced in the MOP (Fig. 14). In magmatic series 1, we propose two general sequences of crystallization (Fig. 14a), including (1) the hornblende gabbro: high-Al amphibole + magnetite → plagioclase (An_{90-80}) → low-Al amphibole; and (2) differentiated intrusions from monzodiorite to tonalite: plagioclase (An_{90-80}, An_{70-50}) → clinopyroxene + and/or interstitial low-Al amphibole + magnetite + plagioclase (An_{50-20}) + biotite + K-feldspar + quartz.

The magmatic series 2 consists of nested gabbroids of various mineral assemblages successively emplaced over ~10 Myr. We have distinguished four sequences of crystallization (Fig. 14b), including (1) early Gabbroids 1: apatite → plagioclase (An_{50-40}) + biotite + clinopyroxene →

high-Al amphibole + plagioclase (An_{40-30}) → interstitial K-feldspar + late zeolites, (2) Gabbroids 2, 3, 4 and monzonite: apatite → plagioclase ($An_{80-75,}$ An_{60-50}) → clinopyroxene + olivine (Fo_{50}) + plagioclase (An_{50-30}) + magnetite → biotite (± high-Al amphibole in monzonite) + poikilitic K-feldspar (± nepheline exsolution), (3) nepheline-bearing monzogabbro dike (essexite): apatite + Cu-Fe sulphides + magnetite + biotite + clinopyroxene → poikilitic nepheline, and (4) Gabbroids 5 and 6 and coeval differentiated quartz monzodiorite dike and hosted-MMEs fine-grained hornblende gabbro: apatite → clinopyroxene + magnetite + high-Al amphibole → plagioclase (An_{75-50}) + phlogopite → plagioclase (An_{40-20}) + low-Al amphibole + quartz + interstitial K-feldspar. Magmatic series 3 is characterized by early emplacement of calc-alkaline lamprophyres followed by differentiated granodioritic intrusions and dikes. Two sequences of crystallization are suggested (Fig. 14c), including (1) calc-alkaline lamprophyres: clinopyroxene + high-Al amphibole + phlogopite → plagioclase + K-feldspar (± quartz), and (2) porphyritic granodiorite and andesitic dikes: plagioclase (An_{65-45}) → plagioclase (An_{30-10}) + low-Al amphibole + biotite + quartz + K-feldspar.

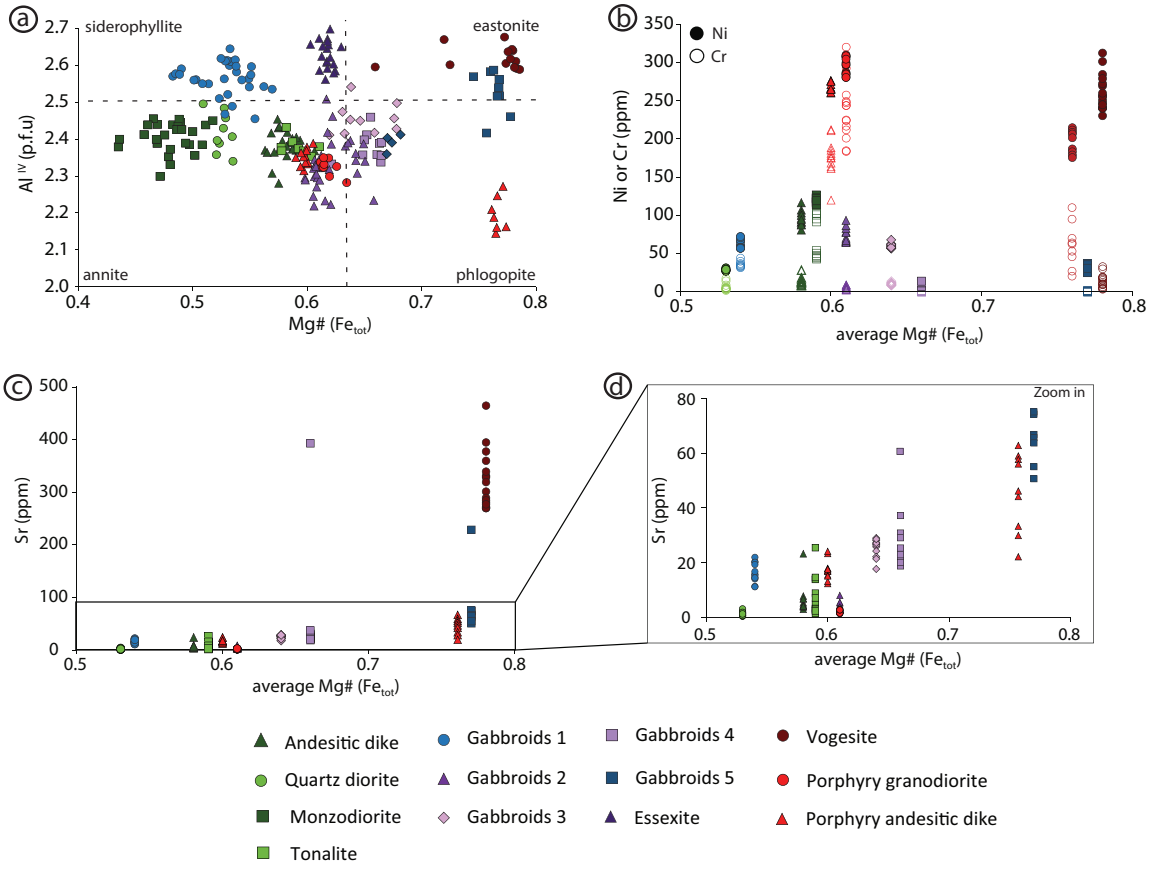

Figure 13: a) Biotite classification scheme after Deer et al. (1992), b) Cr or Ni (ppm) vs. average Mg# for representative samples for each magmatic series, c) Sr (ppm) vs. average Mg#, and d) zoom in c).

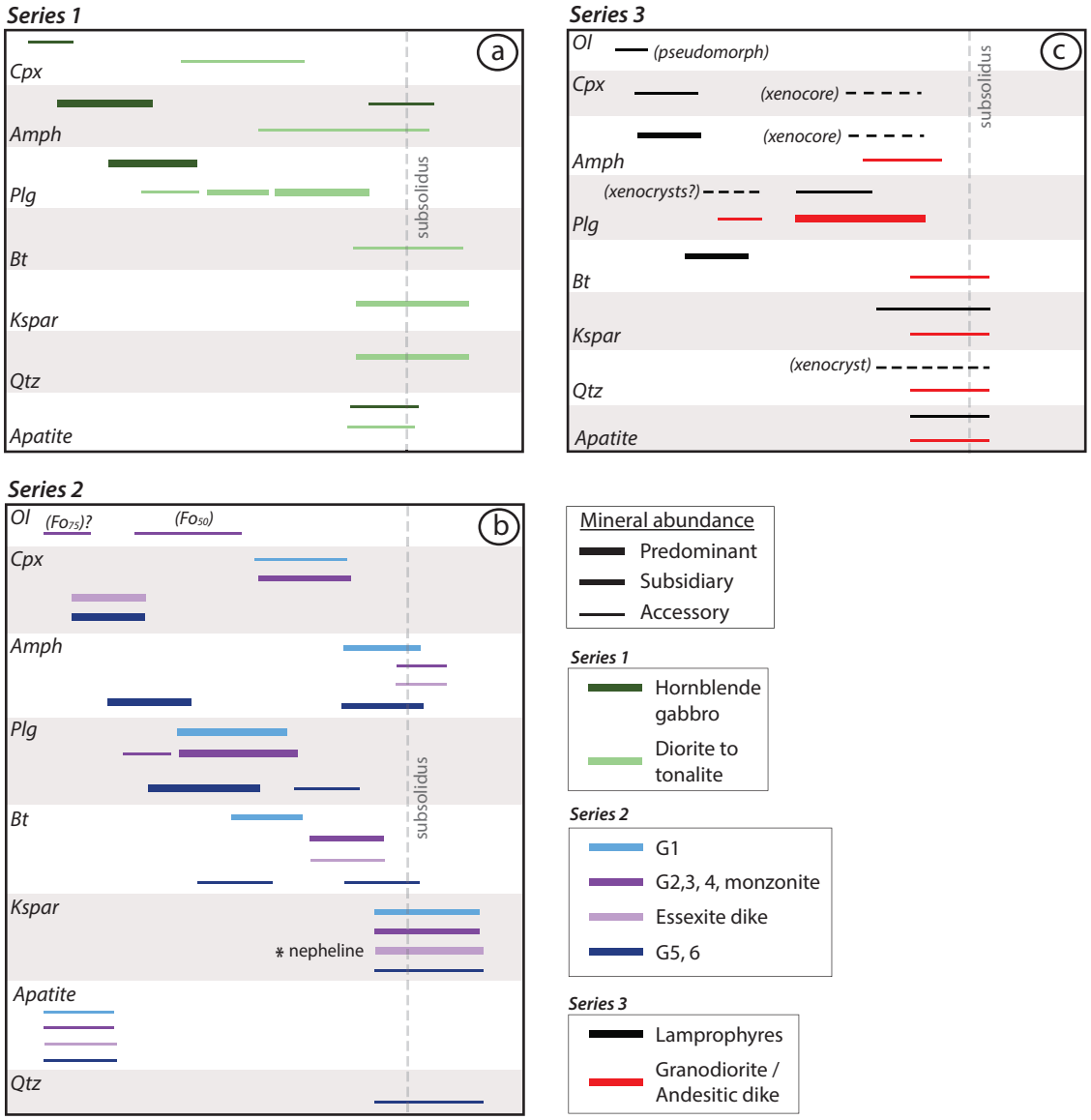

Figure 14: Sequence of crystallization for main mineral constituents for representative samples for each individual magmatic series. a) magmatic series 1, b) magmatic series 2, and c) magmatic series 3. See text for description. Abbreviations: ***Amph*** Amphibole, ***Bt*** Biotite, ***Cpx*** Clinopyroxene, ***Hbl*** Hornblende, ***Kspar*** K-feldspar, ***Ol*** Olivine, ***Plg*** Plagioclase, ***Qtz*** Quartz.

6. THERMOBAROMETRY

6.1 Al-in-hornblende thermometry

It has long been recognized that edenite and Ti-Tschermak substitutions are a very effective quantitative thermometer (Hammerstrom & Zen 1986; Holland & Blundy, 1994; Anderson & Smith, 1995; Erdman et al., 2014; Putirka, 2016). In the MOP, amphibole compositions display positive correlations with T-sensitive Edenite and Ti-Tschermak substitutions (Figs. 12c,d) and allow us to provide quantitative temperature estimates using the new amphibole-only calibration

of Putirka (2016; eq. 5) (Figs. 15a,b; Supplementary Table B.4 and Electronic Appendix E.4). Magmatic series 1 displays an average temperature ranging from 930¡C ± 23¡C to 760¡C ± 8¡C, with hornblende gabbro yielding the highest range of temperatures of 960-880¡C, and more differentiated magmas characterized by lower temperatures of 850-760¡C. In the magmatic series 2, Mg-hastingsite hosted in Gabbroids 1, 5, 6 and in monzonite yields a range of crystallization temperatures between 960¡C ± 10¡C and 870¡C ± 11¡C. By contrast, differentiated quartz monzodiorite dike and hosted-MMEs fine-grained hornblende gabbro crosscutting gabbroid 5 of similar age yield significantly lower temperatures of ~780¡C. In the magmatic series 3, calc-alkaline lamprophyres display average amphibole crystallization temperature of 1020¡C ± 7¡C for vogesite dikes, and reversely zoned amphibole phenocrysts in spessartite consist of a xenocore crystallized at 850¡C ± 2¡C overgrown by a rim yielding a significantly higher temperature of 990¡C ± 14¡C, which indicates crystal core inheritance by host-rock assimilation. Amphibole from porphyry granodiorite yields significantly lower average temperatures of 770¡C ± 24¡C. Noteworthy is that we observe a very good match with the plagioclase-hornblende geothermometer B of Holland & Blundy (1994) calibrated using a thermodynamic approach, which is valid for both silica-saturated and silica-undersaturated rocks (Fig. 15b; Supplementary Table B.4 and Electronic Table E.4).

For comparison, quantitative temperature estimates using Putirka (2016, eq. 5) have been tested on amphibole crystallized from a series of fractional crystallization experiment at various pressure and temperature using different starting composition, such as hydrous andesite fractionation at 8Ð12 kbar (Alonso-Perez et al., 2009), hydrous olivine-tholeiite at 7 kbar (Nandekar et al., 2014), high-Al basalt at 2 kbar (Sisson & Grove, 1993), hydrous basaltic andesite and andesite at 2Ð3 kbar (Moore & Carmichael, 1998), hydrous andesite at 1.3Ð2.5 kbar (Rutherford & Devine, 2003), trachybasalt at 1.5Ð2 kbar (Barclay & Carmichael, 2004). Results support the relatively accurate Al-in-hornblende quantitative temperature estimate for a wide P-T-X range (Fig. 15c).

6.2 Al-in-hornblende barometry

Since decades, Al-in-hornblende barometers have been calibrated based on various experiments (e.g., Hammerstrom & Zen 1986; Hollister et al. 1987; Johnson & Rutherford, 1989; Schmidt 1992; Mutch et al., 2016), thermodynamic calculation (Anderson & Smith, 1995; Ague, 1997), and data compilation (Ridolfi & Renzulli, 2012; Putirka, 2016). In the MOP, chemical composition within individual sample does not correlate with P-sensitive Al-Tschermak substitutions (Fig. 12b), which indicates that the evolution of amphibole composition within individual sample is mainly controlled by temperature (Figs. 12c,d). However, the general positive trend amongst samples within magmatic series correlates with an evolution from mafic

to felsic intrusions and likely indicates amphibole crystallization at variable pressure (Fig. 12b). This allows us to use the Al-in-hornblende geobarometer as a first order pressure estimate, i.e., upper crust vs. middle to lower crust.

Two different Al-in-hornblende geobarometers have been used (Supplementary Table B.4 and Electronic Appendix E.4), including (1) the calibration of Ridolfi & Renzulli (2012, barometer P1b) applicable to a large range of magma compositions and mineral assemblage, and (2) the experimental calibration of Mutch et al. (2016), which is a reassessment of the former calibration of Schmidt (1992) and requires a buffering mineral assemblage consisting of amphibole, plagioclase, biotite, quartz, K-feldspar, Fe-Ti-oxides, and apatite. In the following, we report pressure calculated using the amphibole-only barometer of Ridolfi & Renzulli (2012) because (1) we do not necessarily have the appropriate mineral assemblage to use the thermodynamic approach of Mutch et al. (2016) for each investigated sample, (2) no melt inclusions composition have been reported, and (3) whole-rock composition of intrusives does not represent the melt composition in equilibrium with amphibole crystallization to use the pressure estimates after Putirka (2016). Although the calibration of Ridolfi & Renzulli (2012) has been challenged and questioned (e.g., Erdman et al., 2014; Putirka, 2016), Al-in-hornblende barometers yield reasonable pressure estimates when crosschecked with independent pressure constraints (e.g., Leuthold et al., 2014).

In magmatic series 1, Al-in-hornblende yields two distinct ranges of pressure, including hornblende gabbro crystallized at 380 ± 50 MPa and more evolved intrusions crystallized at lower pressures ranging from 90 ± 10 to 170 ± 20 MPa. In magmatic series 2, amphibole-bearing intrusions are characterized by pressure of amphibole crystallization that progressively decrease over time from 420 ± 40 to 190 ± 20 MPa . In magmatic series 3, acicular, groundmass brown amphibole of vogesite yields a pressure of 500 ± 70 MPa, whereas the more primitive rim composition of amphibole from spessartite yields a slightly lower pressure of 410 ± 40 MPa, but overlapping within errors. By contrast, xenocores yield a significantly lower pressure of 170 ± 10 MPa. Mg-hornblende crystallized in porphyritic granodiorite yield the lowest pressure estimate of 90 ± 20 MPa.

According to experiments, Al^{VI} is generally higher for amphibole crystallized at high pressure (Fig. 12b; Alonso-Perez et al., 2009; Nandedkar et al., 2014) compared to those crystallized at lower pressure (Fig. 12b; Rutherford & Devine, 2003; Barclay & Carmichael, 2004). However, quantitative pressure estimates using Ridolfi & Renzulli (2012, P1b) applied to amphibole crystallized from experiments fail to yield accurate pressure estimates (Fig. 15d). Although it is beyond the scope of this paper to provide an explanation, we notice that amphibole crystallizing from alkali-rich or more medium-K calc-alkaline - tholeiitic starting material yield pressure over-estimated and under-estimated, respectively (Fig. 15d). Therefore it

is very important to be cautious when using the Al-in-hornblende barometer, and be aware of the necessity to crosscheck with other field constraints (i.e. contact metamorphic reaction, diagnostic mineral such as garnet) and/or petrographic mineral assemblage and stability field constraints further discussed below.

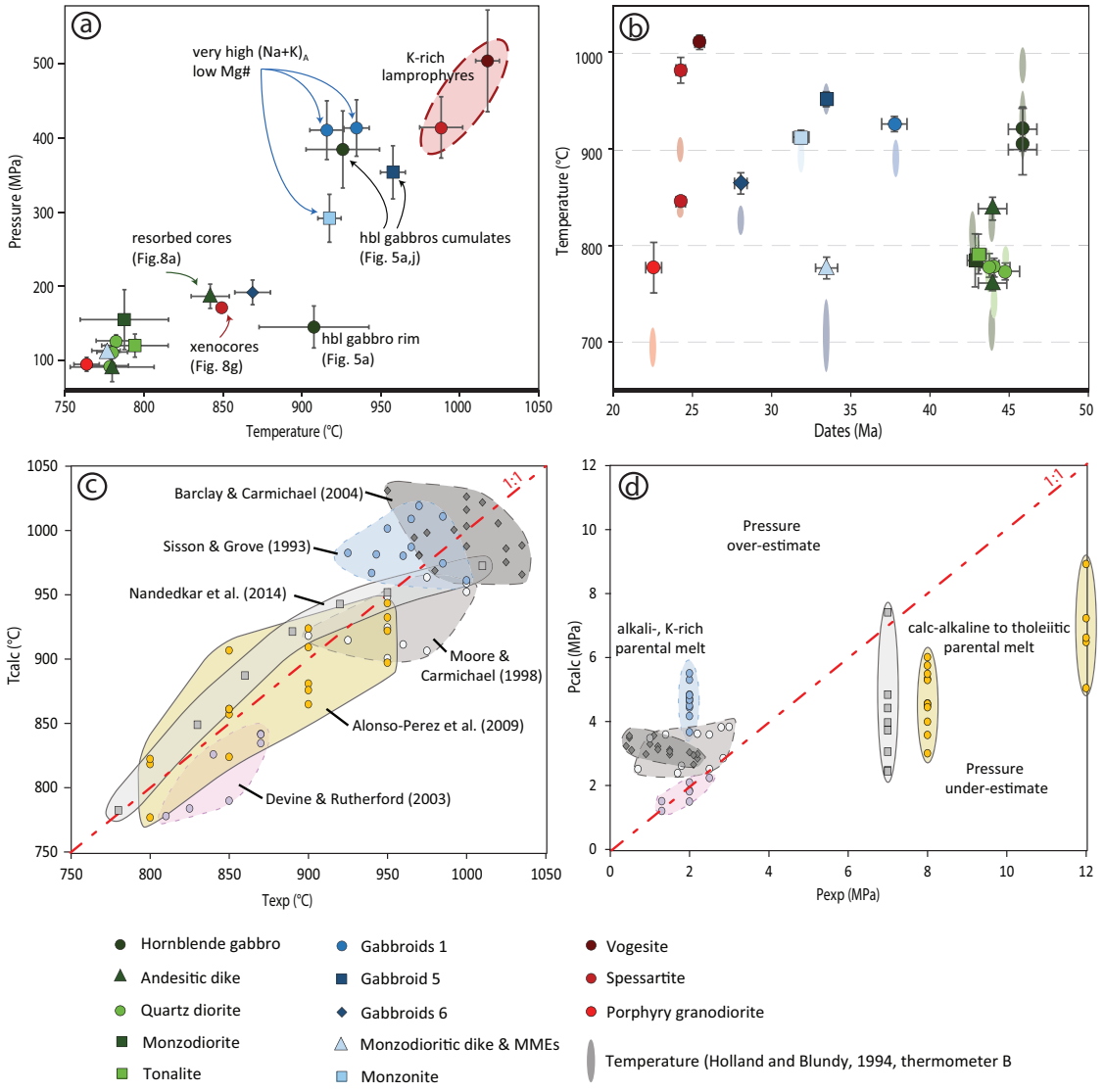

Figure 15: a) Average pressure vs. average temperature plot using calibration of Ridolfi & Renzulli (2012, P1b) and Putirka (2016, eq. 5), respectively. b) Average temperature vs. mean ages from Rezeau et al. (2016). Shaded areas indicate temperature estimates calculated after Holland & Blundy (1994, thermometer B). Error bars correspond to the standard deviation (1s) of analyses for respective samples. c) Comparison between temperature calculated using Putirka (2016, eq. 5) and temperature constrained from experiments. d) Comparison between pressure calculated using Ridolfi & Renzulli (2012, P1b) and pressure constrained from experiments. Experimental data: hydrous andesite fractionation at 8Ð12 kbar (Alonso-Perez et al., 2009); hydrous olivine-tholeiite at 7 kbar (Nandekar et al., 2014); high-Al basalt at 2 kbar (Sisson & Grove, 1993); hydrous basaltic andesite and andesite at 2Ð3 kbar (Moore & Carmichael, 1998); hydrous andesite at 1.3Ð2.5 kbar (Rutherford & Devine, 2003); trachybasalt at 1.5Ð2 kbar (Barclay & Carmichael, 2004).

7. DISCUSSION

7.1 Plagioclase textures and chemistry: an archive of magmatic processes

Three types of plagioclase textures have been identified and average compositions range from bytwonite to oligoclase (Fig. 10). Plagioclase textural features are (1) An-rich cores showing sieved textures overgrown by An-poorer plagioclase, (2) normal zoning from An-rich core to An-poor rim, and (3) complex chemical zoning showing sharp An-rich growth zones within a general normal zoning pattern at crystal scale (Figs. 8b,c,e,i and 9). The composition of plagioclase is function of variable parameters including pressure, temperature, melt composition and melt water content (Sisson & Grove, 1993; Panjasawatwong et al., 1995; Rutherford & Devine, 2003; Ginibre et al., 2007; Krawczynski et al., 2012). Sieved plagioclase cores reflect disequilibrium textures indicating a change of crystallization conditions (Streck, 2008). Sieved textures in concert with the general normal zoning is consistent with calcic core plagioclase crystallization in a deeper magma reservoir and subsequent transfer to a shallow magma reservoir into a derivative felsic melts, which could be controlled by decompression of water-undersaturated magma (Blundy & Shimizu, 1991) and/or by cooling (Sisson & Grove, 1993). Such features are observed in monzodiorite and dioritic to tonalitic intrusions of the magmatic series 1, in Gabbroids 2 and 4 of the magmatic series 2, and in porphyritic granodiorite of the magmatic series 3.

Plagioclase crystals are also characterized by progressive An-rich core to An-poor rim normal zoning without optical zoning. The lack of disequilibrium textures point toward rapid cooling linked to magma emplacement into shallow cold crust, which commonly promote sodic rim plagioclase crystallization together with hornblende and/or biotite (Sisson & Grove, 1993). Decompression of water-saturated magma may also represent an alternative or complementary scenario (Blundy & Cashman, 2008). This would apply for plagioclase hosted in hornblende gabbro of the magmatic series 1, Gabbroids 1, 5 and 6 of the magmatic series 2, and in calc-alkaline lamprophyres and differentiated rocks of the magmatic series 3. Complex textural and chemical zoning in plagioclase consists of episodic An-rich growth zones and An-poor intergrowth, which is reported from andesitic dikes of the magmatic series 1, Gabbroids 3 and monzonite of the magmatic series 2 and in porphyritic granodiorite of the magmatic series 3. This documents episodes of plagioclase growth in a more calcic melt (i.e. in a more mafic melt) generally attributed to mafic magma recharge intermittently supplied from deeper levels (Ruprecht & Wšrner, 2007; Streck, 2008; Bachmann and Huber, 2016). The latter is coherent with occurrences of MMEs and mingling textures reported from field observations (Fig. 4).

Finally, few intrusions are composed of plagioclase characterized by high An content (An_{60-90}; Fig. 10). Best examples are reported from hornblende gabbro cumulates of both magmatic series 1 and 2 (Gabbroid 5), where large optically homogeneous plagioclase crystals

display normal core to rim An-rich zoning. Experimental studies revealed that water content and melt composition (Ca, Al) strongly influence the composition of liquidus plagioclase (Panjasawatwong et al., 1995; Krawczynski et al., 2012), which indicates that water-rich magmas are favourable to form An-rich plagioclase and promote delayed plagioclase crystallization with respect to amphibole at moderate to high pressure conditions, i.e., in the mid- to lower crust. In the MOP, An-rich plagioclases reported from hornblende gabbros post-date Al-rich amphibole crystallization, and indicate relatively high pressure as discussed in the following section (Figs. 14).

7.2 Significance and implications for variable ferromagnesian silicate mineral assemblages

Each magmatic series displays intrusions composed of amphibole indicating distinct pressure and temperature of crystallization (Figs. 15a,b), corresponding to crystallization from magma reservoirs emplaced at mid- to upper crustal levels (~4-15 km). However, mineral assemblages and chemistry differ from one magmatic series to another, as well as sequences of crystallization (Figs. 9 - 14). Based on mineral stability fields determined by experiments (Righter & Carmichael, 1996; Moore & Carmichael, 1998; Rutherford & Devine, 2003; Barclay & Carmichael, 2004; Krawczynski et al., 2012), the sequence of crystallization allows a rough pressure estimate and to a lesser extent temperature, which ultimately challenge quantitative Al-in-hornblende thermobarometers. We believe that each magmatic series deserves a specific attention and they will be further discussed individually.

7.2.1 magmatic series 1

The hornblende gabbro is the oldest investigated mafic rock characterized by the lowest REE contents and a lack of Eu negative anomalies in large brown amphibole, whereas differentiated intrusions and dikes host high REE amphiboles showing marked Eu negative anomalies (Fig. 12d). The former likely represents cumulates fractionated at an early magmatic stage promoting early amphibole fractionation prior to plagioclase (An_{90-95}), which occurs at pressure of >200-350 MPa, i.e., at mid-crustal depth (Fig. 16). By contrast, differentiated magmas rather indicate crystallization at lower pressure (<200-350 MPa) in the upper crust (Fig. 16). The hornblende gabbro displays Mg-hornblende overgrowth over Mg-hastingsite indicative of a second episode of amphibole crystallization at lower pressure and temperature (P <200MPa; T~900¡C). This could correspond to crystallization in the upper crust following decompression and/or cooling during magma transfer from middle to upper crustal level. Overall, quantitative pressure and temperature estimates calculated from Al-in hornblende thermobarometry are in good agreement with respect to the sequence of crystallization and inferred P-T constraints from mineral stability phase diagrams (Figs. 15a,b and 16). In addition,

low-Al clinopyroxene from differentiated rocks can be ascribed to extensive plagioclase co-crystallization or alternatively to the early appearance of amphibole, which subsequently would have limited Al enrichment in clinopyroxene (Dessimoz et al., 2012). Although the lack of trace element characterization limits petrological interpretation, complementary low Mg# in clinopyroxene together with the absence of olivine indicate late stage crystallization in the upper crust from a differentiated melt that has experienced extensive crustal fractionation at depth (MŸntener et al., 2001; Nandedkar et al., 2014). The moderate alkali enrichment of amphiboles in magmatic serie 1 reflects the medium-K calc-alkaline nature of the parental melt (Rezeau et al., 2017), which likely supports a cogenetic link between intrusions crystallized at various crustal depths.

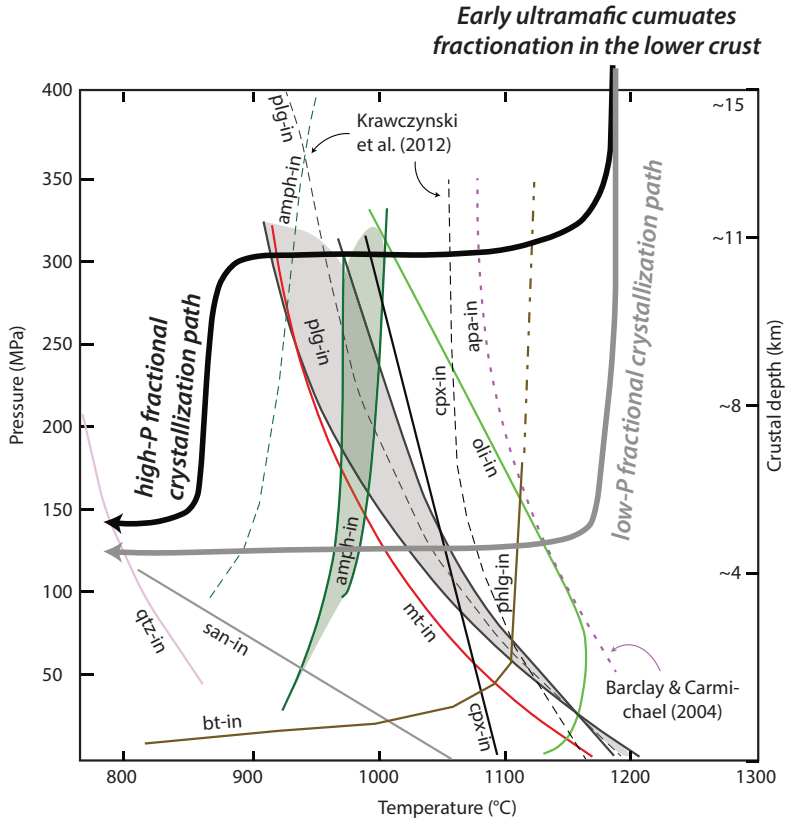

Figure 16: P-T phase diagram based on the experimental data of Righter & Carmichael (1996) for biotite (bt) - phlogopite (phlg); Moore & Carmichael (1998) for amphibole (amph), plagioclase (plg), clinopyroxene (cpx) and olivine (oli); Rutherford & Devine (2003) for quartz (qtz) and sanidine (san); Barclay & Carmichael (2004) for apatite (ap, dotted line), and Krawczynski et al., (2012) for amphibole, plagioclase and clinopyroxene (dotted lines). Shaded green and grey field represent amphibole and plagioclase stability fields for basalt-andesite and andesite starting composition after Moore & Carmichael (1998). Mineral stability fields may vary as a function of parental melt composition, water content and oxygen fugacity as illustrated by the difference of plagioclase and amphibole stability from Moore & Carmichael (1998) and Krawczynski et al. (2012). Two schematic crystallization paths determined from crystallization

sequences proposed in Figure 14. The black arrow represents the evolution of rocks characterized by amphibole crystallization prior to plagioclase fractionation, whereas the grey arrow indicates those characterized by early plagioclase fractionation.

7.2.2 magmatic series 2

The successive emplacement of shoshonitic to high-K calc-alkaline intrusions is extremely complex and four main sequences of crystallization have been identified (Fig. 14). Gabbroids 1 (37.6 - 37 Ma) are composed of clinopyroxene rimmed by brown amphibole displaying low Mg#, visible Eu negative anomalies, and significant enrichment in alkalis and LREE (Fig. 12). Such characteristics suggest post-plagioclase crystallization from a fractionated melt at relatively low pressure (<150-200 MPa; Fig. 16). This is at variance with the Al-in-hornblende barometer yielding significantly higher average pressure of 420 ± 40 MPa (Fig. 15a). As pointed out above, the unrealistic pressure estimate could be influenced by the composition of an alkali-rich parental melt generated by low degree of partial melting of a metasomatized subcontinental lithospheric mantle (Rezeau et al., 2017). On the other hand, Al-in-hornblende quantitative average temperature of 930 ± 10¡C is in agreement with experiments mentioned above (Figs. 15c and 16). High-Al and alkali-rich amphibole are reported from low pressure experiments conducted at 100-300 MPa using shoshonitic to high-K calc-alkaline basalt-andesite starting material (Fig. 15d; Sisson & Grove, 1993; Moore & Carmichael, 1998; Barclay & Carmichael, 2004), which is in agreement with pressure estimation based on petrography. We therefore propose low pressure crystallization of brown amphibole in Gabbroids 1 from an alkali-rich interstitial hydrous fractionated melt following the hydration crystallization reaction: calcic plagioclase + Fe-Ti-oxides + pyroxene + Na-rich hydrous melt ⇒ amphibole + sodic plagioclase + quartz + Na-rich zeolites (Sisson & Grove, 1993; Beard et al., 2004).

Gabbroids 2, 3 and 4 (35.6 - 33.5 Ma) are grouped based on their amphibole-free mineral assemblages and the occurrence of biotite surrounding clinopyroxene, and/or magnetite and/or olivine. Clinopyroxene crystals display marked Eu negative anomalies indicative of crystallization after plagioclase at relatively low pressure (<150-200 MPa; Fig. 16). The formation of biotite overgrowth is explained by the reaction occurring at low pressure: clinopyroxene + K-rich hydrous melt ⇒ biotite (Rutherford & Devine, 2003; Beard et al., 2004; Sisson et al., 2005). Although both amphibole and biotite crystallize from hydrous alkali-rich melts, the former needs an amount of dissolved magmatic H_2O >4 wt% for granitoids emplaced in the upper crust (Naney, 1983), and even up to ~10 wt% for andesitic melts fractionating at higher pressure (Krawczynski et al., 2012), whereas biotite stability field is enhanced by K-rich parental melt (Edgar & Arima 1983; Righter & Carmichael, 1996; Sisson et al., 2005). This

illustrates parental melts characterized by variable initial water and K contents with respect to Gabbroids 1, and consequently suggests two distinct parental reservoirs at depth. The occurence of low Mg olivine (Fo_{50}) in Gabbroid 3 emphasizes crystallization from a melt that experienced extensive fractionation at depth, which would be partly supported by the presence of higher Mg olivine (Fo_{75}) identified in troctolitic MME hosted by the Gabbroid 3, although they do not represent primitive olivine. Additionally, the presence of an alkaline Si-undersaturated parental magma reservoir at depth is evidenced by the emplacement of the nepheline-bearing monzogabbro dike (essexite) composed of clinopyroxene lacking of Eu negative anomalies and displaying the highest Al, Ti and Sr content compared to clinopyroxene in Gabbroids 2, 3 and 4 (Fig. 9). This clearly indicates early clinopyroxene fractionation prior to plagioclase (or feldspathoids) at pressure >150-200 MPa (Fig. 16). Noteworthy is that exsolutions of nepheline in K-feldspar are also observed in Gabbroid 3 (Figs. 6h and 7; Supplementary Table A.2). Although the age is unconstrained for the essexite dike, the spatial relationship and mineral assemblage similarities with gabbroids 2, 3 and 4 would suggest a co-genetic link. The young monzonite (31.9 Ma) is somehow difficult to precisely relate to any of previous intrusions. The general sample texture reminds Gabbroid 3, however, the presence of brown amphibole sharing identical compositions as those reported in Gabbroids 1 could also suggest crystallization from a chemically similar parental magma and/or illustrate remobilization of crystal mush reservoir at depth (Gabbroids 1?). Hence, we propose that clinopyroxene clusters in monzonite represent antecrysts (Miller et al., 2007) reequilibrated at shallower crustal level. The marked Eu negative anomalies together with low Al content in clinopyroxene suggest crystallization from a differentiated melt at low pressure (<150-200 MPa), which does not support Al-in-hornblende barometry pressure estimate of ~300 MPa for similar reasons as proposed above for Gabbroids 1. amphibole surrounding clinopyroxene are resorbed and illustrate rapid near-isothermal decompression (Blundy & Cashman, 2008), which favors the formation of biotite at lower pressure resulting from the reaction of hornblende with K-rich melt (Rutherford & Devine, 2003; Sisson et al., 2005; Molina et al., 2009).

Gabbroid 5 (33.5 Ma) resembles the hornblende gabbro described in the magmatic series 1 with the main difference being the significant enrichment in alkali and LREE observed in both whole-rock and rock-forming silicates (Fig. 12; Rezeau et al., 2017). Such chemical pattern indicates crystallization from an alkali-rich melt. Occurrence of high Mg# biotite surrounding amphibole illustrates the reaction of hornblende with hydrous K-rich melt. The lack of Eu negative anomalies in amphibole indicates relatively high crystallization pressure (>200-350 MPa) and phlogopite crystallization is generally achieved at high temperature compared to biotite (Fig. 16; Righter & Carmichael, 1996). This is in agreement with Al-in-hornblende average thermobarometry (P=350 MPa, T=960¡C, Figs. 15a,b). In addition, syn-magmatic

monzodioritic dike and hosted-MME fine-grained hornblende gabbro display low-Al amphibole crystallizing after plagioclase and likely represent a sequence of crystallization occurring at shallow crustal levels from a differentiated melt (Figs. 15a and 16). Gabbroids 6 (28.3 Ma) represent the youngest hornblende gabbro intrusions of magmatic series 2 and thermobarometry yield moderate pressure and temperature (P~200 MPa, T~870¡C, Figs. 15a,b). They are emplaced in the vicinity of the Kadjaran Cu-Mo deposit (Fig. 2) and suffered from hydrothermal alteration. This hinders us to link with certainty variations in mineral chemistry solely to igneous processes, and consequently to estimate accurate depth of crystallization.

7.2.3 magmatic series 3

In adakitic calc-alkaline lamprophyres (26.6 - 24.3 Ma), the presence of resorbed quartz antecrysts together with amphibole and clinopyroxene reverse zonation clearly illustrate host-rock assimilation and melt hybridization, which also corroborate the occurrence of zircon antecrysts (Rezeau et al., 2016). Vogesite dikes host reversely zoned clinopyroxene showing a core characterized by marked Eu negative anomalies together with low Mg#, Cr, Ni, Ti and Al content, compared to the rim lacking of Eu negative anomalies and displaying high Mg#, Cr, Ni, Ti and Al content close to primitive clinopyroxene crystallized in the lower crust (Figs. 8h and 9; MŸntener et al., 2001). Amphibole displays similar chemical pattern (Figs. 8g and 9) and quantitative pressure estimates yield low and high pressure of ~170 MPa and ~500 MPa for cores and rims, respectively (Fig. 15a). Similarly, acicular brown amphiboles in the groundmass of spessartite dikes yield on average high pressure of crystallization of ~400 MPa (Fig. 15b,c). However, such high pressure of crystallization is difficult to reconcile with (1) the assimilation of host-rocks crystallized in the upper crust and (2) the groundmass composed of acicular silicate crystals, which should have rapidly crystallized at the level of emplacement (<200 MPa). Similarly to Gabbroids 1 and monzonite described above, this apparent discrepency between Al-in-hornblende barometry and petrographic constraints may be explained by crystallization from a more primitive hydrous K-rich parental melt that ascended adiabatically to the upper crust and crystallized and/or equilibrated at low pressure. High temperature average estimates of ~1000¡C (Figs. 15a,b), however, are consistent with crystallization of early phlogopite and amphibole and delayed plagioclase at low pressure from an oxidized primitive K-rich melt. This has been proposed for shoshonitic magmatism and lamprophyres (minettes) emplaced along the Western Mexican volcanic belt (e.g., Righter & Carmichael, 1998; Barclay & Carmichael, 2004).

Porphyritic adakitic granodiorite and andesitic dikes (24.5 - 21.2 Ma) host interstitial low-Al amphibole displaying marked Eu negative anomalies typical for crystallization at shallow depth, which is in agreement with Al-in-hornblende thermobarometry yielding low

crystallization pressure and temperature of 90 MPa and ~780¡C (Figs. 15a,b). Interesting features consist of the presence of two types of biotite in porphyritic andesitic dikes, including high Mg# phlogopite phenocrysts similar to those reported in vogesite (Fig. 13a). In addition to the complex plagioclase textures, this points toward episodes of thermal rejuvenation by more juvenile magmas and syn-magmatic interactions between more mafic (lamprophyres?) and felsic magmas. Alternatively, it could also represent antecrysts assimilated upon magma emplacement.

Based on the systematic and significantly higher Cr and Ni contents in biotite, amphibole and clinopyroxene combined with higher Mg# values, these intrusions and dikes are crystallized from a parental magma that experienced less fractionation compared to magmatic series 1 and 2, and consequently indicate crystallization from a distinct more juvenile mantle source as previously suggested by whole-rock geochemistry (Moritz et al., 2016; Rezeau et al., 2016, 2017).

8. SUMMARY OF THE MAGMATIC PLUMBING SYSTEM EVOLUTION

The successive magmatic series emplaced in the MOP are characterized by a large compositional rock diversity and the chemical evolution from magmatic series 1 to 3 is interpreted in terms of a decreasing degree of partial melting of a mantle garnet lherzolite combined with progressive mantle metasomatism over time with limited crustal assimilation and/or cannibalization of young juvenile crust (Rezeau et al., 2016, 2017). Although the exact mechanism for incremental magma emplacement in the MOP is beyond the scope of this paper, regional strike-slip tectonics in the MOP provided favourable structures for magma ascent (Tayan et al., 1976; Hovakimyan et al., 2016), and incremental crustal growth likely resulted from the amalgamation of dikes and/or sills emplacement in the upper crust as proposed in the literature (e.g., Schoene et al., 2012; Leuthold et al., 2014; Annen et al. 2015). Based on this study, we propose a conceptual reconstruction of magma emplacement in the crust for each individual magmatic series that ultimately shaped the exposed composite MOP (Fig. 17).

8.1 Magmatic series 1

From the south to the north of the MOP, calc-alkaline intrusions ranging from hornblende gabbro to tonalite display a maximum life span of ~2.8 ± 0.8 m.y. emplaced in a subduction-related regional geodynamic setting (Rezeau et al., 2016, 2017). The oldest hornblende gabbro represents a cumulate early crystallized at relatively high pressure (380 ± 50 MPa) corresponding to mid-crustal level (10-15 km), whereas younger differentiated intrusions indicate crystallization at lower pressure (~250-100 MPa) in the upper crust (Figs 15a and 16). Based on the occurrence of Mg-hastingsite rimmed by Mg-hornblende in hornblende gabbro,

we propose that the hornblende gabbro was transferred to the upper crust probably in the aftermath of felsic magma emplacement. Since early fractionation of amphibole in the middle crust drives the liquid line of descent toward SiO_2-rich melts (e.g., Jagoutz, 2010; Nandedkar et al., 2014), we propose a co-genetic relationship between early hornblende gabbro fractionation in the middle crust and subsequent generation of differentiated melts emplaced in the upper crust (Fig. 17a), which is also supported by whole-rock trace element geochemical modelling (Rezeau et al., 2017). The widespread occurrences of moderately alkaline amphibole together with the episode of very calcic plagioclases fractionation in the hornblende gabbro suggest crystallization from hydrous calc-alkaline parental magmas generated by slab-related fluid-fluxed high degree of partial melting of a mantle-related source (Sisson & Grove, 1993; Krawczynski et al., 2012; Rezeau et al., 2017). In the upper crust, plagioclase and amphibole record episodes of thermal rejuvenation by episodic mafic magma recharge and likely polybaric crystallization, respectively (Figs. 8a,b, 10a and 15a), which is corroborated by the widespread occurrence of MMEs.

In the northern part of the MOP at Hanqasar (Fig. 2), the concentric shape of the intrusion and the mafic to felsic magmatic differentiation trend toward its centre supports *in-situ* differentiation from monzodiorite to tonalite during progressive inward cooling of magma emplaced within a cold upper crust (Fig. 2; Bateman & Chappell, 1979; Coleman et al., 2004). Although differentiated intrusions in the southern and northern MOP represent two sub-intrusions suite with distinct crystallization ages, they both exhibit short-term *in situ* crystallization of <1 m.y. (Rezeau et al., 2016). This corroborates the concept of short-lived upper crustal magma reservoirs and relatively fast cooling of an intrusion between <500 kyr up to ~1.5 Myr (e.g., Glazner et al., 2004; Samperton et al., 2015; Bucholz et al., 2016). Whole-rock geochemistry suggests a chemically and isotopically homogeneous magmatic source (Moritz et al., 2016, Rezeau et al., 2017), which allows us to conclude that all intrusions of magmatic series 1 are genetically related.

8.2 Magmatic series 2

Shoshonitic to high-K calc-alkaline intrusions represent a protracted incremental assembly of magmas operating over a maximum period of ~9.7 ± 0.9 m.y. within a collisional environment (Rezeau et al., 2016, 2017). Following the concept of short-lived crystallization mentioned above, it is unlikely that magmatic series 2 represents a single magmatic differentiation series lasting 10 m.y.. Consequently, the investigated samples rather correspond to multiple discrete magmatic pulses, followed by crustal differentiation processes occurring at variable crustal levels. According to this study, the majority of intrusions and dikes in magmatic series 2 crystallized at low pressure in the upper crust (<150-200 MPa), with the exception of the

essexite dike and Gabbroid 5 crystallizing clinopyroxene and amphibole at higher pressure at mid-crustal levels (>200-350 MPa). Repeated emplacement of intrusions in the mid- to upper crust is favorable for maintaining an elevated thermal regime and crystal mush reservoirs over a longer period of time up to several million years (e.g., Annen, 2011; Solano et al., 2012). This would explain the average range of higher temperature (900-950¡C) compared to intrusions in magmatic series 1 (Figs. 15a,b). Additionally, mineral chemistry reveals an overall enrichment in alkalis and LREE (Figs. 3a, 9, 11, 12), which certainly reflects the shoshonitic to high-K calc-alkaline parental melts composition generated by low degree of partial melting of a metasomatized mantle-related source (Rezeau et al., 2017).

In situ differentiation is also suggested for gabbroids that are spatially and temporally associated within 1-2 m.y., which is either revealed by ductile contacts and the occurrence of coeval gabbro and more differentiated intrusions or dikes (gabbroids 1, 5 and 6) or by gabbroids of similar mineral assemblages in concert with overlapping U-Pb zircon dates (gabbroids 2, 3 and 4). We also propose that the non-uniform U-Pb zircon age distributions and overlapping ages throughout the entire magmatic series 2 (Rezeau et al., 2016), together with the occurrence of widespread MMEs and zoned plagioclase, suggest periods of mafic recharge, thermal rejuvenation and crystal mush reactivation followed by chemical reequilibration at mid- to upper crustal levels. Fluctuations in mineral assemblage such as amphibole-bearing rocks or amphibole-free intrusions with biotite (± nepheline) reflect different parental melts with variable water and/or alkali contents (Edgar & Arima, 1983; Beard et al., 2004; Sisson et al., 2005; Molina et al., 2009; Krawczynski et al., 2012). The occurrence of essexite (i.e., nepheline-bearing monzogabbro) also supports the presence of an alkaline magma reservoir at depth (Fig. 17b). The emplacement of Si-undersaturated to Si-critically saturated melts together with amphibole-free to amphibole-bearing intrusions shed light on multiple syn-magmatic crustal magma reservoirs fractionated from parental melts characterized by variable chemical compositions (Fig. 17b).

8.3 Magmatic series 3

The high-K calc-alkaline adakitic magmatism is characterized by the early emplacement of calc-alkaline lamprophyre dikes (vogesite, spessartite) followed by porphyritic granodiorite and andesitic dikes over a maximum timescale of ~5.4 ± 0.4 m.y. within a collisional to post-collisional geodynamic setting (Moritz et al., 2016; Rezeau et al., 2016, 2017). Petrography and mineral reverse zoning reported from spessartite illustrates assimilation and hybridization of a primitive melt crystallizing clinopyroxene, amphibole and phlogopite characterized by the highest Mg# values and Ni and Cr contents (Figs. 9, 12 and 13), which is consistent with their primitive-like whole-rock geochemistry (Kelemen et al., 2003; Rezeau et al., 2017). This

represents the most primitive magmas in the MOP and indicates significantly less ultramafic mineral fractionation at depth compared to older magmatic series 1 and 2 (Fig. 17c). Mineral chemistry in vogesite indicates delay of plagioclase fractionation and the widespread occurrence of acicular brown amphibole and phlogopite in the groundmass suggest fast crystallization from a K-rich hydrous melt. However, assimilation of antecrysts crystallized in the upper crust indicate *in-situ* crystallization occurring at low pressure, which can be achieved at high temperature under water-saturated and oxidized conditions (Carmichael et al., 1996; Righter & Carmichael, 1996; Barclay & Carmichael, 2004). By contrast, porphyry granodioritic melts crystallized at shallow levels and progressive *in-situ* crystallization is inferred from the recognition of three sub-facies in porphyritic granodiorite intrusion (Fig. 2; Tayan, 1976). Ferromagnesian minerals in intrusions from magmatic series 3 are systematically enriched in Ni and Cr compared to rocks from magmatic series 1 and 2, and therefore indicate a less differentiated magmatic source and a potential genetic link with calc-alkaline lamprophyres. Conclusively, the magmatic series 3 represents more primitive magma likely generated during regional lithospheric thinning and concomitant low degree of partial melting of a metasomatized mantle source during the initiation of the collapse of the Arabia-Eurasia orogenic belt (Rezeau et al., 2017). Such geodynamic environment is generally considered favourable for the generation of calc-alkaline lamprophyres (Turner et al., 1999; Prelević et al., 2015). The release of compressional stress facilitates the emplacement of more primitive melts in the upper crust (e.g., Bertrand et al., 2014) and subsequent crustal processes such as fractional crystallization and host-rock would represent a favourable scenario to explain the temporal and spatial association of calc-alkaline lamprophyres and felsic intrusions in the MOP (Rock, 1991; Prelević et al., 2004, 2015).

9. CONCLUDING REMARKS

This study provides the first detailed petrological characterization of the composite MOP illustrating an extreme complexity regarding igneous processes operating over a protracted period of 30 Myr. Careful petrographic observations combined with *in-situ* mineral chemistry analyses allowed us to document each magmatic series and shed light on contrasting sequences of mineral crystallization intimately related to the evolution of magmatic source processes (Rezeau et al., 2017). We revealed interactions between compositionally distinct magmas allowing us to identify open-system magmatic processes for each magmatic series. Independently of the regional geodynamic setting, intrusions and dikes are mainly crystallized

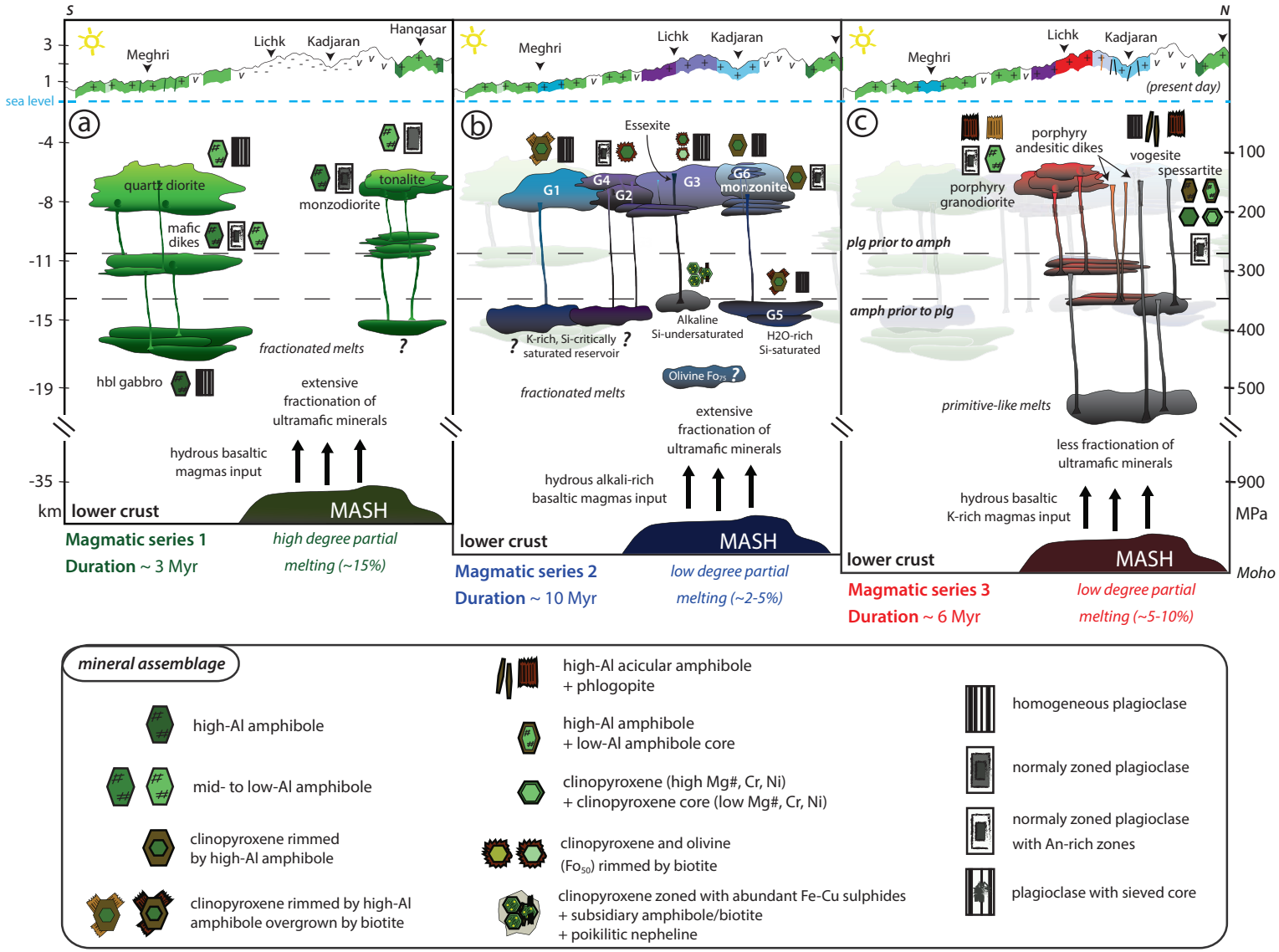
S
N
Meghri
Lichk
Kadjaran
Hanqasar
(present day)
sea level
3
1
-4
-8
-11
-15
-19
-35
km
100
200
300
400
500
900
MPa
Moho
a
b
c
quartz diorite
tonalite
monzodiorite
mafic dikes
fractionated melts
hbl gabbro
extensive fractionation of ultramafic minerals
hydrous basaltic magmas input
lower crust
MASH
Magmatic series 1
Duration ~ 3 Myr
high degree partial melting (~15%)
Essexite
G1
G2
G3
G4
G5
G6
monzonite
K-rich, Si-critically saturated reservoir
Alkaline Si-undersaturated
H2O-rich Si-saturated
Olivine Fo75
hydrous alkali-rich basaltic magmas input
Magmatic series 2
Duration ~ 10 Myr
low degree partial melting (~2-5%)
porphyry andesitic dikes
vogesite
spessartite
porphyry granodiorite
plg prior to amph
amph prior to plg
primitive-like melts
less fractionation of ultramafic minerals
hydrous basaltic K-rich magmas input
Magmatic series 3
Duration ~ 6 Myr
low degree partial melting (~5-10%)
mineral assemblage
high-Al amphibole
mid- to low-Al amphibole
clinopyroxene rimmed by high-Al amphibole
clinopyroxene rimmed by high-Al amphibole overgrown by biotite
high-Al acicular amphibole + phlogopite
high-Al amphibole + low-Al amphibole core
clinopyroxene (high Mg#, Cr, Ni) + clinopyroxene core (low Mg#, Cr, Ni)
clinopyroxene and olivine (Fo50) rimmed by biotite
clinopyroxene zoned with abundant Fe-Cu sulphides + subsidiary amphibole/biotite + poikilitic nepheline
homogeneous plagioclase
normaly zoned plagioclase
normaly zoned plagioclase with An-rich zones
plagioclase with sieved core

Figure 17: Conceptual model of incremental assembly of the MOP based on mineral petrography and chemistry constraints. Duration of magmatism and degree of mantle partial melting are from Rezeau et al. (2016) and Rezeau et al. (2017), respectively. MASH stands for melting, assimilation, storage and hybridization after Hildreth & Moorbath (1989). The apparent N-S cross section is sourced from Google Earth topography, and the present day outcropping intrusions are based on the geological map presented in Figure 2. See text for discussion.

---

in the upper crust with subsidiary rocks early crystallized in the mid- to lower crust. Despite a relative abundance of mafic intrusions in the magmatic series 2 and 3, most of them are interpreted to crystallize at low pressure with a potential for middle crust crystal mush reactivation and subsequent chemical reequilibration during its emplacement in the upper crust. A precise characterization of pressure and temperature of magma crystallization is quite challenging in the MOP due to the successive emplacement of magmatic series of different composition, especially for intrusions crystallizing from alkali-rich parental melts. The lack of diagnostic mineral for pressure (i.e., clinopyroxene-orthopyroxene pairs, garnet, contact metamorphic reactions) combined with alkali-rich amphiboles prevent accurate pressure estimate, and we tried our best to overcome these limitations by using petrography and experimental mineral stability field. This allowed us to distinguish different levels of crystallization and we believe that the reconstruction of the evolution of the composite MOP proposed in Figure 17 is a reasonable preliminary model for the study area and potentially yield new insights regarding the incremental growth of composite plutons in general. We believe that it is an important contribution because it points out the complexity of the magmatic series 2 and the lack of understanding for specific areas in the MOP (i.e., Schvanidzor Gabbroids 1 and Meghri ridge Gabbroid 3, 5 and nepheline-bearing monzogabbro dike), which ultimately helps to raise new questions in order to focus future studies to specific smaller areas.

This study faced several main limitations and future crucial investigations can be summarized as follows: (1) the need of detailed mapping for identifying Gabbroids 1-6 and the recognition of clear contacts between syn-magmatic compositionally different intrusions in order to perform mass balance calculations allowing a quantitative approximation of the relative roles of fractional crystallization and assimilation, (2) a complementary high-precision zircon U-Pb geochronological survey to assess rates of magma emplacement and time scales of magmatic differentiation, (3) in-situ mineral isotope geochemistry to quantify the importance of magma mixing/mingling, and (4) a comprehensive study of mafic magmatic enclaves throughout the entire MOP for each magmatic series in order to have access to the most primitive composition for a better characterization of igneous processes occurring in the mantle source and/or in the lower crust.

REFERENCES

Agard, P., Omrani, J., Jolivet, L., Whitechurch, H., Vrielynck, B., Spakman, W., MoniŽ, P., Meyer, B., & Wortel, R. (2011). Zagros orogeny: a subduction-dominated process. Geological Magazine 148, 692Ð725.

Ague, J. J. (1997). Thermodynamic calculation of emplacement pressures for batholithic rocks, California: Implications for the aluminum-in-hornblende barometer. Geology 25(6), 563-566.

Allen, M.B., & Armstrong, H.A., (2008). ArabiaÐEurasia collision and the forcing of mid-Cenozoic global cooling. Palaeogeography, Palaeoclimatology, Palaeoecology 265, 52Ð58.

Alonso-Perez, R., MŸntener, O. & Ulmer, P. (2009). Igneous gar- net and amphibole fractionation in the roots of island arcs: experimental constraints on andesitic liquids. Contributions to Mineralogy and Petrology 157, 541Ð558.

Anderson, J. L., & Smith, D. R. (1995). The effects of temperature and fO_2 on the Al-in-hornblende barometer. American Mineralogist 80(5-6), 549-559.

Annen, C. (2011). Implications of incremental emplacement of magma bodies for magma differentiation, thermal aureole dimensions and plutonismÐvolcanism relationships. Tectonophysics 500(1), 3-10.

Annen, C., Blundy, J. D., Leuthold, J., & Sparks, R. S. J. (2015). Construction and evolution of igneous bodies: Towards an integrated perspective of crustal magmatism. Lithos 230, 206-221.

Bachmann, O., & Huber, C. (2016). Silicic magma reservoirs in the earth's crust: a review. American Mineralogist 101, 2377-2404.

Ballato, P., Uba, C.E., Landgraf, A., Strecker, M.R., Sudo, M., Stockli, D.F., Friedrich, A., & Tabatabaei, S.H., (2011). ArabiaÐEurasia continental collision: insights from late Tertiary foreland-basin evolution in the Alborz Mountains, northern Iran. Geological Society of America Bulletin 123, 106Ð131.

Barboni, M., Annen, C., & Schoene, B. (2015). Evaluating the construction and evolution of upper crustal magma reservoirs with coupled U/Pb zircon geochronology and thermal modeling: A case study from the Mt. Capanne pluton (Elba, Italy). Earth Planetary Science Letters 432, 436Ð448.

Barclay, J. & Carmichael, I. S. E. (2004). A hornblende basalt from western Mexico: Water-saturated phase relations constrain a pressureÐtemperature window of eruptibility. Journal of Petrology 45, 485Ð506.

Barrier, E., & Vrielynck, B. (2008). Palaeotectonic Maps of the Middle East. CGMW.

Bateman, P. C., & Chappell, B. W. (1979). Crystallization, fractionation, and solidification of the Tuolumne intrusive series, Yosemite National Park, California. Geological Society of America Bulletin 90(5), 465-482.

Beard, J. S., Ragland, P. C., & Rushmer, T. (2004). Hydration crystallization reactions between anhydrous minerals and hydrous melt to yield amphibole and biotite in igneous rocks: Description and implications. The Journal of geology 112(5), 617-621.

Bertrand, G., Guillou-Frottier, L., Loiselet, C. (2014). Distribution of porphyry copper deposits along the western Tethyan and Andean subduction zones: Insights from a paleotectonic approach. Ore Geology Reviews 60, 174-190.

Blundy, J. D., & Shimizu, N. (1991). Trace element evidence for plagioclase recycling in calc-alkaline magmas. Earth and Planetary Science Letters, 102(2), 178-197.

Blundy, J., & Cashman, K. (2008). Petrologic reconstruction of magmatic system variables and processes. In: Putirka, K. D. & Tepley, F. J., III (eds) Minerals, Inclusions and Volcanic Processes. Mineralogical Society of America and Geochemical Society, Reviews in Mineralogy and Geochemistry 69, 179-239.

Broderick, C., Wotzlaw, J.F., Frick, D.A., Gerdes, A., Ulianov, A., GŸnther, D., & Schaltegger, U. (2015). Linking the thermal evolution and emplacement history of an upper-crustal pluton to its lower-crustal roots using zircon geochronology and geochemistry (southern Adamello batholith, N. Italy). Contribution to Mineralogy and Petrology 170 : 28.

Bucholz, C. E., Eddy, M. P., Jagoutz, O., Bowring, S. A., Schmidt, M. W., & Sambuu, O. (2016). Constraining the time scales of magmatic differentiation with U-Pb zircon geochronology. Geology 45(1), 11-14.

Bucholz, C. E., Jagoutz, O., Schmidt, M. W., & Sambuu, O. (2014). Phlogopite-and clinopyroxene-dominated fractional crystallization of an alkaline primitive melt: petrology and mineral chemistry of the Dariv Igneous Complex, Western Mongolia. Contributions to Mineralogy and Petrology 167(4), 1-28.

Buret, Y., Wotzlaw, J. F., Roozen, S., Guillong, M., von Quadt, A., & Heinrich, C. A. (2017). Zircon petrochronological evidence for a plutonic-volcanic connection in porphyry copper deposits. Geology 45(7), 623-626.

Caricchi, L., Simpson, G., & Schaltegger, U. (2014). Zircons reveal magma fluxes in the EarthÕs crust. Nature 511, 457-461.

Carmichael, I. S. E., Lange, R. A., & Luhr, J. F. (1996). Quaternary minettes and associated volcanic rocks of Mascota, western Mexico: a consequence of plate extension above a subduction modified mantle wedge. Contributions to Mineralogy and Petrology 124(3), 302-333.

Cashman, K. V., Sparks, R. S. J., & Blundy, J. D. (2017). Vertically extensive and unstable magmatic systems: A unified view of igneous processes. Science 355 (6331), DOI: 10.1126/science.aag3055.

Chiu, H.-Y., Chung, S.-L., Zarrinkoub, M.H., Mohammadi, S.S., Khatib, M.M., & Iizuka, Y. (2013). Zircon U–Pb age constraints from Iran on the magmatic evolution related to Neotethyan subduction and Zagros orogeny. Lithos 162-163, 70–87.

Coleman, D., Gray, W., & Glazner, A. (2004). Rethinking the emplacement and evolution of zoned plutons: Geochronologic evidence for incremental assembly of the Tuolumne Intrusive Suite, California. Geology 32, p.433-436.

Deer, W.A., Howie, R.A., Wise, W.S., & Zussman, J. (2004). Rock-Forming Minerals. 4B. Framework Silicates: Silica Minerals, Feldspathoids and the Zeolites (2nd edition). Geological Society, London, 982 p.

Deer, W. A., Howie, R. A., & Zussman, J. (1992). An introduction to the rock-forming minerals (Vol. 696). London: Longman.

DeCelles, P. G., & Graham, S. A. (2015). Cyclical processes in the North American Cordilleran orogenic system. Geology 43(6), 499-502.

DeCelles, P. G., Ducea, M.N., Kapp, P., & Zandt, G. (2009). Cyclicity in Cordilleran orogenic systems. Nature Geosciences 2, 251-57.

Delibaş, O., Moritz, R., Ulianov, A., Chiaradia, M., Sara•, C., Revan, K. M., & Gš•, D. (2016). Cretaceous subduction-related magmatism and associated porphyry-type Cu–Mo prospects in the Eastern Pontides, Turkey: New constraints from geochronology and geochemistry. Lithos 248, 119-137.

Dessimoz, M., MŸntener, O., & Ulmer, P. (2012). A case for hornblende dominated fractionation of arc magmas: the Chelan Complex (Washington Cascades). Contributions to Mineralogy and Petrology 163(4), 567-589.

Djrbashyan, R. T. & Tayan, R. N. (2008). Geological Map of the Southern Zangezur, Armenia, Lesser Caucasus. Institute of Geological Sciences, Armenian National Academy of Sciences. Based on the "Geological map of the Zangezur mining district", Scale 1: 50 000. Authors: Karamyan K.A. Guyumdjyan H.P., Djrbashyan R.T., Tayan R.N., 1974.

Edgar, A. D., & Arima, M. (1983). Conditions of phlogopite crystallization in ultrapotassic volcanic rocks. Mineralogical Magazine 47(1), 11-19.

Erdmann, S., Martel, C., Pichavant, M., & Kushnir, A. (2014). Amphibole as an archivist of magmatic crystallization conditions: problems, potential, and implications for inferring magma storage prior to the paroxysmal 2010 eruption of Mount Merapi, Indonesia. Contributions to Mineralogy and Petrology 167(6), 1-23.

Ginibre, C., Wšrner, G., & Kronz, A. (2007). Crystal zoning as an archive for magma evolution. Elements 3(4), 261-266.

Glazner, A. F., Bartley, J. M., Coleman, D. S., Gray, W., & Taylor, R. Z. (2004). Are plutons assembled over millions of years by amalgamation from small magma chambers?. GSA today 14(4/5), 4-12.

Grove, T. L., Elkins-Tanton, L. T., Parman, S. W., Chatterjee, N., MŸntener, O., & Gaetani, G. A. (2003). Fractional crystallization and mantle-melting controls on calc-alkaline differentiation trends. Contributions to Mineralogy and Petrology 145(5), 515-533.

Hammarstrom, J. M., & Zen, E. A. (1986). Aluminum in hornblende: an empirical igneous geobarometer. American Mineralogist 71(11-12), 1297-1313.

Hawthorne, F. C., Oberti, R., Harlow, G. E., Maresch, W. V., Martin, R. F., Schumacher, J. C., & Welch, M. D. (2012). Nomenclature of the amphibole supergroup. American Mineralogist 97(11-12), 2031-2048.

Hildreth, W., & Moorbath, S., (1988). Crustal contributions to arc magmatism in the Andes of central Chile. Contributions to mineralogy and petrology 98, 455-489.

Holland, T., & Blundy, J. (1994). Non-ideal interactions in calcic amphiboles and their bearing on amphibole-plagioclase thermometry. Contributions to mineralogy and petrology 116(4), 433-447.

Hollister, L. S., Grissom, G. C., Peters, E. K., Stowell, H. H., & Sisson, V. B. (1987). Confirmation of the empirical correlation of Al in hornblende with pressure of solidification of calc-alkaline plutons. American Mineralogist 72(3-4), 231-239.

Hovakimyan, S., Moritz, R., Tayan, R., Melkonyan, R., & Harutyunyan, M., (2016). Regional strike-slip tectonics and porphyry Cu-Mo and epithermal ore deposit formation during Cenozoic subduction to post-collisional evolution of the southernmost Lesser Caucasus, Tethyan belt. 14th Swiss Geoscience Meeting, 18-19 November 2016, Geneva, p. 61 (abstract volume).

Jackson, S.E. (2008). Lamtrace data reduction software for LA-ICP-MS. In: Sylvester, P. (Ed.), Laser Ablation ICP-MS in the Earth Sciences: Current Practices and Outstanding Issues. Short Course series, Mineralogical Association of Canada 40, 305Ð307.

Jagoutz, O. E. (2010). Construction of the granitoid crust of an island arc. Part II: a quantitative petrogenetic model. Contributions to Mineralogy and Petrology 160, 359-381.

Johnson, M. C., & Rutherford, M. J. (1989). Experimental calibration of the aluminum-in-hornblende geobarometer with application to Long Valley caldera (California) volcanic rocks. Geology 17(9), 837-841.

Kaislaniemi, L., Van Hunen, J., Allen, M. B., & Neill, I. (2014). Sublithospheric small-scale convection - A mechanism for collision zone magmatism. Geology 42, 291-294.

Kelemen, P. B., Hangh¿j, K. & Greene, A. R. (2003). One view of the geochemistry of subduction-related magmatic arcs, with an emphasis on primitive andesite and lower crust. In: Turekian, K. & Holland, H. (eds) Treatise on Geochemistry, Vol. 3. Oxford: Pergamon, pp. 1Ð70.

Karamyan, K. A., Tayan, R. N., & Guyumdjyan, O. P., (1974). The main features of intrusion magmatism Zangezur region of the Armenian SSR. Proceedings of the National Academy of Sciences of the Republic of Armenia 27, 54-65 (in Russian).

Krawczynski, M. J., Grove, T. L., & Behrens, H. (2012). Amphibole stability in primitive arc magmas: effects of temperature, H2O content, and oxygen fugacity. Contributions to Mineralogy and Petrology 164(2), 317-339.

Kuşcu, İ., Tosdal, R. M., Gencalioğlu-Kuşcu, G., Friedman, R., & Ullrich, T. D. (2013). Late Cretaceous to Middle Eocene magmatism and metallogeny of a portion of the Southeastern Anatolian orogenic belt, East-Central Turkey. Economic Geology 108(4), 641-666.

Leake, B. E., Woolley, A. R., Arps, C. E., Birch, W. D., Gilbert, M. C., Grice, J. D., Hawthorne, F.C., Kato, A., Kisch, H. J., Krivovichev, V. G., Linthout, K., Laird, J., & Mandarino, J. (1997). Nomenclature of Amphiboles: Report of the Subcommittee on Amphiboles of the International Mineralogical Association Commission on New Minerals and Mineral Names. Mineralogical magazine 61(2), 295-321.

Le Maitre, R. W. (ed.) (2002). Igneous Rocks: A Classification and Glossary of Terms. Cambridge: Cambridge University Press, 236 pp.

Leuthold, J., MŸntener, O., Baumgartner, L. P., Putlitz, B., Ovtcharova, M., & Schaltegger, U. (2012). Time resolved construction of a bimodal laccolith (Torres del Paine, Patagonia). Earth and Planetary Science Letters 325, 85-92.

Leuthold, J., MŸntener, O., Baumgartner, L. P., & Putlitz, B. (2014). Petrological constraints on the recycling of mafic crystal mushes and intrusion of braided sills in the Torres del Paine mafic complex (Patagonia). Journal of Petrology 55(5), 917-949.

Lipman, P. W. (2007). Incremental assembly and prolonged consolidation of Cordilleran magma chambers: Evidence from the Southern Rocky Mountain volcanic field. Geosphere 3(1), 42-70.

McDonough, W. F., & Sun, S. S. (1995). The composition of the Earth. Chemical geology 120(3-4), 223-253.

Mederer, J., Moritz, R., Ulianov, A., & Chiaradia, M., (2013). Middle Jurassic to Cenozoic evolution of arc magmatism during Neotethys subduction and arc-continent collision in the Kapan Zone, southern Armenia. Lithos 177, 61Ð78.

Middlemost, E.A.K. (1994). Naming materials in the magma/igneous rock system. Earth Science Reviews 37, 215Ð224.

Miller, J. S., Matzel, J. E., Miller, C. F., Burgess, S. D., & Miller, R. B. (2007). Zircon growth and recycling during the assembly of large, composite arc plutons. Journal of Volcanology and Geothermal Research 167(1), 282-299.

Molina, J. F., Scarrow, J. H., Montero, P. G., & Bea, F. (2009). High-Ti amphibole as a petrogenetic indicator of magma chemistry: evidence for mildly alkalic-hybrid melts during evolution of Variscan basicÐultrabasic magmatism of Central Iberia. Contributions to Mineralogy and Petrology 158(1), 69-98.

Moore, G., & Carmichael, I. S. E. (1998). The hydrous phase equilibria (to 3 kbar) of an andesite and basaltic andesite from western Mexico: constraints on water content and conditions of phenocryst growth. Contributions to Mineralogy and Petrology 130(3), 304-319.

Moritz, R., Rezeau, H., Ovtcharova, M., Tayan, R., Melkonyan, R., Hovakimyan, S., Ramazanov, V., Selby, D., Ulianov, A., Chiaradia, M., & Putlitz, B. (2016). Long-lived, stationary magmatism and pulsed porphyry systems during Tethyan subduction to post-collision evolution in the southernmost Lesser Caucasus, Armenia and Nakhitchevan. Gondwana Research 37, 465-503.

MŸntener, O., Kelemen, P., & Grove, T. (2001). The role of H2O during crystallization of primitive arc magmas under uppermost mantle conditions and genesis of igneous pyroxenites: an experimental study. Contribution to Mineralogy and Petrology 141(6), 643Ð658.

Mutch, E. J. F., Blundy, J. D., Tattitch, B. C., Cooper, F. J., & Brooker, R. A. (2016). An experimental study of amphibole stability in low-pressure granitic magmas and a revised Al-in-hornblende geobarometer. Contributions to Mineralogy and Petrology 171(10), 85.

Nandedkar, R. H., Ulmer, P. & MŸntener, O. (2014). Fractional crystallization of primitive, hydrous arc magmas: an experi- mental study at 0.7GPa. Contributions to Mineralogy and Petrology 167, 1Ð27.

Naney, M. T. (1983). Phase equilibria of rock-forming ferromagnesian silicates in granitic systems. American Journal of Science 283(10), 993Ð1033.

Panjasawatwong, Y., Danyushevsky, L. V., Crawford, A. J. & Harris, K. L. (1995). An experimental study of the effects of melt composition on plagioclaseÐmelt equilibria at 5 and 10 kbar: implications for the origin of magmatic high-An plagioclase. Contributions to Mineralogy and Petrology 118, 420Ð432.

Paterson, S. R. & Ducea, M. N. (2015). Arc magmatic tempos: Gathering the evidence. Elements 11, 91-98.

Pirrie, D., Butcher, A. R., Power, M. R., Gottlieb, P., & Miller, G. L. (2004). Rapid quantitative mineral and phase analysis using automated scanning electron microscopy (QemSCAN);

potential applications in forensic geoscience. Geological Society, London, Special Publications 232(1), 123-136.

Prelević, D., Foley, S. F., Cvetković, V., & Romer, R. L., (2004). Origin of minette by mixing of lamproite and dacite magmas in Veliki Majdan, Serbia. Journal of Petrology 45, 759-792.

Prelević, D., Akal, C., Romer, R. L., Mertz-Kraus, R., & Helvacõ, C. (2015). Magmatic response to slab tearing: constraints from the Afyon Alkaline Volcanic Complex, Western Turkey. Journal of Petrology egv008.

Putirka, K. (2016). Amphibole thermometers and barometers for igneous systems and some implications for eruption mechanisms of felsic magmas at arc volcanoes. American Mineralogist 101(4), 841-858.

Rezeau, H., Moritz, R., Wotzlaw, J. F., Tayan, R., Melkonyan, R., Ulianov, A., Selby, D., d'Abzac F. X. & Stern, R. A. (2016). Temporal and genetic link between incremental pluton assembly and pulsed porphyry Cu-Mo formation in accretionary orogens. Geology 44, 627-630.

Rezeau, H., Moritz, R., Leuthold, J., Hovakimyan, S., Tayan, R. & Chiaradia, M. (2017). 30 Myr of Cenozoic magmatism along the Tethyan margin during Arabia-Eurasia accretionary orogenesis (Meghri-Ordubad pluton, southernmost Lesser Caucasus). Lithos 288-289, 108-124.

Ridolfi, F., & Renzulli, A. (2012). Calcic amphiboles in calc-alkaline and alkaline magmas: thermobarometric and chemometric empirical equations valid up to 1,130¡ C and 2.2 GPa. Contributions to Mineralogy and Petrology 163(5), 877-895.

Righter, K., & Carmichael, I. S. (1996). Phase equilibria of phlogopite lamprophyres from western Mexico: biotite-liquid equilibria and PT estimates for biotite-bearing igneous rocks. Contributions to Mineralogy and Petrology 123(1), 1-21.

Rock, N. M. S. (1991). Lamprophyres. Glasgow: Blackie, 285 pp.

Ruprecht, P., & Wšrner, G. (2007). Variable regimes in magma systems documented in plagioclase zoning patterns: El Misti stratovolcano and Andahua monogenetic cones. Journal of Volcanology and Geothermal Research 165(3), 142-162.

Rutherford, M. J. & Devine, J. D. (2003). Magmatic conditions and magma ascent as indicated by hornblende phase equilibria and reactions in the 1995-2002 Soufri•re Hills magma. Journal of Petrology 44(8), 1433-1454.

Samperton, K.M., Schoene, B., Cottle, J.M., Keller, C.B., Crowley, J.L, & Schmitz, M.D (2015). Magma emplacement, differentiation and cooling in the middle crust: Integrated zircon geochronological–geochemical constraints from the Bergell Intrusion, Central Alps. Chemical Geology 417:322–340.

Schoene, B., Schaltegger, U., Brack, P., Latkoczy, C., Stracke, A., & GÜnther, D. (2012). Rates of magma differentiation and emplacement in a ballooning pluton recorded by UÐPb TIMS-TEA, Adamello batholith, Italy. Earth and Planetary Science Letters 355, 162-173.

Schmidt, M. W. (1992). Amphibole composition in tonalite as a function of pressure: an experimental calibration of the Al-in-hornblende barometer. Contributions to mineralogy and petrology 110(2-3), 304-310.

Sisson, T. W. & Grove, T. L. (1993). Experimental investigations of the role of H_2O in calc-alkaline differentiation and subduction zone magmatism. Contributions to Mineralogy and Petrology 113, 143Ð166.

Sisson, T. W., Ratajeski, K., Hankins, W. B., & Glazner, A. F. (2005). Voluminous granitic magmas from common basaltic sources. Contributions to Mineralogy and Petrology 148(6), 635-661.

Solano, J. M. S., Jackson, M. D., Sparks, R. S. J., Blundy, J. D., & Annen, C. (2012). Melt segregation in deep crustal hot zones: a mechanism for chemical differentiation, crustal assimilation and the formation of evolved magmas. Journal of Petrology 53(10), 1999-2026.

Sosson, M., Rolland, Y., MÜller, C., Danelian, T., Melkonyan, R., Kekelia, S., Adamia, S., Babzadeh, V., Kangarli, T., Avagyan, A., Galoyan, G., & Mosar, J., (2010). Subductions, obduction and collision in the Lesser Caucasus (Armenia, Azerbaijan, Georgia), new insights. In: Sosson, M., Kaymakci, N., Stephenson, R.A., Bergerat, F., Starostenko, V. (Eds.), Sedimentary basin tectonics from the Black Sea and Caucasus to the Arabian platform. Geological Society London, Special publication 340, 329Ð352.

Streck, M. J. (2008). Mineral textures and zoning as evidence for open system processes. In: Putirka, K. D. & Tepley, F. J., III (eds) Minerals, Inclusions and Volcanic Processes. Mineralogical Society of America and Geochemical Society, Reviews in Mineralogy and Geochemistry 69, 595-622.

Tayan, R.N., Plotnikov, E.P., & Abdurakhmanov, R.U., (1976). Some features of emplacement of geological structure of the ZangezourÐNakhichevan region of Lesser Caucasus. Proceedings of the National Academy of Sciences of the Republic of Armenia 29, 12Ð20 (in Russian).

Turner, S. P., Platt, J. P., George, R. M. M., Kelley, S. P., Pearson, D. G., & Nowell, G. M. (1999). Magmatism associated with orogenic collapse of the BeticÐAlboran domain, SE Spain. Journal of Petrology, 40(6), 1011-1036.

Vermeesch P (2012). On the visualisation of detrital age distributions. Chemical Geology 312-313,190-194.

Walker, B. A., Bergantz, G. W., Otamendi, J. E., Ducea, M. N., & Cristofolini, E. A. (2015). A MASH zone revealed: the mafic complex of the Sierra Valle FŽrtil. Journal of Petrology 56(9), 1863-1896.

Wotzlaw, J. F., Schaltegger, U., Frick, D. A., Dungan, M. A., Gerdes, A., & GŸnther, D. (2013). Tracking the evolution of large-volume silicic magma reservoirs from assembly to supereruption. Geology 41(8), 867-870.

Wotzlaw, J. F., Bindeman, I. N., Stern, R. A., DÕAbzac, F. X., & Schaltegger, U. (2015). Rapid heterogeneous assembly of multiple magma reservoirs prior to Yellowstone supereruptions. Scientific reports, 5.

APPENDIX

Appendix A: Summary minerals percentage from QEMSCAN analyses

Supplementary Table A.1: Magmatic series 1

	AG1401	AG1406	AG1402	AG1404	VK1403	HQ1402	HQ1403
Mineral Name	*Area %*	*Area %*	*Area %*	*Area %*	*Area %*	*Area %*	*Area %*
Pyroxene (Augite)	0.02	1.08	0.00	0.26	0.03	0.01	
Amphibole (Hornblende)	50.79	22.22	11.93	10.77	4.09	13.85	8.90
Feldspar_Anorthite	36.07	8.99	1.74	2.02	0.16	12.19	0.39
Plagioclase Feldspar	1.58	50.54	52.19	52.62	26.85	61.30	42.50
Feldspar_Albite	0.05	0.00	0.08	0.12	5.67	0.05	1.95
Biotite/Phlogopite	0.05	4.90	4.62	6.95	3.14	1.71	1.21
K-Feldspar	0.70	4.29	9.43	7.32	33.75	4.64	22.15
Quartz	0.00	6.48	17.22	17.03	23.52	2.60	18.03
Fe-oxides	4.55	1.02	1.03	1.10	1.04	1.34	1.31
Apatite	0.01	0.06	0.18	0.16	0.12	0.18	0.27
Rutile/Anatase	0.00	0.00				0.00	
Sphene	1.37	0.15	0.49	0.15	0.09	0.16	0.88
Zircon		0.00	0.01	0.01	0.03	0.01	0.02
Ilmenite	0.22	0.01	0.00	0.06	0.44	0.03	0.04
Chlorite	1.65	0.04	0.69	0.65	0.05	1.08	1.62
Epidote	0.40	0.00	0.16	0.24	0.13	0.29	0.06
Muscovite	1.83	0.03	0.16	0.38	0.09	0.45	0.54
Calcite	0.05	0.00		0.05	0.01	0.01	0.04
'Kaolinite' (clay)	0.03	0.00	0.02	0.00	0.00	0.00	0.04
Others	0.62	0.06	0.04	0.09	0.77	0.10	0.05
AlSilicate trap		0.12					
Bornite						0.00	
Chalcopyrite			0.00	0.00	0.00	0.00	
Arsenopyrite					0.00		
Pyrite		0.00			0.01		
Background	0.04	2.95	0.32	0.08	0.06	0.02	0.23

Supplementary Table A.2: Magmatic series 2

	AG1308A1	VK1404	MR1403	LI1303A1	MR1402	KJ1317_mafic	KJ1317_felsic	KJ0901A	KJ1006A	KJ1308	KJ1508
Mineral Name	*Area %*	*Area %*	*Area %*	*Area %*	*Area %*	*Area %*	*Area %*	*Area %*	*Area %*	*Area %*	*Area %*
Olivine			1.30								
Pyroxene (Augite)	1.79	6.13	12.03	7.20	1.17	0.14	1.54	1.76	1.20	0.00	1.40
Amphibole (Hornblende)	27.57	15.88	0.25	2.50	42.92	20.53	7.07	2.43	6.81	0.42	38.75
Feldspar_Anorthite	0.84	8.24	0.77	24.44	39.23	0.75	0.24	2.18	0.00	0.00	24.34
Plagioclase Feldspar	30.51	53.70	36.38	43.70	3.15	71.87	68.57	48.10	25.36	26.27	21.38
Feldspar_Albite	4.22	0.01	0.54	0.12	0.02	0.16	0.17	1.05	14.54	7.63	0.02
Biotite/Phlogopite	7.07	9.51	6.93	9.91	1.07	0.15	0.03	2.51	6.56	4.55	1.61
K-Feldspar	14.42	1.39	35.49	3.43	1.18	0.89	6.12	36.69	41.99	54.41	2.16
Quartz	0.00	0.00		0.00	0.00	0.49	13.67	1.17		3.71	0.00
Nepheline			1.88								
Fe-oxides	0.40	2.90	1.89	2.22	3.66	2.54	1.04	1.18	0.68	0.88	2.28
Apatite	1.91	1.08	1.30	0.91	3.06	0.28	0.51	0.54	0.72	0.23	0.73
Rutile/Anatase				0.00	0.00	0.00	0.00	0.01	0.00	0.02	0.00
Sphene	0.30	0.49		0.27	0.11	0.06	0.07	0.39	0.64	0.23	0.56
Zircon	0.00	0.01		0.02	0.00	0.01	0.01	0.00	0.00	0.05	
Ca-sulphate	0.00	0.00		0.00				0.00			0.00
Ilmenite	0.01	0.00	0.07	0.32	0.41	0.34	0.20	0.09	0.03	0.58	0.00
Chlorite	0.13	0.06	0.02	2.61	2.20	0.89	0.25	1.17	0.07	0.86	4.00
Epidote	0.70	0.20	0.00	1.00	1.11	0.07	0.17	0.11	0.30	0.04	2.09
Muscovite	0.72	0.19	1.10	0.77	0.45	0.18	0.04	0.21	0.50	0.09	0.24
Calcite	0.34	0.00	0.01	0.28	0.00			0.04	0.08		
'Kaolinite' (clay)	0.35	0.00	0.01	0.03	0.04	0.14	0.01	0.00	0.00	0.00	0.00
Ca-Mg-Fe_carb			0.00						0.01		0.00
Others	0.84	0.17	0.01	0.27	0.22	0.34	0.20	0.27	0.54	0.02	0.39
Scolesite	3.82										
Thomsonite	4.00										
AlSilicate trap						0.15	0.07				
Chalcopyrite		0.04	0.00	0.00				0.09	0.00		0.02
Pyrite	0.03	0.00		0.00				0.00	0.00		
Bornite					0.00						0.03
Pyrrhotite			0.00								
Background	0.84	0.03	0.10	0.61	1.47	0.44	0.41	0.49	0.12	0.41	0.43

Supplementary Table A.3: Magmatic series 3

	KJ1303A2	MR1401	LI1301	KJ1313
Mineral Name	*Area %*	*Area %*	*Area %*	*Area %*
Pyroxene (En-Fs)	0.02	0.08	0.01	0.01
Amphibole (Hornblende)	10.82	0.06	11.26	0.21
Feldspar_Anorthite	0.01	0.00		0.00
Plagioclase Feldspar	17.87	24.74	25.17	23.91
Feldspar_Albite	1.33	10.59	10.10	3.70
Biotite/Phlogopite	5.67	1.30	6.13	5.21
K-Feldspar	26.58	30.73	22.80	20.36
Quartz	5.29	9.53	21.96	5.24
Si-K-rich matrix		14.02		30.55
Fe-oxides	1.18	1.22	0.62	0.38
Apatite	0.56	0.36	0.32	0.35
Rutile/Anatase	0.01	0.07		0.20
Sphene	0.34	0.00	0.43	0.00
Zircon	0.00	0.00	0.01	0.01
Ca-sulphate	0.00			
Ilmenite	0.00	0.01	0.00	0.00
Alteration product of olivine/px	18.17			
Talc	3.51			
Chlorite	4.02	6.04	1.01	0.08
Epidote	0.03	0.00	0.00	0.01
Muscovite	0.06	0.25	0.12	0.09
Calcite	0.22	0.56	0.00	3.28
Ca-Mg-Fe_carb	2.26			3.97
Dolomite	0.00			
'Kaolinite' (clay)	0.00	0.07	0.02	0.72
Others	2.01	0.39	0.03	1.68
Pyrite	0.02			0.00
Chalcopyrite				0.00
Pyrrhotite	0.00			
Background	0.05	2.77	0.93	0.12

Appendix B: EPMA summary EPMA major and LA-ICP-MS trace element analysis

Table 1: Olivine major elements composition and clinopyroxene major and trace elements compositions.

	Olivine (series 2)				*Clinopyroxene (series 1)*						*Clinopyroxene (series 2)*					
Sample	**Gabbroids 3**		**Gabbroids 3 (MME)**		**Diorite**		**Andesitic dike**		**Monzodiorite**		**Gabbroids 1**		**Gabbroids 2**		**Gabbroids 3**	
Sample #	*MR1403*		*ROD7409*		*AG1402*		*AG1406*		*HQ1402*		*AG1308A/A1*		*VK1404*		*MR1403*	
Mean of:	*(n=18)*	*1s*	*(n=16)*	*1s*	*(n=5)*	*1s*	*(n=15)*	*1s*	*(n=16)*	*1s*	*(n=21)*	*1s*	*(n=13)*	*1s*	*(n=48)*	*1s*
SiO_2 (wt%)	34.55	0.23	37.59	0.14	52.98	0.22	52.67	0.46	53.04	0.38	49.53	0.76	51.44	1.05	50.86	0.66
TiO_2	0.01	0.01	0.01	0.01	0.14	0.05	0.32	0.04	0.10	0.06	0.74	0.16	0.59	0.23	0.77	0.10
Al_2O_3	-	-	-	-	0.78	0.15	1.67	0.37	0.66	0.22	3.75	0.59	2.11	0.74	2.99	0.43
FeO	39.77	0.70	22.94	0.43	8.98	0.07	8.40	0.42	10.71	0.56	9.06	1.22	6.72	0.78	7.73	0.49
MnO	2.39	0.24	0.47	0.03	0.61	0.10	0.49	0.08	0.68	0.09	0.44	0.23	0.37	0.07	0.43	0.11
MgO	23.33	0.26	37.98	0.39	14.21	0.29	14.42	0.18	11.99	0.28	11.88	1.01	15.18	0.49	13.65	0.76
CaO	0.07	0.02	n.a	n.a	22.81	0.44	21.27	0.47	21.98	0.50	23.25	0.33	22.83	0.61	22.58	0.34
Na_2O					0.34	0.02	0.33	0.03	0.26	0.03	0.89	0.12	0.43	0.10	0.73	0.19
K_2O					-	-	-	-	-	-	-	-	-	-	-	-
Cr_2O_3	<0.01	-	0.02	0.00	-	-	-	-	-	-	-	-	-	-	-	-

NiO	<0.03	-	0.05	0.01	-	-	-	-	-	-	-	-	-	-	-	-
Total	100.12	-	99.00	-	100.85	-	99.56	.	99.43	-	99.57	-	99.67	-	99.76	-
Forsterite (Fo)	0.51	0.01	0.75	0.00												
Mg-no					0.74	0.00	0.76	0.02	0.64	0.01	0.70	0.04	0.80	0.02	0.76	0.02
Ti (a.p.f.u)	-	-	-	-	0.004	0.002	0.009	0.001	0.003	0.002	0.021	0.004	0.016	0.006	0.022	0.003
Al					0.034	0.007	0.073	0.016	0.029	0.010	0.165	0.026	0.092	0.032	0.131	0.019
Mean of:	n.a	n.a	n.a	n.a	n.a	n.a	n.a	n.a	n.a	n.a	*(n=7)*	*1s*	n.a	n.a	*(n=16)*	*1s*
Li (μg/g)	-	-	-	-	-	-	-	-	-	-	15.786	0.970	-	-	14.080	2.437
Cs	-	-	-	-	-	-	-	-	-	-	-	-	-	-	0.020	0.010
Rb	-	-	-	-	-	-	-	-	-	-	0.261	0.256	-	-	0.197	0.302
Ba	-	-	-	-	-	-	-	-	-	-	0.555	0.310	-	-	1.694	1.960
Th	-	-	-	-	-	-	-	-	-	-	0.940	0.109	-	-	1.908	0.546
U	-	-	-	-	-	-	-	-	-	-	0.161	0.024	-	-	0.446	0.146
Nb	-	-	-	-	-	-	-	-	-	-	1.937	0.460	-	-	1.090	0.197
Ta	-	-	-	-	-	-	-	-	-	-	0.366	0.103	-	-	0.138	0.030
La	-	-	-	-	-	-	-	-	-	-	44.357	3.731	-	-	32.386	4.180
Ce	-	-	-	-	-	-	-	-	-	-	128.057	17.423	-	-	107.688	10.039
Pb	-	-	-	-	-	-	-	-	-	-	0.888	0.102	-	-	0.767	0.405
Pr	-	-	-	-	-	-	-	-	-	-	17.929	3.932	-	-	17.180	1.425
Sr	-	-	-	-	-	-	-	-	-	-	113.500	12.258	-	-	87.575	13.604
Nd	-	-	-	-	-	-	-	-	-	-	75.943	22.569	-	-	84.856	6.495
Zr	-	-	-	-	-	-	-	-	-	-	656.429	158.190	-	-	324.799	125.151
Hf	-	-	-	-	-	-	-	-	-	-	18.071	2.716	-	-	10.012	4.056
Sm	-	-	-	-	-	-	-	-	-	-	16.837	6.521	-	-	20.775	1.601
Eu	-	-	-	-	-	-	-	-	-	-	3.479	1.182	-	-	3.662	0.262
Gd	-	-	-	-	-	-	-	-	-	-	13.633	5.860	-	-	17.812	1.404
Tb	-	-	-	-	-	-	-	-	-	-	1.834	0.762	-	-	2.388	0.204
Dy	-	-	-	-	-	-	-	-	-	-	10.753	4.181	-	-	14.104	1.240
Y	-	-	-	-	-	-	-	-	-	-	50.586	16.698	-	-	70.278	6.505
Ho	-	-	-	-	-	-	-	-	-	-	1.927	0.703	-	-	2.593	0.248
Er	-	-	-	-	-	-	-	-	-	-	5.230	1.614	-	-	6.968	0.732
Yb	-	-	-	-	-	-	-	-	-	-	6.157	1.173	-	-	6.802	0.887
Lu	-	-	-	-	-	-	-	-	-	-	1.070	0.177	-	-	1.037	0.145
Tm	-	-	-	-	-	-	-	-	-	-	0.817	0.199	-	-	1.004	0.119
Cr	-	-	-	-	-	-	-	-	-	-	10.017	7.161	-	-	8.541	8.563
Ni	-	-	-	-	-	-	-	-	-	-	6.140	0.113	-	-	12.231	1.741

Supplementary Table B.1 (continued)

					Clinopyroxene (series 3)	
Essexite	**Gabbroids 4**	**Gabbroids 5**	**Monzonite**	**Gabbroids 6**	**Spessartite**	**Spessartite**
MR1404	*LI1303A1*	*MR1402*	*KJ1006A*	*KJ1508*	*KJ1307*	*KJ1411*

(n=24)	*1s*	*(n=11)*	*1s*	*(n=13)*	*1s*	*(n=25)*	*1s*	*(n=15)*	*1s*	*core (n=23)*	*1s*	*rim (n=20)*	*1s*	*core (n=6)*	*1s*	*rim (n=7)*	*1s*
49.41	0.55	51.33	0.76	51.91	1.39	51.72	0.86	52.87	0.28	52.08	0.69	52.02	0.65	53.92	0.25	52.78	1.05
1.00	0.19	0.46	0.17	0.50	0.21	0.52	0.19	0.23	0.06	0.52	0.13	0.53	0.12	0.16	0.03	0.48	0.22
4.90	0.69	2.18	0.68	2.42	0.76	2.08	0.47	1.15	0.19	2.84	0.45	2.88	0.41	1.01	0.12	2.77	1.18
9.14	0.21	7.35	0.42	6.24	0.68	8.64	0.66	6.88	0.23	4.76	0.59	4.80	0.57	7.24	0.24	5.09	0.90
0.31	0.01	0.52	0.04	0.48	0.16	0.48	0.08	0.56	0.06	0.10	0.06	0.10	0.06	0.61	0.03	0.21	0.19
10.62	0.25	14.45	0.45	14.92	0.46	12.59	0.49	15.04	0.17	16.34	0.40	16.31	0.37	14.01	0.24	15.45	0.94
23.02	0.18	22.72	0.51	22.79	0.73	22.60	0.53	22.80	0.32	22.97	0.35	22.94	0.33	22.47	0.30	22.37	0.52
0.92	0.07	0.38	0.08	0.48	0.14	1.14	0.13	0.34	0.04	0.36	0.03	0.36	0.03	0.55	0.05	0.37	0.05
-	-	-	-	-	-	-	-	-	-	-	-	-	-	-	-	-	-
-	-	-	-	-	-	-	-	-	-	-	-	-	-	0.03	0.01	0.48	0.14
-	-	-	-	-	-	-	-	-	-	-	-	-	-	-	-	-	-
99.30	-	99.37	-	99.74	-	99.80	-	99.87	-	99.97	-	99.94	-	99.98	-	99.92	-
0.73	0.01	0.78	0.01	0.81	0.02	0.72	0.02	0.84	0.01	0.86	0.02	0.86	0.02	0.77	0.01	0.84	0.03
0.028	0.005	0.013	0.005	0.014	0.006	0.015	0.005	0.006	0.002	0.014	0.004	0.014	0.003	0.004	0.001	0.013	0.006
0.218	0.030	0.096	0.030	0.106	0.033	0.091	0.021	0.050	0.008	0.122	0.020	0.124	0.018	0.044	0.005	0.120	0.051
(n=10)	*1s*	*(n=16)*	*1s*	n.a	n.a	*(n=19)*	*1s*	n.a	n.a	*core (n=3)*	*1s*	*rim (n=4)*	*1s*	n.a	n.a	n.a	n.a
16.716	1.537	15.192	1.692	-	-	10.768	3.889	-	-	3.991	1.997	1.404	0.198	-	-	-	-
0.038	0.019	-	-	-	-	0.146	0.142	-	-	0.074	-	0.012	-	-	-	-	-
0.141	0.136	0.094	0.046	-	-	0.631	1.258	-	-	0.080	0.056	0.019	0.006	-	-	-	-
0.499	0.485	0.844	0.929	-	-	1.394	1.949	-	-	1.942	2.502	0.126	0.110	-	-	-	-
0.696	0.690	1.174	0.492	-	-	2.010	1.482	-	-	0.179	0.142	0.046	0.011	-	-	-	-
0.105	0.118	0.266	0.114	-	-	0.446	0.286	-	-	0.044	0.043	0.009	0.001	-	-	-	-
2.649	0.555	0.564	0.189	-	-	1.124	0.868	-	-	0.054	0.006	0.040	0.004	-	-	-	-
0.227	0.043	0.090	0.036	-	-	0.121	0.080	-	-	0.008	0.002	0.008	0.002	-	-	-	-
30.385	6.827	23.266	3.923	-	-	35.591	12.341	-	-	13.943	4.711	3.191	0.362	-	-	-	-
83.290	19.156	94.107	12.837	-	-	112.535	39.115	-	-	52.815	12.826	11.027	1.412	-	-	-	-
0.832	1.016	0.713	0.163	-	-	1.437	1.266	-	-	0.605	0.057	0.103	0.011	-	-	-	-
12.184	3.032	16.979	2.307	-	-	17.420	5.659	-	-	8.790	1.594	1.969	0.263	-	-	-	-
282.697	30.997	60.578	5.842	-	-	50.810	17.641	-	-	42.563	11.346	110.150	2.022	-	-	-	-
55.514	13.611	90.749	13.045	-	-	81.947	24.214	-	-	43.398	6.239	11.120	1.357	-	-	-	-
188.615	60.911	209.764	62.677	-	-	315.435	203.011	-	-	18.366	1.112	15.364	2.438	-	-	-	-
5.511	1.977	9.293	2.701	-	-	10.489	6.500	-	-	1.012	0.094	0.695	0.118	-	-	-	-
11.450	2.823	26.516	3.737	-	-	20.141	4.779	-	-	11.765	1.377	3.087	0.354	-	-	-	-
2.753	0.573	3.956	0.787	-	-	2.599	0.393	-	-	1.699	0.138	0.894	0.104	-	-	-	-
8.471	2.280	25.396	3.770	-	-	17.639	3.301	-	-	10.632	1.058	2.841	0.296	-	-	-	-
1.019	0.264	3.610	0.513	-	-	2.518	0.492	-	-	1.496	0.122	0.346	0.039	-	-	-	-
5.744	1.590	22.452	2.975	-	-	15.578	2.963	-	-	9.055	0.716	1.953	0.207	-	-	-	-
27.285	7.535	107.323	15.555	-	-	79.276	15.132	-	-	44.110	3.397	8.799	0.972	-	-	-	-
1.005	0.283	4.251	0.584	-	-	2.961	0.577	-	-	1.637	0.123	0.340	0.036	-	-	-	-
2.619	0.718	11.606	1.620	-	-	8.193	1.660	-	-	4.322	0.339	0.802	0.124	-	-	-	-

2.504	0.687	11.290	1.710	-	-	8.676	2.033	-	-	4.169	0.255	0.626	0.066	-	-	-	-
0.407	0.115	1.673	0.254	-	-	1.376	0.379	-	-	0.623	0.019	0.082	0.009	-	-	-	-
0.361	0.100	1.666	0.239	-	-	1.224	0.263	-	-	0.615	0.044	0.101	0.008	-	-	-	-
0.698	-	1.102	0.476	-	-	6.201	8.269	-	-	75.028	87.604	4291.793	251.710	-	-	-	-
1.920	-	-	-	-	-	7.493	2.967	-	-	49.238	13.973	196.241	7.273	-	-	-	-

Supplementary Table B.2: Plagioclase major elements composition

	Plagioclase (series 1)																			
Sample	**hornblende**				**Diorite**												**Andesitic dike**			
Sample #	*AG1401*				*AG1402/AG1403/AG1404*												*AG1406*			
	core		**rim**		**core**		**rim**		**core**		**rim**		**core**		**rim**		**core**		**xenocore**	
Mean of:	*(n=24)*	*1s*	*(n=26)*	*1s*	*(n=17)*	*1s*	*(n=18)*	*1s*	*(n=12)*	*1s*	*(n=13)*	*1s*	*(n=14)*	*1s*	*(n=11)*	*1s*	*(n=16)*	*1s*	*(n=7)*	*1s*
SiO_2 (wt%)	45.8	1.0	45.7	0.8	55.2	1.4	57.6	1.0	55.9	1.2	59.6	1.4	53.4	2.7	58.3	1.7	53.9	2.1	50.5	2.3
Al_2O_3	33.8	0.6	34.0	0.6	28.1	0.9	26.5	0.6	27.6	0.9	25.2	0.8	29.1	1.8	25.7	1.0	28.8	1.4	31.2	1.7
FeO	0.1	0.1	0.2	0.1	0.1	0.0	0.2	0.2	0.2	0.1	0.2	0.1	0.2	0.1	0.2	0.1	0.2	0.0	0.2	0.0
CaO	17.9	0.8	17.9	0.7	10.8	1.1	8.9	0.8	10.3	1.0	7.4	1.0	12.1	2.1	8.1	1.3	11.9	1.6	14.7	2.0
Na_2O	1.6	0.4	1.5	0.4	5.8	0.7	6.9	0.5	5.8	0.6	7.5	0.6	4.8	1.2	7.1	0.8	5.1	0.9	3.5	1.2
K_2O	0.0	0.0	0.0	0.0	0.1	0.0	0.2	0.0	0.2	0.0	0.2	0.1	0.2	0.1	0.2	0.1	0.2	0.0	0.1	0.1
Total	99.4	-	99.3	-	100.2	-	100.3	-	100.1	-	100.1	-	99.9	-	99.6	-	100.0	-	100.2	-
An	86	4	87	3	50	5	41	4	49	5	35	5	58	10	38	7	56	8	69	10

																			Plagioclase (series 2)	
Sample			**Monzodiorite**						**Tonalite**						***Gabbroids 1***					
Sample #			*HQ1402*						*HQ1403*						*AG1308A/A1*					
	rim		**core**		**inter**		**rim**		**core**		**inter**		**rim**		**core**		**rim**		**core**	
Mean of:	*(n=15)*	*1s*	*(n=16)*	*1s*	*(n=15)*	*1s*	*(n=18)*	*1s*	*(n=30)*	*1s*	*(n=10)*	*1s*	*(n=31)*	*1s*	*(n=26)*	*1s*	*(n=30)*	*1s*	*(n=21)*	*1s*
SiO_2 (wt%)	57.3	2.5	48.5	2.1	54.6	2.0	59.0	0.8	57.4	1.2	55.1	2.4	60.3	1.5	56.5	1.0	56.9	0.7	*56.9*	*0.9*
Al_2O_3	26.7	1.4	32.5	1.4	28.6	1.0	25.7	0.6	26.8	0.8	28.4	1.5	25.0	1.0	27.0	0.9	26.5	0.6	27.0	0.7
FeO	0.2	0.1	0.3	0.1	0.2	0.0	0.2	0.0	0.2	0.0	0.2	0.0	0.2	0.0	0.2	0.1	0.2	0.1	0.2	0.1
CaO	9.3	1.8	16.3	1.7	11.5	1.3	8.0	0.7	9.2	0.9	11.0	1.9	7.0	1.2	9.1	0.8	8.7	0.5	9.0	0.6
Na_2O	6.6	0.9	2.5	1.0	4.9	0.3	7.1	0.3	6.6	0.5	5.6	1.0	7.8	0.7	6.5	0.6	6.8	0.4	6.6	0.4
K_2O	0.2	0.1	0.1	0.1	0.2	0.0	0.3	0.1	0.2	0.1	0.1	0.0	0.2	0.1	0.2	0.1	0.3	0.0	0.3	0.1
Total	100.3	-	100.1	-	100.0	-	100.4	-	100.3	-	100.3	-	100.5	-	99.5	-	99.4	-	99.8	-
An	43	8	78	8	55	4	38	3	43	4	52	9	33	6	43	4	41	3	42	3

Sample			**Gabbroids 2**								***Gabbroids 3***				***Gabbroids 4***					
Sample #			*VK1404/VK1405*								*MR1403*				*LI13030A1*					
	rim		**core**		**rim**		**core**		**rim**		**core**		**rim**		**core**		**xenocore**		**rim**	
Mean of:	*(n=23)*	*1s*	*(n=23)*	*1s*	*(n=12)*	*1s*	*(n=52)*	*1s*	*(n=19)*	*1s*	*(n=21)*	*1s*	*(n=17)*	*1s*	*(n=15)*	*1s*	*(n=5)*	*1s*	*(n=16)*	*1s*
SiO_2 (wt%)	*57.8*	*0.5*	53.8	1.0	58.2	1.2	55.4	0.8	56.5	1.5	56.8	1.3	58.1	1.4	48.6	3.3	48.9	2.5	55.0	0.8
Al_2O_3	26.5	0.4	28.3	0.8	26.0	0.4	26.9	0.5	26.2	0.8	27.0	1.2	25.8	1.2	31.7	2.5	31.6	1.7	27.6	0.6
FeO	0.2	0.1	0.4	0.2	0.3	0.1	0.3	0.2	0.4	0.7	0.2	0.1	0.2	0.1	0.3	0.0	0.3	0.0	0.3	0.0
CaO	8.3	0.2	11.5	0.6	8.3	0.6	9.9	0.5	9.0	0.8	9.1	1.0	7.8	1.1	15.8	2.9	15.5	2.0	10.8	0.6
Na_2O	6.9	0.2	5.1	0.3	7.0	0.4	6.0	0.3	6.5	0.5	6.3	0.6	7.0	0.5	2.7	1.5	2.8	1.0	5.4	0.3
K_2O	0.3	0.1	0.2	0.0	0.2	0.0	0.2	0.1	0.2	0.1	0.5	0.1	0.6	0.4	0.1	0.1	0.1	0.1	0.3	0.1
Total	99.9	-	99.3	-	100.0	-	98.8	-	98.9	-	99.9	-	99.4	-	99.2	-	99.2	-	99.4	-
An	39	1	55	3	39	3	47	2	43	4	43	5	37	5	76	14	75	10	51	3

Plagioclase (series 2)

Sample	*Gabbroids 5*				*Felsic dike crosscutting Gabbroids 5*						*MME in felsic dike (Gabbroids 5)*								*Monzonite*	
Sample #	*MR1402*				*KJ1319*						*KJ1318*								*KJ1006A/KJ0901A*	
	core		**rim**		**core 1**		**recharge**		**rim**		**core**		**rim**		**core**		**rim**		**core**	
Mean of:	*(n=30)*	*1s*	*(n=26)*	*1s*	*(n=13)*	*1s*	*(n=8)*	*1s*	*(n=21)*	*1s*	*(n=8)*	*1s*	*(n=8)*	*1s*	*(n=8)*	*1s*	*(n=8)*	*1s*	*(n=10)*	*1s*
SiO_2 (wt%)	49.3	0.5	52.1	1.1	57.0	1.9	57.1	2.1	61.2	1.3	51.2	4.0	60.5	0.8	56.0	1.7	58.2	1.1	59.9	1.6
Al_2O_3	31.5	0.5	29.8	0.9	26.4	1.4	26.4	1.2	23.9	0.8	30.7	2.7	24.4	0.6	27.2	1.0	25.9	0.7	24.9	1.3
FeO	0.3	0.0	0.3	0.0	0.1	0.1	0.1	0.1	0.1	0.1	0.2	0.1	0.3	0.1	0.2	0.2	0.2	0.1	0.1	0.0
CaO	15.0	0.4	12.9	0.9	8.8	1.5	8.8	1.5	5.8	0.9	13.9	3.0	6.4	0.5	9.9	1.2	8.2	0.8	7.3	1.4
Na_2O	3.1	0.2	4.4	0.6	6.6	0.8	6.6	0.7	8.2	0.5	3.8	1.8	8.0	0.3	6.1	0.6	7.2	0.4	7.7	0.7
K_2O	0.0	0.0	0.1	0.0	0.3	0.1	0.2	0.1	0.4	0.1	0.1	0.1	0.4	0.1	0.3	0.1	0.2	0.0	0.2	0.1
Total	99.2	-	99.5	-	99.2	-	99.2	-	99.5	-	99.9	-	100.1	-	99.7	-	99.9	-	100.1	-
An	72	2	62	5	42	7	42	7	27	4	66	15	30	2	47	6	38	4	34	6

Plagioclase (series 3)

Sample		*Gabbroids 6*			*Spessartite*				*Porphyry andesitic dike*				*Porphyry andesitic dike*				Porphyry granodiorite					
Sample #		*KJ1508*			*KJ1307*				*MR1401*				*KJ1313*				*LI1301*					
	rim		**core**		**rim**		**core**		**rim**		**core**		**rim**		**core**		**rim**		**core**		**xenocore**		**rim**	
Mean of:	*(n=12)*	*1s*	*(n=20)*	*1s*	*(n=20)*	*1s*	*(n=8)*	*1s*	*(n=8)*	*1s*	*(n=5)*	*1s*	*(n=4)*	*1s*	*(n=28)*	*1s*	*(n=37)*	*1s*	*(n=45)*	*1s*	*(n=13)*	*1s*	*(n=47)*	*1s*
SiO_2 (wt%)	63.5	1.5	53.6	0.9	53.8	0.6	59.4	3.3	55.8	0.4	59.8	1.2	61.1	1.2	59.3	0.9	61.0	0.8	61.0	1.4	53.1	1.1	61.6	1.3
Al_2O_3	22.6	0.9	28.7	0.8	28.7	0.3	24.9	2.1	27.2	0.3	24.6	0.9	23.6	0.5	25.2	0.6	23.9	0.4	24.0	0.7	28.8	0.7	23.6	0.7
FeO	0.2	0.1	0.3	0.0	0.3	0.1	0.4	0.2	0.5	0.0	0.5	0.1	0.4	0.1	0.2	0.0	0.2	0.0	0.2	0.0	0.2	0.0	0.2	0.0
CaO	4.4	1.2	11.6	1.0	11.5	0.4	7.2	2.7	9.9	0.3	7.1	0.9	5.8	0.5	7.1	0.7	5.6	0.3	5.8	0.7	11.0	0.8	5.3	0.8
Na_2O	9.4	0.8	5.2	0.5	5.2	0.2	7.2	1.4	5.6	0.2	7.1	0.3	7.6	0.3	7.2	0.3	7.9	0.2	8.1	0.4	5.3	0.5	8.4	0.5
K_2O	0.2	0.1	0.1	0.0	0.1	0.0	0.9	0.3	0.5	0.0	1.1	0.3	1.3	0.3	0.6	0.1	0.9	0.1	0.6	0.1	0.2	0.0	0.5	0.1
Total	100.2	-	99.5	-	99.7	-	99.9	-	99.6	-	100.1	-	99.9	-	99.6	-	99.4	-	99.7	-	98.5	-	99.7	-
An	20	6	55	4	55	2	34	13	48	2	33	4	28	3	34	3	27	2	27	3	53	4	25	4

Supplementary Table B.3: Plagioclase trace elements composition

	Plagioclase (Series 1)						*Plagioclase (Series 2)*					
Sample	**Hornblende gabbro**		**Andesitic dike**		**Diorite**		**Monzodiorite**		**Tonalite**		**Gabbroids 1**	
Sample #	*AG1401*		*AG1406*		*AG1402*		*HQ1402*		*HQ1403*		*AG1308A1*	
Mean of:	*(n=14)*	*1s*	*(n=16)*	*1s*	*(n=16)*	*1s*	*(n=16)*	*1s*	*(n=14)*	*1s*	*(n=16)*	*1s*
Li (µg/g)	2.76	3.14	5.39	2.84	19.90	31.60	8.88	10.98	0.65	0.26	-	-
Cs	0.99	1.00	0.60	0.44	4.61	8.18	20.88	38.59	0.38	0.45	-	-
Rb	6.41	13.43	9.13	17.06	8.41	18.16	35.28	69.01	1.58	2.89	0.47	0.21
Ba	46.23	19.26	470.86	1047.35	148.14	82.86	249.46	181.29	345.91	175.84	210.59	54.87
Th	0.00	0.01	0.23	0.37	0.93	2.69	0.35	1.29	0.04	0.09	0.01	0.02
U	-	-	0.07	0.07	0.02	0.05	0.02	0.03	0.01	0.02	0.00	0.00
Nb	-	-	0.16	0.23	0.04	0.06	0.07	0.08	0.01	0.02	0.05	0.08
Ta	-	-	0.02	0.02	0.01	0.01	0.01	0.00	0.00	0.00	0.01	0.00
La	0.84	0.48	7.79	1.92	7.33	2.68	3.34	2.00	7.47	1.66	38.34	1.74
Ce	1.10	0.51	9.07	2.63	9.24	3.67	4.12	2.16	8.60	1.91	33.46	2.78
Pb	3.76	0.41	8.87	2.24	10.58	2.07	9.95	3.89	11.34	2.10	13.27	0.83
Pr	0.11	0.04	0.69	0.25	0.76	0.34	0.34	0.16	0.65	0.16	1.87	0.24
Sr	896.76	52.50	897.68	99.51	730.44	149.57	1833.07	560.21	1290.30	158.80	3452.61	205.60
Nd	0.42	0.16	2.11	0.89	2.35	1.19	1.09	0.45	1.86	0.50	4.14	0.74

Zr	0.17	0.14	3.02	4.19	0.76	1.29	0.58	0.53	0.46	0.55	0.20	0.36
Sm	0.06	0.02	0.26	0.13	0.28	0.16	0.14	0.08	0.20	0.09	0.26	0.05
Eu	0.17	0.08	0.70	0.17	0.72	0.31	0.58	0.31	0.68	0.14	1.16	0.15
Gd	0.05	0.02	0.18	0.09	0.18	0.11	0.09	0.04	0.11	0.05	0.11	0.02
Tb	-	-	0.02	0.01	0.02	0.01	0.01	0.00	0.01	0.01	0.01	0.00
Dy	0.02	0.02	0.08	0.06	0.11	0.10	0.04	0.03	0.04	0.03	0.04	0.01
Y	0.10	0.12	0.35	0.28	0.54	0.70	0.17	0.10	0.17	0.12	0.11	0.03
Ho	0.00	0.00	0.01	0.01	0.02	0.02	0.01	0.00	0.01	0.01	0.00	0.00
Er	0.01	0.01	0.04	0.03	0.05	0.07	0.02	0.01	0.02	0.02	0.01	0.01
Yb	0.02	0.02	0.04	0.04	0.05	0.08	0.02	0.01	0.02	0.02	0.01	0.00
Lu	-	-	0.01	0.01	0.01	0.02	0.00	0.00	0.00	0.00	0.00	0.00
Tm	-	-	0.01	0.01	0.01	0.01	0.00	0.00	0.00	0.00	0.00	0.00

Plagioclase (Series 3)

Sample	**Gabbroids 2**		**Gabbroids 3**		**Gabbroids 4**		**Gabbroids 5**		**Monzonite**		**Porphyry granodiorite**	
Sample #	*VK1404*		*MR1403*		*LI1303A1*		*MR1402*		*KJ1006A/KJ0901A*		*LI1301*	
Mean of:	*(n=28)*	*1s*	*(n=16)*	*1s*	*(n=16)*	*1s*	*(n=16)*	*1s*	*(n=32)*	*1s*	*(n=16)*	*1s*
Li (µg/g)	0.87	0.43	0.46	0.46	5.55	2.33	0.40	0.23	1.09	1.40	2.32	2.06
Cs	0.12	0.16	0.04	-	0.04	-	0.15	0.14	0.26	0.58	0.34	0.35
Rb	2.58	1.82	0.47	0.19	0.49	0.77	0.25	0.22	1.65	3.21	5.74	13.65
Ba	684.66	192.37	514.12	206.87	206.14	64.82	260.12	105.51	347.28	304.09	428.91	180.46
Th	0.14	0.33	0.57	2.11	0.02	0.04	0.01	0.01	0.08	0.14	0.01	0.03
U	0.02	0.02	0.13	0.48	0.01	0.02	0.00	0.00	0.02	0.07	0.00	0.01
Nb	0.05	0.07	0.04	0.04	0.01	0.01	0.01	0.02	0.18	0.84	0.01	0.01
Ta	0.00	0.00	0.01	0.00	-	-	-	-	0.07	0.11	0.01	-
La	23.17	9.29	41.17	15.07	34.13	8.14	22.46	2.41	33.96	14.14	11.61	4.68
Ce	27.69	10.02	48.08	27.13	45.90	10.67	26.54	2.55	35.64	20.51	9.97	3.87
Pb	8.81	2.11	16.50	3.85	19.32	4.45	7.61	2.44	14.08	5.27	14.84	5.38
Pr	2.18	0.69	3.69	2.88	3.73	0.89	2.01	0.20	2.50	1.74	0.58	0.23
Sr	2252.76	445.40	2468.94	363.10	2608.78	584.72	3314.74	402.20	1475.73	697.88	2175.69	835.93
Nd	6.35	1.79	10.29	10.50	11.02	2.72	5.66	0.64	6.62	5.12	1.32	0.53
Zr	0.40	0.73	0.22	0.31	0.73	-	0.05	0.07	0.16	0.28	0.26	-
Sm	0.59	0.14	0.97	1.54	1.07	0.27	0.47	0.07	0.56	0.47	0.09	0.04
Eu	1.56	0.31	2.20	0.32	2.24	0.49	1.03	0.14	1.75	1.05	0.90	0.40
Gd	0.28	0.06	0.48	0.98	0.54	0.15	0.20	0.03	0.27	0.23	0.03	0.01
Tb	0.02	0.01	0.05	0.10	0.05	0.02	0.02	0.00	0.02	0.02	0.00	0.00
Dy	0.11	0.02	0.23	0.59	0.20	0.06	0.07	0.02	0.11	0.09	0.01	0.01
Y	0.40	0.10	0.96	2.76	0.73	0.23	0.22	0.06	0.46	0.42	0.04	0.02
Ho	0.02	0.00	0.03	0.10	0.03	0.01	0.01	0.00	0.02	0.01	0.00	0.00
Er	0.03	0.01	0.09	0.27	0.06	0.03	0.02	0.00	0.04	0.03	0.00	0.00
Yb	0.03	0.01	0.07	0.24	0.03	0.01	0.01	0.01	0.03	0.03	0.00	0.00
Lu	0.00	0.00	0.01	0.04	0.00	0.00	0.00	0.00	0.00	0.00	0.00	0.00
Tm	0.00	0.00	0.01	0.04	0.01	0.00	0.00	0.00	0.01	0.00	0.00	0.00

Supplementary Table B.4: Amphibole major and trace elements compositions

	Amphibole (series 1)															
Sample	**Hornblende gabbro**				**Andeisitic dike**				**Diorite**						**Monzodiorite**	
(Sample #)	*AG1401*				*AG1406*				*AG1402/AG1403/AG1404*						*HQ1402*	
	core		**rim**		**amph 1**		**amph 2**									
Mean of:	*(n=37)*	*1s*	(n=15)	1s	*(n=30)*	*1s*	*(n=29)*	*1s*	*(n=36)*	*1s*	*(n=30)*	*1s*	*(n=75)*	*1s*	*(n=25)*	*1s*
SiO_2 (wt%)	41.48	0.56	46.38	1.34	44.85	0.68	48.65	0.49	46.46	0.38	46.07	0.60	46.50	0.85	45.06	1.57
TiO_2	2.44	0.18	1.16	0.51	2.21	0.14	1.10	0.10	1.51	0.20	1.17	0.14	1.19	0.13	1.51	0.26
Al_2O_3	12.62	0.46	8.07	1.17	8.39	0.25	5.72	0.27	7.32	0.19	6.74	0.31	6.90	0.44	8.06	1.16
FeO	12.63	1.72	13.80	0.74	12.77	1.10	12.66	0.36	14.81	0.86	15.34	0.28	15.40	0.56	16.38	0.90
MgO	12.58	1.01	13.33	0.91	14.18	0.96	14.78	0.36	12.74	0.55	12.93	0.34	12.87	0.64	11.40	0.86
MnO	0.12	0.15	0.23	0.18	0.36	0.05	0.43	0.05	0.60	0.09	0.61	0.13	0.59	0.11	0.75	0.04
CaO	12.24	0.15	12.30	0.23	11.57	0.32	12.12	0.20	11.97	0.27	11.56	0.26	11.72	0.30	11.78	0.20
Na_2O	1.65	0.17	0.96	0.20	1.74	0.27	0.87	0.12	0.98	0.13	1.33	0.07	1.22	0.08	1.14	0.22
K_2O	0.44	0.08	0.47	0.09	0.83	0.14	0.56	0.05	0.78	0.07	0.71	0.07	0.73	0.09	0.77	0.11
Total	96.35	0.41	96.71	0.43	96.98	0.49	97.03	0.52	97.39	0.46	96.68	0.51	97.29	0.41	96.97	0.48
Mg-no	0.71	0.05	0.65	0.03	0.72	0.04	0.72	0.02	0.65	0.03	0.66	0.02	0.65	0.03	0.60	0.03
Si (a.p.f.u)	6.17	0.06	6.81	0.17	6.63	0.07	7.11	0.05	6.88	0.04	6.88	0.06	6.90	0.08	6.76	0.19
AlIV	1.83	0.06	1.19	0.17	1.37	0.07	0.89	0.05	1.12	0.04	1.12	0.06	1.10	0.08	1.24	0.19
AlVI	0.38	0.04	0.21	0.06	0.09	0.04	0.10	0.04	0.16	0.03	0.07	0.04	0.10	0.04	0.18	0.05
Ti	0.27	0.02	0.13	0.06	0.25	0.01	0.12	0.01	0.17	0.02	0.13	0.02	0.13	0.01	0.17	0.03
$(Na+K)_A$	0.53	0.04	0.33	0.08	0.57	0.04	0.30	0.03	0.38	0.03	0.44	0.04	0.42	0.05	0.42	0.08
T (°C) (Putirka, 2016)	926.20	23.34	908.32	34.61	865.79	18.55	763.46	8.04	782.14	12.66	779.71	9.81	775.75	9.01	787.45	28.06
T (°C) (HB'94 - eq. B)	973.64	20.74	925.20	51.69	855.38	25.38	716.87	22.13	773.43	23.11	743.36	17.86	789.75	10.91	808.86	23.84
P (MPa) (RR2012 - eq. P1b)	384.32	52.21	1.44	0.28	172.03	15.14	93.78	9.50	125.60	8.03	110.30	6.99	112.17	7.56	154.21	40.49
P (MPa) (Mutch et al. 2016)	619.13	35.93	2.99	0.65	313.80	16.41	180.76	10.97	257.42	9.54	232.45	15.13	238.38	23.23	307.46	71.93
Mean of:	(n=13)	1s	n.a.	n.a.	(n=13)	1s	n.a.	n.a.	(n=10)	1s	n.a.	n.a.	n.a.	n.a.	(n=14)	1s
Li ((µg/g)	1.24	0.53	-	-	0.89	0.33	-	-	3.41	0.31	-	-	-	-	3.65	1.06
Cs	0.11	0.07	-	-	0.31	0.42	-	-	0.02	-	-	-	-	-	0.07	0.04
Rb	2.17	1.27	-	-	3.27	4.63	-	-	2.28	0.38	-	-	-	-	2.29	0.71
Ba	130.18	47.35	-	-	28.15	21.76	-	-	72.14	43.50	-	-	-	-	154.82	39.46
Th	0.23	0.22	-	-	0.72	0.92	-	-	0.25	0.05	-	-	-	-	0.40	0.20
U	0.09	0.06	-	-	0.32	0.54	-	-	0.06	0.02	-	-	-	-	0.33	0.20
Nb	1.40	0.48	-	-	8.21	2.28	-	-	20.69	3.96	-	-	-	-	14.15	2.30
Ta	0.09	0.04	-	-	0.54	0.21	-	-	0.81	0.23	-	-	-	-	0.43	0.08
La	2.75	1.82	-	-	16.43	11.64	-	-	26.02	4.06	-	-	-	-	20.59	3.43
Ce	8.75	4.54	-	-	48.24	17.35	-	-	93.46	15.02	-	-	-	-	65.72	8.11
Pb	1.21	0.54	-	-	0.63	0.13	-	-	1.55	0.18	-	-	-	-	2.12	0.35
Pr	1.52	0.55	-	-	6.93	1.70	-	-	15.25	3.11	-	-	-	-	10.41	1.25
Sr	158.98	85.32	-	-	25.67	6.26	-	-	39.49	6.04	-	-	-	-	119.38	36.52
Nd	9.19	2.83	-	-	33.08	7.26	-	-	75.48	21.81	-	-	-	-	51.89	5.88

Zr	25.56	9.94	-	-	29.54	5.51	-	-	42.46	9.24	-	-	-	-	73.55	16.28
Hf	1.15	0.42	-	-	1.82	0.46	-	-	2.75	0.32	-	-	-	-	3.29	0.41
Sm	3.55	1.12	-	-	8.60	1.68	-	-	20.06	9.32	-	-	-	-	14.33	1.52
Eu	1.31	0.39	-	-	1.69	0.27	-	-	3.06	0.62	-	-	-	-	2.92	0.17
Gd	4.83	1.57	-	-	9.13	1.77	-	-	21.11	12.04	-	-	-	-	14.70	1.37
Tb	0.77	0.25	-	-	1.43	0.27	-	-	3.35	1.98	-	-	-	-	2.26	0.21
Dy	5.23	1.70	-	-	9.77	1.96	-	-	22.82	13.68	-	-	-	-	14.87	1.39
Y	26.80	8.46	-	-	58.80	11.21	-	-	127.93	68.47	-	-	-	-	85.66	8.89
Ho	1.06	0.34	-	-	2.01	0.40	-	-	4.63	2.68	-	-	-	-	2.98	0.29
Er	2.85	0.89	-	-	6.01	1.16	-	-	13.41	7.18	-	-	-	-	8.52	0.83
Yb	2.38	0.70	-	-	6.35	1.12	-	-	13.69	5.39	-	-	-	-	8.66	0.68
Lu	0.32	0.09	-	-	0.96	0.15	-	-	1.98	0.66	-	-	-	-	1.28	0.10
Tm	0.38	0.11	-	-	0.89	0.17	-	-	1.98	0.93	-	-	-	-	1.26	0.12
Cr	0.29	-	-	-	210.95	201.11	-	-	5.21	1.07	-	-	-	-	2.11	2.27
Ni	8.62	1.35	-	-	51.68	7.09	-	-	16.87	3.05	-	-	-	-	10.77	1.23

Amphibole (series 2)

Sample	**Tonalite**		***Gabbroids 1***		***Gabbroids 5***		***Monzonite***		***Felsic dike crosscutting Gabbroids 5***		***MME in felsic dike (Gabbroids 5)***		***Gabbroids 6***	
(Sample #)	*HQ1403*		*AG1308A/A1*		*MR1402*		*KJ1006A*		*KJ1319*		*KJ1318*		*KJ1508*	
Mean of:	*(n=39)*	*1s*	*(n=50)*	*1s*	*(n=81)*	*1s*	*(n=19)*	*1s*	*(n=17)*	*1s*	*(n=21)*	*1s*	*(n=15)*	*1s*
SiO_2 (wt%)	47.89	0.80	38.17	0.48	41.88	0.51	38.89	0.48	48.91	0.60	48.95	1.13	44.03	0.63
TiO_2	1.41	0.25	2.57	0.23	2.68	0.12	2.77	0.30	1.17	0.11	1.26	0.19	2.00	0.14
Al_2O_3	6.64	0.59	12.36	0.28	11.80	0.24	11.27	0.43	5.30	0.33	5.51	0.68	9.20	0.38
FeO	12.67	0.51	18.18	0.91	10.95	0.27	19.16	0.64	11.13	0.52	11.30	0.70	12.55	0.47
MgO	14.33	0.43	8.94	0.55	14.00	0.23	8.50	0.26	15.99	0.30	15.64	0.70	13.65	0.45
MnO	0.74	0.09	0.65	0.14	0.25	0.20	0.60	0.06	0.62	0.12	0.63	0.10	0.35	0.03
CaO	11.93	0.13	11.53	0.11	11.95	0.27	11.10	0.09	11.85	0.16	12.00	0.19	12.05	0.13
Na_2O	1.26	0.16	2.21	0.05	2.18	0.09	2.65	0.06	1.04	0.12	1.01	0.12	1.57	0.14
K_2O	0.64	0.07	2.23	0.09	1.11	0.15	1.87	0.05	0.50	0.05	0.56	0.09	0.96	0.07
Total	97.82	0.31	96.84	0.71	96.81	0.49	96.82	0.49	96.50	0.46	96.85	0.57	96.36	0.33
Mg-no	0.70	0.02	0.52	0.02	0.73	0.02	0.48	0.01	0.78	0.01	0.76	0.02	0.70	0.02
Si (a.p.f.u)	7.00	0.09	5.92	0.06	6.21	0.05	6.05	0.07	7.13	0.07	7.13	0.12	6.56	0.07
AlIV	1.00	0.09	2.08	0.06	1.79	0.05	1.95	0.07	0.87	0.06	0.87	0.12	1.44	0.07
AlVI	0.14	0.03	0.18	0.06	0.27	0.05	0.12	0.05	0.04	0.03	0.07	0.05	0.17	0.03
Ti	0.16	0.03	0.30	0.03	0.30	0.01	0.32	0.03	0.12	0.02	0.14	0.02	0.22	0.02
$(Na+K)_A$	0.41	0.06	1.02	0.03	0.79	0.03	1.02	0.02	0.31	0.03	0.32	0.05	0.60	0.05
T (°C) (Putirka, 2016)	794.14	21.11	927.37	9.60	958.06	7.92	917.54	7.49	778.07	9.32	778.41	15.21	868.89	11.33
T (°C) (HB'94 - eq. B)	793.09	17.90	885.44	20.97	945.87	17.40	895.24	19.10	706.77	44.65	716.00	29.86	824.81	15.77
P (MPa) (RR2012 - eq. P1b)	119.05	15.71	418.27	39.45	353.41	35.91	298.56	30.34	91.09	7.33	94.64	13.82	191.02	16.65
P (MPa) (Mutch et al. 2016)	220.37	28.02	642.06	26.82	545.16	18.62	551.09	37.16	164.49	13.11	173.20	28.53	366.65	25.67

Mean of:	(n=12)	1s	(n=8)	1s	(n=16)	1s	(n=9)	1s	n.a.	n.a.	n.a.	n.a.	n.a.	n.a.
Li (μg/g)	4.52	1.21	16.70	2.95	2.25	2.86	5.44	1.22	-	-	-	-	-	-
Cs	0.11	0.03	0.06	-	0.19	0.18	0.06	0.04	-	-	-	-	-	-
Rb	1.71	0.32	20.50	1.43	5.66	1.83	21.11	1.22	-	-	-	-	-	-
Ba	78.88	39.54	162.63	20.87	493.33	48.95	31.64	6.12	-	-	-	-	-	-
Th	0.27	0.20	1.57	0.09	0.98	0.16	1.34	0.49	-	-	-	-	-	-
U	0.07	0.07	0.44	0.10	0.22	0.09	0.17	0.06	-	-	-	-	-	-
Nb	17.18	2.24	116.38	7.46	27.41	2.75	224.61	83.40	-	-	-	-	-	-
Ta	0.50	0.10	4.63	0.40	1.07	0.11	9.25	4.38	-	-	-	-	-	-
La	21.92	2.56	100.69	5.98	39.36	4.19	120.49	32.95	-	-	-	-	-	-
Ce	76.20	6.56	246.63	15.33	114.55	15.15	309.28	97.81	-	-	-	-	-	-
Pb	1.25	0.48	3.47	0.14	3.13	0.57	3.18	0.53	-	-	-	-	-	-
Pr	12.59	1.30	29.75	3.57	17.12	2.63	39.12	13.33	-	-	-	-	-	-
Sr	61.93	15.44	322.38	13.10	509.61	50.50	61.25	6.54	-	-	-	-	-	-
Nd	63.63	7.62	115.30	21.86	82.68	13.42	151.10	53.53	-	-	-	-	-	-
Zr	46.45	14.08	763.25	53.30	165.97	15.79	1235.48	248.78	-	-	-	-	-	-
Hf	2.39	0.51	18.44	1.99	5.34	0.57	35.59	9.52	-	-	-	-	-	-
Sm	16.90	2.83	21.64	5.32	18.52	3.05	27.63	10.25	-	-	-	-	-	-
Eu	2.62	0.43	4.62	0.98	5.94	0.47	3.11	0.61	-	-	-	-	-	-
Gd	16.43	3.33	16.61	4.20	15.85	2.55	20.65	7.73	-	-	-	-	-	-
Tb	2.47	0.54	2.11	0.48	2.04	0.32	2.82	1.08	-	-	-	-	-	-
Dy	16.08	3.69	11.96	2.45	11.79	1.70	16.78	6.45	-	-	-	-	-	-
Y	93.89	20.65	59.49	8.51	58.54	8.38	88.15	32.34	-	-	-	-	-	-
Ho	3.16	0.72	2.14	0.35	2.17	0.32	3.20	1.22	-	-	-	-	-	-
Er	9.02	2.06	5.84	0.70	5.68	0.80	9.06	3.38	-	-	-	-	-	-
Yb	8.77	1.86	6.13	0.43	5.05	0.59	10.18	3.31	-	-	-	-	-	-
Lu	1.28	0.26	0.96	0.07	0.73	0.08	1.75	0.48	-	-	-	-	-	-
Tm	1.31	0.30	0.87	0.07	0.78	0.10	1.39	0.49	-	-	-	-	-	-
Cr	33.02	12.01	46.80	9.69	2.26	0.49	9.55	1.49	-	-	-	-	-	-
Ni	69.66	7.34	17.85	5.49	11.86	0.89	17.31	0.80	-	-	-	-	-	-

	Amphibole (series 3)							
Sample		***Spessartite***			***Vogesite***		***Porphyry granodiorite***	
(Sample #)		*KJ1307*			*KJ1303A*		*LI1301*	
	core		**rim**					
Mean of:	*(n=4)*	*1s*	*(n=22)*	*1s*	*(n=29)*	*1s*	*(n=31)*	*1s*
SiO_2 (wt%)	45.34	0.26	41.77	0.36	39.01	0.82	48.71	1.36
TiO_2	1.52	0.03	3.27	0.39	*3.57*	*0.20*	1.05	0.30
Al_2O_3	8.08	0.09	11.85	0.40	13.42	0.66	5.71	0.95
FeO	13.10	0.06	10.34	0.85	11.37	0.76	12.91	0.69
MgO	13.95	0.08	14.60	0.71	13.22	0.86	14.70	0.72
MnO	0.39	0.02	0.13	0.05	0.10	0.08	0.51	0.18
CaO	11.70	0.11	11.77	0.29	12.08	0.19	11.84	0.25

Na_2O	1.87	0.04	2.42	0.07	2.37	0.05	1.33	0.18
K_2O	1.13	0.03	1.14	0.09	1.38	0.09	0.60	0.14
Total	97.08	0.42	97.29	0.36	96.51	0.48	97.36	0.51
Mg-no	0.68	0.00	0.75	0.03	0.71	0.03	0.70	0.03
Si (a.p.f.u)	6.73	0.01	6.15	0.04	5.85	0.08	7.12	0.14
AlIV	1.27	0.01	1.85	0.04	2.15	0.08	0.88	0.14
AlVI	0.15	0.00	0.21	0.05	0.23	0.06	0.11	0.03
Ti	0.17	0.00	0.36	0.04	0.40	0.02	0.12	0.03
$(Na+K)_A$	0.69	0.02	0.82	0.02	0.92	0.04	0.42	0.09
T (°C) (Putirka, 2016)	849.42	2.38	988.67	13.66	1018.15	7.50	773.61	23.70
T (°C) (HB'94 - eq. B)	836.16	5.03	896.68	12.74	-	-	699.52	16.38
P (MPa) (RR2012 - eq. P1b)	170.29	3.90	414.11	41.51	504.09	68.84	89.45	16.45
P (MPa) (Mutch et al. 2016)	295.46	4.59	539.52	29.83	696.92	65.90	182.77	39.40

Mean of:	(n=8)	1s	(n=1)	1s	(n=14)	1s	(n=10)	1s
Li (µg/g)	4.34	0.50	7.68	-	6.54	6.42	6.93	2.88
Cs	0.02	0.01	0.02	-	0.34	0.18	0.10	0.10
Rb	5.03	0.10	4.92	-	7.65	3.18	2.42	0.40
Ba	316.87	21.27	353.17	-	656.87	213.35	18.33	10.91
Th	0.20	0.03	0.40	-	1.07	0.90	1.39	2.05
U	0.05	0.01	0.10	-	0.10	0.07	0.36	0.57
Nb	13.77	0.97	28.18	-	13.64	4.89	24.78	8.40
Ta	0.73	0.05	1.23	-	0.76	0.29	0.68	0.35
La	10.76	0.66	21.45	-	24.08	8.64	34.29	9.38
Ce	34.80	2.17	68.06	-	67.08	19.82	98.52	31.57
Pb	0.90	0.01	1.75	-	1.16	0.87	1.31	0.43
Pr	5.84	0.31	11.06	-	10.68	2.94	13.15	4.74
Sr	702.94	27.14	542.83	-	936.23	252.59	48.61	24.57
Nd	31.22	1.43	57.00	-	53.24	13.36	56.50	21.27
Zr	57.19	4.04	90.50	-	142.63	56.54	28.86	6.97
Hf	2.26	0.18	3.42	-	5.40	1.99	1.70	0.31
Sm	7.97	0.24	14.11	-	12.09	2.85	11.58	4.52
Eu	2.37	0.06	3.63	-	3.46	0.73	2.24	0.85
Gd	7.43	0.26	12.64	-	10.46	2.57	9.25	3.30
Tb	0.93	0.03	1.66	-	1.26	0.29	1.26	0.45
Dy	5.29	0.23	9.74	-	6.92	1.74	7.54	2.65
Y	24.24	0.76	46.57	-	30.99	8.24	37.89	11.92
Ho	0.92	0.03	1.73	-	1.18	0.32	1.38	0.45
Er	2.25	0.09	4.44	-	2.92	0.86	3.71	1.16
Yb	1.70	0.10	3.70	-	2.18	0.69	3.53	0.95
Lu	0.23	0.01	0.51	-	0.32	0.10	0.51	0.11
Tm	0.28	0.01	0.60	-	0.38	0.11	0.52	0.15
Cr	227.41	80.95	272.04	-	9.39	5.94	207.76	52.44
Ni	447.29	38.70	263.61	-	71.05	44.96	185.05	8.33

Supplementary Table B.5: Biotite major and trace elements compositions

	Biotite (series 1)						*Biotite (series 2)*							
Sample	**Diorite**		**Andesitic dike**		**Monzodiorite**		**Tonalite**		***Gabbroids 1***		***Gabbroids 2***		***Gabbroids 3***	
Sample #	*AG1402*		*AG1406*		*HQ1402*		*HQ1403*		*AG1308A1/A*		*VK1404/05*		*MR1403*	
Mean of:	*(n=10)*	*1s*	*(n=20)*	*1s*	*(n=26)*	*1s*	*(n=8)*	*1s*	*(n=24)*	*1s*	*(n=33)*	*1s*	*(n=10)*	*1s*
SiO_2 (wt%)	35.93	0.59	36.75	0.34	35.88	0.33	36.85	0.41	34.88	0.43	37.16	0.64	36.49	0.44
TiO_2	3.27	1.03	4.34	0.47	4.44	0.44	4.21	0.13	3.44	0.48	2.91	0.22	5.11	1.03
Al_2O_3	14.20	0.82	13.49	0.32	13.35	0.42	13.59	0.21	14.51	0.31	13.40	0.46	13.87	0.40
FeO	18.94	0.43	16.96	0.33	20.49	0.87	16.33	0.41	18.78	0.69	15.98	0.66	14.12	0.60
MnO	0.46	0.05	0.30	0.05	0.35	0.08	0.65	0.08	0.54	0.09	0.44	0.09	0.25	0.07
MgO	11.60	0.33	13.14	0.38	10.63	0.48	13.23	0.44	12.13	0.56	14.61	0.48	14.70	0.90
CaO	0.06	0.14	0.03	0.05	0.01	0.02	0.00	0.00	0.01	0.02	0.01	0.03	0.00	0.00
Na_2O	0.09	0.03	0.02	0.03	0.11	0.01	0.08	0.04	0.22	0.03	0.04	0.04	0.14	0.04
K_2O	9.41	0.68	9.65	0.32	9.22	0.32	9.49	0.16	9.52	0.40	9.53	0.41	9.78	0.22
Cr_2O_3	-	-	-	-	-	-	-	-	-	-	-	-	-	-
NiO	-	-	-	-	-	-	-	-	-	-	-	-	-	-
Total	93.96	-	94.69	-	94.48	-	94.43	-	94.02	-	94.07	-	94.45	-
Fo	-	-	-	-	-	-	-	-	-	-	-	-	-	-
Mg-no	0.52	0.01	0.58	0.01	0.48	0.02	0.59	0.01	0.54	0.02	0.62	0.02	0.65	0.02
Al iv (a.p.f.u)	2.41	0.05	2.39	0.03	2.40	0.04	2.38	0.02	2.57	0.05	2.33	0.07	2.45	0.04
Xphlog	0.47	0.01	0.53	0.01	0.43	0.02	0.53	0.01	0.49	0.02	0.58	0.02	0.58	0.03
Xsid	0.26	0.04	0.19	0.01	0.23	0.02	0.19	0.01	0.28	0.01	0.16	0.03	0.18	0.02
Xann	0.27	0.04	0.29	0.01	0.33	0.03	0.28	0.01	0.23	0.01	0.27	0.03	0.24	0.02
Mean of:	(n=12)	1s	(n=11)	1s			(n=12)	1s	(n=12)	1s	(n=12)	1s	(n=12)	1s
Li (mg/g)	142.42	10.62	32.79	2.32	-	-	325.20	57.58	125.55	11.64	79.58	8.45	90.58	7.08
Cs	7.93	2.09	21.35	3.20	-	-	7.97	5.47	7.14	3.29	7.90	4.05	14.60	1.07
Rb	497.08	31.09	538.12	19.07	-	-	407.83	214.53	639.55	92.72	604.48	61.47	491.35	35.99
Ba	1495.38	456.13	2013.21	192.04	-	-	3618.83	1957.80	2337.41	1099.42	2156.21	812.81	3176.02	323.52
Th	0.00	0.00	0.49	0.62	-	-	0.40	0.61	0.00	0.00	0.74	1.05	0.03	0.05
U	0.00	0.00	0.18	0.25	-	-	0.24	0.32	0.00	0.00	0.89	1.34	0.02	0.04
Nb	2.36	1.45	6.63	4.45	-	-	15.14	5.58	76.09	21.47	65.60	33.51	141.66	20.50
Ta	0.07	0.05	0.47	0.27	-	-	0.29	0.12	3.04	0.85	1.82	0.96	4.86	0.86
La	0.02	0.01	0.62	1.31	-	-	8.03	11.62	0.02	0.01	4.65	7.28	0.04	0.03
Ce	0.01	0.01	0.97	2.22	-	-	11.45	16.60	0.01	0.01	14.37	21.85	0.07	0.08
Pb	0.72	0.15	1.29	0.60	-	-	2.28	2.06	1.18	0.21	3.49	9.13	3.51	0.48
Pr	0.00	0.00	0.11	0.21	-	-	0.98	1.40	0.00	0.00	2.06	3.32	0.01	0.01
Sr	1.67	0.78	6.99	5.67	-	-	8.73	7.25	16.16	3.51	15.91	39.98	25.25	3.40
Nd	0.02	0.02	0.50	0.88	-	-	3.48	5.05	0.01	0.00	8.44	14.25	0.06	0.08

Zr	0.10	0.05	33.39	77.26	-	-	0.86	0.49	16.37	12.43	9.72	18.39	7.15	2.05
Hf	0.00	0.00	0.82	1.94	-	-	0.08	0.03	0.46	0.31	0.33	0.50	0.61	0.16
Sm	0.00	0.00	0.10	0.16	-	-	0.70	0.89	0.00	0.00	1.82	3.28	0.02	0.03
Eu	0.01	0.00	0.04	0.03	-	-	0.11	0.12	0.01	0.00	0.48	0.88	0.03	0.01
Gd	0.01	-	0.23	0.19	-	-	0.71	0.85	-	-	1.44	2.53	0.04	0.03
Tb	0.00	0.00	0.02	0.03	-	-	0.08	0.10	-	-	0.19	0.35	0.00	0.00
Dy	0.00	0.00	0.10	0.16	-	-	0.45	0.59	-	-	1.13	2.02	0.02	0.02
Y	0.03	0.02	0.63	0.92	-	-	2.69	3.72	0.02	0.01	6.52	11.49	0.08	0.10
Ho	0.00	0.00	0.02	0.03	-	-	0.08	0.12	0.00	0.00	0.21	0.38	0.01	0.01
Er	0.00	0.00	0.07	0.10	-	-	0.26	0.34	0.00	0.00	0.61	1.06	0.01	0.01
Yb	0.00	0.00	0.11	0.13	-	-	0.25	0.31	0.01	0.00	0.71	1.17	0.01	0.01
Lu	0.00	0.00	0.02	0.03	-	-	0.04	0.05	0.00	0.00	0.10	0.17	0.00	0.00
Tm	0.00	0.00	0.02	0.01	-	-	0.04	0.05	0.00	0.00	0.10	0.16	0.00	0.00
Cr	8.57	4.69	16.03	5.65	-	-	76.60	29.14	47.64	15.79	6.96	2.35	11.76	1.72
Ni	28.82	1.35	96.18	10.12	-	-	119.80	3.83	61.40	5.75	73.55	9.76	59.85	3.30

Biotite (series 3)

Sample	***Essexite***		***Gabbroids 4***		***Gabbroids 5***		***Vogesite***		***Porphyry andesitic dike***		***Porphyry andesitic dike***		***Porphyry granodiorite***	
Sample #	*MR1404*		*LI1303A1*		*MR1402*		*KJ1303A*		*MR1401*		*KJ1313*		*LI1301*	
Mean of:	*(n=21)*	*1s*	*(n=10)*	1s	*(n=9)*	*1s*	*(n=13)*	*1s*	*(n=7)*	1s	(n=12)	1s	(n=9)	1s
SiO_2 (wt%)	34.83	0.48	36.62	0.48	36.90	0.29	35.93	0.35	37.24	0.24	37.20	0.16	37.54	0.31
TiO_2	5.30	0.29	5.52	0.21	4.34	0.25	4.29	0.32	5.52	0.44	4.58	0.12	3.97	0.14
Al_2O_3	15.00	0.37	13.36	0.21	15.03	0.39	15.17	0.21	12.07	0.33	13.19	0.13	13.30	0.12
FeO	15.03	0.27	13.97	0.52	10.02	0.44	9.94	1.37	9.80	0.18	16.56	0.19	15.75	0.36
MnO	0.24	0.02	0.21	0.04	0.06	0.09	0.05	0.10	0.06	0.06	0.19	0.03	0.26	0.03
MgO	13.51	0.28	14.83	0.39	18.13	0.32	17.79	1.12	17.99	0.25	13.80	0.11	14.31	0.17
CaO	0.04	0.05	0.00	0.00	0.16	0.12	0.17	0.25	0.00	0.00	0.00	0.00	0.00	0.00
Na_2O	0.20	0.03	0.13	0.02	0.39	0.10	0.75	0.06	0.66	0.03	0.44	0.03	0.13	0.02
K_2O	8.84	0.15	9.84	0.32	8.07	0.47	8.84	0.25	9.01	0.10	9.09	0.17	9.41	0.12
Cr_2O_3	-	-	-	-	-	-	-	-	-	-	-	-	-	-
NiO	-	-	-	-	-	-	-	-	-	-	-	-	-	-
Total	92.99	-	94.48	-	93.10	-	92.95	-	92.35	-	95.05	-	94.67	-
Fo	-	-	-	-	-	-	-	-	-	-	-	-	-	-
Mg-no	0.62	0.01	0.65	0.01	0.76	0.01	0.76	0.04	0.77	0.00	0.60	0.00	0.62	0.01
Al iv (a.p.f.u)	2.64	0.06	2.38	0.04	2.53	0.06	2.62	0.03	2.15	0.05	2.35	0.02	2.32	0.02
Xphlog	0.54	0.01	0.58	0.01	0.69	0.01	0.69	0.04	0.68	0.01	0.54	0.00	0.56	0.01
Xsid	0.27	0.02	0.16	0.01	0.16	0.01	0.18	0.02	0.07	0.01	0.16	0.01	0.15	0.01
Xann	0.19	0.02	0.26	0.01	0.15	0.01	0.13	0.01	0.25	0.01	0.30	0.01	0.28	0.00
Mean of:	n.a.	n.a.	(n=12)	1s	(n=8)	1s	(n=16)	1s	(n=12)	1s	(n=10)	1s	(n=14)	1s

Li (mg/g)	-	-	51.76	7.76	133.45	20.98	15.73	6.89	18.67	11.44	65.86	7.71	158.07	16.81
Cs	-	-	7.44	1.43	12.58	3.78	2.57	0.62	3.79	0.79	4.13	1.61	5.26	1.48
Rb	-	-	372.07	43.96	389.01	164.25	298.01	8.87	301.36	24.70	396.45	63.47	535.86	59.87
Ba	-	-	2887.84	464.14	6176.20	1080.06	8295.73	455.97	3745.75	998.48	3405.48	1820.10	2096.43	789.68
Th	-	-	0.01	0.01	0.01	0.01	0.45	0.35	0.06	0.14	0.15	0.27	0.13	0.18
U	-	-	0.03	0.01	0.02	0.01	0.09	0.07	0.04	0.04	0.08	0.07	0.06	0.07
Nb	-	-	107.01	19.05	20.91	1.31	6.77	0.46	35.71	3.93	37.48	13.38	30.97	5.07
Ta	-	-	3.44	0.84	0.84	0.09	0.35	0.03	0.79	0.08	1.07	0.33	0.61	0.18
La	-	-	0.30	0.82	0.81	0.63	7.36	6.65	0.77	1.51	0.70	1.70	0.59	0.73
Ce	-	-	0.41	1.09	0.69	0.58	17.76	16.17	1.78	2.81	1.34	3.77	0.51	0.62
Pb	-	-	4.10	0.74	5.55	5.08	1.11	0.92	1.75	0.70	2.91	1.05	0.72	0.26
Pr	-	-	0.04	0.09	0.14	0.10	2.30	2.11	0.22	0.30	0.16	0.41	0.04	0.05
Sr	-	-	55.64	106.30	84.88	58.62	322.19	54.80	17.19	3.49	43.53	15.48	1.87	0.52
Nd	-	-	0.13	0.28	0.61	0.39	9.95	9.45	1.10	1.18	0.66	1.57	0.14	0.16
Zr	-	-	16.67	7.01	6.54	2.36	15.26	6.47	3.72	0.34	12.47	4.96	0.57	0.22
Hf	-	-	0.99	0.34	0.16	0.02	0.43	0.16	0.12	0.02	0.37	0.11	0.03	0.01
Sm	-	-	0.02	0.03	0.20	0.13	1.98	1.76	0.22	0.22	0.11	0.26	0.02	0.02
Eu	-	-	0.05	0.06	0.13	0.09	0.50	0.42	0.05	0.04	0.06	0.04	0.01	0.01
Gd	-	-	0.05	0.03	0.24	0.17	1.47	1.38	0.19	0.19	0.19	0.28	0.04	0.02
Tb	-	-	0.01	0.00	0.04	0.02	0.18	0.15	0.03	0.03	0.01	0.02	0.00	0.00
Dy	-	-	0.03	0.03	0.23	0.16	0.82	0.78	0.10	0.16	0.07	0.13	0.02	0.01
Y	-	-	0.11	0.13	1.98	1.51	3.65	3.67	0.36	0.59	0.30	0.64	0.09	0.06
Ho	-	-	0.00	0.01	0.05	0.03	0.13	0.12	0.02	0.03	0.01	0.02	0.00	0.00
Er	-	-	0.02	0.02	0.12	0.09	0.31	0.31	0.05	0.07	0.03	0.05	0.01	0.01
Yb	-	-	0.02	0.02	0.10	0.07	0.24	0.25	0.04	0.05	0.04	0.04	0.01	0.01
Lu	-	-	0.01	0.00	0.02	0.01	0.04	0.04	0.01	0.01	0.01	0.00	0.00	0.00
Tm	-	-	0.00	0.00	0.02	0.01	0.05	0.04	0.01	0.01	0.01	0.01	0.00	0.00
Cr	-	-	1.94	0.60	2.20	0.74	18.40	14.46	177.27	23.93	62.98	27.35	236.19	38.04
Ni	-	-	10.87	1.71	31.38	4.14	261.50	23.36	267.77	5.57	197.00	14.81	295.24	11.26

Electronic Appendix: *In-situ* major and trace element detailed analysis (see attached CD)

Electronic Appendix E.1: Olivine

Electronic Appendix E.2: Clinopyroxene

Electronic Appendix E.3: Plagioclase

Electronic Appendix E.4: Amphibole

Electronic Appendix E.5: Biotite

CHAPTER 4

Optimal tectonic, magmatic and hydrothermal conditions for the generation of large porphyry Cu-Mo systems in a collision zone: Insights from the Meghri-Ordubad pluton, southernmost Lesser Caucasus

HervŽ Rezeau[1], Robert Moritz[1], Rodrik Tayan[2] and Samvel Hovakimyan[1,2]

[1]Department of Earth Sciences, University of Geneva, 1205 Geneva, Switzerland; [2]Institute of Geological Sciences, National Academy of Sciences, 0019 Yerevan, Armenia

ABSTRACT

The Afro-Arabian collision zone, which encompasses Eastern Turkey, Lesser Caucasus, Iran and western Pakistan, represents a highly metal endowed segment along the Alpine-Himalayan orogenic belt. Mesozoic and mid-Paleogene magmatism results from the subduction of the northern branch of the Neotethyan Ocean, followed by mid-Paleogene to Quaternary syn- to post-collisional magmatism linked to the final closure of the southern branch of the Neotethyan ocean and the Arabia-Eurasia continental collision. The majority of economical porphyry Cu-Mo(-Au) deposits (PCDs) in the region is associated with subduction and post-subduction magmatism during the Cenozoic. The southernmost Lesser Caucasus hosts the composite Meghri-Ordubad pluton, which was incrementally assembled over 30 m.y., from the Middle Eocene to Early Miocene. The composite pluton is composed of three temporally and compositionally distinct magmatic differentiation series: (1) Middle Eocene subduction-related medium- to high-K calc-alkaline series, (2) Late Eocene Ð Middle Oligocene collisional shoshonitic to high-K calc-alkaline series, and (3) Late Oligocene Ð Early Miocene post-collisional high-K calc-alkaline "adakite-like" series. The evolution of magma chemistry over time reflects variable degrees of partial melting of the mantle source concomitant with progressive metasomatism of the subcontinental lithospheric mantle and a change in regional stress from a compressive to extensional regime. The subduction-related magmatism is associated with small PCDs, whereas the syn- to post-collisional magmatism is linked to the formation of the world-class Kadjaran Cu-Mo porphyry-epithermal deposit. This emphasizes the crucial role of magmatic source and crustal processes in metal crustal endowment and their availability to the exsolved magmatic hydrothermal fluids responsible for the formation of economic PCDs. A careful review of geochemical, petrological, geochronological and tectonic features allows a comparison of different tectono-magmatic conditions associated with variably-sized PCDs in the upper crust. In conclusion, the Meghri-Ordubad pluton offers a unique opportunity to assess a set of key controlling factors leading to the formation of large PCDs in a

collision zone and this study aims at providing new insights for mining compagnies to identify fertile magmatic provinces during greenfield mineral exploration campaigns in order to optimize their quest for the "*Giants*" in continental collision zone.

Keywords: Porphyry Cu-Mo systems; Subduction- and collision-related metallogeny; Tethyan orogenic belt; Zangezur-Ordubad Cu-Mo district; Lesser Caucasus

1. INTRODUCTION

Metal resources are critical for the development of our modern societies and their extraction is generally limited to the first kilometer of the Earth continental crust (e.g., Arndt et al., 2017). Porphyry Cu ± Mo ± Au systems (PCDs) represent main Cu suppliers with ~75% of the world production and a significant amount of Mo and Au worldwide (e.g., Sillitoe, 2010). They are mainly associated with arc magmatism in subduction and post-subduction collision zones (e.g., Cooke et al., 2005; Richards, 2009; Hou et al., 2011;Moritz et al., 2016a,b). However, the generation of fertile magmatic provinces and large economic deposits primarily depends on a favourable set of tectono-magmatic conditions (e.g., Tosdal & Richards, 2001; Richards, 2003, 2011, 2013, 2016; Wilkinson, 2013; Rezeau et al., 2016; Chiaradia & Caricchi, 2017). A widely accepted model for PCD formation describes mantle-derived hydrous basalt underplating at the base of the crust experiencing melting, assimilation, segregation and hybridization, followed by the ascent of intermediate to silicic calc-alkaline to mildly alkaline magmas to the upper crust (e.g., Hildreth & Moorbath, 1988; Annen et al., 2006; Richards, 2011). Cooling of intrusions in the upper crust focuses the accumulation of volatile-, sulfur- and metal-rich magmatic fluids (H_2O, SO_2, H_2S, Cl, S, Cu) in the cupola and the cyclic overpressure triggers ore-forming hydrothermal pulses (e.g., Burnham, 1979; Chelle-Michou et al., 2017).

The Lesser Caucasus is located along the Turkish-Iranian plateau in the central part of the Alpine-Himalayan orogenic belt. The successive closure of the northern and southern branches of the Neotethys oceanic domains during the Mesozoic and Cenozoic, respectively, are linked with the formation of prospective ore provinces (Fig. 1; Richards, 2015a), including the Eastern Pontides in Turkey (e.g., Delibaş et al., 2016), the Artvin-Bolnisi zone, the Somkheto-Karabagh belt, the Kapan zone and the Zangezur-Ordubad region in the Lesser Caucasus (e.g., Mederer et al., 2014; Moritz et al., 2016a,b; Rezeau et al., 2016), and the Urumieh–Dokhtar magmatic arc together with the Lut and Tabas blocks in Iran (e.g., Aghazadeh et al., 2015; Richards and Sholeh, 2016). In the Lesser Caucasus, the Meghri-Ordubad pluton (MOP) represents the largest mineralized district characterized by successive ore-forming cycles from Middle Eocene to Early Miocene resulting in the formation of porphyry Cu-Mo systems and precious and base metal epithermal deposits, including the large Oligo-Miocene Kadjaran Cu-

Mo porphyry-epithermal deposit (e.g., Tayan, 1998; Moritz et al., 2016a,b; Rezeau et al., 2016). Mineralizing pulses are associated with medium- to high-K calc-alkaline subduction-related magmatism during the Middle Eocene and with shoshonitic to high-K calc-alkaline adakite-like post-subduction collisional magmatism during the Oligo-Miocene (Rezeau et al., 2016). The temporal evolution of tectonic, magmatic and hydrothermal features in the MOP offers a unique opportunity to characterize and compare subduction-related and post-subduction collisional PCDs in order to assess optimal tectonic, magmatic and hydrothermal conditions for the generation of large PCDs.

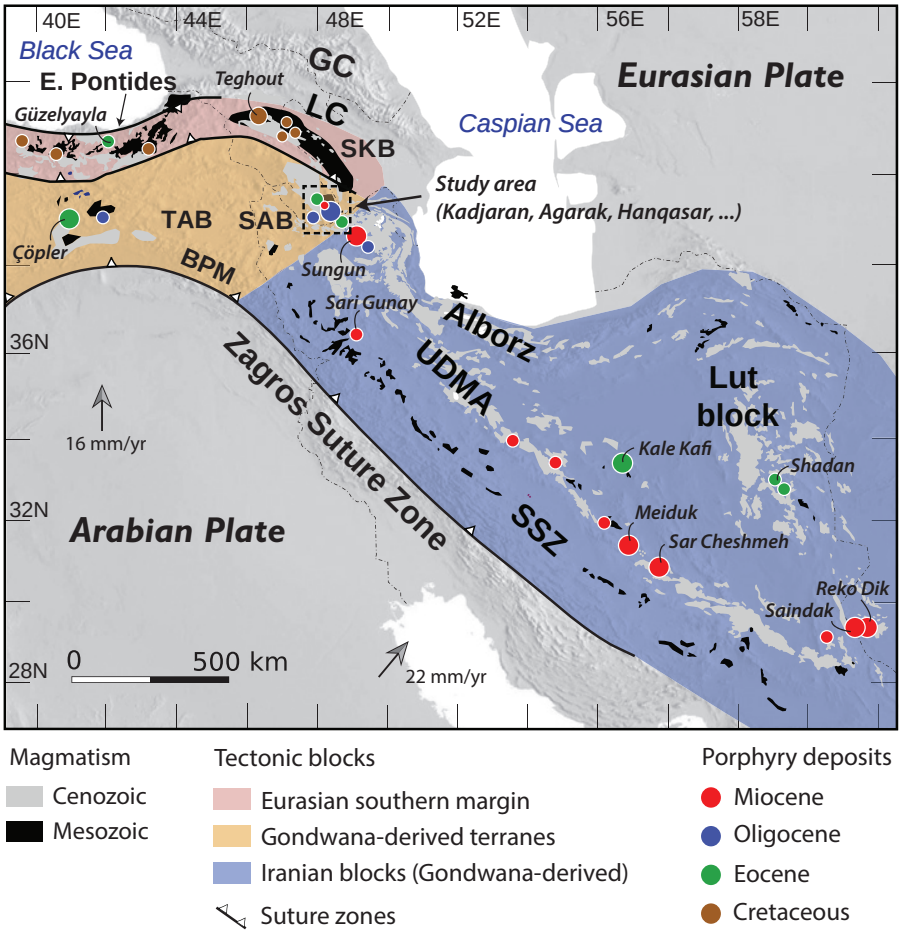

Figure 1: Regional topographic map of the Turkish-Caucasus-Iranian collision zone showing the main tectonic features, suture zones and volcanic belts modified after Sosson et al. (2010) and Mouthereau et al. (2012). The distribution of Cenozoic and Mesozoic mamgatism is compiled after Chiu et al., (2013), Kuşcu et al. (2013), Mederer et al., (2013), and Delibaş et al. (2016). Spatial and temporal distribution of porphyry Cu±Mo±Au deposits along the Turkish-Iranian plateau is reported after Richards (2015a) and Moritz et al., (2016b). Large and small dots indicate large (>100 Mt resources) and small (<100 Mt resources) deposits, respectively, and major deposits are indicated. Abbreviations correspond to Bitlis-PŸturge massif (BPM), Greater Caucasus (GC), Lesser Caucasus (LC), South Armenian block (SAB), Sanandaj-Sirjan zone (SSZ), Somkheto-Karabagh belt (SKB), Tauride-Anatolian block (TAB), and Urumieh-Dokhtar magmatic arc (UDMA).

This study aims at summarizing the tectono-magmatic evolution of the MOP within a comprehensive temporal framework in order to place the incremental growth of the long-lived composite pluton within a regional geodynamic context. The occurrence of variable-sized PCDs allows for discussion of favourable tectono-magmatic controlling factors leading to the formation of large porphyry systems. We present characteristics of subduction-related and post-subduction collision-related PCDs based on field crosscutting relationships, mineral paragenesis and alteration patterns. A special attention on the large post-subduction collision-related Kadjaran Cu-Mo porphyry-epithermal system allows us to propose a magmatic-hydrothermal genetic model of formation constrained in time and space. Based on the evolution of the regional geodynamic and local petrogenesis (Rezeau et al., 2017, Chapter 3) and structural constraints (Hovakimyan et al., 2017), we discuss multiscale tectonic, magmatic and hydrothermal controls and their influence regarding the three main ore-forming events in the MOP. Magmatic source and crustal processes are also discussed in detail with respect to Cu and Mo endowment and the lack of Au. Ultimately, we summarize a combination of favourable controlling factors that could help the mining industry to identify fertile magmatic provinces during greenfield mineral exploration campaign and to assess the potential for major discoveries in collision zone.

2. TECTONO-MAGMATIC EVOLUTION ALONG THE TETHYAN MARGIN

2.1 Regional geodynamic evolution

The Lesser Caucasus and adjoining regions experienced the accretion of Gondwana-derived terranes and the closure of the northern branch of the Neotethys during the late Mesozoic-early Cenozoic, followed by the closure of the southern branch of the Neotethys, the initiation of Arabia-Eurasia continental collision and the post-collisional relaxation during mid- to late Cenozoic (e.g., Barrier and Vrielynck, 2008; Rolland, 2017). The Somkheto-Karabagh belt and the Kapan zone constitute the southern Eurasian margin and result from the NNE-verging convergence of the South Armenian block (SAB) with the Eurasian margin during the Middle Jurassic - Late Cretaceous (Sosson et al., 2010; Mederer et al., 2013). The Sevan-Akera suture zone is characterized by overthrusted ophiolitic nappes that illustrate the progressive closure of the northern branch of the Neotethys ended at 88-83 Ma ($^{40}Ar/^{39}Ar$ dating; Rolland et al., 2009; HŠssig et al., 2013, 2015, 2016). The southwestern limit of the SAB coincides with the accretionary boundary with the Bitlis-PŸtŸrge terrane docked at 74-71 Ma ($^{40}Ar/^{39}Ar$ dating; OberhŠnsli et al., 2010; Rolland et al., 2012). Consequently, the subduction jumped to the SW of the Bitlis-PŸtŸrge massif and initiated the NNE-verging subduction of the southern branch of the Neotethys related to the convergence of the Arabian plate toward the Eurasian margin and accreted terranes (e.g., Rolland et al., 2012). The Cenozoic magmatism along the Turkish-

Iranian plateau (Fig. 1) is characterized by a complex magmatic evolution from middle Eocene subduction-related medium- to high-K calc-alkaline magmatism to Oligo-Miocene collisional-related shoshonitic to high-K calc-alkaline "adakite-likeÓ magmatism, to Pliocene-Quaternary post-collision alkaline ÒOIB-likeÓvolcanism (e.g., Keskin, 2003; Castro et al., 2013; Chiu et al., 2013; Neill et al., 2015; Rezeau et al., 2017) related to the Arabia-Eurasia accretionary orogenesis (e.g., Allen & Armstrong, 2008; Agard et al., 2011; Ballato et al., 2011; Verdel et al., 2011; Chiu et al., 2013; McQuarrie & van Hinsbergen, 2013; Moritz et al., 2016a; Rezeau et al., 2017). Several scenarios are proposed to explain the late Oligocene to Miocene collisional to post-collisional magmatism, including slab roll-back (e.g., Zagros orogeny, Agard et al., 2011; Mouthereau et al., 2012), slab break-off (e.g., E. Anatolia, Keskin, 2003; NW Iran, Aghazadeh et al., 2011; SE Iran, Shafiei et al., 2009) or lithospheric delamination (e.g., E. Anatolia, Pearce et al., 1990; southernmost Lesser Caucasus, Moritz et al., 2016a; central Iran, Haschke et al., 2010). The Pliocene-Quaternary alkaline volcanism is rather ascribed to small-scale lithospheric delamination following a slab break-off and/or roll-back (e.g., Kaislaniemi et al., 2014; Neill et al., 2015).

2.2 Magmatism in the Zangezur-Ordubad region

The MOP outcrops over 1000 km^2 in the Zangezur-Ordubad region at the limit between the South Armenian block and the Kapan zone, across the territories of southern Armenia, Nakhitchevan, and NW Iran (Fig. 2). It is emplaced in and surrounded by Mesozoic, Cenozoic and Quaternary sedimentary and volcanic rocks (Fig. 2; Karamyan et al., 1974; Djrbashyan & Tayan, 2008). Intrusions mainly outcrop in the eastern uplifted Zangezur block separated from the western downthrown Nakhitchevan block by the NW-trending dextral strike-slip OrdubadÐ Salvard fault, and from the Eurasian margin by the NW-trending, dextral strike-slip Khustup-Giratakh fault (Fig. 2; Tayan et al., 1976). In the central part of the Zangezur block, the occurrence of porphyry deposits and epithermal prospects defines an ore-bearing corridor in which mineralized systems are structurally controlled by the central NW-trending dextral strike-slip Tashtun fault active at least since the Eocene and subsequently reactivated (Tayan, 1998; Hovakimyan et al., 2017).

The composite MOP experienced three long lasting episodes of magmatism over ~30 m.y. from Middle Eocene to Early Miocene (Fig. 2; Karamyan et al., 1974; Melkonyan et al., 2008, 2010; Moritz et al., 2016a; Rezeau et al., 2016). Three main magmatic series are recognized, including medium- to high-K calc-alkaline magmatism (hereafter referred to as series 1) dated between 48.9 ± 0.6 Ma and 43.1 ± 0.5 Ma, shoshonitic to high-K calc-alkaline magmatism (hereafter referred to as series 2) dated between 37.8 ± 0.8 Ma and 28.1 ± 0.4 Ma,

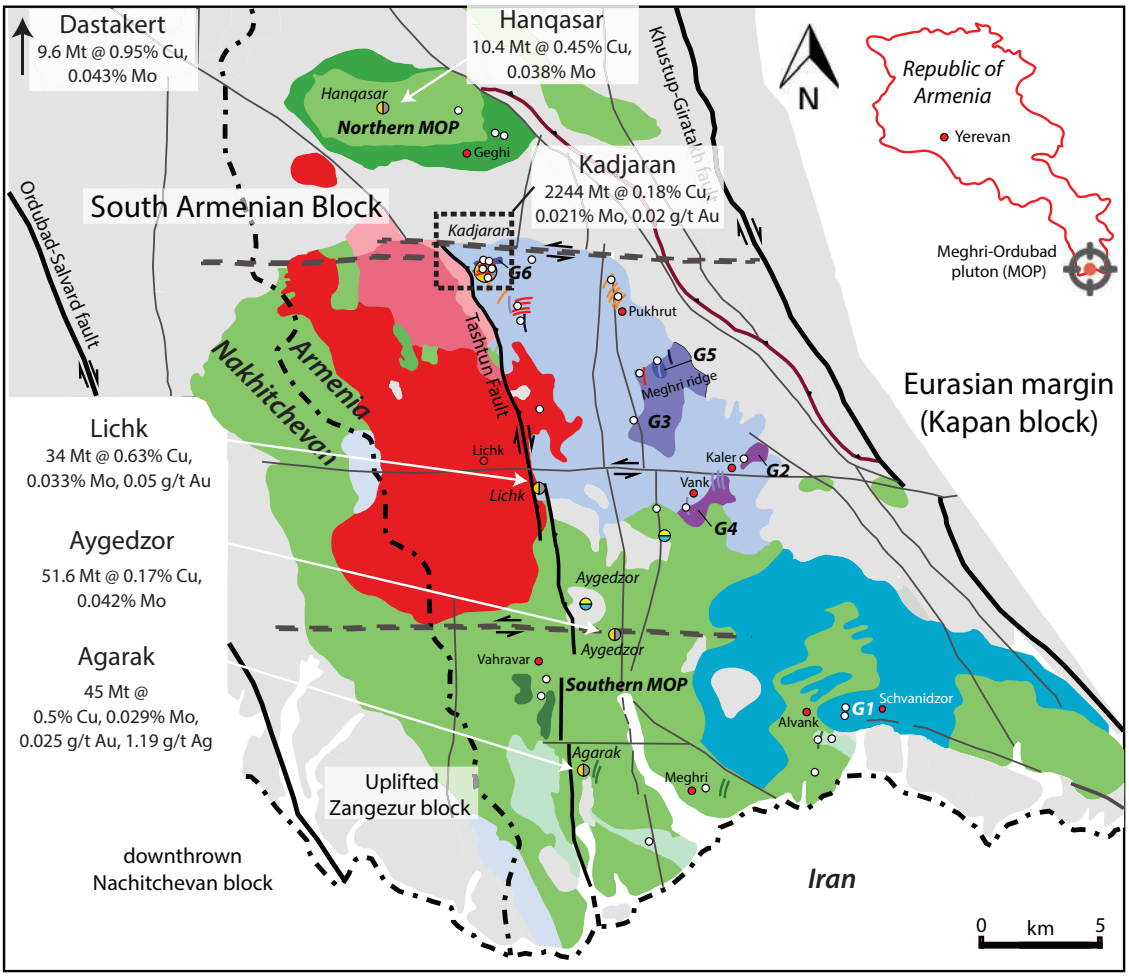

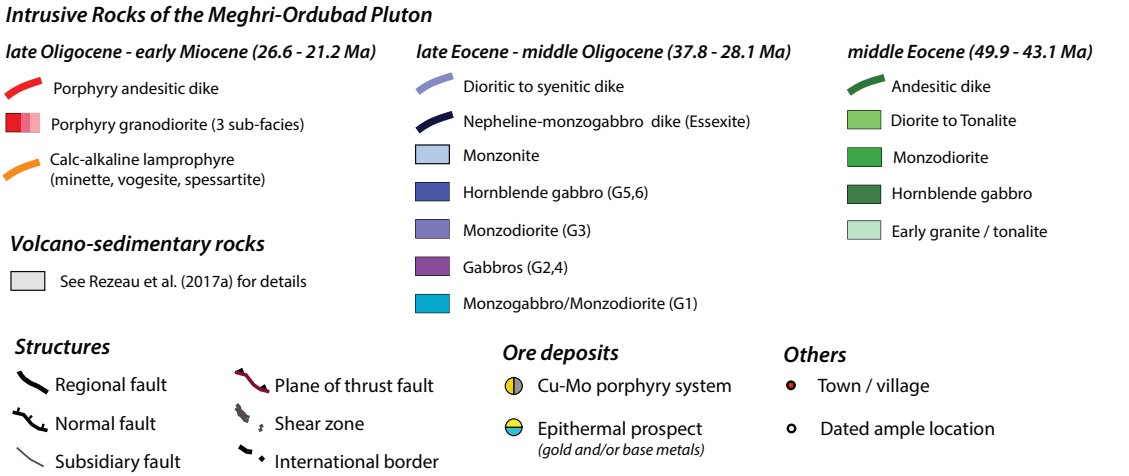

Figure 2: Simplified geological map of the composite Meghri-Ordubad pluton together with the main structural features and the location of major porphyry Cu-Mo ore deposits and base metal - Au epithermal prospects. Modified after Karamyan et al. (1974) and the updated version of Djrbashyan & Tayan (2008). Information relative to ore grades and resources are from Moritz et al. (2016a,b) and references therein. The top right inset indicates the location of the Zangezur-Ordubad zone in southern Armenia at the border with northwestern Iran.

and high-K calc-alkaline "adakite-like" magmatism (hereafter referred to as series 3) emplaced between 26.6 ± 0.3 Ma and 21.1 ± 0.3 Ma (Figs. 3a,b; Rezeau et al., 2016, 2017). Each magmatic series has been emplaced under specific geodynamic environments and they display variable magma composition reflecting contrasting petrological processes (Rezeau et al., 2017, b). Series 1 is characterized by low Sr/Y and La/Yb ratios and flat rare earth element (REE) patterns generated by a high degree of partial melting of a mantle lherzolite promoted by the dehydration of the subducted Neotethys slab (Figs. 3c,d and 4a; Rezeau et al., 2017). Although the entire series was emplaced over 5.8 ± 0.8 m.y., the differentiation series consisting of early emplacement of hornblende gabbro in the middle crust and subsequent dioritic to tonalitic melts emplaced in the upper crust corresponds to only 2.8 ± 0.8 m.y. (Rezeau et al., 2016, Chapter 3). Series 2 was emplaced during 9.7 ± 0.9 m.y. and displays higher Sr/Y and La/Yb ratios together with a significant enrichment in large-ion lithophile elements (LILE), high-field strength elements (HFSE) and light rare earth elements (LREE) without Y and HREE depletion (Figs. 3c,d and 4b; Rezeau et al., 2017). This is interpreted as the result of a low degree of partial melting of a metasomatized mantle lherzolite related to a lower amount of slab-related fluid release and associated with the initiation of Arabia-Eurasia collision (Rezeau et al., 2017). Two differentiation subseries are identified, including (1) hornblende-free gabbroids, (± foids-bearing) and (2) hornblende-bearing gabbroids (Rezeau et al., in prep). Series 3 is composed of early high-K calc-alkaline lamprophyres (spessartite, vogesite) followed by the emplacement of porphyritic granodiorite and porphyritic andesitic dikes over 5.4 ± 0.4 m.y. (Rezeau et al., 2016, 2017, Chapter 3). They are characterized by high Sr/Y and La/Yb ratios in concert with fractionated REE patterns showing depletion in Y and HREE (Figs. 3c,d and 4c), accompanied by an overall increase in Mg#, and enrichment in Ni and Cr (Rezeau et al., 2017, in prep). The "adakite-like" signature inheritance is ascribed to interaction between slab-related silicic melts and peridotite in the mantle wedge rather than high pressure crustal fractionation (Rezeau et al., 2017). Calc-alkaline lamprophyres display the appropriate composition to be qualified as a primitive melt, i.e., Mg# 65Ð70, Cr=280Ð450 ppm, and Ni=140Ð200 ppm (e.g., Kelemen et al., 2003), and that ascent to upper crustal levels was facilitated by an extensional stress regime linked to the initiation of post-collisional orogenic relaxation (Rezeau et al., 2017, Chapter 3). Whole-rock radiogenic isotopic compositions indicate an overall mantle-related magmatism ($^{87}Sr/^{86}Sr$ = 0.70407 - 0.70466 and εNd= +2.3 - 4.9; Moritz et al., 2016a; Rezeau et al., 2017). Complementary zircon εHf (+8 to +11) and $\delta^{18}O$ (+5.2 - +6 ä) values support a predominance of mantle-derived magmas with limited crustal contribution, although the limited isotopic contrast between each magmatic series cannot rule out cannibalization of young juvenile magmas in the lower crust formed just prior to magma generation (Rezeau et al., 2016). A summary of the above mentioned characteristics for each series is provided in Table 1.

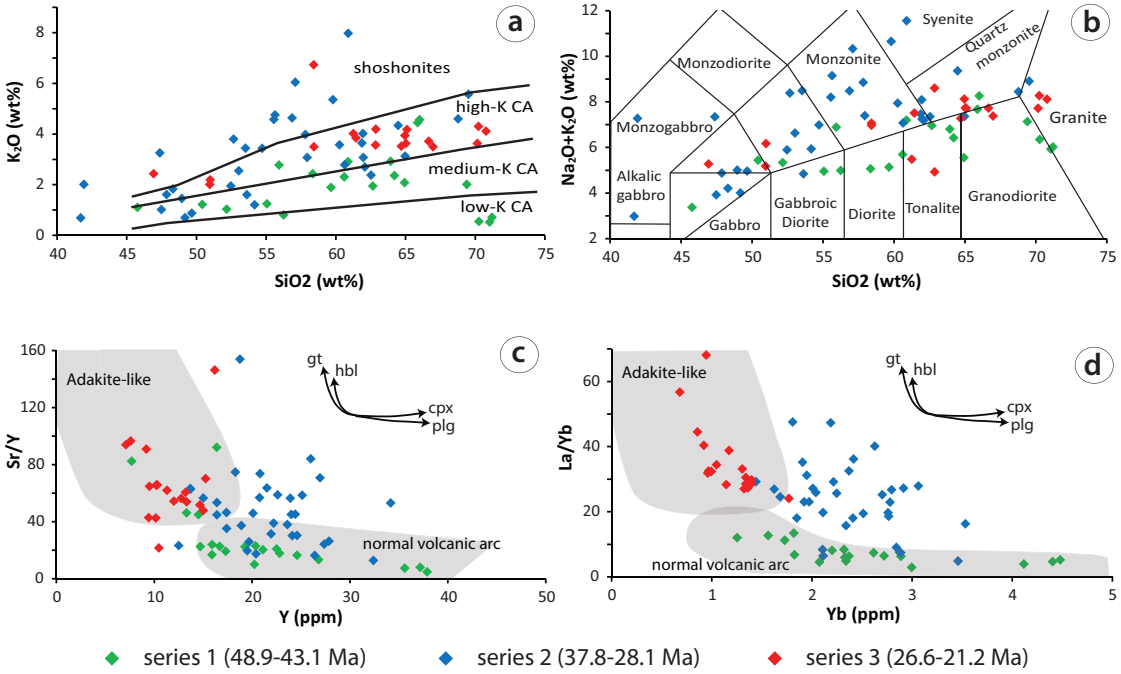

Figure 3: Whole-rock geochemistry for each magmatic series (after Moritz et al., 2016a and Rezeau et al., 2017). a) TAS diagram after Middlemost, (1994), b) K_2O vs. SiO_2 after Pecerillo & Taylor (1976). c-d) Sr/Y vs. Y (ppm) and La/Yb vs. Yb (ppm) plots showing adakite-like and normal arc volcanic rocks fields after Richards & Kerrich (2007).

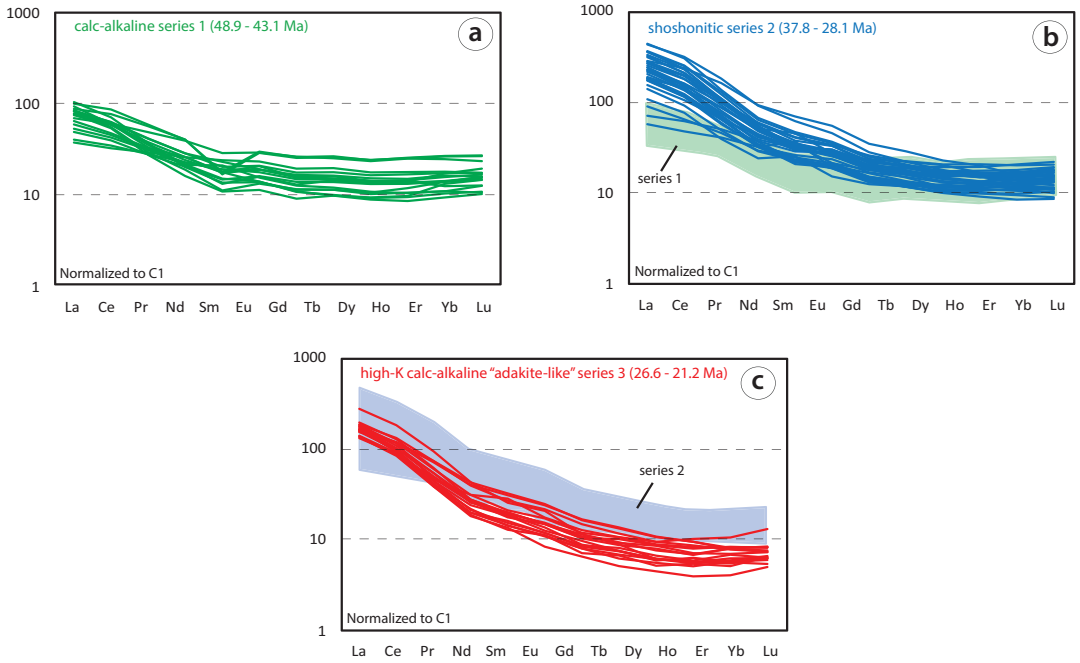

Figure 4: Rare earth element plots normalized to chondrite compositions (C1; Sun & McDonough, 1989) for magmatic series 1 (a), series 2 (b), and series 3 (c) emplaced in the MOP. Data from Moritz et al. (2016b) and Rezeau et al. (2017).

Table 1: Summary of main tectonic, magmatic, and hydrothermal features for each magmatic series incrementally emplaced in the MOP over ~30 m.y..

	magmatic series 1	***magmatic series 2***		***magmatic series 3***
	middle Eocene	***early to middle Oligocene***	***middle to late Oligocene***	***late Oligocene - early Miocene***
Geodynamic setting	subduction-related (closure of the Neotethys) (+)	collision-related (Arabia-Eurasia collision) (+)		post-collisional transition (orogeny relaxation) (+)
Stress regime	compressional (+/-)	highly compressive (-)		transition to extensional/transtensional (+)
Igneous series	medium-K calc-alkaline (+)	shoshonitic to high-K calc-alkaline (+)		high-K calc-alkaline "adakite-like" (high Mg#, Ni, Cr) (+)
Source processes	high-degree (15-20%) of partial melting of a peridotite (slab-related fluid) (?)	low-degree (1-5%) of partial melting of a metasomatized peridotite (decreasing amount of slab-related fluid) (?)		low-degree (5-10%) of partial melting of a garnet-bearing peridotite (slab-related hybridized melt) (?)
Differentiation series	Hbl-gabbro - diorite - tonalite (cpx-plg ± hbl fractionation) (+)	gabbros - monzodiorite - syenite ± foids (cpx-plg-bt fractionation) (-)	hbl-gabbro - monzonite - syenite (cpx-hbl-plg fractionation) (+)	calc-alkaline lamprophyres & porphyry granodiorite (hbl fractionation; limited plg) (+)
Magma chemistry	low Sr/Y & La/Yb flat REE patterns (-)	high Sr/Y & La/Yb & enriched in LREE-MREE (no depletion in Y and Yb) (+/-)		high Sr/Y & La/Yb & depletion of Y and HREE (+)
Duration of magmatism (surface exposure)	2.8 ± 0.8 m.y. (~450 km^2) (-)	9.7 ± 0.9 m.y. (~300 km^2) (+)		5.4 ± 0.4 m.y. (~250 km^2) (+)
Magma/fluid focusing	poorly focused (-)	focused (+)		focused (+)
Mineralization	**small PCDs (10-50 Mt)**	**no PCDs**	**porphyry-related stage in the large Kadjaran Cu-Mo**	**epithermal-related stage in the large Kadjaran Cu-Mo**

(+) prospective; (+/-) unlikely prospective; (-) unprospective; (?) link to magma fertility unknown

abbreviations: bt biotite; cpx clinopyroxene; hbl hornblende; plg plagioclase

3. CHARACTERISTICS OF PORPHYRY CU-MO SYSTEMS HOSTED IN THE MOP

The MOP hosts four economic subduction-related (Agarak, Aygedzor, Hanqasar, Dastakert) and three economic post-subduction collision-related (Kadjaran, Paragachay, Lichk) PCDs emplaced during the Middle Eocene and Middle Oligocene to Early Miocene, respectively (Moritz et al., 2016a,b; Rezeau et al., 2016). Access to operating or closed mines and exploration galleries of subduction-related PCDs was restricted and consequently prevented extensive sampling and field observations. By contrast, the large Kadjaran porphyry-epithermal system formed in a post-subduction collisional environment was fairly well accessible, allowing us to provide detailed field and petrographic descriptions, as well as the recognition of two magmatic-hydrothermal events tightly constrained in time and space.

3.1 Subduction-related porphyry Cu-Mo deposits

The *Agarak* porphyry Cu-Mo deposit is located in the southern part of the MOP, where it is hosted by a tonalitic stock dated at 44.03 ± 0.02 Ma by high-precision chemical abrasion isotope dilution thermal ionization mass spectrometer (CA-ID-TIMS) zircon U-Pb geochronology (Fig. 2; Moritz et al., 2016a). The ore-body is truncated by the Spetri strike-slip dextral normal fault as evidenced by the adjacent Pliocene Nor Arevik sequence (Fig. 5a; Hovakimyan et al., 2017). Proven and probable reserves are estimated at 45 Mt @ 0.5% Cu, 0.029% Mo, 0.025 g/t Au, and 1.19 g/t Ag (Fig. 2, Moritz et al., 2016a, b). In the open-pit, the host-rock displays mingling of gabbroic and tonalitic magmas, which were subsequently crosscut by stockwork-like Cu-Mo veinlets (Fig. 5b). Molybdenite Re-Os geochronology yields a date of 44.2 ± 0.22 Ma, overlapping within errors with the emplacement of the tonalite host-rock (Moritz et al., 2016a). Representative mineralization styles observed in the Agarak open-pit consist of stockwork-like veinlets of quartz-chalcopyrite-molybdenite, quartz-molybdenite, and quartz-pyrite (Figs. 5c,d). Previously, Karamyan (1978) described a paragenetic sequence including a succession of quartz-magnetite, quartz-molybdenite, quartz-chalcopyrite, quartz-pyrite, quartz-sphalerite-galena and late carbonate veins (Fig. 6). Hydrothermal alteration in the ore body is mainly potassic as illustrated by hydrothermal schreddy biotite (Fig. 5e). Further away from the deposit, there is a transition to propylitic alteration characterized by epidotisation of the neighboring igneous rocks (Moritz et al., 2016a).

The *Hanqasar* porphyry Cu-Mo deposit is located in the northern part of the MOP and is hosted by monzodiorite and tonalite yielding laser ablation inductively coupled plasma mass spectrometer (LA-ICP-MS) zircon U-Pb dates of 42.9 ± 0.5 Ma and 43.1 ± 0.5, respectively (Fig. 2; Rezeau et al., 2016). Molybdenite yielded Re-Os dates of 43.14 ± 0.17 and 43.07 ± 0.18 Ma (Moritz et al., 2016a,b; Rezeau et al., 2016), which are in agreement with the coeval magmatism recorded by the host rock. Underground mining operations are currently developped

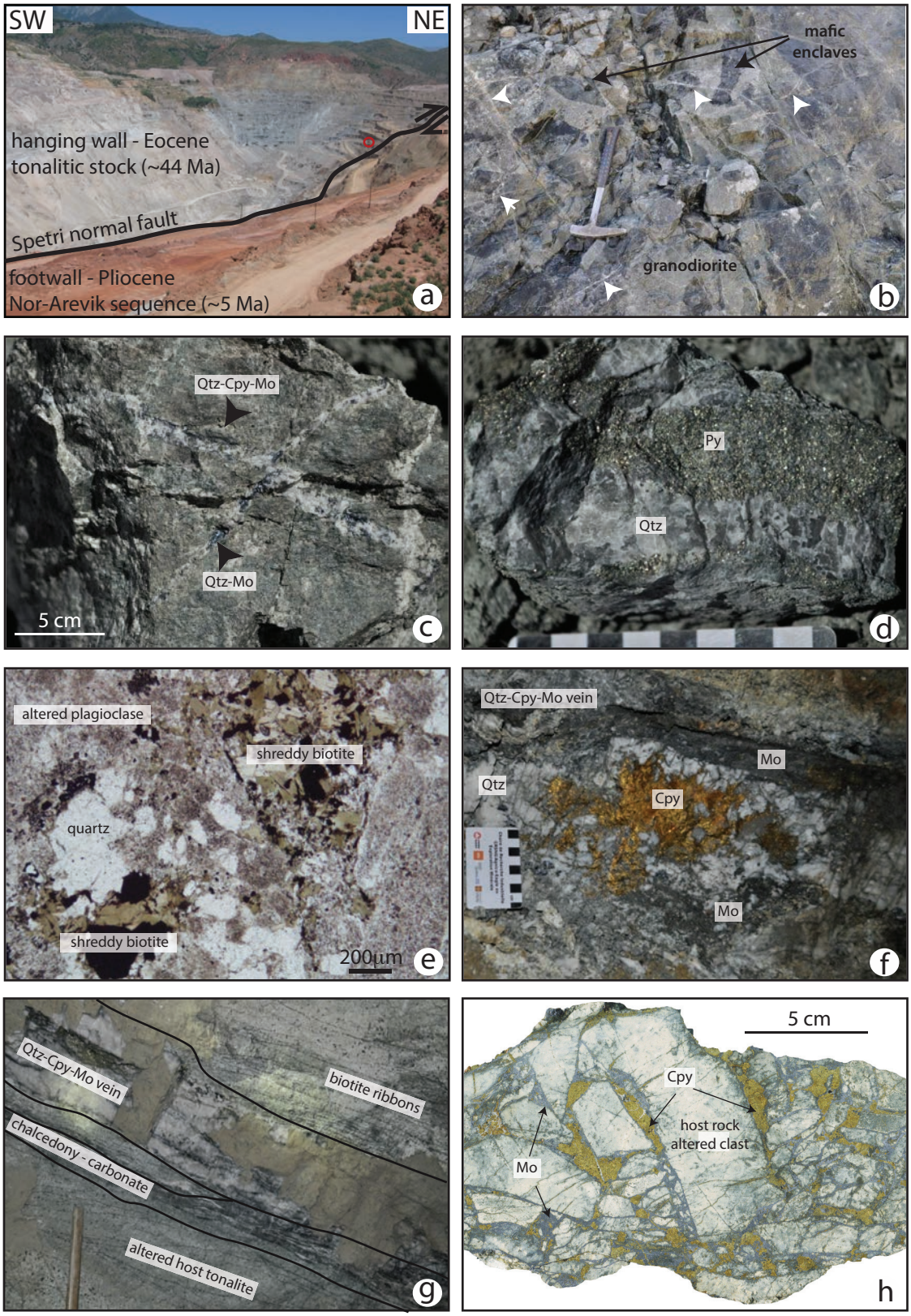

Figure 5: Representative field observations from three middle Eocene PCDs, including Agarak (a-e), Hanqasar (f,g) and Dastakert (h). a) General view of the Agarak open-pit showing the role of the Spetri normal fault that offsets the eastern part of the deposit to depth as illustrated by the adjacent Pliocene Nor Arevik sequence. The red circle indicates a Haul truck for scale. b) Magmatic mingling textures overprinted

by mineralized Cu-Mo stockwork-like veinlets (white arrows). c) Relative temporal relationship between an early quartz-chalcopyrite-molybdenite veinlet crosscut by a quartz-molybdenite veinlet. d) Larger quartz-pyrite veins. e) Altered tonalite host-rock displaying shreddy biotite indicative of potassic alteration and the presence of quartz is attributed to silicification. f) Quartz-molybdenite-chalcopyrite mineralized veins of several tens of centimeters width at the Hanqasar underground mine. g) A meter wide mineralized vein showing early biotitic ribbons crosscut by a quartz-chalcopyrite-molybdenite vein and a late chalcedony-carbonate vein at the Hanqasar underground mine. h) Mineralized monoclastic breccia from the Dastakert deposit showing mineralized cement consisting in equally distributed chalcopyrite and molybdenite. This sample was taken by Rodrik Tayan during the exploitation in the soviet times.

---

and estimated reserves and ore grades are of 10 Mt @ 0.45% Cu and 0.04% Mo (Fig. 2, Moritz et al., 2016a, b). The deposit is characterized by a set of sub-parallel veins steeply dipping to both NE and SW, and they display higher ore grades near the intersection with fault zones (mining staff, personal communication, 2013). The deposit includes various types of veins, including early biotite ribbon veinlets, large quartz-molybdenite-chalcopyrite veins, and late chalcedony-carbonate veins (Figs. 5f,g). By contrast to the stockwork-like veinlets at the Agarak Cu-Mo porphyry deposit, mineralized quartz-molybdenite-chalcopyrite veins in Hanqasar are generally several tens of centimeters up to a meter wide with early molybdenite and late chalcopyrite (Figs. 5f,g). The relative sequence of mineralization presented in Figure 6 is solely based on our limited field observations and may change in the future according to new field and petrographic observations. The alteration pattern is poorly constrained and consists of silicification, sericitization and late carbonate (Karamyan, 1978).

The *Aygedzor* porphyry Cu-Mo deposit is located north of the Agarak porphyry deposit in the central part of the MOP (Fig. 2). Re-Os molybdenite dating yields ages between 43.19 ± 0.17 and 42.62 ± 0.17 Ma (Moritz et al., 2016b), which overlap within uncertainties with Middle Eocene magmatism dated by LA-ICP-MS zircon U-Pb geochronology between 44.8 ± 0.9 Ma and 43.1 ± 0.5 Ma (Rezeau et al., 2016). This deposit is no longer in exploitation but proven reserves, indicated resources and ore grades are 51.6 Mt @ 0.17% Cu and 0.04% Mo (Fig. 2, Moritz et al., 2016a, b). Ore characterization as well as the sequence of mineralizing events relies on former soviet studies that report early quartz-molybdenite-chalcopyrite and quartz-chalcopyrite stockwork-like veinlets, followed by quartz-pyrite, sphalerite-galena veins, and quartz-arsenopyrite veins crosscut by late carbonate and anhydrite-gypsum veins (Fig. 6; Karamyan, 1978). Hydrothermal alteration is described as potassic to propylitic overprinted by sericitization and argillic alteration (Karamyan, 1978). Late moderate acidic alteration can be explained by epithermal mineralization reported in Tey-Lichkvaz, which is interpreted to be structurally linked to the Aygedzor porphyry system (Hovakimyan et al., 2017). However,

younger K-Ar dates of 38.0 ± 2.5 Ma and 37.5 ± 0.5 Ma for hydrothermal sericite (Bagdasaryan et al., 1969) rather suggest two unrelated mineralizing events using the same structures.

The ***Dastakert*** Cu-Mo porphyry deposit is located further north to the MOP associated with the Bargushat intrusive complex and yield molybdenite Re-Os ages significantly younger between 40.22 ± 0.16 and 39.97 ± 0.16 Ma, which appear to be temporally unrelated to any of the intrusive rocks dated in the MOP (Melkonyan et al., 2008, 2010; Moritz et al., 2016b; Rezeau et al., 2016). The granodioritic host-rock has not been dated so far, but biotite K-Ar ages of 42.5 ± 2.5 Ma are reported from a neighboring olivine-bearing gabbro, located in the western Bargushat pluton (Guyumjyan, 1973), which indicate igneous activity further north in the Bargushat pluton. The Dastakert porphyry Cu-Mo deposit was mined in the past, but it is currently not in exploitation. According to Karamyan (1978), the mineralization is characterized by quartz-chalcopyrite, quartz-molybdenite-chalcopyrite, quartz-pyrite, quartz-sphalerite-galena and late carbonate veins (Fig. 6). Monomictic hydrothermal breccia with a mineralized chalcopyrite-molybdenite matrix is also reported (Fig. 4h). Although further zircon U-Pb geochronology on the immediate host rock is needed to accurately determine the magmatic-hydrothermal relationship, this younger mineralizing event defines a younger magmatic-hydrothermal cycle in the Bargushat pluton not recorded or identified so far in the MOP.

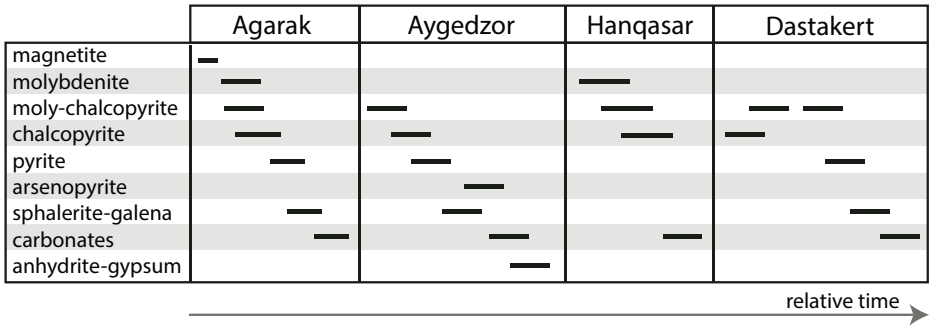

Figure 6: Paragenetic sequences for Agarak, Aygedzor and Dastakert as reported by Karamyan (1978). The paragenetic sequence of Hanqasar is based on our preliminary and limited field observations.

3.2 The major post-subduction Kadjaran porphyry-epithermal Cu-Mo system

3.2.1 Temporal framework and spatial distribution

The large Kadjaran porphyry Cu-Mo system is located in the northwestern part of the MOP. Proven and probable reserves are estimated at 2244 Mt @ 0.18% Cu, 0.021% Mo, 0.02 g/t Au (Fig. 2; Moritz et al., 2016a,b). At the level of exposure, mineralization is hosted by a weakly altered hornblende gabbro and a heavily altered monzonite yielding LA-ICP-MS zircon U-Pb dates of 28.3 ± 0.4 Ma and 28.1 ± 0.4 Ma, respectively (Fig. 7a, Rezeau et al., 2016). Three main mineralized zones are recognized in the open-pit (Figs. 7a,b), including the central ore zone with stockwork-like Cu-Mo mineralization, the adjacent Mo-rich "six veins block"

(hereafter referred to as "6VB"), and the Cu-rich Schlorkut zone. A mineralized prospect named Atkis is reported outside of the open-pit on the other side of the Kadjaran town (Figs. 7a,b).

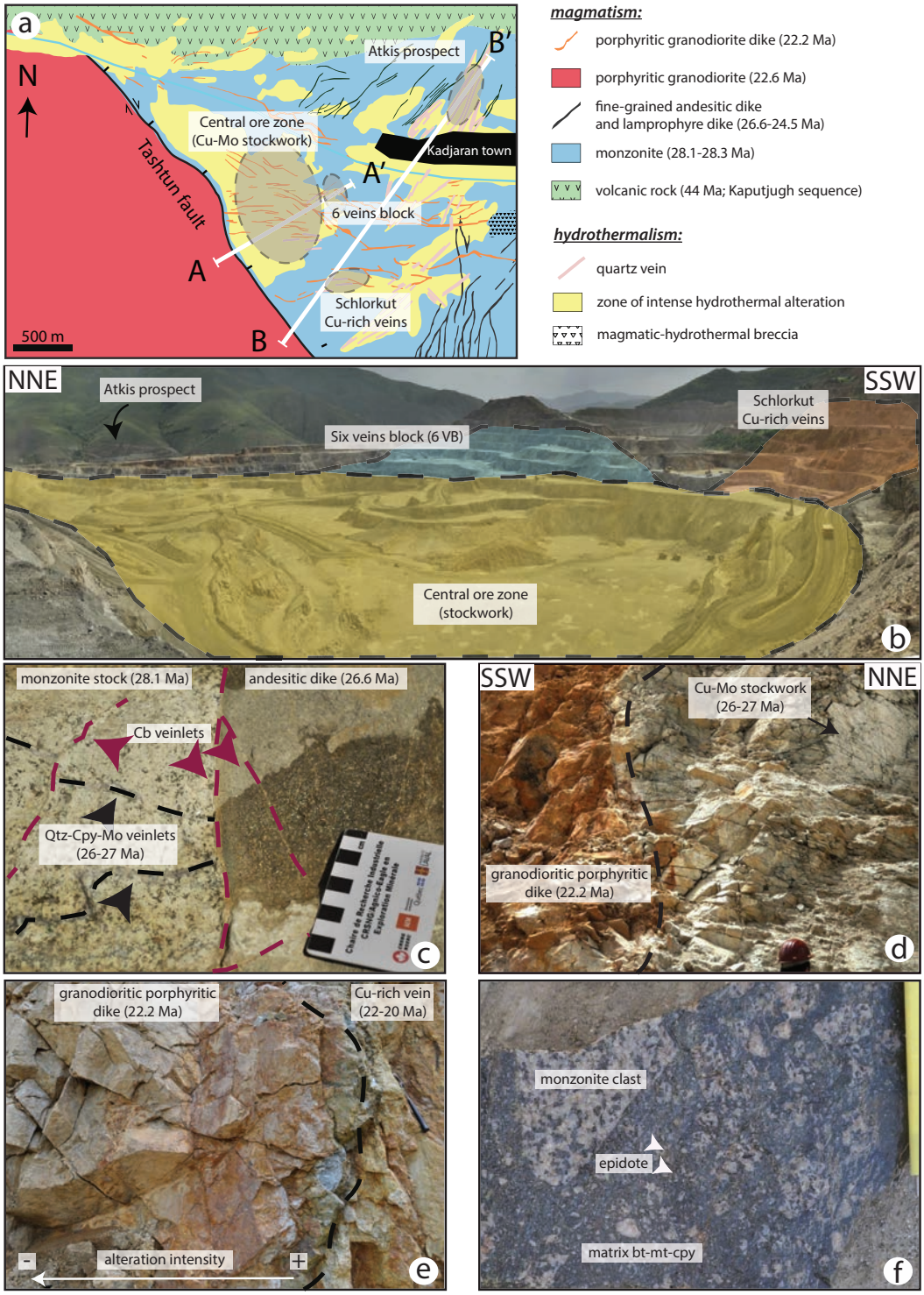

Figure 7: (a) Geological map of the Kadjaran porphyry-epithermal Cu-Mo system simplified after Tayan et al. (2006). Section A-A' and B-B' are represented in Figure 17. (b) Photography of the Kadjaran open-pit in 2013 showing the spatial distribution of the different mineralized zones identified in this study. Field crosscutting relationships in the central ore zone showing (c) a mafic dike and a porphyritic granodioritic dike (d) post-dating stockwork Cu-Mo mineralization, (e) Decrease of hydrothermal alteration intensity from

the Cu-rich vein to the center of the porphyrytic granodioritic dike indicates mineralization post-dating the dike emplacement in Schlorkut area. (f) Monzonite clast from the monomictic magmatic-hydrothermal breccia altered by epidote, suggesting sodic-calcic or propylitic alteration. Field observations are in agreement with zircon U-Pb and molybdenite Re-Os geochronology summarized in Figure 8.

Relative crosscutting relationships show that mineralization pre- and post-dates the emplacement of altered N-S-oriented lamprophyre and E-W-oriented porphyritic granodioritic dikes dated at 26.6 ± 0.3 Ma and 22.2 ± 0.3 Ma, respectively (Figs. 7c-e; Rezeau et al., 2016). A magmatic-hydrothermal breccia occurs in the SE part of the deposit and is characterized by a matrix-supported monomictic breccia with clasts of monzonite in a fine-grained matrix composed of quartz, magnetite, biotite and sulfides together with propylitic to potassic alteration (Figs. 7a,f; Haruntunyan et al., 2004). Finally, molybdenite Re-Os dating reveals two temporally distinct mineralizing events of 27.28 ± 0.14 to 26.43 ± 0.13 Ma and 20.48 ± 0.1 Ma (Rezeau et al., 2016), which is in agreement with complementary K-Ar cooling ages of 22.2 ± 2 Ma in Kadjaran and 24 ± 1 Ma in Atkis reported from hydrothermal sericite (Bagdasaryan et al., 1969). This corroborates magmatic-hydrothermal field relationships described above and summarized in Figure 8.

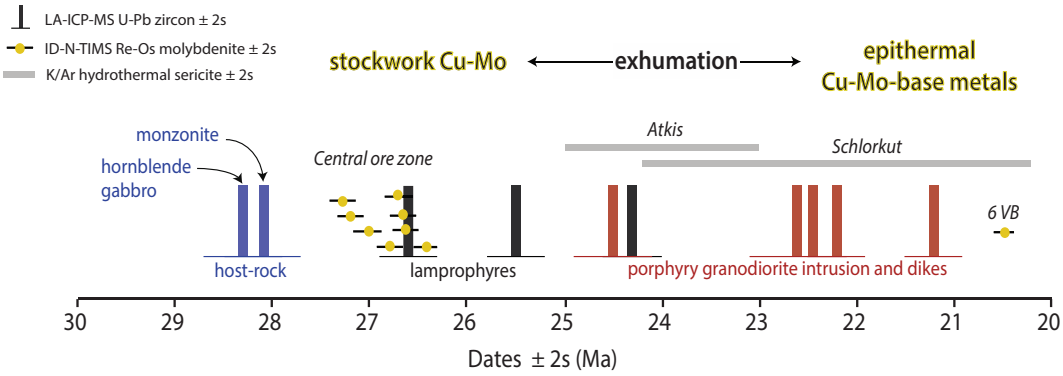

Figure 8: Summary of the sequence of events in the Kadjaran porphyry-epithermal Cu-Mo system based on geochronology and field-based crosscutting relationships. Zircon U-Pb and molybdenite Re-Os dates are from Rezeau et al. (2016) and hydrothermal sericite K-Ar dates are from Bagdasaryan et al. (1969).

3.2.2 Mineralization and hydrothermal alteration

The Central ore zone corresponds to the main exploitation area in the open-pit and it consists of stockwork-like Cu-Mo veinlets (Figs. 9a,b). It represents the main economic stage characterized by the emplacement of mm to cm wide quartz-pyrite, quartz-molybdenite, quartz-molybdenite-chalcopyrite ± bornite, and quartz-chalcopyrite ± bornite veinlets (Figs. 9c,d).

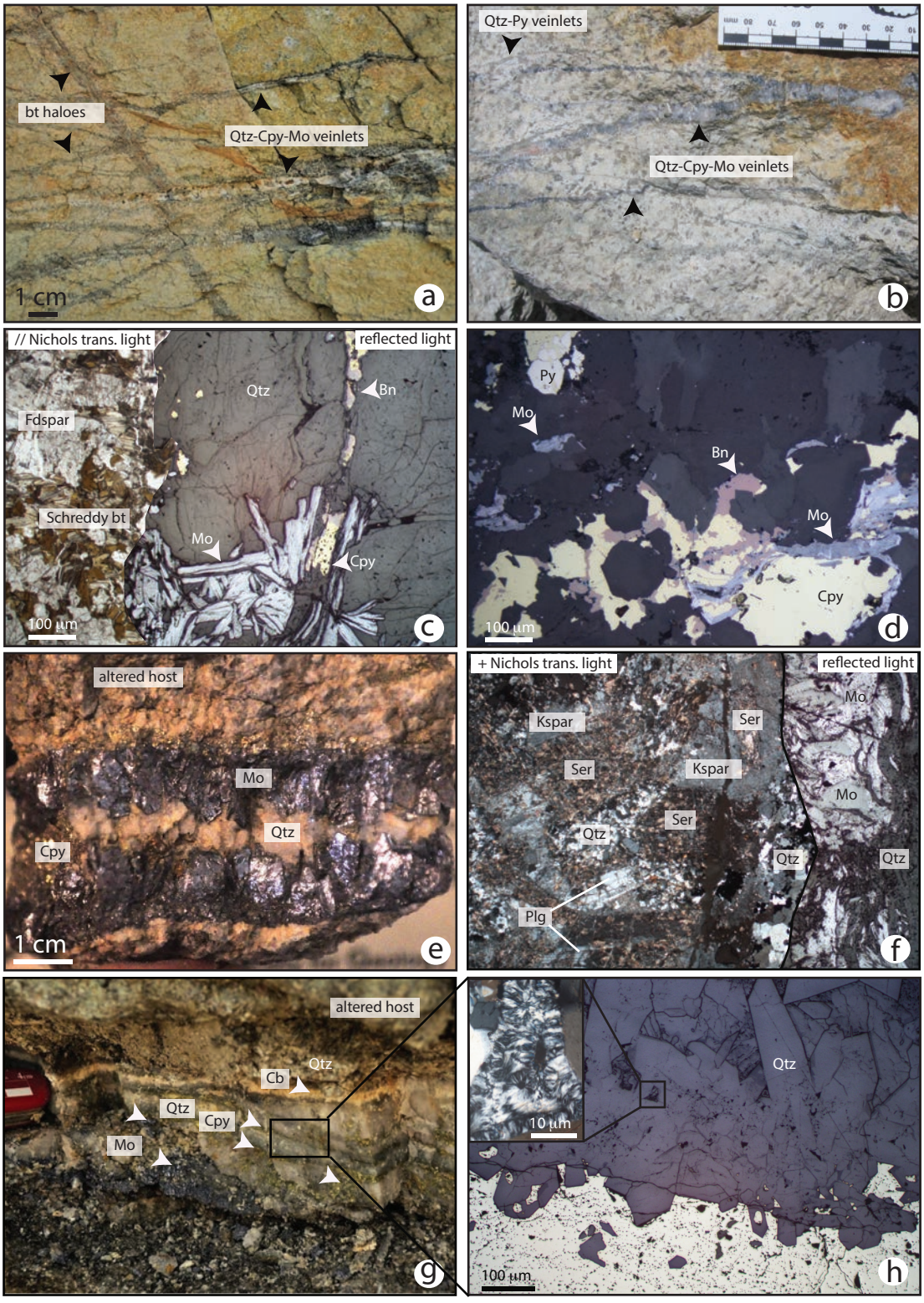

Figure 9: Field and petrographic observations in the central ore zone of the Kadajaran open-pit. (a, b) stockwork-like mineralized veinlets, (c) Composite picture showing early molybdenite followed by chalcopyrite and bornite (reflected light) associated with potassic alteration envelope and shreddy biotite (transmitted light, // Nichols), (d) Reflected light picture showing early chalcopyrite and bornite crosscut by molybdenite. (e) B-vein type showing early molybdenite at the selvage of the vein and inner chalcopyrite precipitation. (f) Composite picture showing B-vein with molybdenite mineralization along the edge of the

quartz vein (reflected light) and associated potassic to sericitic alteration (transmitted light, + Nichols), (g) Subhorizontal vein showing from bottom to top the successive precipitation of quartz-molybdenite, quartz-chalcopyrite and late carbonate. (h) Reflected light picture of the quartz-chalcopyrite layer showing euhedral quartz with interstitial flamboyant quartz (see top left inset in crossed Nichols transmitted light). Abbreviations: Bn Bornite, Bt biotite, Cpy, Chalcopyrite, Kspar feldspar potassic, Mo Molybdenite, Plg plagioclase, Qtz quartz, Py Pyrite, Ser sericite.

Noteworthy is that early quartz-magnetite veinlets were reported by Karamyan (1978). The relative timing between molybdenite and chalcopyrite is difficult to assess since both crosscut each other (Figs. 9c,d). Some of the veinlets display molybdenite along the selvages and chalcopyrite ± bornite in the center documenting early precipitation of molybdenite (Figs. 9e,f). Quartz commonly experienced deformation showing microscale shearing, whereas the least deformed crystals are grayish to translucent euhedral quartz likely crystallized as open-space filling (Figs. 9g,h). Flamboyant quartz is filling interstitial space between euhedral quartz (Fig. 9h). Late stage chalcedony and carbonate minerals are ascribed to low temperature hydrothermal fluid percolation. Hydrothermal alteration envelopes are cryptic to dominantly potassic with K-feldspar or biotite along the vein selvages, whereas sericitization of plagioclase is poorly developed (Figs. 9a-f; Karamyan, 1978). Mineralized hydrothermal stockwork-like veinlets reported in the central ore zone could correspond to early dark micaceous (EDM), M-, A- and B- veins reported from porphyry-related stage in porphyry Cu systems worldwide (e.g., Seedorff et al., 2005; Sillitoe, 2010).

The *Six Veins Block* is composed of a set of dominantly NNW-SSE to E-W oriented, dm-wide steeply dipping parallel veins (Figs. 10a,b). It consists of early quartz - chalcopyrite - molybdenite veins (Fig. 10c), subsequently reopened by quartz - galena - sphalerite - chalcopyrite - tenantite - molybdenite - pyrite mineralization (Figs. 10d-f) and subsidiary quartz - chalcopyrite - enargite (± barite, anhydrite). In addition, clasts of mineralized chalcedony are surrounded and crosscut by late carbonate minerals along the same structures (Figs. 10g,h). Chalcedony clasts in carbonate contain sericite associated with molybdenite - chalcopyrite - sulfosalts - pyrite (Fig. 10h). Complementary XRD analyses of hydrothermal alteration observed on the selvages of mineralized subvertical veins reveal the presence of illite and sericite together with albite (Figs. 11a,b). A careful investigation of hydrothermal quartz crystallizing in open-space filling by secondary electron microscopy Ð cathodoluminescence (SEM-CL) and by electron probe micro-analyzis (EPMA) reveal complex textural and geochemical trace element (Al, Ti) patterns (Fig. 12, Supplementary Table A.1). Three generations of quartz are identified (Fig. 12): (1) a homogeneous luminescent core Q1 with a moderate Al content of 100-300 ppm and "high" Ti contents of 15-35 ppm evolving to a transitional quartz Q1' depleted in Al and characterized by oscillatory zoning, dissolution zones

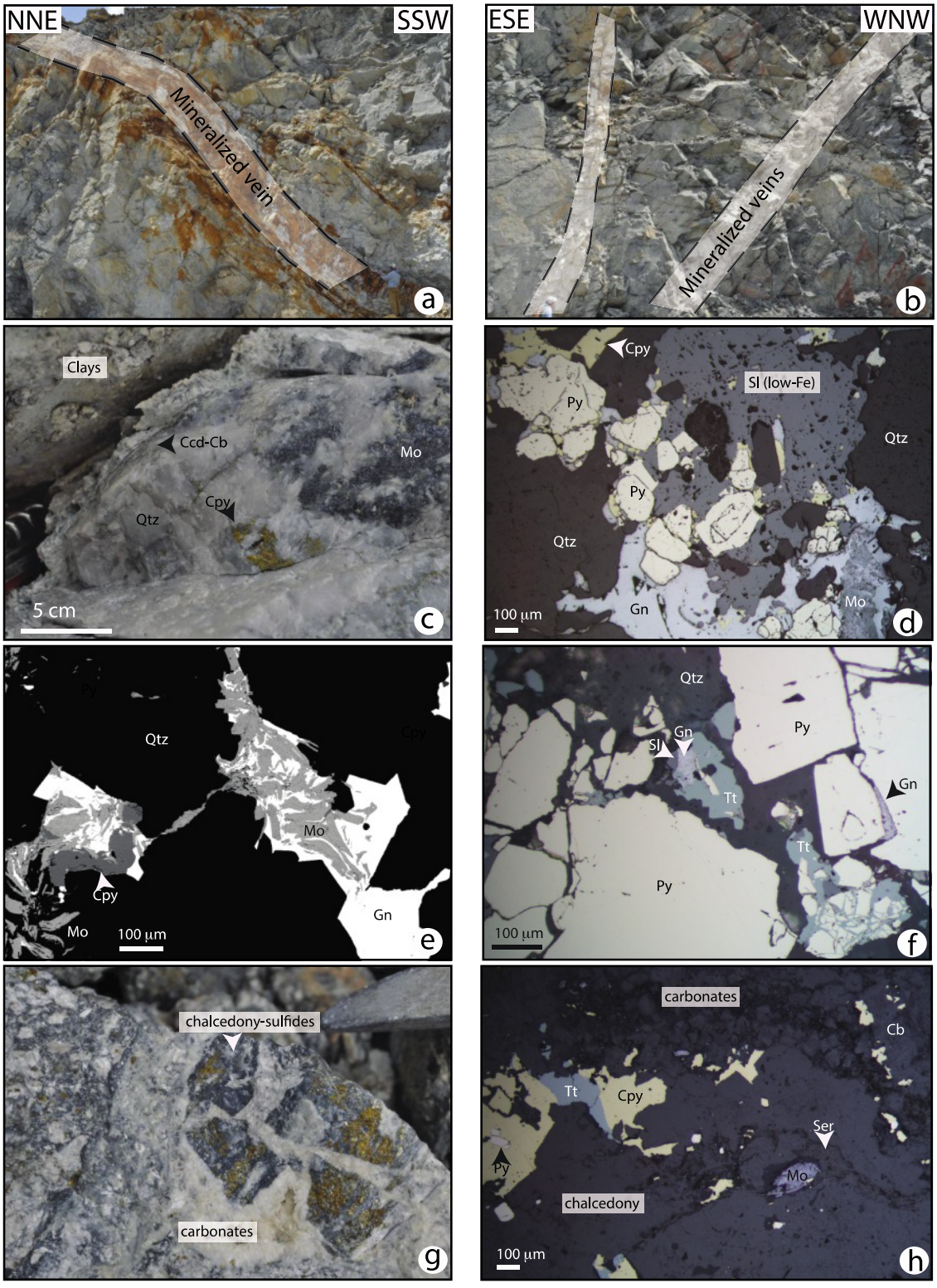

Figure 10: Field and petrographic observations in the 6 veins block zone of the Kadjaran open-pit. (a, b) representative subvertical Cu-Mo and base metal mineralized veins, (c) early quartz-chalcopyrite-molybdenite veins, (d) Reflected light picture showing a late reopening mineralizing event with early pyrite and later galena-sphalerite-chalcopyrite-molybdenite. (e) Backscattered electron image of molybdenite and galena intergrowth together with subsidiary chalcopyrite. (f) Reflected light picture showing early pyrite crosscut by galena-sphalerite-tennantite. (g) Clasts of mineralized black chalcedony in late carbonate

matrix, and (f) reflected light picture zoom on the black chalcedony clast mineral assemblage consisting in molybdenite-chalcopyrite-tenantite together with hydrothermal sericite. Abbreviations: Cb Carbonates, Cpy, Chalcopyrite, Gn Galena, Mo Molybdenite, Qtz quartz, Py Pyrite, Ser Sericite, Sl Sphalerite, Tt Tenantite.

---

and a decrease in luminescence; (2) a less luminescent patchy quartz Q2, associated with chalcopyrite, enargite and anhydrite (± barite), showing chaotic dissolution textures with low Al contents of 10-200 ppm and barely detectable Ti; and (3) a non-luminescent quartz Q3 associated with molybdenite characterized by a significant enrichment in Al up to 1000-5000 ppm and undetectable Ti (<13 ppm).

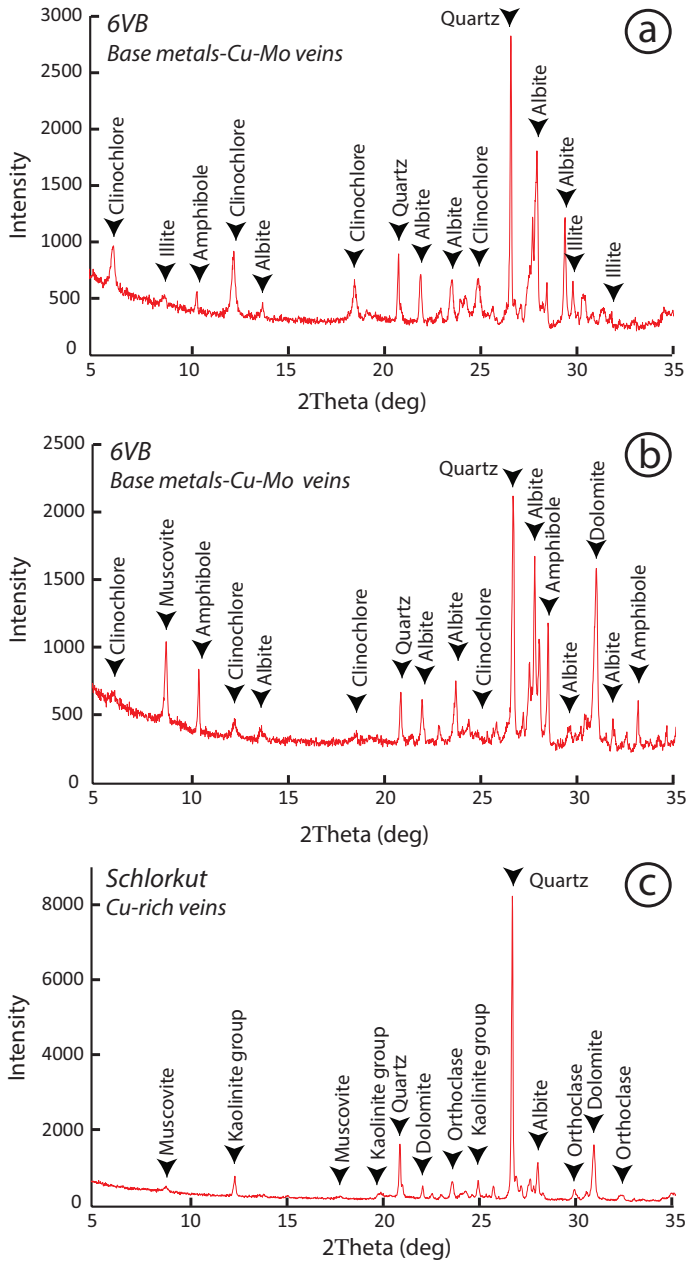

Figure 11: XRD spectra from alteration envelope along a base-metals veins in 6VB (a, b) and a Cu-rich vein in Schlorkut (c). The mineral characterization was carried out on fine fraction samples powder randomly oriented using the Panalytical-Empyrean X-ray diffractometer (XRD) at the University of Geneva. The analyses were performed in continuous scan mode using Bragg-Brentano geometry with a step size of 0.013¡2Theta/step and a counting time/step of 100 sec in the range of 5 to 70¡ (45 kV, 40 mA, Cu Kα). The preparation, sample treatment and analysis of the XRD-pattern follows the recommendations by Moore and Reynolds (1997), and the mineral determination was assisted by using the software HighScore Plus 3.0e. Detection limit for qualitative mineral identification is around 5 wt%.

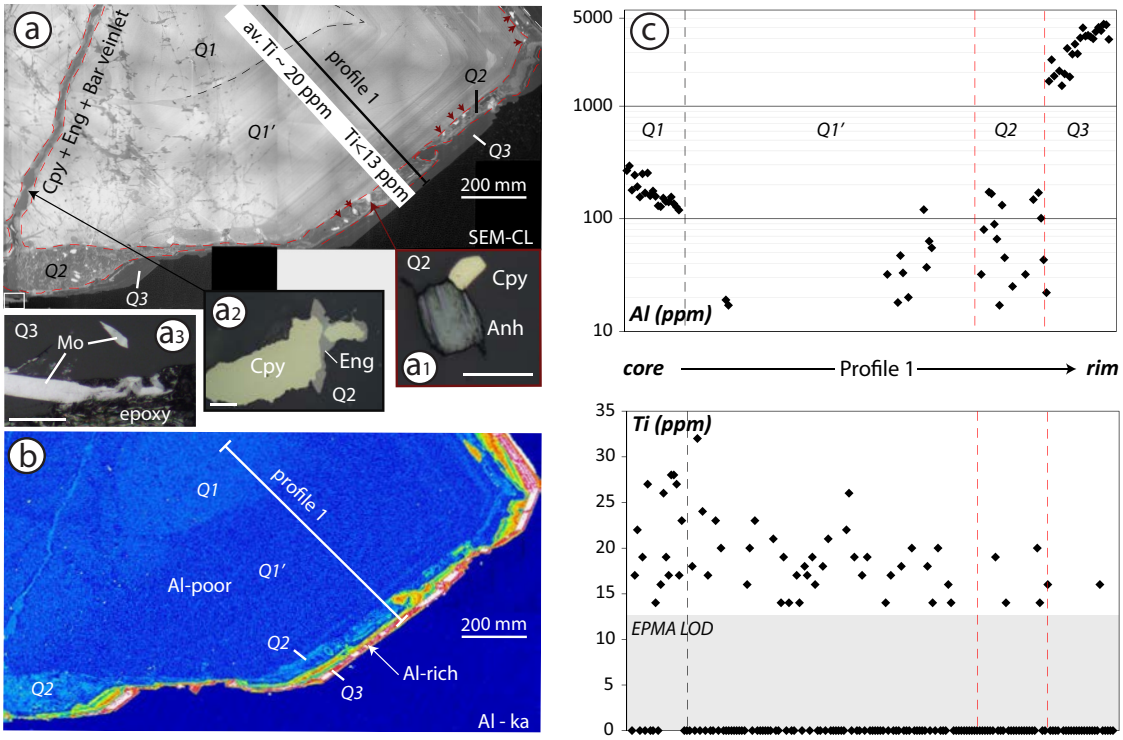

Figure 12: Hydrothermal euhedral quartz crystal from the 6 veins block (a) Scanning Electron Microscope - Cathodoluminescence (SEM-CL) image showing a complex texture from core to rim including three main zone Q1-1', Q2 and Q3. The growth zone Q2 is associated with the precipitation of anhydrite-chalcopyrite (a1) and chalcopyrite-enargite-barite (a2), whereas Q3 co-precipitated with molybdenite dated at 20.5 Ma (a3). Average Ti content is also reported from core to rim. (b) Electron Probe Micro-Analyzer (EPMA) elemental Al mapping. (c) Al and Ti content along the profile 1 in (a) and (b). See text for discussion and Supplementary Table A.1 for detailed analyses. EPMA measurements were carried out at the University of Lausanne using a JEOL JXA 8200 SuperProbe. Results were acquired using a 200 nA electron beam accelerated at 15 kV with a 2-5 µm beam diameter. One spectrometer was dedicated to Al and three for Ti in order to optimize the limit of dectection at ~13 ppm. Standards and X-ray emission lines were set up as follows: albite (Al-Kα) and rutile (Ti-Kα). Counting times of 300 s for the peak and 150 s for the background on both sides of the peak were used. The elemental map was treated with ImageJ software (Schneider et al. 2012).

The *Schlorkut* area exposes a set of E-W oriented subvertical parallel veins reaching up to one meter width and characterized by a greenish staining indicative of Cu enrichment (Fig. 13a). There are various quartz textures in these veins, including milky to greyish quartz, black chalcedony, saccharoidal quartz and vuggy quartz (Figs. 13b,c). The mineralization is dominated by early quartz - pyrite assemblage followed by quartz - digenite - bornite - enargite - chalcopyrite (Figs. 13d-f). In addition to the presence of vuggy quartz, hydrothermal alteration features along the veins and in the quartz vugs are characterized by sericitic to argillic alteration

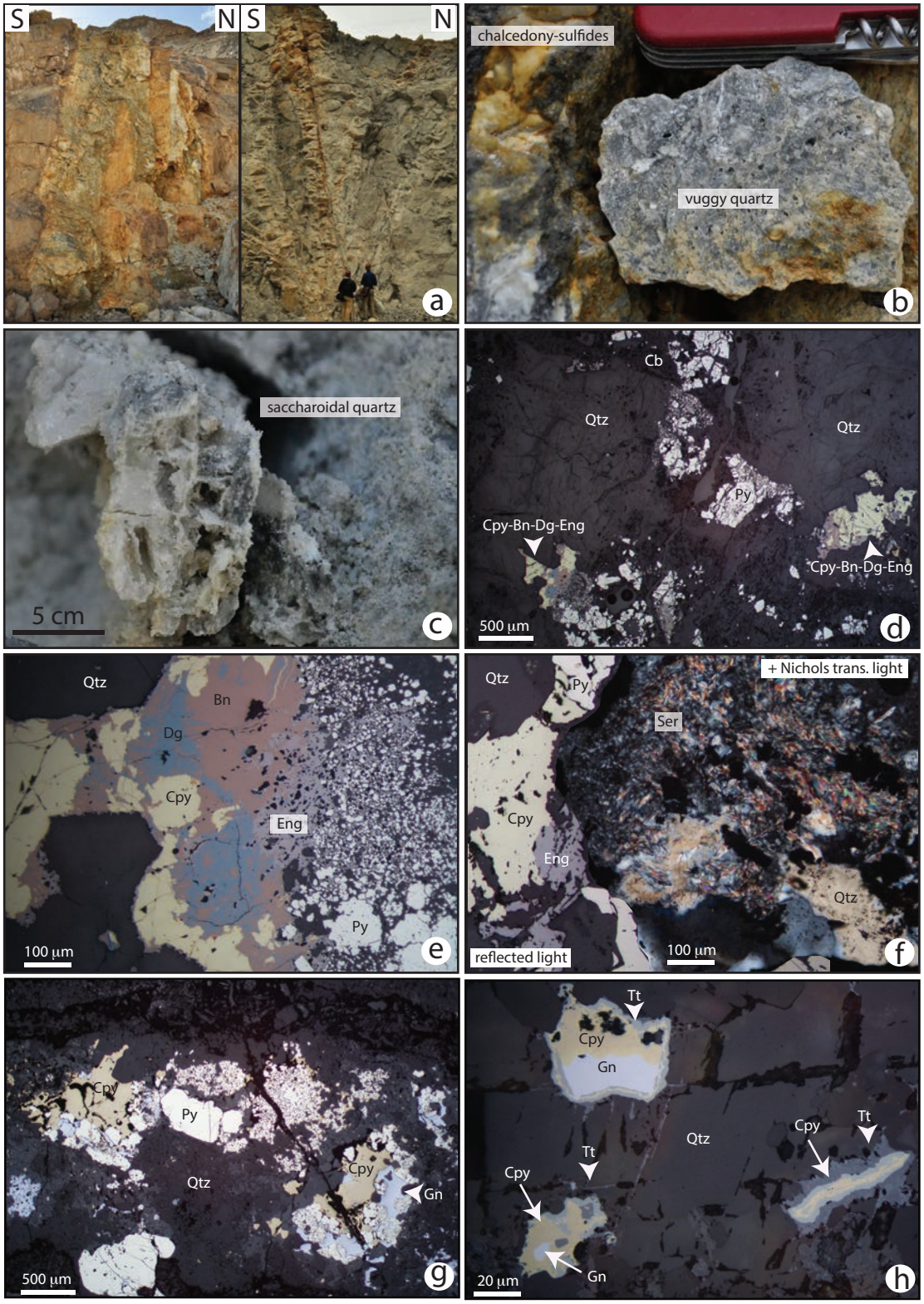

Figure 13: Field and petrographic observations in the Schlorkut area (a-f) in the Kadjaran open-pit and the Atkis prospect (g-h) located outside the open-pit. (a) Representative subvertical Cu-rich veins, (b) Occurrence of vuggy silica together with black chalcedony, (c) Saccharoidal quartz is observed at the edge of the veins at the contact with the monzonite host-rock. (d) Reflected light picture showing early pyrite crosscut by Cu-rich sulfides, (e) Zoom in the Cu-rich sulfide mineral assemblage displaying digenite-

bornite-enargite-chalcopyrite that brecciate early pyrite, (f) Hydrothermal sericite alteration (crossed Nichols, transmitted light) is associated with chalcopyrite-enargite (reflected light), (g) Reflected light picture showing early pyrite crosscut by galena-chalcopyrite, (h) Reflected light picture zoom showing galena-chalcopyrite rimmed by tennantite and oxides. Abbreviations: Cb Carbonates, Cpy, Chalcopyrite, Dg Digenite, Eng Enargite, Gn Galena, Qtz quartz, Py Pyrite, Ser Sericite, Tt Tenantite.

(illite and/or kaolinite, Fig. 11c). Along the upper part of these veins, the host monzonite contains disseminated pyrite and supergene malachite and azurite. Carbonate minerals are late stage phases. This combination of features is extensively reported for intermediate to high sulfidation epithermal deposits emplaced in shallow crustal environments (< 1km, Arribas, 1995; Hedenquist et al., 2000; Einaudi et al., 2003; Simmons et al., 2005).

The *Atkis* prospect is an outcrop restricted to few scraped m^2 on the eastern side of the Kadjaran town. Mineralized samples consist of alternations of milky quartz, chert and carbonate minerals. The mineralization is associated with milky crystalline quartz and consists of early pyrite followed by chalcopyrite - galena - tennantite (Figs. 13g,h). Limited outcrop conditions do not allow us to provide more information, except that hydrothermal sericite used for K-Ar dating (Bagdasaryan et al., 1969) must indicate the presence of sericitic alteration associated with these veins.

To summarize, we propose a new mineral paragenetic sequences in Figure 14 based on field observations and ore petrography described above for each mineralized zone identified in and around the Kadjaran open-pit. This will be further discussed below with respect to the temporal and spatial evolution of the Kadjaran porphyry-epithermal Cu-Mo deposit.

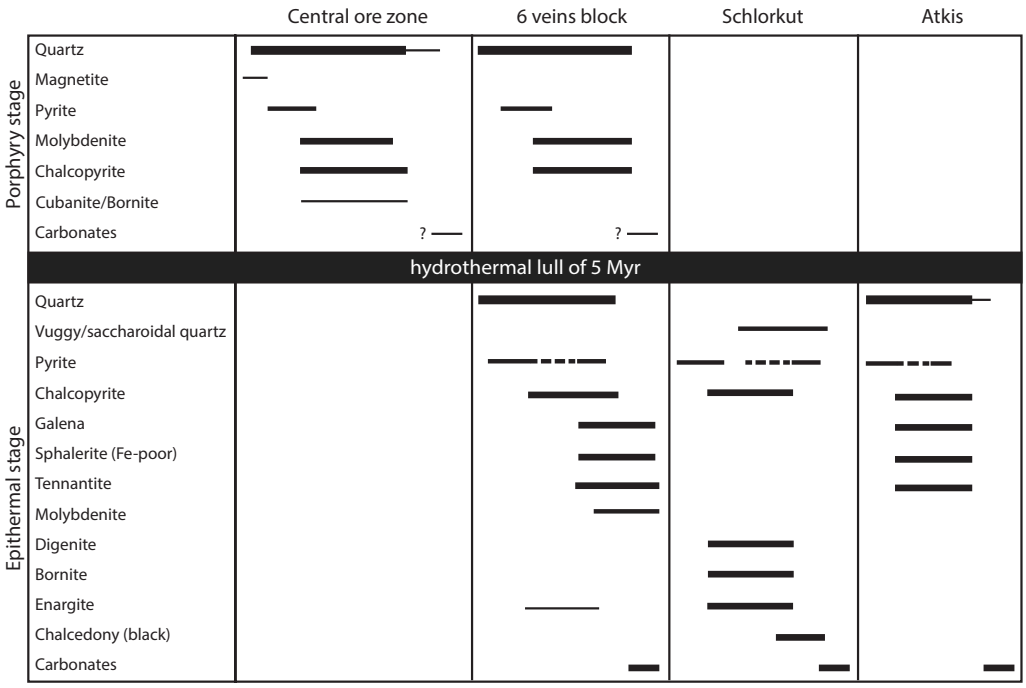

Figure 14: Mineral paragenetic sequence of the Kadjaran porphyry Cu-Mo system based on our new field observations and former ones reported by Karamyan (1978). The sequence is divided in two temporally distinct mineralizing events referred as the porphyry and epithermal stage. See text for discussion.

---

4. DISCUSSION

In the following, we aim at reviewing and comparing tectonic, magmatic and hydrothermal conditions for each magmatic series emplaced in the MOP in order to provide additional understanding regarding the combination of key factors leading to the formation of large porphyry Cu-Mo systems in collisional setting. For an extensive review of the regional geodynamic evolution linked to the incremental emplacement of the MOP and the petrogenesis of the MOP, the reader is referred to Moritz et al. (2016a,b) and Rezeau et al., (2016, 2017, in prep).

4.1 Regional geodynamic evolution and structural features in the Meghri-Ordubad pluton

The major Cenozoic orogenic event along the Lesser Caucasus corresponds to the closure of the Neotethyan ocean as a consequence of the NNE-oriented convergence of the Arabian and Eurasian plates and their subsequent collision (Fig. 15a). Most of recent studies advocate for an onset of collision during the Oligocene and/or early Miocene (e.g., Vincent et al., 2007; Allen and Armstrong, 2008; Ballato et al., 2011; Van Hunen and Allen, 2011; Mouthereau et al., 2012; Bertrand et al., 2014; Moritz et al., 2016a; Rezeau et al., 2017), whereas the Pliocene to Quaternary magmatism represents a transition to a pure post-collisional environment with widespread "OIB-like" volcanism (e.g., Kaislaniemi et al., 2014; Neill et al., 2015) and major exhumation correlated with a thin lithosphere below the Turkish-Iranian plateau at present day (e.g., Austermann and Iaffaldano, 2013; Robert et al., 2015). Paleotectonic reconstructions and the convergence rate of the Arabian plate toward the Eurasian plate highlight two main transitions, including (1) a moderate to highly compressional stress regime imposed to the overriding plate (SAB-Eurasia in Fig. 15a) from the Middle Eocene to Middle Oligocene, followed by (2) the initiation of extensional/transtensional stress regime during the late Oligocene and early Miocene (e.g., Bertrand et al., 2014). In addition, plate kinematics was reorganized during the Oligo-Miocene, due to the rotation of the converging Arabian plate from NE-SW to N-S (e.g., Avagyan et al., 2010). In the MOP, ore formation episodes (~44-40 Ma, 26-27 Ma and 22-20.5 Ma) occurred first in a compressional stress regime during the late Eocene, and at the transition to the extensional regime during the Late Oligocene - Early Miocene (Figs. 15a,b; Bertrand et al., 2014; Rezeau et al., 2017). The latter generally represents a favorable tectonic setting for facilitating the transfer of magma to the upper crust (Glazner et al., 1992; Tosdal and Richards, 2001; Campbell et al., 2014).

ⓐ Regional geodynamic evolution

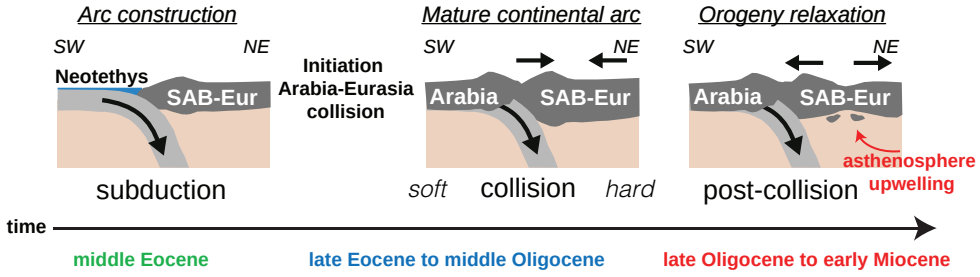

ⓑ Magmatic-hydrothermal temporal relationships in the MOP

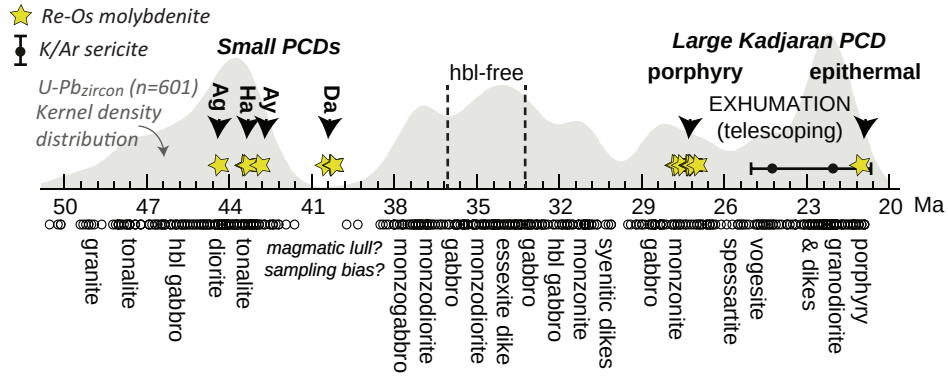

ⓒ Whole-rock geochemistry evolution in the MOP

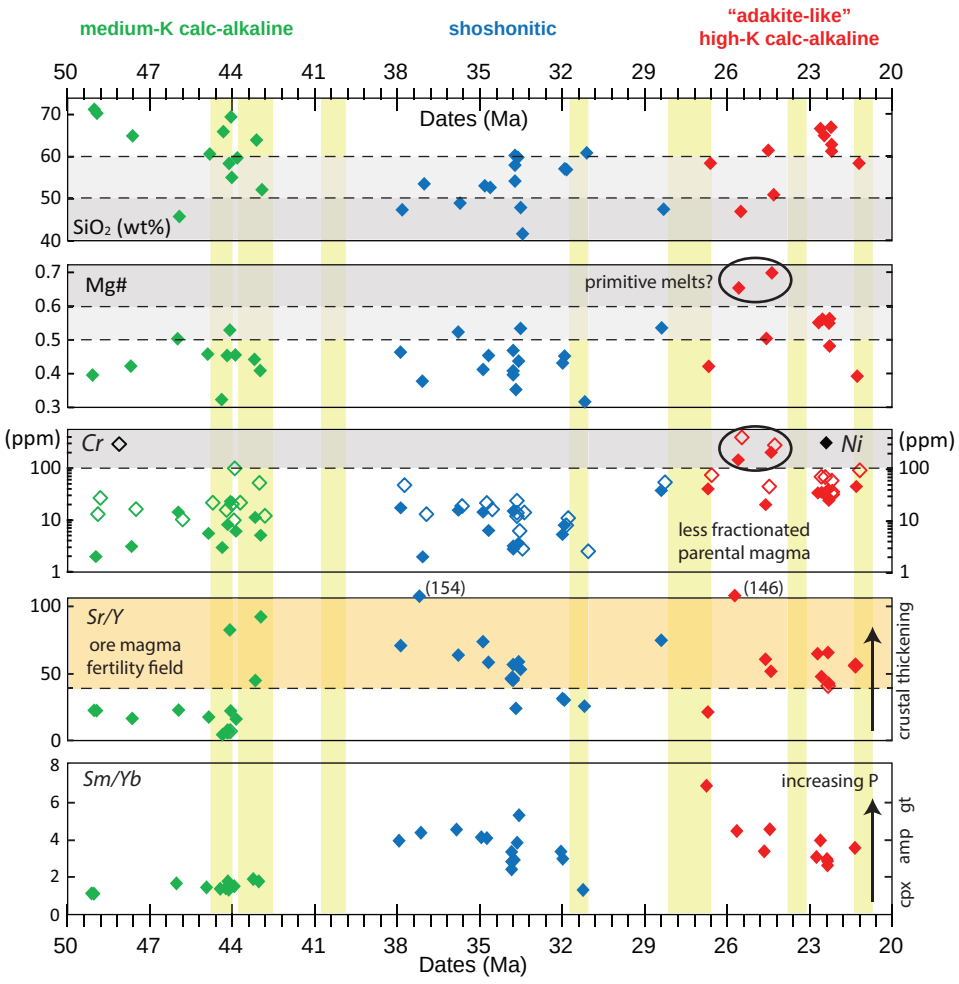

Figure 15: Summary of (a) regional geodynamic evolution, (b) temporal magmatic-hydrothermal relationships and (c) whole-rock geochemistry evolution over 30 m.y. showing the evolution of SiO_2, Mg#, Ni, Cr, Sr/Y and Sm/Yb. Kernel density curve in (b) after Vermeesch (2012). In (c), yellow bars represent ore-forming events and "ore magma fertility field" is after Loucks (2014) and Chiaradia & Caricchi (2017). Abbreviations: amp amphibole, cpx clinopyroxene, gt garnet. See text for discussion.

At the MOP scale, the normal, strike-slip Tashtun fault and the recognition of the Meghri-Tey graben support extensional to transtensional tectonics in the MOP during the Late Oligocene - Early Miocene (Tayan, 1998; Hovakimyan & Tayan, 2008; Hovakimyan et al., 2016). This is also inferred from the Cenozoic exhumation of the Zangezur block described by Tayan et al. (1976) and correlated by the Late Oligocene porphyry-style mineralization overprint by early Miocene epithermal mineralization within ~5-6 m.y. in the world-class Kadjaran porphyry Cu-Mo deposit (Fig. 8; Rezeau et al., 2016), which is widely reported worldwide and generally attributed to an episode of exhumation (e.g., Sillitoe, 2010) and further discussed below.

Based on apparent surface exposure in the MOP (Fig. 2), middle Eocene rocks outcrop over a large area compared to younger intrusions, which are restricted in space for a given time (Fig. 2; Rezeau et al., 2016). It has been argued that focusing of magma emplacement in the upper crust is a key controlling factor to focus, transfer and accumulate "ore ingredients" (H_2O, S, Cl, metals) in the upper crust to ultimately form large deposits (Burnham, 1979; Tosdal & Richards, 2001; Richards, 2003; Candela & Piccoli, 2005; Cooke et al., 2005; Sillitoe, 2010; Richards, 2013; Wilkinson, 2013). This could be an additional feature to explain the dispersed distribution of many small tonnage PCDs formed during the middle Eocene, contrasting with the occurrence of the unique and major Oligo-Miocene Kadjaran PCD. For a detailed discussion about the structural evolution of the MOP and the implications for PCDs, the reader is referred to Hovakimyan et al. (2016).

4.2 Magmatic-hydrothermal cycles in the Meghri-Ordubad pluton

4.2.1 Temporal evolution and magmatic processes operating in the MOP

Three long-lived magmatic series of variable compositions can be recognized in the MOP with respective durations of 5.8 ± 0.8 m.y., 9.7 ± 0.9 m.y., and 5.4 ± 0.4 m.y. (Rezeau et al., 2016). Isotopic signatures and trace element geochemical modeling indicate crustal processes dominated by fractional crystallization of mantle-derived hydrous magmas (Fig. 15c; Rezeau et al., 2017, Chapter 3). Crustal assimilation is difficult to quantify in the MOP because mantle-dominated isotopic signatures either result from limited crustal contamination of radiogenic felsic crust or from cannibalization of previously emplaced young and juvenile magmas having limited isotopic contrast (Rezeau et al., 2016). The latter may be supported by

evidence for crystal mush recycling during the long-lived emplacement of the series 2 and host-rock assimilation by lamprophyres (Chapter 3). In addition, each magmatic series evolved as an open-magmatic system characterized by episodes of mafic magma resplenishment in a shallower felsic reservoir, as illustrated by magma mingling textures, sieved calcic cores and Ca-rich zoning in plagioclase and reverse zoning textures in clinopyroxene and amphibole (Chapter 3). Such mechanism represents a critical step to explain the transfer of "ore ingredients" stored at mid- to lower crustal levels and their subsequent ascent to the upper crust, implying that a reservoir at depth acts as metal, sulfur and volatile supplier and thermal engine through pulsed mafic recharge (Hattori et al. 1993; Hattori & Keith, 2001; Core et al., 2006; Scaillet, 2010; Wilkinson, 2013; Tapster et al., 2016; Buret et al., 2016, 2017).

Recent numerical Monte Carlo simulations indicate that an efficient magma transfer and accumulation needs time (~2-3 Ma) and highly depends on the ability to sustain thermal conditions suitable to form and accumulate hybrid fertile melts in the mid- to lower crust (e.g., Chiaradia & Caricchi, 2017). Complementary numerical modelling sheds light on the mutual and positive correlation among duration of magmatism, magmatic flux and formation of large PCDs (Caricchi et al., 2014; Chelle-Michou et al., 2017). The modelling shows that for a similar magma flux, the duration of magmatism is the first-order controlling factor on the fertility of a magmatic system showing that large PCDs are associated with long-lived magmatic systems of >1-2 m.y.. In the MOP, each differentiation series represent incremental emplacement of short-lived upper crustal magma reservoirs forming a succession of long-lived magmatic series lasting between 5 to 10 m.y. (Figs. 15b,c; Rezeau et al., 2016, Chapter 3). Based on the apparent surface outcrop of the respective magmatic series, apparent average magma fluxes for each magmatic series range from 8.10^{-4} to 2.10^{-3} km^3/yr for the series 1, and from 2.10^{-4} to 5.10^{-4} km^3/yr for series 2 and 3. This was computed using a minimum and a maximum thickness estimate of stacked sill-shaped intrusions varying between 5 and 10 km, assuming that they were emplaced over several million years (e.g., Annen, 2011). Such magma flux approximations illustrate a decrease over time, but remain in agreement with the average magma fluxes calculated for long-lived composite plutons and batholiths worlwide ranging from 1.10^{-4} to 1.10^{-2} km^3/yr (e.g., Menand et al., 2015). This certainly indicates that long-lived magmatism results in favourable thermal conditions to sustain the production of hybridized melts in the mid- to lower crust and increases its ability to feed upper crustal magma reservoirs over several million years. Although it represents a pre-requisite to form PCDs (Richards, 2003; Rohrlack and Loucks, 2005; Caricchi et al. 2014; Rezeau et al. 2016; Chelles-Michou et al., 2017; Chiaradia & Caricchi, 2017), this does not seem to be the ultimate controlling factor to generate large PCDs since barren composite pluton incrementally emplaced over several millions years are also documented (e.g., Coleman et al., 2004). Important to note that barren

pluton at the level of exposure may have experienced surface erosion leading to the removal of ore deposits formed at shallower levels.

4.2.2 Major PCDs and high Sr/Y "adakite-like" magmas systematics

The development of high Sr/Y signature is generally interpreted as indicative for fertile magmatic provinces due to their spatial and temporal association with economic PCDs worldwide (Richards & Kerrich, 2007; Chiaradia et al., 2012; Chiaradia, 2014, 2015; Loucks, 2014; Lu et al., 2015; Chiaradia & Caricchi, 2017). Recent stochastic numerical modelling using Monte Carlo simulations demonstrated that large PCDs are preferentially associated with high Sr/Y (50-150) magmas stored in the mid- to lower crust for a minimum of ~2-3 m.y., whereas low Sr/Y melts are rather restricted to magmas that have experienced short-lived upper crustal processes and generally associated with small PCDs (Chiaradia and Caricchi, 2017). High Sr/Y ratios reflect early amphibole (± garnet) crystallization in the mid- to lower crust and delayed plagioclase fractionation promoting the formation of a residual melt depleted in Y and enriched in Sr. This is explained by the contrasting high partition coefficient of Y and Sr with respect to amphibole and plagioclase, respectively ($\mathbf{Kd_Y^{amph/melt}}$ = 1.2-9, Nandedkar et al., 2016; $\mathbf{Kd_{Sr}^{plg/melt}}$ = 1.5-1.7, Aignertorres et al., 2007). In arc magmas, early amphibole fractionation and delayed plagioclase crystallization is promoted by higher pressure of crystallization (>200-350 MPa) and melt water content (>4-6 wt% H_2O) (Moore and Carmichael, 1998; Chiaradia et al., 2012; Krawczinsky et al., 2012; Louck, 2014; Lu et al., 2016).

In the MOP, Middle Eocene medium- to high-K calc-alkaline intrusions display on average low Sr/Y ratios and host low tonnage PCDs of similar ages (Figs. 15b,c). Intrusions emplaced in the southern part are characterized by REE pattern with Eu negative anomalies indicative of fractional crystallization dominated by plagioclase fractionation (Sr/Y <35), whereas those emplaced in the north display a concave-up "spoon"-shaped REE pattern typical for amphibole and/or clinopyroxene fractionation (Sr/Y >35) (Fig. 4; Rezeau et al., 2017). By contrast, younger shoshonitic to high-K magmatic series 2 and 3 display on average higher Sr/Y ratios (25-150), and are both characterized by concave-up "spoon"-shaped REE patterns (Fig. 4). Each series culminates in ore-forming pulses at 26-27 Ma and 22-20 Ma, which are recognized in the large Kadjaran porphyry-epithermal system further discussed below (Figs. 15b,c). The progressive construction of high Sr/Y "adakite-like" magmatism genetically linked to a large PCD in the MOP is very similar to the evolution of the mineralized Tampakan district in the Phillipines (Papua-New Guinea), where a multi-stage magmatism is reported and the large PCD system is associated with high Sr/Y "adakite-like" magmatism in a thickened crust.

Complementary studies document a positive correlation between high Sr/Y and crustal thickness in the North American Cordillera (Chapman et al., 2015), the Central Andes (e.g., Mamani et al., 2010), and by the extensive whole-rock geochemical data compilation of Pliocene-Quaternary arc magmas (Chiaradia, 2015). By analogy, if we consider the regional Arabia-Eurasia collisional context during the incremental emplacement of the MOP, we suggest a progressive thickening of the crust from an early juvenile arc construction in the Middle Eocene to a mature thickened continental arc in the Late Oligocene - Early Miocene.

Although magmatic series 2 and 3 display high Sr/Y and Sm/Yb ratios, it is important to note that the magmatic series 2 is characterized by variable whole-rock Y and Yb contents similar to the magmatic series 1, whereas the magmatic series 3 is more depleted in Y and HREE (Figs. 3c,d). This indicates contrasting magma petrogenesis such as magmatic series 2 is dominated by clinopyroxene-dominated (± amphibole) fractionation of a LILE- and LREE-rich parental melts ($\mathbf{Kd_Y^{cpx/melt}}$ = 0.6-2.5, Vannucci et al., 1998), and magmatic series 3 reflects amphibole-dominated fractionation of a primitive parental magma (high Mg#, high Cr and Ni content) (Rezeau et al., 2017, Chapter 3). Both processes result in the generation of melt displaying high Sr/Y, La/Yb, and Sm/Yb ratios. Increase of LREE/HREE and MREE/HREE ratios is also considered as the consequence of crystallization of high pressure minerals in a thickened continental crust (Fig. 15c; Kay and Mpodozis, 2001; Mamani et al., 2010), and generally proposed as favourable conditions to generate large PCDs (Kay & Mpodozis, 2001; Richards & Kerrich, 2007; Chiaradia et al, 2012; Loucks, 2014; Lu et al., 2016; Chiaradia & Caricchi, 2017). Conclusively, there is a positive correlation between the size of PCDs and magma fertility in the MOP (Fig. 15b,c), which is in perfect agreement with model predictions (e.g., Loucks, 2014; Chiaradia & Caricchi, 2017).

4.2.3 Temporal and spatial evolution of the major Kadjaran Cu-Mo deposit

The large Kadjaran Cu-Mo porphyry-epithermal system is characterized by temporally distincts styles of mineralization, including (1) Cu-Mo stockwork veinlets and subvertical Cu-Mo veins dated at 26-27 Ma, and (2) epithermal-like subvertical mineralized veins composed of Cu-rich and Cu-Mo-base-metals bracketed between 22.2 Ma and 20.5 Ma (Figs. 8 and 14). In the 6VB, field observations reveal reopening of Cu-Mo subvertical veins by Cu-Mo-base metals veins. Molybdenite Re-Os dating reveals two distinct mineralizing events (26.65 ± 0.14 Ma and 20.48 ± 0.1 Ma) along the same structure, which is supported by the chemical evolution of the associated hydrothermal quartz showing a porphyry-type core and epithermal-like overgrowths, including Q2 associated with chalcopyrite-enargite-barite-anhydrite and Q3 associated with molybdenite dated at 20.5 Ma (Fig. 12a). Trace element composition of hydrothermal quartz

from epithermal environments generally display significant enrichment in Al (>1000 ppm) and low Ti content (<10 ppm) compared to porphyry-related quartz precipitated by high temperature fluids, characterized by low to moderate Al and very low to detectable Ti concentrations (Fig. 16; Rusk et al., 2008; Tanner et al., 2013; Maydagan et al., 2015). However, low to moderate Al and very low to detectable Ti contents in hydrothermal quartz are also consistent with deposition under epithermal conditions as shown by Figure 16 and demonstrated at Kadjaran by chalcopyrite and enargite associated with Q2 (Fig. 12c). TitaniQ geothermometry (Wark and Watson, 2006; Huang and AudŽtat, 2012) indicates deposition of the epithermal-related Ti-poor quartz (<10 ppm) at temperatures <450¡C (Rusk et al., 2008), whereas Ti-rich quartz (>20 to 100s of ppm) from the porphyry environment is consistent with a higher temperature range of ~500-600¡C (Supplementary Table A.1, e.g., Wark and Watson, 2006; Rusk et al., 2008; Huang and AudŽtat, 2012). This is in broad agreement with preliminary fluid inclusion results yielding minimum homogenization temperatures of 250-300¡C from quartz-molybdenite-base metals veins emplaced in 6VB and higher temperatures for stockwork-like Cu-Mo veinlets (Hovakimyan et al., 2015). Chemical features identified in hydrothermal quartz in Kadjaran are representative of porphyry-related quartz Q1 (high Ti) precipitated by high temperature fluids, and two episodes of epitermal quartz overgrowth precipitated by low temperature fluids, including Q2 associated with chalcopyrite-enargite and Q3 (high Al) associated with molybdenite (Figs. 12 and 16).

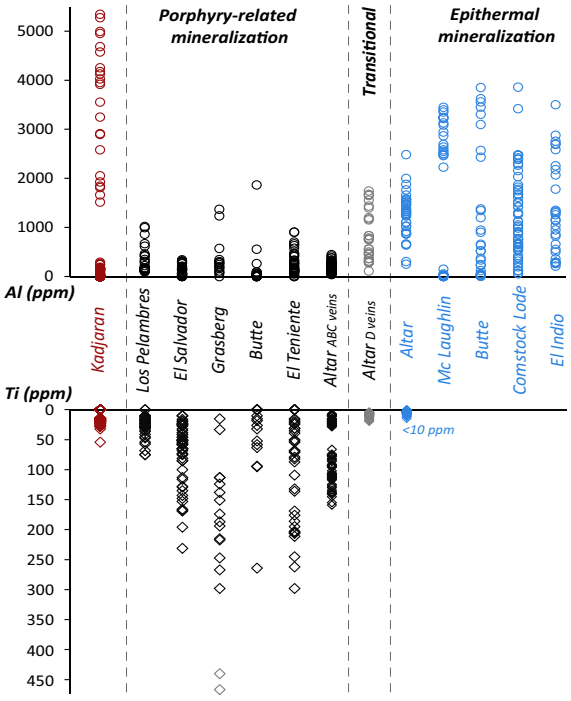

Figure 16: Compilation of Al and Ti concentration (ppm) in porphyry-related and epithermal hydrothermal quartz from different localities. Literature compilation data: Los Pelambres, El Salvador, Grasberg, Butte, El Teniente, McLaughlin and Comstock Lode (Rusk et al., 2008), El Abra (Maydagan et al., 2015), and El Indio (Tanner et al., 2013).

It is important to consider the closure temperature of molybdenite ranging between ~500-600¡C (McInnes et al., 2005) together with Re-Os systematics of molybdenite, which precludes the incorporation of common Os in the isotopic systems (Selby & Creaser, 2001). These two characteristics rule out the possibility of molybdenite remobilization from stockwork mineralization by low-temperature epithermal fluids ranging from 350¡C to 200¡C and emphasize an epithermal-related molybdenite mineralization. Furthermore, the occurrence of quartz - chalcopyrite - enargite pre-dating the second generation of molybdenite (Fig. 12) strongly favors a spatial link to Cu-rich enargite-bearing epithermal veins described in Schlorkut that post-date porphyritic granodioritic dikes dated at 22.2 Ma (Figs. 7, 8, 10d-f). This allows us to bracket the age of the intermediate to high sulfidation Cu-rich epithermal mineralization between 22.2 ± 0.3 Ma and 20.5 ± 0.1 Ma, which is in agreement with the hydrothermal sericite K-Ar cooling age of 22.2 ± 2 Ma reported from Cu-rich veins in Kadjaran (Fig. 8; Bagdasaryan et al., 1969).

Epithermal veins overprint the porphyry-related mineralization at least 4 m.y. later (Fig. 8; Rezeau et al., 2016), which represent a significant time gap difficult to reconcile with a single magmatic-hydrothermal event. According to the genetic model of porphyry systems proposed by Sillitoe (2010), stockwork-like mineralization is likely emplaced at 2 to 5 km depth, whereas epithermal veins are emplaced at shallower levels (<1 km). The juxtaposition of these two mineralization styles indicates telescoping/overprinting and requires a phase of exhumation in between (e.g., Sillitoe, 1994). In Kadjaran, we estimate an average low exhumation rate of 0.2-0.5 mm/yr, assuming a relative surface uplift of 1-2 km within 4 to 6 m.y. corresponding to the minimum and maximum temporal gap between porphyry-related and epithermal-related mineralization. Such low exhumation rate is likely linked to the progressive crustal thickening related to the Arabia-Eurasia collision rather than delamination promoting isostatic rebound and fast exhumation rates (England and Molnar, 1990; Platt and England, 1993).

To summarize, we propose the first temporal and spatial genetic model for the multi-stage formation of the large Kadjaran Cu-Mo porphyry-epithermal system in Figure 17. The early stockwork-like Cu-Mo veinlets and peripheral subvertical Cu-Mo veins are associated with a blind porphyry center at depth since the monzonite host-rock, dated at 28.1 ± 0.4 Ma, is too old to be genetically related to the stockwork mineralization (26.4-27.3 Ma) and calc-alkaline lamprophyre dike dated at 26.6 ± 0.6 Ma is coeval but crosscut mineralized stockwork-like veinlets. Potassic alteration is predominant. Following an exhumation phase at ~26-23 Ma, epithermal-related mineralization stages (22.2-20.5 Ma) overlap within error with porphyryitic granodioritic magmatism (22.6-21.2 Ma), which strongly suggest a link with a hidden porphyry center at depth. We also suspect potential additional resources corresponding to porphyry-related stockwork Cu-Mo mineralization at depth. The latter would be coeval to the large

Sungun PCD formed at ~21 Ma in northern Iran, 70 km southeast of the Kadjaran deposit (Aghazadeh et al., 2015; Richards & Sholeh, 2016).

In the 6VB, chalcopyrite-base metals-tennantite-molybdenite veins are comparable to typical intermediate to high sulfidation base-metal epithermal mineralization (e.g., Hedenquist et al., 2000; Simmons et al., 2005), but they could also correspond to distal veins of porphyry systems, such as transitional to D-veins with intermediate to high sulfidation state mineral assemblages (e.g., Seedorff et al., 2005; Sillitoe, 2010;). Subvertical Cu-rich veins reported in Schlorkut are more typical of high sulfidation veins centered above the porphyry stock (e.g., Sillitoe, 2010). The successive emplacement of early Cu-rich enargite-bearing to late chalcopyrite-tenantite-base metals-molybdenite mineralization tends to indicate a decrease of the sulfidation state of the hydrothermal fluid over time (e.g., Einaudi et al., 2003). This is illustrated by the SW to NE metal zoning observed at the deposit scale likely related to host-rock buffering and cooling by fluid percolation through pre-existing structures (e.g., Sillitoe, 2010; Kouzmanov & Pokrovski, 2012). Hydrothermal alteration associated with epithermal mineralization ranges from sericitic to argillic (Figs. 11). Finally, the set of parallel ore veins at 6VB and Schlorkut reveal the importance of the structural control on ore-forming fluid flow throughout the multiple magmatic-hydrothermal cycles at Kadjaran.

4.3 Source of Mo in porphyry Cu-Mo deposits

The increase of Mo concentrations during igneous crustal processes indicates a strong incompatibility of Mo with progressive fractional crystallization and once magmas reach water-saturation exsolution, Mo is preferentially partitioned into hydrothermal aqueous fluids to form economic PCDs (AudŽtat & Petkke, 2003; Mustard et al., 2006; AudŽtat, 2010; Lerchbaumer & AudŽtat, 2012; Li & AudŽtat, 2015). Economic Mo porphyry deposits are recognized to be genetically linked to rift-related intraplate bi-modal magmatism or subduction-related alkali-rich magmatism (e.g., Carten et al., 1993). However, the source of Mo is still controversial between crustal origin (e.g., Sinclair et al., 2007; Zhu et al., 2009) or derived from metasomatized mantle-derived mafic magmas (e.g., Carten et al., 1993; Pettke et al., 2010), although intraplate riflt-related setting and the recent report of Mo-rich mantle xenoliths (e.g., Song et al., 2016) advocate for mantle-derived origin. In the MOP, each magmatic series is characterized by mantle-derived mafic to felsic crustal fractionation trends and culminate in the formation of variable-sized porphyry Cu-Mo deposits (Moritz et al., 2016; Rezeau et al., 2016, 2017), which represents indirect evidence regarding the mantle-derived origin for molybdenum.

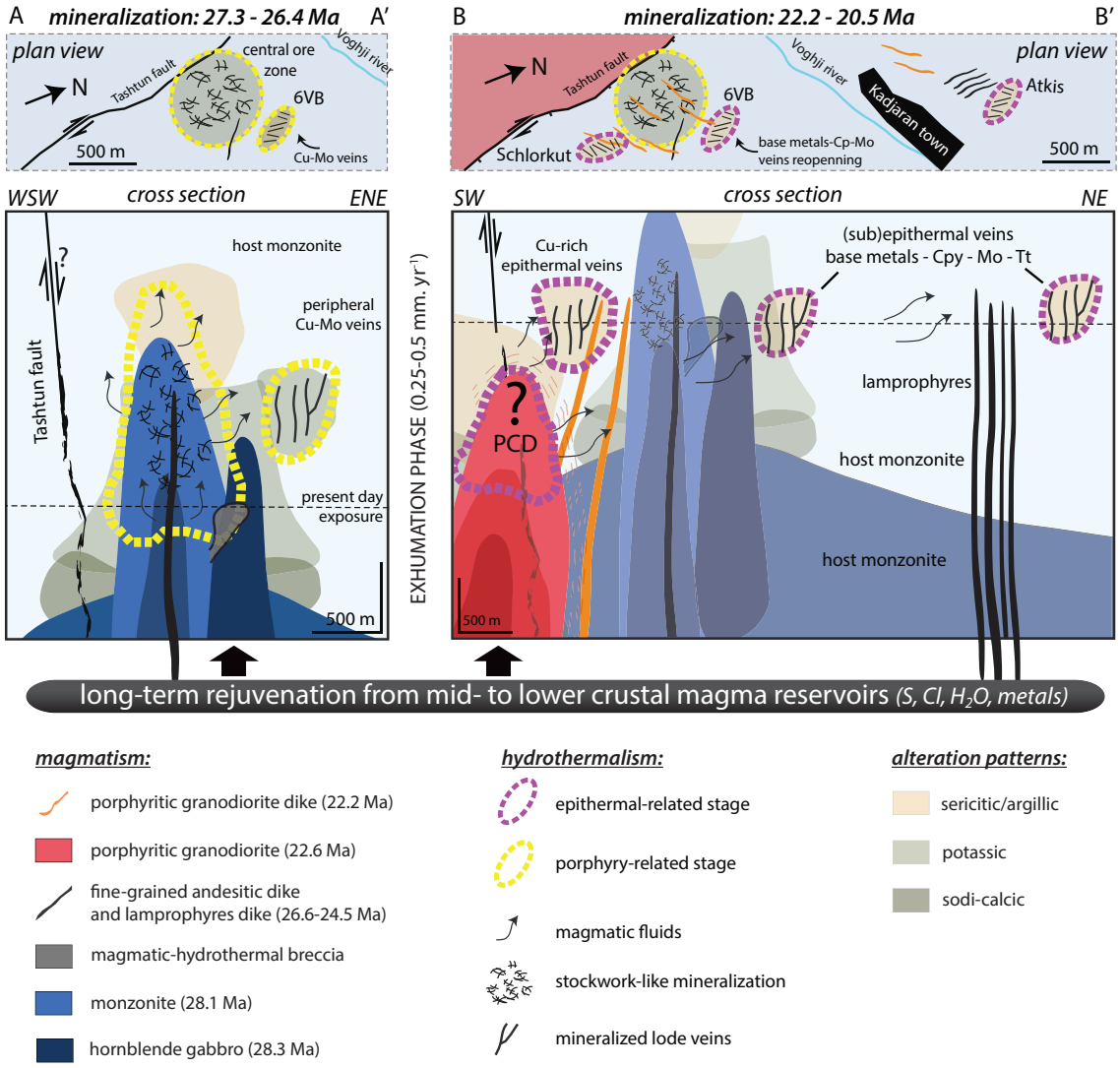

Figure 17: Schematic genetic model showing the spatial and temporal evolution of the large Kadjaran porphyry-epithermal system through two cross sections A-A' and B-B' in Figure 7a, which respectively illustrate the porphyry-related stage at 26-27 Ma followed by the emplacement of Cu-rich and base metals epithermal veins between 24 and 20 Ma. Adapted according to the genetic model of porphyry systems proposed by Sillitoe (2010). See text for discussion.

In-situ LA-ICP-MS analyses in biotite from representative intrusions of the MOP reveal exponential positive correlation between Mo and Nb (also with Ta, not shown) (Fig. 18; Supplementary Tables B.1 and B.2). Similar observations are reported from young Basin and Range subduction-related magmatism in the Western US (Fitton, 1995) and in xenoliths-hosted rutile (Zack et al., 2002). This reflects coupled substitution due to their similar ionic radius, i.e., 0.65 • for Mo^{4+} and 0.64 • for Nb^{5+} at magmatic conditions (e.g., Fitton, 1995). In the MOP, the highest average Mo content (1-4 ppm) corresponds to peritectic biotite crystallized in amphibole-free magmas in the shoshonitic series 2 (Chapter 3) and it represents unusually high Mo concentrations compared to other biotite from surrounding intrusions in the MOP (0.03-1

ppm; Fig. 18) and published values from Kos calc-alkaline volcanic rocks in the Aegean arc (e.g., Voegelin et al., 2014). We believe that such high Mo geochemical anomalies must be intrinsically related to the parental magma composition. In addition, high Mo and Nb contents in biotite are correlated with a significant increase of Nb content and suprachondritic Nb/Ta ratios (>20) in the respective whole-rock composition (Rezeau et al., 2017). Subchondritic Nb/Ta ratios (<17) in continental and mantle rocks are commonly referred to as the "missing Nb paradox" and suggest a complementary high Nb/Ta suprachondritic reservoir at depth, which could either correspond to amphibole- and phlogopite-bearing metasomatic veins formed in the subcontinental lithospheric mantle (e.g., Ionov & Hofman, 1995), to eclogites composed of high Nb/Ta rutile and generated by long-term metasomatism of the subcontinental lithospheric mantle (e.g., Aulbach et al., 2008), and to mid to lower crustal bearing granulites (e.g., Stepanov & Hermann, 2013). This indicates that mantle source processes play a crucial role in generating HFSE- and Mo-rich melts.

In the MOP, the generation of medium- to high-K calc-alkaline series 1 during the middle Eocene is promoted by fluid-fluxed melting in response to the dehydration of the subducted slab and characterized by whole-rock subchondritic Nb/Ta whole-rocks values and low Mo content in biotite. This illustrates crystallization from a HFSE- and Mo-poor parental melt emphasizing the preferential partioning of these elements in rutile rather than in the fluid phase upon slab dehydration (Brenan et al., 1994; Stolz et al., 1996). Alternatively, if we consider that the parental magma composition rather reflects further reequilibration in the subcontinental lithospheric mantle, the formation of rutile-bearing eclogite and/or Nb-Ta-rich metasomatic veins would also decrease Nb/Ta ratios and the Mo content of the generated partial melt. By contrast, the shoshonitic magmatic series 2 displays whole-rock composition characterized by high LILE, LREE and HFSE content and suprachondritic Nb/Ta signature, which is attributed to low degree of partial melting of a K-rich metasomatized subcontinental lithospheric mantle combined with a decrease of slab-related fluid at the expense of slab-related melt (Rezeau et al., 2017). This would be coherent with the partial melting of a Mo-rich suprachondritic reservoir either at the slab-mantle interface and/or in the metasomatized subcontinental lithospheric mantle. The series of shoshonitic intrusions is subdivided by an early amphibole-free barren intrusions composed of Mo-rich biotite (35.7-33.5 Ma), followed by amphibole-bearing intrusions composed of Mo-poor biotite (33.5-28.1 Ma) (Fig. 18). On one hand, we propose that the appearance of amphibole at the expense of biotite illustrates a progressive increase of the initial water content in the parental magma (e.g., Naney, 1983; Bucholz et al., 2014; Rezeau et al., in prep), and therefore emphasizes the critical role of early water saturation to preferentially partition Mo into the exsolved magmatic hydrothermal fluids promoting an efficient metal extraction from the melt. On the other hand, Mo-poor biotite may

simply reflect crystallization from syn-magmatic co-existing parental melt reservoirs of variable composition at depth, which have experienced contrasting source processes due to subcontinental lithospheric mantle heterogeneities. An alternative scenario arising from whole-rock radiogenic isotopes implies the potential contribution of an older HIMU-type mantle source at the transition between magmatic series 1 and 2 (Rezeau et al., 2017), and could correspond to a subcontinental lithospheric mantle metasomatized by subduction fluids during the closure of the northern branch of the Neotethys in Jurassic to Cretaceous times (e.g., Rolland et al., 2012; Mederer et al., 2013) and potentially anomalously enriched in Mo. Such scenario was proposed in the Western US to explain the large Mo anomalies in the underlying mantle (Pettke et al., 2010). The Òadakitic-likeÓ series 3 is characterized by a general decrease of LILE, HFSE, LREE and HREE related to an input of more juvenile magmas generated by higher degree of partial melting at greater depths in the presence of higher modal proportions of garnet (Rezeau et al., 2016; 2017). Intrusions display subchondritic Nb/Ta whole-rock values and low Mo content in biotite illustrating a significant change of mantle source conditions and processes between series 2 and 3.

To summarize, we propose that the early subduction-related magmatism represents an important pre-enrichment step for Mo and HFSE, and further remelting may result in remobilization and enrichment of Mo in residual melts as proposed for Cu (e.g., Richards, 2009; Lee et al., 2012; Chiaradia, 2014). This mechanism will certainly influence the quantity of Mo available in the system and consequently explain the formation of small Cu-Mo porphyry deposits (10-50 Mt @ 0.05% Mo) during the middle Eocene compared to the large Kadjaran porphyry Cu-Mo deposit (2200 Mt @ 0.05% Mo) associated with the shoshonitic series 2. Although we have reported molybdenite precipitation during the epithermal stage linked to the "adakite-like" series 3, it seems negligible compared to the porphyry-related stage. Although additional effort is required to validate this hypothesis, we believe that identifying igneous rocks having suprachondritic Nb/Ta ratios and high Mo concentrations in biotite may represent a good indicator for a metasomatized source enriched in Mo and it could be potentially used as a "Mo ore fertility" exploration vector for the mining industry.

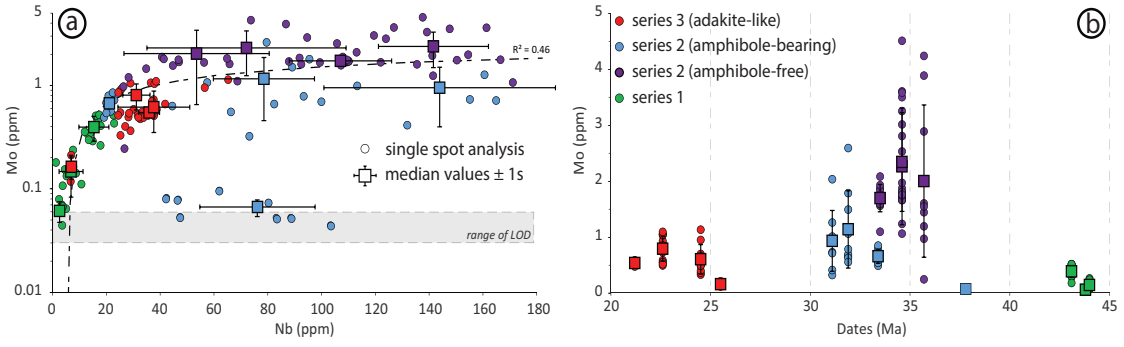

Figure 18: a) Mo vs. Nb content in biotite. b) Mo content vs. time. Full data set are detailed in Supplementary Tables B.1 and B.2, and LA-ICP-MS analytical conditions are presented in Chapter 3.

4.4 Post-subduction magmatism in the MOP: an evolution from barren to fertile magmatism

In the MOP, the magmatic series 2 displays an overall shoshonitic to high-K calc-alkaline trend (Fig. 3), including early hornblende-free barren intrusions and an alkaline nepheline-bearing monzogabbro dike (essexite) extremely enriched in primary Fe-Ti-oxides and Cu-Fe-sulfides, followed by the emplacement of amphibole-bearing intrusions culminating in the formation of the large Kadjaran Cu-Mo porphyry-epithermal system (Figs. 15B,C and 19; Rezeau et al., 2016). The P-T mineral stability field and the sequence of mineral crystallization during crustal fractionation highly depend on the primitive arc magma chemistry and water content (Moore & Carmichael, 1998; Righter & Carmichael, 1996; Sisson et al., 2005; Tatsumi et al., 2008; Krawczynski et al., 2012). Hornblende-free barren shoshonitic intrusions are characterized by clinopyroxene- and phlogopite-dominated fractional crystallization and subsidiary occurrence of nepheline indicative of crystallization from a water-undersaturated (2-4 wt% H_2O) alkaline parental magma (Naney, 1983; Bucholz et al., 2014; Chapter 3). The late Eocene essexite (or nepheline monzogabbro) dike of the MOP magmatic series 2 is of particular interest since it contains abundant primary magmatic Cu-Fe sulfides inclusions (>1 vol.%; Fig. 19) in clinopyroxene. The absence of any Eu negative anomaly revealed by both whole-rock and clinopyroxene gecohemistry constrains early magmatic sulfide saturation at a pressure of > 250-350 MPa (Chapter 3). Magmatic sulfides are the main repositories of chalcophile metals in silicate melts and the timing of magmatic sulfide saturation with respect to an aqueous fluid is of great importance for metal transfer to upper crustal magmatic-hydrothermal systems (Richards, 2009, 2015b, 2016; Lee et al., 2012; Chiaradia, 2014; FontbotŽ et al., 2017). If sulfide saturation predates water saturation, chalcophile metals will be sequestered in Ò*metal-rich*Ócrustal cumulates in the mid- to lower crust. By contrast, during an early fluid saturation, chalcophile metals and volatiles will be efficiently partitioned into the magmatic hydrothermal fluid, and can ultimately lead to the formation of economic PCDs. Coeval abundant crystallization of magnetite recognized in the essexite (nepheline monzogabbro) dike of the MOP maybe evidence of the so-called "magnetite crisis" described by Jenner et al. (2010), which generally triggers magmatic sulfide saturation and precipitation. There is an ongoing debate whether early sulfide saturation in mid- to lower arc crust cumulates will inhibit magma fertility or represents a potential metal reservoir during subsequent remelting (see discussion in Richards, 2015b, p.35-36). We believe that they are complementary steps over the lifetime of arc construction in both oceanic and continental settings, since incremental assembly of mid- to upper crustal batholith is the consequence of several m.y.-long pulsed magmatism, independent

of the geodynamic setting, whether subduction or collision-related magmatism (Coleman et al., 2004; Annen et al., 2015; Menand et al., 2015; Rezeau et al., 2016).

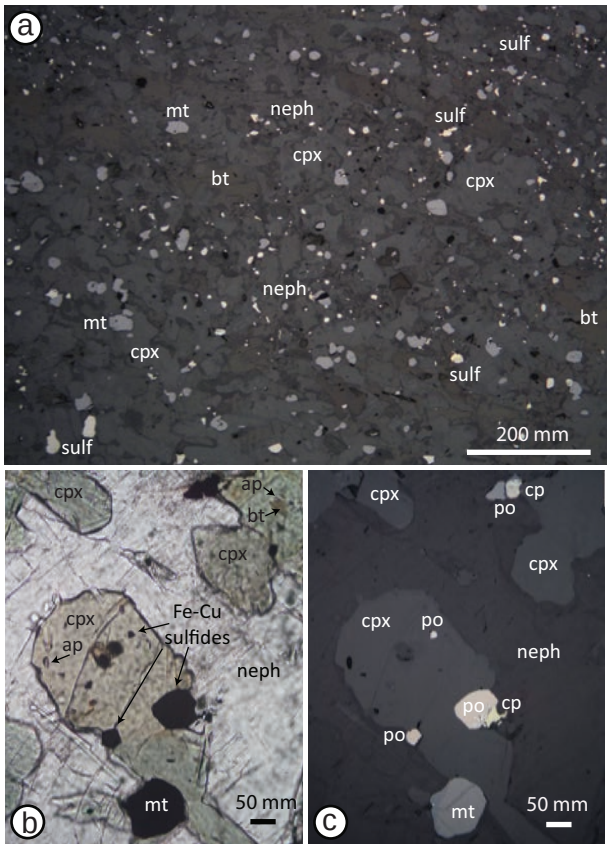

Figure 19: (a) Reflected light microscope photography showing abundant Cu-Fe sulfides (>1 vol.%) in a nepheline-bearing monzogabbro dike, (b) Transmitted (Nichols //) and (c) reflected light photography showing primary Fe-Cu sulfide inclusions in clinopyroxene and associated magnetite. Abbreviations: bt biotite, cp chalcopyrite, cpx clinopyroxene, mt magnetite, neph nepheline, po pyrrhotite, sulf sulfides.

In the MOP, the high abundance of primary Cu-Fe magmatic sulfides (>1 vol.%, Fig. 19) observed in the essexite (nepheline monzogabbro) dike is interpreted as an evidence for abundant accumulation of Cu-Fe magmatic sulfides stored in the mid- to lower crust. Such a high abundance certainly plays a crucial role regarding the economic potential of the complementary fractionated ascending melt in magmatic arcs (e.g., Richards, 2009), which is well correlated with the lack of any reported economic deposits during the late Eocene in the MOP at ca. 38-34 Ma (Fig. 15B). This sheds light on favorable magmatic conditions leading to a very effective sequestration of Cu-Fe magmatic sulfides, and emphasizes the crucial role of water-saturated parental magmas in the transport of "ore ingredients" to upper crustal levels generation of PCDs (e.g., Wilkinson, 2013; Loucks, 2014; Richards, 2016; Chiaradia & Caricchi, 2017). Subsequent water-saturated magmatism channeled by the same crustal structures is a major process to remobilize these sources of metals by oxidation of Cu-Fe magmatic sulfides (Larocque et al., 2000; Nadeau et al., 2010; Scaillet, 2010; Simon & AudŽtat, 2012) and consequently enhance magma ore fertility. In this case, the early magmatic sulfide sequestration step may represent an additional source of metals complementary to the initial

mantle-derived metals and volatiles. This specific sequence of events may represent an important process for the formation of large PCDs in the upper crust and may elegantly explain the temporal association of the large Kadjaran Cu-Mo deposits with amphibole-bearing magmas at the end of the long-lived (10 m.y.) shoshonitic series 2 during the collisional event (Fig. 15B, Rezeau et al., 2016).

5. CONCLUSIONS AND PERSPECTIVES

The study of the mineralized composite MOP illustrates that long-lived mantle-derived magmatism is a prerequisite for the formation of economic PCDs, independently of the geodynamic setting. However, petrological processes together with local tectonics and stress regime seem to play a major role in modulating the size of PCDs. Differentiation series dominated by mid- to lower crustal fractionation of amphibole appear to be favorable for the accumulation of "ore ingredients" and subsequent formation of large deposit, whereas those dominated by shallow crustal processes indicate lower ore potential. Water-rich magmas (i.e. amphibole-bearing) are also crucial to exsolve magmatic fluids early in the fractionation series and consequently to partition chalcophile elements compared to "dryer" (i.e. amphibole-free) magmas promoting early magmatic sulfide saturation responsible for the depletion of differentiated melts emplaced in the upper crust. In addition, local structures and tectonic stress regime certainly play an important role regarding the magma and fluid focusing in the MOP. Although strike-slip faults are reactivated over time, the Middle Eocene magmatic series 1 is emplaced over a large area during a short period of time (1-2 m.y.) compared to Late Eocene to Early Miocene characterized by the successive emplacement of small short-lived magma batches over a long period of time in the same area. This allows to sustain a relatively high thermal regime in the crust promoting cycles of mafic magma transfer from the lower crust and a large accumulation of "ore ingredients" culminating in the formation of a major PCD, where the immediate precursor magmatism is highly focused over a restricted area, i.e., around Kadjaran. It is important to note that the recognition of overlapping mineralizing stages in the large Kadjaran deposit may also contribute to the large tonnage. To summarize, a careful review of the tectono-magmatic evolution over 30 m.y. (Table 1) revealed that the large Kadjaran porphyry-epithermal system illustrates very well the concept of a "special combination of regional to local scale conditions allow[ing] the successful transfer of deep Cu accumulations to shallower levels and the formation of large porphyry copper systems" (Chiaradia, 2014) and the "optimum coincidence of common geological processes to build unusually large accumulations of metal" (Richards, 2013).

From a mineral exploration point of view, the recognition of similar sequences of magmatism within fairly limited areas must be very promising for new discoveries along the

Turkish-Iranian plateau and most likely elsewhere. Shoshonitic to high-K calc-alkaline magmatism in collisional to post-collisional geodynamic setting is relatively common and the distinction between amphibole-free and amphibole-bearing intrusions seems to be crucial since the former may sequester magmatic sulfides, whereas the latter allows partitioning into magmatic fluids. However, the succession of both may represent the perfect combination for an early crustal metal enrichment and a subsequent remobilization of metals to form large resources for both Cu and Mo. The Mo endowment and the lack of Au at the belt scale likely represent their respective initial enrichment in the mantle source and not necessarily indicate specific crustal processes, although (re)melting of a metasomatized mantle source together with sulfide-bearing lower cumulates certainly represent a significant additional source of metals to the initial mantle-derived metal budget. Conclusively, collisional- to post-collisional PCDs represent important resources for our societies and future joint effort for a better understanding regarding their genesis along the Tethyan metallogenic belt will undoubtely offer new perspectives for mineral exploration.

REFERENCES

Agard, P., Omrani, J., Jolivet, L., Whitechurch, H., Vrielynck, B., Spakman, W., MoniŽ, P., Meyer, B., and Wortel, R., 2011, Zagros orogeny: a subduction-dominated process. Geological Magazine, v. 148, p. 692ÐD725.

Aghazadeh, M., Hou, Z., Badrzadeh, Z., and Zhou, L., 2015, TemporalÐspatial distribution and tectonic setting of porphyry copper deposits in Iran: constraints from zircon UÐPb and molybdenite ReÐOs geochronology: Ore Geology Reviews, v. 70, p. 385-406.

Aghazadeh, M., Castro, A., Badrzadeh, Z., and Vogt, K., 2011, Post-collisional polycyclic plutonism from the Zagros hinterland: the Shaivar Dagh plutonic complex, Alborz belt, Iran: Geological Magazine, v. 148, p. 980-1008.

Aignertorres, M., Blundy, J., Ulmer, P., and Pettke, T., 2007. Laser Ablation ICPMS study of trace element partitioning between plagioclase and basaltic melts: an experimental approach: Contributions to Mineralogy and Petrology, v. 153, p. 647-667.

Allen, M.B., and Armstrong, H.A., 2008, ArabiaÐEurasia collision and the forcing of mid-Cenozoic global cooling: Palaeogeography, Palaeoclimatology, Palaeoecology, v. 265, p. 52ÐD58.

Annen, C., 2011, Implications of incremental emplacement of magma bodies for magma differentiation, thermal aureole dimensions and plutonismÐvolcanism relationships: Tectonophysics, v. 500, p. 3-10.

Annen, C., Blundy, J. D., and Sparks, R. S. J., 2006, The genesis of intermediate and silicic magmas in deep crustal hot zones : Journal of Petrology, v. 47, p. 505-539.

Annen, C., Blundy, J. D., Leuthold, J., and Sparks, R. S. J., 2015, Construction and evolution of igneous bodies: Towards an integrated perspective of crustal magmatism: Lithos, v. 230, p. 206-221.

Arndt, N. T., FontbotŽ, L., Hedenquist, J. W., Kesler, S. E., Thompson, J. F., & Wood, D. G., 2017, Metals and Minerals, Now and in The Future. Geochemical Perspectives, 6(1), pp. 171.

Arribas Jr, A., 1995, Characteristics of high-sulfidation epithermal deposits, and their relation to magmatic fluid: Mineralogical Association of Canada Short Course, v. 23, p. 419-454.

AudŽtat, A., 2010, Source and evolution of molybdenum in the porphyry Mo (ÐNb) deposit at Cave Peak, Texas. Journal of Petrology, v. 51(8), p. 1739-1760.

AudŽtat, A., and Pettke, T., 2003, The magmatic-hydrothermal evolution of two barren granites: a melt and fluid inclusion study of the Rito del Medio and Canada Pinabete plutons in northern New Mexico (USA). Geochimica et Cosmochimica Acta, v. 67(1), p. 97-121.

AudŽtat, A., and Simon, A. C., 2012, Magmatic controls on porphyry copper genesis. In: Hedenquist JW, Harris M, Camus F (eds) Geology and Genesis of Major Copper Deposits and Districts of the World: A Tribute to Richard H. Sillitoe. Society of Economic Geologists Special Publication, v. 16, p. 553-572.

Aulbach, S., O'reilly, S. Y., Griffin, W. L., and Pearson, N. J., 2008, Subcontinental lithospheric mantle origin of high niobium/tantalum ratios in eclogites. Nature Geoscience, v. 1(7), p. 468.

Austermann, J., Iaffaldano, G., 2013. The role of the Zagros orogeny in slowing down Arabia-Eurasia convergence since ~5 Ma, Tectonics 32, 351Ð363.

Avagyan, A., Sosson, M., Karakhanian, A., Philip, H., Rebai, S., Rolland, Y., Melkonyan, R., and Davtyan, V., 2010, Recent tectonic stress evolution in the Lesser Caucasus and adjacent regions: Geological Society London Special Publications, v. 340, p. 393-408.

Bagdasaryan, G.P., Gukasyan, R.Kh., and Karamyan, K.A., 1969, Absolute dating of Armenian ore formations: International Geology Review, v. 11, p. 1166Ð1172.

Ballato, P., Uba, C.E., Landgraf, A., Strecker, M.R., Sudo, M., Stockli, D.F., Friedrich, A., and Tabatabaei, S.H., 2011, ArabiaÐEurasia continental collision: insights from late Tertiary foreland-basin evolution in the Alborz Mountains, northern Iran: Geological Society of America Bulletin, v. 123, p. 106Ð131.

Barrier, E., Vrielynck, B. (Eds.), 2008, Palaeotectonic Maps of the Middle East. CGMW.

Bertrand, G., Guillou-Frottier, L., and Loiselet, C., 2014, Distribution of porphyry copper deposits along the western Tethyan and Andean subduction zones: Insights from a paleotectonic approach: Ore Geology Reviews, v. 60, p. 174-190.

Bissig, T., and Cooke, D. R., 2014, Introduction to the special issue devoted to alkalic porphyry Cu-Au and epithermal Au deposits: Economic Geology, v. 109, p. 819-825.

Brenan, J. M., Shaw, H. F., Phinney, D. L., and Ryerson, F. J., 1994, Rutile-aqueous fluid partitioning of Nb, Ta, Hf, Zr, U and Th: implications for high field strength element depletions in island-arc basalts. Earth and Planetary Science Letters, v. 128(3-4), p. 327-339.

Bucholz, C. E., Jagoutz, O., Schmidt, M. W., and Sambuu, O., 2014, Fractional crystallization of high-K arc magmas: biotite- versus amphibole-dominated fractionation series in the Dariv Igneous complex, Western Mongolia: Contributions to Mineralogy and Petrology, v. 168, p. 1-28.

Buret, Y., von Quadt, A., Heinrich, C., Selby, D., WŠlle, M., and Peytcheva, I., 2016, From a long-lived upper-crustal magma chamber to rapid porphyry copper emplacement: Reading the geochemistry of zircon crystals at Bajo de la Alumbrera (NW Argentina). Earth and Planetary Science Letters, v. 450, p. 120-131.

Buret, Y., Wotzlaw, J. F., Roozen, S., Guillong, M., von Quadt, A., and Heinrich, C. A., 2017, Zircon petrochronological evidence for a plutonic-volcanic connection in porphyry copper deposits: Geology, v. 45, p. 623-626.

Burnham, C. W., 1979, Magmas and hydrothermal fluids, In: Barnes, H.L. (ed) Geochemistry of hydrothermal ore deposits, 2nd edn. Wiley, New York, pp 71-136.

Campbell, I. H., Stepanov, A. S., Liang, H. Y., Allen, C. M., Norman, M. D., Zhang, Y. Q., and Xie, Y. W., 2014, The origin of shoshonites: new insights from the Tertiary high-potassium intrusions of eastern Tibet: Contributions to Mineralogy and Petrology, v. 167, p. 1-22.

Candela, P.A., Piccoli, P.M., 2005 Magmatic processes in the development of porphyry-type ore systems: Economic Geology, v. 100th anniversary, p. 25-37.

Caricchi, L., Simpson, G., and Schaltegger, U., 2014, Zircons reveal magma fluxes in the EarthÕs crust: Nature, v. 511, p. 457Ð461.

Carten, R. B., White, W. H. and Stein, H. J., 1993, High-grade granite-related molybdenum systems: Classification and origin. In: Kirkham, R. V., Sinclair, W. D., Thorpe, R. I. & Duke, J. M. (eds) Mineral Deposit Modeling. Geological Association of Canada, Special Papers v. 40, p. 521-554.

Castro, A., Aghazadeh, M., Badrzadeh, Z., and Chichorro, M., 2013, Late EoceneÐOligocene post-collisional monzonitic intrusions from the Alborz magmatic belt, NW Iran. An example of monzonite magma generation from a metasomatized mantle source: Lithos, v. 180, p. 109-127.

Chapman, J. B., Ducea, M. N., DeCelles, P. G., Profeta, L., 2015, Tracking changes in crustal thickness during orogenic evolution with Sr/Y: An example from the North American Cordillera : Geology, v. 43, p. 919-922.

Chelle-Michou, C., Rottier, B., Caricchi, L., and Simpson, G., 2017, Tempo of magma degassing and the genesis of porphyry copper deposits: Scientific Reports, v.7, 40566.

Chiaradia, M., 2015, Crustal thickness control on Sr/Y signatures of recent arc magmas: an Earth scale perspective : Scientific reports, v. 5, 8115.

Chiaradia, M., 2014, Copper enrichment in arc magmas controlled by overriding plate thickness: Nature Geoscience, v. 7, p. 43-46.

Chiaradia, M., and Caricchi, L., 2017, Stochastic modelling of deep magmatic controls on porphyry copper deposit endowment: Scientific Reports, v. 7.

Chiaradia, M., Ulianov, A., Kouzmanov, K., and Beate, B., 2012, Why large porphyry Cu deposits like high Sr/Y magmas?: Scientific reports, 2.

Chiu, H.-Y., Chung, S.-L., Zarrinkoub, M.H., Mohammadi, S.S., Khatib, M.M., and Iizuka, Y., 2013, Zircon U-Pb age constraints from Iran on the magmatic evolution related to Neotethyan subduction and Zagros orogeny: Lithos, v. 162-163, p. 70-87.

Coleman, D.S., Gray, W., and Glazner, A.F., 2004, Rethinking the emplacement and evolution of zoned plutons: Geochronologic evidence for incremental assembly of the Tuolumne intrusive suite, California: Geology, v. 32, p. 433-436.

Cooke, D. R., Hollings, P., and Walshe, J. L., 2005, Giant porphyry deposits: Characteristics, distribution, and tectonic controls: Economic Geology, v. 100, p. 801-818.

Core, D. P., Kesler, S. E., and Essene, E. J., 2006, Unusually Cu-rich magmas associated with giant porphyry copper deposits: Evidence from Bingham, Utah: Geology, v. 34, p. 41-44.

Davidson, J., Turner, S., Handley, H., Macpherson, C., and Dosseto, A., 2007, Amphibole ÒspongeÓin arc crust?: Geology, v. 35, p. 787-790.

Delibaş, O., Moritz, R., Ulianov, A., Chiaradia, M., Sara•, C., Revan, K. M., and Gš•, D., 2016, Cretaceous subduction-related magmatism and associated porphyry-type Cu-Mo prospects in the Eastern Pontides, Turkey: New constraints from geochronology and geochemistry: Lithos, v. 248, p. 119-137.

Djrbashyan, R. T. and Tayan, R. N., 2008, Geological Map of the Southern Zangezur, Armenia, Lesser Caucasus. Institute of Geological Sciences, Armenian National Academy of Sciences. Based on the "Geological map of the Zangezur mining district", Scale 1: 50 000. Authors: Karamyan K.A. Guyumdjyan H.P., Djrbashyan R.T., Tayan R.N., 1974.

Einaudi, M. T., Hedenquist, J. W., and Inan, E. E., 2003, Sulfidation state of fluids in active and extinct hydrothermal systems: transitions from porphyry to epithermal environments. Special Publication-Society of Economic Geologists, v. 10, p. 285-314.

England, P., and Molnar, P., 1990, Surface uplift, uplift of rocks, and exhumation of rocks: Geology, v. 18, p. 1173-1177.

Fitton, J.G., 1995, Coupled molybdenum and niobium depletion in continental basalts. Earth and Planetary Science Letters, v. 136, p. 715–721.

Fontbotž, L., Kouzmanov, K., Chiaradia, M., and Pokrovski, G. S., 2017, Sulfide minerals in hydrothermal deposits: Elements, v. 13, p. 97-103.

Glazner, A. F., Bartley, J. M., Coleman, D. S., Gray, W., and Taylor, R. Z., 2004, Are plutons assembled over millions of years by amalgamation from small magma chambers?: GSA today, v. 14, p. 4-12.

Guyumjyan, H.P., 1973, Magmatic plutonic formation of the Western Bargushat. Proceedings of the National Academy of Sciences of the Republic of Armenia, Earth Sciences, v. 26, №1, p.52-65 (in Russian).

Harutunyan, M. A., Mnatsakanyan, A. Kh., and Tayan R. N., 2004, Explosive breccia bodies of the Kadjaran ore field and conditions of their formation. Proceedings of the National Academy of Sciences of the Republic of Armenia, Earth Sciences, v. 57, №2, p.9-16 (in Russian with English abstract).

Haschke, M., Ahmadian, J., Murata, M., and McDonald, I., 2010, Copper mineralization prevented by arc-root delamination during Alpine–Himalayan collision in Central Iran: Economic Geology, v. 105, p. 855–865.

HŠssig, M., Duretz, T., Rolland, Y., and Sosson, M., 2016, Obduction of old oceanic lithosphere due to reheating and plate reorganization: Insights from numerical modelling and the NE Anatolia-Lesser Caucasus case example: Journal of Geodynamics, v. 96, p. 35-49.

HŠssig, M., Rolland, Y., and Sosson, M., 2015, From seafloor spreading to obduction: Jurassic-Cretaceous evolution of the northern branch of the Neotethys in the Northeastern Anatolian and Lesser Caucasus regions: Geological Society, London, Special Publications, v. 428, SP428-10.

HŠssig, M., Rolland, Y., Sosson, M., Galoyan, G., Sahakyan, L., Topuz, G., , elik, …F., Avagyan, A., and MŸller, C., 2013, Linking the NE Anatolian and Lesser Caucasus ophiolites: evidence for large-scale obduction of oceanic crust and implications for the formation of the Lesser Caucasus-Pontides Arc: Geodinamica acta, v. 26, p. 311-330.

Hattori, K., 1993, High-sulfur magma, a product of fluid discharge from underlying mafic magma: evidence from Mount Pinatubo, Philippines : Geology, v. 21, p. 1083-1086.

Hattori, K. H., and Keith, J. D., 2001, Contribution of mafic melt to porphyry copper mineralization: evidence from Mount Pinatubo, Philippines, and Bingham Canyon, Utah, USA: Mineralium Deposita, v. 36, p. 799-806.

Hedenquist, J. W., Arribas, A., and Gonzalez-Urien, E., 2000, Exploration for epithermal gold deposits: Reviews in Economic Geology, v. 13, p. 45-77.

Hildreth, W., and Moorbath, S., 1988, Crustal contributions to arc magmatism in the Andes of central Chile: Contributions to mineralogy and petrology, v. 98, p. 455-489.

Hou, Z., Zhang, H., Pan, X., and Yang, Z., 2011, Porphyry Cu (±Mo±Au) deposits related to melting of thickened mafic lower crust: examples from the eastern Tethyan metallogenic domain: Ore Geology Reviews, v. 39, p. 21-45.

Hovakimyan, S.E., and Tayan, R.N., 2008, Fractures of the Lichk-Ayguedzor ore field and mineralization controls: Proceedings of the National Academy of Sciences of the Republic of Armenia, Earth Sciences, v. 61, p. 3-12 (in Russian with English abstract).

Hovakimyan, S., Moritz, R., Tayan, R., Harutyunyan, M., and Rezeau, H., 2015, The World-Class Kadjaran Mo-Cu-Porphyry Deposit, Southern Armenia, Lesser Caucasus: Structural Controls, Mineral Paragenesis and Fluid Evolution. In: AndrŽ-Mayer, A.-S., Cathelineau, M., Muchez, P., Pirad, E., Sindern, S. (Eds.), Mineral resources in a sustainable world. 13th SGA Biennial Meeting, 24±27 August 2015, France, Nancy 1, p. 295±298.

Hovakimyan, S., Moritz, R., Tayan, R., Melkonyan, R., and Harutyunyan, M., 2016, Regional strike-slip tectonics and porphyry Cu-Mo and epithermal ore deposit formation during Cenozoic subduction to post-collisional evolution of the southernmost Lesser Caucasus, Tethyan belt. 14th Swiss Geoscience Meeting, 18-19 November 2016, Geneva, p. 61 (abstract volume).

Huang, R., and AudŽtat, A., 2012, The titanium-in-quartz (TitaniQ) thermobarometer: a critical examination and re-calibration: Geochimica et Cosmochimica Acta, v. 84, p. 75-89.

Ionov, D. A., and Hofmann, A. W., 1995, Nb-Ta-rich mantle amphiboles and micas: Implications for subduction-related metasomatic trace element fractionations. Earth and Planetary Science Letters, v. 131(3-4), p. 341-356.

Jenner, F.E., O'Neill, H.S.C., Arculus, R.J., and Mavrogenes, J., 2010, The Magnetite Crisis in the Evolution of the Arc-related Magmas and the Initial Concentration of Au, Ag and Cu: Journal of Petrology, v. 51, p. 2445-2464.

Kaislaniemi, L., Van Hunen, J., Allen, M. B., and Neill, I., 2014, Sublithospheric small-scale convection - A mechanism for collision zone magmatism: Geology, v. 42, p. 291-294.

Karamyan, K.A., 1978, Geology, structure and condition of formation copper±molybdenum deposits of Zangezour ore region. Publishing House of the Academy of Sciences Armenian SSR, Yerevan, pp. 179 (in Russian).

Karamyan, K.A., Tayan, R.N., and Guyumdjyan, O.P., 1974, The main features of intrusion magmatism Zangezur region of the Armenian SSR: Proceedings of the National Academy of Sciences of the Republic of Armenia, v. 27, p. 54-65 (in Russian).

Kay, S. M., and Mpodozis, C., 2001, Central Andean ore deposits linked to evolving shallow subduction systems and thickening crust. GSA today, v. 11(3), p. 4-9.

Kelemen, P. B., Hangh¿j, K. and Greene, A. R., 2003, One view of the geochemistry of subduction-related magmatic arcs, with an emphasis on primitive andesite and lower crust. In: Turekian, K. & Holland, H. (eds) Treatise on Geochemistry, Vol. 3. Oxford: Pergamon, pp. 1Ð70.

Keskin, M., 2003. Magma generation by slab steepening and breakoff beneath a sub- ductionÐ accretion complex: an alternative model for collision-related volcanism in Eastern Anatolia, Turkey. Geophysical Research Letters 30, 8046-8050.

Kouzmanov, K., and Pokrovski, G. S., 2012, Hydrothermal controls on metal distribution in porphyry Cu (-Mo-Au) systems. In: Hedenquist JW, Harris M, Camus F (eds) Geology and Genesis of Major Copper Deposits and Districts of the World: A Tribute to Richard H. Sillitoe. Society of Economic Geologists Special Publication, v. 16, p. 573-618.

Krawczynski, M. J., Grove, T. L., and Behrens, H., 2012, Amphibole stability in primitive arc magmas: effects of temperature, H2O content, and oxygen fugacity: Contributions to Mineralogy and Petrology, v. 164, p. 317-339.

Kuşcu, İ., Tosdal, R. M., Gencalioğlu-Kuşcu, G., Friedman, R., and Ullrich, T. D., 2013, Late Cretaceous to Middle Eocene magmatism and metallogeny of a portion of the Southeastern Anatolian orogenic belt, East-Central Turkey: Economic Geology, v. 108, p. 641-666.

Larocque, A. C., Stimac, J. A., Keith, J. D., and Huminicki, M. A., 2000, Evidence for open-system behavior in immiscible Fe-S-O liquids in silicate magmas: implications for contributions of metals and sulfur to ore-forming fluids: The Canadian Mineralogist, v. 38, p. 1233-1249.

Lee, C. T. A., Luffi, P., Chin, E. J., Bouchet, R., Dasgupta, R., Morton, D. M., Le Roux, V., Yin, Q-Z and Jin, D., 2012, Copper systematics in arc magmas and implications for crust-mantle differentiation. Science, v. 336(6077), p. 64-68.

Lerchbaumer, L., and AudŽtat, A., 2012, High Cu concentrations in vapor-type fluid inclusions: An artifact?. Geochimica et Cosmochimica Acta, v. 88, p. 255-274.

Li, Y., and AudŽtat, A., 2015, Effects of temperature, silicate melt composition, and oxygen fugacity on the partitioning of V, Mn, Co, Ni, Cu, Zn, As, Mo, Ag, Sn, Sb, W, Au, Pb, and Bi between sulfide phases and silicate melt. Geochimica et Cosmochimica Acta, v. 162, p. 25-45.

Loucks, R. R., 2014, Distinctive composition of copper-ore-forming arc magmas: Australian Journal of Earth Sciences, v. 61, p. 5-16.

Lu, Y. J., Loucks, R. R., Fiorentini, M. L., Yang, Z. M., and Hou, Z. Q., 2015, Fluid flux melting generated postcollisional high Sr/Y copper oreÐforming water-rich magmas in Tibet: Geology, v. 43, p. 583-586.

McInnes, B. I., Evans, N. J., Fu, F. Q., and Garwin, S., 2005, Application of thermochronology to hydrothermal ore deposits: Reviews in Mineralogy and geochemistry, v. 58, p. 467-498.

Mamani, M., Wšrner, G., and Sempere, T., 2010. Geochemical variations in igneous rocks of the Central Andean orocline (13 S to 18 S): Tracing crustal thickening and magma generation through time and space: Geological Society of America Bulletin, v. 122, p.162-182.

Maydag‡n, L., Franchini, M., Rusk, B., Lentz, D., McFarlane, C., Impiccini, A., R'os, F.J., and Rey, R., 2015, Porphyry to epithermal transition in the Altar Cu-(Au-Mo) Deposit, Argentina, studied by cathodoluminescence, LA-ICP-MS, and fluid inclusion analysis: Economic Geology, v. 110, p. 889-923.

McQuarrie, N., and van Hinsbergen, D. J., 2013, Retrodeforming the Arabia-Eurasia collision zone: Age of collision versus magnitude of continental subduction: Geology, v. 41, p. 315-318.

Mederer, J., Moritz, R., Ulianov, A., and Chiaradia, M., 2013, Middle Jurassic to Cenozoic evolution of arc magmatism during Neotethys subduction and arc-continent collision in the Kapan Zone, southern Armenia: Lithos, v. 177, p. 61Ð78.

Mederer. J., Moritz, R., Zohrabyan, S., Vardanyan, A., and Melkonyan, R., 2014, Base and precious metal mineralization in the Jurassic-Cretaceous arc of the Lesser Caucasus - a comparison of the contrasting Drmbon, Alaverdi and Kapan mining districts: Ore Geology Reviews, v. 58, p. 185-207.

Melkonyan, R.L., Ghukasian, R.Kh., Tayan, R.N., and Haruntunyan, M.A., 2008, Geochronometry of the Meghri pluton monzonites (Armenia) - results and consequences: Proceedings of the National Academy of Sciences of the Republic of Armenia, v. 61, p. 3-9 (in Russian with English abstract).

Melkonyan, R.L., Ghukasian, R.Kh., Tayan, R.N., Khorenyan, R.A., and Hovakimyan, S.E., 2010, The stages of copperÐmolybdenum ore formation in Southern Armenia (by the results of RbÐSr isotope age estimations): Proceedings of the National Academy of Sciences of the Republic of Armenia, v. 63, p. 21Ð32 (in Russian with English abstract).

Menand, T., Annen, C., and de Saint Blanquat, M., 2015, Rates of magma transfer in the crust: Insights into magma reservoir recharge and pluton growth: Geology, v. 43, p. 199-202.

Middlemost, E.A.K., 1994, Naming materials in the magma/igneous rock system: Earth-Science Reviews, v. 37, p. 215Ð224.

Moore, G., and Carmichael, I. S. E., 1998, The hydrous phase equilibria (to 3 kbar) of an andesite and basaltic andesite from western Mexico: constraints on water content and conditions of phenocryst growth: Contributions to Mineralogy and Petrology, v. 130, p. 304-319.

Moore, D. M., and Reynolds, R. C. JR.,1997, X-ray Diffraction and the Identification and Analysis of Clay Minerals. Oxford University press, Oxford, pp. 378.

Moritz, R., Rezeau, H., Ovtcharova, M., Tayan, R., Melkonyan, R., Hovakimyan, S., Ramazanov, V., Selby, D., Ulianov, A., Chiaradia, M., andPutlitz, B., 2016a, Long-lived, stationary magmatism and pulsed porphyry systems during Tethyan subduction to post-collision evolution in the Southernmost Lesser Caucasus, Armenia and Nakhitchevan: Gondwana Research, v. 37, p. 465-503.

Moritz, R., Melkonyan, R., Selby, D., Popkhadze, N., Gugushvili, V., Tayan, R., and Ramazanov, V., 2016b, Metallogeny of the Lesser Caucasus: From arc construction to post-collision evolution: In : Richards, J. (ed), Tethyan Tectonics and Metallogeny, Special Publication of the Society of Economic Geology, v. 19, p.157-192.

Mouthereau, F., Lacombe, O., and VergŽs, J., 2012, Building the Zagros collisional orogen: timing, strain distribution and the dynamics of Arabia/Eurasia plate convergence: Tectonophysics, v. 532, p. 27-60.

Mustard, R., Ulrich, T., Kamenetsky, V. S., and Mernagh, T., 2006, Gold and metal enrichment in natural granitic melts during fractional crystallization. Geology, v. 34(2), p. 85-88.

Nadeau, O., Williams-Jones, A. and Stix, J., 2010, Sulphide magma as a source of metals in arc-related magmatic hydrothermal ore fluids: Nature Geosciences, v. 3, p. 501-505.

Nandedkar, R. H., HŸrlimann, N., Ulmer, P. and MŸntener, O., 2016, Amphibole-melt trace element partitioning of fractionating calc-alkaline magmas in the lower crust: an experimental study: Contributions to Mineralogy and Petrology, v.171, p. 71.

Naney, M. T., 1983, Phase equilibria of rock-forming ferromagnesian silicates in granitic systems: American Journal of Science, v. 283, p. 993–1033.

Neill, I., Meliksetian, K., Allen, M. B., Navasardyan, G., and Kuiper, K., 2015, Petrogenesis of mafic collision zone magmatism: The Armenian sector of the Turkish–Iranian Plateau: Chemical Geology, v. 403, p. 24-41.

OberhŠnsli, R., Candan, O., Bousquet, R., Rimmele, G., Okay, A., and Goff, J., 2010, Alpine HP evolution of the eastern Bitlis complex, SE Turkey. In: Sosson, M., Kaymakci, N., Stephenson, R.A., Bergerat, F., Starostenko, V. (Eds.), Sedimentary Basin Tectonics From the Black Sea and Caucasus to the Arabian Platform: Geological Society London, Special publication, v. 340, p. 461-483.

Peccerillo, A., and Taylor, S.R., 1976, Geochemistry of Eocene calc-alkaline volcanic rocks from the Kastamanou area, northern Turkey: Contributions to Mineralogy and Petrology, v. 58, p. 63-81.

Pearce, J., Bender, J., De Long, S., Kidd, W., Low, P., Guner, Y., Saroglu, F., Yilmaz, Y., Moorbath, S., and Mitchell, J., 1990, Genesis of collision volcanism in Eastern Anatolia, Turkey: Journal of Volcanology and Geothermal Research, v. 44, p. 189-229.

Pettke, T., Oberli, F., and Heinrich, C. A., 2010, The magma and metal source of giant porphyry-type ore deposits, based on lead isotope microanalysis of individual fluid inclusions. Earth and Planetary Science Letters, v. 296(3), p. 267-277.

Platt, J., and England, P., 1994, Convective removal of lithosphere beneath mountain belts-Thermal and mechanical consequences. American Journal of Science, v. 294(3), p. 307-336.

Rezeau, H., Moritz, R., Wotzlaw, J. F., Tayan, R., Melkonyan, R., Ulianov, A., Selby, D., d'Abzac F. X. and Stern, R. A., 2016, Temporal and genetic link between incremental pluton assembly and pulsed porphyry Cu-Mo formation in accretionary orogens: Geology, v. 44, p. 627-630.

Rezeau, H., Moritz, R., Leuthold, J., Hovakimyan, S., Tayan, R. and Chiaradia, M., 2017, 30 Myr of Cenozoic magmatism along the Tethyan margin during Arabia-Eurasia accretionary orogenesis (Meghri-Ordubad pluton, southernmost Lesser Caucasus). Lithos, v. 288-289, p.108-124.

Rezeau, H., Leuthold, J., Moritz, R., Tayan, R. Hovakimyan, S., Ulianov, A., and Kouzmanov, K., (in prep), Petrological characterization of subduction- and collision-related magmatism in the composite Meghri-Ordubad pluton, southernmost Lesser Caucasus (Tethyan Orogenic Belt). In prep for Journal of Petrology.

Richards, J. P., 2016, Economic geology: Clues to hidden copper deposits: Nature Geoscience, v. 9, P.195-196.

Richards, J. P., 2015a, Tectonic, magmatic, and metallogenic evolution of the Tethyan orogen: From subduction to collision: Ore Geology Reviews, v. 70, p. 323-345.

Richards, J. P., 2015b, The oxidation state, and sulfur and Cu contents of arc magmas: implications for metallogeny: Lithos, v. 233, p. 27-45.

Richards, J. P., 2013, Giant ore deposits formed by optimal alignments and combinations of geological processes: Nature Geoscience, v. 6, p. 911-916.

Richards, J. P., 2011, Magmatic to hydrothermal metal fluxes in convergent and collided margins. Ore Geology Reviews, v. 40, p. 1-26.

Richards, J. P., 2009, Postsubduction porphyry Cu-Au and epithermal Au deposits: Products of remelting of subduction-modified lithosphere: Geology, v. 37, p. 247-250.

Richards, J. P., 2003, Tectono-magmatic precursors for porphyry Cu-(Mo-Au) deposit formation: Economic Geology, v. 98, p.1515-1533.

Richards, J. P., and Sholeh, A. (2016). The Tethyan Tectonic History and Cu-Au Metallogeny of Iran. In : Richards, J. (ed), Tethyan Tectonics and Metallogeny, Special Publication of the Society of Economic Geology, v. 19, p.193-212.

Richards, J. P., and Kerrich, R., 2007, Special paper: adakite-like rocks: their diverse origins and questionable role in metallogenesis: Economic geology, v. 102, p. 537-576.

Righter, K., & Carmichael, I. S., 1996, Phase equilibria of phlogopite lamprophyres from western Mexico: biotite-liquid equilibria and PT estimates for biotite-bearing igneous rocks. Contributions to Mineralogy and Petrology, v. 123(1), p. 1-21.

Robert, A. M., Fernˆndez, M., JimŽnez-Munt, I., and VergŽs, J., 2015, Lithospheric structure in Central Eurasia derived from elevation, geoid anomaly and thermal analysis: Geological Society, London, Special Publications, v. 427, http://doi.org/10.1144/SP427.10.

Rohrlach, B. D., Loucks, R. R., and Porter, T. M., 2005, Multi-million-year cyclic ramp-up of volatiles in a lower crustal magma reservoir trapped below the Tampakan copper-gold deposit by Mio-Pliocene crustal compression in the southern Philippines: Super porphyry copper and gold deposits: A global perspective: Adelaide, PGC Publishing, v. 2, p. 270.

Rolland, Y., 2017, Caucasus collisional history: Review of data from East Anatolia to West Iran: Gondwana Research, doi: 10.1016/j.gr.2017.05.005

Rolland, Y., Perincek, D., Kaymakci, N., Sosson, M., Barrier, E., and Avagyan, A., 2012, Evidence for ~80ÐÐ75 Ma subduction jump during AnatolideÐTaurideÐArmenian block accretion and ~48 Ma ArabiaÐEurasia collision in Lesser CaucasusÐEast Anatolia: Journal of Geodynamics, v. 56ÐÐ57, p. 76ÐÐ85.

Rolland, Y., Billo, S., Corsini, M., Sosson, M., and Galoyan, G., 2009, Blueschists of the Amassia-Stepanavan suture zone (Armenia): linking Tethys subduction history from E-Turkey to W-Iran: International Journal of Earth Sciences, v. 98, p. 533-550.

Rusk, B. G., Lowers, H. A., and Reed, M. H., 2008, Trace elements in hydrothermal quartz: Relationships to cathodoluminescent textures and insights into vein formation: Geology, v. 36, p. 547-550.

Scaillet, B., 2010, Economic geology: Volatile destruction: Nature Geoscience, v. 3, p. 456Ð457.

Schneider, C. A., Rasband, W. S., and Eliceiri, K. W., 2012, NIH Image to ImageJ: 25 years of image analysis: Nature methods, v. 9, p. 671.

Seedorff, E., Dilles, J. H., Proffett, J. M., Einaudi, M. T., Zurcher, L., Stavast, W. J. A., Johnson, D. A., and Barton, M. D., 2005, Porphyry deposits: Characteristics and origin of hypogene features: Economic Geology 100th anniversary, v.29, p. 251-298.

Selby, D., and Creaser, R. A., 2001, Re-Os geochronology and systematics in molybdenite from the Endako porphyry molybdenum deposit, British Columbia, Canada: Economic Geology, v. 96, p. 197-204.

Shafiei, B., Haschke, M., Shahabpour, J., 2009, Recycling of orogenic arc crust triggers porphyry Cu mineralization in Kerman Cenozoic arc rocks, southeastern Iran: Mineralium Deposita, v. 44, p. 265Ð283.

Sillitoe, R. H., 2010, Porphyry copper systems: Economic geology, v. 105, p. 3-41.

Sillitoe, R. H., 1994, Erosion and collapse of volcanoes: Causes of telescoping in intrusion-centered ore deposits: Geology, v. 22, p. 945-948.

Simmons, S. F., White, N. C., and John, D. A., 2005, Geological characteristics of epithermal precious and base metal deposits: Economic Geology 100th anniversary, v. 29, p. 485-522.

Sinclair, W. D., 2007, Porphyry Deposits. in Goodfellow, W. D., ed., Mineral deposits of Canada: A synthesis of major deposit types, district metallogeny, the evolution of geological pro- vinces, and exploration methods: Geological Association of Canada, Mineral Deposits Division, Special Publication v. 5, p. 223Ð243.

Sisson, T. W., Ratajeski, K., Hankins, W. B., and Glazner, A. F., 2005, Voluminous granitic magmas from common basaltic sources. Contributions to Mineralogy and Petrology, v. 148(6), p. 635-661.

Song, W., Xu, C., Smith, M. P., Kynicky, J., Huang, K., Wei, C., Zhou, L. and Shu, Q., 2016, Origin of unusual HREE-Mo-rich carbonatites in the Qinling orogen, China. Scientific reports, v. 6, n¡37377.

Sosson, M., Rolland, Y., MŸller, C., Danelian, T., Melkonyan, R., Kekelia, S., Adamia, S., Babzadeh, V., Kangarli, T., Avagyan, A., Galoyan, G., and Mosar, J., 2010, Subductions, obduction and collision in the Lesser Caucasus (Armenia, Azerbaijan, Georgia), new insights. In: Sosson, M., Kaymakci, N., Stephenson, R.A., Bergerat, F., Starostenko, V. (Eds.), Sedimentary basin tectonics from the Black Sea and Caucasus to the Arabian platform: Geological Society London, Special publication, v. 340, p. 329Ð352.

Stepanov, A. S., and Hermann, J., 2013, Fractionation of Nb and Ta by biotite and phengite: Implications for the Òmissing Nb paradoxÓ Geology, v. 41(3), p. 303-306.

Stolz, A. J., Jochum, K. P., Spettel, B., and Hofmann, A. W., 1996, Fluid-and melt-related enrichment in the subarc mantle: evidence from Nb/Ta variations in island-arc basalts. Geology, v. 24(7), p. 587-590.

Sun, S.-S., and McDonough, W.F., 1989, Chemical and isotopic systematics of oceanic basalts: Implications for mantle composition and processes: Geological Society of London, Special Publication v. 42, p. 313Ð345.

Tanner, D., Henley, R. W., Mavrogenes, J. A., and Holden, P., 2013, Combining in situ isotopic, trace element and textural analyses of quartz from four magmatic-hydrothermal ore deposits: Contributions to Mineralogy and Petrology, v. 166, p. 1119-1142.

Tapster, S., Condon, D. J., Naden, J., Noble, S. R., Petterson, M. G., Roberts, N. M. W. Saunders, A.D., and Smith, D. J., 2016, Rapid thermal rejuvenation of high-crystallinity magma linked to porphyry copper deposit formation; evidence from the Koloula Porphyry Prospect, Solomon Islands: Earth and Planetary Science Letters, v. 442, p. 206-217.

Tatsumi, Y., Shukuno, H., Tani, K., Takahashi, N., Kodaira, S., and Kogiso, T., 2008, Structure and growth of the Izu-Bonin-Mariana arc crust: 2. Role of crust-mantle transformation and the transparent Moho in arc crust evolution: Journal of Geophysical Research: Solid Earth, v. 113(B2).

Tayan, R.N., 1998, On central magma-ore controlling zone of the Zangezur ore region. Proceedings of the National Academy of Sciences of the Republic of Armenia, Earth Sciences, v. 51, No3, p.20-26 (in Russian with English abstract)

Tayan, R.N., Plotnikov, E.P., and Abdurakhmanov, R.U., 1976, Some features of emplacement of geological structure of the ZangezourÐNakhichevan region of Lesser Caucasus: Proceedings of the National Academy of Sciences of the Republic of Armenia, v. 29, p. 12Ð20 (in Russian).

Tayan, R.N., Harutunyan, M. A., Hovhannisyan, A.E, 2006, Geological-structural map of the Kadjaran ore field, Scale 1: 5 000. Based on the "Geological- structural map of the Kadjaran ore field" by Karamyan, K.A., Tayan, R.N., Avagyan, A.A., Arevshatyan, T.A., Vartanesov V.E., Sargsyan, S.P. and Harutunyan, M.A. (1985). Institute of Geological Sciences, Armenian National Academy of Sciences, Yerevan, Armenia.

Tosdal, R. M., and Richards, J. P., 2001, Magmatic and structural controls on the development of porphyry Cu±Mo±Au deposits: Reviews in Economic Geology, v. 14, p. 157-181.

Van Hunen, J., and Allen, M.B., 2011, Continental collision and slab break-off: A comparison of 3-D numerical models with observations: Earth and Planetary Science Letters, v. 302, p. 27Ð37.

Verdel, C., Wernicke, B.P., Hassanzadeh, J., and Guest, B., 2011, A Paleogene extensional arc flare-up in Iran: Tectonics 30, http://dx.doi.org/10.1029/2010tc002809 (TC3008).

Vermeesch, P., 2012, On the visualisation of detrital age distributions: Chemical Geology, v. 312-313, p. 190-194.

Vincent, S. J., Morton, A. C., Carter, A., Gibbs, S., and Barabadze, T. G., 2007, Oligocene uplift of the Western Greater Caucasus: an effect of initial ArabiaÐEurasia collision: Terra Nova, v. 19, p. 160-166.

Vannucci, R., Bottazzi, P., Wulff-Pedersen, E., and Neumann, E. R., 1998, Partitioning of REE, Y, Sr, Zr and Ti between clinopyroxene and silicate melts in the mantle under La Palma (Canary Islands): implications for the nature of the metasomatic agents: Earth and Planetary Science Letters, v. 158, p. 39-51.

Voegelin, A. R., Pettke, T., Greber, N. D., von NiederhŠusern, B., and NŠgler, T. F., 2014, Magma differentiation fractionates Mo isotope ratios: evidence from the Kos Plateau Tuff (Aegean Arc). Lithos, v. 190, p. 440-448.

Wark, D. A., and Watson, E. B., 2006, TitaniQ: a titanium-in-quartz geothermometer: Contributions to Mineralogy and Petrology, v. 152, p. 743-754.

Wilkinson, J. J., 2013, Triggers for the formation of porphyry ore deposits in magmatic arcs: Nature Geoscience, v. 6, p. 917-925.

Zack, T., Kronz, A., Foley, S. F., and Rivers, T., 2002, Trace element abundances in rutiles from eclogites and associated garnet mica schists. Chemical Geology, v. 184(1), p. 97-122.

Zhu, L., Zhang, G., Guo, B., and Lee, B., 2009, He-Ar isotopic system of fluid inclusions in pyrite from the molybdenum deposits in south margin of North China Block and its trace to metallogenetic and geodynamic background. Chinese Science Bulletin, v. 54(14), p. 2479-2492.

APPENDIX

Appendix A:

Supplementary Table A.1: EPMA trace element (Al, Ti) profile analyses from core to rim across hydrothermal quartz crystal crystallized in subvertical veins from the six veins block in Kadjaran porphyry-epithermal Cu-Mo deposit. Crystallization temperatures are also reported using two different "TitaniQ" thermometer from Wark & Watson (2006) and Huang & AudŽtat (2012).

			Wark & Watson 2006 (aTi=1)	*Wark & Watson 2006 (aTi=0.7)*	*Huang & Audétat 2012 (P = 1 kbar)*	*Huang & Audétat 2012 (P = 3 kbars)*
Profile analysis	*Al (ppm)*	*Ti (ppm)*	T(°C)	T(°C)	T(°C)	T(°C)
1	267	54	678.3	717.1	609.6	688.8
2	294	bdl	-	-	-	-
3	179	17	571.3	601.6	509.3	579.4
4	243	22	593.0	625.0	529.6	601.6
5	192	bdl	-	-	-	-
6	156	19	580.5	611.6	517.9	588.9
7	250	bdl	-	-	-	-
8	169	27	611.1	644.5	546.6	620.1
9	254	bdl	-	-	-	-
10	160	bdl	-	-	-	-
11	176	14	555.6	584.8	494.6	563.5
12	158	bdl	-	-	-	-
13	130	16	566.3	596.3	504.7	574.4
14	128	26	607.7	640.8	543.4	616.6
15	152	19	580.5	611.6	517.9	588.9
16	142	17	571.3	601.6	509.3	579.4
17	141	28	614.4	648.0	549.7	623.4
18	156	28	614.4	648.0	549.7	623.4
19	136	27	611.1	644.5	546.6	620.1
20	127	17	571.3	601.6	509.3	579.4
21	119	23	596.9	629.1	533.3	605.6
22	bdl	bdl	-	-	-	-
23	bdl	bdl	-	-	-	-
24	bdl	bdl	-	-	-	-
25	bdl	18	576.0	606.7	513.7	584.3
26	bdl	bdl	-	-	-	-
27	bdl	32	626.7	661.3	561.2	636.0
28	bdl	bdl	-	-	-	-
29	bdl	24	600.6	633.2	536.8	609.4
30	bdl	bdl	-	-	-	-
31	bdl	17	571.3	601.6	509.3	579.4
32	bdl	bdl	-	-	-	-
33	bdl	bdl	-	-	-	-
34	bdl	23	596.9	629.1	533.3	605.6

35	bdl	bdl	-	-	-	-
36	bdl	20	584.8	616.2	522.0	593.3
37	bdl	bdl	-	-	-	-
38	bdl	bdl	-	-	-	-
39	19	bdl	-	-	-	-
40	17	bdl	-	-	-	-
41	bdl	bdl	-	-	-	-
42	bdl	bdl	-	-	-	-
43	bdl	bdl	-	-	-	-
44	bdl	bdl	-	-	-	-
45	bdl	bdl	-	-	-	-
46	bdl	16	566.3	596.3	504.7	574.4
47	bdl	20	584.8	616.2	522.0	593.3
48	bdl	bdl	-	-	-	-
49	bdl	23	596.9	629.1	533.3	605.6
50	bdl	bdl	-	-	-	-
51	bdl	bdl	-	-	-	-
52	bdl	bdl	-	-	-	-
53	bdl	bdl	-	-	-	-
54	bdl	bdl	-	-	-	-
55	bdl	bdl	-	-	-	-
56	bdl	21	589.0	620.7	525.9	597.5
57	bdl	bdl	-	-	-	-
58	bdl	bdl	-	-	-	-
59	bdl	14	555.6	584.8	494.6	563.5
60	bdl	19	580.5	611.6	517.9	588.9
61	bdl	bdl	-	-	-	-
62	bdl	14	555.6	584.8	494.6	563.5
63	bdl	bdl	-	-	-	-
64	bdl	bdl	-	-	-	-
65	bdl	17	571.3	601.6	509.3	579.4
66	bdl	14	555.6	584.8	494.6	563.5
67	bdl	bdl	-	-	-	-
68	bdl	18	576.0	606.7	513.7	584.3
69	bdl	17	571.3	601.6	509.3	579.4
70	bdl	bdl	-	-	-	-
71	bdl	19	580.5	611.6	517.9	588.9
72	bdl	16	566.3	596.3	504.7	574.4
73	bdl	bdl	-	-	-	-
74	bdl	bdl	-	-	-	-
75	bdl	18	576.0	606.7	513.7	584.3
76	bdl	bdl	-	-	-	-
77	bdl	21	589.0	620.7	525.9	597.5
78	bdl	bdl	-	-	-	-
79	bdl	bdl	-	-	-	-
80	bdl	bdl	-	-	-	-
81	bdl	bdl	-	-	-	-
82	bdl	bdl	-	-	-	-

83	bdl	bdl	-	-	-	-
84	bdl	22	593.0	625.0	529.6	601.6
85	bdl	26	607.7	640.8	543.4	616.6
86	bdl	bdl	-	-	-	-
87	bdl	19	580.5	611.6	517.9	588.9
88	bdl	bdl	-	-	-	-
89	bdl	bdl	-	-	-	-
90	bdl	17	571.3	601.6	509.3	579.4
91	bdl	bdl	-	-	-	-
92	bdl	19	580.5	611.6	517.9	588.9
93	bdl	bdl	-	-	-	-
94	bdl	bdl	-	-	-	-
95	bdl	bdl	-	-	-	-
96	bdl	bdl	-	-	-	-
97	bdl	bdl	-	-	-	-
98	bdl	bdl	-	-	-	-
99	bdl	14	555.6	584.8	494.6	563.5
100	bdl	bdl	-	-	-	-
101	32	17	571.3	601.6	509.3	579.4
102	bdl	bdl	-	-	-	-
103	bdl	bdl	-	-	-	-
104	bdl	bdl	-	-	-	-
105	18	18	576.0	606.7	513.7	584.3
106	47	bdl	-	-	-	-
107	33	bdl	-	-	-	-
108	bdl	bdl	-	-	-	-
109	20	20	584.8	616.2	522.0	593.3
110	bdl	bdl	-	-	-	-
111	bdl	bdl	-	-	-	-
112	bdl	bdl	-	-	-	-
113	bdl	bdl	-	-	-	-
114	bdl	bdl	-	-	-	-
115	120	18	576.0	606.7	513.7	584.3
116	37	bdl	-	-	-	-
117	63	14	555.6	584.8	494.6	563.5
118	55	bdl	-	-	-	-
119	bdl	20	584.8	616.2	522.0	593.3
120	bdl	bdl	-	-	-	-
121	bdl	bdl	-	-	-	-
122	bdl	bdl	-	-	-	-
123	bdl	16	566.3	596.3	504.7	574.4
124	bdl	14	555.6	584.8	494.6	563.5
125	bdl	bdl	-	-	-	-
126	bdl	bdl	-	-	-	-
127	bdl	bdl	-	-	-	-
128	bdl	bdl	-	-	-	-
129	bdl	bdl	-	-	-	-
130	bdl	bdl	-	-	-	-

131	bdl	bdl	-	-	-	-
132	bdl	bdl	-	-	-	-
133	bdl	bdl	-	-	-	-
134	bdl	bdl	-	-	-	-
135	bdl	bdl	-	-	-	-
136	bdl	bdl	-	-	-	-
137	32	bdl	-	-	-	-
138	80	bdl	-	-	-	-
139	bdl	bdl	-	-	-	-
140	172	bdl	-	-	-	-
141	166	19	580.5	611.6	517.9	588.9
142	89	bdl	-	-	-	-
143	66	bdl	-	-	-	-
144	17	bdl	-	-	-	-
145	132	14	555.6	584.8	494.6	563.5
146	45	bdl	-	-	-	-
147	bdl	bdl	-	-	-	-
148	bdl	bdl	-	-	-	-
149	25	bdl	-	-	-	-
150	bdl	bdl	-	-	-	-
151	bdl	bdl	-	-	-	-
152	bdl	bdl	-	-	-	-
153	bdl	bdl	-	-	-	-
154	32	bdl	-	-	-	-
155	bdl	bdl	-	-	-	-
156	bdl	bdl	-	-	-	-
157	148	20	584.8	616.2	522.0	593.3
158	bdl	14	555.6	584.8	494.6	563.5
159	170	bdl	-	-	-	-
160	101	bdl	-	-	-	-
161	43	16	566.3	596.3	504.7	574.4
162	22	bdl	-	-	-	-
163	1665	bdl	-	-	-	-
164	2581	bdl	-	-	-	-
165	1843	bdl	-	-	-	-
167	2054	16	566.3	596.3	504.7	574.4
168	1519	bdl	-	-	-	-
169	1926	bdl	-	-	-	-
170	3248	bdl	-	-	-	-
171	1813	bdl	-	-	-	-
172	2894	bdl	-	-	-	-
173	3556	bdl	-	-	-	-
174	2911	bdl	-	-	-	-
175	4027	bdl	-	-	-	-
176	4953	bdl	-	-	-	-
177	4179	bdl	-	-	-	-
178	4253	bdl	-	-	-	-
179	4128	bdl	-	-	-	-

180	3954	bdl	-	-	-	-
181	4575	16	566.3	596.3	504.7	574.4
182	4995	bdl	-	-	-	-
183	4685	bdl	-	-	-	-
184	5346	bdl	-	-	-	-
185	5276	bdl	-	-	-	-
186	3918	bdl	-	-	-	-
Limit of detection	10 ppm	13 ppm				

bdl:below detection limit

Appendix B:

Supplementary Table B.1: Average LA-ICP-MS trace element content of Nb and Mo in biotite for representative dated samples in the MOP. The full spectrum of elements is reported in Chapter 3 (Supplementary Table B.5 and Electronic Table E.5).

Sample	avg Mo ($\mu g.g^{-1}$)	1s ($\mu g.g^{-1}$)	avg Nb ($\mu g.g^{-1}$)	1s ($\mu g.g^{-1}$)	Mean age (Ma)
AG1406	0.15	0.06	6.63	4.45	44
AG1402	0.06	0.01	2.36	1.45	43.8
HQ1403	0.39	0.11	15.14	5.58	43.1
AG1308A1	0.07	0.02	76.09	21.47	37.8
VK1404	2.00	1.36	53.39	27.07	35.7
MR1403	2.27	1.04	72.00	37.11	34.6
MR1403bis	2.34	0.88	141.66	20.50	34.6
LI1303A1	1.70	0.24	107.01	19.05	33.5
MR1402	0.66	0.13	20.91	1.31	33.4
KJ0901A	1.14	0.69	78.50	18.83	31.9
KJ1308	0.93	0.54	143.99	43.16	31.1
KJ1303A2	0.16	0.04	6.77	0.46	25.5
MR1401	0.61	0.26	37.48	13.38	24.5
LI1301	0.79	0.22	30.97	5.07	22.6
KJ1313	0.54	0.03	35.71	3.93	21.2

Supplementary Table B.2: Detailed LA-ICPM-MS trace element content of Nb and Mo in biotite for representative dated samples in the MOP. The full spectrum of elements is reported in Chapter 3 (Supplementary Table B.5 and Electronic Table E.5).

Samples	mean age (Ma)	Mo ($\mu g.g^{-1}$)	Nb ($\mu g.g^{-1}$)	Ta ($\mu g.g^{-1}$)
AG1402				
au22e03	43.8	-	1.028	0.012
au22e04	43.8	-	0.381	0.006
au22e05	43.8	-	2.327	0.077
au22e06	43.8	-	1.785	0.046
au22e07	43.8	0.071	3.311	0.117
au22e08	43.8	0.065	4.942	0.145
au22e09	43.8	-	4.731	0.148
au22e10	43.8	0.045	3.527	0.102
au22e11	43.8	-	1.603	0.050
au22e12	43.8	-	1.377	0.047
au22e13	43.8	-	1.627	0.069
au22e14	43.8	-	1.643	0.041
AG1406				
au22f03	44	0.068	3.747	0.296
au22f04	44	0.264	17.741	0.940
au22f05	44	0.147	5.327	0.498
au22f06	44	0.155	4.478	0.258
au22f07	44	0.134	5.160	0.343
au22f08	44	0.08	2.382	0.175
au22f09	44	0.143	8.679	0.701
au22f10	44	0.108	3.685	0.296
au22f11	44	0.239	7.555	0.604
au22f12	44	0.112	10.667	0.880
au22f13	44	-	3.473	0.231
HQ1403				
au22g03	43.1	0.341	12.937	0.247
au22g04	43.1	0.291	14.884	0.266
au22g05	43.1	0.351	14.116	0.245
au22g06	43.1	0.299	13.383	0.228
au22g07	43.1	0.517	22.531	0.505
au22g08	43.1	0.431	22.768	0.369
au22g09	43.1	0.357	11.913	0.245
au22g10	43.1	0.181	1.205	0.020
au22g11	43.1	0.47	16.982	0.344
au22g12	43.1	0.409	17.801	0.319
au22g13	43.1	0.509	15.964	0.344

au22g14	43.1	0.519	17.245	0.383
AG1308A1				
au22a04	37.8	0.053	47.234	2.219
au22a05	37.8	0.095	61.910	2.650
au22a06	37.8	0.072	80.179	3.029
au22a07	37.8	0.052	83.051	3.153
au22a08	37.8	0.081	42.205	1.689
au22a09	37.8	0.078	46.578	1.715
au22a10	37.8	0.044	103.326	4.186
au22a11	37.8	-	102.453	4.015
au22a12	37.8	0.052	88.520	3.055
au22a13	37.8	-	90.018	3.154
au22a14	37.8	-	88.711	4.020
au22a15	37.8	-	78.927	3.638
VK1404				
au23f04	35.7	0.973	26.248	0.954
au23f05	35.7	0.246	26.639	1.220
au23f06	35.7	1.445	34.672	1.181
au23f07	35.7	1.194	28.147	0.859
au23f08	35.7	3.887	86.595	3.687
au23f09	35.7	4.238	73.535	2.112
au23f11	35.7	1.605	65.626	3.183
au23f12	35.7	2.888	94.463	4.081
au23f13	35.7	1.548	44.603	1.680
MR1403				
au23g03	34.6	1.679	46.887	1.673
au23g04	34.6	1.872	40.525	1.524
au23g05	34.6	1.766	46.705	1.655
au23g06	34.6	1.795	41.230	1.521
au23g07	34.6	1.659	56.208	2.026
au23g08	34.6	1.811	64.729	2.227
au23g09	34.6	1.694	87.668	2.800
au23g10	34.6	4.509	137.361	5.739
au23g11	34.6	3.605	126.667	4.516
MR1403bis				
au23c03	34.6	2.807	123.671	4.147
au23c04	34.6	3.015	119.249	3.659
au23c05	34.6	3.5	147.338	4.817
au23c06	34.6	3.582	161.029	5.355
au23c07	34.6	2.532	105.522	3.678

au23c08	34.6	3.252	138.907	4.257
au23c09	34.6	1.97	154.188	5.611
au23c10	34.6	1.664	121.737	4.474
au23c11	34.6	1.238	141.207	4.694
au23c12	34.6	1.065	170.789	6.015
au23c13	34.6	1.747	150.031	5.337
au23c14	34.6	1.761	166.217	6.260

LI1303A1

au22b03	33.5	2.083	112.794	3.338
au22b04	33.5	1.871	107.629	3.235
au22b05	33.5	1.561	106.980	3.530
au22b06	33.5	1.663	99.181	3.019
au22b07	33.5	1.836	91.625	2.631
au22b08	33.5	1.595	92.285	2.709
au22b09	33.5	1.694	109.823	3.540
au22b10	33.5	1.707	109.892	3.697
au22b11	33.5	1.097	68.541	2.184
au22b12	33.5	1.76	109.266	3.542
au22b13	33.5	1.592	135.197	5.042
au22b14	33.5	1.929	140.905	4.869

MR1402

au23d03	33.4	0.561	21.548	0.867
au23d04	33.4	0.491	19.034	0.729
au23d05	33.4	0.794	20.704	0.755
au23d06	33.4	0.85	22.278	0.900
au23d07	33.4	0.678	19.858	0.799
au23d08	33.4	0.643	21.052	0.837
au23d09	33.4	0.542	19.895	0.816
au23d10	33.4	0.72	22.892	1.006

KJ0901A

au22h03	31.9	0.66	82.198	3.413
au22h04	31.9	0.696	99.730	4.875
au22h05	31.9	1.065	57.349	1.549
au22h06	31.9	0.631	44.354	0.914
au22h07	31.9	1.787	95.268	3.227
au22h08	31.9	1.493	88.908	3.240
au22h10	31.9	0.555	66.137	1.659
au22h11	31.9	0.784	93.153	4.047
au22h12	31.9	2.593	79.396	3.125

KJ1308

au23h03	31.1		102.833	3.183
au23h04	31.1	0.323	72.988	2.019
au23h05	31.1	0.987	113.037	3.532
au23h06	31.1	0.413	131.622	4.646
au23h07	31.1	1.262	160.290	5.372
au23h08	31.1	0.732	154.836	6.575
au23h09	31.1	0.714	164.598	8.189
au23h10	31.1	1.011	182.875	11.523
au23h11	31.1	2.036	212.810	20.131

KJ1303A2

au23a03	25.5	0.119	6.648	0.317
au23a04	25.5	-	7.214	0.405
au23a05	25.5	-	7.192	0.375
au23a06	25.5	0.213	6.876	0.391
au23a07	25.5	0.165	7.640	0.357
au23a08	25.5	-	5.828	0.303
au23a09	25.5	-	7.581	0.422
au23a10	25.5	-	6.607	0.348
au23a11	25.5	-	6.730	0.352
au23a12	25.5	-	6.470	0.353
au23a13	25.5	-	6.775	0.355
au23a14	25.5	0.147	6.424	0.329
au23a15	25.5	-	6.835	0.335
au23a16	25.5	-	6.347	0.318
au23a17	25.5	-	6.668	0.351
au23a18	25.5	-	6.531	0.324

MR1401

au23b03	24.5	1.134	65.126	1.741
au23b04	24.5	0.95	56.433	1.576
au23b05	24.5	0.33	25.135	0.771
au23b06	24.5	0.366	28.838	0.865
au23b07	24.5	0.403	26.914	0.821
au23b08	24.5	0.538	28.345	0.819
au23b09	24.5	0.489	33.652	0.948
au23b10	24.5	0.701	36.856	1.087
au23b11	24.5	0.492	31.757	0.930
au23b12	24.5	0.661	41.721	1.132

LI1301

au22c03	22.6	0.495	28.135	0.740
au22c04	22.6	0.588	30.030	0.776
au22c05	22.6	0.776	31.741	0.569
au22c06	22.6	0.547	25.090	0.336

au22c07	22.6	0.73	37.464	0.794
au22c08	22.6	0.554	33.224	0.573
au22c09	22.6	0.886	24.974	0.530
au22c10	22.6	0.933	25.639	0.382
au22c11	22.6	1.059	36.389	0.814
au22c12	22.6	1.035	37.764	0.736
au22c13	22.6	1.048	28.850	0.526
au22c14	22.6	0.852	24.371	0.363
au22c15	22.6	1.095	38.366	0.854
au22c16	22.6	0.516	31.543	0.591

KJ1313

au22d03	21.2	0.587	38.562	0.778
au22d04	21.2	0.548	36.184	0.806
au22d05	21.2	0.582	37.258	0.802
au22d06	21.2	0.534	37.412	0.801
au22d07	21.2	0.556	38.135	0.842
au22d08	21.2	0.51	37.566	0.779
au22d09	21.2	0.521	36.963	0.820
au22d10	21.2	0.579	37.758	0.841
au22d11	21.2	0.514	24.305	0.578
au22d12	21.2	0.476	32.532	0.696
au22d13	21.2	0.548	36.392	0.857
au22d14	21.2	0.513	35.418	0.855

Detection limit:

AG1308A1	D.L.	0.026	0.002	0.001
LI1303A1	D.L.	0.025	0.004	0.001
LI1301	D.L.	0.029	0.002	0.001
KJ1313	D.L.	0.032	0.002	0.001
AG1402	D.L.	0.032	0.001	0.001
AG1406	D.L.	0.038	0.003	0.001
HQ1403	D.L.	0.031	0.003	0.001
KJ0901A	D.L.	0.033	0.003	0.001
KJ1303A2	D.L.	0.089	0.005	0.004
MR1401	D.L.	0.02	0.002	0.001
MR1403bis	D.L.	0.025	0.002	0.001
MR1402	D.L.	0.025	0.003	0.001
VK1405	D.L.	0.026	0.002	0.001
VK1404	D.L.	0.065	0.004	0.002
MR1403	D.L.	0.028	0.004	0.001
KJ1308	D.L.	0.112	0.004	0.004

GENERAL CONCLUSIONS

This thesis presents new quantitative isotopic and geochemical dataset combined with detailed petrography, including 1) 30 zircon U-Pb weighted mean ages from 601 individual analyses and 2 molybdenite Re-Os ages, 2) 30 weighted mean zircon Hf isotopic analyses from 365 individual analyses, 3) 14 weighted mean O isotopic analyses from 280 individual analyses, 4) 37 whole rock major and trace element geochemical analyses, 5) 29 whole rock radiogenic isotope analyses, 6) 2213 major elements *in-situ* EPMA analyses (olivine, n=18; clinopyroxene, n=262; plagioclase, n=930; amphibole, n=605; biotite, n=212, hydrothermal quartz, n=186), 7) 549 trace elements *in-situ* LA-ICP-MS analyses (clinopyroxene, n=75; plagioclase, n=216; amphibole, n=128; biotite, n= 130), and 7) 22 samples quantitatively analysed by QEMSCAN for mineral phases abundance and distribution. In addition, new field observations regarding the sequence of mineralizing event in the large Kadjaran Cu-Mo porphyry-epithermal deposit have been reported. This new comprehensive database is presented in chapters 1 to 4 and significantly revises and improves previous interpretations for the Cenozoic composite Meghri-Ordubad pluton incrementally emplaced from the Middle Eocene to the Early Miocene. Each chapter is complementary and contributes to our understanding of 1) temporal constraints of the incremental growth of long-lived composite plutons, 2) mantle source processes leading to the generation of compositionally distinct differentiation series (medium-K calc-alkaline, shoshonitic, high-K calc-alakline "adakite-like") related to contrasted geodynamic setting (subduction, collision and post-collision) and stress regime (compression vs. extension), 3) crustal processes occurring at mid- to upper crustal levels and complex open-magmatic system involving fractional crystallization, assimilation, crystal mush remobilization and magma interactions through mafic resplenishment, 4) the temporal and genetic link between magmatism and ore-forming processes, and 5) favorable tectono-magmatic conditions to form large porphyry Cu-Mo deposits, including a new genetic model for the formation of the large Kadjaran Cu-Mo porphyry-epithermal system. Finally, the multi-disciplinary approach carried out in this thesis allowed us to shed light on fundamental geological problematics mentioned above, and also to provide new insights for the mining industry regarding the optimal tectono-magmatic conditions required for the formation of large ore resources in collisional context, especially for future exploration campaigns along the Tethyan metallogenic belt and more specifically along the Turkish-Iranian plateau.

ACKNOWLEDGEMENTS

I would like to thank my supervisor Robert Moritz for the guidance, freedom and support over the past 6 years during my Ph.D. and my M.Sc. thesis. You offered me the possibility to work on contrasting project from Archaean-hosted orogenic gold deposits in Canada to Cenozoic arc magmatism and porphyry Cu-Mo in the Lesser Caucasus. I have learnt a valuable set of skills from both scientific and field experiences as your student and i wish I can transfer these skills in my future academic career.

I am extremely grateful to my colleagues and friends Richard Spikings and Jšrn-Frederik Wotzlaw. The former was continually willing to spend time with me for scientific discussion about regional questions, whereas the latter pushed me hard to achieve my first publication and opened my eyes on the great potential of this Ph.D. project. Finally both of them were always here to have great random chats and laughs around cold beers, round of tequilas or Sambuka and rarely fresh glass of water somewhere in Geneva between the Paquis headquarter, rue de la MŽdecine or the Carouge underground center. Thanks mates!

Thank you to Kalin Kouzmanov for your guidance regarding the analytical methods in general and more specifically the microprobe, but also as an example for being very picky with analytical results. Additionally, thank you for the high quality teaching you provide me during the master class, which made me realize the huge gap i had to fill in order to carry out decent science. I would like to thank prof. Lluis FontbotŽ same way for your guidance, optimism and the tremendous effort you have invested to bring the "Mineral Resources and Geofluids" research group with an international recognition. This is very inspiring. Finally, thanks to Urs Schaltegger for always offering me a helping hand and wise advises when necessary.

A special shout out goes to my 4th floor former and current mates Fran•ois-Xavier d'Abzac, Joshua Davies, Danijela Miletic, Maria Ovtcharova, Massimo Chiaradia, Bjšrn Baresel, Federico farina and Nicolas Greber. It is just a pleasure every morning to see your funny faces and share stupid jokes all day long, although mine were always way funnier than yours. I also highly appreciated daily scientific discussions during coffee breaks or later on around the corner.

Thank you to my colleagues and friends Yannick Buret, Cyril Chelle-Michou, Vincent Casanova, Bertrand Rottier, Ariadni Georgatou, AndrŽ Navin Paul and other PhD students in general for great scientific emulation and after-work beers throughout these years and unforgettable moments in the field and conferences for some of you.

Technical staff members Christine, Fred, Jean-Marie and Fran•ois are deeply acknowledged for their availability, technical skills and their kindness, which are priceless to make our life easier and to carry out high quality science.

I am grateful to my Armenian colleagues for introducing me to their beautiful country and more specifically to the local geology. Thank you to Samvel Hovakimyan and Rodrik Tayan for your assistance during field work and to share your precious knowledge about the fascinating Meghri-Ordubad pluton. Rafa‘l Melkonyan, Arshavir Hovanissyan and Mariana Haruntunyan are acknowledged for their warm welcoming at the Academy of Sciences every year and also to the staff of the Zangezur Copper-Molybdenum Combine and the Agarak Copper-Molybdenum Combine - GeoProMining for access to their mines.

I would like to mention that nothing would have started in Geneva without the complicity of my "twin brother" Pierre Hemon. I am also very grateful to my close friends from the "Mauges", and to the great people i have met during my stay in Geneva, including Moritz, Tilmann, Mathieu, Esther, Carmen, Salima, Maria, Paola, Betiti, Olivia, Jazmin, Prisca, Patricia and Mary Jane, who made my seven years in Geneva very special!

Finally, this long scientific journey would not have been possible without the full support and trust of my parents and my two older brothers. Massive thanks to my mother and my father who are simply genuine and inspiring persons, as well as models for fighting spirit and kindness.